Experimentele analyse en modellering
van het vermoeiingsgedrag van geschroefde buisverbindingen

Experimental Analysis and Modelling
of the Fatigue Behaviour of Threaded Pipe Connections

Jeroen Van Wittenberghe

Promotoren: prof. dr. ir. P. De Baets, prof. dr. ir. W. De Waele
Proefschrift ingediend tot het behalen van de graad van
Doctor in de Ingenieurswetenschappen: Werktuigkunde-Elektrotechniek

Vakgroep Mechanische Constructie en Productie
Voorzitter: prof. dr. ir. P. De Baets
Faculteit Ingenieurswetenschappen en Architectuur
Academiejaar 2011 - 2012

UNIVERSITEIT
GENT

ISBN 978-90-8578-461-6
NUR 950, 978
Wettelijk depot: D/2011/10.500/65

Promotors

prof. dr. ir. P. De Baets
prof. dr. ir. W. De Waele

Ghent University
Faculty of Engineering
Department of Mechanical Construction and Production

Examination Committee

prof. L. Taerwe (Chair)
prof. P. De Baets
prof. W. De Waele
prof. R. Denys
prof. M. Loccufier
prof. J. Degrieck
prof. G. De Roeck
Dr. G. Knauf
Dr. M. Liebeherr

Research Institute

Ghent University
Department of Mechanical Construction and Production
Laboratory Soete
Technologiepark 903
B-9052 Zwijnaarde
Belgium

Tel. +32 9 331 04 73
Fax. +32 9 331 04 90
Jeroen.VanWittenberghe@UGent.be

www.tribology-fatigue.ugent.be

All truths are easy to understand
once they are discovered;
the point is to discover them.

Galileo Galilei

Acknowledgements

Before presenting the findings of my research, I would like to thank everyone who contributed in one way or another to the successful completion of tbis work. First of all, I want to thank my promoters, prof. Patrick De Baets and prof. Wim De Waele, for giving me the opportunity to perform this research at Ghent University, Laboratory Soete, for the given advice and the freedom they provided.

This work would not have been possible without the efforts of many of my colleagues at the Laboratory Soete. Therefore I would like to express my gratitude to the technical staff:

- *Rudy Desmet for sharing his experience on technical drawings, tolerances and production technology;*
- *Josiane Yde for taking good care of me and all the other researchers in the department;*
- *Johan Declercq for all practical help and cheering up the department every day;*
- *Chris Bonne for perfectly preparing the strain gauge measurements;*
- *Hans Van Severen for making flawless welds between the endcaps and the pipes for the resonant bending fatigue setup; Tony Lefevre for using his master skills to mill the notches in the pipes and Filip Lobbestael for taking care of the renovation of the room for the setup.*

Furthermore, I would like to thank my fellow researchers over the last years:

- *Wouter Ost for the conversations, the shared insights and all kinds of assistance;*
- *Gusztav Fekete for coming to visit the lab at the right time and for the holidays in Hungary. I'm happy that you became a colleague;*

- *Yeczain Hermanito Perez, Stijn Hertelé and Matthias Verstraete for all the jokes and the good times during and after work;*
- *Timothy for choosing an interesting PhD subject and thereby continuing the threaded connections research at our university;*
- *Jan De Pauw who performed a lot of tests on small scale threaded pipe connections during his master thesis and started a PhD project afterwards;*
- *All other researchers: Vanessa, Jacob, Felicia, Mohsen, Reza, Hanan, Patrici, Simon and Stijn for the good atmosphere in the department.*

My thanks also goes to the other master thesis students who worked on this subject: Bruno Meertens, Jonas Claeys, Koenraad Roeygens and Jonas Seys.

In addition I am grateful for the support of colleagues from other universities. I would like to thank prof. Guido De Roeck and Tien Thanh Bui from the Catholic University of Leuven for the cooperation and performing the modal analysis measurements. I would like to express my gratitude to the Institute of Mechanical Engineering Technology of the Szent Istvan University in Hungary, where I could stay for an internship. More specifically I would like to thank prof. Gabor Kalacska, prof. Laszlo Zsidai and of course Matyas Ando for all the good care during my stay.

This work would not have been possible without the financial support of BOF fund (B/04939) of the Ghent University and of the FWO Vlaanderen (3G022806).

Parts of my research were possible through cooperation with industrial partners. I would like to acknowledge them for delivering test material and for their support:

- *Mr. Guillaume Delcorte from Delcorte S.A., Maubeuge, France;*
- *Mr. Hans Van Rijzingen from National Oilwell Varco, Etten-Leur, The Netherlands;*
- *Dr. Gerhard Knauf from Salzgitter Mannesmann Forschung GmbH, Duisburg, Germany.*

I would also like to thank my friends to get my mind of the research once in a while: Koen, Leen, Bert, Ellen, Stijn, Michiel, Helmut, Joachim, Kim, Margo, Maarten, Vincent, Ann-Sophie, Christof, Sandra, Tine, Stefaan, Stefanie and Mindy, for all the nice trips, playing pingpong, the holidays, the weekends and the outdoor adventures!

Most of all, I would like to thank my family; my parents Willem and Katrien, for always encouraging me during my studies; my sister Annelies; and of course my wife Emilie for always being supportive and understanding and for believing in me, no matter what.

Jeroen Van Wittenberghe

Ghent, 2011.

Summary

Threaded pipe connections are commonly used in the oil and gas industry in particular to connect casing strings, drillpipe strings or production and transportation risers and pipelines. In order to maintain a sealed and secure connection while in service, the connections are generally preloaded. To introduce this preload, the connections commonly have tapered threads and they are assembled by applying a certain make-up torque. The combination of the make-up torque and external loads results in a multiaxial stress distribution over the coupling, where the coupling's threads act as stress raisers. When used in offshore environments, waves and currents cause dynamic loads acting on the pipelines. The pipe connections remain the weakest points because fatigue cracks can initiate in the connection's threads.

A wide variety of patented threaded pipe connection designs exists, all claiming to improve a connection's fatigue life. However, experimental data for such designs, available in literature, is limited. Published studies generally comprise experiments on a single connection type. In addition, as no uniformity in testing setup, loading conditions and damage detection techniques exists, results from different studies can not be used for a detailed fatigue analysis to compare the designs. Furthermore, current design curves in codes and standards lead to overly conservative or inaccurate results.

The aim of this work is to provide a better understanding of the fatigue mechanisms of threaded pipe connections and to study the effect of different design features on a connection's fatigue life. Final goal is to formulate guidelines for new fatigue resistant connection designs.

In this study, the API Line Pipe connection is used as a reference. Several modifications and design features are applied to this connection type. To simulate the influence of these modifications, a parametric 2D axisymmetric finite element model, called *ThreadGen*, is developed. The results of this model are compared with a 3D finite element simulation to prove its validity

for both make-up and bending. In addition the results of the 2D axisymmetric simulations are validated by static strain gauge measurements during a make-up test, an axial tension test, a bending test and an internal pressure test. The validated model is then used to evaluate the influence of connection properties and design features on the threaded connection's behaviour.

Test rigs are developed to perform fatigue experiments on three scales: the small scale experiments on 1" (33.4 mm outer diameter) connections are performed in four-point bending; the medium scale tests on 4.5" (114.3 mm) connections are carried out under axial tension and in four-point bending; for full scale testing of specimens in the range of 150 mm to 500 mm in diameter a resonant bending fatigue setup is developed. A significant part of this work is dedicated to this last setup. Two plain pipes without a threaded connection are tested in the setup to characterize its dynamic behaviour and to measure the response of a pipe subjected to a certain excitation frequency. The testing of full scale threaded pipe connections in this setup is part of future research.

The majority of the performed fatigue tests comprises small scale experiments. Several modified configurations are tested. For each configuration an *S-N* curve is constructed, so that the effect of a certain configuration on the connection's fatigue life can be quantified. It is observed that a local modification of the threaded connection's geometry as well as the connection's contact conditions can have an important influence on the fatigue life of the connection.

During the medium scale four-point bending tests, advanced measuring techniques are used to monitor the fatigue crack growth during the test. Although these are existing techniques, they are applied to crack sizing in threaded connections for the first time. A dynamic 3D optical displacement measurement system is used to detect changes in the bending deflection shape of the pipe as a result of a propagating crack. Besides, a local crack opening measurement is carried out and modal analysis techniques are applied to monitor changes of the pipe's eigenfrequencies. To visualize the crack fronts at different moments during the tests, a beach marking technique is used so that the exact crack shapes can be seen during post-mortem analysis. It is shown that a crack initiates at the root of the last engaged thread of the male part of the connection, and propagates gradually over a large segment of the circumference, forming a long shallow crack. When the crack penetrates the pipe wall, it rapidly increases in size along two crack fronts. The observed crack shapes do not have a semi-elliptical shape as commonly used in fracture mechanics. A fatigue crack growth analysis that considers the crack as an annular flaw, is effective in describing the crack growth behaviour.

The results from the finite element simulations and the experimentally obtained *S-N* curves are combined in a multiaxial damage evolution law. Using this fatigue analysis, the observed trends in the fatigue lives of the

configurations are explained. The general concept of using a connection's thread load distribution as a measure for its fatigue life is proven to be inaccurate. The main reason for this is that the load distribution is related to the axial stresses over the connection. However, the fatigue life of a threaded connection is determined by the local multiaxial stress distribution and strain range around the root of the last engaged thread. These local conditions are not only the result of the load distribution, but they are also affected by the hoop stress introduced during make-up, which can additionally be affected by a changed connection stiffness.

In addition, the multiaxial damage evolution law is used to analyse the influence of several features on a connection's fatigue life. Not for all patented modifications an increased fatigue life is predicted when applied to the API Line Pipe connection. It is finally stated that to optimize a fatigue resistant connection, it is appropriate to combine several design features. The thread shape can be optimized to obtain a low stress concentration factor and reduce the local strains at the thread root. The connection global geometry and make-up conditions can be optimized to improve the load distribution over the threads and reduce local stresses and strains at the threads.

Samenvatting

(Dutch Summary)

In de olie industrie wordt vaak gebruik gemaakt van schroefkoppelingen voor het verbinden van buizen. Dit soort geschroefde buisverbindingen is terug te vinden in pijpleidingen, boorleidingen en andere leidingen voor de winning en het transport van aardolie en aardgas. Om een voldoende veilige en lekdichte verbinding te garanderen, worden de koppelingen voorgespannen. Hiertoe zijn deze vaak uitgevoerd met conische schroefdraad en worden de koppelingen voorgespannen door ze vast te draaien met een opmaak koppel. Door de combinatie van dit opmaak koppel met uitwendige belastingen, ontstaat een multiaxiale spanningstoestand over de verbinding en de tanden van de schroefdraad zorgen hierbij voor spanningsconcentraties. In offshore toepassingen veroorzaken wind, golven en stromingen dynamische belastingen op de pijpleidingen. De geschroefde verbindingen vormen daarin de zwakste schakel, omdat vermoeiingsscheuren vaak initiëren rond de tanden van de koppeling.

Er bestaat een brede waaier aan gepatenteerde ontwerpen van geschroefde buisverbindingen. Ieder van deze ontwerpen wordt geacht betere vermoeiingseigenschappen te bezitten, maar slechts weinig experimentele resultaten zijn gepubliceerd om deze beweringen te staven. Bestaande studies beperken zich vaak tot één specifiek ontwerp. Aangezien er geen uniformiteit bestaat over te gebruiken testmethodes en schadedetectie technieken, is het onmogelijk om de resultaten van verschillende studies met elkaar te vergelijken in een gedetailleerde vermoeiingsanalyse. Bovendien zijn bestaande normen en richtlijnen te conservatief of onvoldoende nauwkeurig.

Doel van dit werk is een beter inzicht te verschaffen in het vermoeiingsgedrag van geschroefde buisverbindingen en de invloed van bepaalde ontwerpen op de vermoeiingslevensduur van een koppeling te

kunnen inschatten. Met als einddoel richtlijnen te formuleren voor het ontwerp van nieuwe schroefkoppelingen voor vermoeiingstoepassingen.

In dit werk wordt de gestandaardiseerde API Line Pipe verbinding als referentie gebruikt. Verschillende modificaties en ontwerpvariëteiten worden toegepast op deze verbinding. Om de invloed hiervan te simuleren, is een parametrisch eindige elementen model ontwikkeld, genaamd *ThreadGen*. Dit is een tweedimensionaal axisymmetrisch model. Om dit model te valideren, wordt het vergeleken met een driedimensionale eindige elementen simulatie van een opgemaakte verbinding en een opgemaakte verbinding onder buiging. Daarnaast wordt het model nog experimenteel gevalideerd door de resultaten van verschillende simulaties te vergelijken met rekstrookmetingen tijdens het opmaken van de verbinding en tijdens statische testen onder axiale trek, onder buiging en onder inwendige druk. Het gevalideerde model wordt daarna gebruikt om de invloed van verschillende eigenschappen en modificaties op het gedrag van de schroefkoppeling te onderzoeken.

In dit werk zijn verschillende opstellingen ontwikkeld voor het uitvoeren van vermoeiingsexperimenten op drie schaalniveaus: de kleinschalige testen zijn uitgevoerd in vierpuntsbuiging op verbindingen met een diameter van 33.4 mm (nominale maat 1″); op middenschaal (114.3 mm of 4.5″) gebeuren de testen zowel in vierpuntsbuiging als axiale trek; voor testen op volle schaal tussen 150 mm en 500 mm in diameter, is een resonantie vermoeiingsmachine ontwikkeld. Een aanzienlijk deel van dit werk is besteed aan het ontwerp en de constructie van deze opstelling. Om de werkingskarakteristieken van de opstelling te bepalen, zijn twee buizen zonder schroefkoppeling getest. Hierbij werd de dynamische responsie van beide buizen voor verschillende machine-instellingen bepaald en vergeleken met theoretische modellen. Het testen van schroefkoppelingen op volledige schaal in deze opstelling, maakt deel uit van toekomstig onderzoek.

Het merendeel van de experimenten is uitgevoerd op kleinschalig niveau. Diverse modificaties zijn op die manier getest. Voor elke configuratie is een vermoeiingscurve bepaald om de invloed van de modificaties te kwantificeren. Uit de experimenten blijkt dat zowel lokale aanpassingen van de koppelingsgeometrie als een verandering van de contact condities in de koppeling een belangrijke invloed hebben op de vermoeiingslevensduur van de volledige verbinding.

Tijdens de experimenten op middenschaal in, zijn geavanceerde meettechnieken toegepast om de vermoeiingsscheurgroei op te volgen. Hoewel het om bestaande technieken gaat, zijn ze voor het eerst toegepast op geschroefde buisverbindingen in deze studie. Een optische meettechniek wordt gebruikt om veranderingen in de doorbuigingsvorm van de buis, ten gevolge van een propagerende scheur, te detecteren. Daarnaast worden lokale metingen van de scheuropening uitgevoerd en wordt gebruik gemaakt van modale analyse om de eigenfrequenties van de buis met de schroefkoppeling op te volgen. Om de vorm van de vermoeiingsscheur op

bepaalde tijdstippen tijdens het experiment te markeren, is een speciale techniek toegepast die toelaat de scheurvormen tijdens post-mortem analyse te zien. Een vermoeiingsscheur initieert aan de wortel van de laatste ingrijpende tand van het mannelijke deel van de schroefkoppeling. Daarna propageert ze geleidelijk over een breed segment over de omtrek van de koppeling, alvorens in de diepte te propageren. Hierdoor vormt zich een lange ondiepe scheur. Nadat deze scheur door de wanddikte van de buis is gegroeid, propageert de scheur snel verder over twee aparte scheurfronten. De bekomen scheurvormen stemmen niet overeen met de semi-elliptische vorm die vaak ondersteld wordt in de breukmechanica. Een analysetechniek die de scheur beschouwt als een omtreksscheur, kan echter wel voldoende nauwkeurig de scheurgroei voorspellen.

De resultaten van de eindige elementen simulaties en de experimenteel bepaalde vermoeiingscurven worden gecombineerd in een multiaxiaal schade-evolutie model. Met deze vermoeiingsanalyse kunnen de experimenteel geobserveerde trends verklaard worden. De algemeen aanvaarde onderstelling dat tandkrachtverdeling over een schroefkoppeling een maat kan zijn voor diens vermoeiingslevensduur, blijkt onnauwkeurig te zijn. De belangrijkste oorzaak hiervan is dat tandkrachtverdeling een maat is voor de axiale spanningen over de geschroefde buisverbinding, terwijl de vermoeiingslevensduur bepaald wordt door de lokale multiaxiale verdeling van spanningen en rekken aan de wortel van de laatst ingrijpende tand van de koppeling. Deze lokale condities worden niet enkel bepaald door de tandkrachtverdeling, maar ook onder meer door de omtreksspanning ten gevolge van het opmaken van de schroefkoppeling.

Het schade-evolutie model wordt eveneens gebruikt om verschillende modificaties te analyseren. Er wordt aangetoond dat het model niet voor alle gepatenteerde modificaties een verhoging van de vermoeiingslevensduur van de API Line Pipe verbinding voorspelt. Uit de analyse blijkt dat best een combinatie van ontwerpmodificaties gebruikt wordt wanneer een nieuwe schroefkoppeling ontwikkeld wordt. Het schroefdraadprofiel kan aangepast worden om een zo laag mogelijke spanningsconcentratie te bekomen. De globale geometrie van de koppeling kan samen met het opmaak koppel geoptimaliseerd worden om de tandkrachtverdeling en de multiaxiale verdeling van spanningen en rekken aan de wortel van de tanden te verbeteren.

Contents

Symbols and acronyms

Symbols

a	crack depth	µm
A	surface area	m^2
b	fatigue strength exponent	-
c	fatigue ductility exponent	-
C	damping matrix	kg/s
C_i	i^{th} arbitrary constant	-
D	accumulated damage	-
D_b	box outside diameter	mm
D_p	pin outside diameter	mm
E	Young's modulus of elasticity	GPa
f_i	i^{th} eigenfrequency	Hz
F	force matrix	N
F_e	excitation force	N
I	area moment of inertia	m^4
J	mass moment of inertia	$kg \cdot m^2$
k_a	loading mode correction factor	-
k_b	size effect correction factor	-
k_c	surface roughness correction factor	-
K	stiffness matrix	N/m
K	stress intensity factor	$MPa \cdot m^{1/2}$

K'	cyclic strength coefficient	-
K_f	fatigue notch factor	-
K_t	stress concentration factor	-
K_{tg}	gross stress concentration factor	-
K_{tn}	net stress concentration factor	-
l	length	m
L	length	m
L_b	box length	mm
L_c	critical distance	m
m	strain hardening exponent	-
m_b	beam mass	kg
m_l	total mass of the left endweight	kg
m_r	total mass of the right endweight	kg
M	mass or mass matrix	kg
$M(x)$	bending moment	Nm
n	number of stress cycles	-
n'	cyclic strain hardening exponent	-
N	cycle or number of cycles to failure	-
N_i	number of cycles to crack initiation	-
p	pressure	MPa or bar
P	thread pitch	mm
q	notch sensitivity factor	-
R	load ratio	-
R_c	radius of the contact surface	mm
R_i	inside radius	mm
R_o	outside radius	mm
R_V	triaxiality function	
s	distance	m
S	nominal stress	MPa
S_a	stress amplitude	MPa
S_f	fatigue stress	MPa

S_m	mean stress	MPa
S_r	stress range	MPa
t	number of make-up turns	-
T	torque	Nm
TR	transmissibility function	-
$u(x,t)$	deflection	m
$U(x)$	deflection amplitude	m
$U_f(x)$	deflection amplitude due to forced vibration	
Y	geometric factor in the Paris law	-

α	taper angle	°
a	damage evolution law material parameter	
a_e	excenter angel	°
β	damage evolution law material parameter	
γ	wave number	m^{-1}
δ	degree of freedom	
ΔK	difference in stress intensity factor	$MPa \cdot m^{1/2}$
ΔK_{th}	threshold value of ΔK	$MPa \cdot m^{1/2}$
$\Delta\varepsilon$	local strain range	-
$\Delta\sigma$	local stress range	MPa
Δt	taper difference	°
ε	strain	-
ε_f'	fatigue ductility coefficient	-
ε_p	equivalent plastic strain	-
θ	skin depth	mm
κ	Dang Van material parameter	-
λ	Dang Van material parameter	-
φ	half thread angle	°
μ	magnetic permeability	$H \cdot m^{-1}$
ν	Poisson's ratio	-

ρ	density	kg/m^3
σ	(local) stress	MPa
σ_e	electrical conductivity	$S \cdot m^{-1}$
σ_{eq}	von Mises equivalent stress	MPa
σ_f'	fatigue strength coefficient	MPa
σ_H	hydrostatic pressure	MPa
σ_i $(i = 1...3)$	principal stress component	MPa
σ_{UTS}	ultimate tensile strength	MPa
σ_y	yield strength	MPa
ζ	damping ratio	-
τ	shear stress	MPa
ω	angular frequency	s^{-1}
ω_1	first/natural angular eigenfrequency	s^{-1}

Definitions and acronyms

ACFM	alternating current field measurement
ACPD	alternating current potential drop
AM	area method
API	American Petroleum Institute
ASME	American Society of Mechanical Engineers
box	female part of a threaded connection
BSPT	British Standard Pipe Thread
buttress	trapezoidal thread type
CMS	component mode synthesis
COF	coefficient of friction
DCPD	direct current potential drop
DEL	damage evolution law
DIC	digital image correlation
flush	as in *flush connection*: integral connection produced in the pipe material without any local increase in inside or outside diameter

integral	as in *integral connection*: connection type where the pipes have a pin and box at either end; no separate coupling part is used for these connections
ISO	International Organization for Standardization
LET	last engaged thread
load flank	thread flank that carries the connection's load under axial tension
LVDT	linear variable displacement transducer
make-up	the process of assembling a threaded connection to its final state
MPI	magnetic particle inspection
NC	numbered connection style drill pipe acc. to API spec. 7
NDT	non-destructive testing
NPT	National Pipe Thread Taper
OCTG	oil country tubular goods; general term for pipes for casing, tubing, line pipe and transportation pipes for oil and gas
OMA	operational modal analysis
OMAX	operational modal analysis with exogenous inputs
pin	male part of a threaded connection
REG	regular style drill pipe acc. to API spec. 7
SCF	stress concentration factor
SEM	scanning electron microscopy
stab flank	thread flank opposite to the load flank
TCD	theory of critical distance
tpi	number of threads per inch
T&C	threaded and coupled; connection type where the pipes have two pin threads at either side and are connected by a separate box
upset	as in *upset connection*: integral connection where the pin and box are produced in a part with a thicker wall than the other part of the pipe

Chapter 1
Introduction

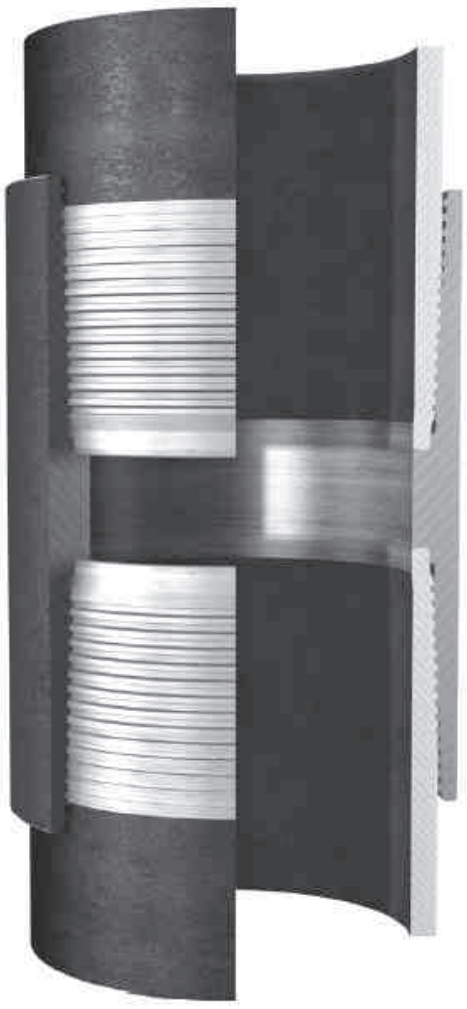

1 An overview of threaded pipe connections

1.1 Applications

Threaded pipe connections are commonly used in the oil and gas industry in onshore as well as in offshore applications. They are used to connect pipelines e.g. in cases where welding is impractical or even impossible. The most common example are probably drill pipes which have to be coupled and uncoupled frequently as illustrated in Figure 1.1. Increased demand for fossil fuels moves the exploration of new sources to greater depths, deeper ocean water and into harsher environments. This results in extreme requirements for the pipelines used and the threaded pipe connections. During well construction, a hole is drilled using a drilling tool connected to a long string of drill pipes. To avoid the well from collapsing, casing pipes are placed inside the well. After well completion, a tubing string is inserted through which the oil and gas flows to the surface. In case of offshore wells, an additional riser pipeline connects the wellhead at the bottom of the sea to a production platform. The drill pipes, casing and tubing, which are regularly called *Oil Country Tubular Goods* (OCTG), and in many cases also the riser pipes, are connected using threaded connections. Additionally, threaded pipe connections are used in structural applications for example to connect tendons of tension leg platforms, to connect offshore caissons, in pillars of offshore structures and columns of vertical pumps.

Figure 1.1: Drill pipe threaded connection

Threaded pipe connections can also be found in pressure pipe fittings and transport pipelines. However, they are most commonly used in OCTG applications.

Interchangeability of threaded connections of different manufacturers is important. During World War I, shortages of equipment caused delays in drilling operations throughout the USA. The industry attempted to overcome this problem by pooling equipment. The program reportedly failed because there was no uniformity of pipe sizes, threads and couplings. Thus, the newly founded *American Petroleum Institute* (API) took up the challenge of developing industry-wide standards [1.1]. Its first specifications were published in 1924 and until present these are updated every couple of years [1.2-3]. Afterwards, a number of fittings, line pipe, casing, tubing and drill pipe connections have been standardized by other organisations such as the *European Committee for Standardization* [1.4], the *American Society of Mechanical Engineers* (ASME) [1.5] and the *International Organization for Standardization* (ISO) [1.6]. However, as can be seen from Table 1.1, the applicability of standard connections is restricted to oil wells and onshore gas wells with limited depth and bottom hole pressure. For more severe duty, so-called *premium* or *proprietary* connections should be used, which are connections developed by private companies. These connections are designed for a better connection performance while still satisfying the standardized minimum requirements and sometimes they remain interchangeable with standard connections. For example, their structural strength, fatigue resistance or leak tightness is improved by changing the connection's geometry or thread shape, adding additional seals or improving the production process. Generally, these improvements are patented, but little is known on how specific features affect the global connection performance.

Standard OCTG connections are typically designed for single or combined static loads to the string, such as tension or compression, bending and internal or external pressure. The main design considerations for these connections are leak tightness and resistance against high bottom hole pressure.

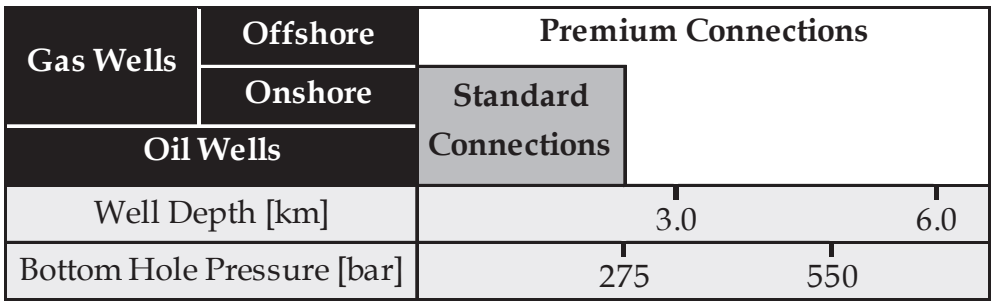

Table 1.1: Applicability of API and premium connections

When dynamic loads act on the connections, their fatigue resistance becomes important. These service loads can be caused by either operational or environmental conditions. In drill strings, dynamic loads are typically caused

by torque vibrations and by bending of the string during drilling service. Fatigue damage due to dynamic bending is the most important cause of failure of drill pipes [1.7-9]. Offshore risers, tendons and columns are also subjected to dynamic environmental loads as illustrated in Figure 1.2. These are mainly caused by waves and currents. The latter can cause vortex induced vibrations (VIV) on the pipe strings. Additionally, wind acting on a floating platform or production vessel can cause the structure to move, creating more fluctuating loads. These load conditions are so severe that fatigue damage is the main failure mode for offshore risers [1.9].

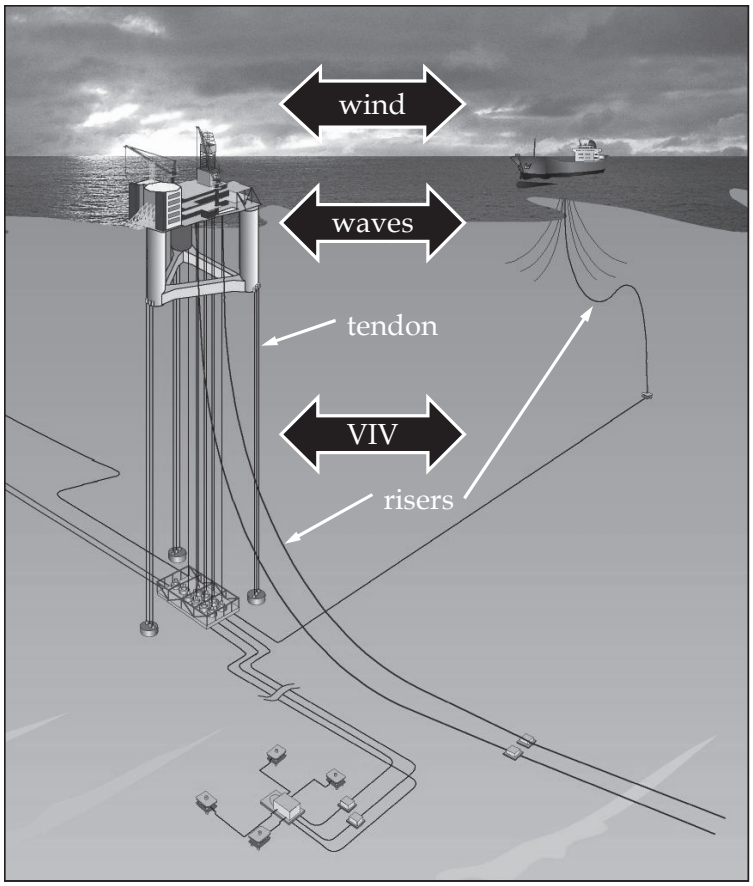

Figure 1.2: Environmental dynamic loads on offshore pipelines.

Even though there exists a wide variety of premium drill connections, during the last years there is a tendency to use casing pipes for drilling particular wells [1.11-13]. This is more cost-effective since no drill pipes are needed and the casing can stay in the well after drilling. However, this practice requires better fatigue properties for the connections as they become subjected to additional dynamic loads resulting from the drilling operation. Hence with changing applications and environmental conditions, threaded connections of all kinds need continuous improvement and fatigue resistance is one of the important features that need attention.

1.2 Principles

1.2.1 Classification

Threaded pipe connections consist of a male and female part, called respectively *pin* and *box*. They can be divided in three main categories based on their method of manufacturing. These three types are illustrated in Figure 1.3. The first type has male threads machined at both pipes that are connected using a separate coupling part. These connections are called *Threaded and Coupled* (T&C, see Figure 1.3a) and are commonly used in casing, tubing and riser applications. The other types are called *Integral* types, since the pipes have a pin and box of the connection at either end. Hence no separate coupling part is used for these connections. When the connection is produced in the pipe material without any local increase in inside or outside diameter, it is called a *flush connection* (as shown in Figure 1.3b). In case the connection is produced in a part with a thicker wall than the other part of the pipe, it is called an *upset connection* (see Figure 1.3.c). Integral flush connections are used in casing pipes while integral upset connections are more common for tubing and drill pipes.

According to reported failure cases and laboratory tests [1.15-17], the location that is most susceptible for fatigue damage for all connection types is the root of the *last engaged thread* (LET) of the pin as shown in Figure 1.4. Although in drill pipes fatigue cracks are also commonly found in the LET of the box [1.18].

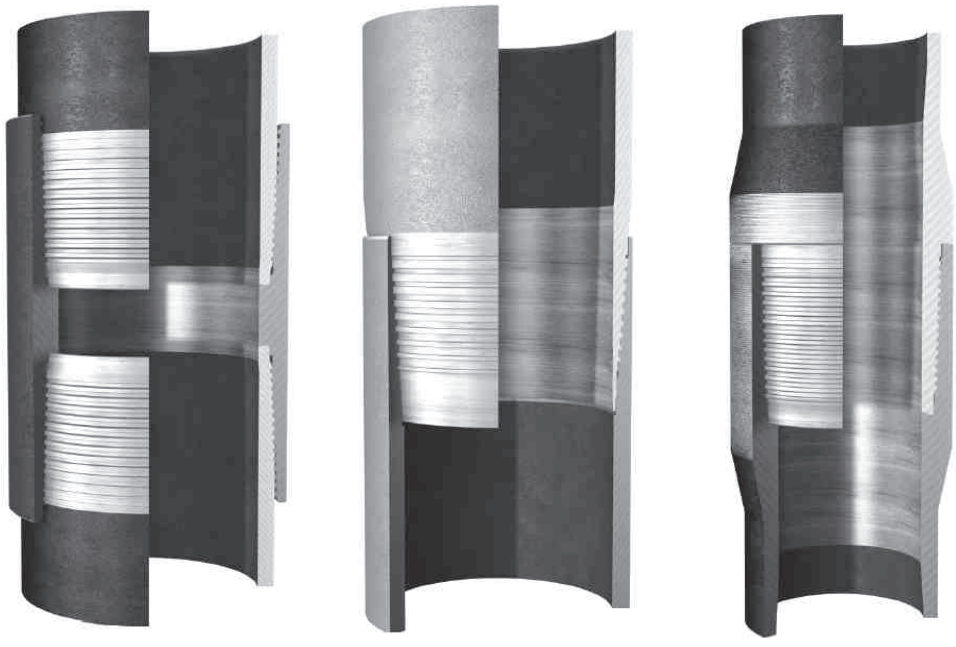

a **b** **c**

Figure 1.3: a) Threaded and Coupled, b) Integral Flush, c) Integral Upset Connection [1.14].

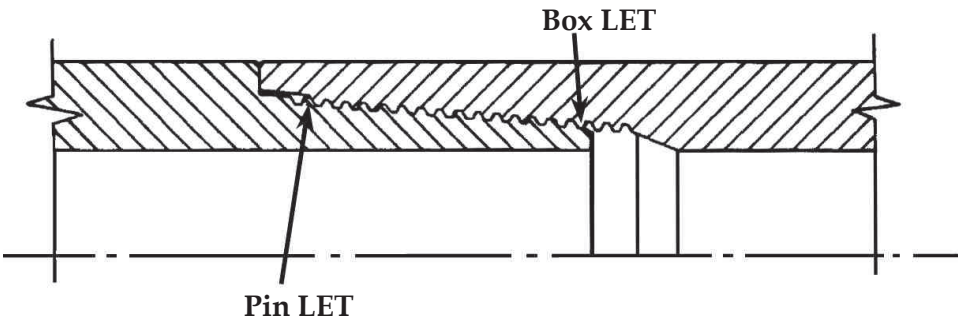

Figure 1.4: Common fatigue crack initiation areas in threaded pipe connections.

1.2.2 Make-up

To ensure adequate sealing capacity and to avoid that the connection loosens due to vibrations, threaded connections are generally preloaded. For this reason, the connections have a conical shape. The preload is then introduced by assembling the connection with a certain torque. The torque applied is different for every connection type and size and is commonly referred to as the *make-up torque*.

In some standardized and several premium connections, one or more *torque shoulders* are added. These are parts of the connection where the pin and box come in contact outside the thread region as shown in Figure 1.5. These shoulders enable a higher make-up torque to be applied to the connection. This can change the load distribution over the threads. Torque shoulders also provide additional sealing. The use of torque shoulders requires more accurate tolerances on the connection's geometry and accurate torque monitoring during make-up. Once the shoulders are in contact, the resulting torque increases rapidly for a given rotation and overtorque can cause the connection to fail. In Figure 1.5 an example is given of both a single and double shoulder configuration. Additional metal-to-metal seals can be provided in the axial direction as can be seen in the double shouldered connection of Figure 1.5.b, resulting in improved sealing that prevents leakage of oil and gas and avoids dirt or seawater to enter into the pipeline.

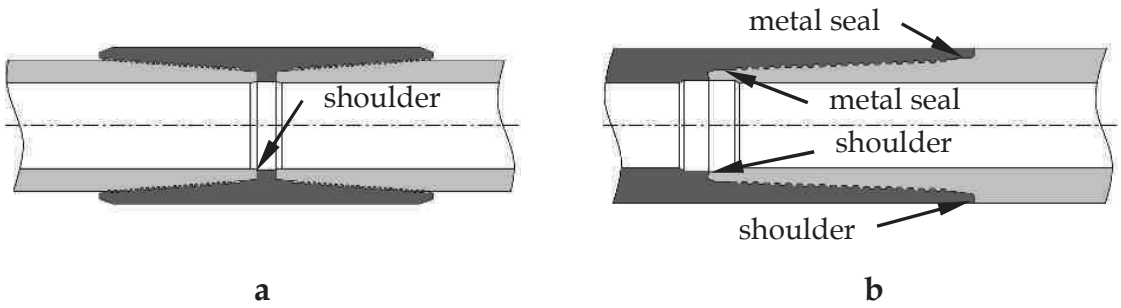

Figure 1.5: a) single shoulder T&C connection; b) double shoulder integral flush connection.

1.2.3 Thread types

Several thread types are in use for threaded pipe connections of which three are standardized by API specification 5B [1.2] (Figure 1.6. a to c). The oldest and most simple thread type has a truncated triangular shape as shown in Figure 1.6.a and is used in the *API Line Pipe* connection. The thread flank that carries the load under axial tension of the connection is referred to as the *load flank*, while the unloaded flank is called the *stab flank*. To obtain a reduced stress concentration when the connection is loaded, the thread roots and crests can be rounded (see Figure 1.6.b). This kind of thread is standardized for *API Round* casing and tubing connections and for *British Standard Pipe Taper* threads (BSPT).

When subjected to an axial load, triangular threads will carry reaction forces with a high radial component. This can cause the pin and box to deform which can result in the connection to leak. Next to this, due to their triangular shape, at the crest the thread is much more narrow than at the root. This means that the thread crests can be easily damaged due to overload. For these reasons, thread types with small flank angles are available. They have a more constant section over the thread height. The most common pipe thread of this kind is the buttress thread which has a rounded trapezoidal shape, as can be seen in Figure 1.6.c. This thread type is standardized for the *API Buttress* connection.

Numerous variations of these three thread types exist for premium connections. For example, the thread angle, flank angles, root geometry or tolerances are changed to get an improved behaviour. Some of those designs are discussed more in detail in Chapter 2. Additionally, completely different thread types can be found such as the wedge type of Figure 1.6.d. This type is capable of carrying high torsion and compression loads together with reliable sealing capabilities. However, wedge threads are more subjected to wear during multiple make-up and break out operations [1.19].

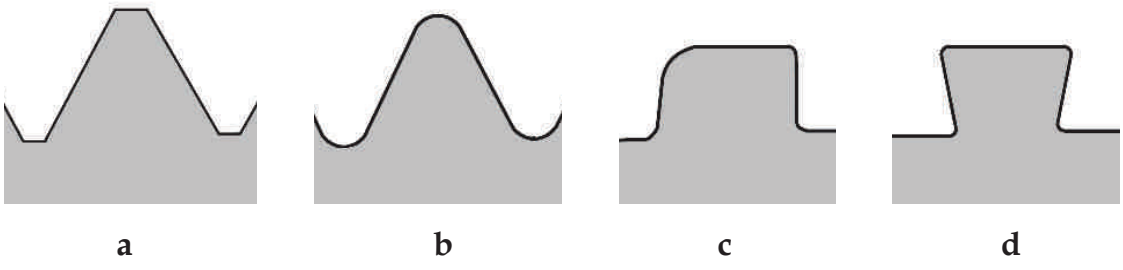

Figure 1.6: Thread types a) triangular; b) round; c) buttress; d) wedge.

2 Scope of this work

The aim of this work is to provide a better understanding of the fatigue mechanisms of threaded pipe connections. Different features that are expected to improve a connection's fatigue life are studied as until now it

remained impossible to quantify their influence. In addition, current design curves in codes and standards lead to overly conservative results. For this reason several connection designs are analysed using an approach combining experimental testing with numerical simulations. In the following chapters, the methodology used, the results obtained and conclusions will be presented.

In Chapter 2 an overview is given of the current knowledge of the fatigue life of threaded pipe connections based on information from literature, codes and standards. The best methodology is selected by comparing existing modelling techniques, fatigue analysis methods and experimental testing facilities.

As there is no general method for online monitoring of fatigue damage in threaded connections, Chapter 3 includes an overview of available measuring techniques and focuses on the techniques used during the experiments. To be able to perform fatigue experiments on full-scale pipes an experimental test rig had to be developed. In Chapter 4 the design and working principles of the constructed resonant bending fatigue test setup are presented. Additionally, experimental tests are carried out at two smaller scales. The test equipment, material and connection type used, the loading conditions applied and results obtained are analyzed in Chapter 5.

Chapter 6 is dedicated to the parametric finite element program that is developed to assess the behaviour of the threaded connections. The modelling details concerning the used assumptions and boundary conditions are explained. The model is validated by comparing with the previously described experimental results. Comparison with results from literature is also provided.

The validated program is then used to perform a parametric study on an *API Line Pipe* connection to quantify the influence of different parameters on the connection's behaviour in Chapter 7.

In Chapter 8 a detailed analysis is carried out in which the experimental observations are compared with standard design curves and the results from the finite element model. Furthermore, local data from the model is used for fatigue analysis in order to explain the observed trends in the connection's fatigue life.

Conclusions related to the fatigue behaviour of threaded pipe connections are formulated in Chapter 9 together with possibilities for future research related to experimental testing and numerical modelling of threaded pipe connections.

Final goal is to use the scientific findings of this work to formulate guidelines for new fatigue resistant premium threaded pipe connection designs.

References

[1.1] API's History, http://www.api.org/, retrieved 24/11/2010.

[1.2] API Specification 5B, Specification for Threading, Gauging and Thread Inspection of Casing, Tubing and Line Pipe Threads (U.S. Customary Units), American Petroleum Institute, fourteenth ed., 1996.

[1.3] API Specification 7, Specification for Rotary Drill Stem Elements, American Petroleum Institute, thirty-ninth ed., 1997.

[1.4] EN 10226-1:2004:E, Pipe threads where pressure tight joints are made on the threads – Part 1: Taper external threads and parallel internal threads – Dimensions, tolerances and designation, European Committee for Standardization, 2004.

[1.5] ANSI/ASME B1.20.1-1983, Pipe Threads, General Purpose (Inch), 1983.

[1.6] ISO 3183, Petroleum and natural gas industries - Steel pipe for pipeline transportation systems, International Organization for Standardization, second ed., 2007.

[1.7] API Recommended Practice 7G, Recommended Practice for Drill Stem Design and Operating Limits, American Petroleum Institute, sixteenth ed., 1998.

[1.8] Vaisberg, O., Vincké, O., Perrin, G., Sarda, J.P., Fay, J.B., Fatigue of drillstring: State of the art, Oil & Gas Science and Technologie, 57(1), 7-37, 2002.

[1.9] MacDonald, K.A., Bjune, J.V., Failure analysis of drillstrings, Engineering Failure Analysis, 14, 1641-1666, 2007.

[1.10] API Specification 16R, Specification for Marine Drilling Riser Couplings, American Petroleum Institute, first ed., 1997.

[1.11] Santi, N. J., Carcagno, G. E., Toscano, R., Premium & Semi-premium Connections Design Optimization for Varied Drilling-with-Casing Applications, Offshore Technology Conference, OTC17221, 2005.

[1.12] Strickler, R.D., Wadsworth, T.M., Drilling with casing: Are you damaging your casing?, World Oil, 3, 51–53, 2005.

[1.13] Carcagno, G.E., Bufalini, A., Conde, L., Toscano, R., Low SCF Integral Premium Connections for Use in Highly Demanding Casing and Tubing Drilling Operations, Offshore Technology Conference, OTC16566, 2004.

[1.14] TenarisHydril, Premium Connections Catalogue, http://www.tenaris.com/tenarishydril/, Version 01, March 2009.

[1.15] Griffin, R.C., Kamruzzaman, S., Strickler, R.D., Casing drilling drill collars eliminate downhole failures, Offshore Technology Conference, OTC16569, 2004.

[1.16] Ferjani, M., Intégration des phénomènes dynamiques dans l'analyse en fatigue des garnitures de forage, PhD Thesis, Ecole Polytechnique, Palaiseau, France, 2006.

[1.17] Sches, C., Desdoit, E., Massaglia, J., Fatigue Resistant Threaded and Coupled Connectors for Deepwater Riser Systems: Design and Performance Evaluation by Analysis and Full Scale Tests, ASME 27th International Conference on Offshore Mechanics and Arctic Engineering, OMAE2008-57603, 2008.

[1.18] MacDonald, K.A., Deans, W.F., Stress Analysis of Drillstring Threaded Connections Using The Finite Element Method, Engineering Failure Analysis, 2, 1-30, 1995.

[1.19] Mallis, D.L., Reynolds, H.A., Wedge Thread with Torque Shoulder, United States Patent US 7,690,696 B2, 2010.

Chapter 2

Fatigue of Threaded Pipe Connections

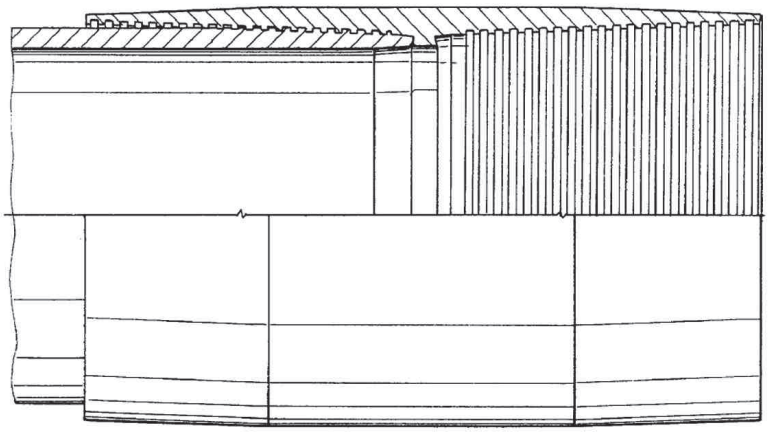

1 Goal

In this chapter the current state of the art in fatigue research on threaded pipe connections is summarized. First a comparison is made between different modelling techniques used to simulate stress distribution over the connection and load distribution over the different threads. Then an overview is given of patented premium connections or connection modifications that claim to improve the connections' fatigue life. After that different fatigue analysis techniques used to evaluate threaded connections are presented. Finally, existing experimental fatigue setups are discussed and available fatigue data of threaded connections is compared to existing standards.

This chapter aims to illustrate the current knowledge on fatigue of threaded connections and to determine the focus of this research project.

2 Stress analysis

2.1 Introduction

Due to the combination of make-up, preload and external load together with the threaded geometry of the connections, a complex multiaxial stress and strain distribution is introduced into the connections. The connection's threads act as stress raisers so cracks can easily be initiated at those locations. As a first indication, the region with the highest appearing stresses can be considered to be the most susceptible to fatigue failure. For a more elaborate fatigue analysis, accurate knowledge about the stress and strain distribution, the different stress components and multiaxiality of stresses is necessary.

The analysis of threaded pipe connections is characterized by two non-linearities. Firstly, high local stresses appear, exceeding the material's yield strength even during the make-up stage. Hence, non-linear elastic-plastic material models are commonly used. Secondly, surface interactions together with small sliding between pin and box result in non-linear behaviour. This makes it necessary that the contact properties, in particular the *coefficient of friction* (COF), are defined accurately.

Before going into detail about fatigue analysis, an overview is given of stress analysis techniques. These models can be used for evaluating static load cases while in section 4 it will be shown how results from these analysis can be used for fatigue modelling.

2.2 Modelling techniques

2.2.1 Analytical modelling

The basic behaviour of threaded pipe connections is related to that of bolts and nuts since they share the same threaded geometry. The first real effort of modelling the load distribution in bolts was performed by Stromeyer in 1918 [2.1]. His analytical model was based on a purely elastic extension of a planar model of riveted joints and did not take into account the actual thread geometry. His analysis suggested that the load is not distributed equally among the threads, with the last loaded thread of the bolt, i.e. the thread furthest away from the free end, carrying the highest load. A qualitative confirmation of his result was provided by means of a planar photo-elastic model, although it was not possible to measure the appearing stresses accurately at that time. In his analysis he proposed the idea that the distribution of the loads over the threads was dependent on the bending deflections of the threads and the relative pitches of nut and bolt. These ideas were confirmed by later investigators [2.2]. It was hereby demonstrated that it should be possible to optimise the load distribution by changing the thread geometry.

In later years it was found that planar methods were not sufficiently adequate to describe the behaviour of threaded fasteners. Their behaviour is not only determined by the axial forces, since also important circumferential stresses are induced. To include these influences in his analysis, Hetényi [2.3] conducted a test program on three dimensional photoelastic models. He found that the load distribution over the threads could be significantly improved by changing the global nut shape. This way the high load concentration at the last engaged thread of the bolt could be reduced. Additionally, the greatest reduction occurred when a tapered thread was used.

Apart from the bending of the threads it was recognized that there is a notch effect stress due to the general axial loads in the bolt. Several investigations were performed to study the notch effect of different thread types, root radii, thread angles etc. The results were subsequently catalogued to be used for design purposes. Perhaps the most famous of those works is that of Peterson [2.4] which was first published in 1974.

2.2.2 Semi-analytical models

It was not until the 1980's, with the development of the finite element method, that threaded pipe connections could be modelled more in detail. Since the computational performance of the computers in that time was rather limited, it was not possible to model full non-linear 3D models. Hence, threaded pipe connections were evaluated using hybrid models [2.5-8]. This technique combines a finite element model with analytical calculations and was applied by Glinka et al in 1986. Using a finite element model of three

threads subjected to different load cases, a plot of stress concentration factor versus tensile load was obtained and the thread's bending stiffness was calculated. This bending stiffness was then used as an input in the analytical model to obtain the load distribution in the connection over the different threads. Knowing this load distribution, the corresponding stress concentrations were calculated using the previously obtained stress concentration plots. The calculated stresses were used in a fatigue analysis of buttress threaded connections of tendons for tension leg platforms. By using this technique, Newport [2.6-7] and Brennan [2.8] showed that shouldered threaded pipe connections with tapered threads behave in a similar way as preloaded bolts. The preload substantially changes the dynamic load acting on the threads and can be either obtained by assembling a tapered connection with a certain torque or by providing a torque shoulder. In the case of a shoulder, the load distribution over the threads is changed since the threads closest to the shoulder will receive the preload. Additionally, they found that there is an optimum in the connection's number of engaged threads. A connection without sufficient threads will have a very high load carried by the last engaged thread of the pin, while a connection with more than the optimal number of threads does not get any benefit from the additional threads. The main advantage of this technique was that it allowed the use of elastic-plastic material models and the introduction of cracks [2.9], while the computational requirements remained limited. Additionally, the influence of thread parameters could easily be studied because this only required changing the finite element model of the threads without changing the global analytical model. Bahai [2.10] tried to generalize the hybrid method by constructing parametric equations based on a large series of simulations. However, this resulted in unpractical empirical equations limited to standard API drill pipe threads.

2.2.3 Two dimensional axisymmetric finite element models

In the early 1990's, the hybrid method could be replaced by 2D axisymmetric models, thanks to increasing computing power. At that time three dimensional finite element models of threaded connections could not be evaluated due to the complexity of the contact interactions. The most important advantage of the 2D approach was the limited size of the models which had a reasonable calculation time. However, next to this major advantage, the approach implied several simplifications. First of all, the thread helix was ignored. Since the pitch of most threaded connections is limited, this simplification was assumed not to have a major effect on the resulting stress distribution. Secondly, the thread run-in and run-out regions can not be modelled, hence it is not possible to study these regions in detail. Nevertheless, this approach was more versatile than the previous semi-analytical technique and results were in good agreement with observations of photo-elastic models.

In 1993 Assanelli and Dvorkin evaluated standard API Round and API Buttress connections using a 2D axisymmetric model with an elastic perfectly plastic material model [2.11]. Additionally detailed analysis of rotary shouldered connections became possible as was illustrated by their analysis of a premium connection.

Although some basic analyses were carried out using simple linear elastic material behaviour [2.12-14], it was pointed out by Hilbert and Kalil [2.15] and Assanelli et al. [2.16] that two basic non-linearities had to be incorporated. First of all elastic-plastic material behaviour should be used instead of linear elastic or elastic perfectly plastic approximations, since the material's yield strength can be exceeded even during make-up. Second, surface interactions of the contacting thread surfaces of pin and box, metal to metal seal surfaces and torque shoulders result in non-linear contact behaviour. The non-linear aspects of surface interactions are contact, sliding and friction. To be able to incorporate all aforementioned aspects in the models, a new element type was created [2.17]. In prior models, contact was modelled by so-called gap elements. These elements did not allow for real sliding since the nodes of two contacting elements were tied together by a gap element. When evaluating the failure behaviour of premium connections a third non-linearity arises. To incorporate extreme loads or large displacements, non-linear deformations have to be allowed.

Special attention has to be paid to the modelling of the connection's make-up. Since the model geometry is only two-dimensional, it is not possible to rotate the pin in the box in the simulations. Hence, make-up is commonly modelled by giving the pin and box a certain radial overlap corresponding to the specified number of make-up turns [2.18]. During the first step of the analysis pin and box are brought into contact and the resulting deformation of pin and box is assumed to be identical to the made up connection.

The same approach of using 2D axisymmetric finite element models with elastic-plastic material behaviour and elaborate contact interaction of the threads is used until today. During the last decade analyses were carried out this way on a wide range of applications of threaded connections. Curley and Prinja were able to explain the failure of a threaded drilling component using a non-linear 2D axisymmetric model, although they simplified the exact geometry of the threads [2.19]. A number of investigations were performed to further understand the behaviour of standard connections. API Round casings were studied in 2003 by Dvorkin and Toscano [2.20] and in later by Yuan et al. [2.21-22]. Both gave a comparison between the simulated strains and strains measured by strain gauges during experimental tests and found a good correspondence, hereby demonstrating the applicability of 2D axisymmetric models. Standard drill pipes were modelled by Kristensen et al. [2.23], Bertini et al. [2.24] and Santus et al. [2.25].

Several studies on premium connections have been published. Since those connections are designed to work under extreme loading conditions, their

analysis is not only limited to axial tension. Premium casings are typically subjected to high internal and external pressure, hence these load cases are included in the models [2.25-28]. Strain gauge measurements on premium connections have been carried out during make-up by Hilbert and Kalil [2.15] and for additional axial loading and internal pressure by Dvorkin et al. [2.17], both obtained a good agreement with their corresponding simulations.

As pointed out in Chapter 1, the main differences between standard and premium designs are that the premium designs include features as rotary torque shoulders, metal-to-metal pressure seals, elastic ring seals and use non standard thread types which are in many cases modified buttress threads. Generally, the thread type design for a premium connection is not intended to seal pressure as is the case for several standard thread types. Modified buttress threads have small or even negative load flank angles which minimize relative sliding and separation between the threads. This makes this kind of threads much more resistant to thread jumpout failure than standard triangular or API Round threads. On the other hand, the leak tightness of premium designs is generally realized by providing diametral interference between metal-to-metal seal faces.

In deviated wells drill pipes are subjected to high bending loads during operation. Casings can also experience high bending during installation. In general these load cases cannot be simulated by axisymmetric models. However, as was noted by MacDonald and Deans [2.12], when the wall thickness to diameter ratio is sufficiently small, the stress gradient over the wall is sufficiently limited to be represented by a uniform membrane load (see Figure 2.1). Alternatively, to model bending in a 2D axisymmetric model, special solid elements can be used that permit non-linear, asymmetrical deformation [2.26, 2.30].

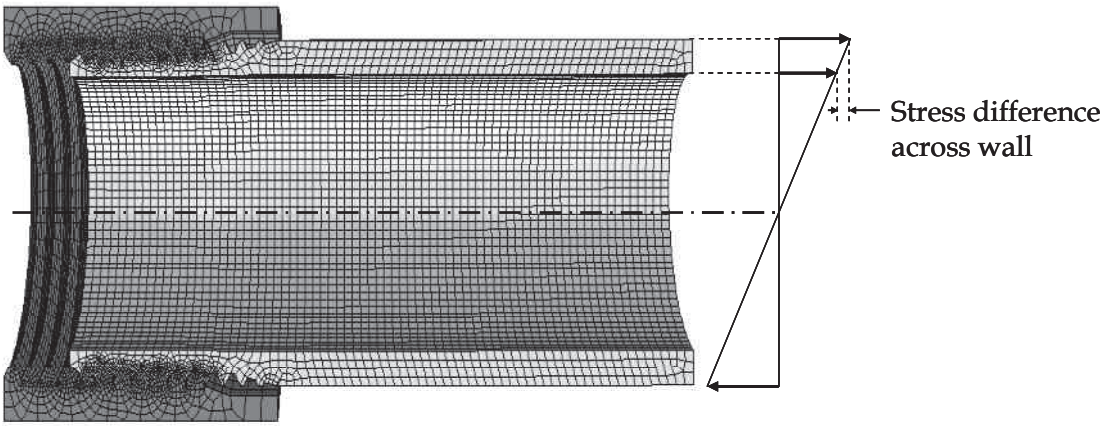

Figure 2.1: Through-wall distribution of the stress in a pipe under bending.

2.2.4 Three dimensional finite element models

The most rigorous way to model bending loads is by using a full three dimensional model. However, despite the vast performance increase of computers over the last decades, full 3D models of threaded couplings still require very long calculation times due to the high number of nodes in the contact analysis. In addition to this, due to their complexity and multiple contacting surfaces, full 3D models tend to be less stable and less convergent. 3D simulations are commonly oversimplified by using linear elastic material properties [2.31] or very coarse meshes [2.32]. This results in inaccurate stress distributions and mesh dependent stress concentration factors without practical use.

It was shown by Zhong [2.28] that 2D axisymmetric models of threaded couplings are in good agreement with full 3D models, but he took only into account the make-up situation. While Chen and Shih [2.33] showed that for axially loaded bolts 2D axisymmetric models are a very good approximation to calculate the real 3D stress distribution. Hence, for axisymmetric load situations as make-up and axial tension, 2D axisymmetric models can be used. A bending load applied on a premium T&C connection was modelled in 3D by Sches et al. [2.34], but only with elastic material behaviour. Ferjani [2.35] evaluated the bending of a standard shouldered drill string connection, with simplified modelling of the make-up stage.

Full 3D models are only used in special cases where the influence of thread run-in and run-out or thread helix are studied or when special load cases are examined as due to their high degree of complexity, calculation times that can be easily 30 times higher than 2D axisymmetric models and as in most cases only limited additional results are generated. In all other cases, conventional 2D axisymmetric models are the preferred modelling technique.

2.3 Considerations

2.3.1 Contact modelling

As mentioned in paragraph 2.2.3, it is of great importance to use the correct contact models in the analysis. But defining correct contact interactions requires accurate knowledge about the contact interface properties, e.g. the *coefficient of friction* (COF). However, a variety of values for the COF are in use. In ISO 10407-1 [2.36] values for the COF are specified between 0.06 and 0.14, mentioning a typical value of 0.08 when thread compounds are used. Assanelli et al. [2.16] and Yuan et al. [2.21] even use a lower value of about 0.02. In experimental studies friction values between 0.06 and 0.09 were obtained by Ertas et al. [2.37] for tests on pipeline steel with different thread compounds and Santus et al. [2.25] measured values of 0.15 during torsion tests on full scale threaded connections. As will be shown further in Chapter 7, this variation of the coefficient of friction has a significant influence on the

thread sliding behaviour and it is important that correct values for the COF are used.

2.3.2 Stress concentration factors

Starting with the hybrid technique it became possible to calculate the stresses appearing at the thread roots. Typically, the highest stress appears at the root of the *last engaged thread* (LET) of the pin for threaded connections without torque shoulders. In Table 2.1 some typical values of stress concentration factors (SCF) at the LET of the pin are given for threaded connections as obtained by analyses with elastic-plastic material behaviour. As can be seen, SCF values between 1.8 and 5.6 are common. However, when linear elastic material properties are used, much higher SCF's are obtained. For example SCF's of 10 and more are obtained this way for drill pipes [2.30-31]. If the hot-spot approach[1] is used instead of the value of the peak stress, similar stress concentration factors are found. This is illustrated in the drill string analysis of Macdonald and Deans [2.12]. They obtained a SCF between 4.9 to 6.5 depending on the applied load. This corresponds well to the value of 5.6 obtained by Ferjani [2.35].

Connection Type	SCF	Source
Metric bolt	3.7	Shoji et al. [2.38]
Drill pipe	5.6	Ferjani [2.35]
Premium riser connection	1.8	Sches [2.34]

Table 2.1: Typical values of stress concentration factors

2.4 Discussion

The discussed 2D axisymmetric and 3D FE studies all consider only one or sometimes two or three distinct connections. In some cases the results of a premium design are compared to the results of a standard connection, but no qualitative or quantitative comparison between a wide range of design features nor a parametric study has been published in open literature. This is the reason why there are no general design rules available for threaded connections and why the influence of several design features on the overall behaviour of the connections has not yet been documented in detail. This is mainly because commercial premium connections are protected by patents. The patent documents, which are freely available in the public domain, only

[1] With the hot-spot approach, the stress at a certain critical distance from the thread root is used to determine the stress concentration factor instead of using the value of the peak stress in a linear elastic analysis. This is discussed more in detail during the fatigue analysis in section 2.3.1 of Chapter 8.

contain claims and the general ideas behind the patented features. No detailed analyses are published as the companies that developed the connection otherwise risk losing their competitive advantage. Nevertheless, even without quantifying the effects, a broad patent overview can identify trends to obtain a certain improvement of the connection's behaviour. This overview is provided in the next section.

3 Patent overview

3.1 The early days

Threaded connections have been used to couple pipes for over a century. Before going into detail about patented features that improve a connection's fatigue resistance, it can be useful to look at the history of threaded pipe connection designs.

It is difficult to define who invented the first modern threaded pipe connection. Although wrought iron fittings had been used before [2.39], the first patented connection that could be considered as a contemporary threaded and coupled connection dates from 1885 and is shown in Figure 2.2.

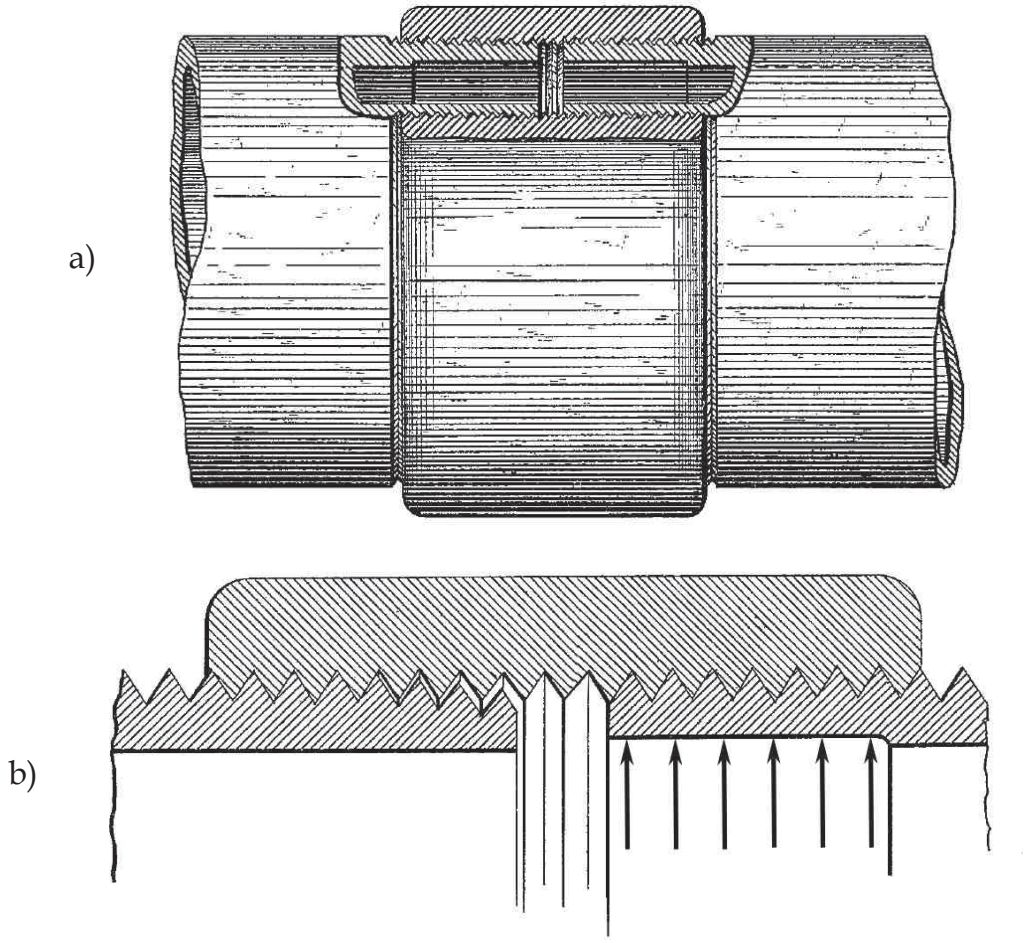

Figure 2.2: Patented connection by W.A. Bole [2.40-41].

This connection and its method of coupling were patented by William A. Bole [2.40-41]. Unpatented T&C connections existed before. Those connections consisted of a tapered pin and a straight box, since internal tapered threads were difficult to produce at that time. The resulting connections had only a limited resistance to internal and external pressures. The improvement of Bole's invention consisted of a method to ensure a leak tight connection that would not loosen. To obtain this, the pin should be screwed as tightly as possible into the box, after which the pin's thread surface is radially expanded to take away all clearance between the threads (see Figure 2.2.b). To apply this plastic deformation a special tube expander was necessary, a device that was patented by Mr. Bole six months earlier [2.42]. Subsequent patents continued focussing on leak and pressure tightness. Instead of using a pipe expander, Higbee developed a special thread type where material of the threads of the pin would plastically flow in the open space between the threads of the box [2.43]. Two years later he added special requirements to the thread taper of his developed connection with tapered pin and a straight box [2.44]. Both patented features can nowadays be found in the standard BSPT connections. In following years more improvements were found to increase pressure tightness. It is notable that most of these patents are based on modifications of the pin of the connection. Several patents propose a special groove to allow for plastic pin deformation [2.45-46] and new pin designs allow for special shoulders with extra sealing capabilities [2.47].

Although pressure tightness remained to be required, structural strength and resistance against external loads began to gain importance starting from the 1950's. Since oil and gas exploration moved to greater depths and deviated wells, the loads on the pipes and pipe joints increased significantly. Consequently, a joint with the same strength as the pipe, i.e. a joint that is 100% efficient, became desirable. This was obtained by the development of upset connections with increased wall thickness at the threaded portion of the pipe. However, the first T&C 100% efficient connection was developed by Webb not earlier than 1956 [2.48]. His connection is shown in Figure 2.3. Its main contribution lays in the fact that the entire thread was engaged, including the last shallow root convolution on the pipe (see detailed thread run-out in Figure 2.3.b). In order to these last threads being efficient, buttress threads were used. It was further stated that the threads should be sufficiently stiff to avoid bending of the threads. Therefore, the width of the threads at the pitch line should be equal to or bigger than the thread height.

Other inventions claimed to improve the resistance to external static loads by enhancing the make-up process of the connection [2.49] or by improving the load distribution by a changing thread profile over the engaged thread length [2.50].

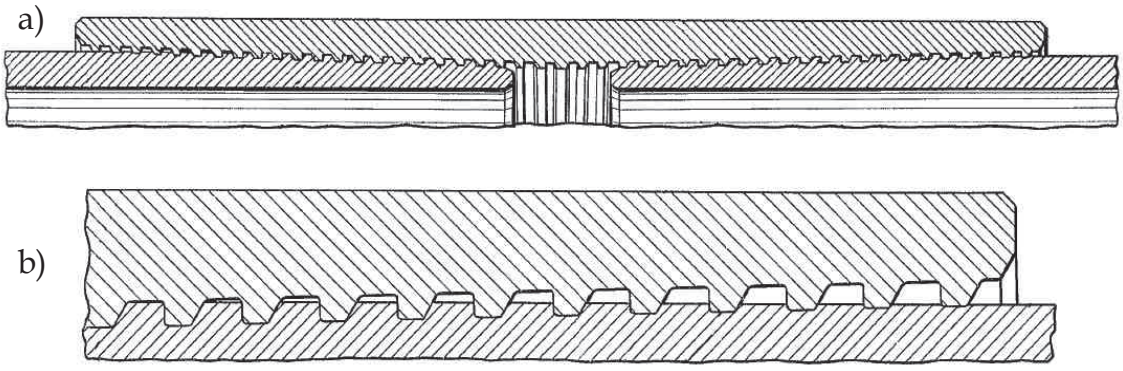

Figure 2.3: First 100% efficient T&C connection by Webb [2.48]

3.2 Fatigue resistant threaded connections

3.2.1 General trends

Starting from the 1960's, threaded connections have been developed which are optimized for the use in dynamic applications. Those fatigue resistant designs all try to reduce the maximum appearing stress peaks in the connection. Through all patents two general trends can be identified to achieve this goal. Firstly, the global box geometry is changed to obtain a more uniform load distribution over the threads and hence reducing the high stresses appearing at the LET. It can be noted that to improve the connection's fatigue strength, the box geometry is changed, while in order to improve the pressure tightness of a connection, generally the pin geometry is modified; as illustrated in section 3.1. The second trend to obtain a fatigue resistant connection is to provide a local modified thread shape. By changing the thread profile, the local stress concentration can be reduced and by altering the thread shape or interference over the engaged thread length, the load distribution can be modified.

3.2.2 Global box geometry modifications

In 1961 a new connection was invented by Bodine [2.51] (illustrated by Figure 2.4.a). This T&C connection was developed to be used in a sonic well pump tubing string. In this application, important fluctuating axial stresses are introduced by the pumping action. Due to the high load carried by the last engaged thread of the pin, fatigue cracks would develop at this location in conventional connections. Bodine's connection however, was constructed in such a way that the loads would be distributed more uniformly over the different threads, hereby lowering the concentrated load at the LET of the pin and hence increasing the fatigue life of the entire connection. This improved distribution was obtained by changing the box geometry. In general, the box of the connection has a bigger wall thickness than the pin and is the most rigid part of the connection.

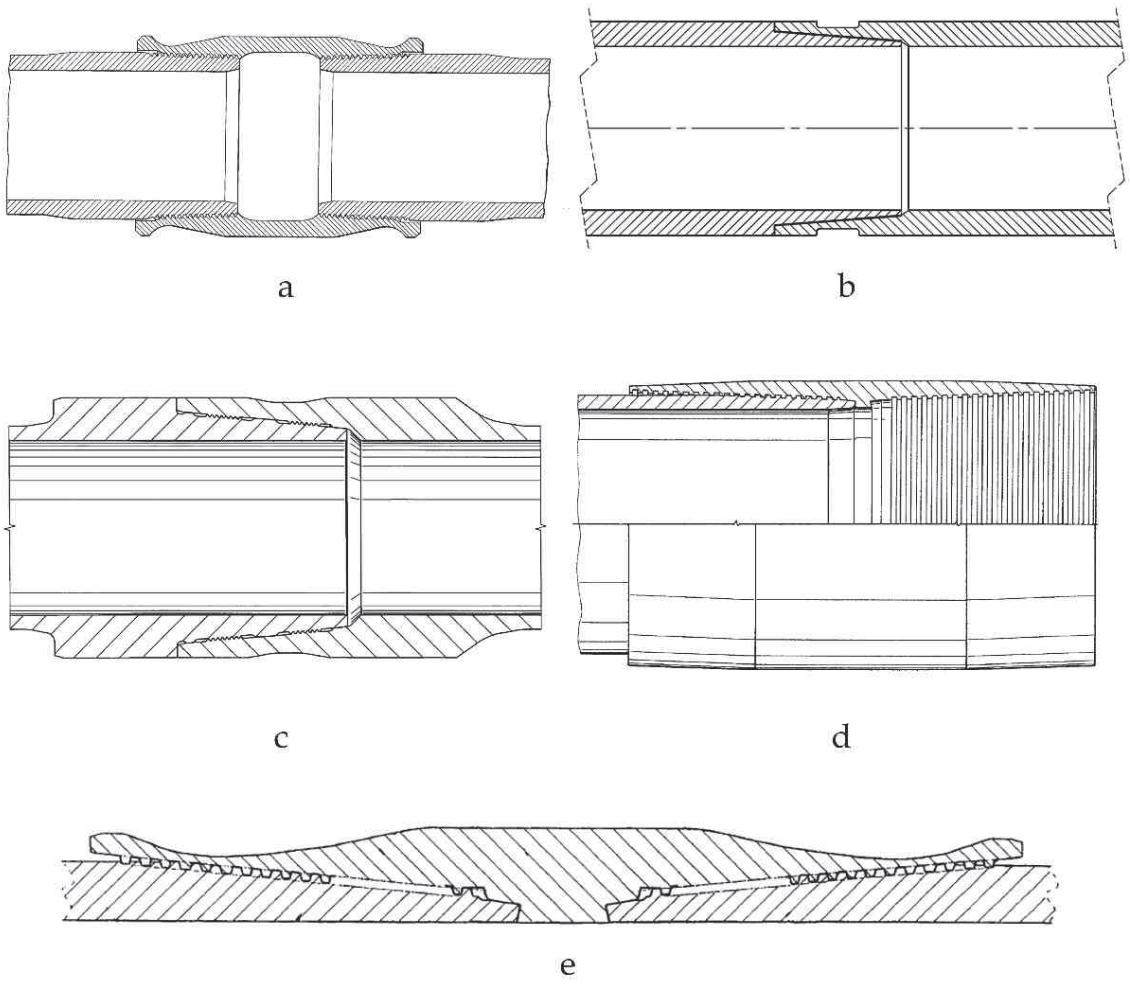

Figure 2.4: Patented box modifications: a) Bodine, 1961 [2.51], b) Schreier, 1963 [2.52], c) Galle et al. 2002 [2.53], d) DeLange and Evans, 2003 [2.54], e) Verdillon, 2004 [2.55].

However, when reducing the stiffness of the box locally, by applying a groove in its outer surface located over the last engaged threads of the pin, the box is able to elastically deform and to transfer the load more easily to the following threads.

The same idea of local stiffness reductions to redistribute loads has been used ever since in a variety of other patents. In 1963 an integral drill string connection with a changed box was patented [2.52]. This connection is shown in Figure 2.4.b.

The offshore riser connection of Galle et al. [2.53] (Figure 2.4.c) uses two conical threaded sections. Those threaded sections are separated by an intermediate unthreaded region. The intermediate region of the box also carries a recessed groove. Again this enables a more uniform distribution of the load carried by the two separate threaded sections.

The T&C coupling by DeLange and Evans [2.54] (Figure 2.4.d) claims to provide better fatigue performance by changing the so-called *stiffness gradient* of the recess region of the box. This modification basically comprises a

gradual chamfer of the box that starts over the last fully engaged thread of the pin and it will be discussed more in detail in during the parametric study in section 3.2.2 of Chapter 7. Additionally, the design of DeLange and Evans includes a feature previously introduced by Webb [2.48]. It proposes to apply a long engaged thread length, including a thread run-out region where the threads are only partly engaged. This long engaged thread region can also be found in the connection of Verdillon [2.55] as shown in Figure 2.4.e. Next to this it uses a waisted groove over the highest loaded threads similar to the original design of Bodine [2.51]. This connection is commercially available and is named the VAM TOP FE connection. Verdillon added the possibility of filling up the machined groove with an elastic filler material, as long as the stiffness of the used filler is sufficiently lower than the stiffness of the material of the connection.

3.2.3 Local thread modifications

To optimize the connection threads for fatigue purposes, the thread profile can be changed to reduce the stress concentration at the thread roots. Additional to this, the thread taper, pitch, interference or tolerances can be changed over the engaged threads to modify the load distribution. Since these modifications generally result in complex thread shapes that require very fine tolerances, local thread modifications can be considered as less robust ways to influence the connection's fatigue behaviour. This is because wear or local damage during service can change those tight tolerances and hence eliminate the desired fatigue properties.

Nevertheless, numerous patented thread modifications exist. The so-called *Reed-thread* developed by Saunders et al. [2.56] as shown in Figure 2.5.a, is a modified rounded triangular thread. It contains a stress relief groove in the thread root with an increased root radius compared to the standard thread shape to reduce the stress concentration factor. Additionally, the connection contains a pin with a slightly lower taper angle than the box. This results in an artificial change in pitch and radial interference which improves the load distribution, a feature that was also adopted in the sucker rod connection by Ernst and Villasante [2.62].

Both Gunderson et al. [2.57] and DeLange et al. [2.58] proposed a modified buttress thread with enhanced fatigue properties to be used for risers, tendons or drill applications (see Figure 2.5.b and c). They both use a zero degree load flank and increased root radii.

The zero degree load flank ensures that the axial load on the connection does not produce any significant radial component which would tend to separate the pin and box. An additional modified buttress thread with a positive load flank and optimized root radius was patented by Verdillon [2.60] (Figure 2.5.e).

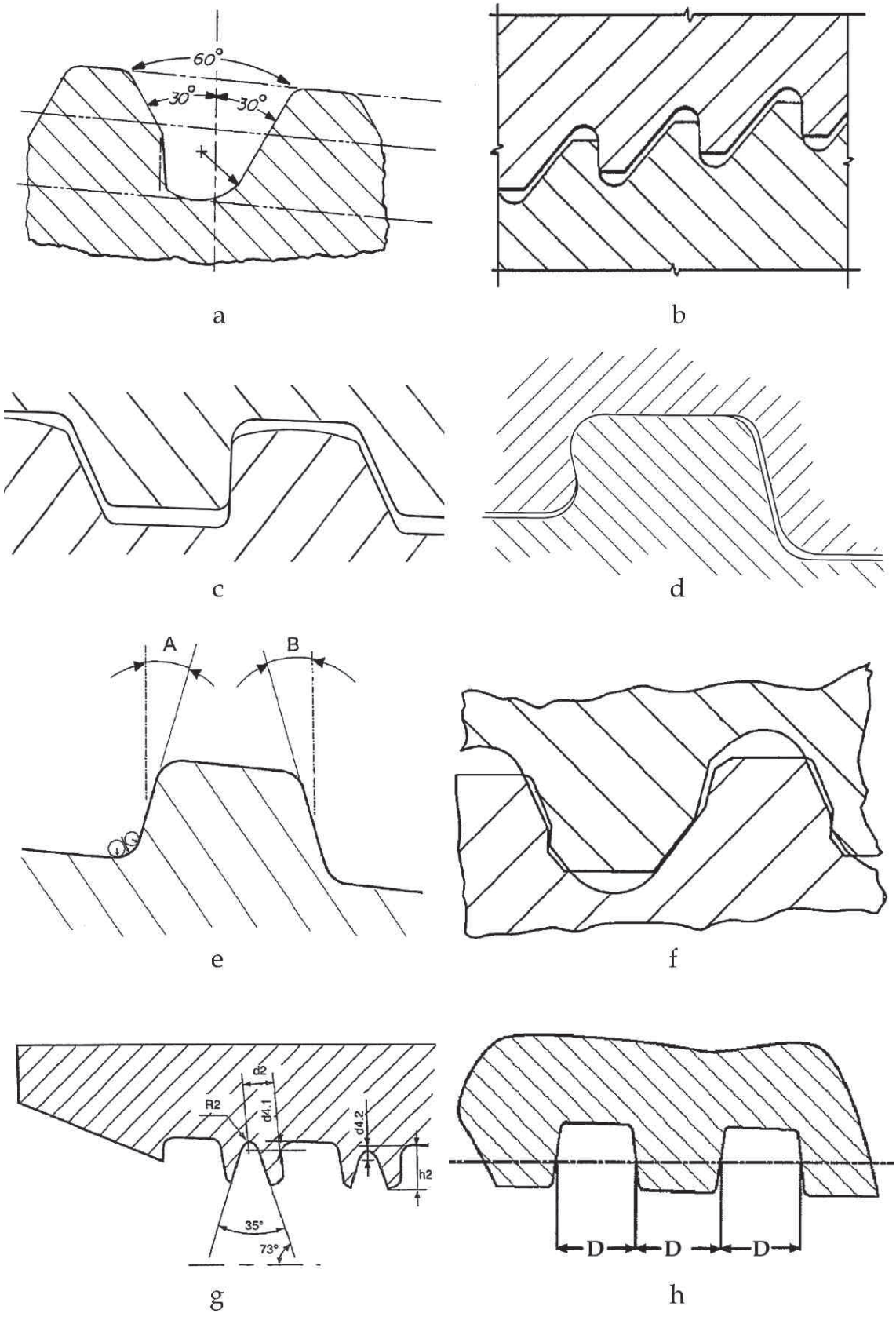

Figure 2.5: Patented thread types: a) Saunders et al., 1985 [2.56], b) Gunderson et al., 1990 [2.57], c) DeLange et al., 1999 [2.58], d) Olivier, 2002 [2.59], e) Verdillon, 2004 [2.60], f) Pallini et al., 2007 [2.61], g) Noel and Roussie, 2009 [2.63], h) Toscano and Di Toro, 2010 [2.64].

Worth mentioning is that modified buttress threads also exist with a negative load flank. An example of this can be found in the drill string thread by Olivier [2.59] as shown in Figure 2.5.d. The negative load flank locks the connection together and prevents separation of the threads. Next to reducing fretting fatigue failure, this kind of threads are generally more resistant to yielding and overtorque. The thread type of Olivier has improved fatigue properties due to the radiused corners of the load flank.

The irregular thread type for riser connections of Pallini et al. [2.61] (Figure 2.5.f) has an S-shaped load flank that provides a variable load angle depending on the radial position along the contact interface. The thread profile uses a combination of thread cuts that vary in shape and pitch to provide load and stab flanks that vary along the axial length of the engaged threads. Due to the changing interference between the threads, the load distribution becomes more uniform over the engaged length. It is obvious that this kind of threads with varying pitch and profile demands extremely tight tolerances and advanced production tools. This results in high production and maintenance costs since connection repairs can only be carried out by specialized workshops equipped with the required tools. Additionally, the irregular thread shape hinders thread inspection.

Noel and Roussie [2.63] developed an additional modification of the buttress thread type. But instead of optimizing the root radii, they provided a portion of the threads with an additional groove in the thread crests as can be seen in Figure 2.5.g. This groove is machined only at the first and last engaged threads. The groove reduces the thread stiffness, so the load is transferred better to the subsequent threads. The improved load distribution should result in an increased fatigue life of the connection. Nevertheless, the extra groove in the threads makes inspection and repair of the threads more difficult.

The symmetrical trapezoidal thread design of Toscano et al. [2.64] for sucker rod connections (Figure 2.5.h) provides contact on both the load and stab flank. The created diametrical interference is claimed to reduce thread disengagement and to have improved fatigue properties compared to prior art sucker rod connections where only axial interference is applied by using a torque shoulder.

3.2.4 Additional fatigue improving features

Next to the two general trends of improving the fatigue strength of a connection either by changing the global box shape or the local thread shape, some other features are used. The fatigue strength of rounded triangular threads can be improved by cold working the thread roots, for example by rolling the threads after they have been milled into the connection as was shown by Knight et al. in their study on drill pipe connections [2.65]. In that way compressive residual stresses are introduced at the location where the fatigue cracks tend to initiate, which is beneficial for the fatigue life of the

connection. A connection where this introduction of residual stresses is proposed was developed by Benedict et al. [2.66].

Stress relief grooves can be used to locally reduce the stiffness of the connection around the first and last engaged thread. This way the load on these locations is partly transferred to the next threads. Since stress relief grooves result in a locally decreased wall, they are only used in upset connections which have a bigger wall thickness than the pipe material. An example of a connection with stress relief grooves is shown in Figure 2.6.

Metal-to-metal surfaces are used as seals to prevent leakage, but when the connection is subjected to dynamic bending loads, those seals can have a beneficial effect on the connection's fatigue life. This is because the metal-to-metal seals also provide structural support for the contacting parts and transmit part of the bending load. This decreases the stresses in the threaded region of the connection. In Figure 2.7 an example of such a connection is given [2.68]. However, as indicated by Santus [2.69], metal-to-metal surfaces can also decrease a connection's fatigue life, as fretting phenomena can initiate fatigue cracks in the sealing contact itself.

Another feature that is claimed to provide better fatigue resistance can be found in the patent of Nisida et al. [2.70]. Although the patent is aimed at bolts, it may be applicable to threaded pipe connections as well. As illustrated in Figure 2.8, the last engaged threads of the connection's pin have crests that are cut off. In that way the last engaged threads of the box will only be partly engaged.

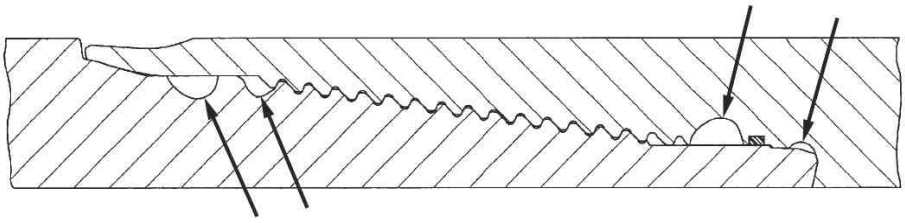

Figure 2.6: Patented connection with stress relief grooves by Pallini et al.[2.67], the grooves are indicated by the arrows.

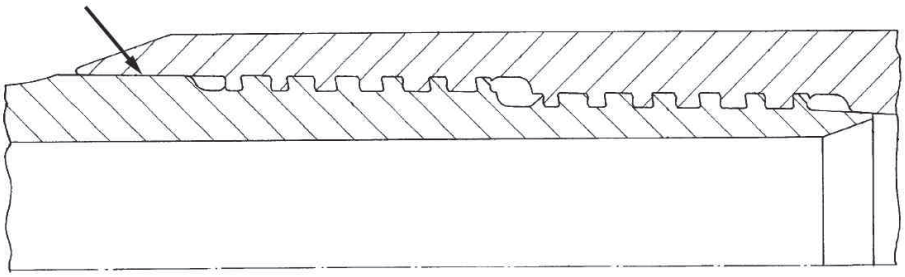

Figure 2.7: Metal-to-metal sealing surfaces (indicated by the arrow) can improve the fatigue resistance of a connection subjected to cyclic bending loads [2.68].

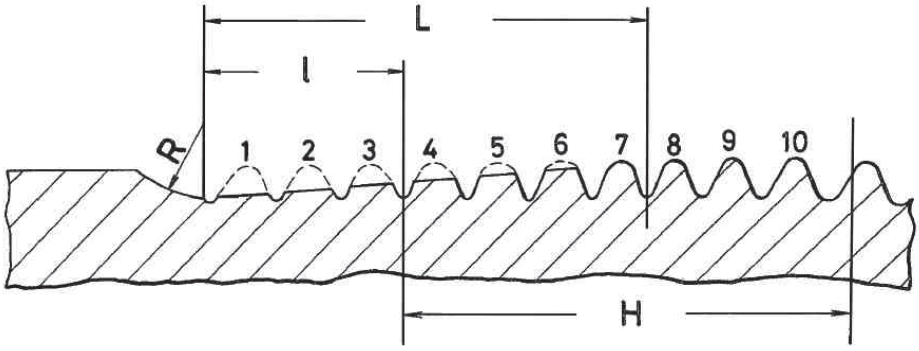

Figure 2.8: Patented thread run-out by Nisida et al [2.70].

When subjected to axial loads, the last engaged threads of the box will bend and the loads will be transmitted to the subsequent threads of the connection. This approach is similar to the grooved threads of Noel and Roussie [2.63] (Figure 2.5.g) and the long thread run-out of DeLange and Evans [2.54] (Figure 2.4.d).

3.3 Discussion

From the described examples it is clear that fatigue life improvement of threaded pipe connections is extensively studied during the last decades. Numerous patented fatigue resistant connections exist and several are commercially available. However, the information provided in the patent documents concern only general ideas and claims about the resulting performance, but no quantifiable results are published to prove such claims. Additionally, this lack of results makes it impossible to make an objective comparison between different designs. Together with the lack of parametric studies of threaded connections (see section 2.4), the need for a uniform approach in evaluating and comparing threaded connections becomes clear.

4 Fatigue analysis [2.71-73]

4.1 Introduction

In this section an overview is given of different fatigue life prediction models. Since it falls beyond the scope of this dissertation to provide a general overview of all existing fatigue modelling techniques, this overview is limited to existing fatigue models relevant for the evaluation of threaded pipe connections. Additionally, the underlying mechanisms of fatigue fracture in general are considered to be general knowledge.

In the early days, in-service fatigue failure was avoided by ensuring that the stress levels in a component were below the material's fatigue limit. The value of this limit is a material property and generally speaking, no fatigue damage will appear when stresses remain lower than the limit value. This meant that the component would have an infinite life. Since this results in an

uneconomic design, nowadays components and structures are commonly designed for a finite life. This has prompted the development of fatigue models and analysis techniques to predict a component's fatigue life. These techniques can be grouped into the following categories:

- stress-life approach;
- local strain models;
- fracture mechanics;
- multiaxial models.

The stress-life approach was the first fatigue prediction technique to be developed. This technique is generally used to predict the total life of a component. Local strain models, however, only consider the crack initiation life. This approach can be used when crack initiation dominates the total fatigue life. On the other hand, fracture mechanics only deals with the crack propagation stage. When both the crack initiation and propagation stage of a component are important, local strain models can be used in conjunction with fracture mechanics to predict the total fatigue life by simply adding the calculated number of cycles in the two stages.

Multiaxial fatigue models take into account the multiaxial stress or strain distribution at notches or crack tips and can either be based on a stress or strain based approach or can be based on energetic criteria. Depending on the criterion, the models predict fatigue crack initiation, propagation or total fatigue life.

4.2 Stress-life approach

4.2.1 S-N curves

The stress-life approach is the oldest among the fatigue analysis techniques. This method was developed by Wöhler and is based on experimental observations. The mathematical relations of this approach are derived from the so-called S-N curve or Wöhler curve of which an example is shown in Figure 2.9. This curve is obtained by subjecting a number of test specimens to fatigue tests at different stress levels. During a single test, the load is fluctuated with a constant amplitude until failure occurs. How failure is defined, depends on the test specimen. For standardized strip- or bar-like specimens, failure means commonly total fracture of the specimen, while for tubular specimens a through-wall crack is generally considered as failure. The resulting number of load cycles to failure N corresponding with a certain stress amplitude S_a is then plotted in the S-N curve. The number of cycles N is plotted on the horizontal axis, which is conventionally put in logarithmic scale. The stress amplitude on the vertical axis can be either logarithmically or linearly plotted.

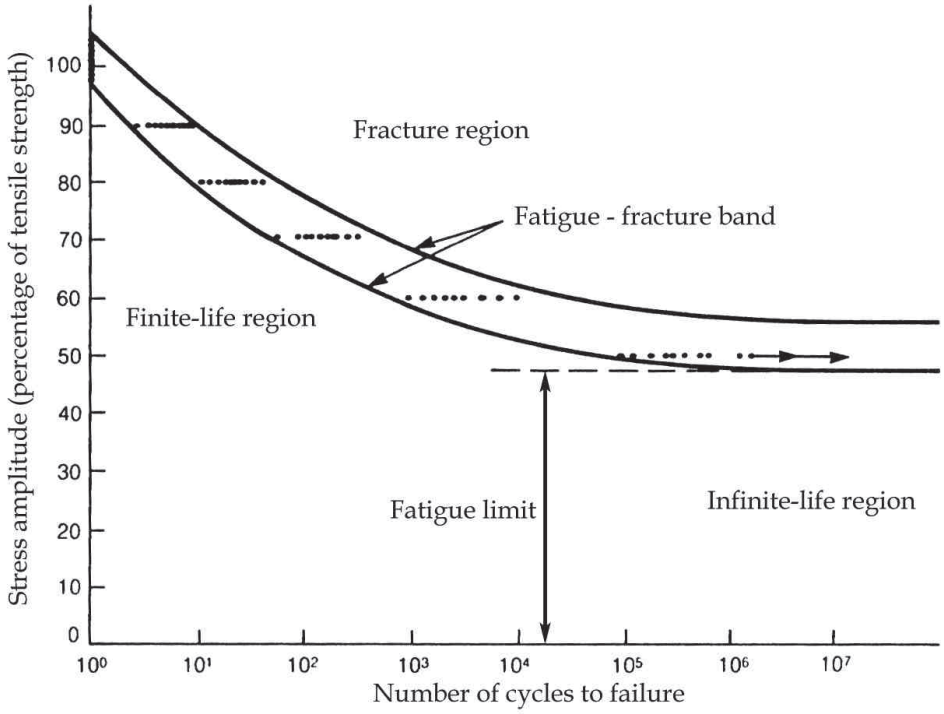

Figure 2.9: Typical S-N curve of a medium-strength steel [2.73]

A typical example of an S-N curve is shown in Figure 2.9. As can be seen, it starts as a sloping curve changing into a horizontal asymptote with the number of cycles to failure becoming infinite. The stress level corresponding to the asymptote is referred to as the *fatigue limit*. Since stresses below the fatigue limit would never result in fatigue failure, tests are generally stopped when a certain number of cycles is reached, for example at $2 \cdot 10^6$ cycles. Fatigue test data are prone to scatter, due to the nature of the fatigue mechanism. Nevertheless, the data can be embedded in a certain fatigue-fracture band wherein the probability of failure changes from a low probability next to the finite-life region, to a high probability next to the fracture region. Typically a mean curve for the finite-life region with a 50 % probability of failure is used according to the Basquin relation:

$$S_a^k \cdot N = \text{constant} \tag{2.2}$$

For design purposes a probability of failure of 50 % is obviously unacceptable. For this reason design curves are used which are obtained by subtracting two times the standard deviation from the mean curve which corresponds to a probability of failure of 4.55 %.

The stress amplitude to which the fatigue life is related to is generally a nominal stress, since it is derived from the forces applied in the experimental test setup. This has the advantage that no complex stress analysis is required to evaluate the test specimens. However, this means that results obtained for a specific component can not easily be extended to a modified component. Additionally, S-N curves are obtained from constant amplitude tests whereas in practice most components are subjected to variable amplitude stresses. To

use S-N data for practical load histories, the cumulative fatigue damage model of Miner can be used:

$$D = \sum_i \frac{n_i}{N_i} \tag{2.3}$$

Miner postulated that fatigue damage accumulates linearly. When a component is subjected to n_i stress cycles at a stress which has N_i cycles to failure, then a fraction of n_i/N_i of the total life is consumed. The damage accumulated over the cycles at different stress levels is summed up to give the total damage D. The component would fail if D becomes one. Miner's theory assumes that damage can be superimposed, that the appearing damage is irreversible and that there is no interaction between different stress levels in the sense that it is unimportant in which order the component experiences the stress cycles.

4.2.2 Mean stress effect

Fatigue tests can be carried out with a fully reversible load with zero mean stress or with a fluctuating load with a certain prestress. To make the test conditions clear, a *load ratio* R as defined by Eq. (2.4) should be mentioned with every S-N curve. Where S_{min} and S_{max} are respectively the minimum and maximum applied stress, as shown in Figure 2.10. Additionally, S_r is the applied stress range and S_m is the mean stress.

$$R = \frac{S_{min}}{S_{max}} \tag{2.4}$$

Many S-N curves are given for a fully reversible fatigue load with zero mean stress or load ratio $R = -1$. In order to compare data obtained in tests conducted at a different load ratio, the Goodman Eq. (2.5) can be used to correct the mean stress effect.

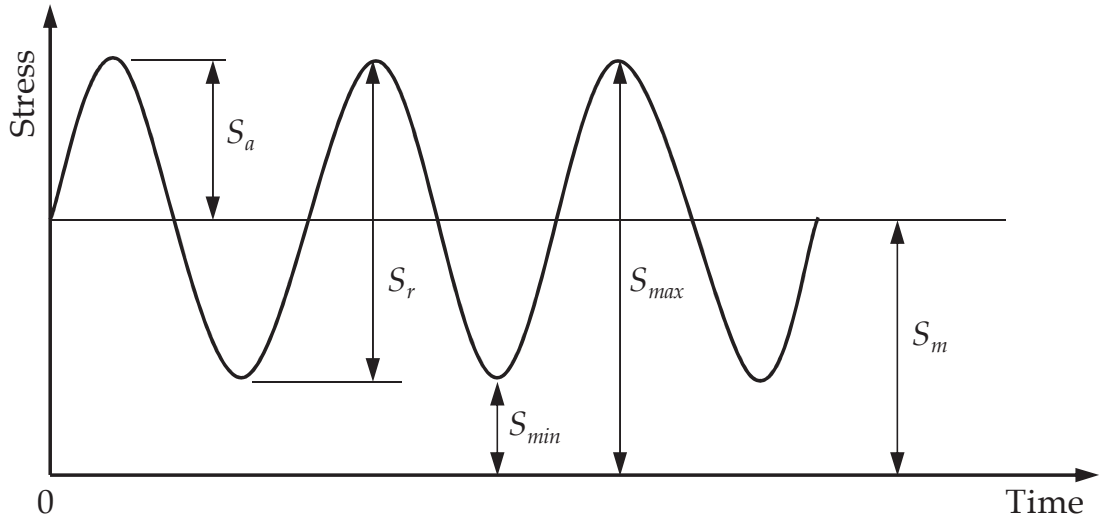

Figure 2.10: Stress definitions.

With this equation the fatigue stress S_f as would occur for a fully reversible fatigue load can be calculated from the applied stress amplitude S_a taking into account the ratio between the applied mean stress S_m and the material's tensile strength σ_{UTS}.

$$\frac{S_a}{S_f} = 1 - \frac{S_m}{\sigma_{UTS}} \tag{2.5}$$

4.2.3 Stress concentrations

To determine the fatigue life of a machined component, the fatigue data of standard test specimens can be used. However, a real-life component has an arbitrary size with a certain stress concentration, an arbitrary surface finish and an arbitrary loading mode, while standard test specimens have prescribed dimensions and a polished surface. To take all these differences into account, the fatigue stress of the machined component $S_{f,comp}$ can be estimated from the fatigue stress of a standard component S_f by introducing a number of correction factors:

$$S_{f,comp} = k_a \cdot k_b \cdot k_c \frac{S_f}{K_f} \tag{2.6}$$

In this equation k_a is a correction factor for the loading mode, since the fatigue behaviour of a component is different when the loads are applied e.g. in tension or bending mode. The factor k_b deals with the size effect, which takes into account that the effect of fatigue failure on small standardized specimens can be different from the effect on a bigger structure. k_c is a surface roughness factor that allows to relate the results of polished standard specimens to machined parts with a higher surface roughness. Finally, K_f is the fatigue notch factor. This can be calculated from the geometrical stress concentration factor K_t by Eq. (2.7) with q the notch sensitivity factor.

$$K_f = 1 + q(K_t - 1) \tag{2.7}$$

When using this technique to evaluate threaded connections based on experimental data of the pipeline steel, one should consider that the factors k_a, k_b, k_c and q are all given by empirical relations or charts which means that each single factor is subjected to a certain amount of uncertainty. Additionally, the input for these relations or charts requires measurements of local parameters such as surface roughness and root radii. Next to this, selecting a certain uniaxial loading mode from a complex stress distribution might be an oversimplification. Due to these assumptions and the scatter of every factor, the calculated life might differ significantly from the real behaviour of the connection.

4.3 Local strain models

Local strain models aim to predict the number of load cycles needed for a crack to initiate in a component. Unfortunately, there is no uniform definition of how long a crack must be to be considered initiated. Consequently, the fraction of the total fatigue life taken by initiation depends on the used criterion. In general, this criterion depends on the practical consideration what the minimum crack size is that can be detected with the available measuring technique. Typical sizes of detectable cracks start from smaller than 0.1 mm using microscopic techniques to cracks over 10 mm for example when internal flaws in welds are sized.

In the local strain approach it is considered that for a component without initial cracks, initiation will most likely take place at the highly stressed tip of a notch. Hereby it is assumed that the number of cycles to initiate a crack at the notch tip is equal to the crack initiation in a plain test specimen subjected to the same stress-strain history. Since in notches the local stresses can easily exceed the material's yield strength even if the nominal stresses remain much lower, a distinction is made between elastic and plastic strains. The dynamic stress-strain behaviour of a material is different from its quasistatic response. Hence, the dynamic stress-strain curve is determined using a stable cyclic tensile test. The cyclic stress-strain relation of metallic materials is commonly described by the Ramberg-Osgood equation (2.8). Where $\Delta\varepsilon$ and $\Delta\sigma$ are respectively the local dynamic strain and stress range, E is Young's modulus of elasticity and K' and n' are material constants, with K' the cyclic strength coefficient and n' the cyclic strain hardening exponent. The first term of the equation is the elastic strain, the second term represents the plastic strain.

$$\frac{\Delta\varepsilon}{2} = \frac{\Delta\sigma}{2E} + \left(\frac{\Delta\sigma}{2K'}\right)^{1/n'} \tag{2.8}$$

Based on the work of Manson and Coffin, this cyclic stress-strain relation can be expressed as a function of fatigue initiation life N_i:

$$\frac{\Delta\varepsilon}{2} = \frac{\sigma_f'}{E}(2N_i)^b + \varepsilon_f'(2N_i)^c \tag{2.9}$$

Where σ_f' is the fatigue strength coefficient, b is the fatigue strength exponent, ε_f' is the fatigue ductility coefficient and c is the fatigue ductility exponent. All four terms are material properties. A typical strain life plot is shown in Figure 2.11. The two asymptotes are the different terms for the elastic and plastic strain range.

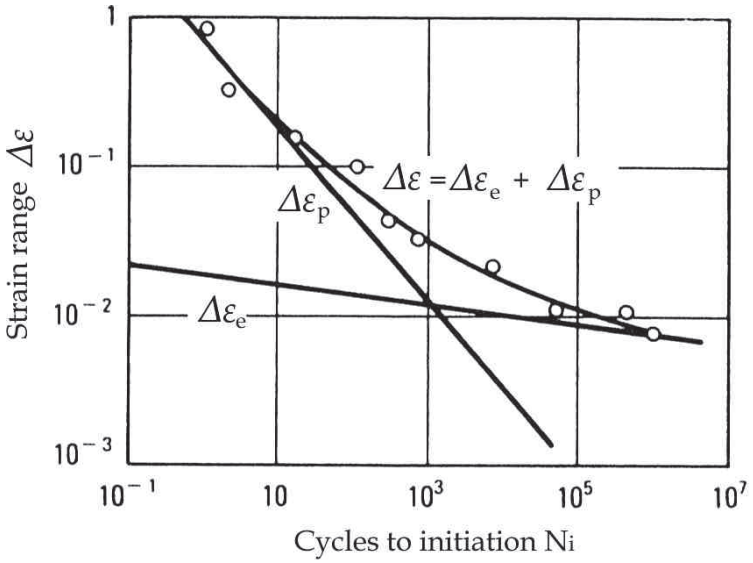

Figure 2.11: Typical strain range versus cycles to initiation curve [2.73]

The above mentioned equations are used to define the material parameters based on experimental fatigue tests of standard test specimens. Once these material parameters are known, a component's fatigue life can be calculated without any additional tests. A possible method uses the stress concentration factor K_t in Eq. (2.10), the so-called Neuber's rule.

$$\Delta\sigma \cdot \Delta\varepsilon = \frac{K_t{}^2 \cdot S_r^2}{E} \tag{2.10}$$

Using Neuber's rule it is possible to calculate the local stress range $\Delta\sigma$ and local strain range $\Delta\varepsilon$ based on the nominal stress range S_r. This is done by finding the intersection between the curves described by the equations (2.8) and (2.10). Once the local strain range is found, the fatigue initiation life can be calculated from Eq. (2.9). Next to Neuber's rule, other methodologies exist to apply the local strain approach to practical applications. The difficulty however, is to define the appropriate stress concentration factor K_t which is not straightforward for the case of preloaded threaded pipe connections.

4.4 Fracture mechanics

To predict the rate of fatigue crack growth in a component, fracture mechanics can be used. That way a component's crack propagation life can be calculated. When looking at crack propagation under cyclic loading, the parameter ΔK is normally used for evaluation of the crack growth behaviour and is expressed in MPa·m$^{1/2}$. This is the difference in stress intensity factor at maximum and minimum applied load. When experimentally measured crack growth rates da/dN, with a the crack depth, are plotted against ΔK, a typical sigmoidal curve is obtained as shown in Figure 2.12. The crack growth rate is generally expressed in µm/cycle.

The curve can be divided into three sections that represent the different regions of fatigue crack growth. The first region exhibits a vertical asymptote at the threshold value ΔK_{th}. ΔK values below this threshold level are too low to cause crack growth. It should be noted that the threshold region is not equal to the crack initiation stage as discussed in section 4.3. The crack initiation stage considers the formation of micro cracks only, while fracture mechanics considers pure macroscopic cracks. Even though it is possible that micro cracks initiate at the material surface, it is possible that they are not able to penetrate into the material due to microstructural barriers if ΔK remains below the threshold value. As discussed before, there is no clear size limit to distinguish between micro and macro cracks.

In region II of Figure 2.12 the crack growth rate is described by a power function known as the Paris-Erdogan law:

$$\frac{da}{dN} = C \cdot \Delta K^m \tag{2.11}$$

Where C and m are material constants. By rearranging and integrating this equation, the number of cycles can be calculated for a crack to grow from one depth to another.

The third region of Figure 2.12 is the stable-tearing crack growth region. In this region the crack growth rate is high, in the order of 0.01 mm/cycle and above. In this region a combination of fatigue crack growth and local ductile tearing takes place. Ductile tearing does not yet occur over the full crack front, but the unstable final failure is imminent. The crack growth life in this region is very limited and hence of less interest for engineering applications. When the maximum appearing crack stress intensity factor exceeds the critical value of K_c, final fracture takes place.

Since da/dN-ΔK plots are commonly presented with a log-log scale, the power function (2.11) appears as a straight line with a slope m in region II. By fitting the results of an experimental crack growth test on small test specimens, the material parameters C and m can be easily determined, but determining the value of the stress intensity factor K of a crack is often much more complex. The crack stress intensity factor can be expressed in the general form (2.12).

$$K = Y \cdot S\sqrt{\pi a} \tag{2.12}$$

Where a is the crack depth, S is a chosen nominal stress and Y is a dimensionless parameter which depends on the specimen, crack and loading conditions. A closed form solution exists for many simple geometries. However, when a complex structure is to be analyzed, the crack stress intensity factor should be calculated through finite element analysis. Since this requires a very fine mesh around the crack tip and the analysis of different crack depths for a full fatigue crack growth analysis, this technique is both complex and time consuming.

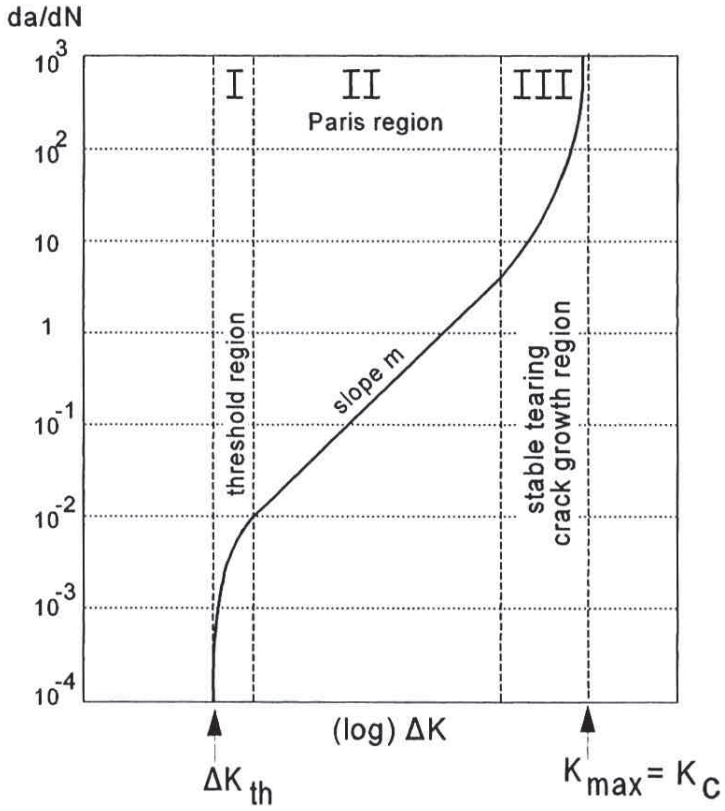

Figure 2.12: Regions of crack growth rate as a function of ΔK [2.72].

4.5 Multiaxial fatigue models

When dealing with structures subjected to complex load cases, the above mentioned fatigue analysis approaches, might not give accurate results since they consider the dynamic loads to be uniaxial. Even in situations where the global acting stress is purely uniaxial, the local stress situation around notches or irregularities can be multiaxial. To describe such load cases more accurately, multiaxial fatigue models were developed. A wide variety of multiaxial fatigue models exist, all with their specific approach and applicability. Nevertheless, they can be classified into two main categories: methods based on an equivalent damage parameter -which can be related to stress, strain or energy- and methods based on searching for a critical plane. Through the available models, few have been validated against real machine components, hence this summary is limited to two approaches relevant for fatigue analysis of threaded pipe connections.

4.5.1 Dang Van criterion [2.74]

A method that is widely used for practical applications is the Dang Van criterion which is based on a microscopic approach of the critical shearing plane. In his approach Dang Van postulated that crack initiation may occur in the critical plane of the most unfavourable oriented grains that are subjected to a plastic deformation even if the bulk stress is elastic [2.75]. Hence the criterion postulates that fatigue damage will appear at a definite

time when the combination of local shear stress $\tau(t)$ and hydrostatic pressure $\sigma_H(t)$ runs out of the safe region during cyclic loading (as shown in Figure 2.13). This criterion can be written as:

$$\max_A \left[\tau(t) + \kappa \cdot \sigma_H(t)\right] \leq \lambda \tag{2.13}$$

Where A is the studied area, κ and λ material parameters that can be obtained by the endurance limits of two fatigue tests, one under reversed bending and the other under reversed torsion. The local shear stress and hydrostatic pressure are calculated according equations (2.14) and (2.15), with σ_1, σ_2 and σ_3 the principal stresses.

$$\tau(t) = \frac{\sigma_1(t) - \sigma_3(t)}{2} \tag{2.14}$$

$$\sigma_H(t) = \frac{1}{3}\left[\sigma_1(t) + \sigma_2(t) + \sigma_3(t)\right] \tag{2.15}$$

Even though the Dang Van criterion as given by Eq. (2.13) does not include predictions for finite fatigue life, using the information of two full S-N curves, the criterion can be extended for this purpose as will be shown in section 4.6.3.

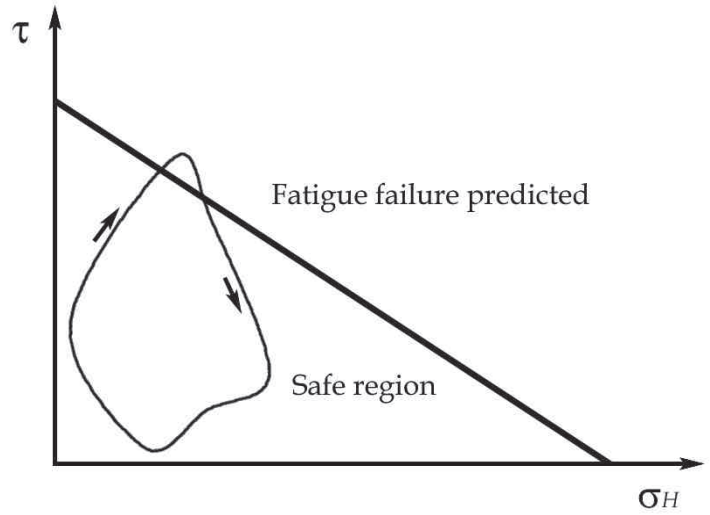

Figure 2.13: Dang Van criterion

4.5.2 Damage evolution law

The damage evolution law of Abdel Wahab et al. [2.76] is a multiaxial fatigue model based on an energy criterion. It is derived using thermodynamic principles, assuming material plasticity at the crack initiation location. Since in the case of threaded connections, plastic deformation can be introduced at the thread roots from the moment the coupling is made up, this methodology can be used for their fatigue life evaluation. The damage evolution law takes into account the multiaxiality of the stress state at the crack initiation place by

introducing a triaxiality function. Accumulated damage is described by the damage parameter D given in Eq. (2.16). D is *0* for the virgin material and *1* for the completely damaged material. In this equation, a and β are damage parameters and material constants, m is the strain hardening exponent of the material according to the Ramberg-Osgood relation. $\Delta\sigma_{eq}$ is the difference between the maximum and minimum von Mises equivalent stress during a load cycle and R_V is the triaxiality function as given in Eq. (2.17) with E the material's Young's modulus and ν the Poisson's ratio. σ_H is the hydrostatic pressure.

$$D = 1 - \left[1 - a(\beta + m + 1)\Delta\sigma_{eq}^{\beta+m} R_V^{\beta/2} N\right]^{\frac{1}{\beta+m+1}} \tag{2.16}$$

$$R_V = \frac{2}{3}(1+\nu) + 3(1-2\nu)\left[\frac{\sigma_H}{\sigma_{eq}}\right]^2 \tag{2.17}$$

The number of cycles to crack initiation N_i is determined from Eq. (2.16) by assuming a fully damaged situation (D = *1*). This results in following relation:

$$N = \frac{\Delta\sigma_{eq}^{-(\beta+m)} R_V^{-\beta/2}}{a(\beta + m + 1)} \tag{2.18}$$

The damage parameters a and β can be estimated by calculating the correlation between the nominal stress and the local stresses and fitting the results of an S-N curve to Eq. (2.18). This makes it possible to apply this method to test results of a real component even if no detailed fatigue properties of the component's material are known.

4.6 Practical applications and recommended approach

4.6.1 Stress-life approach in codes and standards

Due to its simplicity and close relation to experimental testing , the stress life approach is the most widely adopted method for the evaluation of threaded pipe connections. Even though the use of a nominal stress to predict fatigue failure precludes an accurate description of local effects at the thread roots, the stress-life approach is adopted by several codes and standards for the design and evaluation of threaded connections. In the BS 7608 standard a design curve with an endurance limit at $2{\cdot}10^6$ cycles is given for threaded fasteners, mainly bolts, subjected to a dynamic axial load at a load ratio of R=*0*. As can be seen in Eq. (2.19) the material is accounted for by dividing the applied stress range S_r by the material's tensile strength σ_{UTS}. However, it does not take into account the design or geometry of the threads.

$$\left(\frac{S_r}{\sigma_{UTS}}\right)^3 \cdot N = 400 \tag{2.19}$$

A different S-N curve is provided by the ASME codes and given by Eq. (2.20) [2.77]. This relation describes the mean curve of fatigue tests performed by Markl in the 1950's. Tests were performed on a wide range of welds, fittings and joints and for each type a stress intensification factor i was defined. This stress intensification factor should not be confused with common stress concentration factors. Markl used the S-N curve of a butt welded joint as a reference and i describes the relationship between a component and this reference curve. For threaded pipe joints a factor $i = 2.3$ was obtained, which is adopted by the ASME B31.3 code [2.78]. Noting that Eq. (2.20) is a mean curve, a conservative factor of safety of 2 on stress was introduced to obtain the ASME design curve (2.21). No endurance limit is assumed in this standard.

$$i \cdot S_r = 3378 \cdot N^{-0.2} \tag{2.20}$$

$$i \cdot S_r = 1689 \cdot N^{-0.2} \tag{2.21}$$

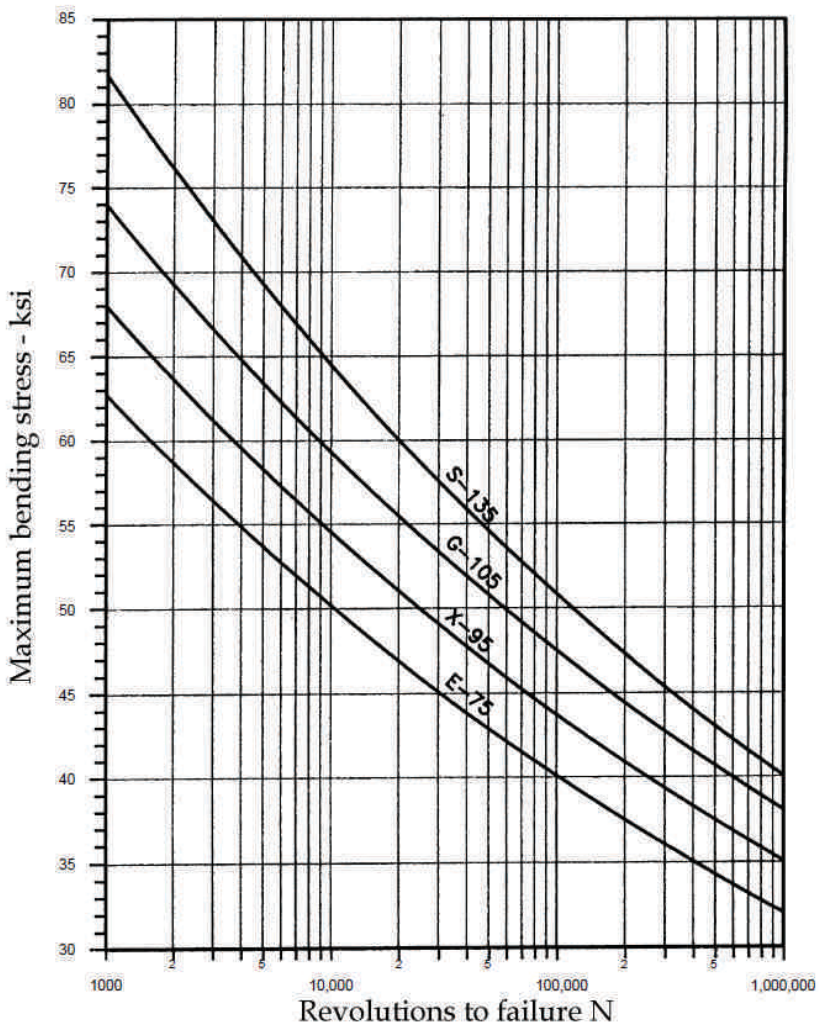

Figure 2.14: Mean S-N curves for API drill pipe connections [2.80]

In analogy with this approach, a number of S-N curves are given in API RP 7G [2.80] for drillpipe connections of different grades. These curves, as shown in Figure 2.14, can be used for fatigue life calculations of standard API drillpipe joints.

The most elaborate specification for the analysis of threaded pipe connections is given by DNV-RP-C203 [2.81]. In this document it is recommended to establish a finite element model with contact surfaces on the threads including non-linear material behaviour to allow for local yielding during make-up. A fine mesh is necessary at the thread roots to describe the stress distribution with sufficient accuracy. By simulating a single load cycle, the local stress range can be obtained. This value can then be used to calculate the stress-life from the S-N curve with following equation:

$$S_r = 5151 \cdot N^{-0.2128} \tag{2.22}$$

When the calculated stress concentration in the connection is dependent on the load level, it is recommended to use the load that the connection is most likely to experience during the first year of service. Additionally, the results should be supported by experimental test results of full-scale connections. It is noted in the procedure's description that based on experience this stress-life approach is more representative for actual fatigue behaviour than that of the initial strain method which is recommended by ISO 19902 and which leads to overly conservative results. Additionally, a simplified approach is given if a linear elastic finite element analysis is performed. In this case the S-N relation (2.23) can be used in combination with the obtained stress range. This approach is more conservative and no experimental validation is required to meet the standard.

$$S_r = 6015 \cdot N^{-0.25} \tag{2.23}$$

4.6.2 Local strain and fracture mechanics models

A general problem with local strain and fracture mechanics models is that they only describe a part of the fatigue process, respectively the crack initiation and propagation phase. This means that in order to get accurate results, two different models have to be combined and two separate sets of material constants are required, which are generally not available. This was illustrated by the work of Schneider et al. [2.82]. However, his experimental results were obtained for M10 bolted joints with a solid shaft. This means that the fatigue crack propagation is more important than in the case of threaded connections where the ratio between wall thickness and diameter can be relatively small. As can be derived from the experimental results of Newport [2.6], the fatigue crack initiation life is about 85 % of the total fatigue life for casing connections. However, when looking at connections with a bigger wall thickness to diameter ratio such as drill pipes, the influence of the fatigue crack growth becomes more important. In the work of Brennan [2.8] it can be found that the part of the fatigue initiation life can

be limited to 10 % and less. Hence it should be noted that it is inaccurate to exclude the impact of either crack initiation or propagation from fatigue life calculations without preliminary test results. An additional complication when using the combination of crack initiation and propagation models is defining the crack size for transition between the two models. Newport [2.6] considered a crack to be initiated if it exceeded a length of 2.5 mm. While Brennan [2.8] and Schneider et al. [2.82] both used the crack depth with a critical value of respectively 0.2 mm and 0.1 mm to define crack initiation. This choice depends in most cases rather on practical considerations, e.g. the resolution of the used crack sizing technique, than on fracture mechanical aspects.

4.6.3 Multiaxial fatigue models

Multiaxial fatigue models make still part of intensive research and new models are developed regularly. Hence there is no real consensus on what model to use in the case of threaded connections. However, application of the Dang Van criterion was reported in different studies of threaded components. Since the criterion itself only describes the boundary of infinite life, fatigue life calculations are not possible. Therefore the criterion was extended to encompass finite life calculations. Such an approach was used by Ferjani [2.35] in his study on the fatigue life of drill string connections. When using this approach, first the parameters κ and λ from the Dang Van criterion (2.13) are calculated using the endurance limits of the S-N curves obtained for the material under cyclic tension and cyclic torsion. The resulting Dang Van relation is plotted as a straight line in a σ_H-τ plot. It is then assumed that the lines corresponding with a finite fatigue life are parallel to this Dang Van line. The distance between the lines can be obtained using the S-N curve for the material under torsion as shown in Figure 2.15.

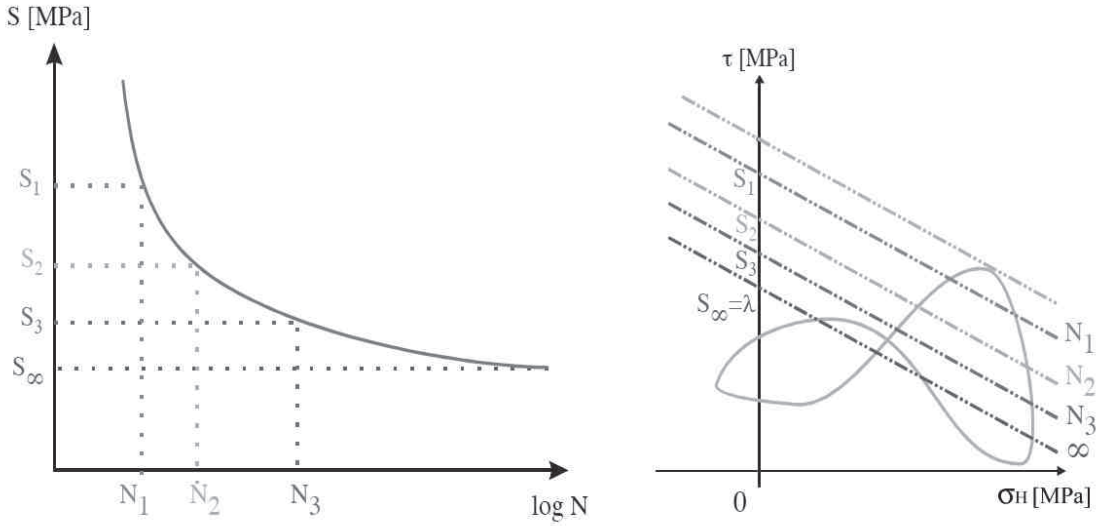

Figure 2.15: Extension of the Dang Van criterion to finite fatigue life calculations [2.35]

A similar approach was used independently by Fares et al. [2.75] for the fatigue life calculation of bolts. In their study the S-N curves of two bolts under different preloading conditions were used to obtain the modified Dang Van graph, hence obliterating the need of separate material testing and showing the usefulness of this approach for evaluating threaded connections.

4.6.4 Recommended approach

To decide which fatigue analysis technique to use, the main advantages and disadvantages of the discussed approaches and models are summarized in Table 2.2.

It should be obvious that, in order to relate the results of this study to existing standards and other studies, a stress-life approach is preferable, because of its close relation to experimental results and its wide application in standards. However, as was noted by Cetin and Härkergard [2.83], if stress-life approaches are used as a design or analysis tool for threaded connections without experimental test results of the considered connection, the obtained fatigue lives are highly dependent of the analysis technique used for the calculation of the stress concentrations.

When using the local strain approach and fracture mechanics, the problem arises that the used material parameters are commonly unknown. Accurate knowledge about these parameters requires significant testing of the base material, while estimation of all parameters will accumulate the uncertainty of the final results. Additionally the lack of a clear distinction between crack initiation and propagation causes additional complications.

The advantage of a multiaxial analysis is that it combines the conventional results from S-N curves based on nominal stresses with the local multiaxial stress situation at the thread roots.

In this study it was chosen to use conventional S-N curves to present the results of experimental tests and to use multiaxial models to perform more detailed analysis. The discussed design curves for threaded components as found in standards will be compared to the obtained experimental and numerical analyses.

Advantages	Disadvantages
Stress-life approach	
• This technique is broadly used because it is relatively simple and quick. • The total connection life is predicted. • The stress to which the fatigue life is related can be the nominal stress, removing the need for complex stress analysis.	• A large number of tests is needed to produce an S-N curve that relates to one specific connection. • S-N curves can rarely be used for other geometries since results are highly dependent on the used theories and calculations. • No distinction is made between crack initiation and propagation. This information can be required for in service inspections.
Local strain models	
• A strain-life curve can be used for any geometry. • For a given material, the results of a set of standard specimens is sufficient, no component testing is required.	• A complex stress analysis is required. Depending on the method used, the obtained stress intensity factor can be significantly different. • Only the crack initiation phase is taken into account, not the total fatigue life. • The required material data is generally not available.
Fracture Mechanics	
• The local behaviour of cracks is addressed. • It can be used for the non-destructive evaluation of remaining fatigue life and for defining inspection intervals.	• A complex stress analysis with several uncertainties is required. • Only the crack propagation phase is considered. • The required material data is generally not available.
Multiaxial models	
• Describes appearing stress concentrations more accurately by considering multiaxiality. • Data of S-N curves can be used as an input.	• A complex stress analysis is required. • Multiaxial models are less common, which means there is no consensus on what models to use.

Table 2.2: Trade-off of different fatigue analysis techniques.

5 Experimental work

5.1 Experimental fatigue setups

5.1.1 Setup types

Even though computer simulations like finite element analysis can significantly increase the efficiency of the design process, experimental tests remain important to obtain reliable predictions of the fatigue life of a threaded connection. Since the stress distribution resulting from make-up and dynamic loads can not be applied to small strip-like specimens, it is required to perform the experiments on threaded tubular specimens.

Fatigue test setups for pipes can by categorized based on the way the load is applied. The three conventional types are illustrated schematically in Figure 2.16. In the first setup shown in this figure, two pipes connected by a threaded coupling are subjected to a fluctuating axial tensile load. For large diameter pipes, this kind of fatigue testing requires extremely high forces. To reduce the required forces, the pipes can be tested in bending. In the four-point bending setup of Figure 2.16.b the bending forces are applied by means of hydraulic cylinders. In this kind of bending setup, only the outer fibres at the top and bottom side of the pipe undergo the maximum load amplitude. Otherwise in a rotational bending setup (see Figure 2.16.c), the pipe is subjected to a constant bending force and then rotated. This means that the entire circumference of the connection is subjected to the same load cycle.

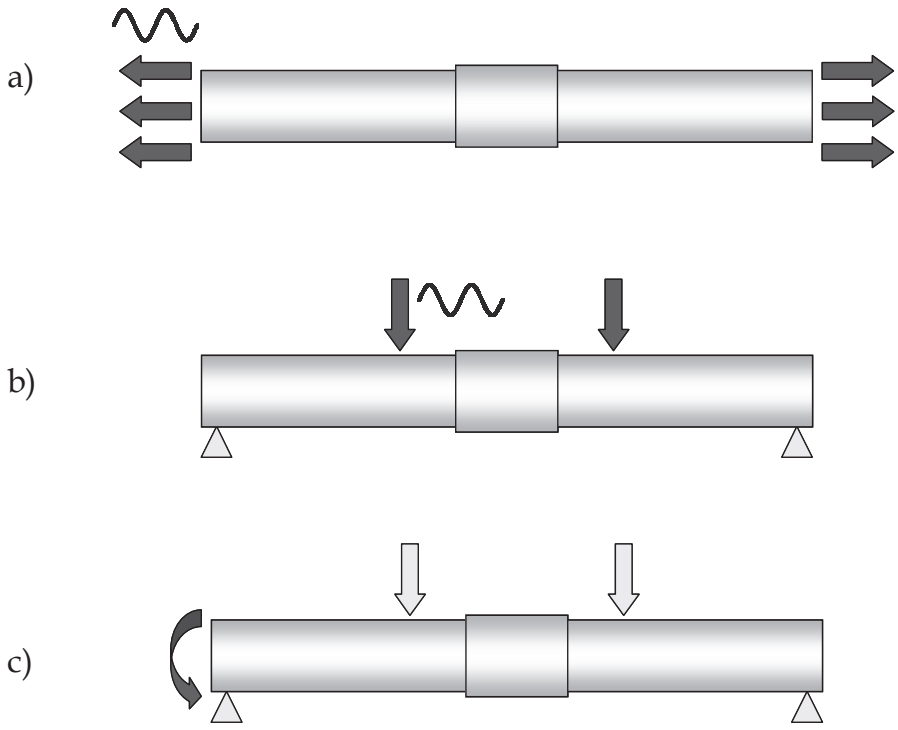

Figure 2.16: Types of fatigue setups: a) axial tension, b) four-point bending, c) rotating bending.

There are three main disadvantages linked to the conventional setup types. Firstly, they consume a considerable amount of power to generate the required forces for deforming the pipe. Secondly, a stiff and strong fatigue resistant load frame is required since it needs to be able to withstand the same fatigue loads as the pipes. Finally, the resulting testing frequencies of these setups are quite low, typically between 0.1 and 5 Hz, which results in long testing times.

Next to the three conventional setup types, there is a fourth type of fatigue setup for pipes. This type is based on resonant bending and overcomes all mentioned disadvantages of the conventional types. A resonance bending fatigue setup is schematically shown in Figure 2.17. In this setup, a pipe is subjected to an excitation with a frequency close to the natural frequency of the pipe. This causes the pipe to come into resonance, which means that the pipe will deform according to a standing wave that rotates at the excitation frequency. The induced stresses in the pipe are similar to the stress situation in a rotating bending setup in the sense that the entire pipe circumference is subjected to the same load cycle. The pipe is supported in the nodes of the standing wave, and consequently the supporting framework is not subjected to dynamic forces. The pipe's natural frequency, which depends mainly on its bending stiffness and mass, should be in the rpm range of commercial electromotors. Since a plain pipe would have to be too long to get within this range, the pipe's natural frequency is lowered by filling it with water and attaching additional weights at both ends of the pipe. This setup type consumes a fraction of the power compared to conventional setups and testing frequencies are typically in the region of 25 to 40 Hz.

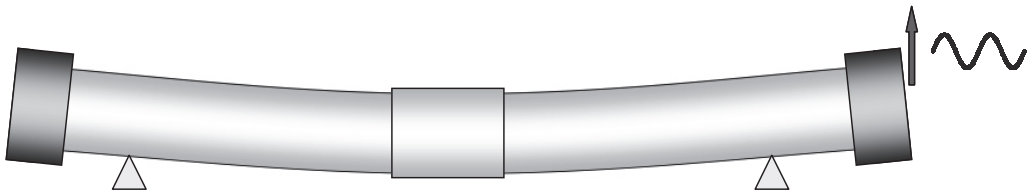

Figure 2.17: Resonant bending fatigue setup.

In the following sections an overview will be given of worldwide existing setups for fatigue testing of pipes. This overview is not limited to threaded connections, since similar setups are being used for the investigation of pipe girth welds e.g. to study the effect of prestrain and misalignment.

5.1.2 Axial tension and four-point bending setups

Since axial fatigue testing requires huge forces, they are only used in few cases. For example, Ferjani [2.35] tested scale models of drill pipes with a reduced diameter of 40 mm, but even these small diameter samples required a force of 138 kN. Next to this, axial fatigue tests where carried out by

Newport [2.6] on T&C casing connections and by Brennan [2.8] on 6.5″ (168.8 mm) drill pipe samples.

An example of a four point bending setup to test the fatigue strength of flawed pipes [2.84] is shown in Figure 2.18. The pipe is placed on two supporting rollers that are 0.96 m apart. The load is introduced by two loading rollers that are moved up and down by a hydraulic actuator at a frequency of 0.1 Hz.

To monitor the presence of a through-wall crack, the pipe is pressurized. At the moment a pressure drop is detected, the test is stopped and the pipe is considered to be failed. The corresponding number of cycles is taken as the fatigue life of the specimen. A similar setup with the same failure criterion was used by Kim and Park [2.85] in their study of notched and wall-thinned pipes. As an alternative for leak detection, the crack opening displacement can be monitored. An example of this can be found in a study of fatigue crack propagation of welded pipes [2.86] where an artificial notch was machined in the heat affected zone of the weld. Also local strains can be monitored by strain gauges, as demonstrated by a study of locally thinned 42 mm diameter pipes [2.87].

In their study of the fatigue properties of threaded connections for casing drilling applications, Carcagno et al. [2.88] used a four-point bending setup that is able of applying an additional axial tensile prestress. Tests were carried out on 4.5″ (114.3 mm) upset connections at a frequency of 5 Hz. Again, the test specimens were pressurized for leak detection.

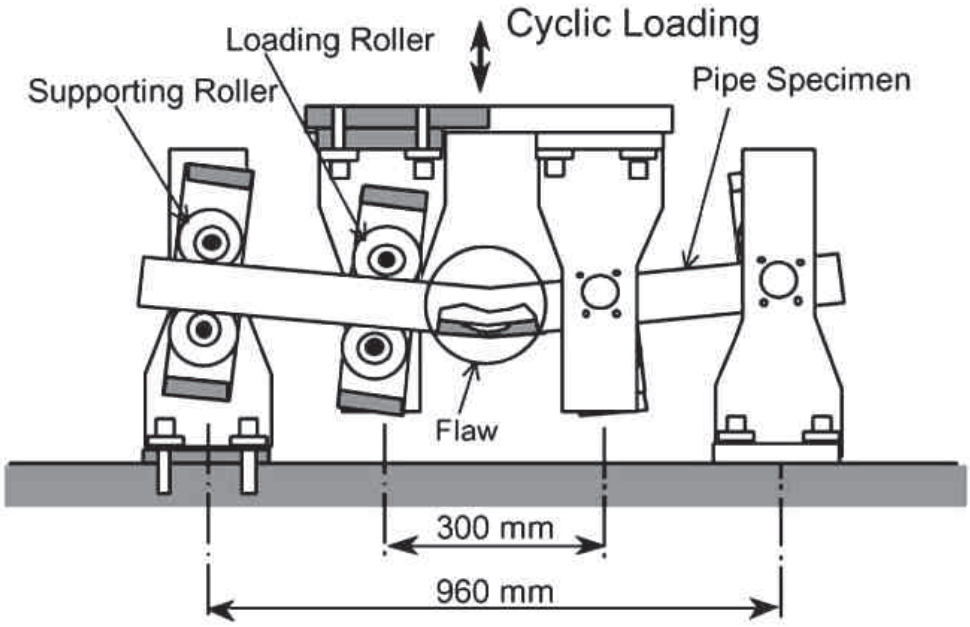

Figure 2.18: Four-point bending setup [2.84].

5.1.3 Rotating bending setups

In Figure 2.19 the rotating bending fatigue setup of Miscow et al. [2.89] is shown. This setup was designed for fatigue tests on steel drill pipe joints and was later used by Plácido et al. [2.32] to study the fatigue of aluminium drill connections and by Netto et al. [2.90] in their study of the fatigue life of defected girth welds. In this setup, the pipe is subjected to a constant bending moment applied by two hydraulic actuators and rotated by a driving mechanism powered by an electromotor. An additional hydraulic actuator is included which is able to pretension the pipe axially during the fatigue test. As can be seen in the lower part of Figure 2.19, the setup needs to be supported by a rigid frame to take up the applied forces.

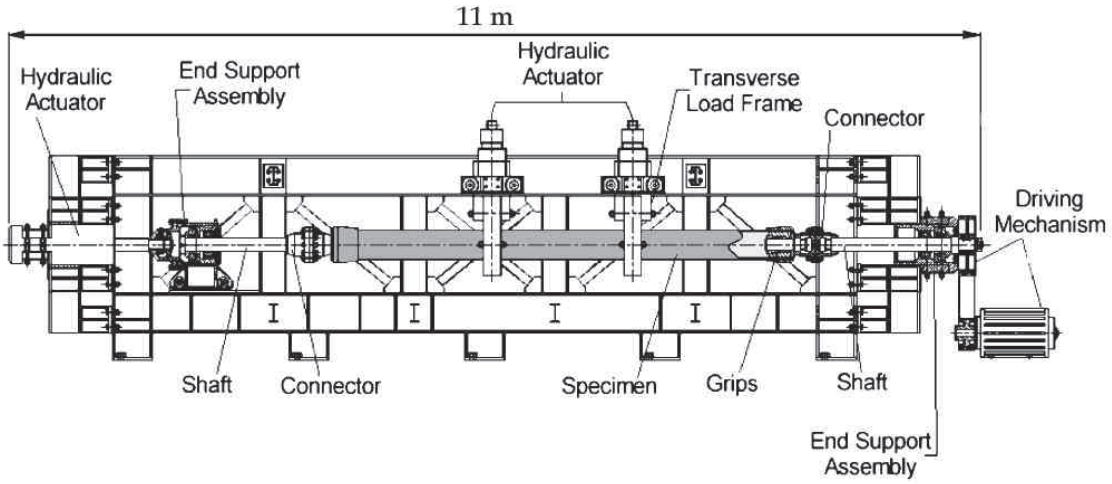

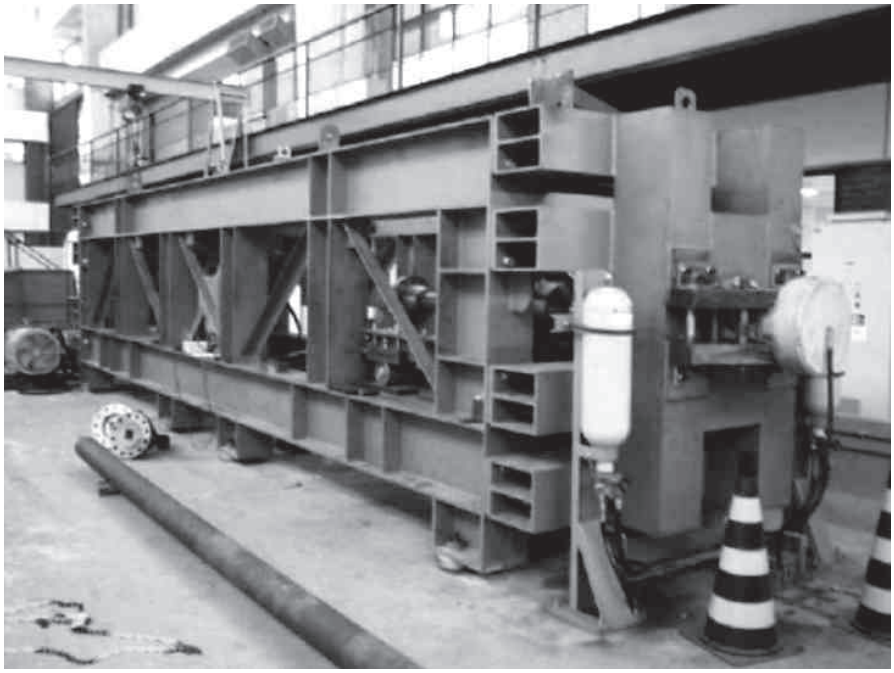

Figure 2.19: Rotating bending fatigue setup. Upper: schematic section view; lower: global setup view [2.89].

Another rotating bending test setup was used by Varma et al. [2.91-92] to test 24" (= 610 mm outer diameter) integral type threaded connections. Interesting to note is that the bending force required to apply a bending stress of 150 MPa on their 24" connection was 138 kN, which is the same force that was needed by Ferjani [2.35] to apply an axial tensile stress of 150 MPa on a sample of only 40 mm diameter. This illustrates the advantages of a bending setup compared to axial tension tests. While in most cases leak detection is used to detect through wall thickness cracks, an increase in deflection amplitude can also be used to stop tests under load control, as is done on the machine of Veidt and Berezovski [2.93].

5.1.4 Resonant bending setups

The dynamics of resonant bending fatigue setups is completely different compared to conventional types. Where in conventional setups, the testing frequency is depending on the flow rates of the hydraulic equipment, the testing frequency in a resonant bending setup depends on the natural frequency of the tested pipe. The value of this natural frequency is dependent on the pipe dimensions (outer diameter, wall thickness and length), the pipe material and additional masses attached to the pipe.

Although it is hard to determine at what exact time the first resonant bending fatigue setup was taken into service, because most of them are owned by private companies that are reluctant to publish test data, it can be stated that the first experiments on large-scale pipelines using pipe resonance where carried out in 1983 [2.94]. In that project, a pipe testing site was constructed in the Severn estuary near Oldburry, UK. The site was selected for the high tidal range of the estuary. Near high water the necessary hydrodynamic flow conditions could be achieved with a sufficient depth to avoid free surface wave effects and at low tide, access was possible allowing the installation of the pipes to be tested. At this location, a pipeline with a free span length of 30 to 50 m could be placed in the tidal current, which excitated the pipe at its natural frequency. This way the total pipeline was subjected to a fatigue load. Tests were carried out on 20" (= 510 mm diameter) pipes with a wall thickness of 12 mm. The natural frequency of this pipe with a free span length of 50 m was 0.35 Hz.

As such large-scale experiments are very expensive and as they require a location with specific conditions, during the last two decades resonant bending fatigue setups have been developed for use in laboratory conditions. Instead of using flow induced vibrations, these setups generally use a rotating excentric mass as a source of excitation. An example of a typical resonant bending setup, used for testing riser welds, is shown in Figure 2.20. As can be seen in this picture, the pipe is supported at two points, which are the nodes of the natural waveform developed by an excitation force introduced by an excentric drive unit at the right. At the left a counterweight is added to obtain a symmetric bending mode.

Figure 2.20: Resonant bending fatigue setup [2.95].

Although a reasonable amount of publications are available, reporting on experimental results obtained by resonant bending fatigue testing, the actual tests are performed by a limited number of private research institutions. Additionally, little information is given about the constructional aspects of the setups which are in general more complex than conventional test rigs. Nevertheless, resonant bending fatigue testing is less energy and time consuming than the latter.

The Welding Institute (TWI) in the UK uses seven resonant bending setups, accommodating diameters in the range of 4" to 36" (100 mm to 914 mm) [2.96]. They have the capability of additionally applying a constant axial tension of 125 MPa to pipes with a diameter of 324 mm [2.97]. The applicable stress ranges from 50 to 400 MPa.

Stress Engineering, located in Houston Texas, explores six resonant bending test setups suitable for a diameter range from 16 mm to 914 mm at stress ranges from 35 MPa to 350 MPa [2.98].

Other institutions using one or more resonant bending setups are Vallourec and Mannesmann Tubes [2.34], Tenaris [2.99] and EWI [2.95]. All these institutions use these setups to perform validation tests for industrial applications. Hence welded pipes or threaded pipe connections are merely tested until leak appears but no additional instrumentation is present and no elaborate studies on the fatigue behaviour, for example the influence of the crack propagation on the dynamic response of the pipe in the setup, are carried out.

Only one academic institution, the University of Pisa, Italy has developed resonant bending fatigue setups. One of their two setups is comparable to that shown in Figure 2.20 and is designed for testing aluminium drill pipes at a maximum stress range of 200 MPa [2.24]. Next to this, they developed a particular type of resonant bending setup for testing steel drill pipes with an outer diameter between 88 and 170 mm. This setup is shown in Figure 2.21

and contains two couples of counter-rotating eccentric masses at the top of two bending arms. The steel drill connection specimen is supported by springs which allow in plane displacements. The rotating masses induce inertial forces on the specimen and alternating bending is applied to the specimen. In contrast to the other described resonant fatigue test rigs, this setup does not subject the specimen to rotating bending. By changing the phase difference between the couples of rotating masses, the bending amplitude can be changed. The test rig operates at a frequency near the natural frequency of the system which means that the resulting bending moment is much larger than that calculated by the forces F_1 and F_2.

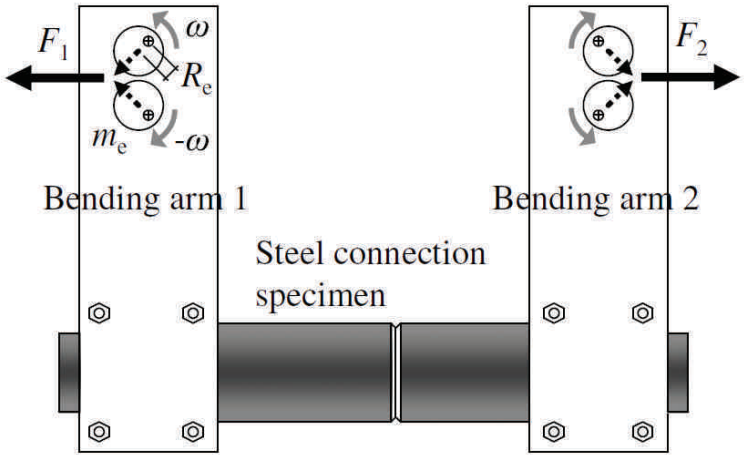

Figure 2.21: Short resonant fatigue setup of Bertini et al. [2.101].

5.2 Available experimental data

The amount of published experimental fatigue test data is limited since most tests are carried out by private research institutions for industrial costumers. The published test data of fatigue tests on threaded pipe connections is summarized in Table 2.3. Results of 175 tests on 18 different connection types and sizes were found. These tests were carried out on the full scale test setups described in the previous section. Considering that there exist more than 60 different casing connection types only [2.100], the total number of 175 available tests can indeed be called very limited. It is mentioned in literature that some research institutions have much larger experimental databases; V&M tubes has performed over 200 experiments on full scale T&C connections [2.107], but the sheer amount of these results has never been published.

In Figure 2.22 the data points of tests that resulted in failure are plotted. Test samples that were subjected to a number of cycles without damage are not included. This way 121 results could be plotted. The S-N graph is given for a load ratio $R = -1$. If the tests were carried out at a different load ratio, the mean stress effect was corrected for by using Eq. (2.5). As a reference two design curves were added in Figure 2.22, the ASME-B31 design curve (2.21)

for threaded pipe joints and the DNV-B curve (2.23). As can be seen from the graph, the ASME-B31 curve is overly conservative since all data points lay considerably above the design curve. This is mainly caused by the factor of safety of 2 on the stress that was used to construct the curve. Next to this, most data points are located below the DNV-B curve. The points closest to and exceeding this curve come from experiments of premium connections that contain several of the patented features discussed in section 3.2.

When the stress amplitude is expressed as a percentage of the material's ultimate tensile stress, the data points can be compared to the BS7608 design curve. This is done in Figure 2.23. It can be seen that the design curve can be adequately used as a conservative lower bound for the stress life data. Only two of the 121 data points are located below the line. This is acceptable since the probability of survival provided by the design curve is supposed to be 95 %. Nevertheless, it is obvious that the fatigue life of a joint is highly dependent on the connection design. For example at a stress amplitude of 10 % of the ultimate tensile strength, fatigue lives are found between 90 000 and $13 \cdot 10^6$ cycles or a difference with a factor 144. Hence, using one single design curve to evaluate threaded connections, will lead to conservative results for the more advanced connection types.

When the data of Table 2.3 is studied more in detail it can be seen that more than half of the tests (99) comprise tests on drill pipe or drill collar connections, 40 tests were carried out on riser connections, 21 on casing and 15 on threaded connections for offshore columns. In many cases, the number of performed tests on the studied connection type or size is limited to 3 or 4. These tests are only performed as a validation against a modelling background or specific standards. This data is not sufficient to construct an S-N curve. Therefore only the studies where 10 or more tests are performed and where the stress and fatigue life data is provided, are discussed more in detail. The six resulting S-N relations are summarized in Table 2.4 and the mean curves for a stress ratio of $R = -1$ are graphically presented in Figure 2.24. The mean curves where determined by finding the best fit using regression analysis.

The high number of experimental tests on drill strings can be explained by the fact that this is the most common application for threaded pipe connections and fatigue loads cannot be avoided during their service. It should be noted here that the API has two main categories of drill pipe connections described by API Spec 7. First of all there is the *Regular style* (REG) and second there is the *Numbered Connection style* (NC). Both contain a thread type with round roots and truncated crests, but the truncation of the NC style is larger than the REG style. Two S-N relations can be derived for NC style connections. Firstly Bertini et al. [2.101] tested full scale NC50 joints in the short resonant fatigue setup shown in Figure 2.21. Secondly Ferjani [2.35] performed a range of tests on a scale model of an NC type drill joint. Both S-N relations are compared in Figure 2.24.

Connection type	Connection size	Number of tests	Source
Drill pipe NC50	168.8 mm	10	Bertini [2.101]
Drill pipe NC50	168.8 mm	8	Brennan [2.8]
Drill pipe NC50	168.8 mm	4	Miscow [2.89]
Drill pipe NC50	168.8 mm	3	Plácido [2.32]
Drill pipe NC26	88.9 mm	8	Bertini [2.24], [2.101]
Drill pipe NC type scale model	40 mm	14	Ferjani [2.35]
Drill pipe 6 5/8 REG	168.8 mm	6	Brennan [2.8]
Drill pipe NQ integral flush	70 mm	18	Veidt [2.93]
Drill pipe ADP-STJ acc. ISO	147 mm	7	Bertini [2.24], [2.101]
Drill collar NC type	152.4 and 168.8 mm	21	Weiner [2.102]
Casing T&C premium	7" (177.8 mm)	3	Santi [2.103]
Casing T&C GB-CD	4.5" (114.3 mm)	2	GB Tubulars [2.104]
Casing T&C GB-CD	7" (177.8 mm)	4	GB Tubulars [2.104-105]
Casing upset premium	7" (177.8 mm)	5	Santi [2.103]
Casing upset premium Tenaris PJD	4.5" (114.3 mm)	4	Carcagno [2.88]
Casing T&C VAM	140 mm	3	Newport [2.6] and Brennan [2.8]
Riser T&C Hydril 500	16" (406.4 mm)	9	Hydril [2.106]
Riser T&C VAM Top FE	7", 13-3/8" and 16" (177.8, 339.7 and 406.4 mm)	31	Sches [2.34] and Schilling [2.107]
Offshore structural column XLSYS	24" (610 mm)	15	Varma [2.91-92]

Table 2.3: Overview of published experimental fatigue data of threaded pipe connections

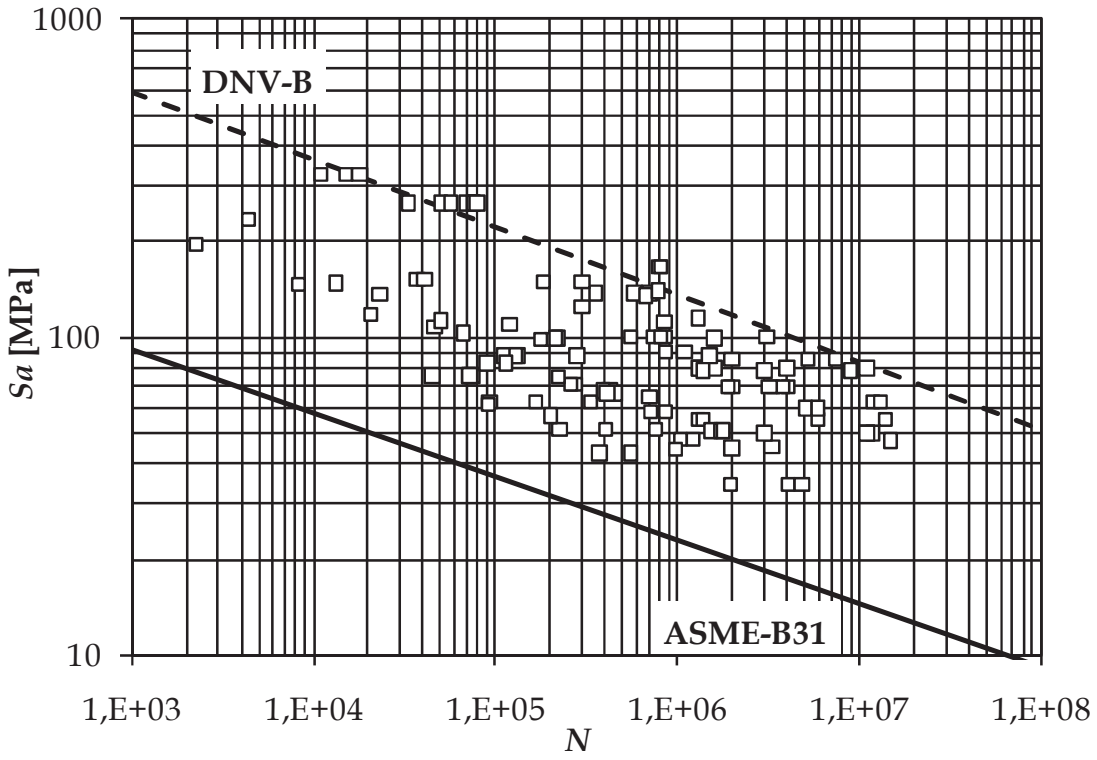

Figure 2.22: Summary of published fatigue life data for threaded pipe connections, compared to the ASME-B31 and DNV-B design curves (*R = -1*).

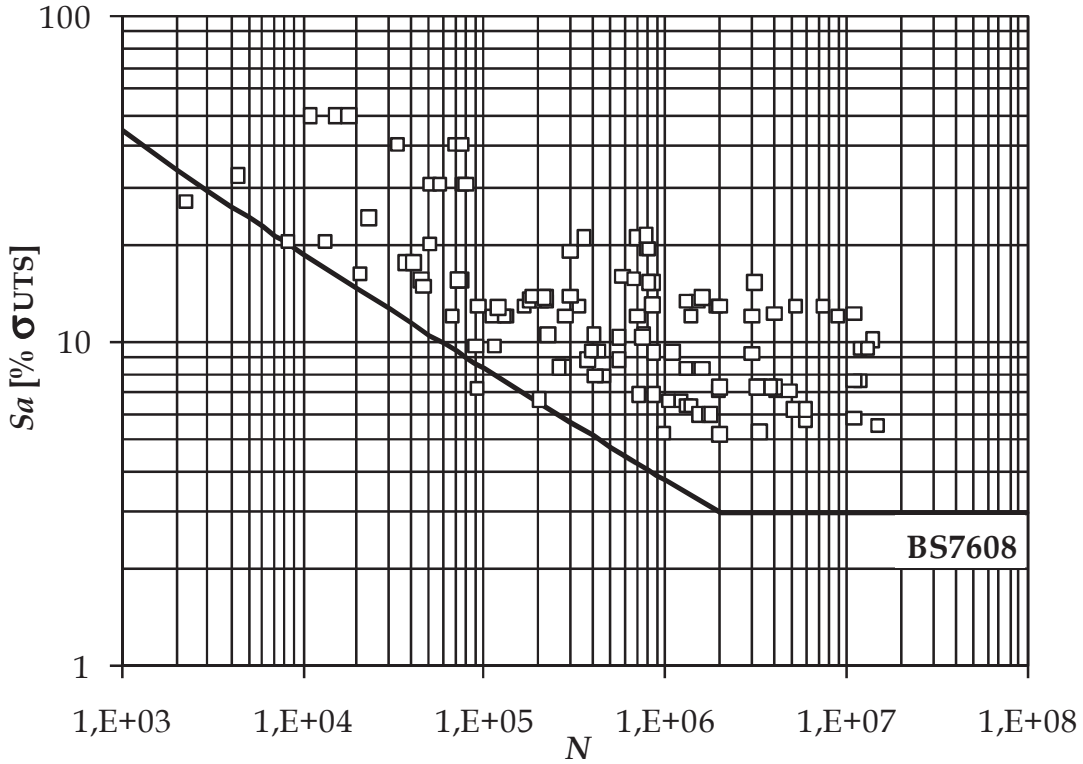

Figure 2.23: Summary of published fatigue life data for threaded pipe connections, compared to the BS7608 (*R = -1*).

Connection Type	S-N relation	Material	UTS [MPa]	Source
Drill pipe NC50	$S_a = 236.3 \cdot N^{-0.2339}$	AISI 4145	965	Bertini [2.101]
Drill pipe NC type scale model	$S_a = 69.4 \cdot N^{-0.1698}$	42CrMo4	850	Ferjani [2.35]
Drill pipe NQ integral flush	$S_a = 124.4 \cdot N^{-0.1938}$	alloy steel	725	Veidt [2.93]
Riser T&C VAM Top FE	$S_a = 542.7 \cdot N^{-0.25}$	API L80	655	Sches [2.34] and Schilling [2.107]
Riser T&C VAM Top FE	$S_a = 412.6 \cdot N^{-0.25}$	API P110	862	Sches [2.34]
Offshore structural column	$S_a = 160.6 \cdot N^{-0.2118}$	API X56	490	Varma [2.91-92]

Table 2.4: Overview of S-N relations, mean curves at $R = -1$, of published experimental fatigue data of threaded pipe connections

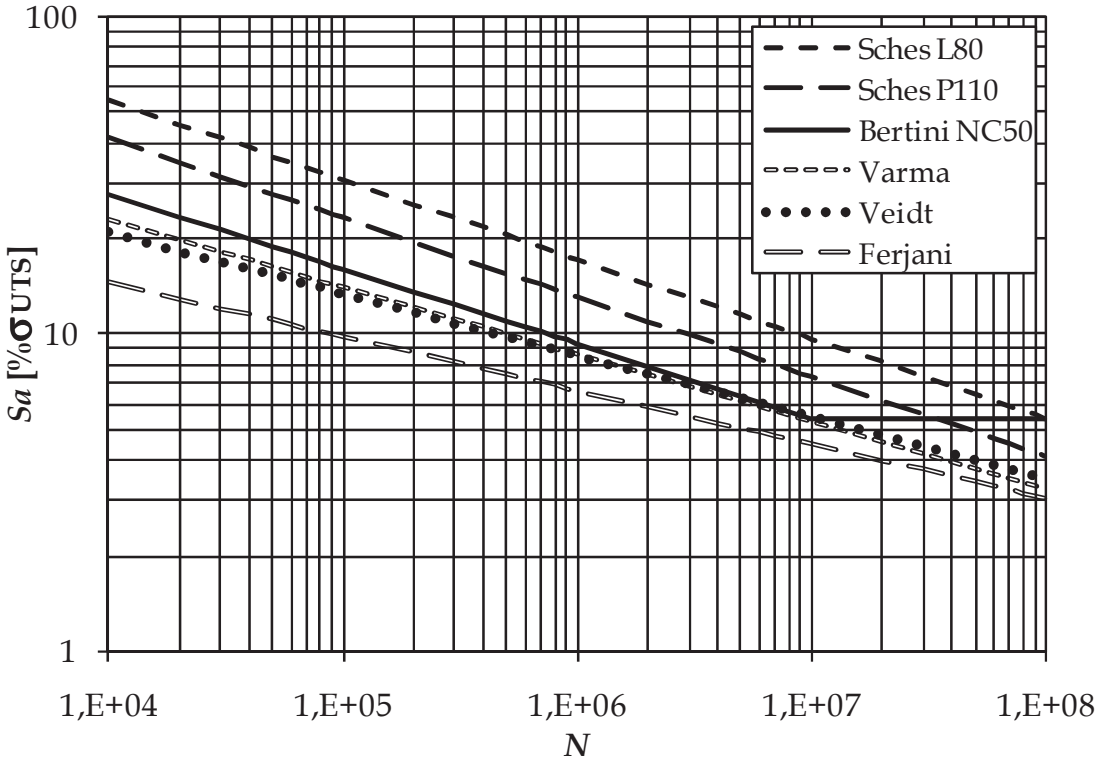

Figure 2.24: Graphical representation of the mean S-N curves of Table 2.4.

It should be noted that the curve obtained by Ferjani is considerably lower than the full-scale curve of Bertini et al. A cause for this might be found in the tolerances of the connection that cannot be scaled.

In most studies no fatigue limit is used, only Bertini et al. assumed one at 10^7 cycles. Except for this fatigue limit, the results obtained by Veidt et al. [2.93] for an ISO NQ drill pipe are comparable to that of Bertini et al. Also the results obtained by Varma et al. [2.91-92] for offshore columns compare very well to the curves of Veidt et al. and Bertini et al.

By far the most extensive study if it comes to number of experiments, was published by Sches et al. [2.34]. They performed tests on a premium riser connection of different sizes and made in two different steel grades. In total 18 connections made out of API L80 steel and 10 made out of API P110 steel were tested until failure. For both steel grades a relation was derived in their publication according to the DNV standard that prescribes a slope of the S-N curve of 0.25. It should be noted that their design of the premium connection uses a combination of patented features to obtain an improved fatigue life. The threads were optimized by features similar to the patent of Verdillon [2.60] (see Figure 2.5.e). The connection contains a waisted groove such as described in [2.55] and shown in Figure 2.4.e. The bending stresses in the threads are reduced by using a metal-to-metal seal that transfers part of the bending stress. Next to this the selected material has improved fatigue properties and the connection size range is designed in such a way that there are no size effects in the available diameter range, as can be seen by comparison with the results of the 13-3/8″ size connection presented by Schilling et al. [2.107].

6 Summary and conclusions

In this chapter an overview has been given of the current knowledge on fatigue behaviour of threaded pipe connections. During the last decades it is been tried to improve the fatigue life by changing the connections global geometry or changing local features such as the thread type or changing the interference over the engaged thread length. This resulted in several patented designs. However, it is impossible to make a qualitative nor a quantitative comparison between these configurations based on published data.

To analyse threaded connections, numerical tools can be used. An overview is given of different analysis techniques for threaded connections that were used in the past. Finite element modelling has been identified as the most commonly used method to calculate stress and strain distributions over the connections. 2D axisymmetric models are preferred due to their calculation efficiency compared to full 3D models. However it is of uppermost importance to take into account the non-linearities of material behaviour and contact conditions. If not, the obtained data will not represent the real situation. Even though some basic parameter studies were carried out using

previous modelling techniques, no parametric studies using finite element models have been published. The finite element model developed in the frame of the present research work will be presented in Chapter 6. This model is constructed in such a way that parametric studies on a connection are possible to study the influence of the connection's properties on its fatigue life.

To perform elaborate fatigue analyses different fatigue models are available which use stresses or strains obtained by the finite element models. The stress-life approach is chosen to present the data obtained by experimental testing. This allows these data to be easily compared to existing results from literature and design curves from standards. However, due to the fact that this approach does not allow to take into account the complex stress distribution at the threads, additional multiaxial fatigue analysis will be carried out.

Since every modelling technique is based on some assumptions and simplifications, experimental tests remain to play an important role in the design process of threaded connections. Different types existing experimental setups for fatigue testing of threaded pipe connections are compared. They are categorized by the way the load is introduced on the pipe.

The amount of published experimental data is rather limited. Hence, in the present study a strong experimental basis has to constructed. For this reason fatigue tests are carried out in four-point bending setups on two different connection sizes. Additionally, to be able to test even bigger connection sizes an additional setup is developed. From the existing experimental test rigs the resonant bending fatigue setup is identified as the most practical setup due to its low energy consumption and fast testing speed. The developed setup together with its working principles are presented in Chapter 4. As most existing resonant bending setups have limited instrumentation, Chapter 3 is dedicated to crack growth measurement techniques.

References

[2.1] Stromeyer, C.E., Stress Distribution in Bolts and Nuts, Trans. Inst. Naval Architects, 60, 112-121, 1918 (as referred in Newport [2.6] p.21).

[2.2] Dragoni, E., Effect of nut geometries on screw thread stress distribution: Photoelastic results, Journal of Strain Analysis for Engineering Design, 27(1), 1-6, 1992.

[2.3] Hetényi, M., The Distribution of Stress in Threaded Connections, Proc. Soc. Exp. Stress Analysis, 1(1), 147, 1943 (as referred in Peterson [2.4] p.388).

[2.4] Pilkey, W.D., Peterson's Stress Concentration Factors, Wiley Interscience, New York, second ed., 1997.

[2.5] Glinka, G., Dover, W.D., Topp, D.A., Fatigue Assessment of Tethers, Inst. Mech. Eng., Int. Conf. on Fatigue and Crack Growth in Offshore Structures, 187-198, 1986.

[2.6] Newport, A., Stress and Fatigue Analysis of Threaded Tether Connections, PhD Dissertation, Dept. of Mech. Eng. University College London, 1989.

[2.7] Newport, A., Glinka, G., Concentration of Cyclic Stresses in Preloaded Threaded Connections, Journal of Engineering Mechanics, 117(6), 1257-1273, 1991.

[2.8] Brennan, F.P., Fatigue and Fracture Mechanics Analysis of Threaded Connections, PhD Thesis, Dept. of Mech. Eng. University College London, 1992.

[2.9] Zhao, H.,Kuang, Z.B.,Li, Z.H., Stress-intensity factor for a semi-elliptical surface crack at the thread root of a screwed-pipe joint, Computers & Structures, 59(3), 419-424, 1996.

[2.10] Bahai, H., A parametric model for axial and bending stress concentration factors in API drillstring threaded connectors, Int. J. of Pressure Vessels and Piping, 78(7), 495-505, 2001.

[2.11] Assanelli, A.P., Dvorkin, E.N., Finite-Element Models of OCTG Threaded Connections, Computers & Structures, 47(4), 725-734, 1993.

[2.12] MacDonald, K.A., Deans, W.F., Stress Analysis of Drillstring Threaded Connections Using The Finite Element Method, Engineering Failure Analysis, 2(1), 1-30, 1995.

[2.13] MacDonald, K.A., The effectiveniss of stress relief features in austenitic drillcollar connections, Engineering Failure Analysis, 3(4), 267-279, 1996.

[2.14] Bahai, H., Glinka, G., Esat, I.I., Numerical and experimental evaluation of SIF for threaded connectors, Engineering Fracture Mechanics, 54(6), 835-845, 1996.

[2.15] Hilbert, L.B., Kalil, I.A., Evaluation of Premium Threaded Connections Using Finite Element Analysis and Full-Scale Testing, IADC/SPE Drilling Conference, SPE 23904, 563-580, 1992.

[2.16] Assanelli, A.P., Xu, Q., Benedetto, F., Johnson, D.H., Dvorkin, E.N., Numerical/experimental analysis of an API 8-round connection, Journal of Energy Resources Technology-Transactions of the ASME, 119(2), 81-88, 1997.

[2.17] Dvorkin, E.N., Assanelli, A.P., Toscano, R.G., Performance of the QMITC Element in Two-Dimensional Elasto-Plastic Analysis, Computers & Structures, 58(6), 1099-1129, 1996.

[2.18] Axisymmetric analysis of a threaded connection, Abaqus 6.6 Example Problems Manual, section 1.1.19, 2006.

[2.19] Curley, J.A., Prinja, N.K., Failure Investigation of an offshore drilling component, ABAQUS Users' Conference, Chester UK, 1999.

[2.20] Dvorkin, E.N., Toscano, R.G., Finite element models in the steel industry: Part II: Analysis of tubular products performance, Computers & Structures, 81(8), 575-594, 2003.

[2.21] Yuan, G., Yao, Z., Han, J., Wang, Q., Stress distribution of of oil tubing thread connection during make and break process, Engineering Failure Analysis, 11, 537-545, 2004.

[2.22] Yuan, G., Yao, Z., Wang, Q., Tang, Z., Numerical and experimental distribution of temperature and stress fields in API Round threaded connection, Engineering Failure Analysis, 13(8), 1275-1284, 2006.

[2.23] Kristensen, A.S., Toor, K., Solem, S., Finite element analysis of jar connections: Modeling considerations, Journal of structural Mechanics, 3, 2005.

[2.24] Bertini, L., Beghini, M., Santus, C., Baryshnikov A., Fatigue on drill string conical threaded connections, test results and simulations, 9th Int. Fatigue Congress, FT588, 2006.

[2.25] Santus, C., Bertini, L., Beghini, M., Merlo, A., Baryshnikov, A., Torsional strength comparison between two assembling techniques for aluminium drill pipe to steel joint connection, Int. J. of Pressure Vessels and Piping, 86, 177-186, 2009.

[2.26] Takano, J., Yamaguchi, M., Kunishige, H., Development of Premium Connection "KSBEAR" for withstanding high compression, high external pressure, and severe bending, Kawasaki Steel Technical Report, 47, 14-22, 2002.

[2.27] Premium Joint, "JFEBEAR" for OCTG, JFE Technical Report, 7, 50-54, 2006.

[2.28] Zhong, A., Thread connection response to critical pressures, Abaqus users' conference, Paris, France, 690-706, 2007.

[2.29] Sugino, M., Nakamura, K., Yamaguchi, S., Daly, D., Briquet, G., Verger, E., Development of an innovative high-performance premium threaded connection for OCTG, Offshore Technology Conference, OTC20734, 2010.

[2.30] Tafreshi, A., SIF evaluation and stress analysis of drillstring threaded joints, Int. J. of Pressure Vessels and Piping, 76, 91-103, 1999.

[2.31] Shahani, A.R., Sharifi, S.M.H., Contact stress analysis and calculation of stress concentration factors at the tool joint of a drill pipe, Materials and Design, 30(9), 3615-3621, 2009.

[2.32] Plácido, J.C.R., Valadão de Miranda, P.E., Netto, T.A., Pasqualino, I.P., Miscow, G.F., de Carvalho Pinheiro, B., Fatigue analysis of aluminum drill pipes, Materials Research, 8(4), 409-415, 2005.

[2.33] Chen, J.J., Shih, Y.S., A study of the helical effect on the thread connection by three dimensional finite element analysis, Nuclear Engineering and Design, 191(2), 109-116, 1999.

[2.34] Sches, C., Desdoit, E., Massaglia, J., Fatigue Resistant Threaded and Coupled Connectors for Deepwater Riser Systems: Design and Performance Evaluation by Analysis and Full Scale Tests, ASME 27th International Conference on Offshore Mechanics and Arctic Engineering, OMAE2008-57603, 2008.

[2.35] Ferjani, M., Intégration des phénomènes dynamiques dans l'analyse en fatigue des garnitures de forage, PhD Thesis, Ecole Polytechnique, Palaiseau, France, 2006.

[2.36] ISO 10407-1, Petroleum and natural gas industries – Drilling and production equipment – Part 1: Drill stem design and operating limits, International Organization for Standardization, 2004.

[2.37] Ertas, A., Cuvalci, O., Carper, H.J., Determination of Friction Characteristics of J-55 OCTG Connections Lubricated with Environmental Safe Thread Compound, Tribology Transactions, 42(4), 881-887, 1999.

[2.38] Shoji, Y., Sawa, T., Stress concentration at the root of bolt thread, ASME Pressure Vessels and Piping Conference, PVP2010-25857, 2010.

[2.39] Morse, J.O., Wrought Iron Coupling for Pipe Sections, United States Patent, US 263943, 1882.

[2.40] Bole, W.A., Pipe Coupling, United States Patent, US 332184, 1885.

[2.41] Bole, W.A., Method of Coupling Pipes, United States Patent, US 331940, 1885.

[2.42] Bole, W.A., Tube Expander, United States Patent, US 319879, 1885.

[2.43] Higbee, C.A., Screw Union or Coupling, United States Patent, US 597000, 1898.

[2.44] Higbee, C.A., Screw Coupling, United States Patent, US 658087, 1900.

[2.45] Pistole, H., Weiner, P.D., Pipe coupling having holding means responsive to high internal fluid pressure, United States Patent, US 3100657, 1963.

[2.46] Weiner, P.D., High pressure, low stress tubular connection, United States Patent, US 3497246, 1970.

[2.47] Stone, F., Beach, R., Stone, A.L., Well Pipe Joint, United States Patent, US 2239942, 1941.

[2.48] Webb, S., Sealed Threaded Pipe Joint, United States Patent, US 2772102, 1956.

[2.49] Ahlstone, A.G., Rigid Connector for Pipe and Method of Making the Same, United States Patent, US 4124229, 1978.

[2.50] Van Der Wissel, H.T., Box-and-Pin Type Threaded Joint, United States Patent, US 3050318, 1962.

[2.51] Bodine, A.G., Sonic well pump tubing string, United States Patent, US 2992613, 1961.

[2.52] Schreier, K., Jonction filetée, notamment pour tige de forage, French Patent, FR 1317815, 1963.

[2.53] Galle, E.M. Sr., Galle E.M. Jr., Threaded Connector for Pipe, United States Patent, US 6494499 B1, 2002.

[2.54] De Lange, R.W., Evans, M.E., Threaded and coupled connection for improved fatigue resistance, United States Patent, US 6609735 B1, 2003.

[2.55] Verdillon, L., Fatigue-resistant threaded bevelled tubular element, United States Patent, US 6752436 B1, 2004.

[2.56] Saunders, D.D., Kalsi, M.S., Chen, G.S., Tool joint, United States Patent, US 4549754, 1985.

[2.57] Gunderson, R.H., Burns, J.Q., Fox, S.A., Fatigue-resistant threaded connector, United States Patent, US 4892337, 1990.

[2.58] De Lange, R.W., Evans, E., Buster, J.L., Threaded Connection for Enhanced Fatigue Resistance, United States Patent, US 5931511, 1999.

[2.59] Olivier, H.P., Connection, United States Patent, US 6485063 B1, 2002.

[2.60] Verdillon, L., Threaded tubular element for fatigue resistant threaded tubular joint and resulting threaded tubular joint, United States Patent, US 6729658 B2, 2004.

[2.61] Pallini, J.W., Munk, B.N., Riha, J.B., Lyle, R.D., Threaded Pipe Connector, United States Patent, US 2007/0063517 A1, 2007.

[2.62] Ernst, H.A., Villasante, J.A., Hollow Sucker Rod Connection with Second Torque Shoulder, United States Patent, US 7431347 B2, 2008.

[2.63] Noel, T., Roussie, G., Fatigue-resistant threaded component for tubular threaded joint, United States Patent, US 751534, 2009.

[2.64] Toscano, R.G., Di Toro N.H.M., Sucker Rod Connection with Improved Fatigue Resistance Formed by Applying Diametrical

Interference to reduce Axial Interference, United States Patent, US 7735879 B2, 2010.

[2.65] Knight, M.J., Brennan, F.P., Dover, W.D., Controlled fatigue design of drillstring threaded connections, Fatigue and Fracture of Engineering Materials and Structures, 26, 1081-1090, 2003.

[2.66] Benedict, D., Düber, H., Flörke, H., Modular Thread Connection With High Fatigue Resistance, United States Patent, US 7150479 B2, 2006.

[2.67] Pallini, J.P., Lyle, R.D., Munk, B.N., Threaded Connector, United States Patent, US 6478344 B2, 2002.

[2.68] Church, K.L., Thread form with multifaced flanks, United States Patent, US 6254146 B1, 2001.

[2.69] Santus, C., Fretting fatigue of aluminum alloy in contact with steel in oil drill pipe connections, modeling to interpret test results, International Journal of Fatigue, 30, 677-688, 2008.

[2.70] Nisida, S., Urashima, C., Masumoto, H., Screwed connection having improved fatigue strength, United States Patent, US 4189975, 1980.

[2.71] Zahavi, E., Life expectancy of machine parts: fatigue design, CRC Press, USA, 1996.

[2.72] Schijve, J., Fatigue of structures and materials, Kluwer Academic Publishers, 2001.

[2.73] Boyer, H.E., Atlas of fatigue curves, American Society for Metals, Ohio, USA, 2003.

[2.74] Mryzglód, M., Zielinski, A.P., Numerical implementation of multiaxial high-cycle fatigue criterion to structural optimization, J. of Theoretical and Applied Mechanics, 44(3), 691-712, 2006.

[2.75] Fares, Y., Chaussumier, M., Daidie, A., Guillot, J., Determining the life of bolts using a local approach and the Dang Van criterion, Fatigue Fract Engng Mater Struct, 29, 588-596, 2006.

[2.76] Abdel Wahab, M.M., Ashcroft, I.A., Crocombe, A.D., Shaw, S.J., Prediction of fatigue thresholds in adhesively bonded joints using damage mechanics and fracture mechanics, J. Adhesion Sci. Technol., 15(7), 763-781, 2001.

[2.77] Rodabaugh, E.C., Comparisons of ASME Code Fatigue Evaluation Methods for Nuclear Class 1 Piping with Class 2 or 3 Piping, US Nuclear Regulatory Commission, NUREG/CR-3243, 1983.

[2.78] ASME B31.3-2002, Process Piping, American Society of Mechanical Engineers, 2002.

[2.79] BS7608:1993, Code of practice for Fatigue Design and Assessment of Steel Structures, British Standards Institution, 1999.

[2.80] API Recommended Practice 7G, Recommended Practice for Drill Stem Design and Operation Limits, American Petroleum Institute, sixteenth edition, 1998.

[2.81] DNV-RP-C203, Recommended Practice: Fatigue Design of Offshore Steel Structures, Det Norske Veritas, 2010.

[2.82] Schneider, R., Wuttke, U., Berger, C., Fatigue analysis of threaded connections using the local strain approach, Procedia Engineering, 2, 2357-2366, 2010.

[2.83] Cetin, A., Härkegard, G., Fatigue life prediction for large threaded components, Procedia Engineering, 2, 1225-1233, 2010.

[2.84] Hasegawa, K., Sakata, K., Miyazaki, K., Kanno, S., Fatigue strength for pipes with allowable flaws and design fatigue curve, International Journal of Pressure Vessels and Piping, 79, 37-44, 2002.

[2.85] Kim, J.W., Park, C.Y., Experimental investigation of the failure behavior of notched wall-thinned pipes, Nuclear Engineering and Design, 236(17), 1838-1846, 2006.

[2.86] Lefevre, A., Waaijenberg, M., Aylwin, E., Triel, H.M., Defect propagation from fatigue loading in 13%Cr pipelines, Pipeline Technology Conference, Ostend 2009-128, 2009.

[2.87] Lourenço, M.I., Netto, T.A., Low cycle fatigue of corroded pipes under cyclic bending and internal pressure, International Pipeline Conference, IPC2010-315710, 2010.

[2.88] Carcagno, G.E., Bufalini, A., Conde, L., Toscano, R., Low SCF Integral Premium Connections for Use in Highly Demanding Casing and Tubing Drilling Operations, Offshore Technology Conference, OTC16566, 2004.

[2.89] Miscow, G.F., de Miranda, P.E.V., Netto, T.A., Plácido, J.C.R., Techniques to characterize fatigue behaviour of full scale size drill pipes and small scale samples, International Journal of Fatigue, 26(6), 575-584, 2004.

[2.90] Netto, T.A., Lourenco, M.I., Botto, A., Fatigue performance of pre-strained pipes with girth weld defects: Full-scale experiments and analyses, International Journal of Fatigue, 30(5), 767-778, 2008.

[2.91] Varma, A.H., Russell, B.W., Wallace, B., Large-scale rotating bending fatigue tests for offshore pipe connections, Experimental Mechanics, 37(2), 147-153, 1997.

[2.92] Varma, A.H., Salecha, A.K., Wallace, B., Russell, B.W., Flexural fatigue behavior of threaded connections for large diameter pipes, Experimental Mechanics, 42(1), 1-7, 2002.

[2.93] Veidt, M., Berezovski, A., Design and application of a drill pipe fatigue test facility, Structural Integrity and Fracture International Conference, 2004.

[2.94] HR Wallingford Ltd, Vibration of Pipeline Spans, Health and Safety Executive - Offshore Technology Information, OTI 92 555.

[2.95] Zelenak, P, Resonance Fatigue Rig, EWI Tech Brief, http://www.ewi.org/, retrieved 24/11/2010.

[2.96] TWI, Variable amplitude fatigue testing of full-scale pipe joints, Connect, 163, 8-8, 2009.

[2.97] Razmjoo, G.R., Hutchens, E.J., Slater, G., Fatigue Performance of Corrosion Resistant Steel Catenary Risers, TWI Proposal, PR5473-2, 2001.

[2.98] Stress Engineering Services, Testing Services Catalog, http://www.stress.com/, retrieved 24/11/2010.

[2.99] Darcis, P., Marines-Garcia, I., Di Vito, L., Richard, G., Ruiz, E., Marqeus, E.C., Dell'Erba, D.N., Armengol, M., Quintanilla, H., Fatigue performance of SMLS SCR girth welds: stress raisers and notch effects, Pipeline Technology Conference, Ostend 2009-042, 2009.

[2.100] 2008-09 Casing Reference Tables, World Oil.

[2.101] Bertini, L., Beghini, M., Santus, C., Baryshnikov A., Resonant test rigs for fatigue full scale testing of oil drill string connections, International Journal of Fatigue, 30, 978-988, 2008.

[2.102] Weiner, P.D., True, M.E., A means of increasing drill collar connection life, Journal of Engineering for Industry, 95, 243-246, 1973.

[2.103] Santi, N. J., Carcagno, G. E., Toscano, R., Premium & Semi-premium Connections Design Optimization for Varied Drilling-with-Casing Applications, Offshore Technology Conference, OTC17221, 2005.

[2.104] GB Tubulars, Test Summary Resonant Fatigue Testing 4-1/2" OD, 11.60 ppf, P-110 GB HB, 7" OD, 23.00 ppf, P-110 GB HB, http://www.gbtubulars.com/, 2009.

[2.105] GB Tubulars, Test Summary Resonant Fatigue Testing 7" OD, 26.00 ppf, P-110 GB CD, http://www.gbtubulars.com/, 2009.

[2.106] Hydril Company, 16" 96.00 & 109.00 lb/ft P-110 Series 500™ Type 563 Fatigue Test for Consumable Drilling Riser Service, Hydril Tech Note, 2002.

[2.107] Shilling, R., Payne, M.L., Massaglia, J., Sches, C., Leyer, J., Pinto, J., High-strength Threaded and Coupled Connectors for Dynamic Riser Applications, SPE International Oil Conference and Exhibition, SPE 108708, 2007.

Chapter 3

Measurement Techniques

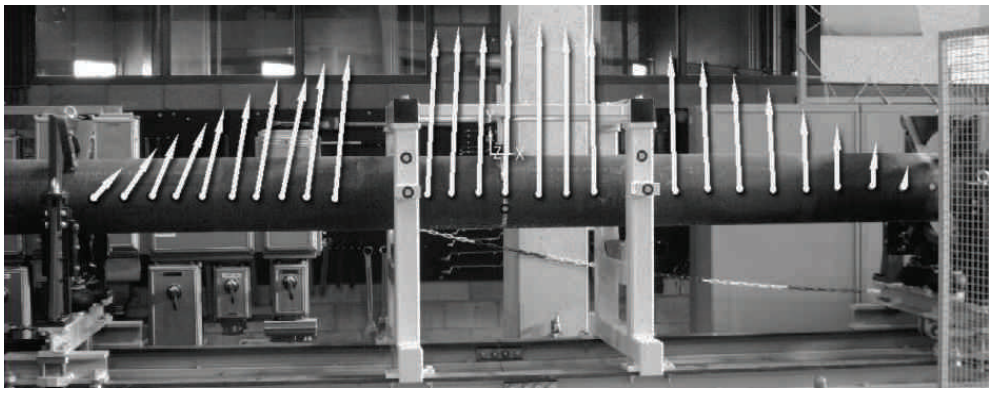

1 Goal

In this chapter an overview is given of measurement techniques that may be suitable for detecting fatigue failure in threaded pipe connections. It is not aimed to give a complete overview of existing crack sizing techniques, as not all techniques can be applied to threaded connections.

Distinction is made between online monitoring and offline crack sizing techniques. From the practical viewpoint, online monitoring techniques are the most interesting as they can be used without interrupting a running fatigue test. However, since fatigue cracks in threaded connections generally initiate at the root of an engaged thread, the region where the crack appears is not directly accessible during the test. This means that with online techniques a crack is generally monitored in an indirect way which might result in a less accurate measurement than in the case of offline crack sizing techniques. However, for the latter a running test has to be stopped and the connection disassembled. This process can have an influence on the fatigue crack growth since the make-up stress is redistributed during consecutive assembly and disassembly steps.

Additional attention is given to other measurement techniques generally not used for crack sizing purposes, but which are used during the current research.

In the last section of this chapter a final comparison between the techniques is made and the techniques are selected that will be used in this study for monitoring fatigue damage in the resonant bending setup described in Chapter 4 and during the experiments described in Chapter 5. Although it is beyond the scope of this project to develop new fatigue crack sizing techniques, three online measurement techniques will be applied to threaded connections for the first time.

2 Overview of crack inspection techniques

2.1 Online crack monitoring

2.1.1 Leak detection

To detect a through wall thickness crack in a tubular specimen, leak detection can be used. This is done by closing both ends of the specimen and applying a certain internal pressure with a fluid or gas (in most cases respectively water or air). The internal pressure is then monitored with a pressure gauge. When a sudden pressure drop is detected, a fatigue crack has propagated through the specimen's wall thickness, creating a leak. Due to its simplicity this method is common practice for fatigue testing of both threaded and welded pipes and it is used in most experimental studies described in the

previous chapter. The only downside of this method is that it only provides information about the specific moment that the through wall thickness crack appears. It does not deliver any additional information on the crack growth rate while penetrating the pipe wall, nor does it give any measure for the actual crack length or shape.

2.1.2 Crack opening measurement

With crack opening measurements, the propagation of a fatigue crack can be monitored continuously. This technique is widely used for the characterisation of material fatigue crack growth properties and adopted by several standards. As an example the so-called *compact tension* or CT specimen, as described in the ASTM E647 designation [3.1], is shown in Figure 3.1. This kind of specimen contains a machined notch at the root of which a fatigue crack will initiate. During the fatigue test the crack opening δ_o is measured using a clip gauge or linear variable displacement transducer (LVDT). To relate the measured crack opening to the crack depth a, the compliance method has to be used. This method is based on analytical solutions, in which the crack depth is a function of the ratio of crack opening to applied load. However, this analytical solution only exists for standard test specimens so no direct method is available to translate measured crack opening values to crack size in a threaded connection. Nevertheless, crack opening measurements have been successfully used on non-standard tubular specimens to provide a qualitative indication of the crack growth rate e.g. to monitor fatigue propagation in pipeline welds [3.2].

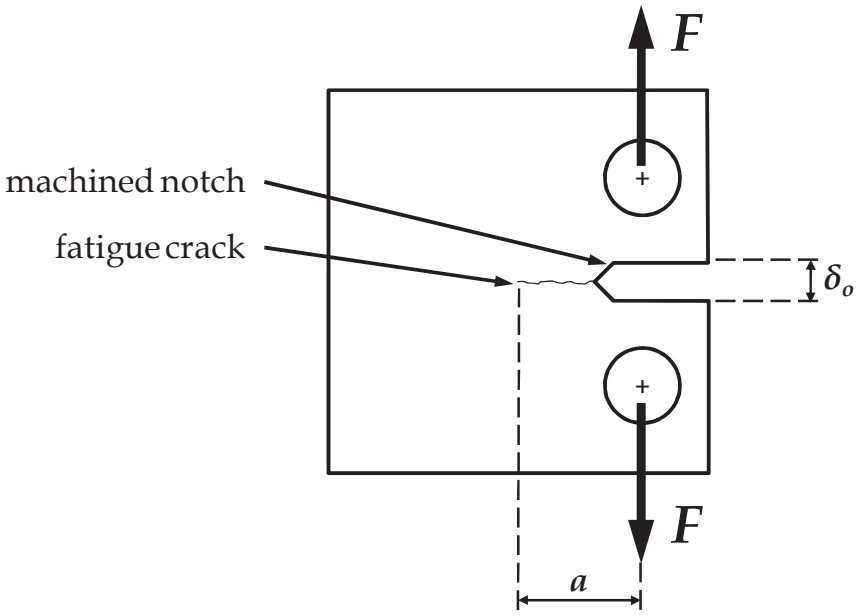

Figure 3.1: Compact tension specimen with crack opening measurement.

2.1.3 Ultrasonic inspection

Ultrasonic inspection is a well established crack sizing technique and can be applied to threaded connections [3.3]. During a measurement an ultrasonic signal is pulsed into a test specimen. When these pulses encounter a surface, e.g. an edge or a thread, they are reflected and captured by the same transducer. This is schematically illustrated in Figure 3.2. If a fatigue crack appears, an extra surface is created on which the pulses are reflected. By monitoring the changes in the reflected signals, the crack growth can be quantified. As the transducer can be placed outside the thread contact zone, the connection can remain coupled. With conventional ultrasonic testing methods it is difficult to distinguish flaws from the signals reflected by the different threads. Therefore, advanced signal processing is necessary to make ultrasonic testing applicable for online monitoring of fatigue crack growth. Additionally, the test should be paused since local displacements due to a variable load can introduce inaccurate readings. Nevertheless, this technique can be considered as an online measuring method since there is no need to remove the threaded connection from the test rig.

Although this technique exists and its feasibility was demonstrated by Suh et al. [3.3] by sizing cracks in bolts with a minimum depth of 0.5 mm and accuracy of 0.2 mm, there exists no off-the-shelf equipment to implement this technique to threaded pipe connections. Consequently, this technique is not applied in this study.

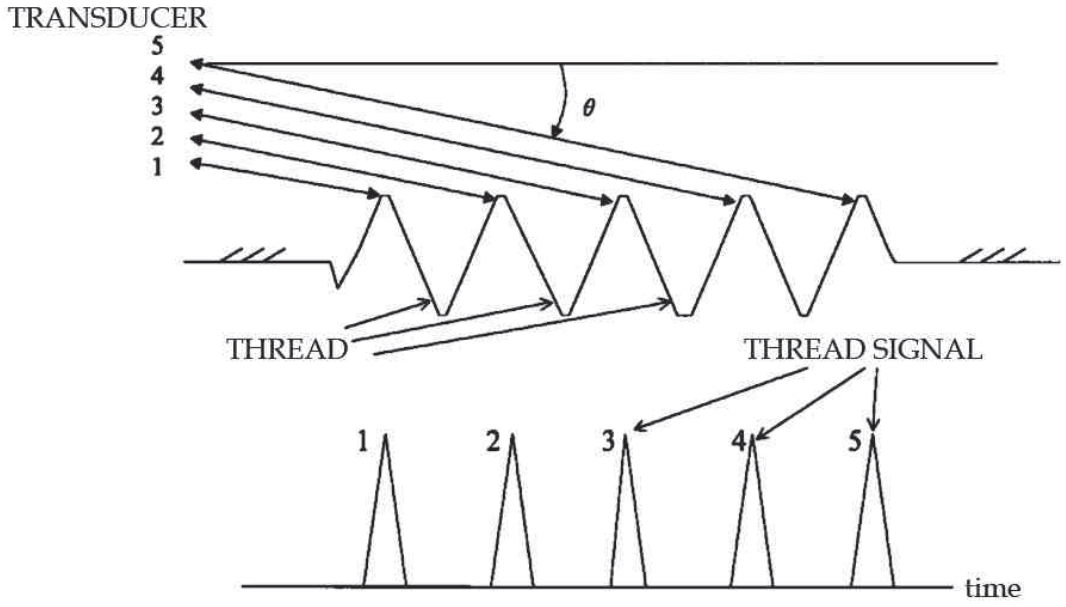

Figure 3.2: Ultrasonic inspection technique for bolts [3.3].

2.1.4 Modal analysis

Damage tends to reduce a structure's stiffness and as a consequence also its eigenfrequencies are reduced. With knowledge of these changes it becomes

possible to determine the extent of cracks or damage in the structure. When also changes in the mode shapes are analysed, both crack size and crack location can be possibly determined [3.4]. In order to use this technique in practical applications, the modal accelerations or modal strains should be measured with respectively accelerometers or modal strain sensors. These sensors should be attached at different locations over the test specimen.

In classical modal analysis, the structure of interest is excitated by one or more measured dynamic forces. The response of the structure to these forces is recorded and the modal parameters in the frequency range of interest are extracted from the analysed data. During the test, the structure is essentially isolated from its operating environment and tested in laboratory conditions. Due to this isolation, the excitation and the boundary conditions may therefore differ significantly from those of a structure's real-life operation. Next to this, these methods are in general less suitable for large structures, since it is very difficult, if not impossible, to create laboratory conditions for testing. As an alternative, output-only or *operational modal analysis* (OMA) techniques have been developed [3.5]. They extract the modal parameters from the dynamic response to ambient forces and in operational condition. Consequently, they deliver a linear model of the structure around the real working point of operation. The unmeasured, ambient forces are usually modelled as stochastic quantities with unknown parameters but with known behaviour. Nevertheless, the existing OMA techniques suffer from several shortcomings. The first one is that output-only measurements do not allow to determine a complete modal model, since the mode shapes can not be scaled in an absolute sense. Secondly, the ambient excitation is sometimes confined to a narrow frequency band, and as a result only a limited number of modes can be extracted with high quality from the ambient vibration data. For these reasons, there has been an increasing interest during the last few years towards combined experimental-operational modal testing techniques, also called *operational modal analysis with exogenous inputs* (OMAX) [3.6]. In this technique, artificial forces are used in operational conditions. The main difference between OMAX and the traditional modal analysis approach is that the operational forces are included in the identified system model. They are not considered as an unwanted noise source, but as useful excitation. Consequently, the amplitude of the artificial forces can be equal to or lower than the amplitude of the unmeasured operational forces. This is of crucial importance for the modal testing of large structures, since it allows to use small excitation devices like impact hammers or shakers.

When applied to fatigue crack growth, crack size and locations are determined by changes in the modal parameters of the structure. Hence, advanced calculation techniques have to be used to relate the measurements to crack data. The modal analysis measurements performed during this project are carried out in cooperation with the Catholic University of Leuven.

2.2 Offline crack sizing

2.2.1 Dye penetrants

Dye penetrants can be used to highlight cracks during visual inspection. The working principles are illustrated in Figure 3.3. After the surface is cleaned and grease free, a dye penetrant is applied to the surface and enters the defect (step *a* in Figure 3.3). This dye has a bright red color. After a certain dwelling time, that enables the dye to penetrate all cracks, the superficial dye is removed (step *b*). In the next step a thin layer of a white developer is sprayed on the surface. The developer has the property to absorb the red dye from the crack which clearly colours the white layer of the developer.

This technique can be used to help locating surface cracks and viewing crack lengths during visual inspection, but it does not provide additional information about crack depth.

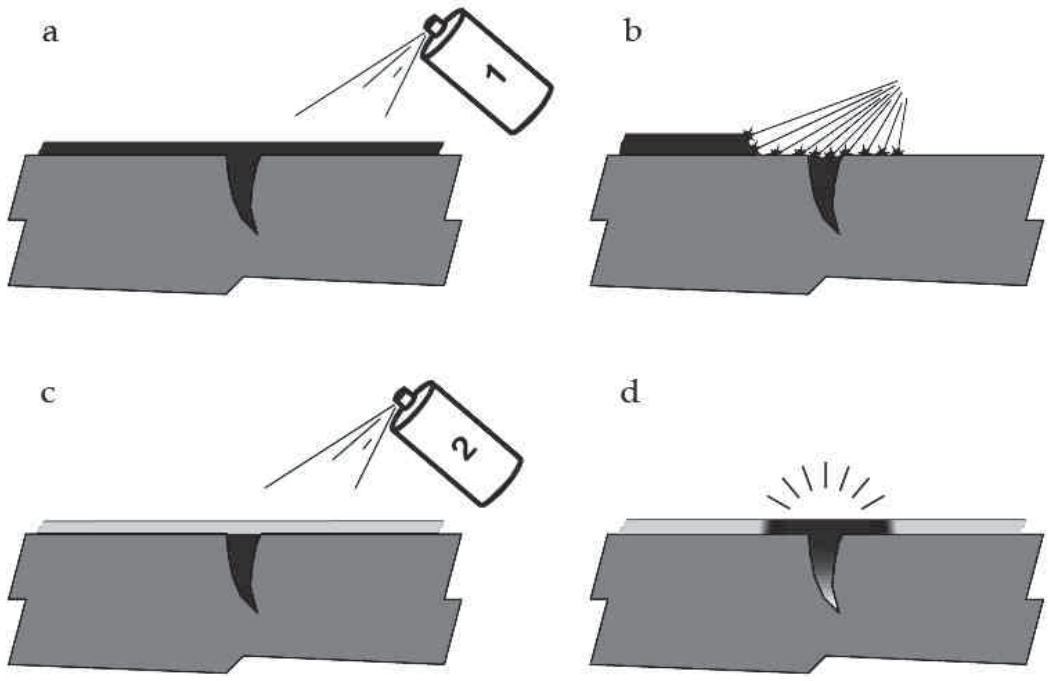

Figure 3.3: Illustration of dye penetrant testing.

2.2.2 Magnetic flux leakage (MFL)

Magnetic flux leakage (MFL) detection is a magnetic *non-destructive testing* (NDT) method in which a very high magnetic field is induced in the test specimen. Sensing coils or Hall probes are used to detect the flux leakage around a flaw. Alternatively, the magnetic field outside the surface of the material can be detected visually with the so-called *magnetic particle inspection* (MPI) technique where the crack is revealed by an accumulation of magnetic particles trapped in its leakage field.

It is possible to use MFL to size cracks in threaded pipe connections as is shown by Ding et al. in two studies, respectively on tubing [3.7] and drill pipe threads [3.9]. Their setup is illustrated by Figure 3.4. A magnetizing exciter, which consists of a soft iron yoke (2) and the electrical coil (3), is inserted in the threaded pipe (1) and magnetizes it to saturation. When the threaded connection is saturated, the magnetic flux will leak into the air at the location of the crack (4). This flux can then be detected by the probe (5). This probe contains 8 Hall sensors and is pulled by a linear motor to scan the threads along the axial direction.

With this method, Ding et al. where able to detect cracks with a minimum depth of 0.3 mm and with a measurement accuracy of about 0.3 mm [3.7]. However, MFL is not applied in the current research project.

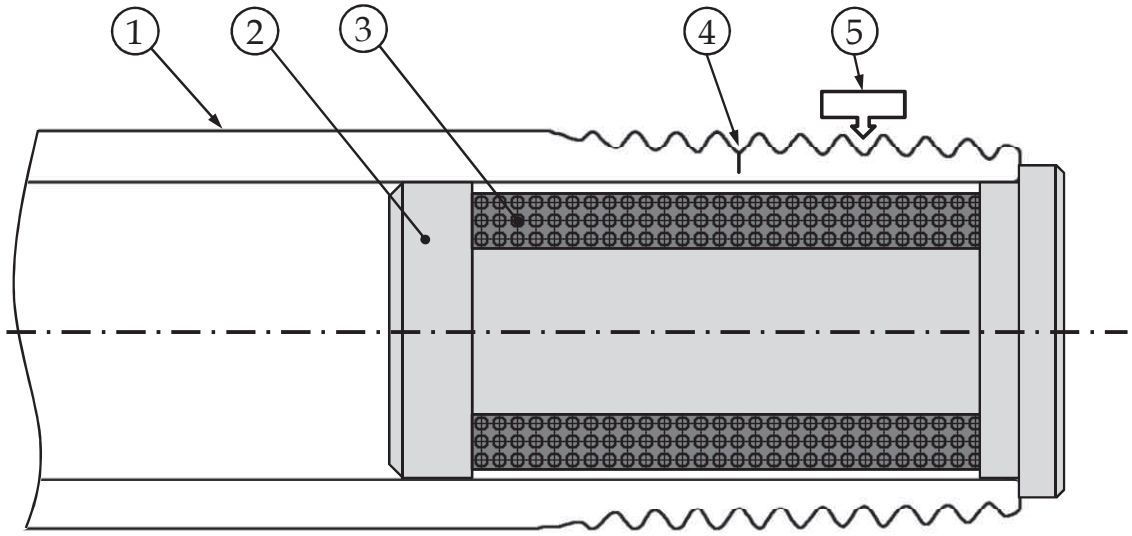

Figure 3.4: Thread inspection by magnetic flux leakage.

2.2.3 Eddy current testing

When a coil with an alternating current passing through is brought in the proximity of an electrically conducting material, the impedance measured at the terminals of the coil changes. As illustrated by Figure 3.5, the magnetic field associated with the current flowing in the coil induces eddy currents in the conducting specimen. These eddy currents create a secondary magnetic field opposite to the magnetic field of the coil, which affects the coil's impedance. When a surface defect is present in the test object, the eddy currents are not able to flow through it and its presence can be detected.

This technique can be applied to detect flaws of approximately 1 mm in depth in bolt threads of non-magnetic metals [3.8]. Its practical applicability for ferromagnetic materials is less straightforward. For the latter, mechanical and thermal production and handling processes can introduce magnetic anomalies or local magnetisation which can interfere with the crack detection process. Consequently, this technique is not used in the current work.

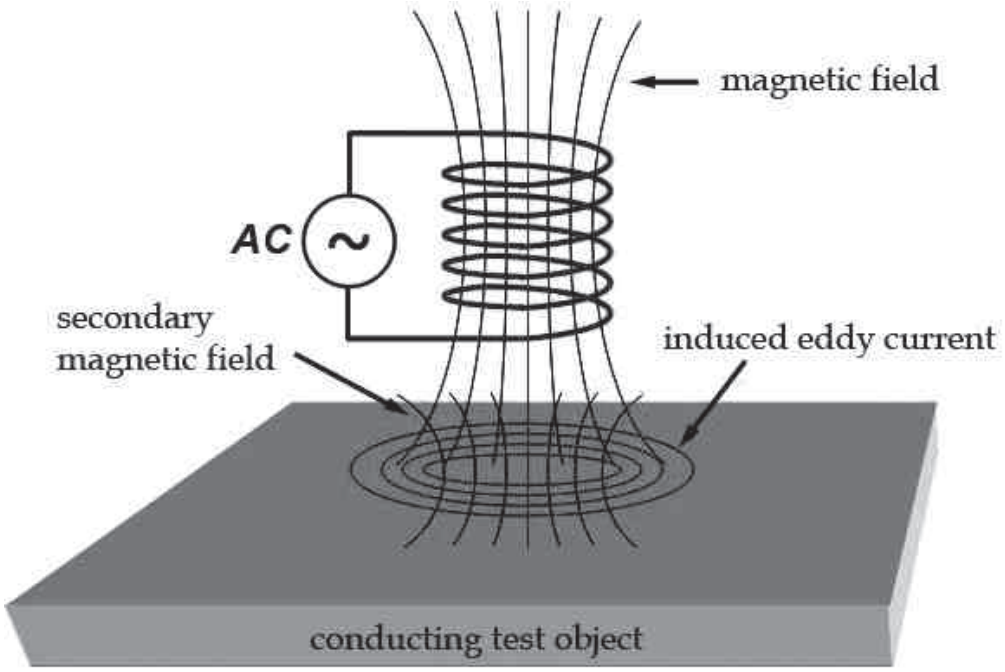

Figure 3.5: Eddy current testing.

2.2.4 Direct Current Potential Drop technique (DCPD)

The *direct current potential drop* (DCPD) technique is among the oldest electromagnetic NDT techniques and has been used for decades to estimate crack depths in plates and to monitor crack initiation and propagation during laboratory tests [3.10-11]. In this relatively simple technique an electrical DC current is injected into a conducting specimen through one pair of electrodes, while a second pair straddles the crack or the area where crack initiation is expected, as illustrated in Figure 3.6 [3.11]. The injecting electrodes should be positioned at a sufficient distance to ensure field uniformity at the inspection area.

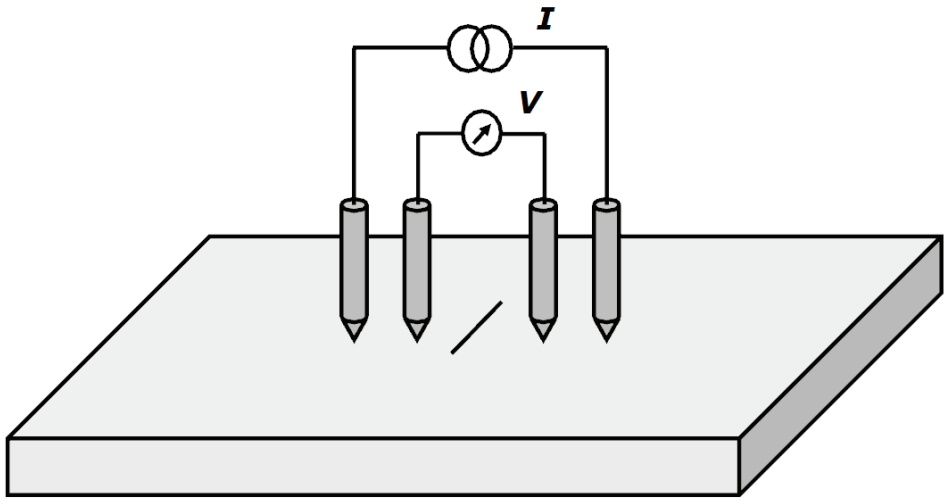

Figure 3.6: Direct current potential drop [3.11].

As the crack size increases, the cross-section of the specimen is reduced, hence increasing the electrical resistance and the potential difference measured between the inner probes. Since the potential differences are relatively small (in the order of μV), large currents (100 A and more) have to be used. In addition the method is very sensitive to changes in distance between the measuring probes and good electrical contact of the measuring probes is necessary. This means in practice that the probes should be spot welded to the part, which makes this method unsuitable to use on threaded pipe connections.

2.2.5 Alternating Current Potential Drop technique (ACPD)

The working principle of the *alternating current potential drop* (ACPD) technique is very similar to DCPD, the main difference being the use of an alternating instead of a direct current. When an alternating current is passed through a conductor, the so-called *skin effect* forces the current to flow in a thin layer on the outer surface. This means the effective cross-section carrying the current is small. As a consequence, sufficiently high potential differences can be generated by relatively low currents (3 A and smaller) [3.11-13]. The thickness of the current-carrying layer, or skin depth θ can be calculated by Eq. (3.1):

$$\theta = \frac{1}{\sqrt{\pi f \sigma_e \mu}} \tag{3.1}$$

Where f is the frequency of the applied alternating current, which can be up to 10 kHz, σ_e is the electrical conductivity and μ is the magnetic permeability. At a frequency of about 5 kHz, for example, ferromagnetic mild steel has a skin depth in the order of 0.1 mm. The presence of an electrically insulating defect, such as a crack, forces the current to flow around and below it. The longer current path results in a higher resistance and a larger potential drop.

ACPD can be used to size cracks in threads [3.13] as illustrated in Figure 3.7. Since fatigue cracks tend to initiate along the thread roots, but the position around the root radius is not known in advance, special voltage probes should be used that contact across adjacent thread crests as illustrated in the figure. If the thread is on a solid component like a bolt, the alternating current is best injected along the bolt's axis as shown in Figure 3.7. This delivers a uniform current field distribution around the thread circumference. For a tubular specimen, it may be better to induce the field using an additional coil that moves with the voltage probe.

Although ACPD system can reach sub-micrometer accuracy if the probes are welded to the specimen, the accuracy of a system with travelling probes is only 0.1 mm and the minimum detectable crack size is approximately 1 mm. In addition, the accuracy is highly dependent on the electrical contact between the probe and the thread crests. This technique is not applied in the current work.

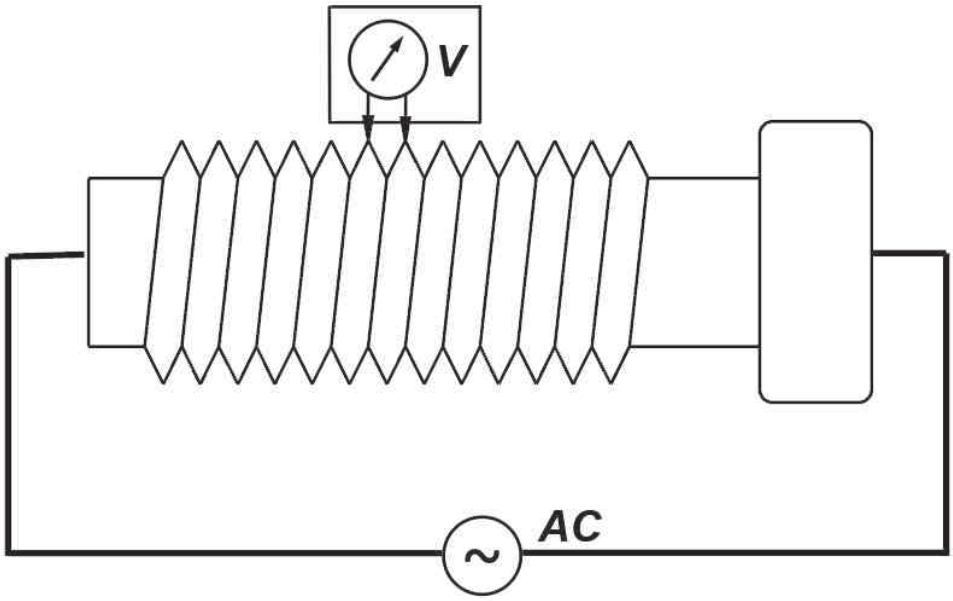

Figure 3.7: ACPD measurement for bolt inspection.

2.2.6 Alternating Current Field Measurement (ACFM)

The *alternating current field measurement* (ACFM) technique was developed to combine the ability of ACPD to size cracks accurately in ferromagnetic materials with the ability of the eddy current technique to work without electrical contact. The latter is achieved by inducing (rather than injecting) uniform currents on the surface of the inspected specimen and by measuring the magnetic field above the surface instead of measuring the surface voltage.

During ACFM inspection two components of the magnetic field B are considered. The x-component B_x according to the coordinate system shown in Figure 3.8 is parallel to the crack, while B_z is perpendicular to the object's surface [3.15]. When no crack is present, both the electric field induced by the current flow in the y-direction and the B_x-component are uniform. A surface flaw diverts the current away from the deepest point of the crack and concentrates it near the ends of the defect (see Figure 3.9). This generates a strong peak in the B_z field above the crack ends, while the B_x field drops in strength. Interpretation of crack depth is based upon the ratio of uniform to minimum B_x levels, whilst crack length is determined by the local maxima and minima in the B_z signal. The magnitudes of these two parameters are recorded over time as the ACFM probe scans the surface under inspection.

Since the 1980's special probes have been developed to optimize ACFM measurements for thread inspection. Consequently, ACFM has been successfully used to size cracks in bolts [3.14] and drill pipe threads [3.15-16]. An example of a drill pipe thread inspection probe is given in Figure 3.10. It incorporates an induction coil to generate the surface current and a pick-up coil to measure the B_x and B_z field components. The detection threshold for crack depths in threads is less than 1 mm and the technique has an accuracy

of about 0.3 mm. The main disadvantage of this technique is that a relatively expensive probe has to be made for every thread type and size. Hence, it has not been applied during this project.

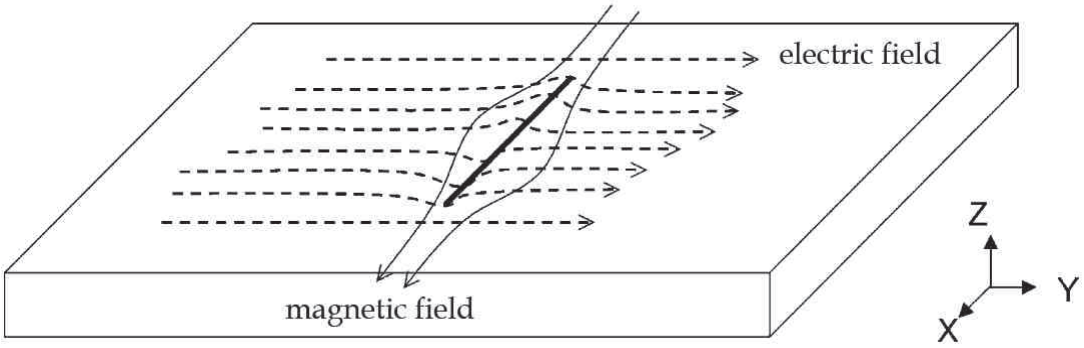

Figure 3.8: Field directions and coordinate system used in ACFM [3.15].

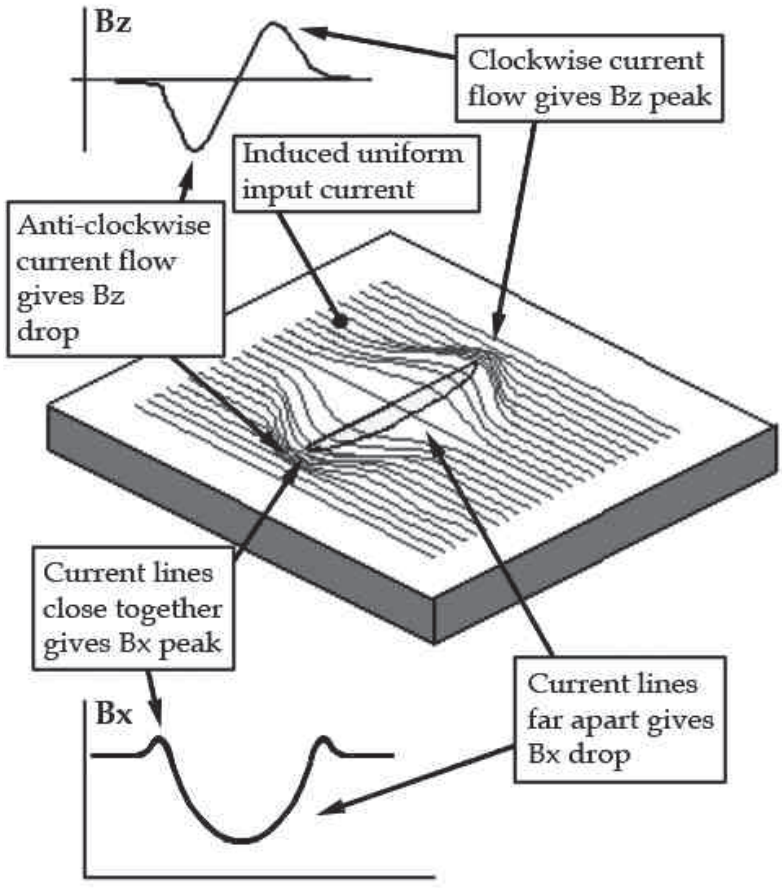

Figure 3.9: Magnetic field components in the vicinity of a defect [3.15].

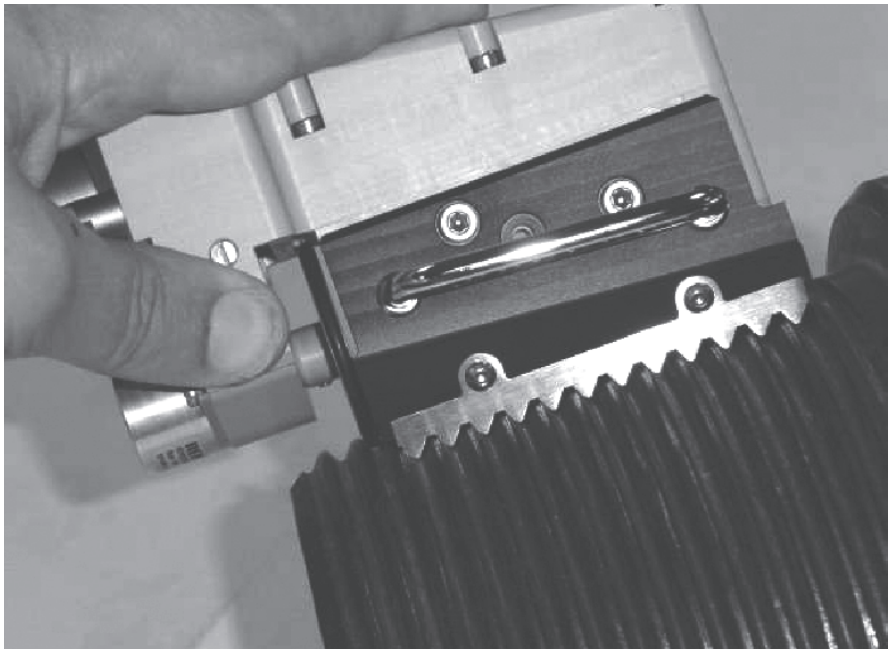

Figure 3.10: Probe for ACFM inspection of drill pipe threads [3.16].

2.2.7 Beach marking

This technique is based on the principles of the crack propagation law of Paris-Erdogan Eq. (2.11) as introduced in Chapter 2. From this theory it is known that the crack growth rate depends on the applied stress range. When the stress range is reduced, the crack growth rate is reduced as well. This changed propagation rate will mark a clear line in the fracture surface of the test specimen as is illustrated in Figure 3.11.

In practice this is done by applying a number of load cycles at a higher stress ratio while keeping the same value of the maximum stress (see Figure 3.12). The majority of the fatigue damage is produced by the stress range $S_{r,test}$. The lower stress range $S_{r,beach}$ can be chosen in such a way that its contribution to the total fatigue damage is negligible.

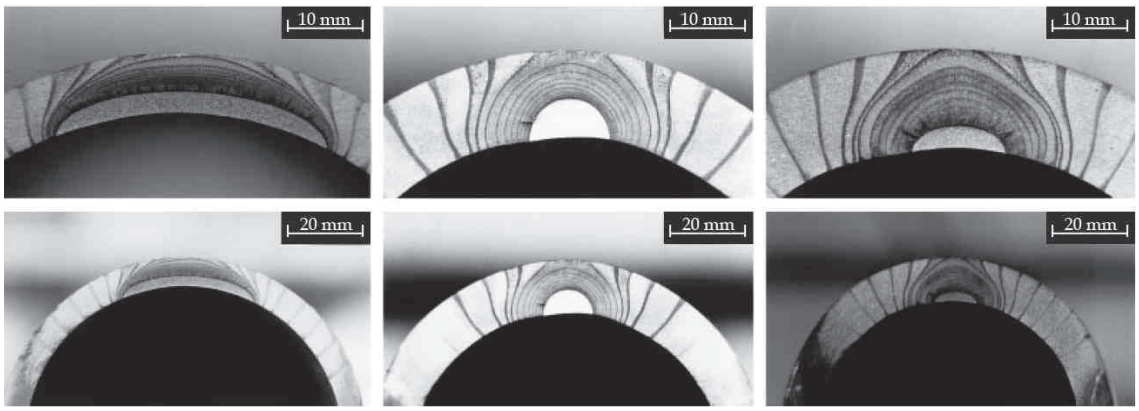

Figure 3.11: Fracture surfaces with beach mark lines of tubes with internal notches of different initial sizes [3.17].

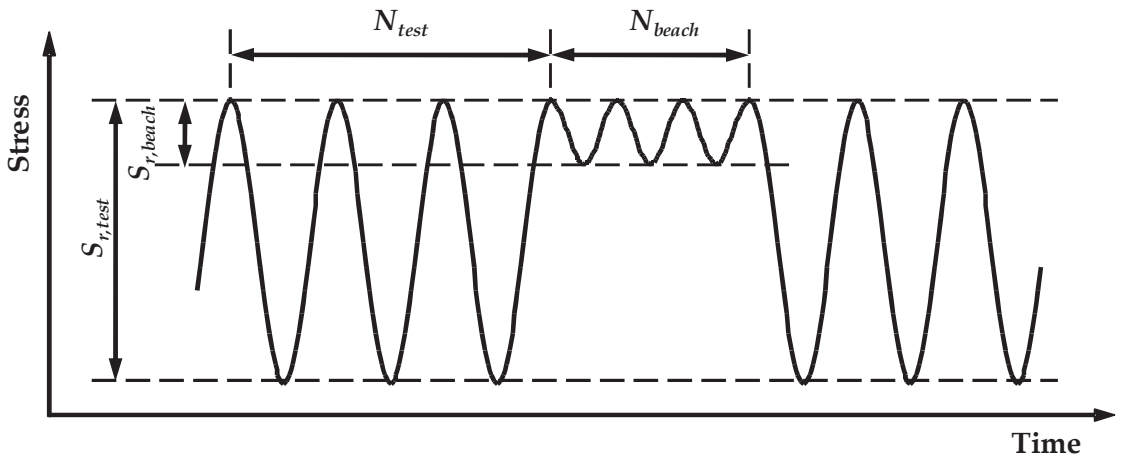

Figure 3.12: Schematic overview of the beach marking technique.

Multiple beach mark load blocks may be applied to create several lines in the fracture surface. The results, however, can only be seen after the test by breaking open the fracture surface. The cracks can then be measured by using an optical measuring microscope. Since this can only done after the test is finished, the beach marking technique requires a certain amount of expertise to determine when to apply the beach mark blocks and to select the correct number of cycles. If the beach mark cycles are applied too early or too few cycles are applied, no beach mark lines will be visible. On the other hand, if too much beach mark blocks or cycles are applied, the crack propagation will be affected by the technique.

Nevertheless, beach marking has been successfully used in different applications [3.17-21] including the work of Brennan on drill pipe connections [3.22]. In most cases, however, the beach mark lines are used as a validation or calibration for an indirect crack sizing technique as described earlier in this chapter. In this study the beach marking technique will be used to investigate the fatigue crack growth in threaded pipe connections more in detail.

2.3 Other measurement techniques

In this section two additional measurement techniques are discussed. They are not specifically developed for crack detection, but will be used in the current research.

2.3.1 Strain gauges

Strain gauges are widely used to locally measure strains in either static or dynamic applications. As mentioned in the literature overview in section 2.2.3 of Chapter 2, strain gauge measurements during static tests have been used for validation of finite element simulations of threaded pipe connections is several studies. In addition, dynamic strain gauge

measurements have been used to control the bending stress of a threaded pipe connection in a resonant bending fatigue setup [3.23].

The working principle of a strain gauge is based on the fact that the resistance of a conductor is both material and geometry dependent. For a material of constant resistivity, the total resistance increases with length and decreases with cross-sectional area. An example of a strain gauge is given in Figure 3.13.a. It consists of a fine wire which runs several times in parallel over the gauge area. When the strain gauge is properly bonded to a surface, the change in length of the surface can be accurately measured by the change in resistance of the wire. Strain gauges are constructed in such a way that the change in resistance is proportional to the applied tensile or compressive strain value [3.24].

In fatigue applications strain gauges are applied to monitor local strains around stress concentrations or a measured strain value can be used as feedback signal for a strain controlled fatigue test.

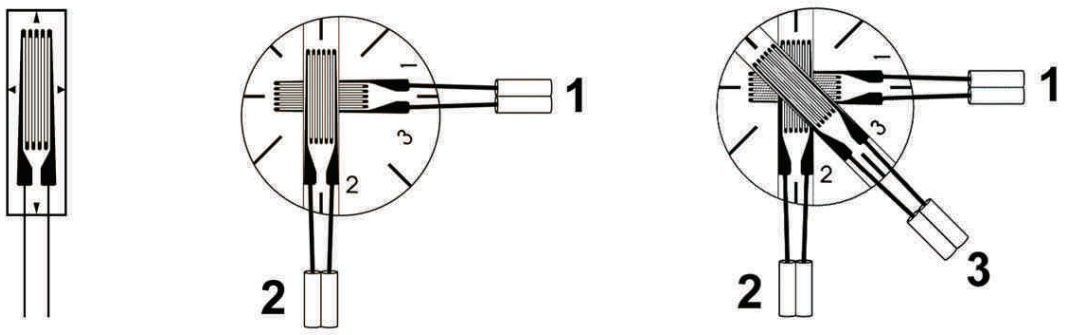

a **b** **c**

Figure 3.13: Strain gauges: a) line gauge, b) cross gauge, c) rosette gauge.

With the type of strain gauge as illustrated in Figure 3.13.a, only the strain in the vertical direction can be measured. This kind of line gauges are used at locations where a uniaxial strain situation is expected to appear. In the elastic region, the uniaxial stress component σ can then be calculated from the measured strain ε according to Hooke's law, with E Young's modulus of elasticity:

$$\sigma = \varepsilon E \tag{3.2}$$

For a biaxial strain situation, a cross gauge as in Figure 3.13.b can be used. With the strain gauge aligned along the principal directions, the elastic stress components σ_1 and σ_2 can be calculated according Eq. (3.3-4), with ν the Poisson coefficient.

$$\sigma_1 = \frac{E}{1-\nu^2}\left(\varepsilon_1 + \nu \cdot \varepsilon_2\right) \tag{3.3}$$

$$\sigma_2 = \frac{E}{1-\nu^2}\left(\varepsilon_2 + \nu \cdot \varepsilon_1\right) \tag{3.4}$$

When also the shear strain ε_{12} has to be measured, for example to determine the principal stress directions, a rosette gauge, as shown in Figure 3.13.c, can be used. In this case, the shear strain is calculated from Eq. (3.5) and the corresponding shear stress σ_{12} is given by Eq. (3.6)

$$\varepsilon_{12} = \varepsilon_3 - \tfrac{1}{2}(\varepsilon_1 + \varepsilon_2) \tag{3.5}$$

$$\sigma_{12} = \frac{E}{1+\nu}\varepsilon_{12} \tag{3.6}$$

2.3.2 Photogrammetry

Photogrammetry is the practice of determining geometric properties of an object from photographic images. Photogrammetric measurement techniques have been extensively improved and optimized during the last two decades thanks to the development of low cost, high resolution digital cameras. When images of the same object, taken from different orientations are analysed, very accurate 3D information related to the coordinates of an object can be obtained, although the images themselves only contain 2D information.

Originally photogrammetry was developed as a fast way to acquire dimensional data of civil engineering constructions. Using a single digital camera to photograph a construction from different angles, a 3D model of the construction can be generated by post-processing the images [3.25-26].

When an object is photographed at different moments, photogrammetry can be used to detect deformation or displacements. Reference points, such as reflective markers, are added to the object in order to size the displacement. Systems have been developed with two cameras positioned on a fixed distance and under a fixed angle, which enables the acquisition of 3D displacement data. Additionally systems exist with more than two cameras. These can be used when very large objects are to be analysed. An example of this is given by Ozbek et al. [3.27] in their analysis of the displacement of a wind turbine with a rotor diameter of 80 m. Due to advanced post-processing techniques a sub-pixel accuracy can be obtained. This makes it possible to detect small displacements and deformations.

The device used in this study is a dynamic 3D optical measurement system as illustrated in Figure 3.14 [3.28]. The system delivers accurate 3D displacement data for a number of reflective markers attached to a test object. When images are captured, the reflective markers are illuminated by an integrated flash LED system. After the data is captured, it is post-processed to identify the markers and to calculate their displacement (see Figure 3.15). The system consists of two high-speed digital cameras placed on a rigid bar with calibrated length L of 1200 mm and under a certain angle α which can be changed between 15° and 40°. This way the focal point of the system is located at the measuring distance D. All markers inside a certain cubic measuring volume around this point can be captured.

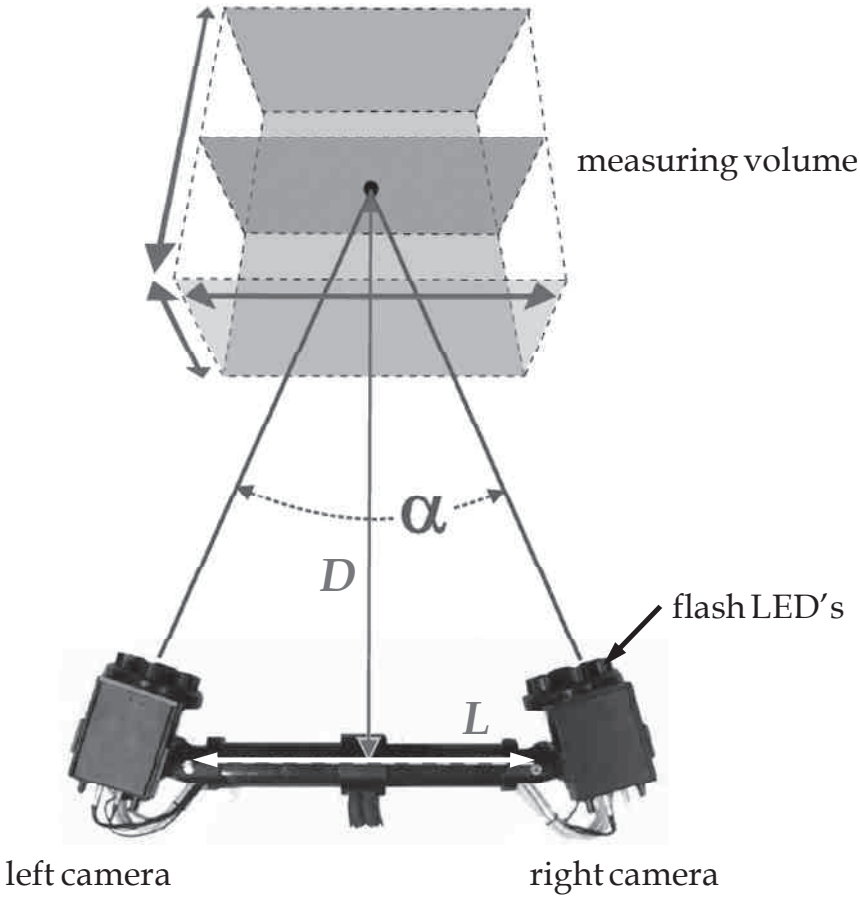

Figure 3.14: Dynamic 3D optical measurement system.

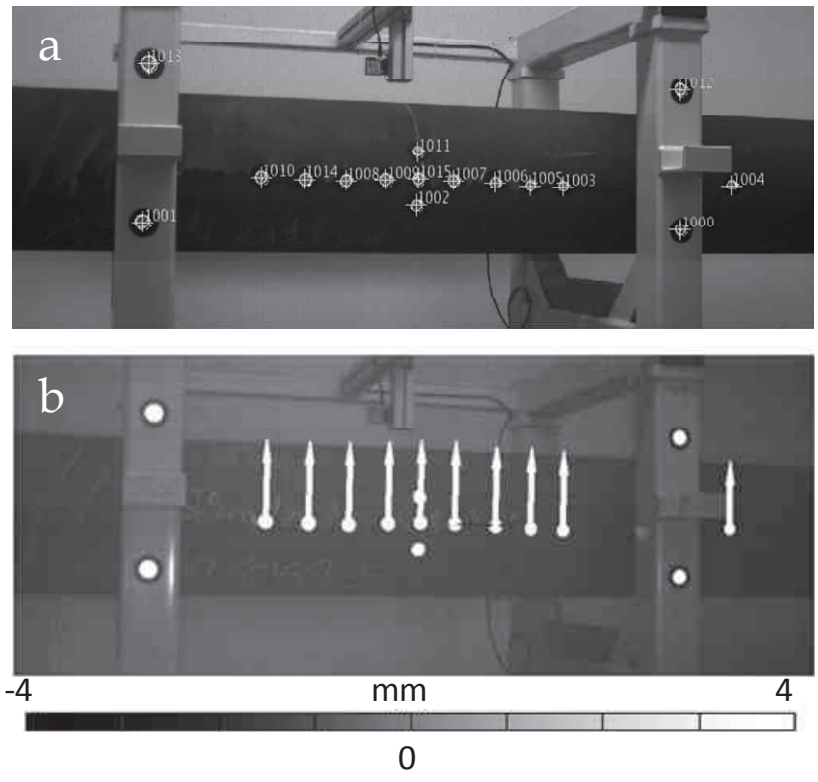

Figure 3.15: a) Identified markers, b) calculated displacements.

With this configuration the measuring distance *D* can be altered from 1.6 m to 4.6 m and the corresponding edge length of the measuring volume is between 1.6 m and 3.5 m. The dynamic 3D optical measurement system uses digital cameras with a 20 mm lens and 1.3 MPixel resolution that can capture images at a rate up to 500 Hz. The system's accuracy is typically about 0.02 pixels, which corresponds, to 20 μm to 50 μm in this setup, depending on the measuring volume.

3 Summary and conclusions

3.1 Comparison of crack sizing techniques

In Table 3.1 an overview is given of the quantitative crack sizing techniques described in the previous sections that were used for inspecting threads or threaded connections in the past. All techniques can detect cracks with a minimum depth between 0.3 mm and 1 mm and have an crack depth measurement accuracy from 0.1 mm to 0.5 mm. These techniques all require specialised equipment and it should be noted that the only online crack sizing technique for threaded connections is ultrasonic inspection, while the other techniques require the connection to be uncoupled for inspection. Next to this, the ultrasonic technique described in [3.3] requires advanced signal processing and no systems are currently available that include this option.

Measurement technique	Crack detection threshold [mm]	Crack depth accuracy [mm]	Online / offline
Ultrasonic inspection	0.5	0.2	online
MFL	0.3	0.3	offline
Eddy current	1	0.5	offline
ACPD	1	0.1	offline
ACFM	1	0.3	offline

Table 3.1: Overview of crack sizing techniques applied to threads.

3.2 Applied techniques

In this study three online techniques will be applied to threaded connections for the first time, as no quantitative online crack sizing method for threaded connections is currently available. First, crack opening measurements will be used to size propagating cracks in a four-point bending setup as described in Chapter 5. For these measurements, conventional clip gauges or LVDT's are employed, no other specialized equipment is required. Second, OMAX

techniques will be applied to specimens in the same setup. The modal analysis measurements are performed in cooperation with the Catholic University of Leuven. Third, a dynamic 3D optical measurement system is used to detect changes in the global deformation behaviour of a threaded pipe sample and crack sizes are determined by reverse engineering.

In order to relate the measured signals by these three techniques to actual crack sizes, beach marking will be applied to visualize crack fronts which are sized by a measuring microscope after the test. Next to this, leak detection is applied where possible, since this allows for a reliable detection of a through wall thickness crack. Dye penetrant investigation is in some cases used to confirm the presence of fatigue cracks without additional sizing.

During the static tests described in Chapter 5 strain gauges are attached to the specimens in order to validate strain distributions simulated by the finite element model described in Chapter 6.

Although the techniques applied in this study are suitable for crack sizing in laboratory conditions, no online monitoring technique is currently available to size cracks in real applications. The current results might be useful for future research to develop online monitoring techniques applicable in the field.

References

[3.1] ASTM E647, Standard test method for measurement of fatigue crack growth rates, ASTM International, 2000.

[3.2] Lefevre, A., Waaijenberg, M., Aylwin, E., Triel, H.M., Defect propagation from fatigue loading in 13%Cr pipelines, Pipeline Technology Conference, Ostend 2009-128, 2009.

[3.3] Suh, D.M., Kim, W.H., Chung, J.G., Ultrasonic inspection of studs (bolts) using dynamic predictive deconvolution and wave shaping, IEEE Transactions on Ultrasonics, ferroelectrics, and frequency control, 46(2), 457-463, 1999.

[3.4] Swamidas, A.S.J., Chen, Y., Monitoring crack growth through change of modal parameters, Journal of Sound and Vibration, 186(2), 325-343, 1995.

[3.5] Peeters, B., De Roeck, G., Stochastic system identification for operational modal analysis: A review, ASME Journal of Dynamic Systems, Measurement, and Control, 123(4), 659-667, 2001.

[3.6] Guillaume, P., De Troyer, T., Devriendt, C., De Sitter, G., OMAX - Operational Modal Analysis in presence of eXogenous inputs, Proceedings of the 25th International Modal Analysis Conference, Orlando, USA, 2007.

[3.7] Ding, J.F., Kang, Y., Wu, X., Tubing thread inspection by magnetic flux leakage, NDT&E International, 39, 53-56, 2006.

[3.8] Koshti, A., Ruffino, N., Stanley, D., Files, B.S., Process specification for eddy current inspection, NASA, PRC-6509 Rev. B, 2008.

[3.9] Ding, J.F., Kang, Y., Wu, X., Research on the method for drill pipe thread inspection, Key Engineering Materials, 321-323, 472-475, 2006.

[3.10] Andersson, M., Persson, C., Melin, S., Experimental and numerical investigation of crack closure measurements with electrical potential drop technique, International Journal of Fatigue, 28(9), 1059-1068, 2006.

[3.11] Sposito, G., Advances in potential drop techniques for non-destructive testing, PhD Thesis, Dept. of Mech. Eng. Imperial College London, 2009.

[3.12] Venkatasubramanian, T.V., Unvala, B.A., An AC potential drop system for monitoring crack length, Journal of Physics E: Scientific Instruments, 17, 765-771, 1984.

[3.13] Lugg, M.C., An introduction to ACPD, Document TSC/MCL/1146, Technical Software Consultants Ltd., 2002.

[3.14] Dover, W.D., Dharmavasan, S., Inspection of threaded components using ACFM, Proceedings International Seminar organised by NDE Centre, University College London, 1988.

[3.15] Knight, M.J., Brennan, F.P., Dover, W.D., Effect of residual stress on ACFM crack measurements in drill collar threaded connections, NDT&E International, 37, 337-343, 2003.

[3.16] Topp, D., Lugg, M.C., Advances in thread inspection using ACFM, 3rd Middle East Nondestructive Testing Conference & Exhibition, Bahrain, 2005.

[3.17] Yoo, Y.S., Ando, K., Circumferential inner fatigue crack growth and penetration behaviour in pipe subjected to a bending moment, Fatigue and Fracture of Engineering Materials and Structures, 23, 1-8, 2000.

[3.18] Liu, J., Bowen, P., DC potential drop calibration in matrix-cladded Ti MMC specimens with a corner notch, International Journal of Fatigue, 25, 671-676, 2003.

[3.19] Raghava, G., Mithun, I.K., Gandhi, P., Vaze, K.K. , Bhate, S.R., Bhattacharya, A., Application of beach marking technique to the study of fatigue crack growth in steel plate specimens subjected to tensile loads, Journal of Structural Engineering, 32 (3), 229-232, 2005.

[3.20] Cai, C.Q., Shin, C.S., A normalized area-compliance method for monitoring surface crack development in a cylindrical rod, International Journal of Fatigue, 27, 801-809, 2005.

[3.21] Lihavainen, V.M., A novel approach for assessing the fatigue strength of ultrasonic impact treated welded structures, PhD Thesis, Lappeenranta University of Technology, 2006.

[3.22] Brennan, F.P., Fatigue and Fracture Mechanics Analysis of Threaded Connections, PhD Thesis, Dept. of Mech. Eng. University College London, 1992.

[3.23] Sches, C., Desdoit, E., Massaglia, J., Fatigue Resistant Threaded and Coupled Connectors for Deepwater Riser Systems: Design and Performance Evaluation by Analysis and Full Scale Tests, ASME 27th International Conference on Offshore Mechanics and Arctic Engineering, OMAE2008-57603, 2008.

[3.24] Lee, Y.L., Pan, J., Hathaway, R., Barkey, M., Fatigue testing and analysis (Theory and practice), Elsevier Butterworth-Heinermann, Burlington, USA, 2005.

[3.25] Henze, F., Siedler, G., Vetter, S., Integration of digital image analysis for automated measurements into a photogrammetric stereo evaluation system, Proceedings of the 36th International Society for Photogrammetry and Remote Sensing Workshop, Hanover, Germany, 2006.

[3.26] Armesto, J., Lubowiecka, I., Ordóñez, C., Rial, F.I., FEM modeling of structures based on close range digital photogrammetry, Automation in Construction, 18(5), 559-569, 2009.

[3.27] Ozbek, M., Rixen, D.J., Erne, O., Sanow, G., Feasibility of monitoring large wind turbines using photogrammetry, Energy, 35, 4802-4811, 2010.

[3.28] Pontos, User information - Hardware, revision b, GOM optical measuring techniques, 2007.

Chapter 4

Design of a Resonant Bending Fatigue Setup

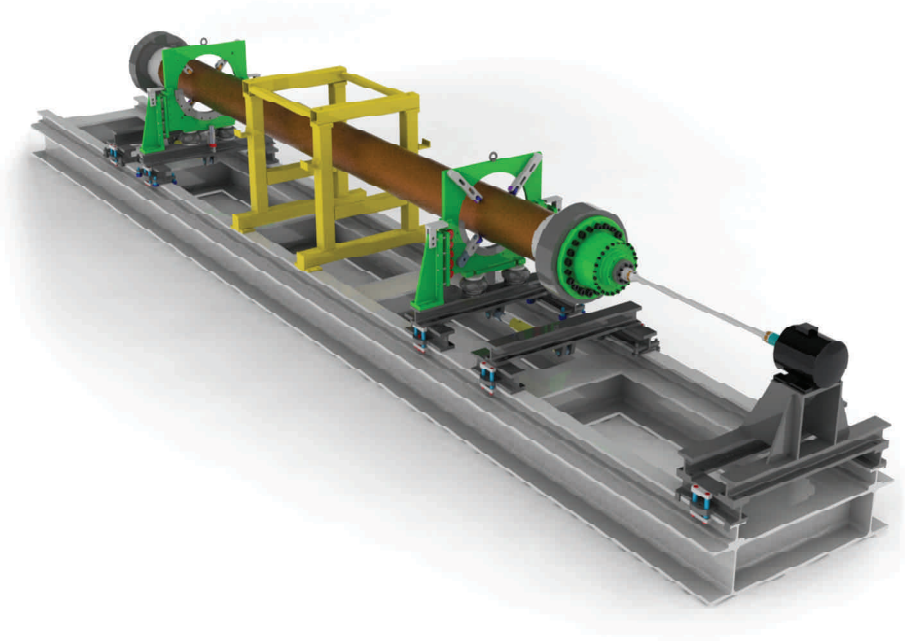

1 Goal

In this chapter the design and working principles of the developed resonant bending fatigue setup are discussed. The setup is completely designed, produced, assembled and taken in operation as part of this PhD project. As mentioned in Chapter 2, the advantages of this setup type over conventional experimental setups are its low energy consumption, the limited dynamic forces on the machine structure and the fast testing speed.

Next to this it is aimed in this design to develop a machine with following unique features compared to existing resonant bending setups.

- The machine should be capable of testing a wide range of pipe diameter at high bending stresses.
- As it is known that a propagating crack can reduce the bending stiffness of the pipe, the deformation shape of the pipe in the setup can change. Therefore the supports should be repositioned to the new location of the nodes.
- To detect such a changed mode shape a suitable measuring system should be integrated.

In the following paragraphs an overview of the setup is given. Afterwards the dynamic behaviour of the pipe is explained by two mathematical models that were used to determine the input required for the structural setup design. The theoretical calculations are compared to measurements obtained from a test series on two plain test pipes and at the end of the chapter the results of a complete fatigue test are presented.

2 Setup design

2.1 Working principles

In a resonant bending fatigue setup, a pipe is subjected to a dynamic excitation with a frequency close to its natural frequency. This causes the pipe to come into resonance, which means that the pipe will deform according to a standing wave that rotates at the excitation frequency. The pipe is supported in the nodes of this wave, hence the supporting framework should not be subjected to high dynamic forces. To achieve this, the pipe's natural frequency, which depends mainly on its bending stiffness and mass, should be in the range of commercial electromotors, which is about 20 to 50 Hz for a motor with a frequency drive. Since a plain pipe would be too long to stay within this range, the pipe's natural frequency is lowered by filling it with water and attaching endweights at both ends of the pipe (the higher the weight of the pipe, the lower its natural frequency).

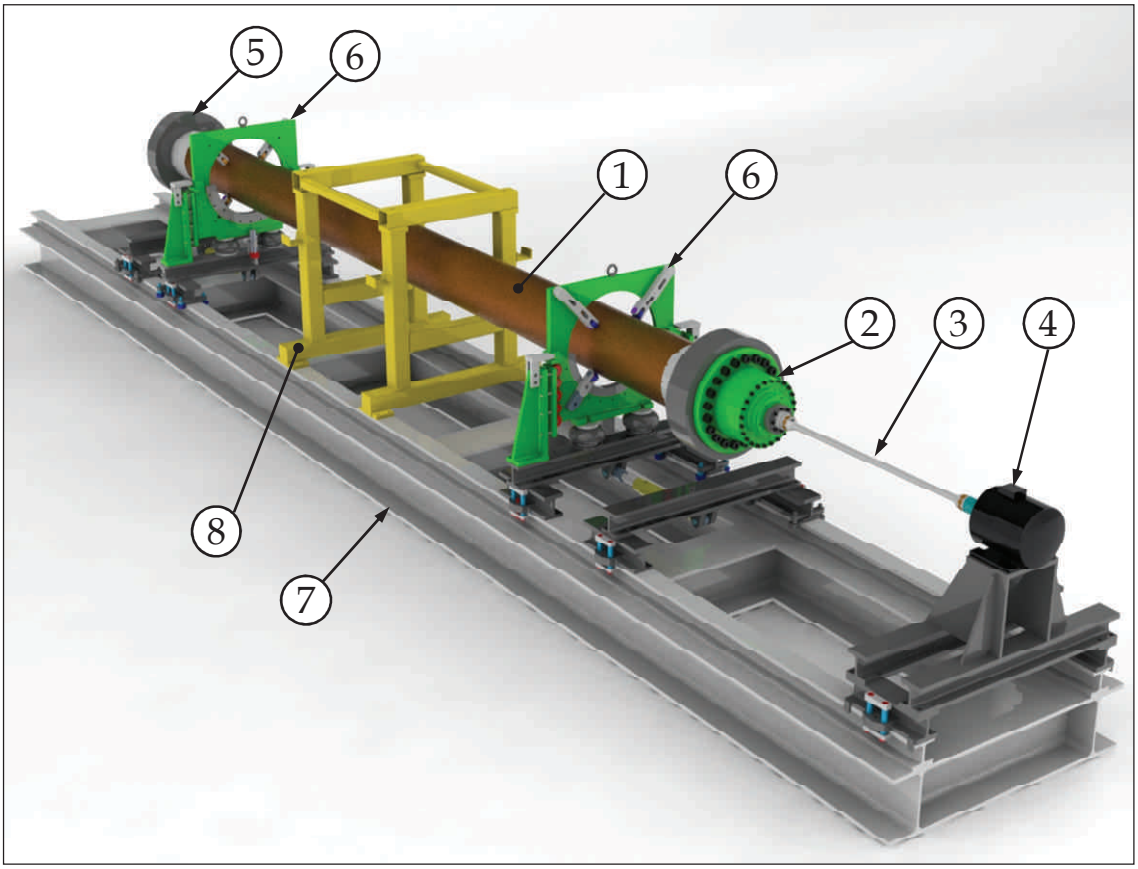

Figure 4.1: Overview of the designed resonant bending fatigue setup.

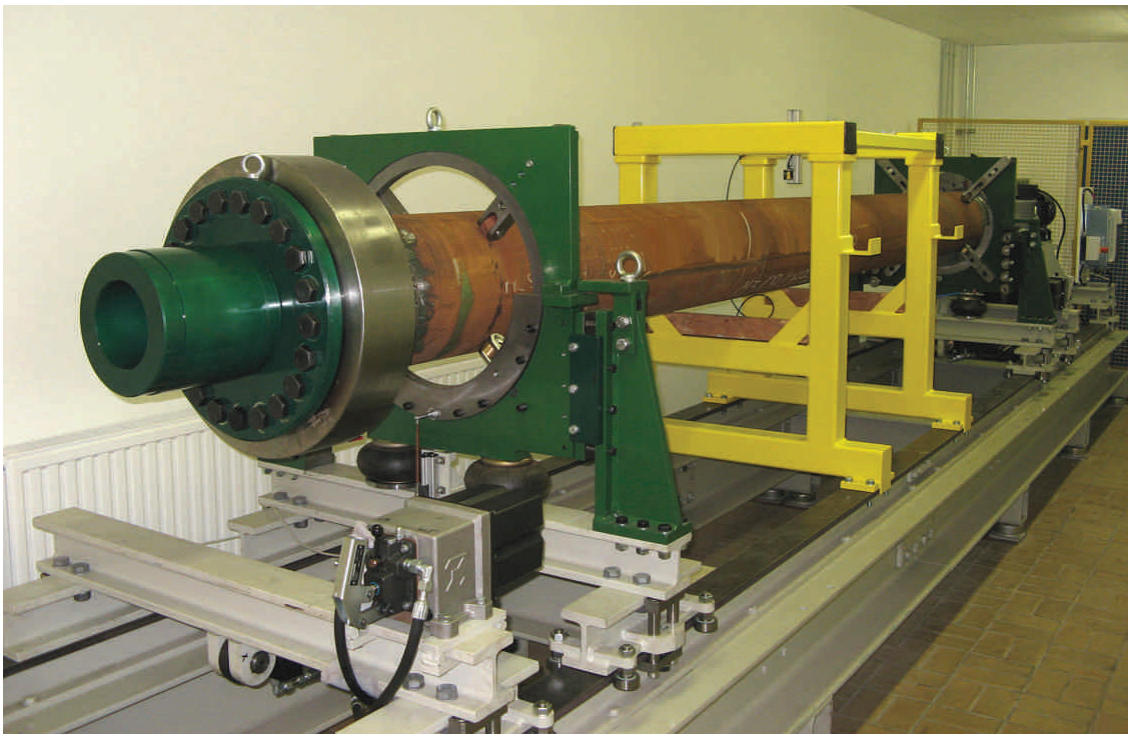

Figure 4.2: View of the completed setup from the side with the compensating mass.

2.2 Setup Overview

An overview of the developed setup is shown in Figure 4.1 together with a picture of the completed setup in Figure 4.2. The test pipe (1) that should contain a central joint, which can be a threaded connection, weld or other type of joint, is excitated by a drive unit (2). This unit is powered via a cardan shaft (3) by an electrical motor (4). At the other pipe end a compensating mass (5) is attached to obtain a more symmetric deformation wave in the pipe. The pipe is supported by the two supports (6) which are placed in the nodes of the first eigenmode of the pipe. The weight is carried vertically by air springs. The total setup is placed on a heavy framework (7) with a length of 9.50 m and a width of 1.29 m as can be seen in Figure 4.3. The total setup height is 1.75 m. An additional safety frame (8) is placed over the central section of the pipe. This central section, which contains the pipe connection, will be subjected to the highest cyclic stresses over the entire circumference during the fatigue test.

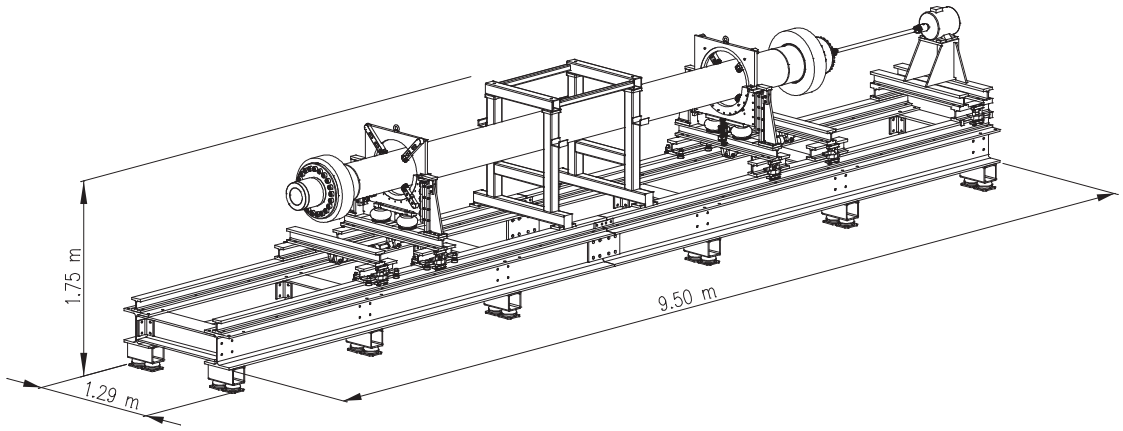

Figure 4.3: Dimensions of the setup.

2.2.1 Mounting the pipe

Before installation special endcaps are installed at both sides of the pipe. The setup is constructed in such a way that the top of the supports and the safety frame can be removed so that the pipe can be hoisted in the setup. Therefore a tailor made gantry crane is used. Subsequently, the upper parts of the supports and safety frame are replaced. Once the pipe is in the setup, two locking assemblies are installed on the endcaps to which the drive unit and the compensating mass are bolted. This installation process is schematically shown in Figure 4.4.

Before starting the test, the pipe is filled with water as to lower its natural frequency. Additionally, when this water is slightly put under pressure, a pressure measurement can be used to detect leaks.

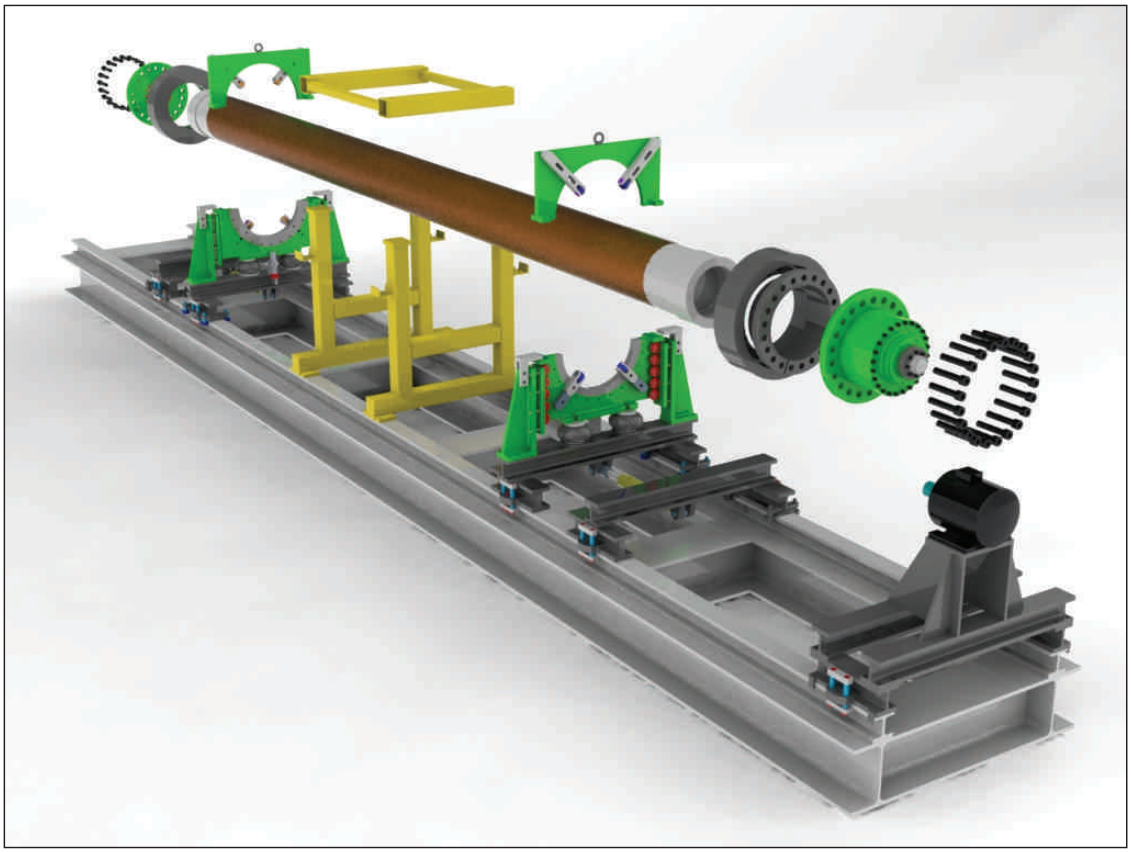

Figure 4.4: Mounting a pipe in the setup.

2.2.2 Drive unit

The drive unit consists of two excentric masses whose relative position can be changed. By altering the angle between 0° and 180° the resulting excenter force at a certain frequency is controlled between zero and a maximum. The two excenters can be seen in Figure 4.5, their maximum rotation speed is 2400 rpm or 40 Hz. This limit is implied by the maximum excitation force which depends quadratically on the rotation speed.

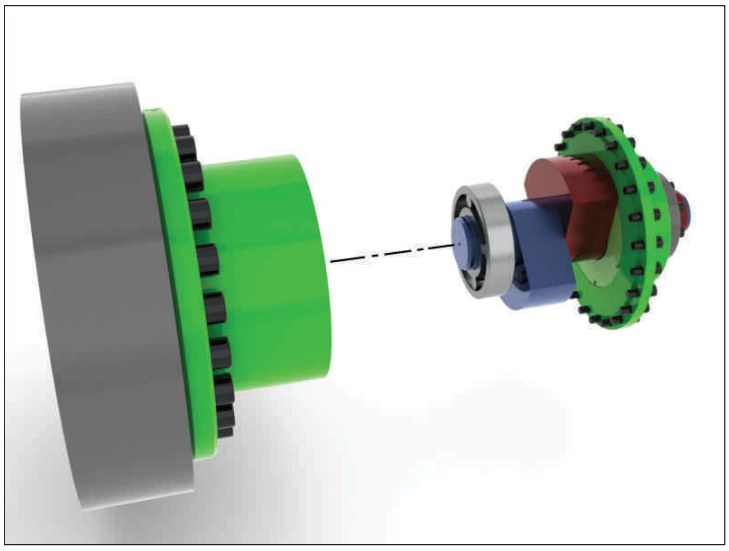

Figure 4.5: Drive unit with two excenters positioned at 0°.

2.2.3 Supports

A detailed view of a support is given in Figure 4.6. The pipe is directly supported by the rollers (1) whose position can be changed to allow for installation of pipes with different diameters. The supports are placed in the nodes of the deformation mode of the pipe in resonance. However, before the resonance frequency of the pipe is reached, a flexible suspension is desirable to allow for movement of the pipe. This is obtained by suspending the central plate on airsprings (2) to allow for vertical movement. The wire springs (3) allow for horizontal displacement. The suspension is designed in such a way that the total vertical stiffness of the airsprings matches the total horizontal stiffness of the wire springs. The displacement of a pipe in the support is monitored by the displacement transducer (4). The support is guided over a rail that is attached to the heavy framework by cam rollers (5) and the support can be clamped to this rail using a mechanical clamping system (6).

To move the supports along the rail, the clamps are released and the support's position can be changed by a hydraulic jack connected to a rigid beam clamped to the rail. This process is illustrated in Figure 4.7.

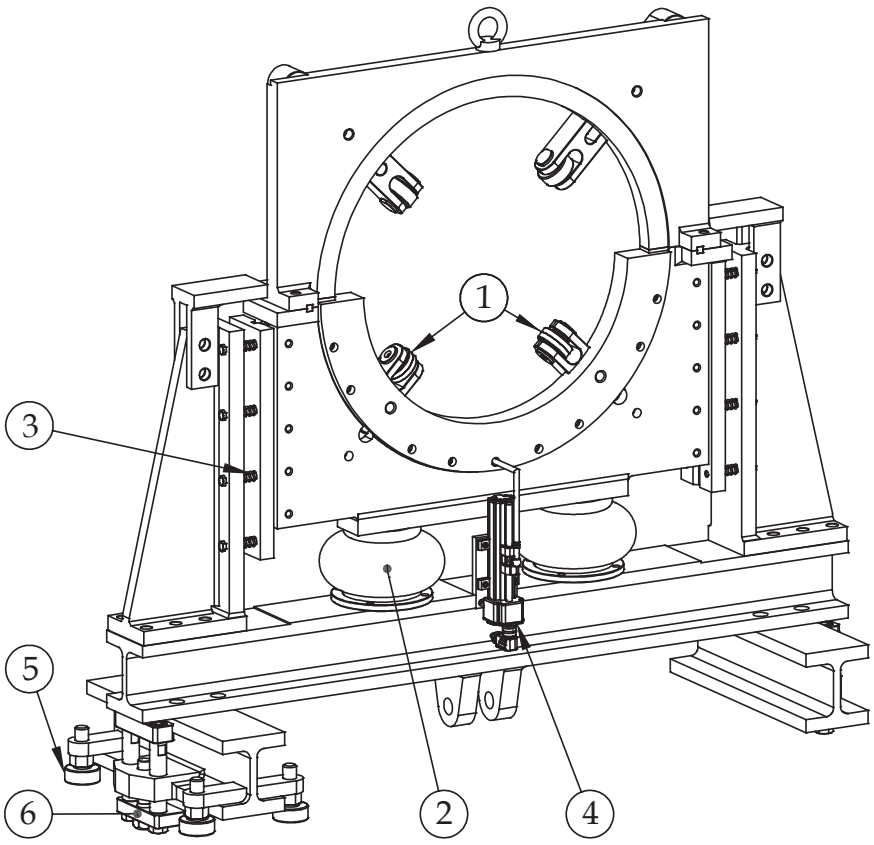

Figure 4.6: Detailed view of a support.

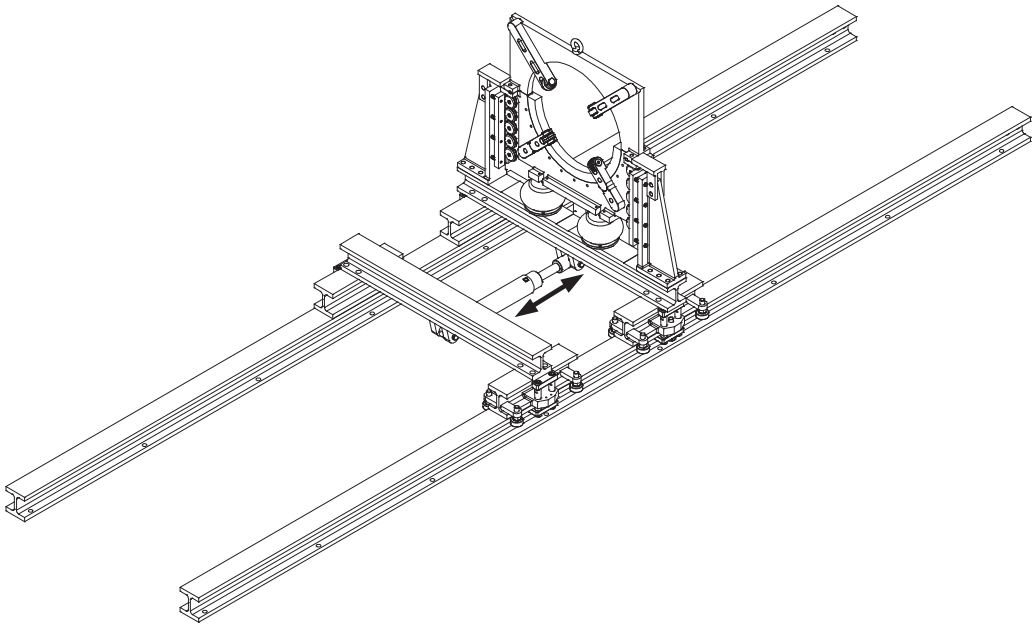

Figure 4.7: Moving the support along the rail.

2.2.4 Frame

The supporting frame is shown in Figure 4.8. It consists of two identical parts (1) and (2) with a length of 4.75 m. These two parts are bolted together using the connection plate (3). The entire frame is supported by 24 flexible dampers (4). The beams and position of the dampers have been dimensioned to avoid the frame itself to come into resonance when vibrations of the pipe are transferred to the frame.

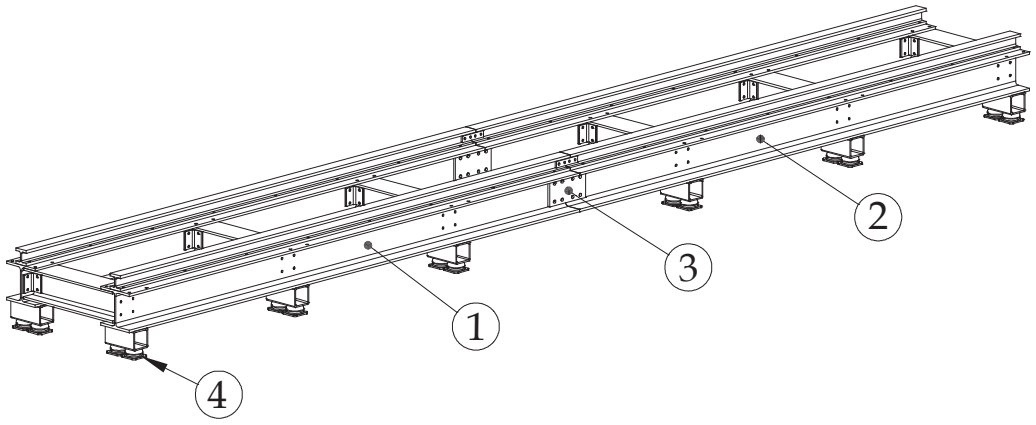

Figure 4.8: Supporting frame of the resonant bending setup.

The natural frequency of a beam depends on its boundary conditions [4.1]. For a simply supported beam with an additional mass at the centre (see Figure 4.9.a) the first angular eigenfrequency or the natural angular frequency ω_1 is given by Eq. (4.1). For a beam with fixed boundaries at both sides and additional central mass as shown in Figure 4.9.b ω_1 is given by

Eq. (4.2). With m_b the total mass of the beam, M the additional concentrated mass, L the beam length, E Young's modulus of elasticity and I the area moment of inertia of the cross section of the beam. The corresponding natural frequency f_1 can be calculated from the angular frequency according to Eq. (4.3).

$$\omega_1 = \sqrt{\frac{48 \cdot EI}{L^3\left(M + \frac{17}{35} m_b\right)}} \tag{4.1}$$

$$\omega_1 = \sqrt{\frac{196 \cdot EI}{L^3\left(M + \frac{3}{8} m_b\right)}} \tag{4.2}$$

$$f_1 = \frac{\omega_1}{2\pi} \tag{4.3}$$

These equations are evaluated for different beam lengths with the properties of the final design of the frame and a concentrated mass $M = 1400\ kg$. This value of M corresponds to the maximum weight of a loaded support. The resulting natural frequencies for different beam lengths are summarized in Table 4.1. In order to stay out of resonance, the beam's natural frequency should be at least three times higher than the maximum excitation frequency of the drive unit. Since the maximum excitation frequency is 40 Hz, the minimum natural frequency of the beams should be 120 Hz.

As can be seen from Table 4.1 it is not sufficient to support the frame only at its ends. Such a simply supported beam with a length of 9.5 m would have a natural frequency of only 7.8 Hz. Additionally, if the two sections of the frame are supported individually, this would result in a natural frequency that is too low even if a beam with fixed boundaries is considered. For this reason the dampers are positioned 1.70 m apart in the region where the supports can be placed.

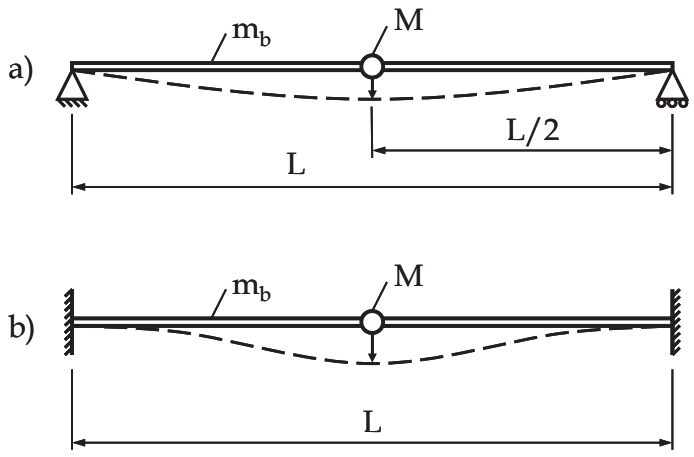

Figure 4.9: a) Simply supported beam, b) beam with fixed boundaries.

	f_1 [Hz]	
L [m]	**Simply supported beam**	**Fixed-fixed beam**
9.50	7.8	16.4
4.75	24.3	50.2
2.50	66.9	137.1
1.70	121.7	248.3

Table 4.1: Natural frequencies of the beams of the frame.

If the beams are considered simply supported, the natural frequency is sufficiently high. In the central section of the beam, the dampers are 2.50 m apart. At this location the section of the beam can be considered to have fixed boundaries and the resulting natural frequency is high enough. However, it is unlikely that the supports are placed in this section of the frame.

2.3 Measured signals

In Figure 4.10 the measured signals and the control circuit are schematically shown. During a test, the excitation frequency f_e of the excenters in the drive unit is continuously measured and controlled by a variable frequency drive circuit. Additionally the motor current is measured to monitor the consumed power. To check if the supports are positioned exactly at the nodes of the deformation wave, the displacements u_1 and u_2 in the supports are continuously monitored by the displacement transducers shown in Figure 4.6.

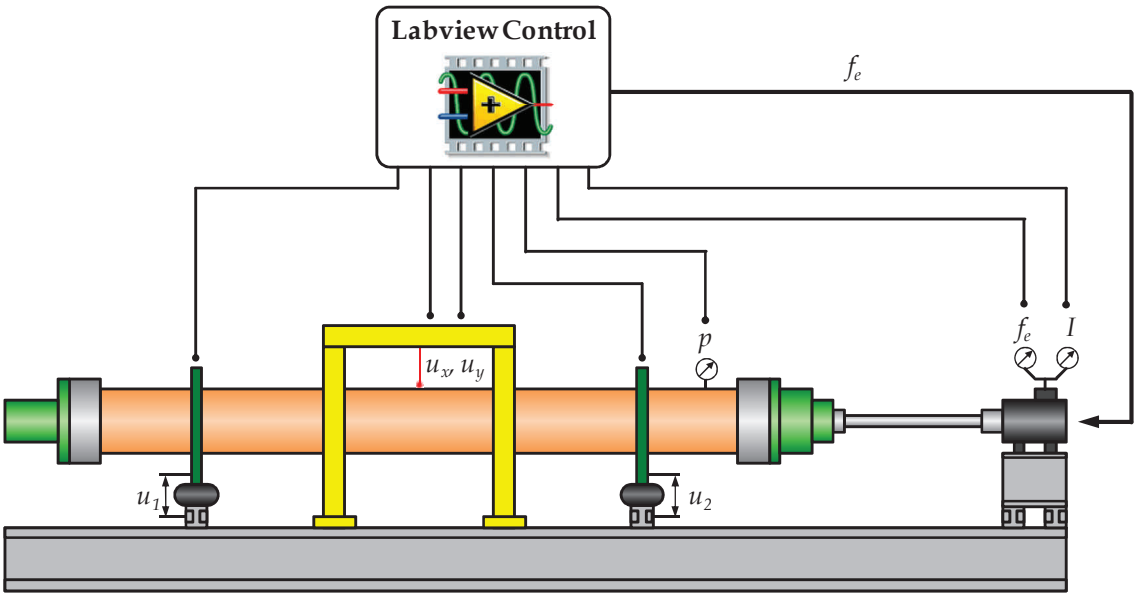

Figure 4.10: Schematic overview of the measured signal and the used control circuit.

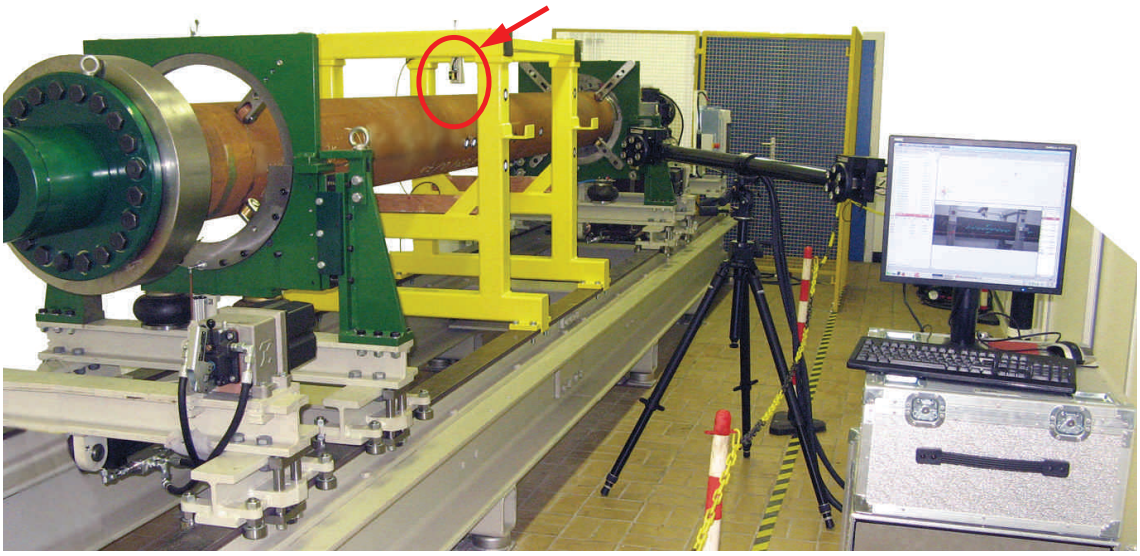

Figure 4.11: Setup with optical measurement system.

If necessary, the position of the supports can be changed by the hydraulic cylinders. A through thickness fatigue crack can be detected by pressurizing the water in the pipe and monitoring the pressure p. When a leak appears, the pressure drops and the test is stopped. The horizontal and vertical deflection of the pipe at its centre (u_x and u_y in Figure 4.10) are measured by two independent laser sensors mounted on the safety frame. The vertical laser is indicated by the arrow in Figure 4.11.

Next to the described continuously measured signals, the deformation shape of the pipe is measured using the high speed dynamic 3D optical measuring system that was described in section 2.3.2 of Chapter 3. The system is used to deliver accurate 3D displacement data for a number of markers attached to the pipe and is shown in Figure 4.11. The measurements provide more detailed data on the bending mode of the pipe than the signals obtained by the laser sensors since these only capture the deflection at the pipe centre. As will be explained later, the deflection measurements are used to calculate the corresponding bending stress in the pipe.

Strain gauges can be attached to the pipe to measure the strains at different locations along the pipe length. From these strains the corresponding stresses can be calculated and compared to the stress values derived from the displacement measurements.

3 Mathematical model

3.1 Analytical model of free floating pipe

In order to calculate the eigenfrequencies and eigenmodes of a water filled plain pipe with end masses attached, a simple model of a free floating pipe is used as shown in Figure 4.12. Where m_l and m_r are the total mass of the endweights, s_l and s_r are the distance of the centres of mass of the endweights

from the pipe ends, J_l and J_r are the mass moments of inertia of the endweights (around the axis through the centre of mass and perpendicular to the plane of Figure 4.12), respectively at the left and the right.

The deflection $u(x,t)$ of the pipe can be calculated using the partial differential Eq. (4.4), which describes the pipe's dynamic force equilibrium. The first term in this equation is the bending force necessary to give the pipe a certain deflection, while the second term is the inertial force due to the dynamic motion. With EI being the bending stiffness of the pipe and $A\rho$ is the mass per meter of the filled pipe.

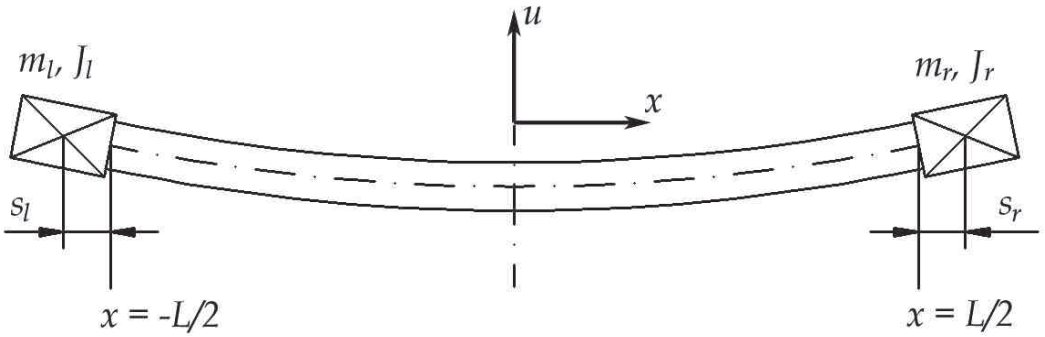

Figure 4.12: Model of a free floating pipe.

$$EI \cdot \frac{\partial^4 u}{\partial x^4} + A\rho \cdot \frac{\partial^2 u}{\partial t^2} = 0 \ , \ \forall x \in \left]\frac{-L}{2}, \frac{L}{2}\right[\tag{4.4}$$

The general solution (4.5) of this partial differential equation can be written as a product of a time-dependent harmonic term and a position-dependent amplitude $U(x)$ with ω the angular frequency and φ the phase difference.

$$u(x,t) = U(x) \cdot e^{i(\omega t + \varphi)} \tag{4.5}$$

Where $U(x)$ is given by equation (4.6) with C_1, C_2, C_3 and C_4 arbitrary constants and wave number γ as defined by equation (4.7).

$$U(x) = C_1 \cdot \sinh(\gamma x) + C_2 \cdot \cosh(\gamma x) + C_3 \cdot \sin(\gamma x) + C_4 \cdot \cos(\gamma x) \tag{4.6}$$

$$\gamma^2 = \omega\sqrt{\frac{A\rho}{EI}} \tag{4.7}$$

The values of the arbitrary constants can be obtained by substituting the boundary conditions at both pipe ends into the partial differential equation. These boundary conditions are schematically shown in Figure 4.13 and Figure 4.14. Since four unknown values of the constants need to be determined, four equations are necessary. The first two equations (4.8) are obtained by expressing the moment and force equilibrium for the free end at the left of the pipe (x=–L/2). While the last two equations (4.9) define the moment and force equilibrium at the right end (x=L/2) of the pipe where the excitation force F_e is applied.

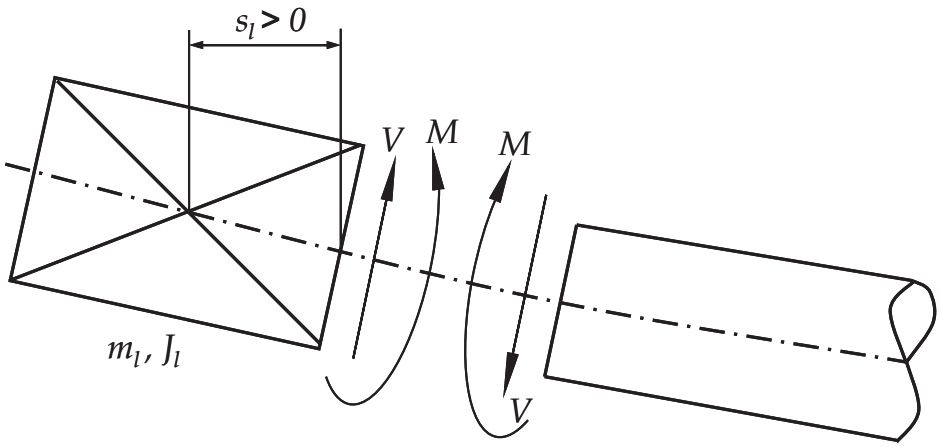

Figure 4.13: Boundary conditions at the free end (left).

$$\forall t : x = -\frac{L}{2}$$

$$\begin{cases} EI \cdot \dfrac{\partial^2 u}{\partial x^2} + m_l \cdot s_l \cdot \dfrac{\partial^2 u}{\partial t^2} - (J_l + m_l \cdot s_l^{\,2}) \cdot \dfrac{\partial^3 u}{\partial x \partial t^2} = 0 \\ EI \cdot \dfrac{\partial^3 u}{\partial x^3} + m_l \cdot \dfrac{\partial^2 u}{\partial t^2} - m_l \cdot s_l \cdot \dfrac{\partial^3 u}{\partial x \partial t^2} = 0 \end{cases} \tag{4.8}$$

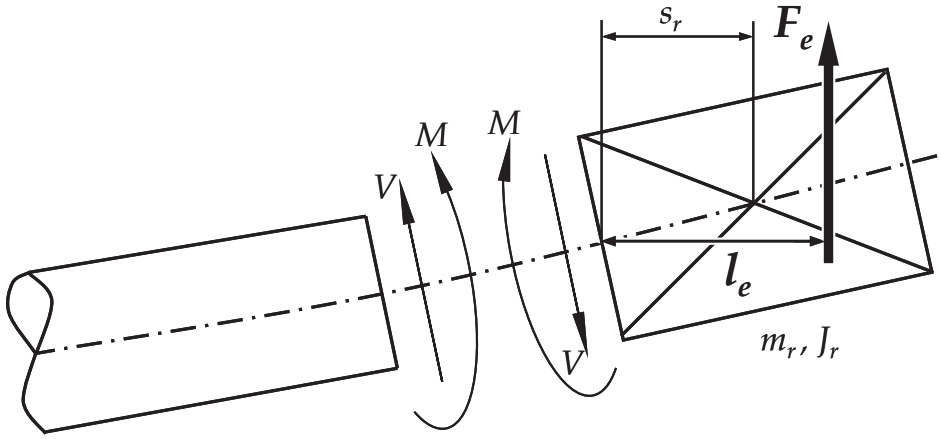

Figure 4.14: Boundary conditions at the right end with excenter force F_e.

$$\forall t : x = \frac{L}{2}$$

$$\begin{cases} EI \cdot \dfrac{\partial^2 u}{\partial x^2} + m_r \cdot s_r \cdot \dfrac{\partial^2 u}{\partial t^2} + (J_r + m_r \cdot s_r^{\,2}) \cdot \dfrac{\partial^3 u}{\partial x \partial t^2} = F_e \cdot l_e \\ -EI \cdot \dfrac{\partial^3 u}{\partial x^3} + m_r \cdot \dfrac{\partial^2 u}{\partial t^2} + m_r \cdot s_r \cdot \dfrac{\partial^3 u}{\partial x \partial t^2} = F_e \end{cases} \tag{4.9}$$

When the equations are solved with the excitation force $F_e(t)$ equal to zero, the different eigenmodes and eigenfrequencies are found. The resulting eigenmodes for a 12" pipe (diameter D = 323.9 mm) with wall thickness 12.7 mm and total length L = 4.80 m, filled with water and with the endweigths attached, are shown in Figure 4.15 and the eigenfrequencies are summarized in Table 4.2. The first eigenfrequency f_1 = 35.11 Hz is often called the *natural frequency* of the pipe.

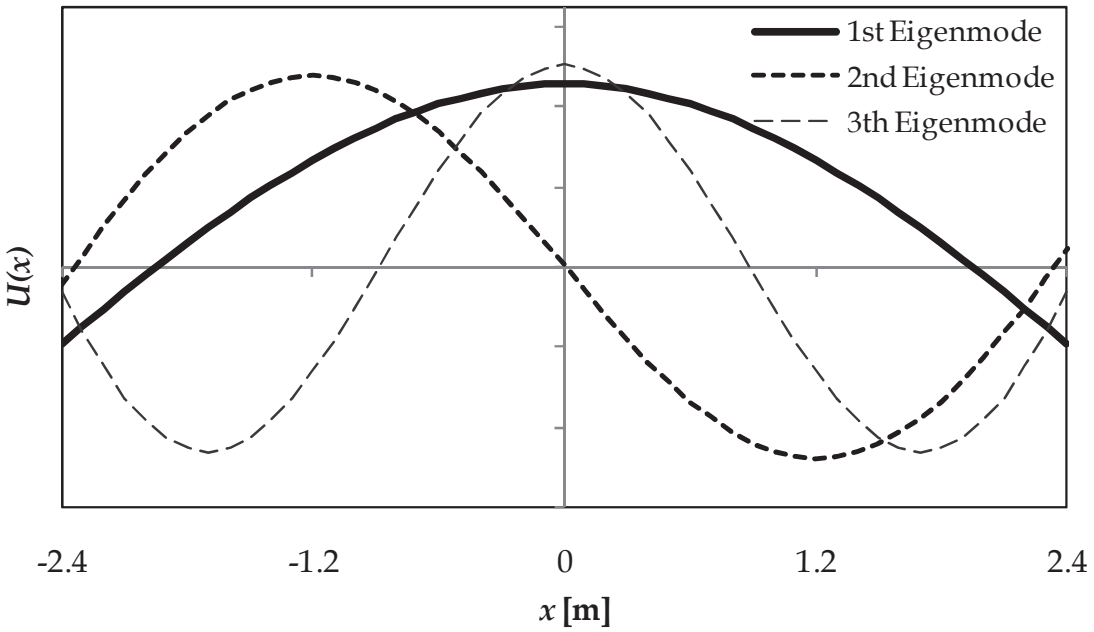

Figure 4.15: First three eigenmodes of the free floating pipe.

f_1	f_2	f_3	f_4
35.11	110.44	224.18	386.66

Table 4.2: First four eigenfrequencies [Hz] of the free floating pipe.

When the response of the pipe to a certain excitation force is of interest, $F_e(t)$ can be expressed as:

$$F_e(t) = m_e \cdot r_e \cdot \omega_e^2 \cdot e^{i \cdot \omega_e \cdot t} \tag{4.10}$$

With m_e and r_e respectively the excenter mass and excentricity, ω_e is the angular excitation frequency. Since the model does not contain any damping term, choosing $\omega_e = \omega_n$ would result in an infinite deflection amplitude (with ω_n the natural angular frequency of the free floating pipe). For this reason a slightly lower angular excitation frequency of $\omega_e = 0.98 \cdot \omega_n$ is chosen; the resulting deflection is given by Eq. (4.11).

$$u(x,t) = U_f(x) \cdot e^{i \cdot \omega_e \cdot t} \tag{4.11}$$

From the deflection amplitude $U_f(x)$ resulting from the forced vibration, the bending moment $M(x)$ and the maximum resulting stress amplitude at the pipe surface $\sigma(x)$ can be calculated according to equations (4.12) and (4.13). In Figure 4.16, $U_f(x)$ and $\sigma(x)$ are plotted for a certain setting of the drive unit. At the center of the pipe (x = 0), the deflection has an amplitude of 9 mm and the bending stress reaches a value of 180 MPa. The nodes of the deflection are located at x = -1.94 m and x = 2.01 m. These are the locations where the pipe should be supported in the test setup. The pipe deflection shape is not perfectly symmetric as the excitation frequency is slightly lower than the pipe's natural frequency.

$$M(x) = EI \cdot \frac{d^2 U_f(x)}{dx^2} \tag{4.12}$$

$$\sigma(x) = \frac{M(x) \cdot D/2}{I} \tag{4.13}$$

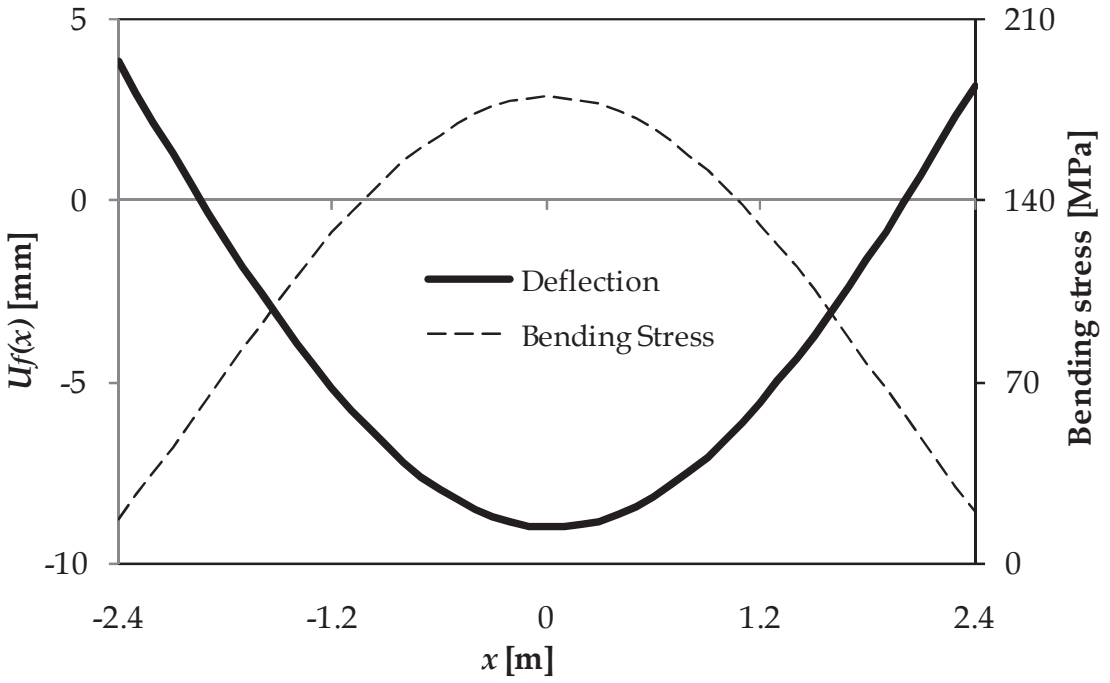

Figure 4.16: Deflection and bending stress with forced vibration.

3.2 Semi-analytical model of the total setup

To model the behaviour of the pipe in the setup and to quantify the influence of a threaded connection on the behaviour of the pipe, a more complex model is introduced as shown in Figure 4.17. In this model the setup is divided into 10 components. Components 1 and 8 are the endweights and 9 and 10 are the supports. The pipe is modelled using *component mode synthesis* (CMS) [4.2] and divided into 6 components. The central components 4 and 5 are introduced to model the influence of a threaded pipe connection.

The basic approach in CMS is to divide the system into a number of subsystems. Then a limited number of mode shapes of the subsystems are used to calculate approximate mode shapes of the complete system. In this analysis, five mode shapes are considered for each pipe section and the Hermite interpolation method [4.3] is used to combine the different components. The interpolation functions used, are defined by Eq. (4.14) and illustrated in Figure 4.18. In the equations x' is the normalized distance along the section length $x' = x/L$. Since the pipe is excited at its first eigenfrequency, taking into account five mode shapes of each segment is sufficient to accurately describe the pipe's response to the excitation.

The resulting model contains 46 degrees of freedom δ : 30 degrees of freedom are the coefficients of the five mode shapes of each of the six pipe sections, 14 degrees of freedom are prone to the deflection and rotation of the end points of each pipe section and the two last degrees of freedom are the support displacements. The complete model can be written in the form of Eq. (4.15). K, M and F are respectively the [46 × 46] stiffness matrix, the [46 × 46] mass matrix and the [46 × 1] force matrix of the system.

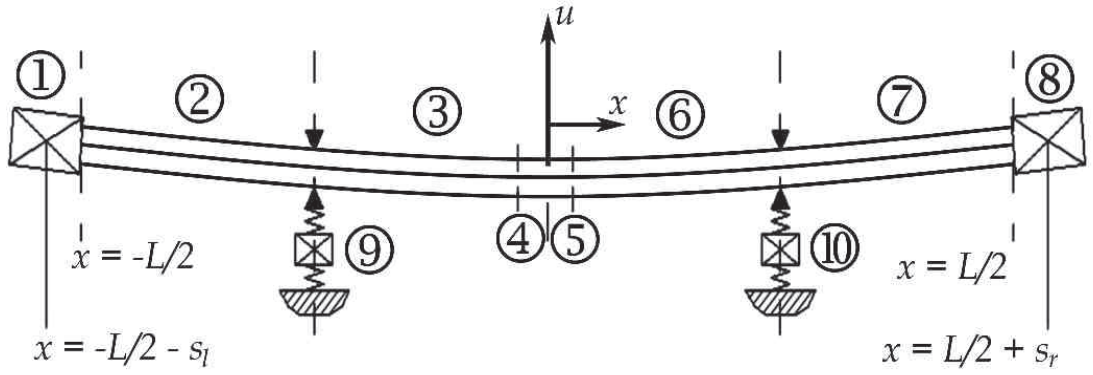

Figure 4.17: Model of the total setup.

$$h_1(x') = 1 - 3x'^2 + 2x'^3 \qquad h_3(x') = 3x'^2 - 2x'^3$$
$$h_2(x') = L\left(x' - 2x'^2 + x'^3\right) \qquad h_4(x') = L\left(2x'^2 + x'^3\right) \tag{4.14}$$

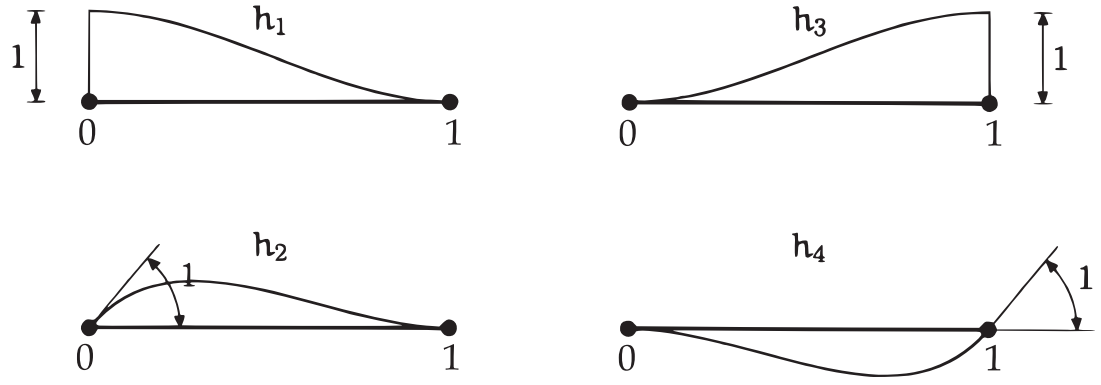

Figure 4.18: Hermite interpolation curves [4.4].

With this elaborated model the deflection and bending stress of the pipe can again be calculated. However, for the same conditions as used in the free floating pipe model, the differences are negligible: the maximum difference in deflection and in bending stress between the two models is only 0.03 mm and 0.6 MPa respectively. Nevertheless, with the more complex CMS model, the influence of misplaced supports can be studied, the required power can be estimated and by changing the properties of pipe segments 4 and 5 in Figure 4.17, the influence of a threaded connection and the joint integrity can be modelled. This will be discussed more in detail in the following sections.

$$K \cdot \delta + M \cdot \frac{d^2\delta}{dt^2} = F \tag{4.15}$$

4 System characterisation

4.1 Dynamic behaviour of the pipe

To understand the dynamic behaviour of the pipe in the setup, the frequency response can be calculated by the CMS model. This model does not contain any damping term, so the resonance peak of the bending stress amplitude will reach an infinite value when it approaches the pipe's natural frequency of 35.11 Hz, as can be seen in Figure 4.19. When the natural frequency is exceeded, the bending stress amplitude will decrease again. In the real application damping will appear due to viscous effects of the water in the pipe and damping in the supports. To estimate the effects of damping, the frequency response is multiplied by the transmissibility function TR of an unbalanced rotating machine which is mathematically described by the differential equation (4.17) (see reference [4.5]). In Eq. (4.16) ζ is the damping coefficient and in Eq. (4.17) C is the damping matrix. It should be noted that, apart from the damping term, this differential equation is similar to Eq. (4.15) which justifies the use of the specific transmissibility function. The frequence response of the damped oscillation is described by Eq. (4.18), where X is a parameter obtained by fitting equation Eq. (4.18) to the undamped frequency response with $\zeta = 0$.

$$TR = \frac{\left(\frac{\omega}{\omega_e}\right)^2}{\sqrt{\left(1-\left(\frac{\omega}{\omega_e}\right)^2\right)^2 + 4\zeta^2\left(\frac{\omega}{\omega_e}\right)^2}} \tag{4.16}$$

$$K \cdot \delta + C \cdot \frac{d\delta}{dt} + M \cdot \frac{d^2\delta}{dt^2} = F \tag{4.17}$$

$$\sigma_{damped}(f_e) = X \cdot TR \cdot \sigma \tag{4.18}$$

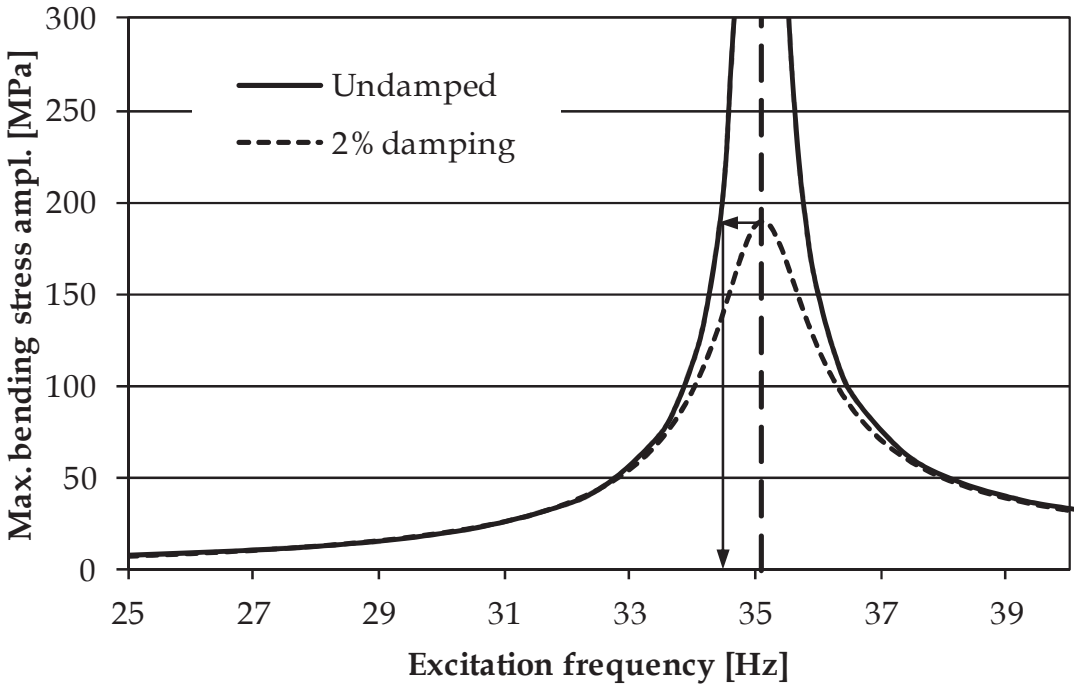

Figure 4.19: Frequency response of a pipe in the setup.

In Figure 4.19 the frequency response is given for a damping ratio of 2%. The resulting maximum bending stress amplitude is 188.9 MPa. The same stress value appears in the undamped CMS model at a frequency of 34.5 Hz. This is about 98% of the natural frequency which justifies the chosen value of $0.98 \cdot \omega_n$ for the excitation frequency ω_e in paragraph 3.1.

4.2 Pipe dimensions

4.2.1 Influence of the pipe length

With the analytical model of the free floating pipe, the influence of the pipe length on its natural frequency can be easily assessed. Results for the considered 12" pipe with a wall thickness of 12.7 mm are shown in Figure 4.20. To obtain a natural frequency below 40 Hz for a plain pipe without any additional endweights and not filled with water, the pipe should have a length of over 7.2 m. When the same pipe is filled with water, a length of 6.2 m is sufficient. When the used endweights are attached as well, the minimum pipe length is reduced to 4.5 m. This example illustrates the necessity of the endweights and beneficial effect of filling the pipe with water, otherwise the required pipe length would be too large. As mentioned above, the tested pipe has a length of 4.8 m, corresponding with a natural frequency of 35.11 Hz.

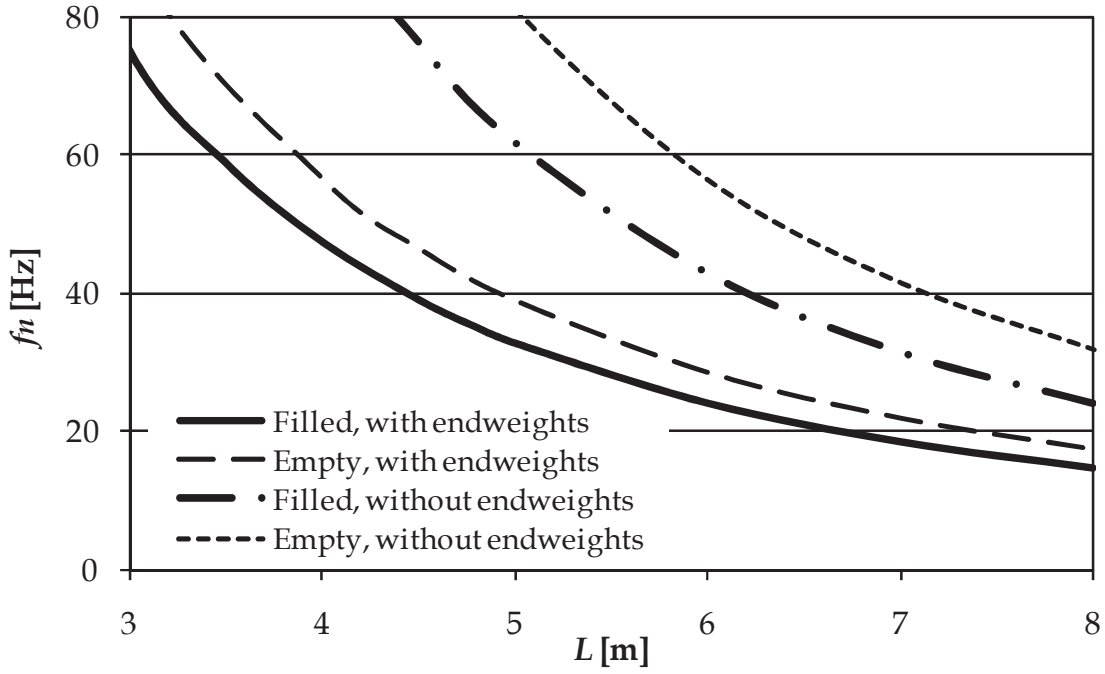

Figure 4.20: Influence of the pipe length on its natural frequency.

4.2.2 Influence of the pipe diameter and wall thickness

To illustrate the effect of pipe diameter *D* and pipe wall thickness *WT*, a pipe is considered with a fixed length of 5 m. Furthermore, the pipe is considered filled with water and the endweights of the actual setup are attached. When the analytical model of the free floating pipe is evaluated for pipes with a changing diameter and wall thickness, the natural frequencies as given in Figure 4.21 are found.

It can be seen that for a given wall thickness, the natural frequency is a close to linear function of the pipe diameter. Also it is observed that for all dimensions of the wall thickness, the natural frequency of a filled pipe of 0.10 m diameter and 5 m long with the endweights attached has a natural frequency of about 7.5 Hz. This is mainly because for these small diameters, the pipe weight becomes relatively small compared to the mass of the endweights. For this reason the practical minimum pipe size for the setup with the current set of endweights is about 6" or 168 mm in diameter.

This chart also illustrates the interaction between pipe diameter and wall thickness in the sense of the setup capabilities. Since 40 Hz is the maximum rotation speed of the excenters it is clear that for an increasing pipe diameter, the maximum pipe wall thickness that can be tested is reduced. While pipes with a *WT* = 4 mm can be tested up to 600 mm in diameter, pipes with *WT* = 40 mm can only be tested up to about 310 mm diameter.

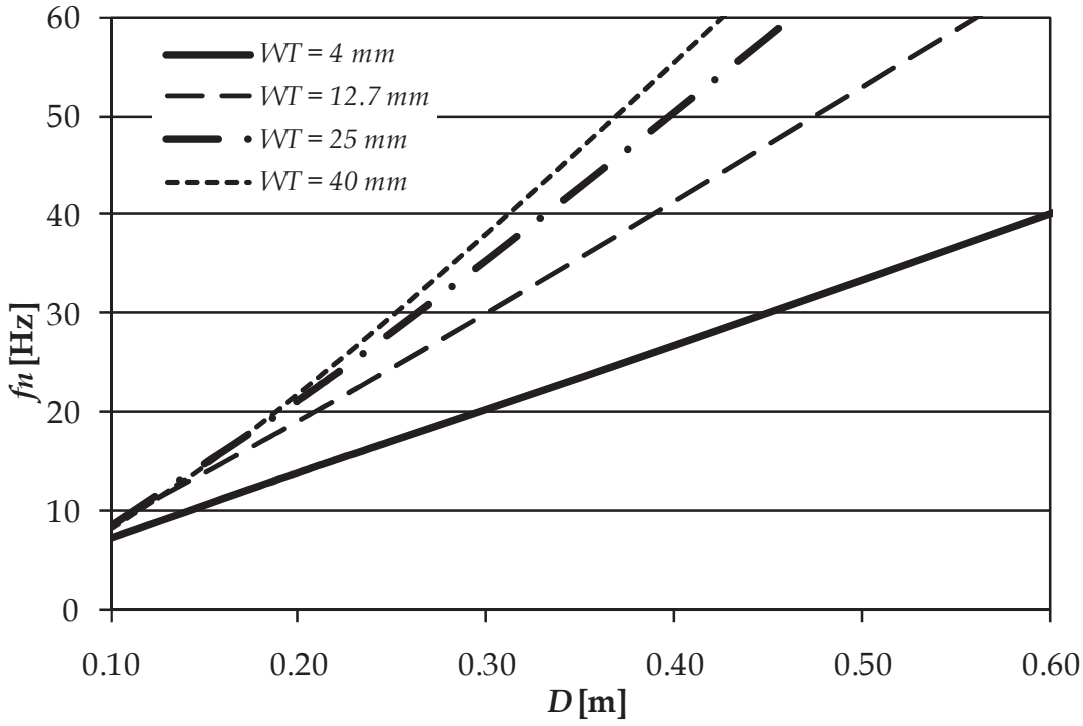

Figure 4.21: Influence of the pipe diameter and wall thickness on its natural frequency.

4.2.3 Simplified relation

From the analysis of the resulting natural frequencies it is observed that the wave number γ as defined by Eq. (4.7) is inversely proportional to the pipe length. Using this relation, Eq. (4.7) could be simplified to a simple relation between the pipe standard dimensions of length, diameter and wall thickness and the resulting natural frequency of the pipe. For a steel pipe filled with water, this is given by Eq. (4.19) with all dimensions in meter and the frequency in Hz.

$$f_n = \frac{15.7 \cdot 10^3}{L^2} \cdot WT^{0.4} \cdot (D - 0.1) + 7.5 \tag{4.19}$$

This equation can be used for a first estimation of the natural frequency of a plain or welded pipe in the setup and clearly shows the influence of the different pipe dimensions. It can be observed that the natural frequency is inversely proportional to the square of the pipe length. Hence to lower the natural frequency of a pipe of a certain size, the pipe length should be increased. There is a linear relation between the natural frequency and the pipe diameter, which corresponds to the observations made in Figure 4.21. When the pipe diameter is equal to 100 mm, the natural frequency will be 7.5 Hz, no matter what the length or wall thickness is. Obviously this simplification only holds true within the boundaries of the setup size. Which means that only pipes should be considered with a length that fits in the setup and having a realistic wall thickness. Finally, the influence of the pipe

wall thickness on the pipe's natural frequency is a power function with exponent 0.4. This means that the change in natural frequency corresponding to an increase in wall thickness of for example 1 mm will decrease for a higher value of the wall.

4.2.4 Influence of a threaded connection

To investigate the influence of a pipe connected by a threaded coupling in the setup, the CMS model is used, where the pipe sections 4 and 5 (as in Figure 4.17) are given the outer dimensions of the connection. To illustrate this, the model is evaluated for a set of standard API connection dimensions given in Table 4.3. The considered connection types are the API Line Pipe connection, both the short and long API Round Casing connection, the API Buttress Casing connection and the API Buttress SC (Special Clearance) Casing connection. The considered pipe size is 8 5/8" with an outer diameter of 219.1 mm and wall thickness of 8.2 mm because all considered connections are available in this size. The total pipe length is 4.4 m for all considered cases and the excitation frequency is 23.07 Hz or 98 % of the natural frequency of the plain pipe without a connection.

Connection Type	Box diameter [mm]	Box length [mm]	Added mass [kg]	U_f [mm]	f_n
Plain pipe 8 5/8"	-	-	-	7.8	23.54
API Line Pipe	244.5	133.4	9.7	8.1	23.51
API Round Short Casing	244.5	196.9	14.3	7.8	23.52
API Round Long Casing	244.5	254.0	18.4	7.4	23.54
API Buttress Casing	244.5	269.9	19.6	7.3	23.55
API Buttress SC Casing	231.8	269.9	9.5	5.4	23.74

Table 4.3: Influence of a threaded connection.

In Figure 4.22 the deformation shape $U_f(x)$ is shown for the plain pipe together with the pipe with three different connections. In combination with the data from Table 4.3 following observations can be made: the deformation shape of the pipe with an API Line Pipe connection has a higher deformation amplitude U_f than the plain pipe. This is due to the limited length of the coupling which makes it behave as a concentrated mass added to the centre of the pipe. This decreases the natural frequency of the system and as the excitation frequency is kept constant, the deformation amplitude increases.

When the API Buttress Special Clearance Casing is considered, which is a buttress casing connection with a decreased box outer diameter, it can be seen that the added mass is similar to that of the API Line Pipe connection. However, the box length is about double of the length of the latter. This means that the added stiffness of the central pipe sections becomes more pronounced and increases the natural frequency of the system which gives a decrease in bending deflection. For the other connection types given in Table 4.3, the change in natural frequency is less pronounced since they all have the same box diameter. This means that a box with an increased length will also have an increased mass.

Due to the large variety of existing connections, it is hard to determine a priori what the pipe deflection will be. For this reason threaded pipe connections should be analysed on an individual basis to determine their dynamic behaviour in the setup.

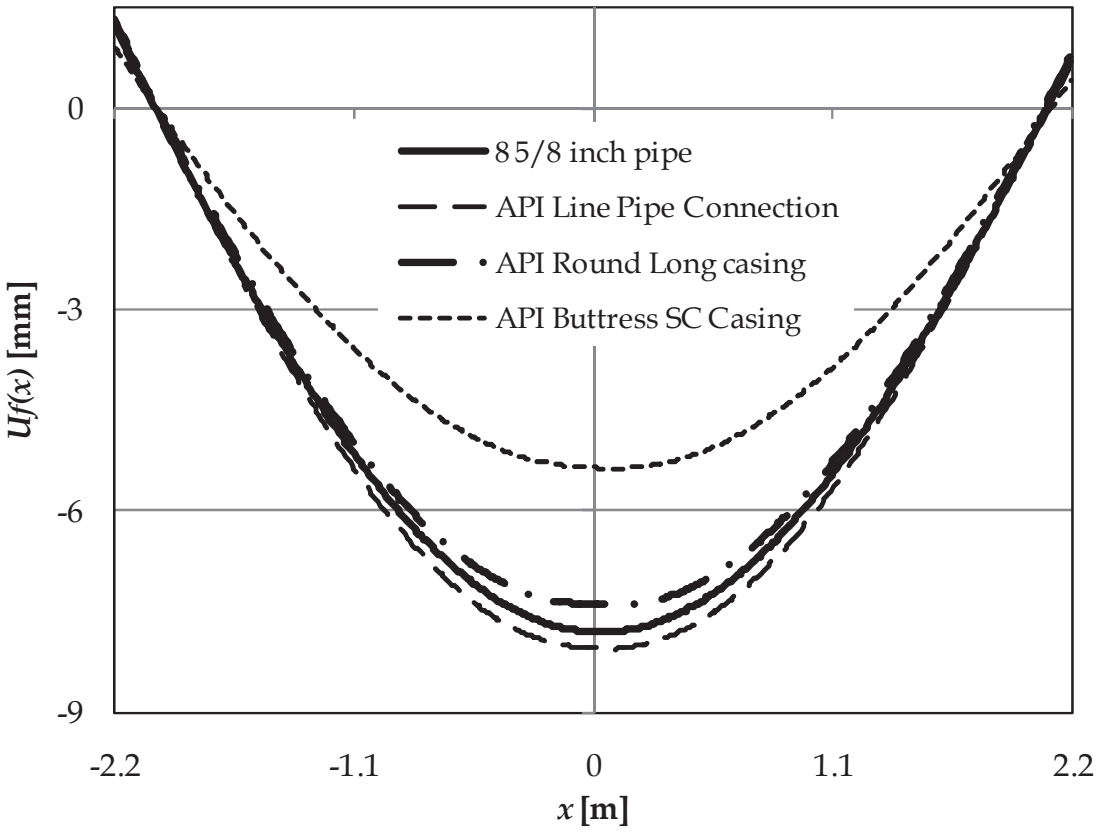

Figure 4.22: Influence of a threaded connection on the pipe deformation

4.3 Setup configuration and requirements

4.3.1 Influence of the excenter force and required drive accuracy

In section 2.2.2 it was shown that the drive unit contains two excenters whose relative position can be changed to control the resulting excenter force. This relative position is described by the excenter angle a_e. In Figure 4.5 the drive

unit is illustrated with the excenters totally out of phase or an excenter angle of $a_e = 0°$. For any given position of the excenters, the corresponding excenter mass m_e is given by Eq. (4.20). The resulting excenter force is defined by Eq. (4.10). As can be seen by this equation, the excenter force can be changed not only by the excenter angle a_e but also by controlling the excitation frequency ω_e. However, as was shown in Figure 4.19, the resonance peak is very steep which requires a very accurate control of the excitation frequency to be able to control the corresponding bending stress. If the bending stress amplitude is to be controllable up to 2 MPa, the excitation frequency should be controlled as accurate as 0.01 Hz, which is practically impossible. For this reason the excenter angle can be changed and the bending stress amplitude can be controlled accordingly. Nevertheless the accuracy of the drive speed should not be less than 0.05 Hz.

$$m_e = m_{e,max} \cdot cos\frac{180° - a_e}{2} \tag{4.20}$$

4.3.2 Influence of the support positions

During the design process of the setup, the CMS model was used to evaluate the stiffness of the airsprings used in the supports. If their stiffness would be too high, a small deviation of the supports from their theoretical position would lead to high dynamic reaction forces. The influence of such a deviation of the supports on the reaction forces for the chosen airsprings is shown in Figure 4.23. As can be seen, the dynamic forces remain limited to 100 N in both supports if the supports do not deviate more than ± 40 mm from the nodes of the first eigenmodes. Because of practical considerations it is possible to position the supports with an accuracy of about 10 to 20 mm, but this will not result in important dynamic forces during the tests.

It should be noted that the discussed dynamic forces are evaluated when the pipe is in resonance. However, before this situation is reached the excitation frequency has to increase from zero to the resonance frequency. During the start up the pipe is not in resonance and the dynamic forces on the supports can be much more important. This is illustrated in Figure 4.24 where the reaction force in the right support closest to the drive unit is plotted as a function of the excitation frequency. It can be seen that at the resonance frequency of the pipe the dynamic forces become zero. But at a much lower frequency of about 3.2 Hz, the support force becomes much more important. This is because the natural frequency of the loaded airsprings is located in this region. To avoid too high forces in the supports the start-up procedure of the test setup is defined to increase the excitation frequency rapidly to 15 Hz in order to avoid resonance of the airsprings. As soon as this frequency is reached the dynamic forces on the right support remain limited between 300 and 400 N. Since the left support is located further away from the drive unit, the dynamic forces at this location are much lower than at the right support.

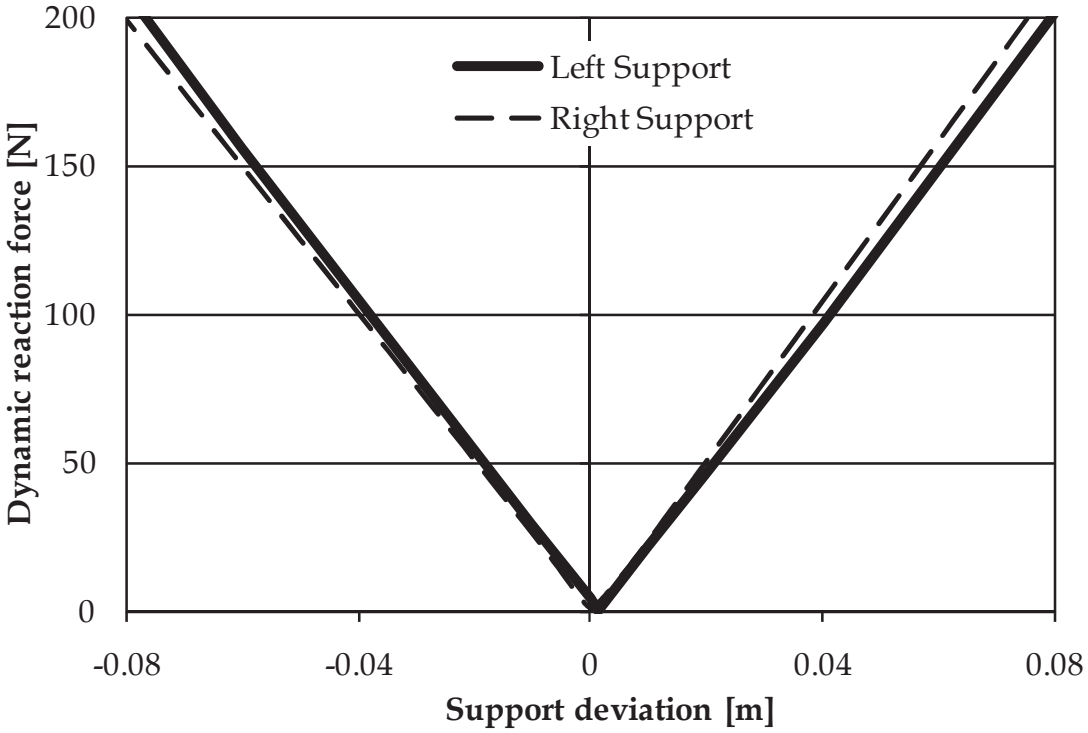

Figure 4.23: Reaction forces in the supports.

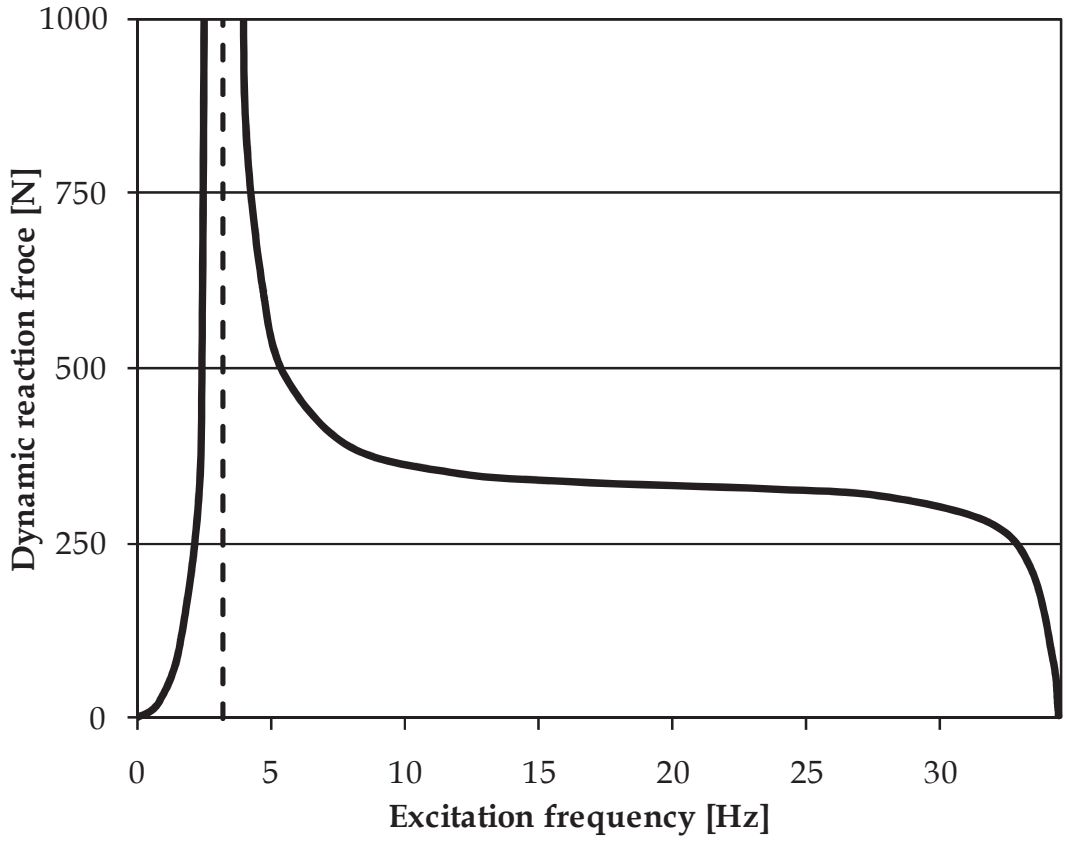

Figure 4.24: Dynamic force in the right support during start-up.

4.3.3 Required power

After startup, the pipe is describing a harmonic deformation and the required power is determined by internal damping in the system. However, as the CMS model does not contain any damping terms, the dissipated power is estimated from the amount of potential energy V in the system, with V calculated from the stiffness matrix K according to Eq. (4.21). The dissipated power P is then calculated by assuming that a certain amount of this potential energy is dissipated by damping during each cycle, see Eq. (4.22). As described earlier, the damping expressed by the damping ratio ζ is expected to come from viscous effects of the water in the pipe and damping in the airsprings. This damping ratio was determined to be between 0.035 and 0.047 by substituting the measured effective motor power with the dissipated power P in Eq. (4.22).

$$V = \frac{1}{2}\delta^T \cdot K \cdot \delta \tag{4.21}$$

$$P = \zeta \cdot V \cdot \frac{\omega_e}{2\pi} \tag{4.22}$$

5 Applicability range of the setup

The effective power needed to obtain a certain stress amplitude in any pipe size can be estimated using the obtained damping value. In Table 4.4 the resulting power is given for a range of pipe diameter and wall thickness sizes to obtain a bending stress amplitude of 180 MPa which corresponds with a bending stress range of 360 MPa. This stress range is comparable to the stress range of 350 MPa of the resonant bending setups of Stress Engineering [4.6] and 400 MPa of the TWI test rigs [4.7] and is considerably higher than the bending stress range of 200 MPa of the setup at the University of Pisa [4.8].

The table contains data for pipes within the diameter range from 6" (168.3 mm) to 20" (508.0 mm) with commercially available wall thicknesses up till 40 mm. For a given pipe size, the table provides the required pipe length L, the corresponding natural frequency f_n and the support positions together with the deflection amplitude and dissipated power corresponding to a bending stress range of 360 MPa.

For the applicability range of the setup there are three limiting factors. First, the dissipated power should remain below the maximum effective power of the drive motor. The nominal power of the drive motor is 7.5 kW, which means that the effective power is about 6 kW as the drive motor has an efficiency between 80 and 85 %. Second, the length of the pipe should not exceed 6 m in order to fit inside the setup. There is no strict minimum length, but as can be seen from Table 4.4, none of the given pipes has a length shorter than 3.7 m. The third limiting factor is the excitation frequency that should remain below 40 Hz as explained in section 2.2.2.

D		*WT*	*L*	Support Positions		f_n	U_f	*P*
[inch]	[mm]	[mm]	[m]	[m]	[m]	[Hz]	[mm]	[kW]
6	**168.3**	**12.5**	4.0	-1.89	1.95	22.87	16.1	1
6	**168.3**	**25**	3.8	-1.73	1.78	27.04	13.4	1
6	**168.3**	**40**	3.7	-1.63	1.68	28.45	12.1	2
8	**219.1**	**5.6**	4.5	-2.09	2.16	20.24	15.1	1
8	**219.1**	**12.7**	4.3	-1.92	1.99	27.33	12.9	1
8	**219.1**	**25**	4.1	-1.75	1.81	33.36	10.8	3
8	**219.1**	**40**	4.0	-1.64	1.70	36.17	9.5	3
10	**273.0**	**5.6**	4.8	-2.12	2.19	22.49	12.5	1
10	**273.0**	**12.7**	4.6	-1.95	2.02	31.18	10.7	2
10	**273.0**	**25**	4.5	-1.80	1.87	37.65	9.3	4
10	**273.0**	**40**	4.4	-1.69	1.75	41.74	8.2	6
12	**323.9**	**8**	5.0	-2.07	2.14	28.27	10.1	2
12	**323.9**	**12.7**	4.8	-1.94	2.01	35.11	9.0	3
12	**323.9**	**25**	4.8	-1.83	1.90	41.77	7.9	6
12	**323.9**	**40**	4.6	-1.69	1.75	48.69	6.9	9
14	**355.6**	**8**	5.2	-2.08	2.16	29.18	9.5	2
14	**355.6**	**12.7**	5.1	-1.99	2.07	35.19	8.7	3
14	**355.6**	**25**	4.9	-1.82	1.89	45.23	7.3	7
14	**355.6**	**40**	4.7	-1.68	1.75	53.07	6.3	11
16	**408.4**	**7.9**	5.4	-2.07	2.15	31.52	8.2	2
16	**408.4**	**12.7**	5.3	-1.99	2.06	38.47	7.5	4
16	**408.4**	**25**	5.1	-1.82	1.89	50.00	6.4	9
16	**408.4**	**40**	4.9	-1.69	1.76	59.13	5.6	15
18	**457.0**	**8**	5.6	-2.07	2.15	33.54	7.4	3
18	**457.0**	**12.7**	5.5	-1.99	2.07	40.93	6.8	5
18	**457.0**	**25**	5.3	-1.84	1.91	53.56	5.9	11
18	**457.0**	**40**	5.1	-1.71	1.78	63.63	5.1	18
20	**508.0**	**7.8**	5.7	-2.05	2.13	36.00	6.5	3
20	**508.0**	**12.7**	5.6	-1.97	2.04	44.56	6.0	6
20	**508.0**	**25**	5.4	-1.83	1.90	58.71	5.2	14
20	**508.0**	**40**	5.2	-1.71	1.77	70.08	4.5	23

Table 4.4: Range of applicability of the test setup.

For the pipe sizes where one of the three limits is exceeded, the cells are marked in grey, which means they can not be tested in the test rig. For a given pipe diameter, the pipe length is reduced for an increased wall thickness size since the dissipated power increases by both the weight and volume of the pipe. Hence, when the pipe wall thickness is increased, the length is reduced to try to limit the power needed. However, when the pipe length is reduced, its natural frequency will increase (see Eq.(4.19)). As can be seen from grey marked cells in Table 4.4, a further decrease in pipe length is not possible, since the natural frequency of the pipe is exceeding 40 Hz.

6 Experimental validation

To validate the results of the mathematical models, several tests have been carried out on two different pipes which are called *Pipe 1* and *Pipe 2* in the remainder of this chapter. Their properties are summarized in Table 4.5. Pipe 1 is an X65 electric resistance welded plain pipe with outer diameter of 12" or 323.9 mm, a wall thickness of 12.7 mm and a length of 4.81 m. Pipe 2 is a seamless X65 pipe with outer diameter of 323.9 mm, wall thickness of 23.9 mm and length of 5.27 m. First the frequency response of the pipe deflection as a function of the applied excitation frequency is studied. Then the deformation shape of the pipes are measured with the 3D optical measuring system.

Test pipe	D [mm]	WT [mm]	L [m]	f_n [Hz]
Pipe 1	323.9	12.7	4.81	35.1
Pipe 2	323.9	23.9	5.27	35.3

Table 4.5: Properties of the two test pipes.

6.1 Frequency response

6.1.1 Experimental and theoretical deflection

The frequency response of the pipe deflection is measured by the laser sensors that are mounted on the safety frame. Both the horizontal z-deflection and the vertical y-deflection are a harmonic signal with the same amplitude but with a phase difference of 90°. This means that a section of the pipe describes a circle as illustrated by Figure 4.25 where the dots are the measured deflections and the black line is a circle with a radius of 3.4 mm. This deflection is obtained for Pipe 1 with an excenter angle of 35° at an excitation frequency of 34 Hz. In Figure 4.25 it can be seen that the measured data is clustered in 18 groups, this is because of the sampling rate of the data acquisition system. When a signal with a frequency of 34 Hz is sampled at a rate of 600 Hz, each cycle is sampled 17 or 18 times.

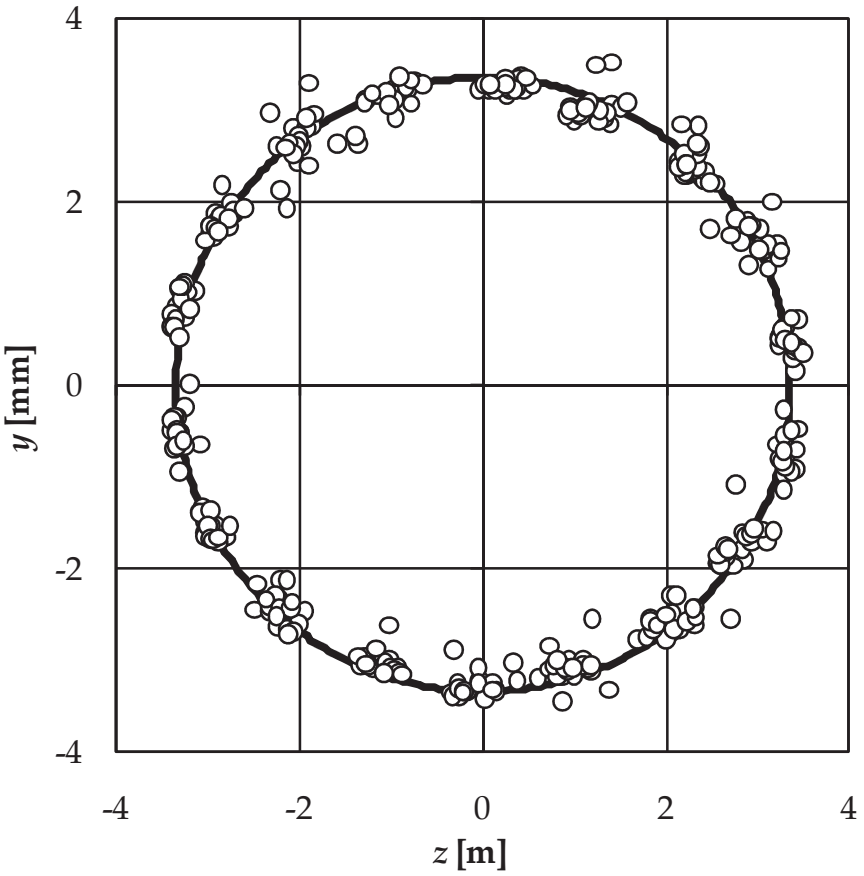

Figure 4.25: Pipe 1 *y*- and *z*-deflection as measured by the two lasers.

To describe the frequency response, only the vertical deflection is used. Using the horizontal deflection does not provide any additional information and does not result in different deflection values. During service of the test rig, both signals are monitored continuously, during post-processing the signals can be compared to filter away noise on one of the sensors.

The measured vertical deflection at the center of the pipe $U_f(0)$ as a function of the excitation frequency, is compared to the deflection calculated with the semi-analytical model for Pipe 1 with an excenter angle of 75°. As can be seen in Figure 4.26, there is a good correlation between both curves. When moving closer to the natural frequency of the pipe however, the measured deflection becomes increasingly smaller than the calculated values. In Figure 4.27 the frequency response for Pipe 1 with an excenter angle of 20° is plotted, while Figure 4.28 shows the frequency response for Pipe 2 with an excenter angle of 135°. For both figures a similar observation can be made. For frequencies below 34 Hz, the correspondence between the theoretical and measured values is good, but the response deviates increasingly for higher frequencies. This is because in the theoretical model, no damping is considered, while in reality the damping has an important influence on the resonance peak.

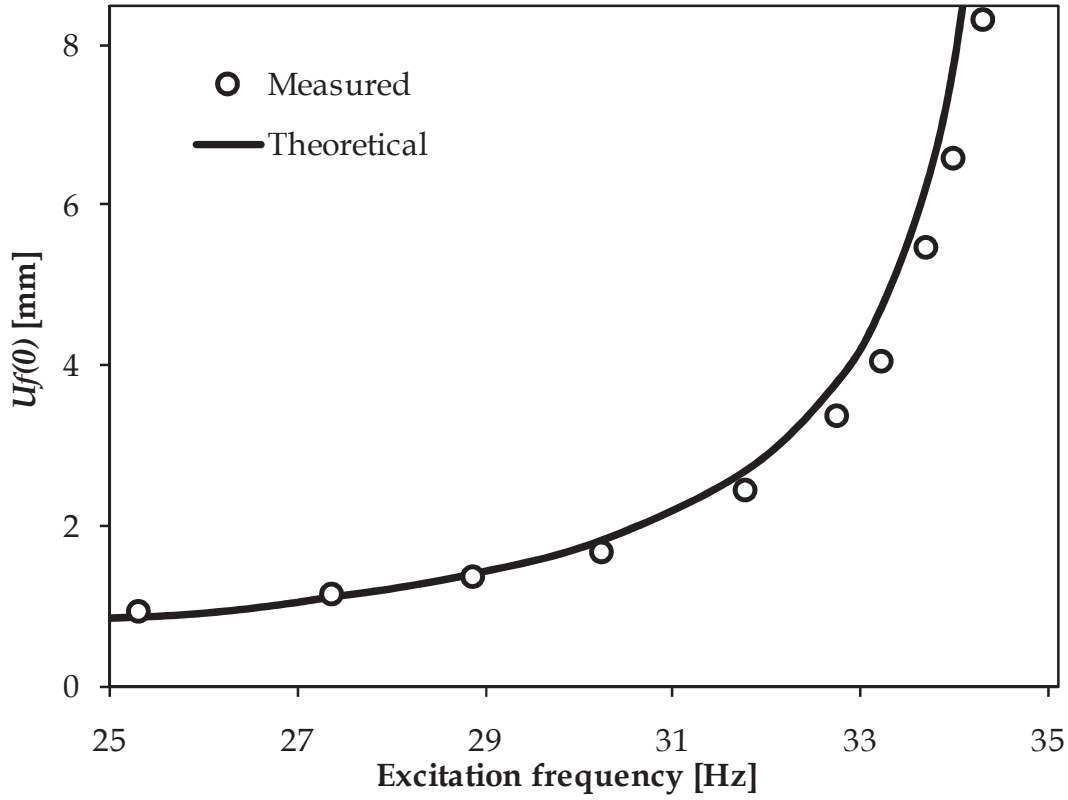

Figure 4.26: Pipe 1 frequency response for an excenter angle of 75°.

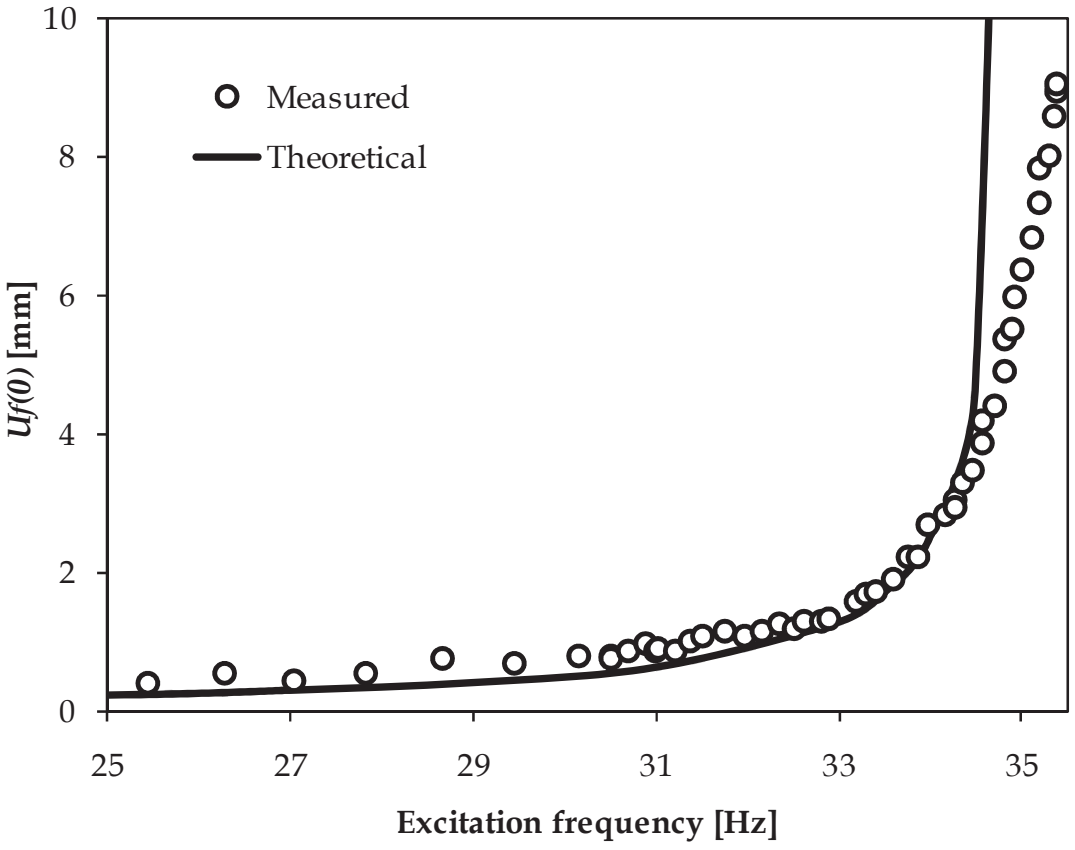

Figure 4.27: Pipe 1 frequency response for an excenter angle of 20°.

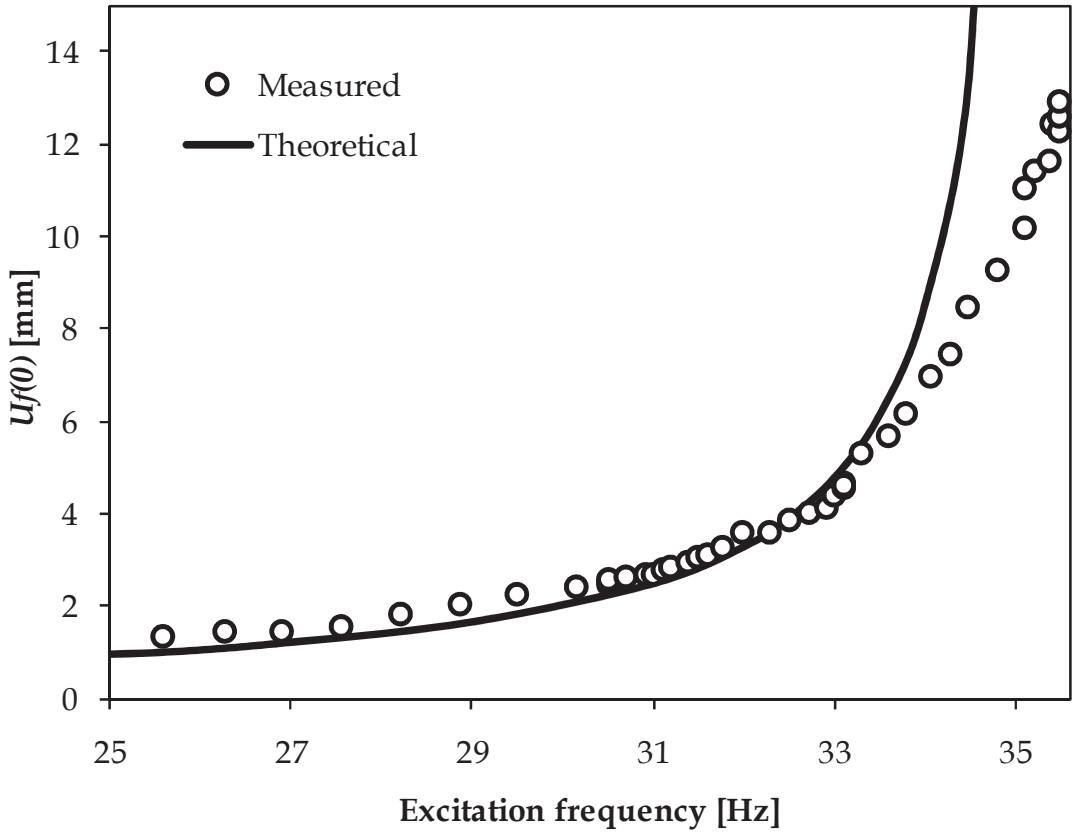

Figure 4.28: Pipe 2 frequency response for an excenter angle of 135°.

When moving up on the resonance peak, the damping becomes more important and the occurring deflection becomes increasingly lower than the theoretical undamped values.

In Figure 4.28 it can be seen that the maximum deflection amplitude for Pipe 2 is 13.1 mm. This corresponds to a bending stress amplitude of 245 MPa (the deflection-stress relationship is discussed more in detail in section 6.3.4). The obtained stress range of 490 MPa is considerably higher than the reported maximum stress range of 350 MPa of the Stress Engineering setups and the stress range of 400 MPa of the setups of TWI as presented in section 5.1.4 of Chapter 2.

6.1.2 Resonance peak

To investigate the behaviour of the setup in the frequency range above $0.98 \cdot f_n$ more in detail, the excenters were positioned at an angle of 5° so that the resulting excenter force would be limited. This in order to avoid too high stresses in the pipe when moving on the resonance peak. It was expected that a frequency response similar to that of the damped system illustrated in Figure 4.19 would be obtained.

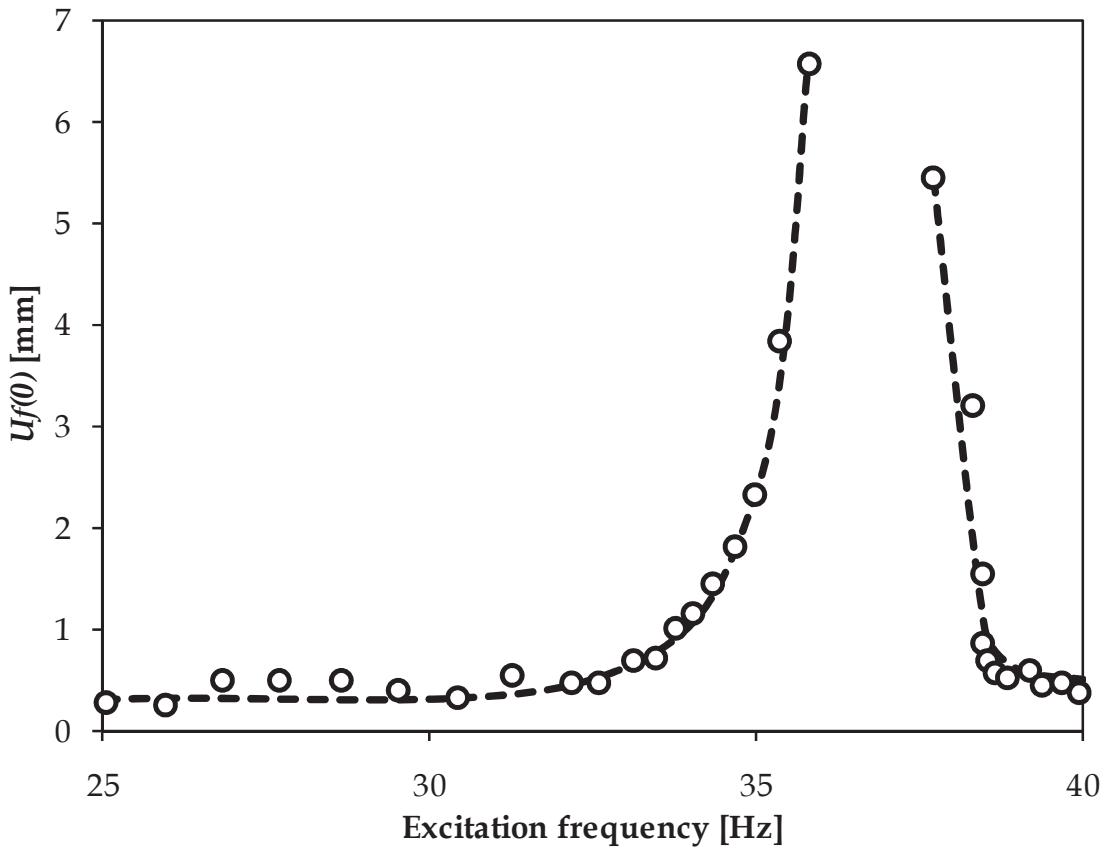

Figure 4.29: Pipe 1 frequency response when moving over the resonance region with an excenter angle of 5°.

However, when the excitation frequency was increased slowly the resulting deflection amplitude increased asymptotically showing a clear resonance peak. But it was not possible to exceed a frequency of 35.6 Hz. Note that this value is slightly higher than the calculated value of 35.11 Hz for the natural frequency. The resulting deflection amplitude at that time reached a value of about 8 mm, which is considerably high for this small excenter angle. A further increase in excitation speed could not be obtained since the electromotor reached its maximum power while the rate of deflection increase did not seem to saturate.

This observation gives the impression that the damping caused by viscous effects in the water in the pipe becomes less important in a narrow band around the resonance frequency. This would mean that the damping coefficient of the system is not constant. Nevertheless, it is possible to move over the resonance region by increasing the frequency more rapidly over the resonance peak. The resulting frequency response is shown in Figure 4.29. The maximum deflection amplitude measured is now only 6.6 mm. Because the frequency is increased rapidly and because of the inertia of the pipe, no useful data is available for frequencies between 35.8 and 37.7 Hz. Hence the exact behaviour on the resonance peak itself remains unknown. For this reason the outer points are not connected by a line in Figure 4.29. Due to the difficulties to map this region in the frequency response, it is not possible to

get an accurate assessment of the damping coefficient of the system. Hence the damping can only be estimated indirectly by comparing the delivered motor power with Eq. (4.22).

6.2 Deformation shape

Due to the dimensions of the room where the setup is placed, only a limited length of the pipe (1.2 m) can be captured by the dynamic 3D optical measurement system. Since the largest pipe deflection occurs at the centre of the pipe (position x = 0), reflective markers are attached at 10 locations along the pipe axis as illustrated in Figure 4.30 in a region between approximately -0.6 m < x < 0.6 m. Additionally, 4 markers are placed on the safety frame (indicated by the arrows in Figure 4.30), which remains stationary during the tests. These points are selected as the global transformation points for all the markers. This means that the coordinates of the markers on the pipe are calculated in a coordinate system linked to the safety frame. Data is captured at a measuring frequency of 500 Hz. The measured deformation shape of the pipe at an excitation frequency of 33.2 Hz is compared to the deformation shape with the same deflection amplitude at the pipe centre calculated with the semi-analytical model (see Figure 4.31). As can be seen, both results correspond very well. The RMS deviation is only 0.03 mm, which is the accuracy of the optical measuring system.

In Figure 4.32 the pipe deflection over time in the yz-plane (perpendicular to the longitudinal x-axis of the pipe) of the marker at the pipe centre is shown. It can be seen that the y- and z-deflection have the same amplitude, but that the z-deflection has a phase delay of 90°. This means that the marker describes a clockwise circular movement as illustrated in Figure 4.33. This confirms the results obtained by the horizontal and vertical laser sensors shown in Figure 4.25.

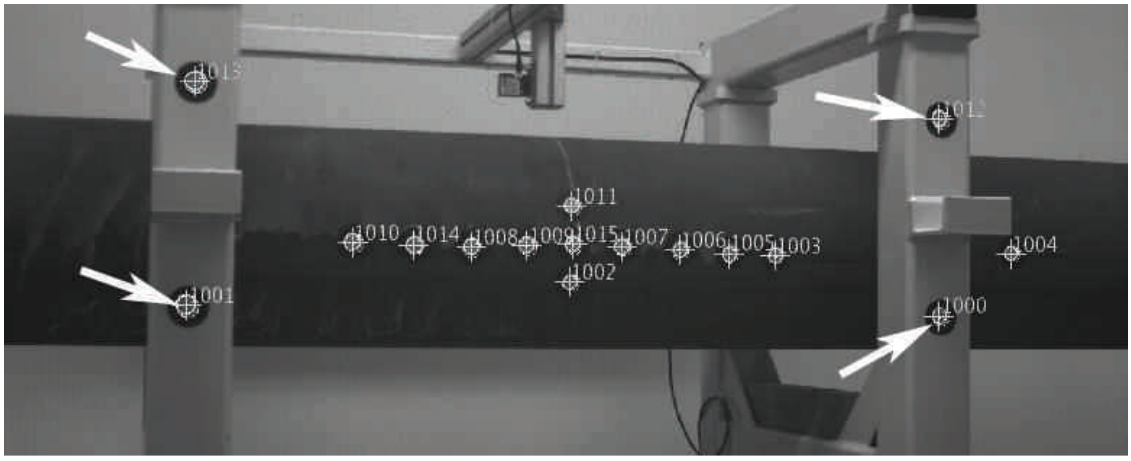

Figure 4.30: Markers as identified by the optical measuring system on Pipe 1 (arrows indicate stationary markers on the safety frame).

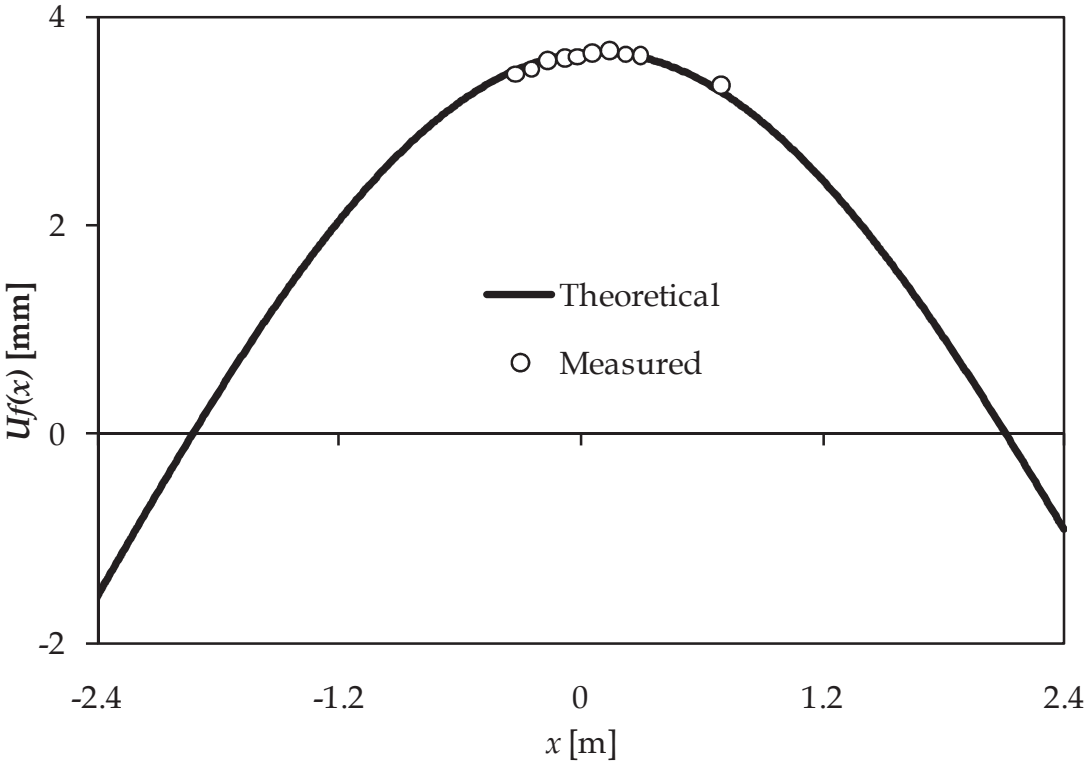

Figure 4.31: Pipe 1 calculated and measured deformation shape.

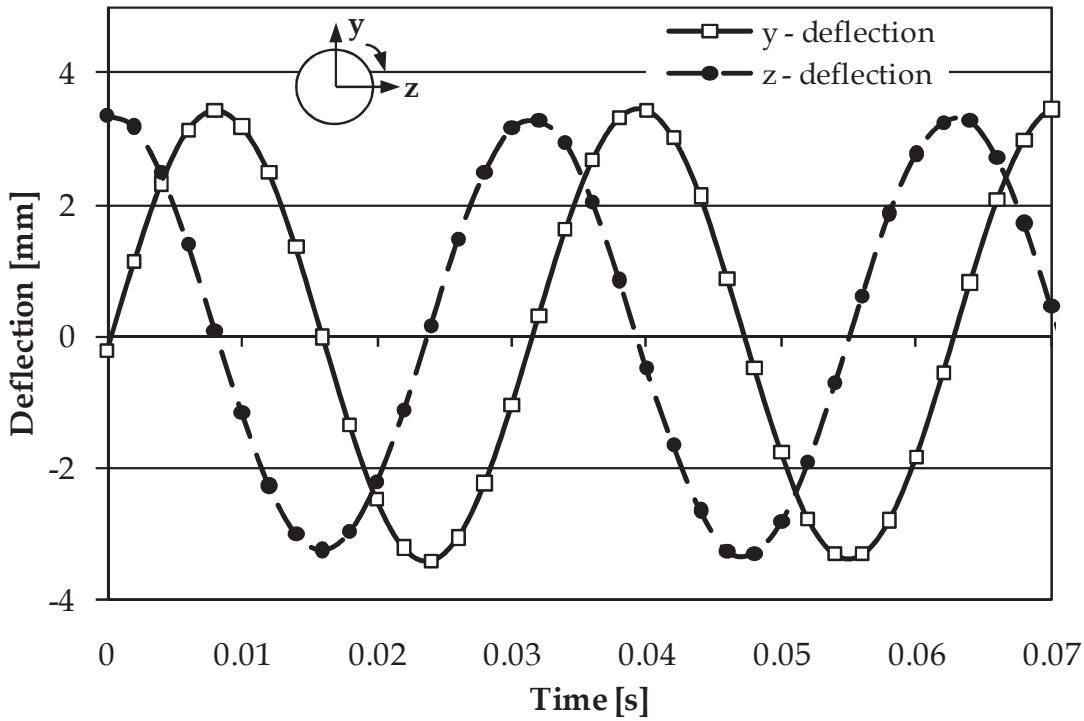

Figure 4.32: Pipe 1 movement of the central point.

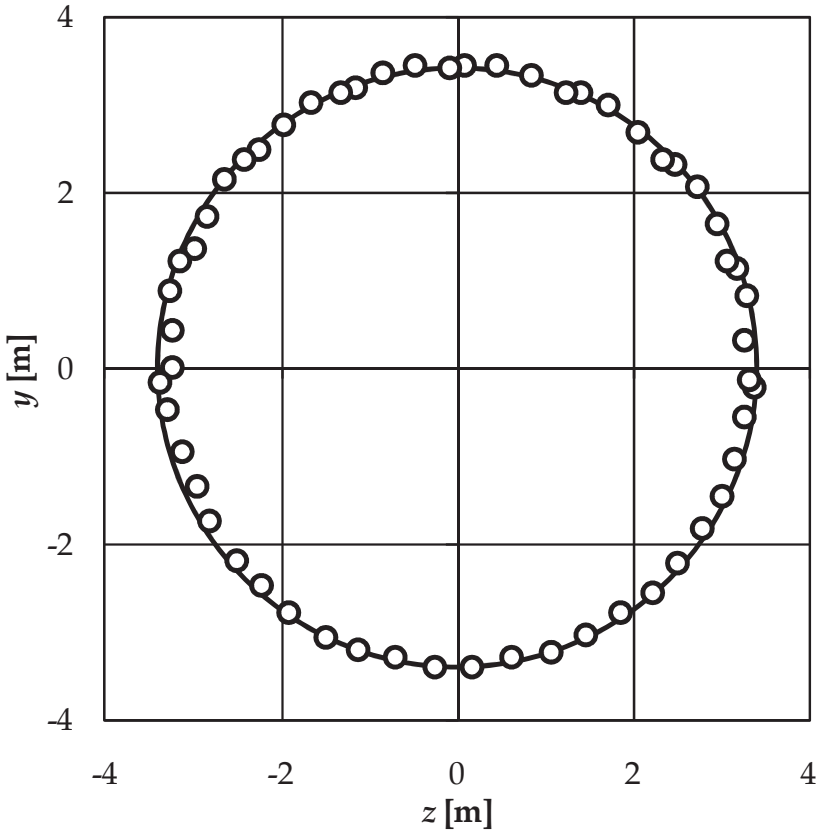

Figure 4.33: Pipe 1 *y*- and *z*-deflection as measured by the dynamic 3D optical measurement system.

6.3 Bending stress and strain

6.3.1 Strain measurements and stress calculation

To monitor the bending strain at the pipe circumference, five strain gauges are attached in the axial direction at different locations over the length of Pipe 1. Since the bending stress remains within the elastic region, it can be calculated from the measured strains according to Hooke's law of elasticity Eq. (4.23).

$$\sigma = \varepsilon \cdot E \tag{4.23}$$

6.3.2 Pipe 1 response for different excenter angles

Similar to the bending deflection frequency response, the bending stress frequency response can be plotted. This signal is smoother since the data acquisition system of the strain gauges contains an internal 100 Hz low-pass filter which means the signal is less prone to noise as is the case for the laser sensor measurements. The bending stress response of Pipe 1 has been determined for 8 different positions of the excenters going from an excenter angle of 5° to 125°. Only 6 response curves are plotted for in Figure 4.34 in order not to overload the graph. For each excenter position, the same maximum stress level can be reached (in case of the excenter positions of 30°

and 60° this was not the case due to operator settings). The difference however, is the slope of the resonance peak. In case of an excenter angle of 5°, the bending stress amplitude only exceeds 40 MPa at 34.5 Hz, while the same stress level is reached at an excitation frequency of 29.5 Hz when the excenter angle is 125°.

Even though it is easier to accurately control the bending stress amplitude on a less steep slope, it is advised to use lower excenter angles for low stress levels. This in order to keep the excitation frequency not too far away from the natural frequency of the pipe. When the excitation frequency is lower, the deformation shape might deviate more from the theoretical harmonic shape and the supports will not be located exactly in the nodes.

In Figure 4.35 the influence of the excenter mass m_e is illustrated. The excenter mass given by Eq. (4.20) is here expressed relative to the maximum excenter mass when the excenter angle a_e = 180°. It should also be noted that according to Eq. (4.20) the excenter mass for an excenter angle of 125° is 89 % of the maximum excenter mass.

It can be seen that for a given excitation frequency, the resulting bending stress amplitude depends linearly on the excenter mass. This result is in correspondence with Eq. (4.10) where it can be seen that a linear increase in excenter mass results in a linear increase in excenter force. When a certain excitation frequency is needed, e.g. 34 Hz, it is easy to determine the required excenter mass with the help of Figure 4.35 and to calculate the corresponding excenter angle according to Eq. (4.20).

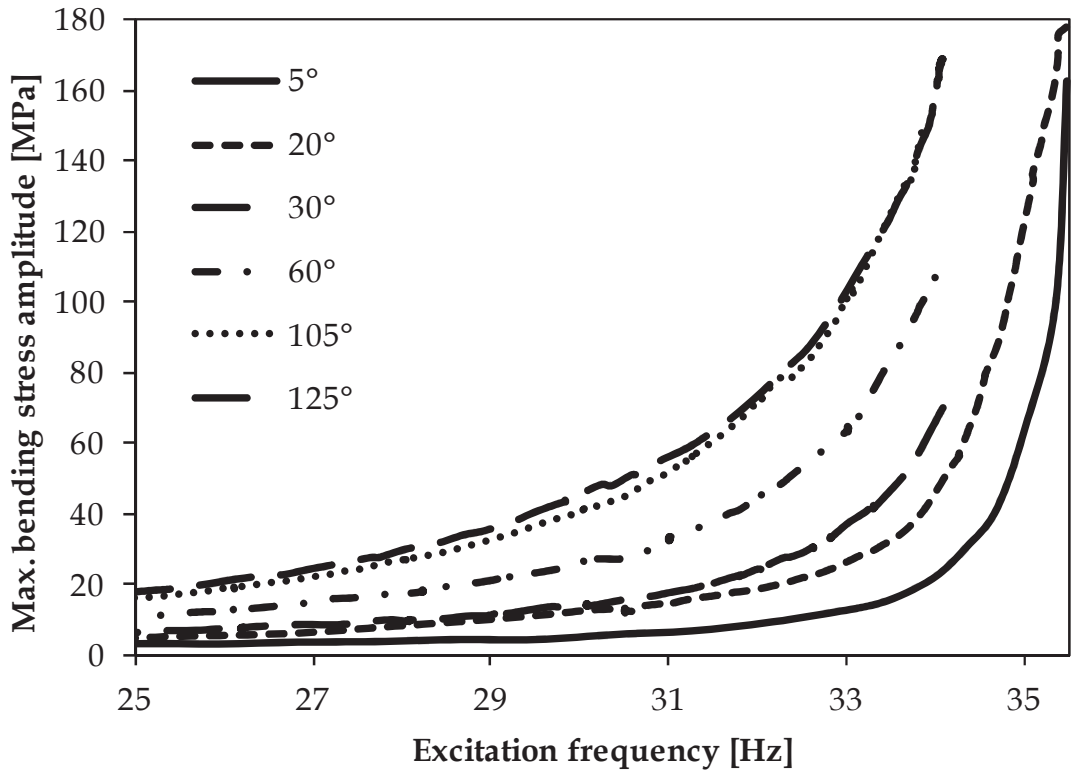

Figure 4.34: Pipe 1 bending stress response for different excenter angles.

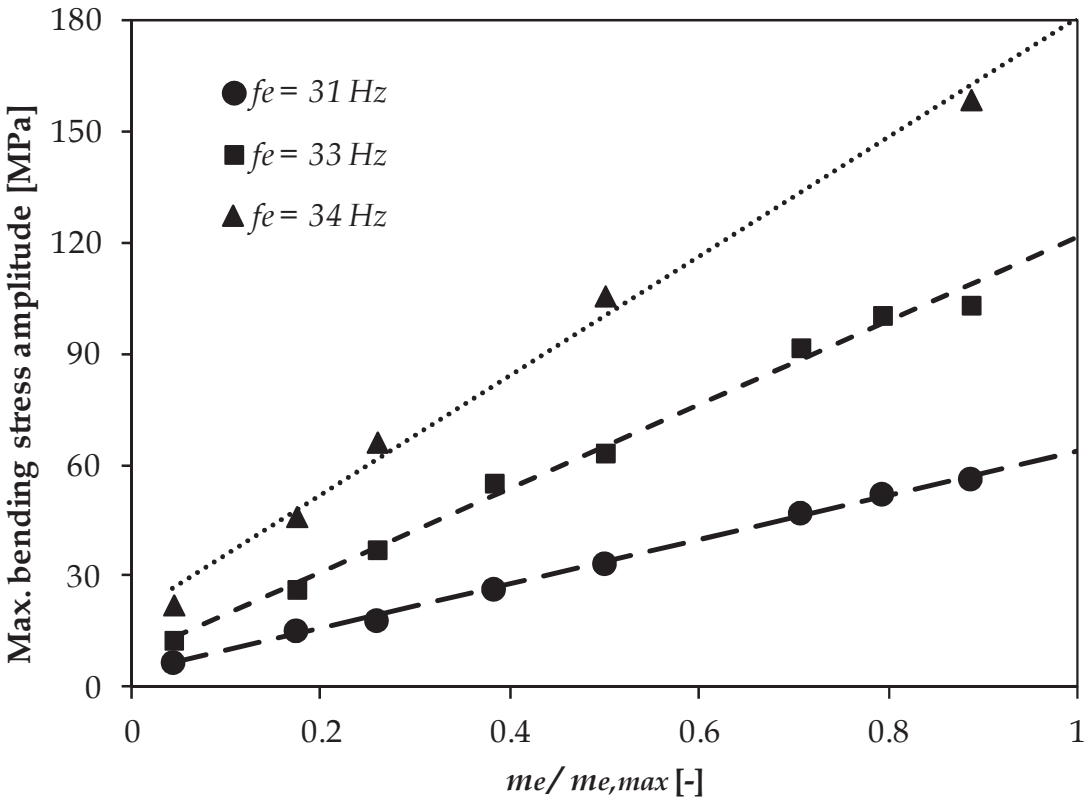

Figure 4.35: Pipe 1 bending stress as a function of the relative excenter mass.

6.3.3 Strain distribution over the pipe

Using the five axial strain gauges attached over the pipe length, it is possible to get an idea of strain and consequently also stress distribution in the pipe's axial direction. In Figure 4.36 the bending stress values obtained by the strain gauges measurements using Eq. (4.23) are compared to the theoretically calculated stress distribution. The measurements were carried out with an excenter angle of 20°.

In the graph the points represent the measurements and the curves the theoretical distributions. The stresses are compared for four different excitation frequencies. For the lower frequencies, the measured and calculated stresses correspond both in a qualitative and quantitative way. While for the higher frequencies the difference in stress amplitude increases with increasing excitation frequency. However, there is still a good qualitative agreement between the shapes of the stress distribution.

The observed difference is again caused by the damping which is not included in the model. As previously shown in Figure 4.27, the influence of the damping is limited for frequencies below 34.5 Hz, but causes an substantial difference in bending amplitude for higher values of the excitation frequency.

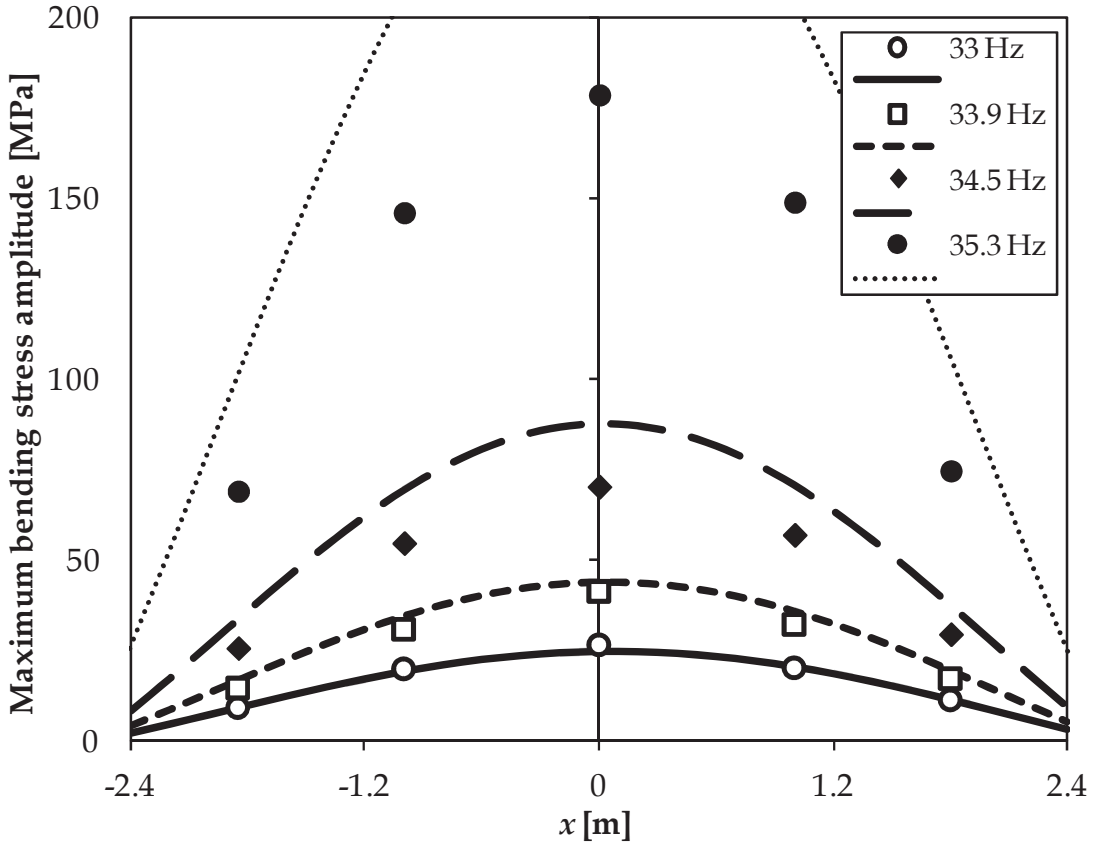

Figure 4.36: Comparison between Pipe 1 measured stress (points) and theoretical calculated stress (lines) for different excitation frequencies.

6.3.4 Deflection-stress relationship

As shown in section 3 of this chapter the developed mathematical models can be used to calculate the pipe deflection and corresponding bending stress. Since no damping is considered in the models, there is an important difference between calculated and measured values in the region of the pipe's natural frequency. Nevertheless, in this paragraph the validity of the relationship between bending deflection and stress amplitude, even in this region, is illustrated.

In Figure 4.37 the bending stress amplitude is presented as a function of the deflection amplitude $U_f(0)$. Using the CMS model a linear relation between both parameters is found. Additionally, the deflection amplitude measured by the laser sensors and the corresponding bending stress derived from the strain gauges measurements are included in the plot. The results shown are from the test on Pipe 1 with an excenter angle of 20°. An excellent correspondence between the measured and modelled data can be seen. The measured data clearly follows the linear relation and the *RMS* deviation is limited to 3.2 MPa.

The results from the same test have been previously used to provide the frequency response plot Figure 4.27. In that graph the measured and modelled deflections start to deviate once the deflection exceeds 4 mm due to

the absence of damping in the model. However, the deflection-stress relationship in Figure 4.37 is valid over the entire deflection range. This means that the CMS model can be used to accurately calculate the bending stress from the measured pipe deflection data even without considering damping effects. Consequently, stress related data can be derived from the deflection measurements without performing additional strain gauge measurements.

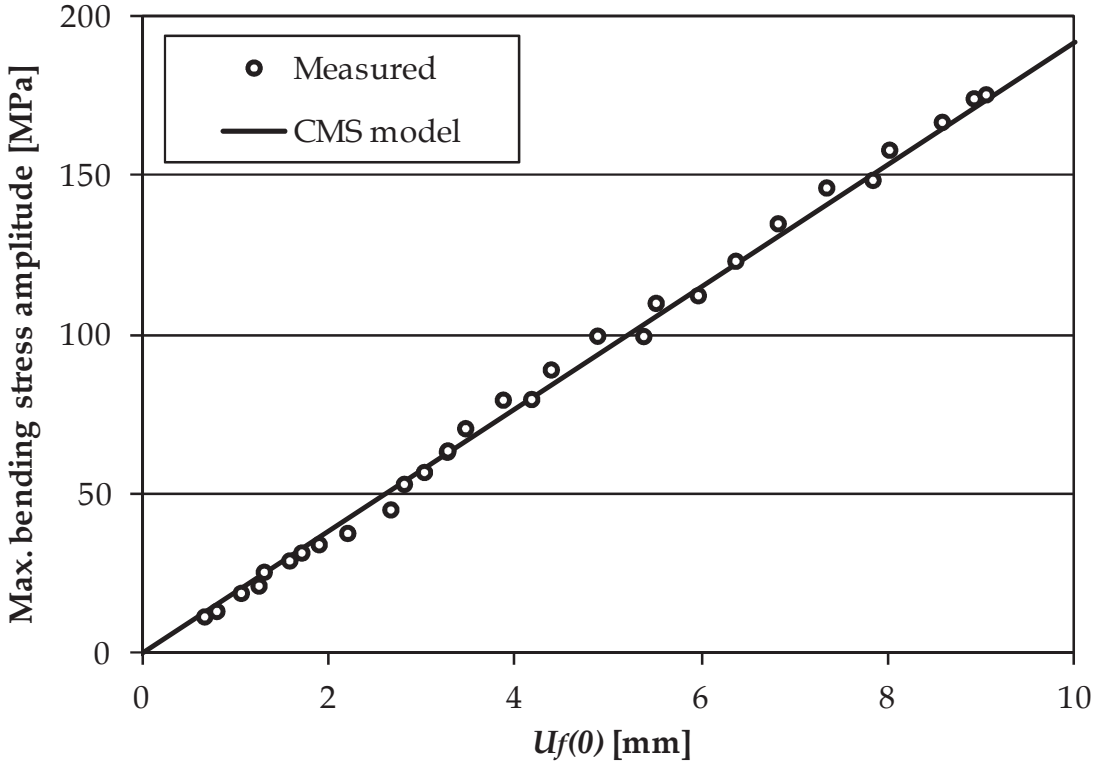

Figure 4.37: Comparison between measured and modelled deflection-stress relation for Pipe 1.

6.3.5 Pipe 2 response for different excenter angles

The response of Pipe 2 for different excenter angles is illustrated in Figure 4.38. The bending stress amplitude values are derived from the displacement measurements as described in the previous paragraph since no strain gauges are applied to this test specimen. Consequently, the curves are less smooth than in Figure 4.34, as the strain gauge data acquisition system contains a low-pass filter. The laser sensor measurements are performed without any filtering and as a consequence more prone to noise.

In Figure 4.39 the influence of the excenter mass m_e is illustrated. The behaviour of Pipe 2 is similar to that of Pipe 1 described in 6.3.2. Again, the resulting stress amplitude depends linearly on the excenter mass.

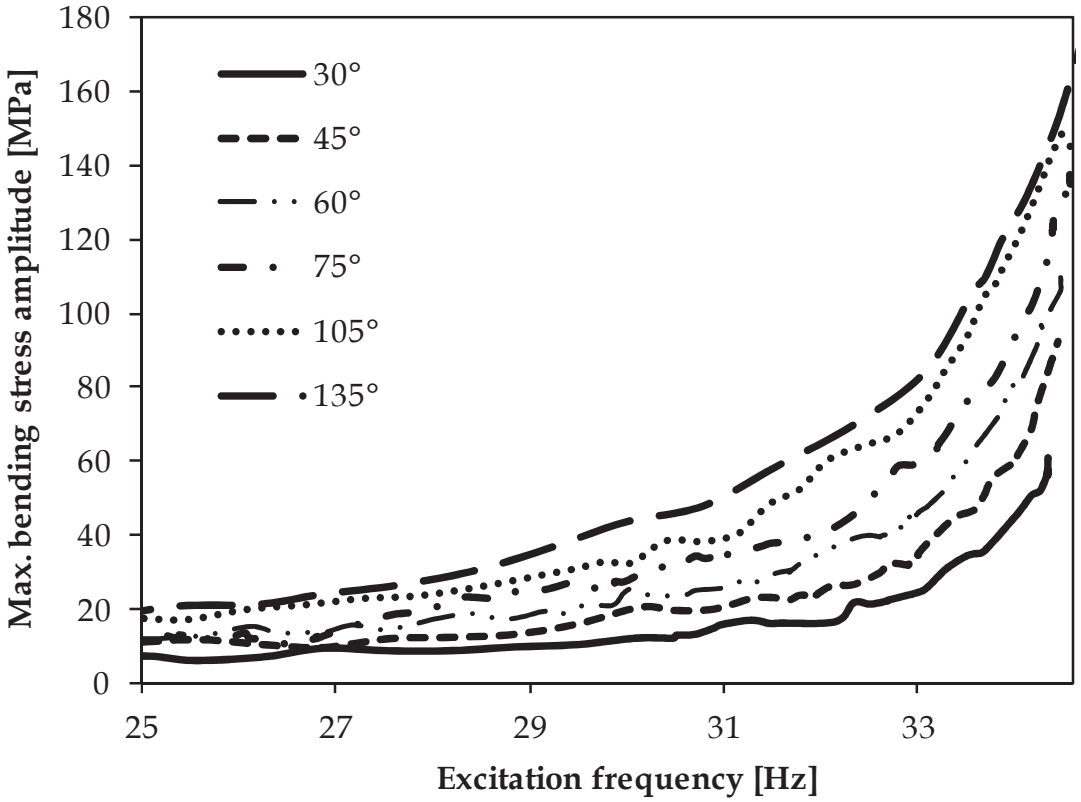

Figure 4.38: Pipe 2 bending stress amplitude response for different excenter angles.

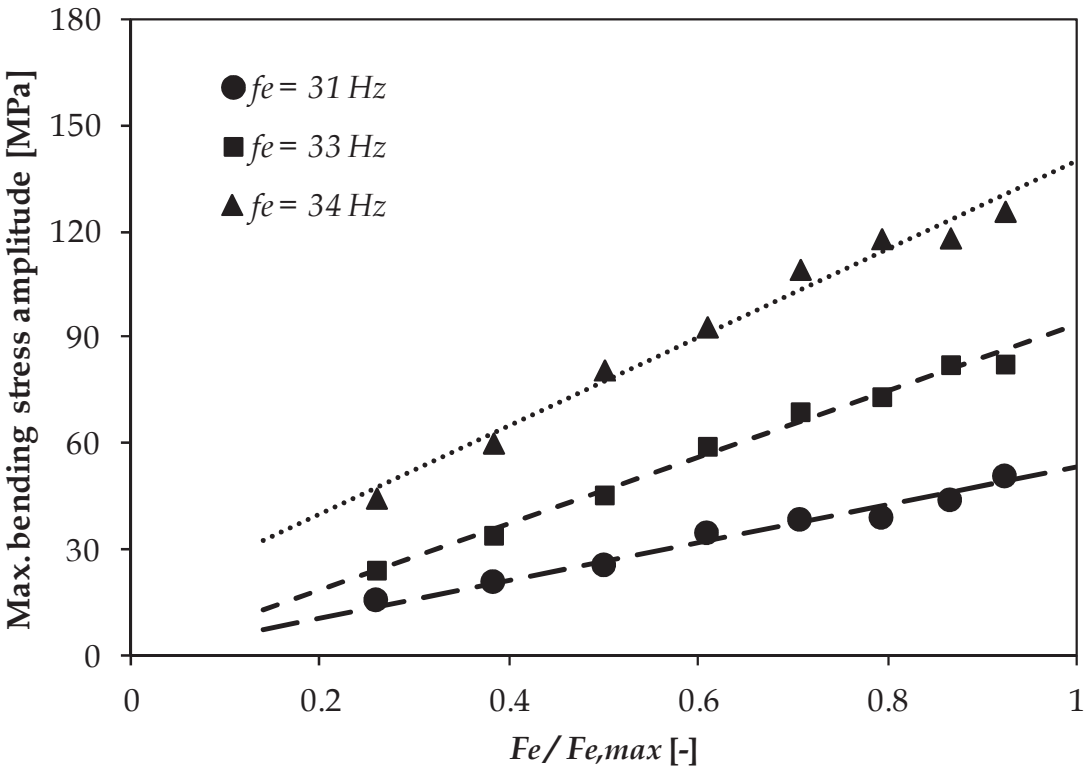

Figure 4.39: Pipe 2 bending stress amplitude as a function of the relative excenter mass.

6.4 Fatigue test

6.4.1 Test conditions

On Pipe 2 a fatigue test until leakage is carried out. In order to create stress concentrations for fatigue cracks to initiate, three notches are milled in the pipe as shown in Figure 4.40 and with dimensions according to Table 4.6. The notches are applied after the previous short tests to determine the pipe's frequency response while the pipe remains in the setup. They are milled in two steps using a special milling tool illustrated in Figure 4.41. In the first step the global dimension of the notch is milled. In the second step the notch is finished with a finer blade to obtain a root radius of 0.075 mm. This is a typical value for milled notches to initiate fatigue cracks as it is described by the ASTM E647 designation [4.9] e.g. to be applied to the compact tension specimen shown in the previous chapter in Figure 3.1.

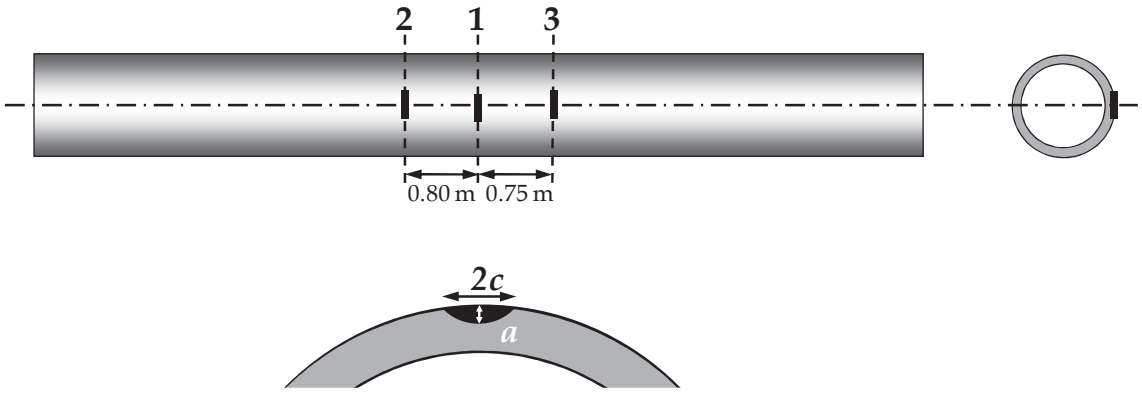

Figure 4.40: Notch locations in Pipe 2.

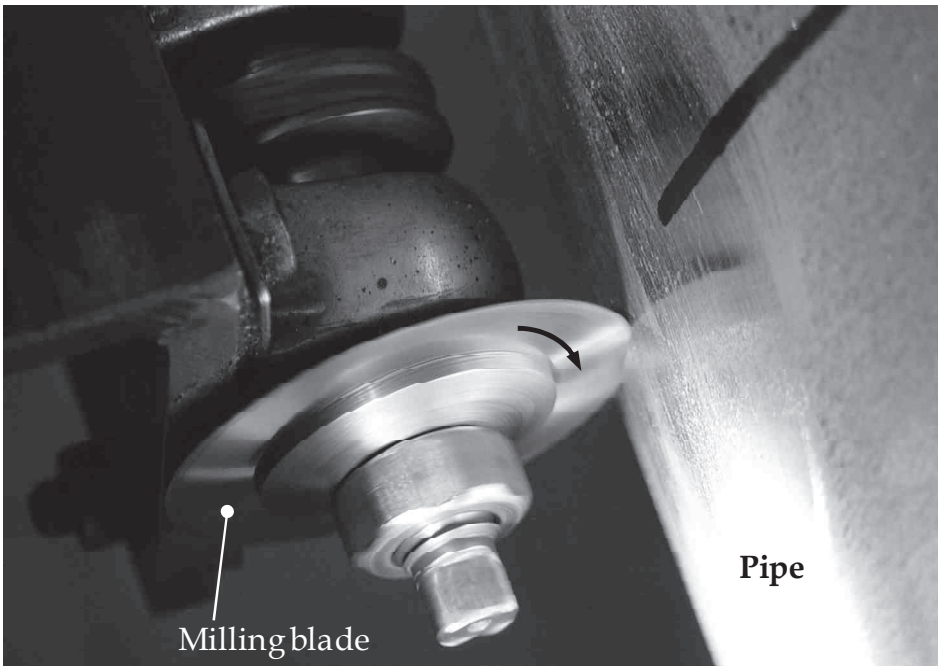

Figure 4.41: Milling of a notch.

Notch number	Notch depth *a* [mm]	Notch length *2c* [mm]	Stress amplitude [MPa]
1	7.0	37	83.3
2	8.0	45	66.5
3	8.0	40	71.7

Table 4.6: Pipe 2 notch dimensions.

During the fatigue test, a load is applied with a stress amplitude of 83.3 MPa at the centre of the pipe, which is the location of notch 1. At notch 2 and 3 the respective stress amplitudes are 66.5 MPa and 71.7 MPa. To obtain these stress levels an excenter angle of 45° is used with an excitation frequency of 34.4 Hz. The resulting deflection amplitude at the centre of the pipe is about 4.5 mm.

6.4.2 Test results

A leak appeared at notch 1 after 654 300 load cycles, after which the test was stopped. The total test took less than 5 hours. Compared to a conventional bending test setup, this is very efficient: e.g. a four-point bending test at a frequency of 2 Hz would need 4 days to perform the same number of cycles.

In Figure 4.42 the bending deflection amplitude at the centre $U_f(0)$ measured by the vertical laser sensor and the excitation frequency f_e are plotted. During the first 50 000 cycles the excitation frequency is adjusted several times by the operator between 34.3 and 34.4 Hz. These changes affected the resulting deflection amplitude. A similar single adjustment is performed at 600 000 cycles. At that point the adjustment was made by the operator to reduce the bending deflection to its original value of 4.5 mm. Between 50 000 cycles and 600 000 cycles, the excitation frequency is kept constant at 34.4 Hz. In this region, the deflection amplitude starts to slightly increase at about 230 000 cycles (indicated by the dashed vertical line in Figure 4.42). It is assumed that this is a consequence of the presence of a propagating crack that locally decreases the bending stiffness of the pipe. It is noted that although there is a sudden deflection decrease at 600 000 cycles due to the reduced excitation frequency, the same trend can be observed.

The deflection measurements obtained with the laser sensor are confirmed by the results of the 3D optical displacement measurement system presented in Figure 4.43. In this graph the deformation shapes at 62 000, 191 000, 295 000 and 515 000 cycles are compared. The deformation shape at 62 000 cycles is in very good agreement with the deflection obtained by the CMS model which is also shown (*RMS* deviation = 0.01 mm). Next to this, it is confirmed that after 230 000 cycles the pipe deflection is increasing. For the measurements taken at 295 000 and 515 000 cycles, a quadratic trend line is added.

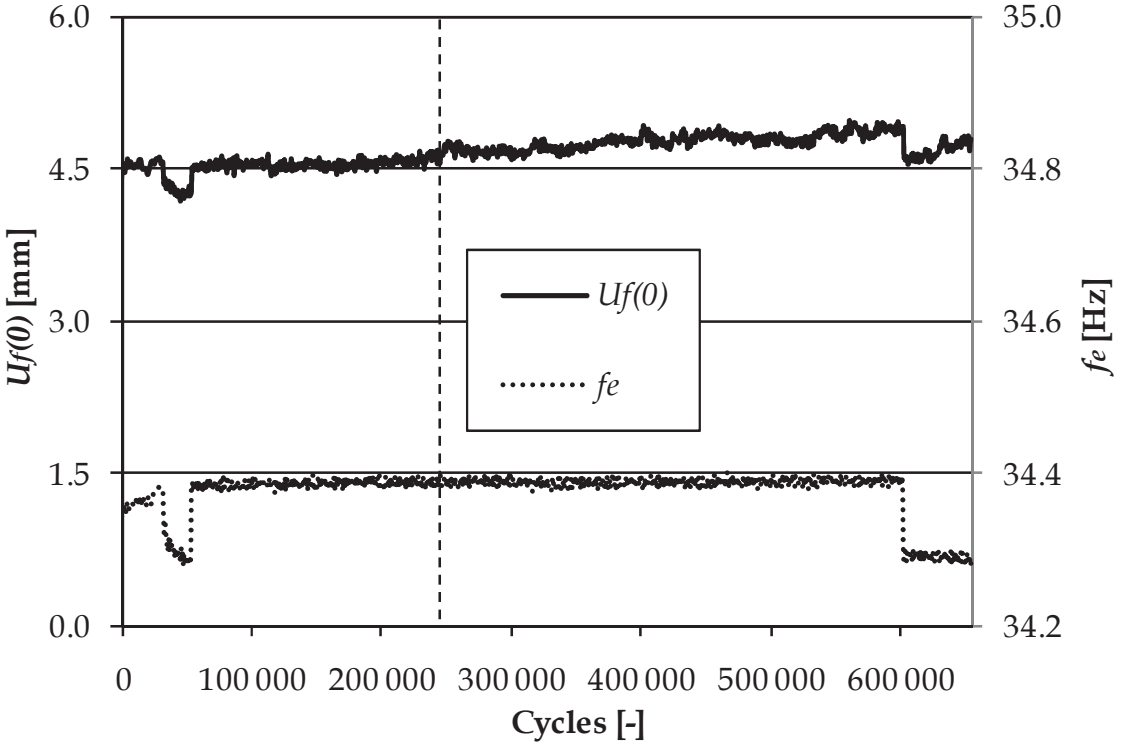

Figure 4.42: Pipe deflection amplitude and excitation frequency during the test.

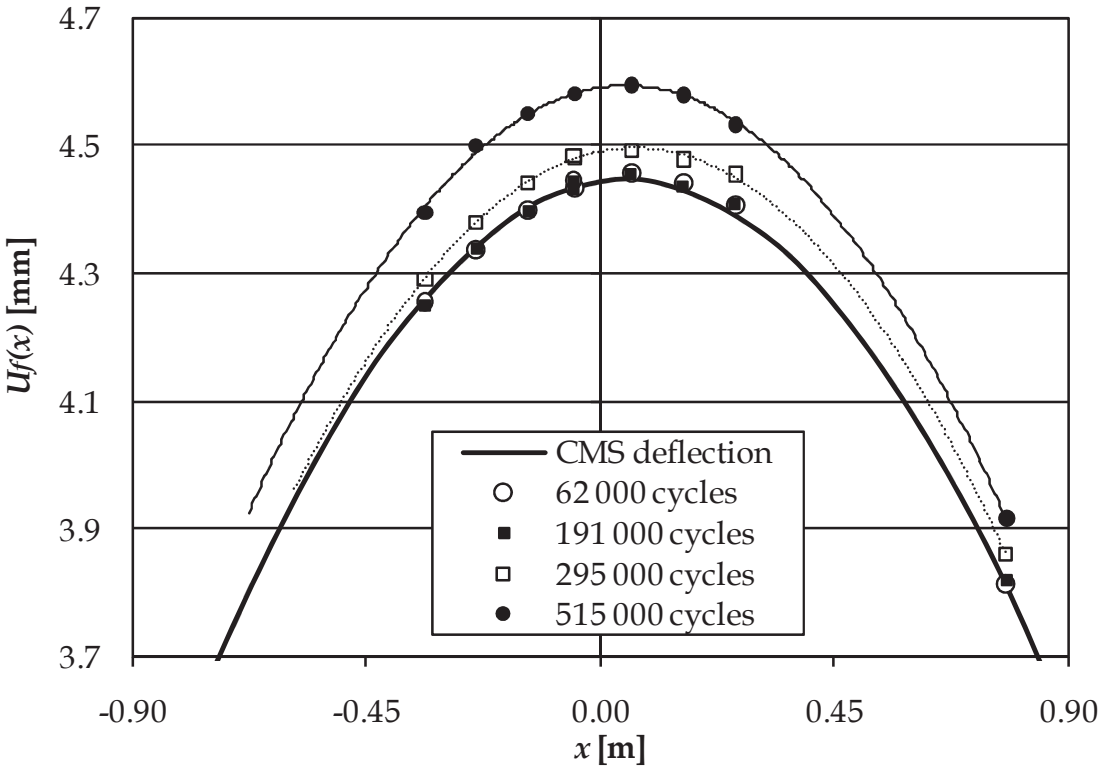

Figure 4.43: Change in bending deflection during the fatigue test.

6.4.3 Fracture analysis

After dismounting the pipe from the setup, the material around the three notches is cut out of the pipe, cooled in liquid air and a brittle fracture is forced so that the fatigue crack becomes visible. In Figure 4.44 the fracture surface at notch 1 is shown. It is clear that the crack initiated from the notch and propagated through the wall of the pipe while keeping its semi-elliptical shape. When the crack penetrates the wall, a small leak is created. Part of the fatigue fracture surface has a darker colour since it is slightly corroded after coming into contact with the water that leaked out. The crack length of the fatigue crack is 103 mm and the crack depth equals the pipe wall thickness.

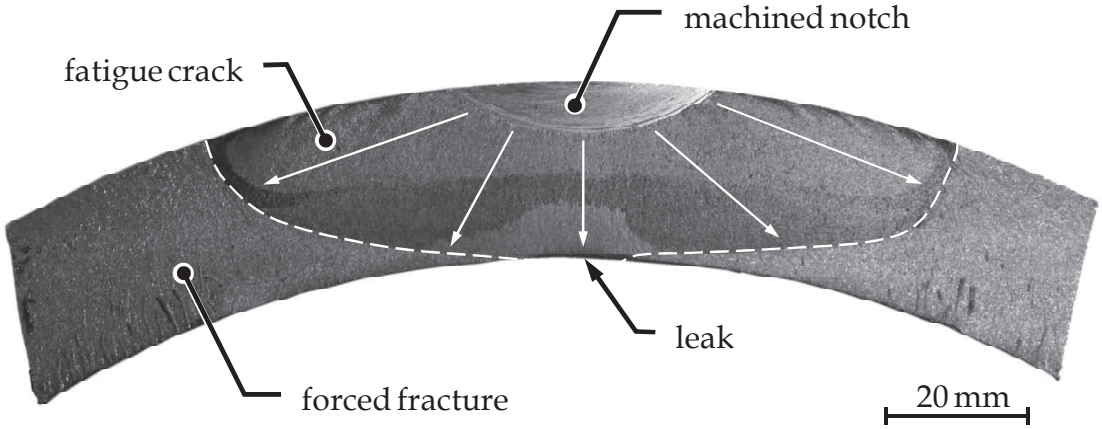

Figure 4.44: Fatigue crack at notch 1.

The fracture surfaces at notch 2 and notch 3 are shown in Figure 4.45-46. From both figures it is visible that the crack fronts have a semi-elliptical shape. The crack dimensions at the end of the test are summarized in Table 4.7. Crack 2 and 3 initiated from a notch with the same initial depth, but the notch length of notch 2 is 5 mm longer than notch 3, nevertheless the final crack size propagated from notch 3 exceeds the dimensions of crack 2 which can be explained by the higher stress amplitude at the location of notch 3.

Crack number	Crack depth a [mm]	Crack length $2c$ [mm]
1	23.9	103
2	16.6	54
3	18.3	60

Table 4.7: Size of the appearing fatigue cracks after 654 300 cycles.

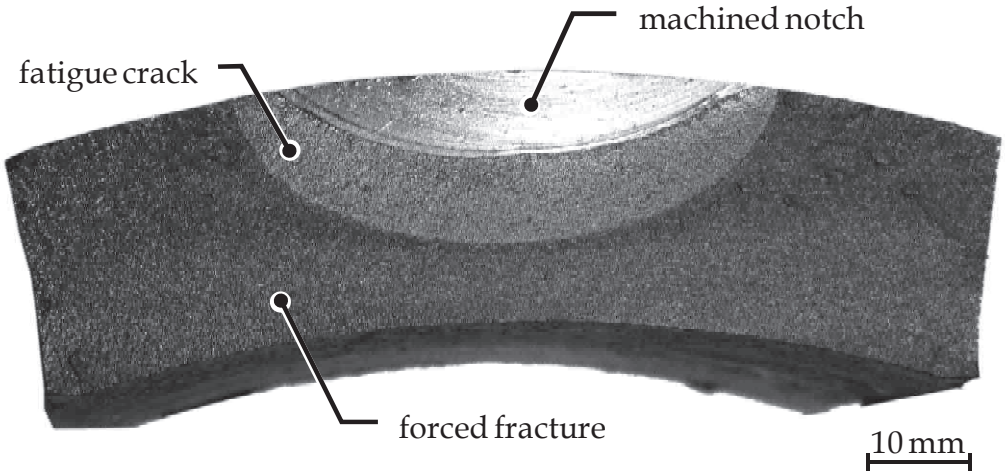

Figure 4.45: Fatigue crack at notch 2.

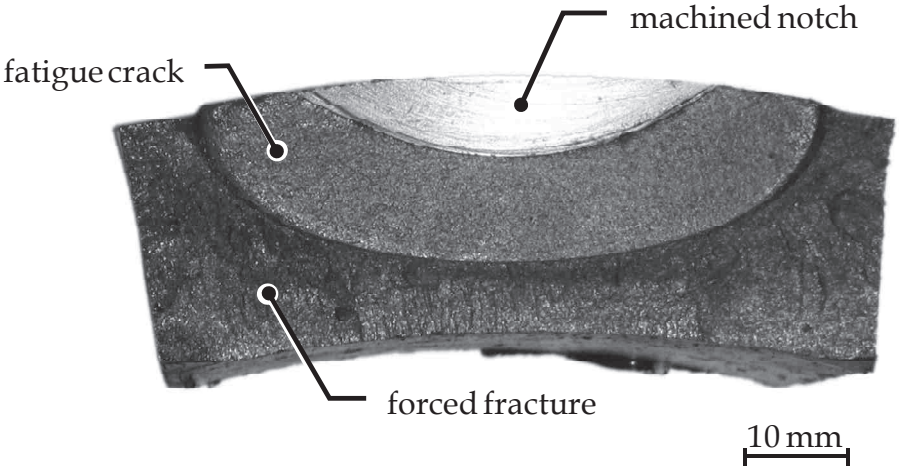

Figure 4.46: Fatigue crack at notch 3.

7 Summary and conclusions

In this chapter the resonant bending fatigue setup developed during this PhD project is discussed in detail. The working principles, design and constructional aspects are presented. The completed setup is suitable of performing fatigue tests on pipe joints from 6″ to 20″ and exhibits several unique features:

- a drive unit with two variable excentric masses, resulting in a setup that is applicable for a wide diameter and wall thickness range;
- supports that are designed to allow continuous control of their position;
- elaborate measuring equipment, including a dynamic 3D optical measuring system to monitor the deformation shape and deflection amplitude of the pipe and of the supports;

- a bending stress range of up to 490 MPa can be applied, which is considerably higher than the reported maximum stress ranges of other existing resonant bending fatigue setups for pipes.

Two mathematical models are developed to predict the dynamic behaviour of a pipe in the setup. An analytical model is used to calculate the eigenmodes and eigenfrequencies of a free floating pipe. Secondly, a more complex semi-analytical model, using component mode synthesis, models the pipe in the setup. By applying advanced measuring techniques on two different pipes in the setup, the following correspondence is found between the models and the behaviour of the test setup:

- for a given pipe diameter, wall thickness and pipe length the models can accurately predict the necessity to fill the pipe with water, the required mass of the endweigths, the system's natural frequency and the position of the supports;
- if the excitation frequency remains under 0.98 times the natural frequency of the system, the influence of the damping remains limited and the model's frequency response accurately predicts the pipe deflection;
- no additional running-in period is needed to adjust the position of the supports;
- a point on the surface of the pipe in resonance, describes a circle. This means it can be guaranteed that all points at the circumference of the pipe at a certain location along the pipe axis undergo the same load cycle during one excitation cycle;
- by strain gauge measurements it is shown that the deflection-stress relation obtained by the models accurately predicts the stress corresponding to a specific deflection amplitude.

It can be concluded that the setup functions properly and that the pipe's behaviour can be predicted accurately using the presented mathematical models.

In the final part of this chapter, a fatigue test is described on a seamless X65 pipe with an outer diameter of 323.9 mm and wall thickness of 23.9 mm. Prior to the test three notches are milled to act as stress concentrations. A leak appeared at the central notch after 654 300 cycles. Changes in bending deflection due to crack propagation are detected both by the laser sensors as the 3D measurement system. Post mortem analysis shows that fatigue cracks propagated from the two other notches as well. The test took less than 5 hours, which illustrates the effectiveness and efficiency of the developed setup.

References

[4.1] Klotter, K., Technische Schwingungslehre, 1er Band: Einfache Schwinger, Teil A: Lineare Schwingungen, Springer-Verlag, Berlin, Germany, third edition, 1981.

[4.2] Maia, N.M.M., Silva, J.M.M, Theoretical and Experimental Modal Analysis, John Wiley & Sons Ltd, Chichester, UK, 1997.

[4.3] Argyris, J., Mlejnek, H.P., Dynamics of Structures, Texts on Computational Mechanics, vol. 5, Elsevier Science Pub., Amsterdam, The Netherlands, 1991.

[4.4] Verhegghe, B., The Element Method in Applied Mechanics, Course notes Faculty of Engineering, Ghent University, 2003.

[4.5] Noldus, E., Loccufier, M., Mechanical Vibrations, Course notes Faculty of Engineering, Ghent University, 2005.

[4.6] Stress Engineering Services, Testing Services Catalog, http://www.stress.com/.

[4.7] TWI Engineering Facilities, http://www.stress.com/, 11-02-2011.

[4.8] Bertini, L., Beghini, M., Santus, C., Baryshnikov A., Fatigue on drill string conical threaded connections, test results and simulations, 9th Int. Fatigue Congress, FT588, 2006.

[4.9] ASTM E647, Standard test method for measurement of fatigue crack growth rates, ASTM International, 2000.

Chapter 5
Experimental Results

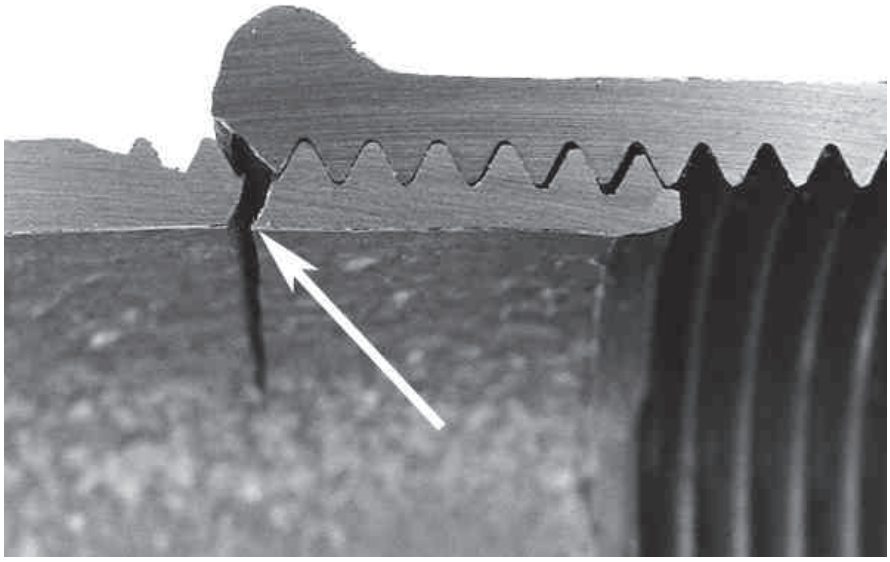

1 Goal

In underlying chapter the experimental test program conducted in the framework of this study is presented. The experiments are conducted in order to generate the data needed to validate the numerical model described in Chapter 6 and to create a database with fatigue data of threaded pipe connections. The tests have been performed on different setups that are designed and constructed in this study. Next to providing the experimental results, the relevant aspects of the developed setups are discussed as well as the implementation of the selected measurement techniques of Chapter 3 and the methodology used to perform the fatigue tests.

In the following chapters, the obtained test data will be used to validate the performed simulations and is analysed more in detail to reveal the general trends in the fatigue behaviour of threaded pipe connections.

2 Experimental test program

2.1 Test program overview

An overview of the experimental test program is given in Figure 5.1. Both static tests and fatigue tests are performed. Static torque, axial tension and internal pressure tests are performed on threaded pipe connections. These tests serve as a validation for the finite element model. Next to this, the torque tests are used to determine the coefficient of friction of the contact between the threads of pin and box.

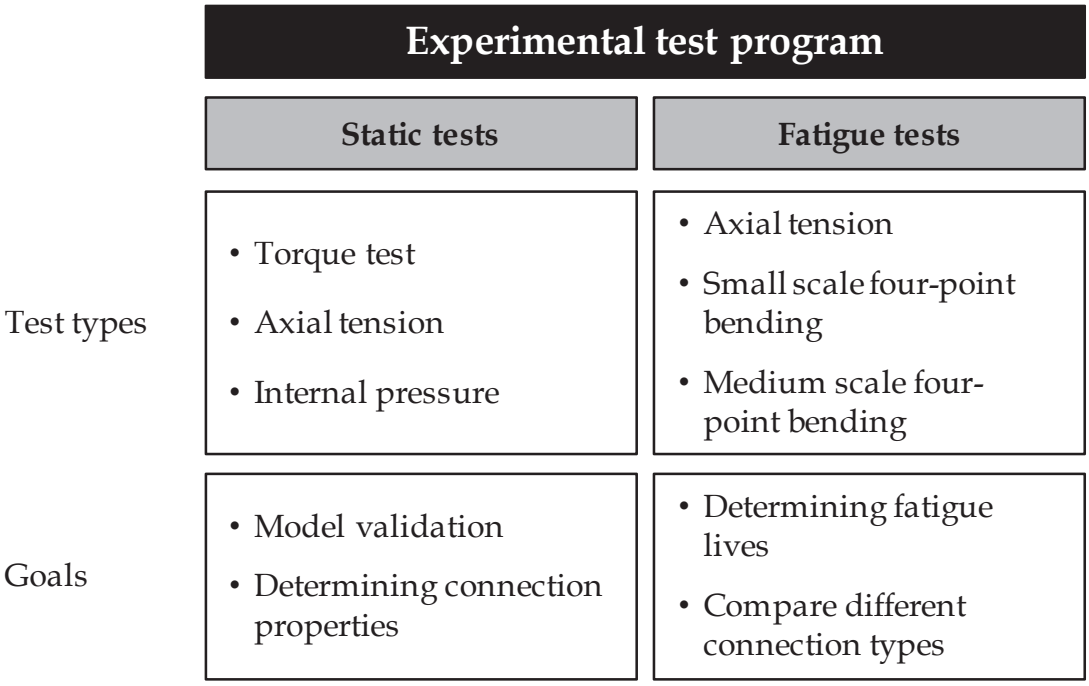

Figure 5.1: Overview of the experimental test program.

The fatigue tests are performed in three different setup types: axial tension, small and medium scale four-point bending. During these tests the fatigue lives for different threaded connection types subjected to a range of dynamic loads are determined.

Additionally the specimen's material properties are determined by tensile tests on the pipe material.

2.2 Test specimen selection

2.2.1 API Line Pipe connection

In this study the API Line Pipe connection is used as a reference. As illustrated in Figure 5.2, this is a T&C connection with truncated triangular threads. The male and female thread both have a thread angle of 60° and a taper of 1/16. The thread geometry is specified by the API 5B specifications [5.1] and lays within the tolerances of the *National Pipe Thread Taper* (NPT) described in [5.2]. The box dimensions as well as the mechanical properties of the API Grade B material used for all API Line Pipe samples, are specified by the API 5L specifications [5.3].

Although not optimized for fatigue service, this connection is selected because it is widely available as a standardized connection type. Moreover it is available in a wide diameter range; API Line Pipe couplings are available with a pin diameter starting from D_p = 10.3 mm (1/8″) to as large as 508.0 mm (20″). This makes it possible to perform small and larger scale tests on the same connection type. As a comparison, the API Buttress connection is only available starting from a diameter D_p = 114.3 mm. A final practical reason to use the API Line Pipe connection is the make-up torque which is lower than other standard API connection types of the same size. Consequently, the make-up can be performed in laboratory conditions by the torque machine described in section 3.2.

Two sizes of API Line Pipe connections are tested: the 1″ and 4.5″ size. The 1″ connection has a pin diameter D_p = 33.4 mm, for the 4.5″ size D_p = 114.3 mm. The pin wall thickness *WT*, box diameter D_b, box length L_b (as in Figure 5.2), and the number of threads per inch *tpi* for both connection sizes are given in Table 5.1. Both the minimum specified material properties and the values obtained by tensile testing are summarized in Table 5.2. The tabulated values are the mean of three tensile tests. For the 1″ specimen a tubular specimen is tested, while the properties of the 4.5″ connection are determined by three tests on strip specimens. It can be seen that the values obtained meet the minimum required properties.

The 4.5″ size is extensively tested in both static and fatigue tests to validate the finite element model that will be described later. The 1″ size samples are easy to handle and to modify. Hence, a large number of fatigue tests is

carried out on this connection size to study the influence of geometrical modifications on its fatigue life.

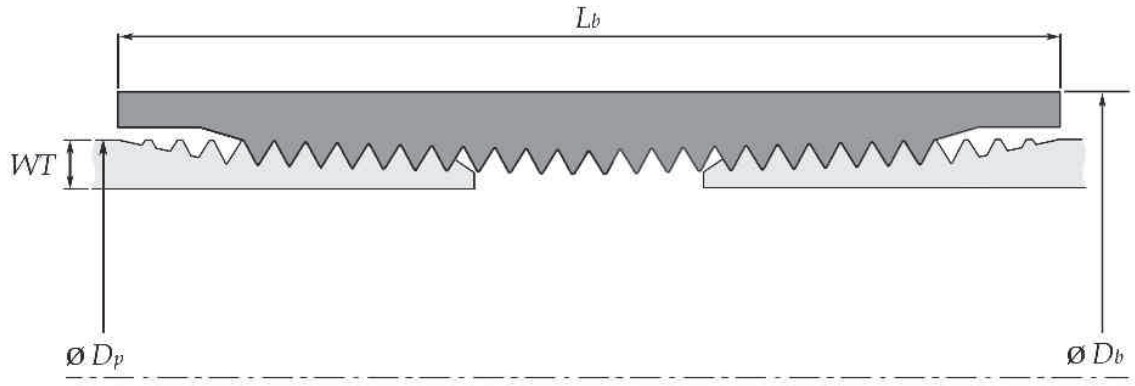

Figure 5.2: Schematic view of the API Line Pipe connection.

Connection type	D_p [mm]	WT [mm]	D_b [mm]	L_b [mm]	*tpi*	Thread type
1″ API Line Pipe	33.4	3.4	40.0	66.7	11.5	triangular
4.5″ API Line Pipe	114.3	6.0	132.1	114.3	8	triangular
1″ BSPT	33.4	3.4	38.6	44.5	11	round

Table 5.1: Geometrical **p**roperties of the used test specimens; dimensions as in Figure 5.2.

Material	σ_y [MPa]	σ_{UTS} [MPa]	ε [%]
API Grade B: minimum specified [5.3]	241	414	27.0
API Grade B: 1″ samples	356	482	31.1
API Grade B: 4.5″ samples	355	502	30.9
St 33 minimum specified [5.4]	185	290	18
St33: 1″ BSPT samples	285	410	> 20

Table 5.2: Material properties of the test specimens.

2.2.2 BSPT connection

The second connection type used in the experiments is the *British Standard Pipe Thread* or BSPT connection as specified by [5.5] and illustrated in Figure 5.3. In this T&C connection type, only the male threads are tapered (taper equal to 1/16), while the female thread is straight. The connection uses round triangular threads with thread angle of 55° and 11 threads per inch.

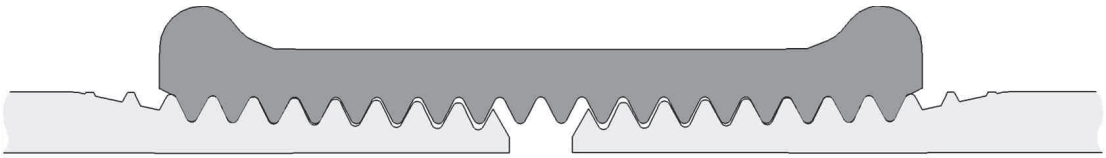

Figure 5.3: Schematic view of the BSPT connection.

The test specimens used in this study have a nominal size of 1″ or D_p = 33.4 mm, so they can be tested in the same setup as the 1″ API Line Pipe samples. The other sample dimensions are summarized in Table 5.1, the material properties are given in Table 5.2. Since the box is a malleable fitting, it has a bulb-like profile at either end. The box diameter D_b, however, is defined as the diameter of the straight part at the centre.

3 Static tests

3.1 Overview of the static tests

The performed static tests are schematically summarized in Figure 5.4. First the results of the torque tests are presented, performed on a 4.5″ API Line Pipe connection using a torque machine. These tests are used to characterize the make-up behaviour of the connection. The test sample is prepared in such a way that an additional tensile test can be performed after make-up. The final test described in this section, is an internal pressure test on a 1″ API Line Pipe connection.

	Static tests		
	Torque test	**Axial tension**	**Internal pressure**
Setup	Torque machine	ESH 1000 kN	Pressure pump
Connection	4.5″ API Line Pipe	4.5″ API Line Pipe	1″ API Line Pipe
Number of tests	3	1	1
Measured signals	• strains • torque • rotation	• strains • load	• strains • internal pressure

Figure 5.4: Overview of static tests.

3.2 Torque test

3.2.1 Setup description

To make-up a threaded connection properly, it is necessary to accurately control the applied rotation and to measure the resulting torque. In order to do this, a setup was constructed by refurbishing an existing torque machine. The original machine is illustrated in Figure 5.5 [5.6]. It uses a counterweight of 300 kg on a lever arm to apply a certain torque and was originally developed to determine the torsional stiffness of materials. The original capacity of the setup was 1500 Nm.

In order to perform fully instrumented make-up tests with this setup, several parts are modified or added and its original capacity is increased. The most important modification is that the counterweight is removed and the torque is measured by a loadcell instead of being based on the displacement of the counterweight. The new adapted setup is presented in Figure 5.6. The test specimen (1), consisting of a pin and box, is mounted in the torque machine by the use of flanges that are welded to pin and box, as shown in Figure 5.7. These flanges are designed to be compatible with the universal testing machine used for the axial tension test described in section 3.3.

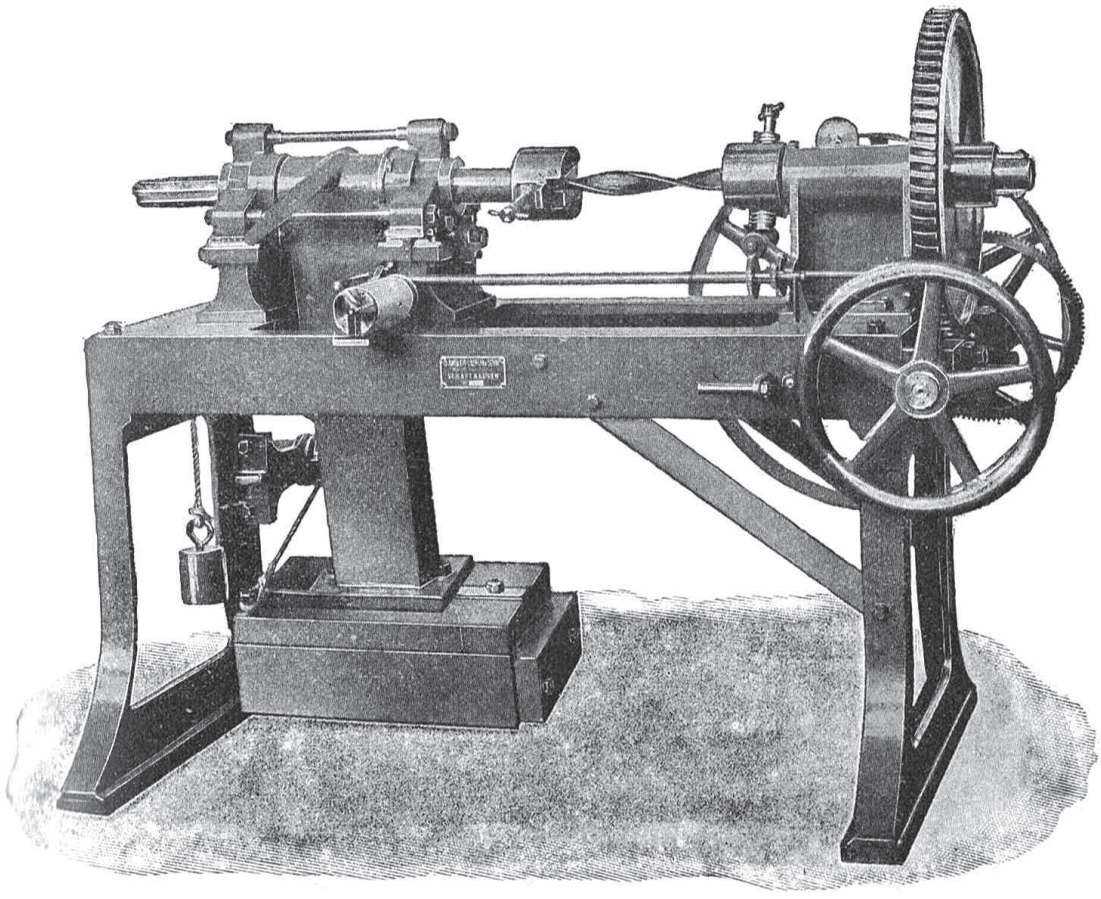

Figure 5.5: Original torque machine with counter-weight as in [5.6].

The drive wheel (2) rotates a worm which drives the gear (3). This causes the pin of the test specimen (1) to rotate with respect to the stationary box. The resulting torque is transmitted to the lever arm (5) which is connected to the loadcell (4). The measured load multiplied by the length of the lever arm (1.00 m) equals the acting torque. To allow an axial motion during make-up, a new linear guiding system (6) is added. The modified torque machine has a capacity of 2500 Nm, and the maximum test specimen length is 400 mm.

The test specimen is instrumented with 11 strain gauges at the positions shown in Figure 5.8. Strain gauges 1 to 4 and strain gauge 11 are attached to the inner surface of the pin, strain gauges 5 to 10 are attached to the outer surface of the box. Strain gauges 1 to 9 are biaxial cross gauges (type TML FCA-3-11 with a gauge length of 3 mm for mild steel applications) to measure both axial and circumferential strains, gauges 10 and 11 are triaxial rosette gauges (type TML FRA-3-11 with a gauge length of 3 mm for mild steel applications) that additionally measure the shear strain.

Gauges 1 to 8 are located on the same circumferential position, while gauges 9 and 10 are located on the box at the same axial position as gauge 7, at respectively 180° and 90° along the box circumference. Strain gauge 11 is on the pin at the axial position of gauge 3 but at 90° along the circumference.

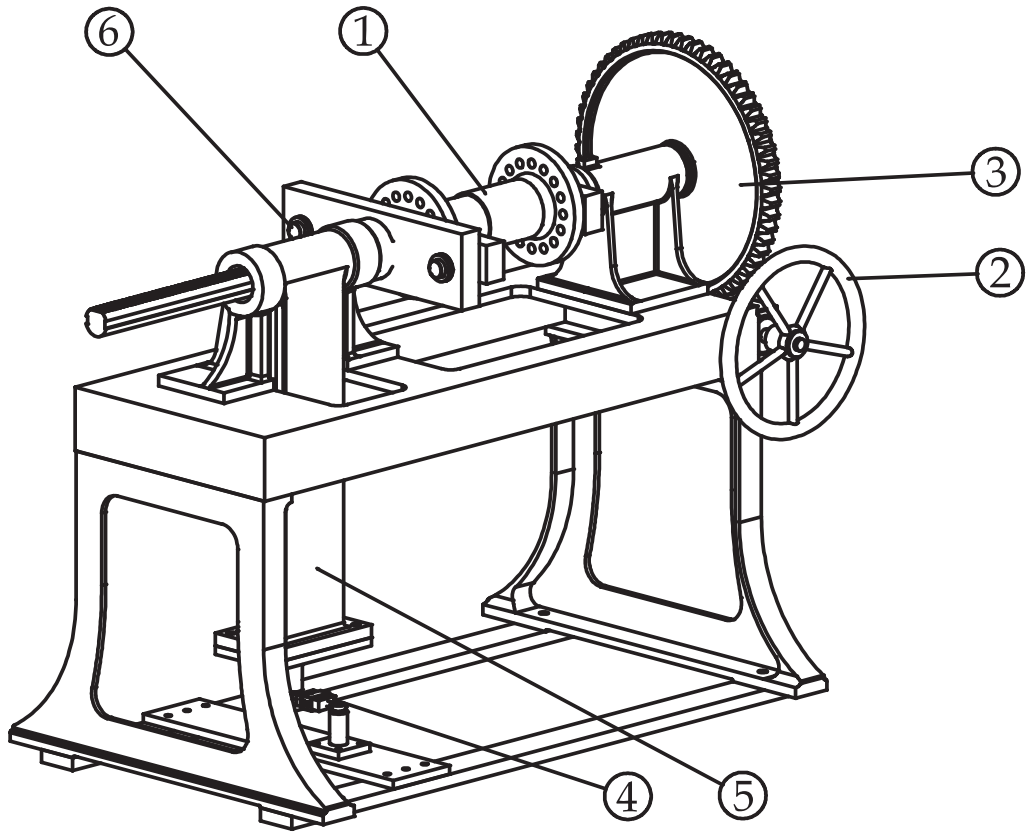

Figure 5.6: Schematic view of the torque machine.

All signals from the loadcell, rotation sensor and strain gauges are recorded at a frequency of 10 Hz by a 16 bit 24 channel data acquisition system with internal conditioner type NI SCXI-1001, manufactured by National Instruments.

3.2.2 Test specimen configuration

The test specimen configuration has dimensions according to Figure 5.8. The total length L_{tot} should not exceed the maximum test specimen size of 400 mm in order to fit in the torque machine. The length of the flanges L_f at both ends is 75 mm. A complete API Line Pipe coupling with box length L_b = 114.3 mm is welded to the left flange. In order to fit in the setup, the pipe length of the pin L_p should be smaller than 136 mm. To avoid any influence of the boundary conditions in the threaded region of the specimen, L_p should exceed a minimum required value defined by Eq. (5.1), with R the pin outside radius and WT the pin wall thickness. This distance is defined in the shell theory [5.7] as the so-called *bending boundary layer*, which is the distance at which 99.4 % of any oscillation in a tube caused by its boundaries is decayed. For the 4.5" API Line Pipe pin dimensions, this results in a minimum length of 74 mm. For the test specimen L_p = 130 mm which makes that the configuration fits in the setup without significant disturbance of the boundary conditions.

$$L_p \geq 4 \cdot \sqrt{R \cdot WT} \tag{5.1}$$

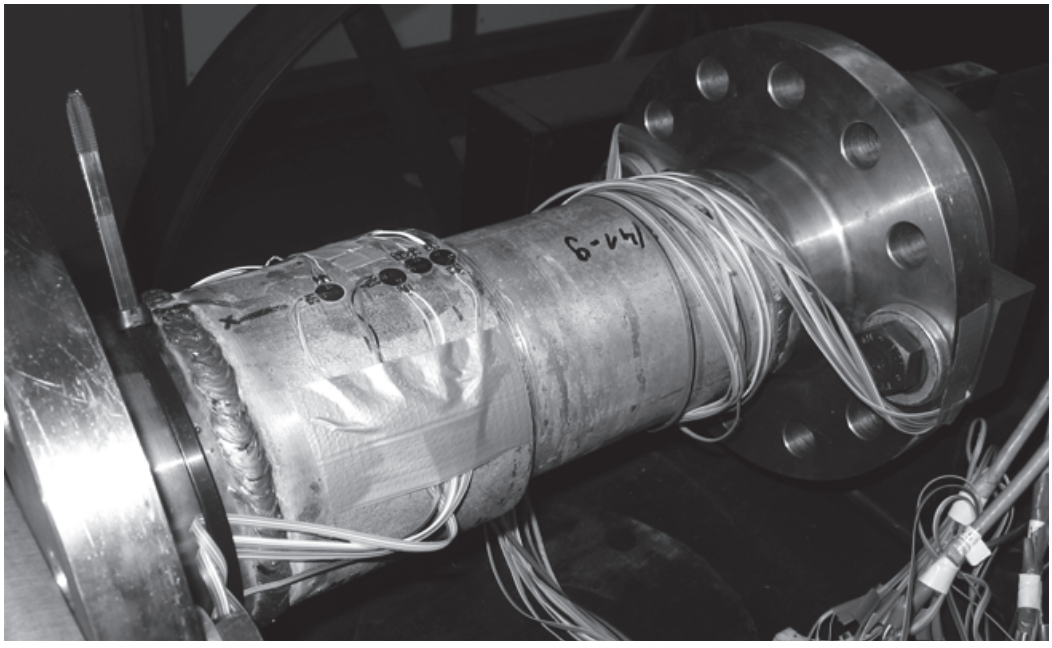

Figure 5.7: Test specimen instrumented with strain gauges.

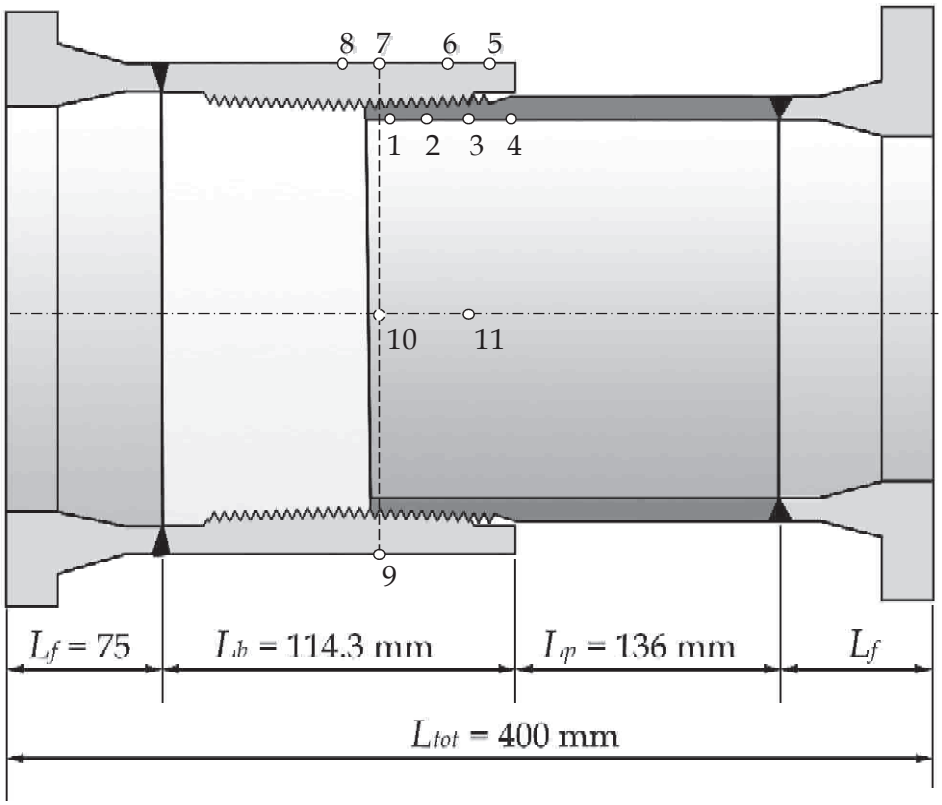

Figure 5.8: View of the test specimen with strain gauge locations.

3.2.3 Test results

Three torque tests are performed on the same sample by consecutive assembling and disassembling. The resulting torque-turn graphs of the tests are shown in Figure 5.9. The number of rotations is put to zero at the point where the torque starts to increase, this is the so-called *hand-tight* situation. It can be seen that there is a difference in torque behaviour between the different tests. This is because plastic deformation of the connection occurs during make-up. The most important deformation takes place during the first assembly, since the torque-turn lines of tests 2 and 3 are closer to each other. This is discussed more in detail in Chapter 6, where a comparison is made between the measured strains and the strains according to the model. Nevertheless, all three curves show the same trend. The torque increase during the first 0.4 rotations remains limited. This is because every connection has some geometrical deviations and the connection needs to settle before the threads of pin and box are completely in contact with each other. Due to the plastic deformation that took place during the first test, the torque required to force this settlement is smaller during the consecutive tests. The number of rotations needed for this, stays however the same. Once this settlement has taken place, the torque increase becomes more important and follows the path of the linear fit as shown for test 1 in Figure 5.10. After the total number of 1.09 make-up turns a torque value of about 1400 Nm is reached in all tests. This value of 1.09 rotations lays within the specified 1 to 3 make-up turns according to API 5B [5.1] and the measured make-up torque

of 1400 Nm conforms API 5C3 [5.8], that specifies the make-up torque should be between 1149 Nm and 1915 Nm.

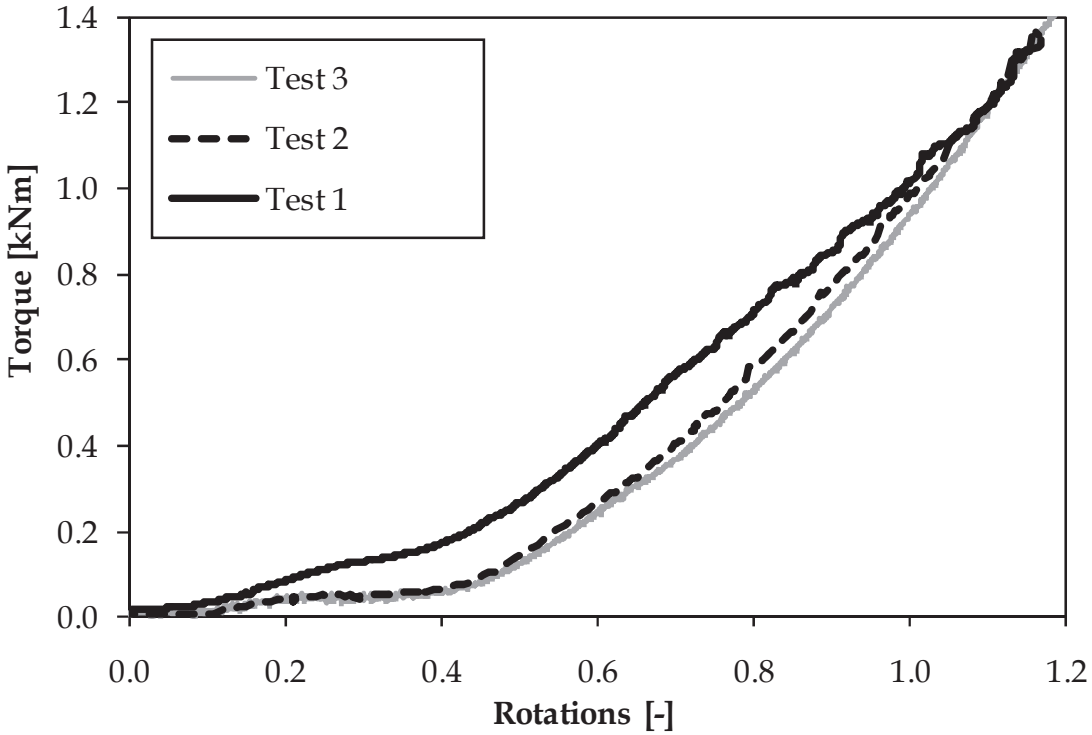

Figure 5.9: Torque vs. number of turns for the three torque tests.

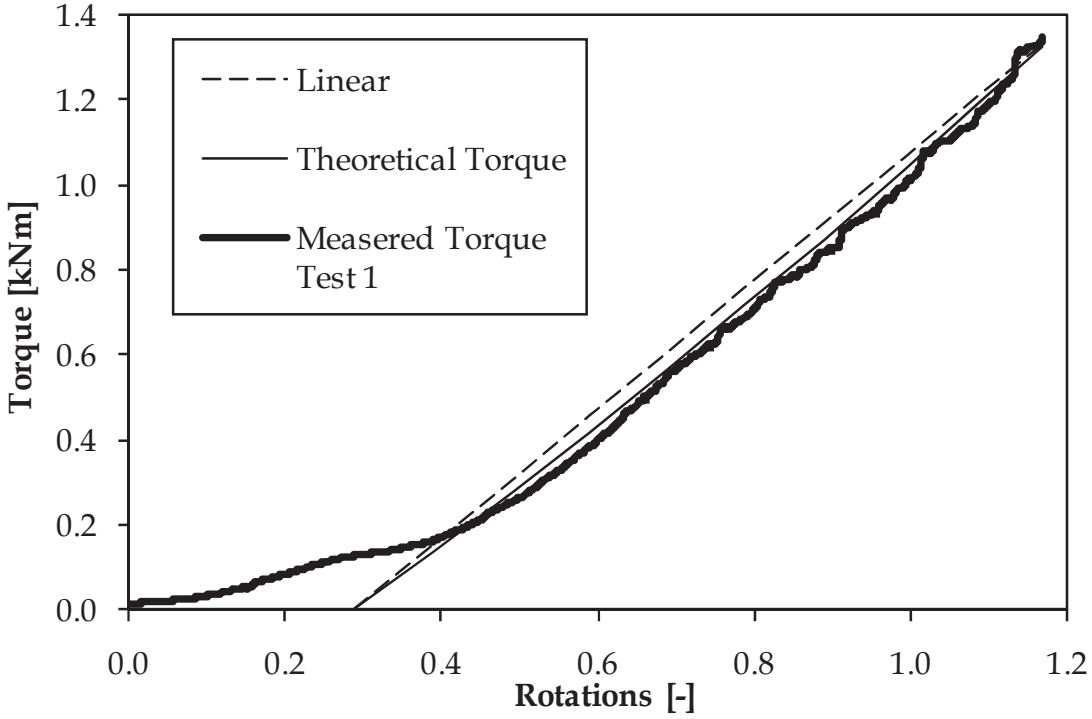

Figure 5.10: Analysis of the torque-turn data of test 1.

The linear fit shown in Figure 5.10 becomes zero at a value of 0.29 rotations. Hence, it looks like the torque-turn line is shifted over this distance and it can be considered that the shifted effective number of make-up turns is only 1.09 – 0.29 = 0.80. When the make-up behaviour of a connection is analysed or simulated numerically, this effective value of make-up turns should be used as an input since there is a perfect match between the geometry of pin and box in the models. In a previous study of Assanelli et al. [5.9] an analogue shift in torque behaviour was observed for an API 8-round threaded connection.

During the torque tests, strain gauge measurements are performed. In Figure 5.11 the results of selected strain gauges are shown. For these measurements the rotation was stopped at certain moments during the make-up in order to get a stable signal. The results are shown for strain gauges 3 and 11, located at the inside of the pin on the same axial distance, but at 90° along on the circumference, and for strain gauges 7 and 9, at the outside of the box on the same axial distance, but 180° rotated. For these four strain gauges the measured axial and circumferential strains are shown, respectively noted with a letter A and C in figure Figure 5.11.

It can be seen that the corresponding strains on pin and box at the same axial position, but rotated over the circumference, correspond well. Differences can appear due to the thread helix which changes the axial position of the threads over the circumference, hence influencing the stress and strain distribution.

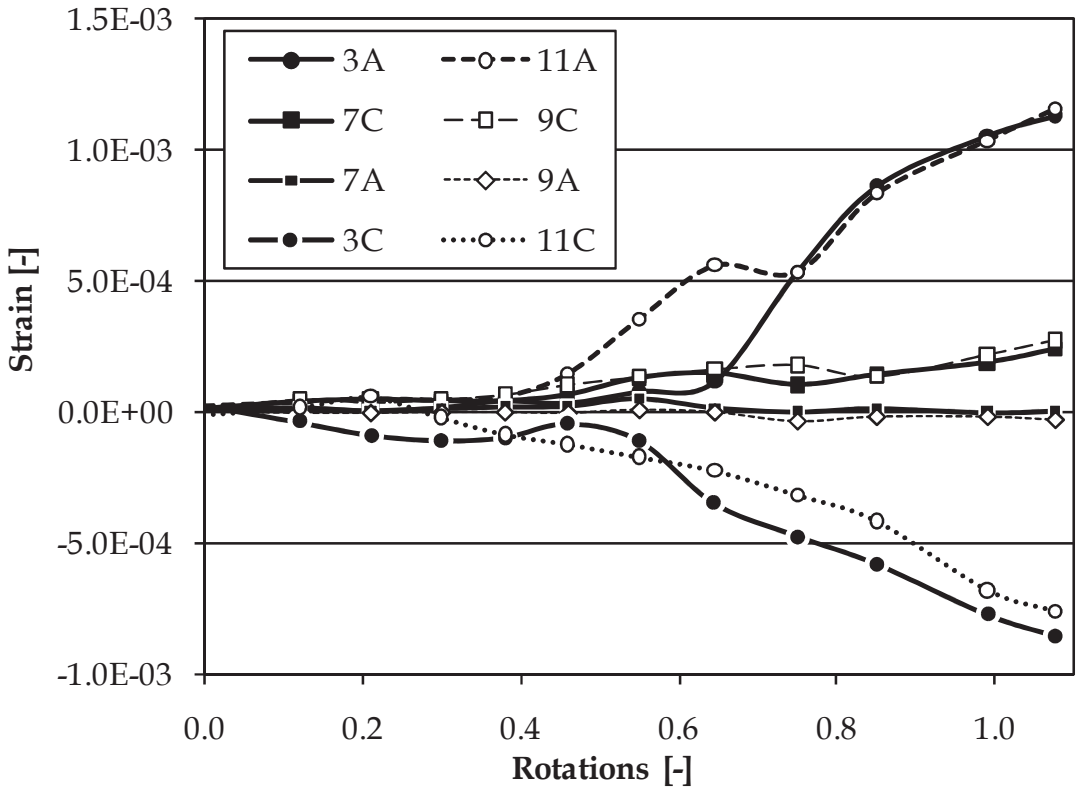

Figure 5.11: Strain measurement during the make-up test.

The resulting strains at the pin are much larger than at the box, since the box is the most rigid part. The circumferential pin hoop strain is negative or compressive, while the hoop strain in the box is positive. This is because the pin is shrunk into the box, compressing the pin and stretching the box. The strains are not a perfect linear function of the number of rotations, as they are affected by small geometrical deviations of pin and box. These fluctuations are not unusual, a similar behaviour was reported before by Yuan et al [5.10].

The strains measured by all strain gauges will be analysed more in detail in Chapter 6, where they are used as a part of the validation of the finite element model.

3.2.4 Determination of the coefficient of friction

From the torque-turn data the mean coefficient of friction between the contacting threads of pin and box can be calculated. This is done by finding the best fit between the experimentally measured and analytically calculated torque versus turn behaviour. The analytical calculations are based on Timoshenko's beam theory [5.11]. By modifying the analytical solution of the shrink fit of two concentric tubes as shown in Figure 5.12.a, this theory can be used to calculate the contact pressure between pin and box of a threaded connection. The contact pressure p between two concentric tubes is given by following equation:

$$p = \frac{E \cdot \delta}{R_c} \frac{\left(R_c^{\,2} - R_i^{\,2}\right) \cdot \left(R_o^{\,2} - R_c^{\,2}\right)}{2 \cdot R_c^{\,2}\left(R_o^{\,2} - R_i^{\,2}\right)} \tag{5.2}$$

With R_i, R_o and R_c respectively the internal radius, outside radius and radius at the contact surface between the two tubes. E is Young's modulus of elasticity and δ the radial overlap at the interface between the two tubes.

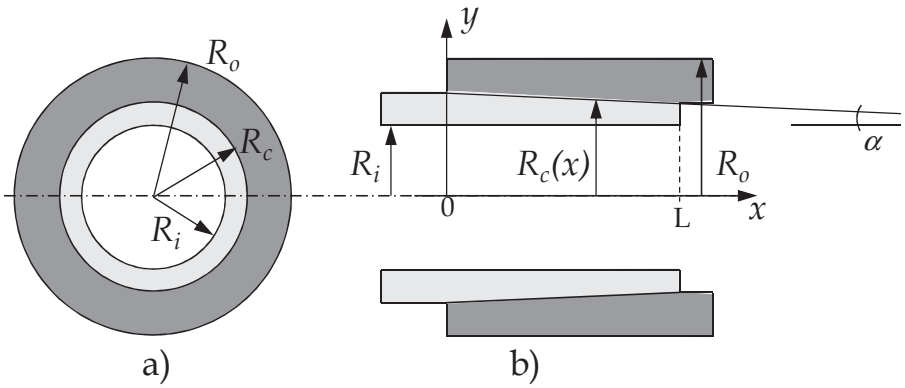

Figure 5.12: Shrink fit symbols.

This theory can be applied to threaded connections since the advancement of a pin into a box approximates that of a wedge. The exact thread shape is neglected and the radius of the contact surface R_c is a function of the axial position x and changes according to the thread pitch line (see Figure 5.12.b).

Hence Eq. (5.2) becomes the function $p(x)$ that describes the radial contact pressure:

$$p(x) = \frac{E \cdot \delta}{R_c(x)} \frac{\left(R_c(x)^2 - R_i^{\,2}\right) \cdot \left(R_o^{\,2} - R_c(x)^2\right)}{2 \cdot R_c(x)^2 \left(R_o^{\,2} - R_i^{\,2}\right)} \tag{5.3}$$

Where the interference δ is depending on the number of make-up turns t, thread pitch P, and the taper angle α :

$$\delta = t \cdot P \cdot tan(\alpha) \tag{5.4}$$

Weiner and Sewell [5.12] showed by strain gauge measurements that this approach can be used to model longitudinal and hoop stresses in a tubular connection. Schneider [5.13] used this same technique to analyse the stresses in standard API casing and tubing threaded connections.

The resulting radial force component dF_r (along the y-direction in Figure 5.12.b) on a segment $d\theta$ of the circumference can be calculated from the radial pressure component $p(x)$ as follows:

$$dF_r = \int_0^L p(x) \cdot R_c(x) \cdot dx \cdot d\theta \tag{5.5}$$

Where L is the length of the contact surface between pin and box. A force dF normal to the tapered contact surface corresponds to this radial component dF_r, with dF given by Eq. (5.6).

$$dF = \frac{dF_r}{cos(\alpha)} \tag{5.6}$$

According to the analytical calculations by Clinedinst [5.14], the contact pressure introduced by make-up results on each fully engaged thread in two equal force components dN normal to the thread flanks. This is illustrated in Figure 5.13. Both load and stab flank are subjected to the same normal force components as during make-up no external axial load is applied. The normal components dN are calculated by Eq. (5.7), with φ the half thread angle (φ = 30° for the API Line Pipe connection).

$$dN = \frac{dF}{2 \cdot sin(\varphi)} \tag{5.7}$$

During make-up the normal thread forces dN will create a frictional force μdN which contributes to the make-up torque. Where μ is the coefficient of friction. It is assumed constant over the different threads, so it can be considered as a mean friction value for the entire contact surface. Next to this friction, the wedge effect accounts for an important part of the total torque value. The total make-up torque T can be calculated using the virtual work balance Eq. (5.8).

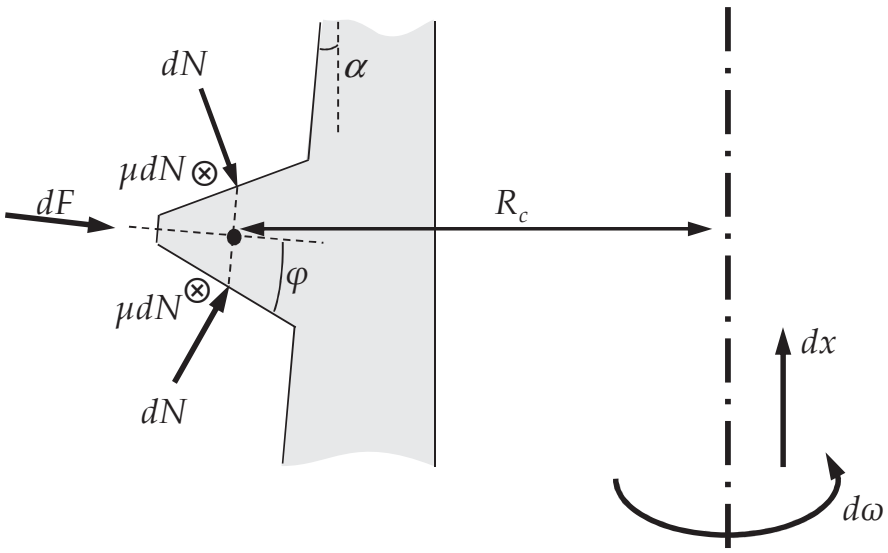

Figure 5.13: Forces acting on a thread.

$$T \cdot d\omega = \left(2 \cdot \mu \cdot \int_0^{2\pi} dN \cdot R_c(x) \cdot d\theta \right) \cdot d\omega + \left(\int_0^{2\pi} dF \cdot sin(\alpha) \cdot d\theta \right) \cdot dx \tag{5.8}$$

This equation expresses that the virtual work applied by the make-up torque T over a certain virtual angular displacement $d\omega$ consists of two terms. The first term is the work for the virtual angular displacement of the frictional torque caused by the contribution of the frictional forces μdN integrated over the circumference.

When the virtual angular displacement is applied, a virtual axial displacement dx will take place due to the helical effects of the threads. This dx is related to $d\omega$ as in Eq. (5.9). The second term in the virtual work balance Eq. (5.8) is the work for dx of the axial component of the contact force dF integrated over the circumference. Thus, this is the virtual work caused by the wedge effect.

$$d\omega = \frac{dx}{P} 2\pi \tag{5.9}$$

Using Eq. (5.9) and Eq. (5.5-7) the virtual work balance can be used to calculated the make-up torque T:

$$T = \frac{2\pi}{cos(\alpha)} \int_0^L p(x) \cdot R_c(x) \cdot \left(\frac{\mu \cdot R_c(x)}{sin(\varphi)} + \frac{P}{2\pi} sin(\alpha) \right) \cdot dx \tag{5.10}$$

Since the integration length L, which is the length of the contacting surface between pin and box, is a function of the number of make-up turns A, it is hard to solve this equation analytically. Nevertheless, numerical evaluation is possible. For a steel connection with known dimensions, the only unknown parameter in this equation is μ. Hence when an experimental torque-turn relation is known, Eq. (5.10) can be fitted to the experimental data to determine the value of the coefficient of friction.

This is done for the three performed make-up tests. In Figure 5.10 the theoretical curve is compared to the measured torque-turn data of test 1 and a corresponding value of $\mu = 0.12$ is calculated. For the two consecutive tests a friction value $\mu = 0.15$ was obtained. The difference between the values can be explained by local changes in the connection geometry due to the plastic deformation during the first test. Nevertheless, all obtained values are within the range that can be found in literature and that have been obtained in experimental tests as was discussed earlier in section 2.3.1 of Chapter 2.

3.3 Axial tension

3.3.1 Setup description

As mentioned earlier, the flanges welded to the test specimen are designed to be compatible with the 1000 kN ESH servo-hydraulic universal testing machine. Hence, after the third make-up the test, the sample was prepared for an axial tensile test.

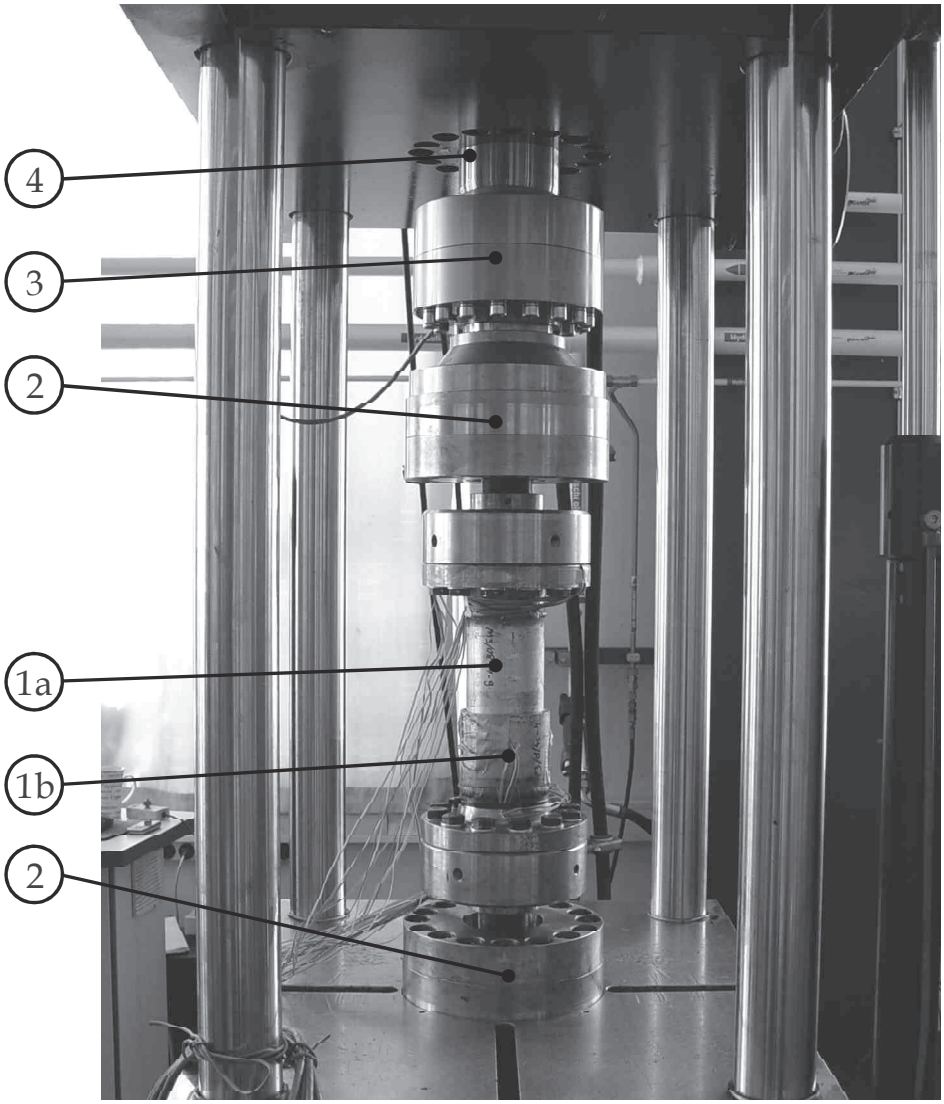

Figure 5.14: Axial tensile test on 4.5″ API Line Pipe Connection.

The total test setup is shown in Figure 5.14. The specimen, consisting of the pin (1a) and the box (1b), is placed vertically in the test rig. To compensate for any misalignment errors, the sample is connected to two ball joints (2) at the top and bottom. The upper ball joint is connected to the load cell (3) that measures the load applied by the vertical hydraulic actuator (4). During the test an axial tensile load is gradually applied. The corresponding strains measured by the strain gauge configuration according to Figure 5.8 are continuously logged.

3.3.2 API Line Pipe joint strength

During the test an axial tensile load is applied to the specimen at a rate of 50 kN/min. At four moments during the test (given in Table 5.3), the test is paused for 30 s to allow for a stable strain measurement. These measurements will be used as part of the validation of the finite element model in Chapter 6.

Axial Load [kN]	Axial Stress [MPa]
50.0	24.5
204.1	100
306.2	150
328.8	161

Table 5.3: Load steps during the static tests.

The tabulated axial stress is the gross stress in the pipe body calculated by dividing the axial load by the cross-sectional area of the unthreaded part of the pipe.

The maximum applied axial load is 328.8 kN, which corresponds to an axial stress in the pipe body of 161 MPa. The joint strength of the 4.5" API Line Pipe connection can be calculated using the empirical formulas given by Clinedinst [5.14]. These relations were determined based on 162 tensile tests on API Line Pipe connections as reported in [5.15]. Two joint strength values are defined: the fracture strength P_f and pull-out strength P_p.

The fracture strength P_f represents the necessary force to break the connection at its minimum cross-section and is calculated by multiplying the specimen's ultimate tensile stress with the cross-sectional area of the pipe wall under the last perfect thread. Using the known dimensions and the determined tensile stress, a value of $P_f = 596$ kN is calculated. This corresponds to an axial pipe body stress of 292 MPa.

However, it is likely that the connection fails at a lower load due to shearing of the threads or due to thread jumpout. The latter occurs when the connection is separated due to the applied load as explained by Figure 5.15.

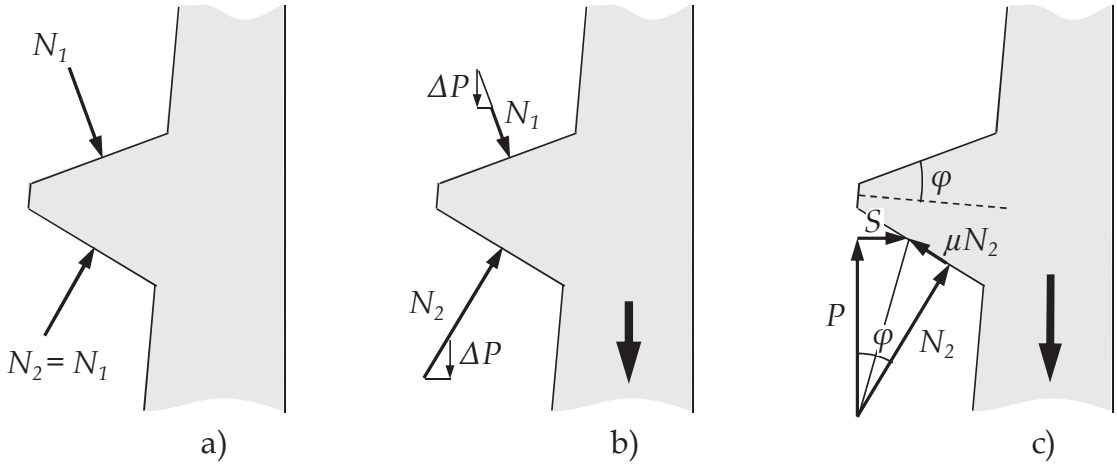

Figure 5.15: Thread forces during axial loading.

As shown previously in section 3.2.4, the make-up induces normal forces on the thread flanks indicated by N_1 and N_2 in Figure 5.15.a. This figure represents a thread of the pin. When no axial load is applied, both normal forces are equal. After an increment ΔP of axial load, the amount of normal force on the upper thread flank (the so-called non load-carrying *stab flank*) is reduced, while the force on the lower flank (the *load flank*) is increased. This is schematically shown in Figure 5.15.b. When a certain amount of axial load is exceeded, the normal load on the stab flank will become zero and all the load is carried by the load flank. Jumpout cannot occur until this condition is reached. The forces acting on the thread at that time are shown in Figure 5.15.c. Due to the large thread angle φ, the axial load does not only cause a normal force N_2 on the load flank, but also an important separation force S that tries to disengage the threads. The separation force is partly countered by the friction force μN_2. As soon as this friction force is exceeded, the threads can start to slide. And due to the sliding, the resulting load will act closer to the thread crest where the thread cross-section is smaller. If the sliding becomes too high, the threads can be completely disengaged or thread shearing can occur. These phenomena are called respectively thread jumpout and thread pull-out.

The API Line Pipe thread pull-out strength P_p can be calculated according to the empirical equation (5.11) given in [5.14].

$$P_p = A \cdot L_e \left[\frac{2.39(2h)^{0.59} D_p^{-0.59} \sigma_{UTS}}{0.5L_e + 0.14D_p} + \frac{\sigma_y}{L_e + 0.14D_p} \right] \tag{5.11}$$

Where A is the cross-sectional area of the pipe wall under the last perfect thread, L_e is the engaged thread length, h is the thread height, D_p is the pin outside diameter, σ_y is the yield strength and σ_{UTS} the ultimate tensile strength. It should be noted that for this empirical equation all lengths should be inputted in inches and the stress values in psi.

Using this equation a pull-out strength $P_p = 503$ kN is obtained, this corresponds to an axial pipe body stress of 246 MPa. The maximum applied axial load during the test is 328.8 kN or 65 % of the connection pull-out strength.

3.3.3 Test results

During the application of the load, the strain gauge signals are continuously monitored. In Figure 5.16 a selection of the measured signals is shown. All measured signals will be discussed more in detail in Chapter 6 where they are compared to the modelled strains. Two axial strain values (noted by a letter A) and a circumferential strain value are plotted (noted by a letter C). The strain numbering is in accordance with Figure 5.8. The strain values are relative strains compared to the made-up situation. The absolute values of the strains can be obtained by adding the strains caused by make-up to the values caused by axial tension.

It can be seen that strain gauges 8A and 5C follow a linear path as a function of the applied axial stress, which means they are behaving linear elastic. The strain in 11A, located at the inside pin wall at the LET, is non-linear caused by local plasticity at this location.

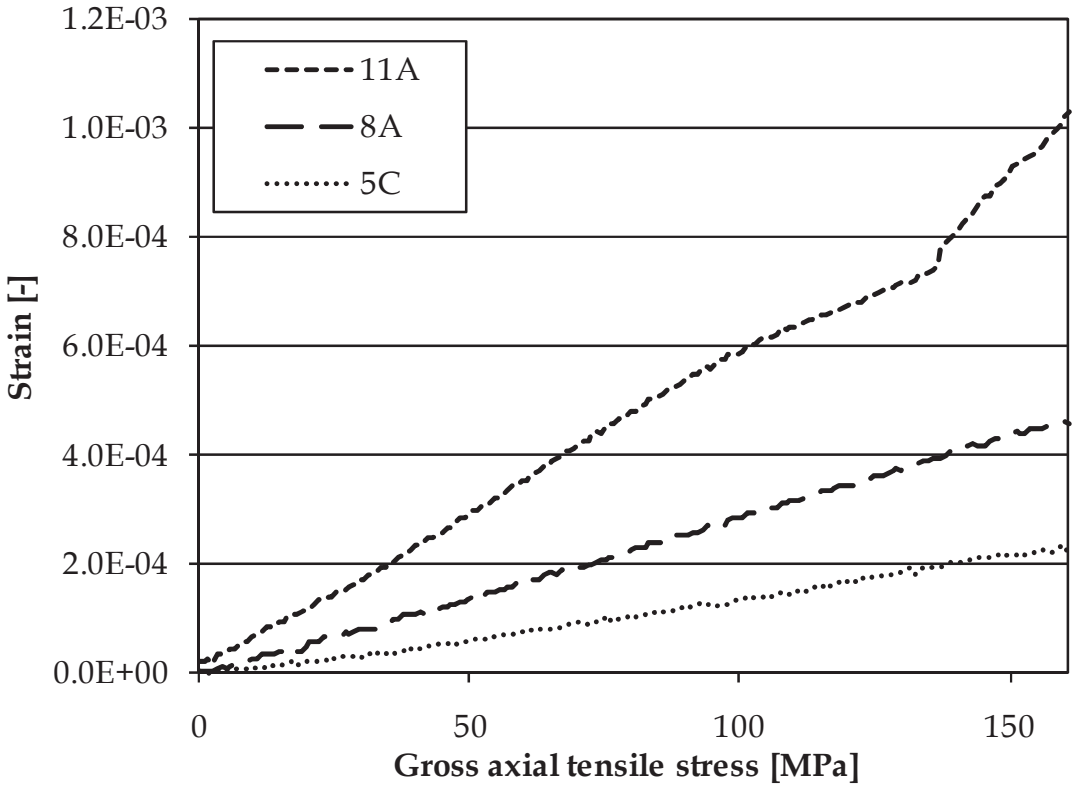

Figure 5.16: Strain measurement during axial tension.

3.4 Internal pressure

3.4.1 Setup description

The internal pressure test is carried out on a 1″ API Line Pipe connection in the setup shown in Figure 5.17. The test sample consists of a box (1a) and two threaded pin samples (1b) with an end piece welded at their free ends. Internal water pressure is applied on the specimen through the inlet in the endpiece (2). The end piece (3) has an air vent to which a pressure sensor is attached after the sample is filled with water. During the test, strains are measured by the strain gauges (4). In total 6 biaxial strain gauges (type TML FCA-3-11 with a gauge length of 3 mm for mild steel applications) are attached at the locations shown in Figure 5.18, capturing both the axial and hoop strains.

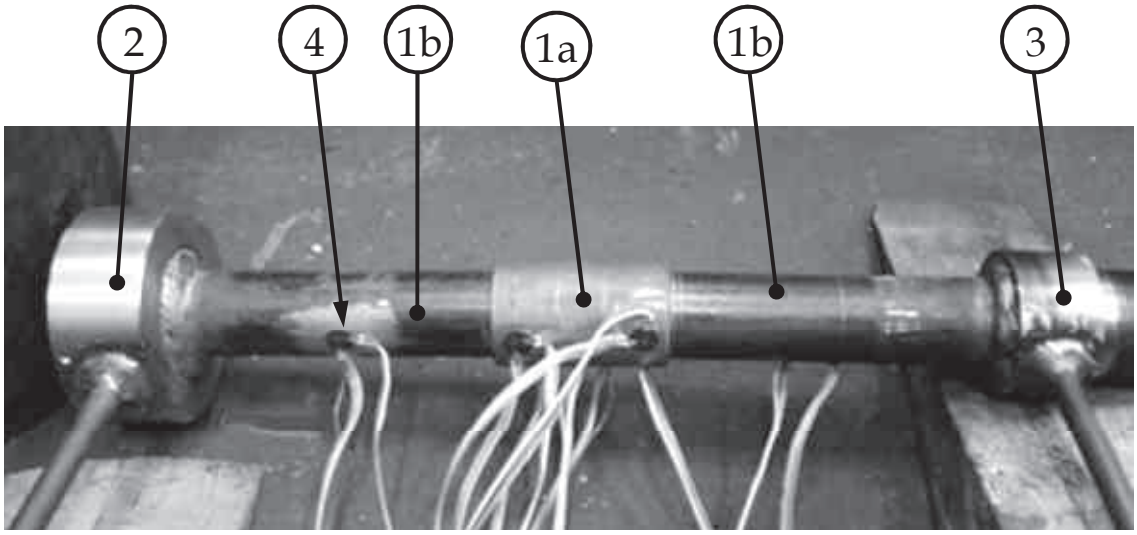

Figure 5.17: Setup of the internal pressure test.

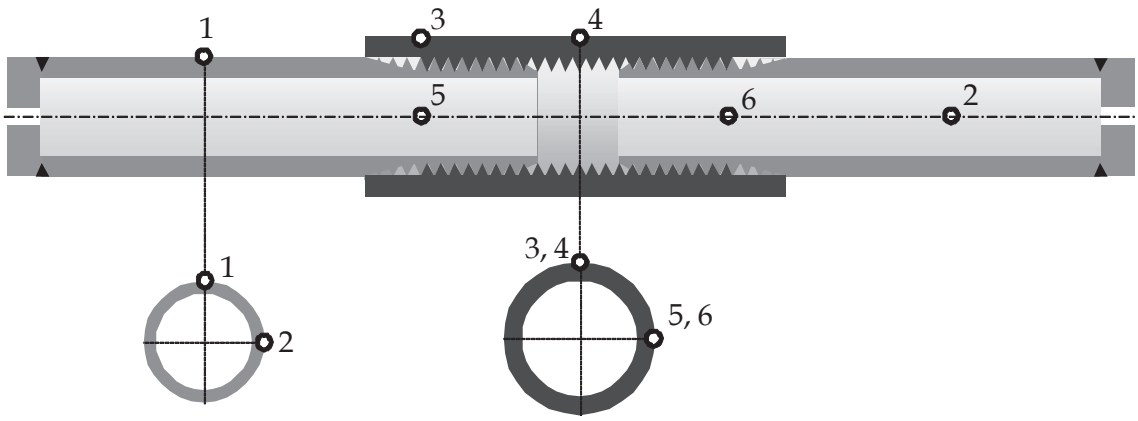

Figure 5.18: Strain gauge locations during the internal pressure test.

3.4.2 Test results

During the test the internal pressure is gradually increased to 500 bar. The results of 7 different strain directions are given as a function of the pressure

in Figure 5.19. All given strain values change linearly with the applied pressure. Since the pressure induces an axisymmetric load on the connection, the circumferential hoop strains and axial strains measured by strain gauges 1 and 2 and the hoop strains measured by strain gauges 3, 5 and 6 show an almost identical behaviour.

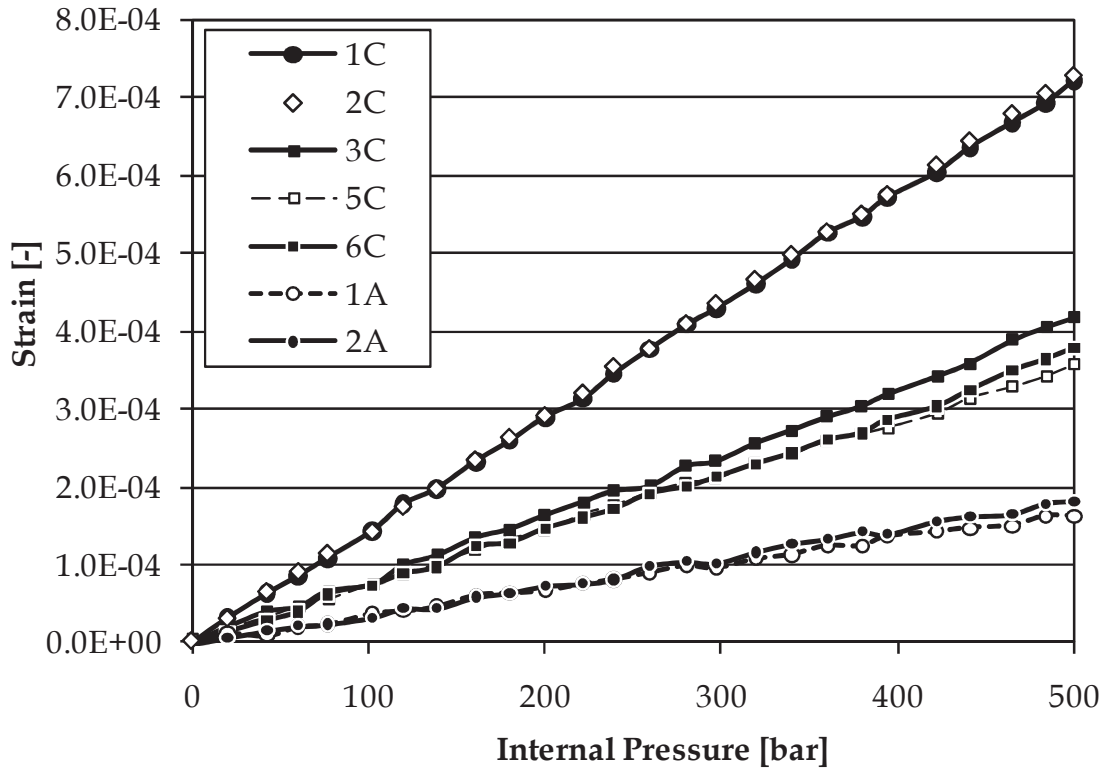

Figure 5.19: Strain measurement during the internal pressure test.

3.4.3 Pipe wall stress analysis

The measured strains are now compared with analytical solutions for pipe wall stresses under hydrostatic pressure. The pressure acting on the endpieces introduces an axial load in the test specimen. The resulting axial stress σ_{xx} in the pipe body is calculated with Eq. (5.12). Where p is the acting internal pressure and R_i and R_o are the internal and external radius of the pipe. The hoop stress σ_{zz} in the pipe body can be calculated using Lamé's pipe stress equation (5.13). The corresponding axial and hoop strains ε_{xx} and ε_{zz} can be calculated based on Hooke's law of elasticity Eq. (5.14).

$$\sigma_{xx} = \frac{pR_i^{\,2}}{R_o^2 - R_i^2} \tag{5.12}$$

$$\sigma_{zz} = \frac{2pR_i^{\,2}}{R_o^2 - R_i^2} \tag{5.13}$$

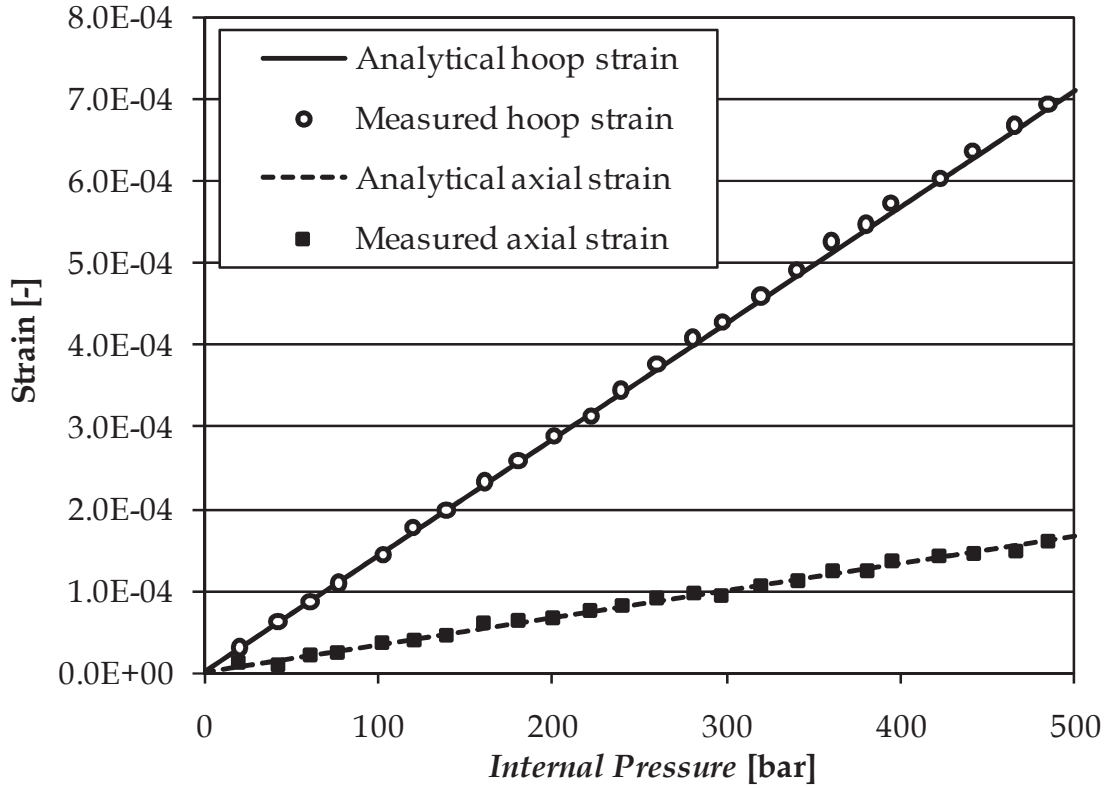

Figure 5.20: Comparison between measured strains at strain gauge 1 and analytical solution.

$$\varepsilon_{xx} = \frac{1}{E}\left(\sigma_{xx} - \nu \cdot \sigma_{zz}\right)$$
$$\varepsilon_{zz} = \frac{1}{E}\left(\sigma_{zz} - \nu \cdot \sigma_{xx}\right) \tag{5.14}$$

In Figure 5.20 the analytically calculated strains in the pipe body are compared to the values measured with strain gauge 1. An excellent agreement is observed. The RMS deviation is only 6 με.

4 Fatigue tests

4.1 Overview of the fatigue tests

In the following sections the performed fatigue tests are discussed. As shown in Figure 5.21, three setups have been used. One axial tension fatigue test is performed in the 1000 kN universal tensile testing machine on the 4.5″ API Line Pipe specimen used in the static torque tests and static axial tension test.

The main part of fatigue tests, however are performed on a small scale four-point bending setup. More than 100 tests are carried out. The test specimens consist of standard 1″ API Line Pipe and 1″ BSPT connections as well as several modified configurations manufactured from 1″ API Line Pipe specimens.

	Fatigue tests		
	Axial tension	**Small scale four-point bending**	**Medium scale four-point bending**
Setup	ESH 1000 kN	ESH 100 kN	Four-point bending setup
Connection	4.5″ API Line Pipe	1″ API Line Pipe 1″ BSPT	4.5″ API Line Pipe
Number of tests	1	104	4
Measured signals	• load • number of cycles • strains	• load • number of cycles • internal pressure	• load • number of cycles • crack opening • optical deflection measurement • modal analysis

Figure 5.21: Overview of experimental fatigue tests.

The third fatigue setup used is the medium scale four-point bending test rig. On this setup 4.5″ API Line Pipe connections are tested. During these tests advanced measuring techniques are used to distinguish between fatigue crack initiation and propagation and to monitor the fatigue crack growth in the connections.

It should be noted that the resonant bending fatigue setup described in Chapter 4 is considered to be a full scale setup. The resonant bending setup has been developed as part of this research project, but hasn't been used yet to perform fatigue tests on threaded pipe connections. Nevertheless, its applicability for fatigue testing of pipe joints is illustrated by the tests on the two plain pipes as discussed in Chapter 4. Performing a full scale test program with the resonant bending test setup on threaded pipe connections is considered to be part of future research work as discussed in the final chapter of this work.

4.2 Axial tension fatigue test

Following the quasistatic axial tensile test described in section 3.3 a dynamic fatigue test is carried out on the same 4.5″ API Line Pipe specimen in the 1000 kN ESH setup illustrated in Figure 5.14. This test serves mostly as a comparison for the samples of the same connection type tested in the medium scale four-point bending setup.

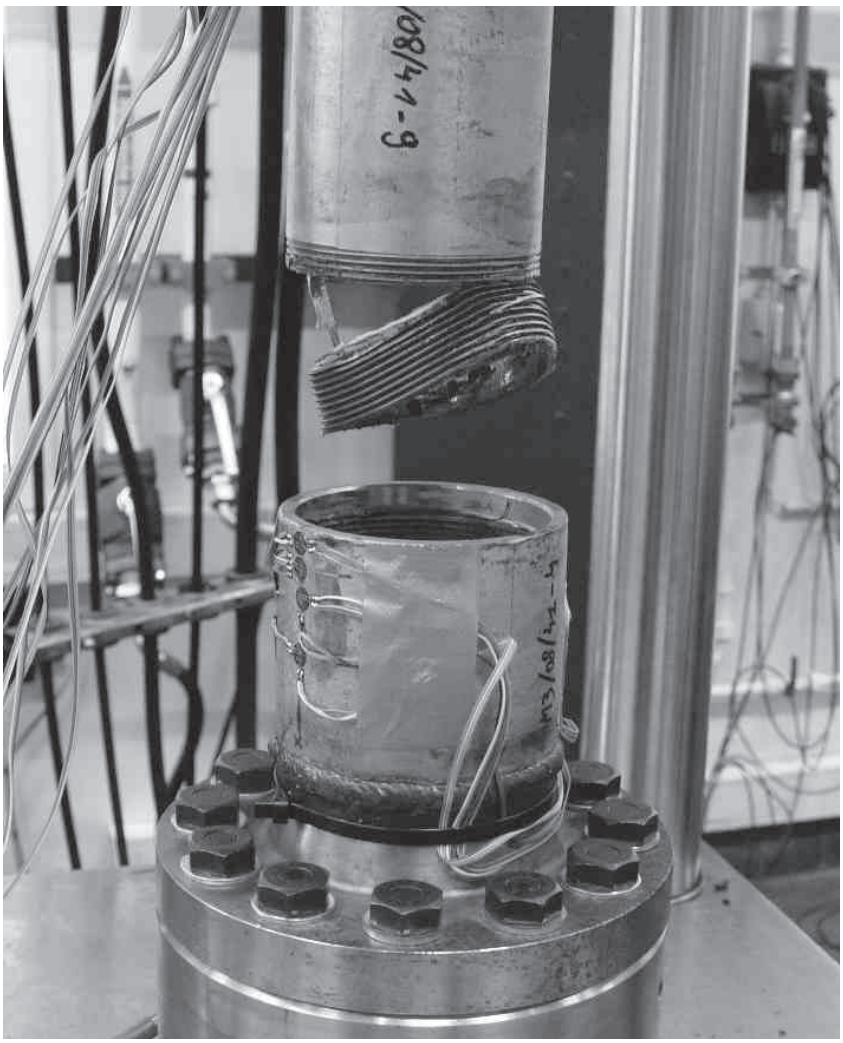

Figure 5.22: Failed 4.5″ API Line Pipe specimen.

The fatigue test is performed at a load ratio of R = 0.1, with a maximum gross stress in the pipe body of 161 MPa or 32 % of σ_{UTS}. The corresponding stress amplitude S_a is 72.5 MPa and the test frequency is 3 Hz.

The connection failed after 10 712 cycli as shown in Figure 5.22. Several mechanisms contributed to the connection's failure. Firstly, a fatigue crack initiated at the last engaged thread of the pin and propagated over part of the pin's cross-section. This caused the load to concentrate on the remaining section and the partition of the threads in this area. Once this area became too small, the threads sheared of in this region and finally jumpout occurred as can be seen in Figure 5.22.

4.3 Small scale four-point bending tests

4.3.1 Setup description

The small scale tests are performed in four-point bending on an ESH 100 kN universal test machine in the setup shown in Figure 5.23. The test sample (schematically illustrated in Figure 5.24) consists of a central box (1a) with

two made up threaded pipes (1b) and is supported by the two outer load points (indicated by the white arrows in Figure 5.23). A dynamic load is applied by the hydraulic actuator (2) and transferred through the load cell (3) to a transverse beam that carries the two inner load points. To avoid a bending moment in the load cell, it is connected to the transverse beam through a hinge (4).

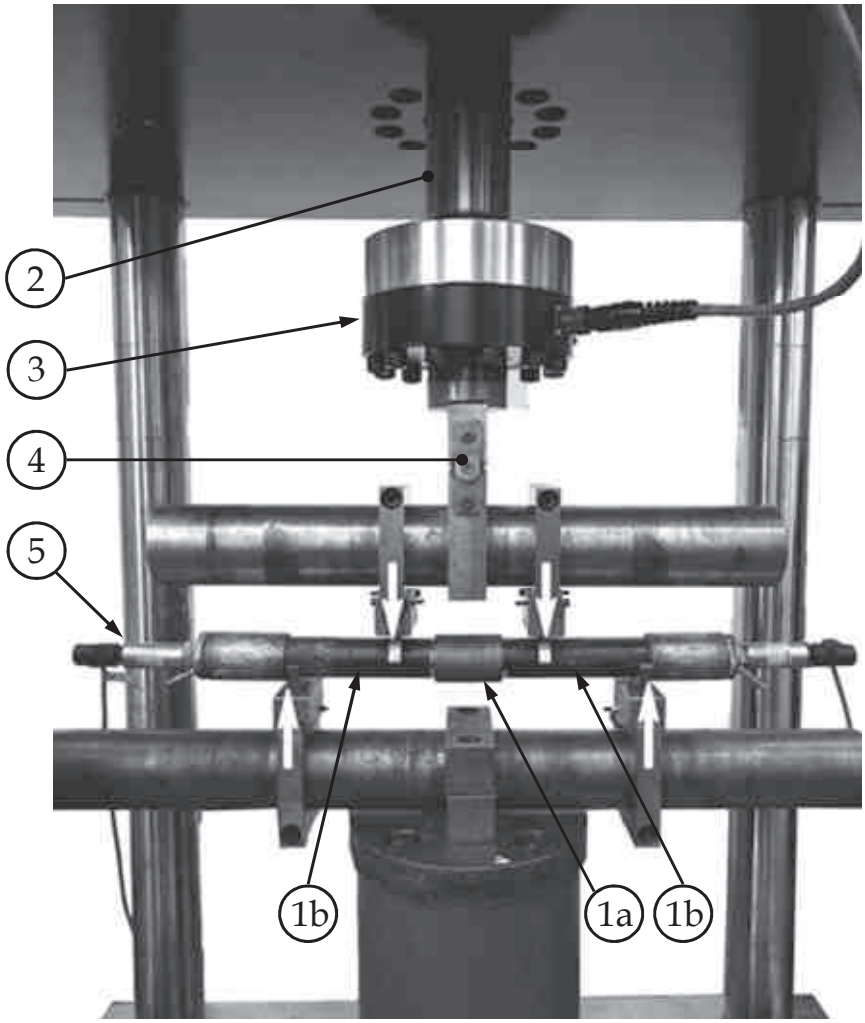

Figure 5.23: Small scale four-point bending setup for 1″ connections.

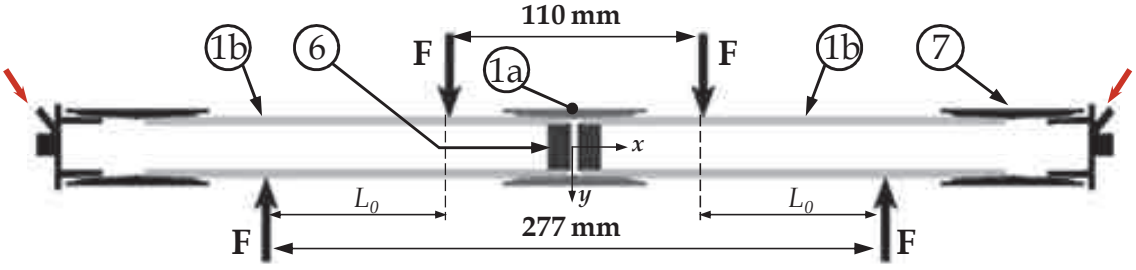

Figure 5.24: Schematic section view of a test specimen.

For a given vertical force F as in Figure 5.24, the bending moment M_z between the two inner points is constant and given by Eq. (5.15). As a result, any material fibre in this region is subjected to a bending stress that is tensile below the neutral axis of the pipe segment and compressive above. The bending stress σ_b is given by Eq. (5.16).

$$M_Z = F \cdot L_0 \tag{5.15}$$

$$\sigma_b = \frac{M_z \cdot y}{I_z} \tag{5.16}$$

Where y is the vertical distance between the considered material fibre and the neutral axis, with the sign of y corresponding to the direction of the y-axis in Figure 5.24. This way tensile bending stresses have a positive sign, and compressive stresses are negative. The x-axis coincides with the centreline of the test specimen. I_z is the area moment of inertia of the cross section of the pipe.

The tests are carried out under load control with a load ratio R = 0.1 and at a testing frequency of 15 Hz. To enable the detection of through thickness fatigue cracks, the tubular samples are pneumatically pressurized at a pressure of around 2 bar. When a crack is propagated through the wall thickness of the pipe, the pressure drops below a threshold and the test is automatically stopped. The number of elapsed load cycles N up to this event, is referred to as the fatigue life of the connection that is used throughout the S-N curves given in the following sections.

Two separate pressure chambers are created for the two pipe samples by inserting plugs (6) (see Figure 5.24) and both free ends of the test specimen are closed using a special end cap (7) with a pressure inlet. This way a crack in either pipe sample can be distinguished from each other. The internal pressure in the two pipes is continuously monitored using the pressure transducers (5) at the end caps. When a pressure drop occurs, the connection is disassembled and the exact crack location is found using dye penetrant investigation. The failed pipe is then replaced by a dummy sample and the test continued until failure of the second pipe specimen occurs.

4.3.2 Tested configurations overview

With the small scale four-point bending setup, 8 different connection types are tested. The first two types are the standard 1" API Line Pipe connection as shown in Figure 5.2 and the standard 1" BSPT connection as shown in Figure 5.3. Then a standard API Line Pipe configuration is tested, where prior to the make up PTFE tape (Teflon) was applied to the threads. Finally, 5 additional configurations are tested, derived from the standard API Line Pipe type, with a modified geometry.

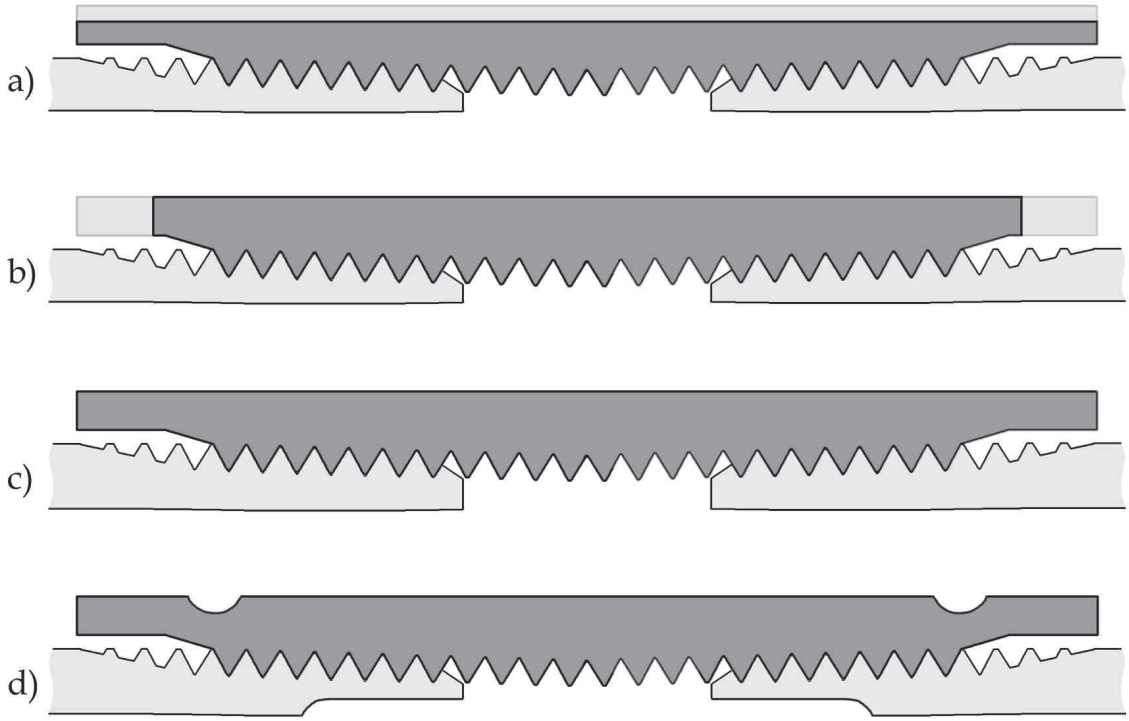

Figure 5.25: Modified configurations: a) reduced box wall, b) reduced box recess, c) increased pin wall, d) modified pin and box.

These modifications are inspired on the threaded connection designs described in the patent overview in section 3.2.2 of Chapter 2. There it has been shown that the general idea behind fatigue resistant threaded connections based on box geometry modifications is to use stiffness reductions to redistribute the thread loads. The modified configurations used in this research are shown in Figure 5.25. In the first two configurations the global stiffness of the box is lowered by reducing the box wall thickness as illustrated by Figure 5.25.a. In one configuration the box wall thickness reduction is 1 mm, in the other 2 mm. In the next configuration the box recess length is reduced by 5 mm at both sides as shown in Figure 5.25.b. Configuration c in Figure 5.25 has a pin with an increased wall thickness and in the final configuration d, the pin has the same wall thickness increase of configuration c and in addition both pin and box are modified. In this last modification two stress relief grooves are applied, as previously described in section 3.2.4 of Chapter 2. Their geometry is based on the work of Venkatesan and Kinzel [5.16] who showed that a bolt-nut connection with similar optimized bolt and nut geometry gives a significantly decreased stress concentration due to a more uniform load distribution.

4.3.3 Standard 1″ API Line Pipe

4.3.3.1 S-N curve

In total 15 tests are conducted on standard 1″ API Line Pipe specimens (shown in Figure 5.2), 13 of which failed due to leakage caused by a fatigue

crack. The other two specimens did not fail and the test was stopped after exceeding 2 million cycles. Each test is represented by a single data point in Figure 5.26. The number of cycles to failure N is shown together with the applied gross bending stress amplitude S_a. This is the amplitude of the maximum bending stress in the pipe material of the pin calculated by Eq. (5.16) without taking into account the stress concentrations of the threads.

The data is processed according the BS 7608 fatigue standard [5.17], in which a fatigue limit is assumed at 2 million cycles. The fatigue data is expected to follow a Basquin relation, as introduced in section 4.2.1 of Chapter 2, written in the form of Eq. (5.17).

$$S_a = A \cdot N^{-B} \tag{5.17}$$

The factors A and B of this mean curve are found by regression analysis of the data points of the tests for which leak occurred. The best least-squares fit of the mean curve to the data points has a standard deviation STD = 5.14 MPa and is given in by Eq. (5.18). The design curve shown in Figure 5.26 is calculated according to [5.17] as the mean curve minus two times the standard deviation. Hence, the design curve is associated with a 95.4 % probability of survival.

$$S_a = 848.7 \cdot N^{-0.2233} \tag{5.18}$$

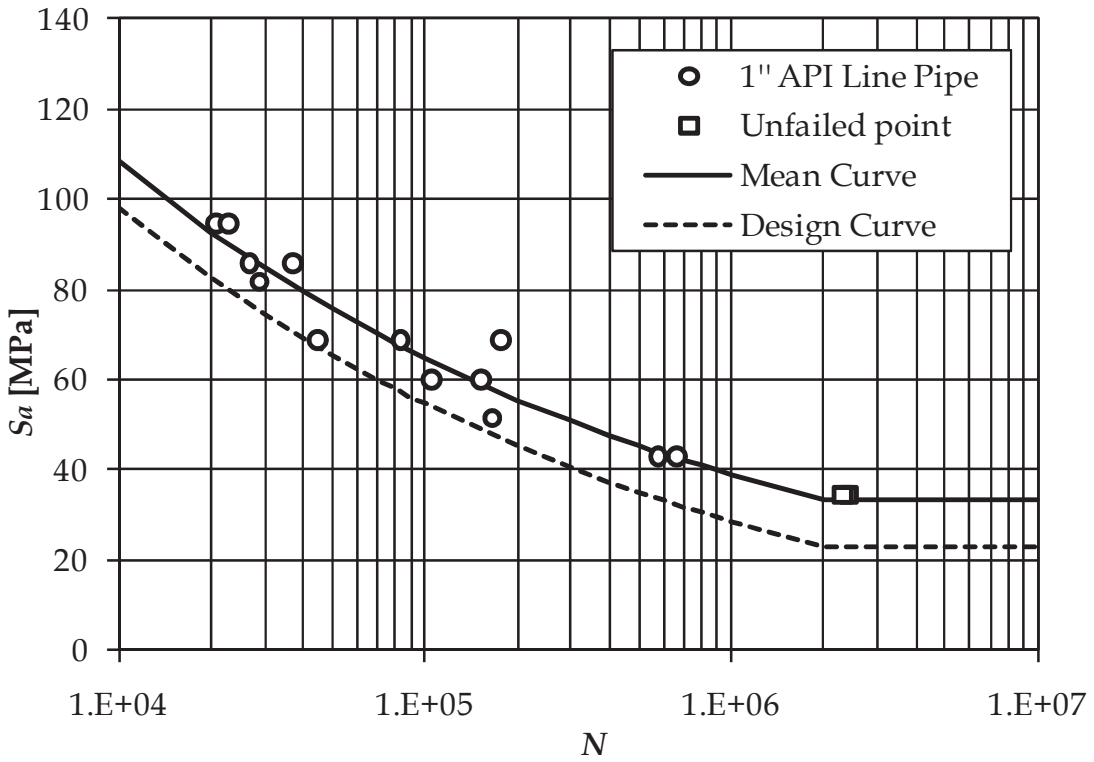

Figure 5.26: S-N curve for the standard 1″ API Line Pipe connection (load ratio R = 0.1).

4.3.3.2 Fracture surface analysis

For the standard 1″ API Line Pipe connection a detailed analysis is made of the fracture surface to get a better understanding of the fatigue crack growth behaviour of the connection. In order to do this, either longitudinal or transverse sections were made by cutting the specimen or by forcing brittle fracture of the pin after cooling the samples in liquid air.

All observed cracks appear at the last fully engaged thread of the pin as illustrated in the section view in Figure 5.27. The crack is indicated by the arrow and is oriented perpendicular to the cutting surface. The root of the LET of the pin is the expected location for the cracks to initiate, according to reported failure cases and laboratory tests as described in section 1.2.1 of Chapter 1. This also corresponds to the location where the highest stress concentrations occur (cfr. section 2.3.2 of Chapter 2).

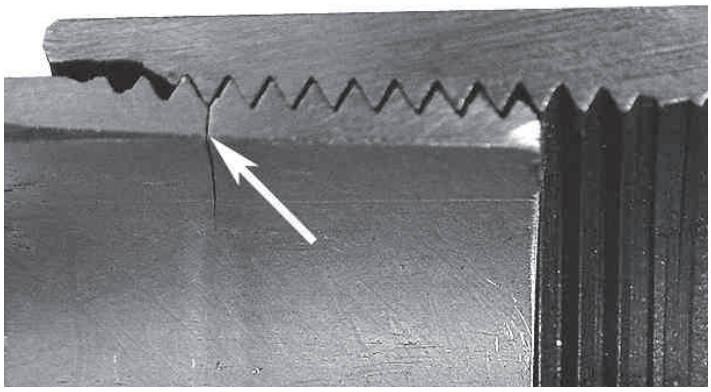

Figure 5.27: Fatigue crack initiated at the LET of the pin of a standard 1″ API Line Pipe specimen.

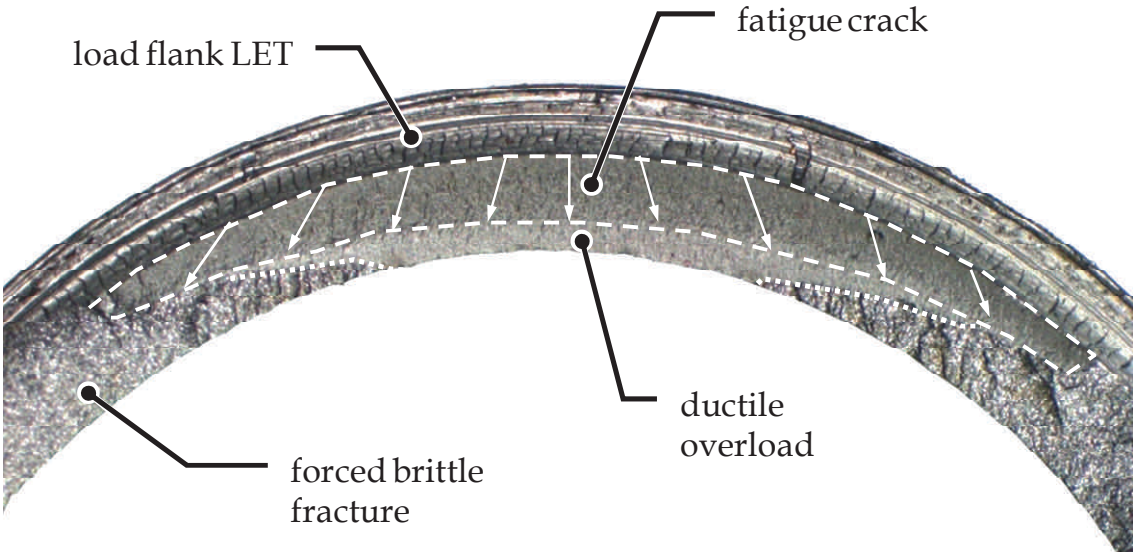

Figure 5.28: Fracture surface of a fatigue crack in a standard 1″ API Line Pipe specimen.

In the fracture surface shown in Figure 5.28 the shape of the fatigue crack for a test with stress amplitude S_a = 94.5 MPa can be seen. To obtain this view, the sample is cooled down in liquid air to a temperature of about -180°C and a brittle fracture is forced to open up the fracture surface. From the figure it can be seen that the fatigue crack initiated along the root of the LET and propagated through the wall of the pin. While doing this, the crack propagated over a wide segment of the circumference. When the remaining wall thickness became insufficient to withstand the applied stress, a ductile overload fracture occurred, creating a through-thickness crack. The pressurized air escaped and the test was stopped. In several cases the ductile overload is much smaller or negligible, but the global shape of the entire fatigue crack is comparable for all observed fracture surfaces.

4.3.4 Standard 1″ BSPT

4.3.4.1 S-N curve

On the standard 1″ BSPT connection shown in Figure 5.3, 8 tests are performed. The test results together with the mean and design curves corresponding to the data are shown in Figure 5.29. The mean curve has a standard deviation of 10.4 MPa compared to the measured data and is described by the following relation.

$$S_a = 811.8 \cdot N^{-0.2075} \tag{5.19}$$

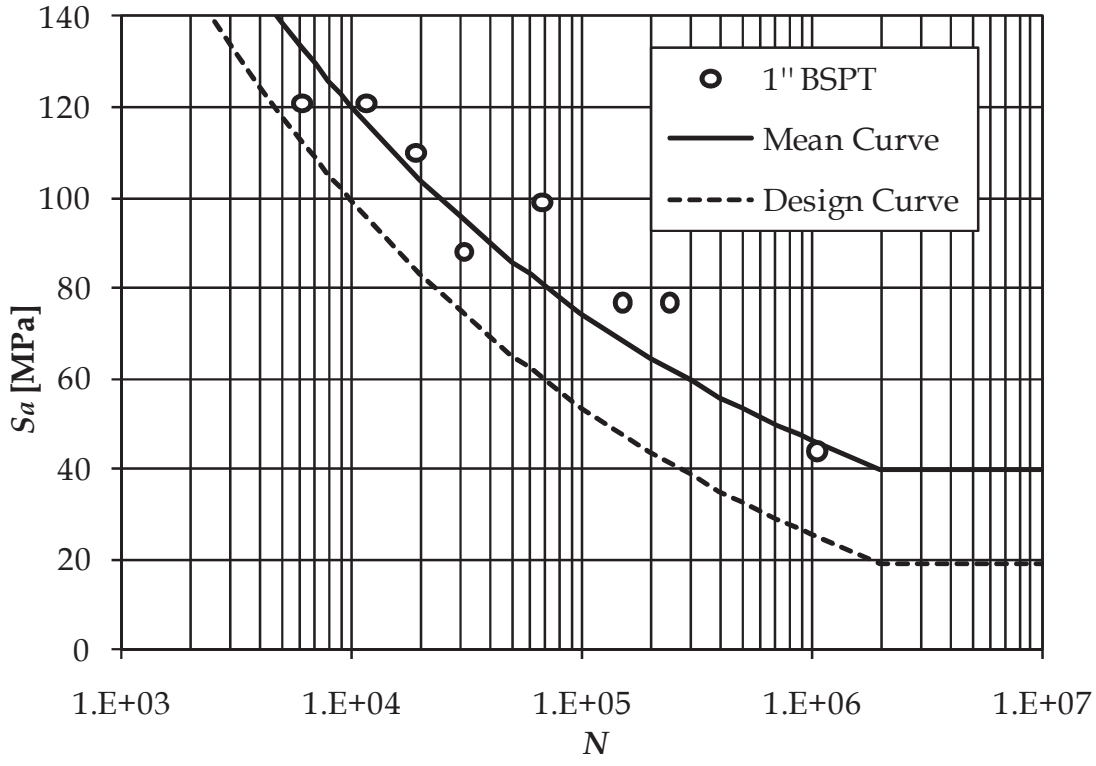

Figure 5.29: S-N curve for the standard 1″ BSPT connection (R = 0.1).

4.3.4.2 Fracture surface

A section view of a failed standard 1″ BSPT specimen is provided in Figure 5.30. It can be seen that the fatigue crack initiated at the LET of the pin as was the case for the standard API Line Pipe connection. From Figure 5.31 it can be seen that the shape of the fracture is similar as well. While penetrating the wall thickness, the fatigue crack propagated over a wide segment of the pin circumference. It should be noted that in this case, there is no significant ductile overload region.

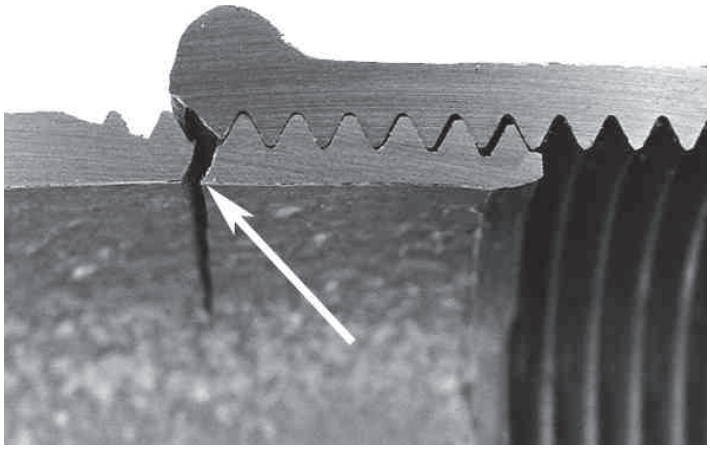

Figure 5.30: Fatigue crack initiated at the LET of the pin of a standard 1″ BSPT specimen.

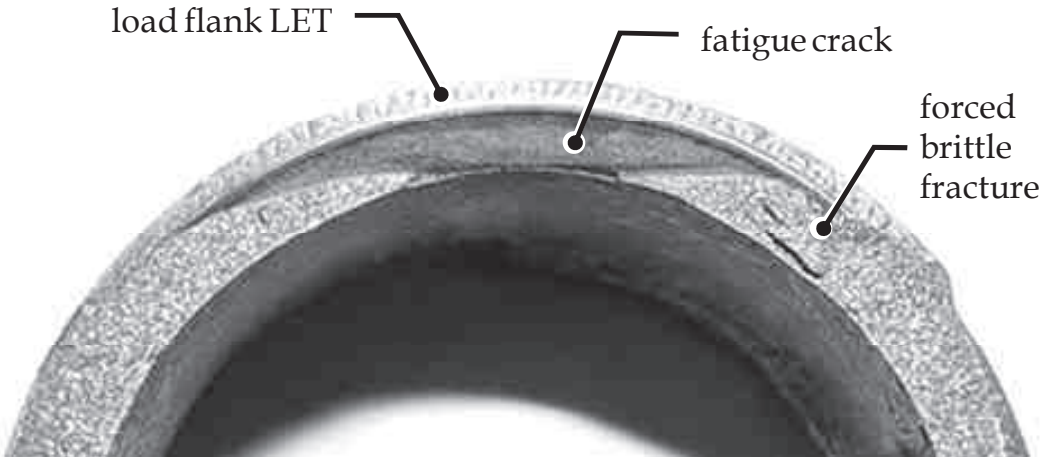

Figure 5.31: Fracture surface of a fatigue crack in a standard 1″ BSPT specimen.

4.3.5 Standard 1″ API Line Pipe with PTFE tape

4.3.5.1 S-N curve

Fourteen tests are carried out on standard 1″ API Line Pipe connections with PTFE between the threads, of which 2 did not fail after 2 million cycles. The test results together with the mean and design curves corresponding to the data are shown in Figure 5.32.

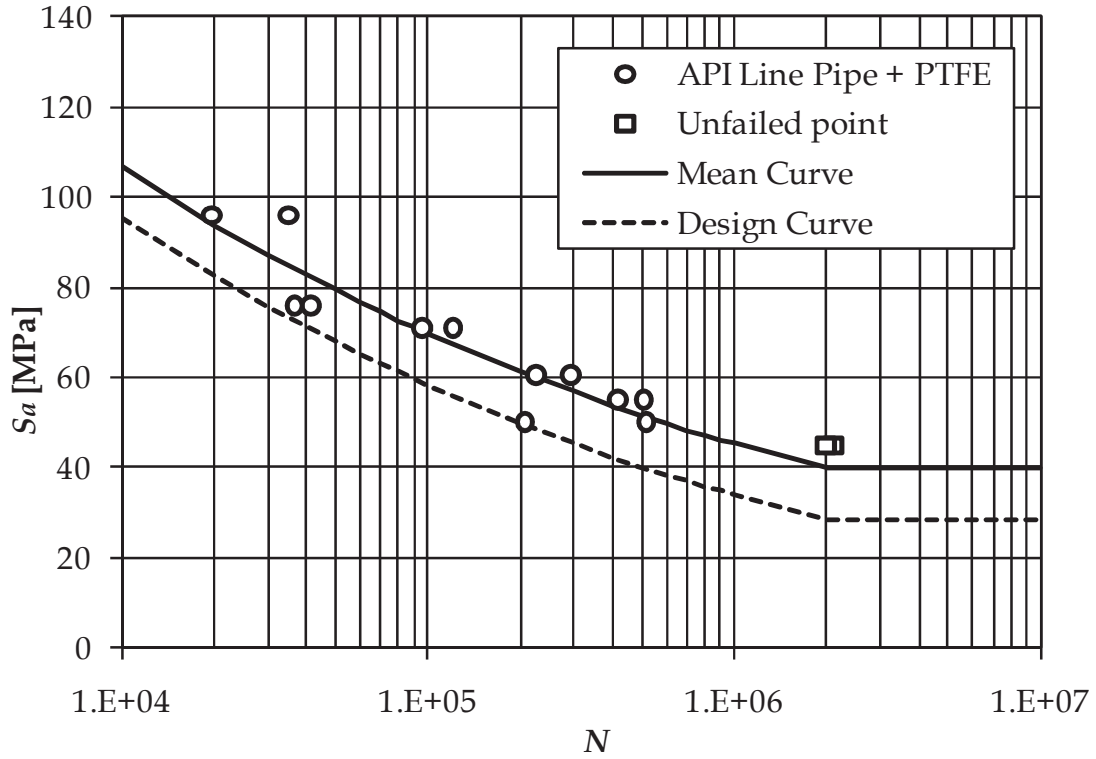

Figure 5.32: S-N curve for the 1″ API Line Pipe connection with PTFE (R = 0.1).

The mean curve has a standard deviation of 5.74 MPa compared to the measured data and is described by the following relation.

$$S_a = 597.2 \cdot N^{-0.1866} \tag{5.20}$$

4.3.5.2 Fracture surface

The fracture surface for a fatigue test with a stress amplitude of S_a = 90 MPa is shown in Figure 5.33. A leak appeared in the specimen after 35 220 cycles. In order to quantify the fatigue crack growth, this surface is investigated using *scanning electron microscopy* or SEM. With this microscopic technique, magnification factors of several thousands can be achieved and individual fatigue striations can visualised. Hence cyclic crack depth increments can be measured. This was done at the three locations indicated in Figure 5.33. Location 1 is near the thread root where the fatigue crack initiated. Location 2 is near the inside wall of the pin and location 3 is at the border between the fatigue crack and the forced brittle fracture zone.

In Figure 5.34 a SEM micrograph of this last location at a magnification of 750 times is shown. Two different regions, divided by the dotted line, can be clearly observed. The lower region is the brittle fracture surface. It has a faceted aspect of a cleavage fracture pattern caused by the brittle fracture of the pin that was forced after subcooling. In the region above the dotted line striations can be observed, which are caused by fatigue fracture. A detailed view of the region inside the white rectangle in Figure 5.34 with a

magnification factor of 3000 is given in Figure 5.35. In this figure individual fatigue striations can be clearly distinguished (two striations are indicated by the white arrows). The crack propagation direction is perpendicular to the striations or upwards in the figure. The mean cyclic crack depth increase in this region is determined to be da/dN = 0.56 µm. The same procedure is used to determine the da/dN values at location 1 and 2. The total crack depth, measured as the distance between the thread root where the crack initiated and the pin inner wall, is 1.889 mm.

Additionally, crack depth increases are measured in a second sample tested at the same stress amplitude of S_a = 90 MPa and with a total fatigue life N = 19 663 cycles. The three measured locations in this additional sample are numbered in the same way as in the sample shown in Figure 5.33. The measured da/dN and total crack depth values in both samples are summarized in Table 5.4. The fatigue crack growth behaviour of the small scale specimens is discussed further in section 4.3.11.2.

Fatigue life *N*	35 220	19 663
Crack depth [mm]	1.889	1.835
***da/dN* location 1 [µm]**	0.44	0.45
***da/dN* location 2 [µm]**	0.54	0.53
***da/dN* location 3 [µm]**	0.56	0.65

Table 5.4: Cyclic crack depth increase values.

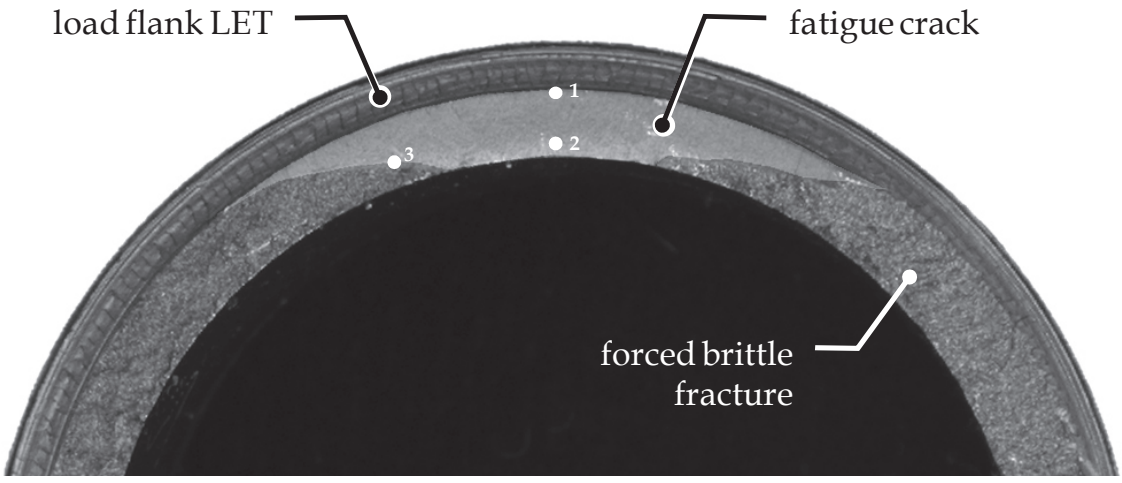

Figure 5.33: Fracture surface of a 1″ API Line Pipe specimen with PTFE.

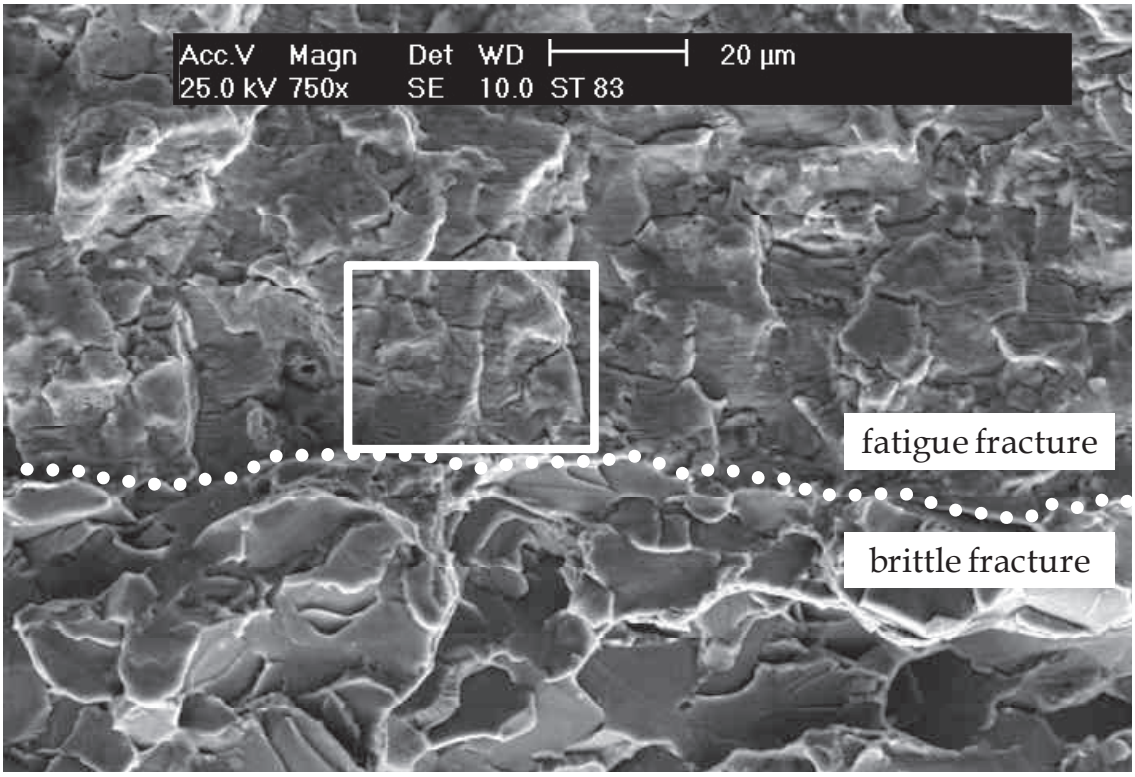

Figure 5.34: SEM micrograph of the boundary between the fatigue crack and the forced brittle fracture (magnification 750x).

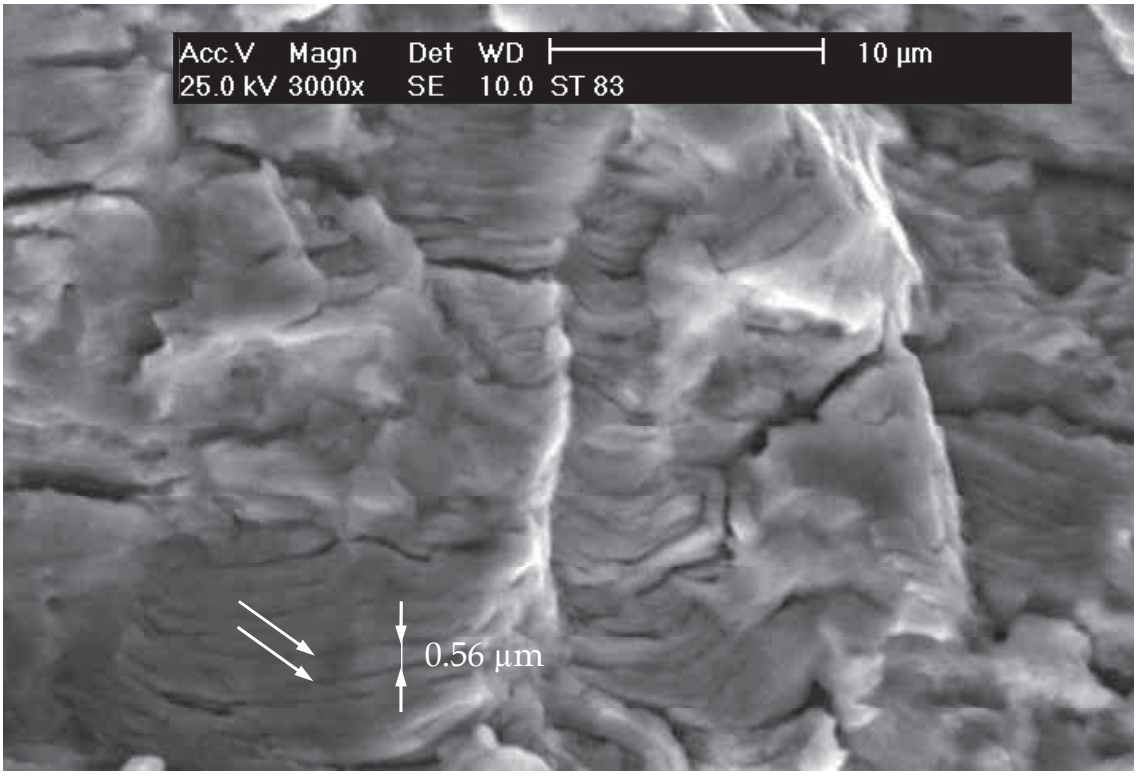

Figure 5.35: SEM micrograph of fatigue crack surface showing fatigue striations (magnification 3000x).

4.3.6 Reduced box wall thickness -1 mm

4.3.6.1 S-N curve

Thirteen tests are carried out on modified 1″ API Line Pipe connections. The modification consists of a reduction in box wall thickness of 1 mm (D_b = 38 mm) as shown in Figure 5.25.a. Two of the specimens had not failed after 2 million cycles. The test results together with the mean and design curves corresponding to the data are shown in Figure 5.36. The mean curve has a standard deviation of 4.47 MPa compared to the measured data and is described by the following relation.

$$S_a = 970.8 \cdot N^{-0.2256} \tag{5.21}$$

When this mean curve is compared to the mean curve of the standard API Line Pipe connection in Figure 5.26, it is clear that the current modification exhibits an improved fatigue life. Hence, this is a first experimental confirmation of the idea that a box stiffness reduction can improve a connection's fatigue life. A more detailed comparison between the obtained fatigue curves of the different tested configurations will be provided in section 4.3.11.1.

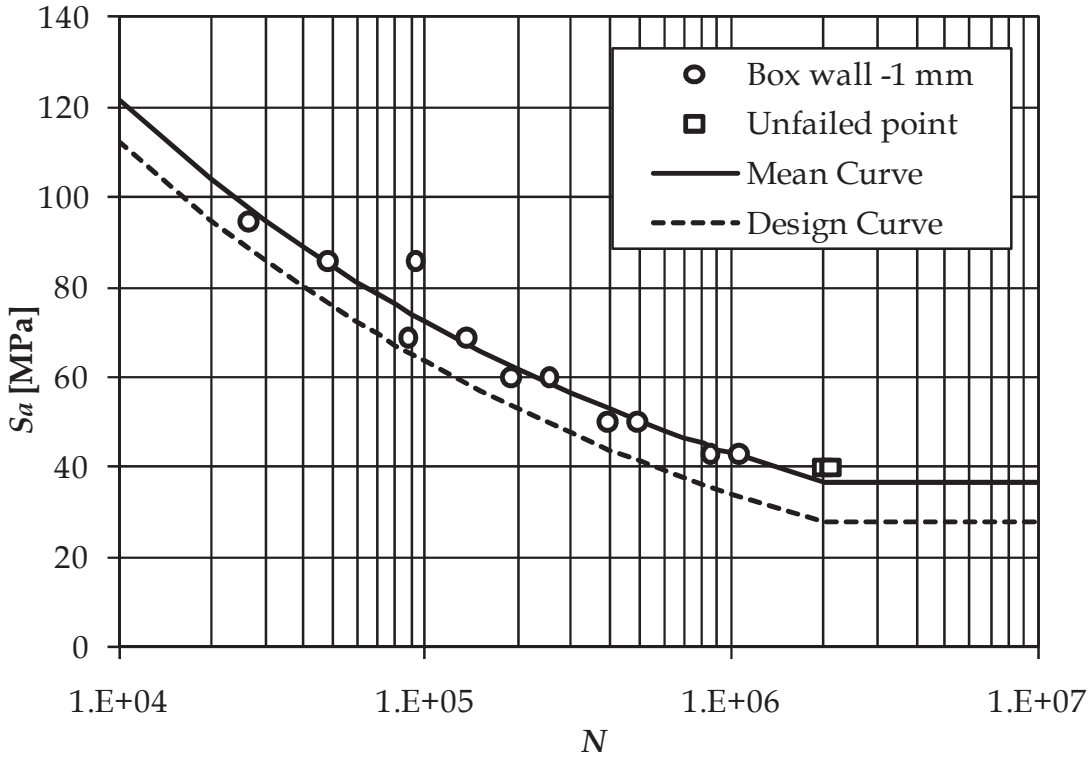

Figure 5.36: S-N curve for the 1″ API Line Pipe connection with box wall thickness reduction of 1 mm (R = 0.1).

4.3.6.2 Fracture surface

The fracture surface of a fatigue test with a stress amplitude of S_a = 60 MPa is shown in Figure 5.37. A leak appeared in the specimen after 253 836 cycles. Analogue to the procedure described in section 4.3.5.2, SEM micrographs are used to determine the crack depth increase values at the three locations indicated in Figure 5.37. The SEM micrograph taken at the boundary between the fatigue and brittle fracture is given in Figure 5.38 and the resulting measured *da/dN*-values are summarized in Table 5.5.

Fatigue life *N*	253 836
Crack depth [mm]	1.812
***da/dN* location 1 [µm]**	0.40
***da/dN* location 2 [µm]**	0.48
***da/dN* location 3 [µm]**	0.48

Table 5.5: Cyclic crack depth increase values.

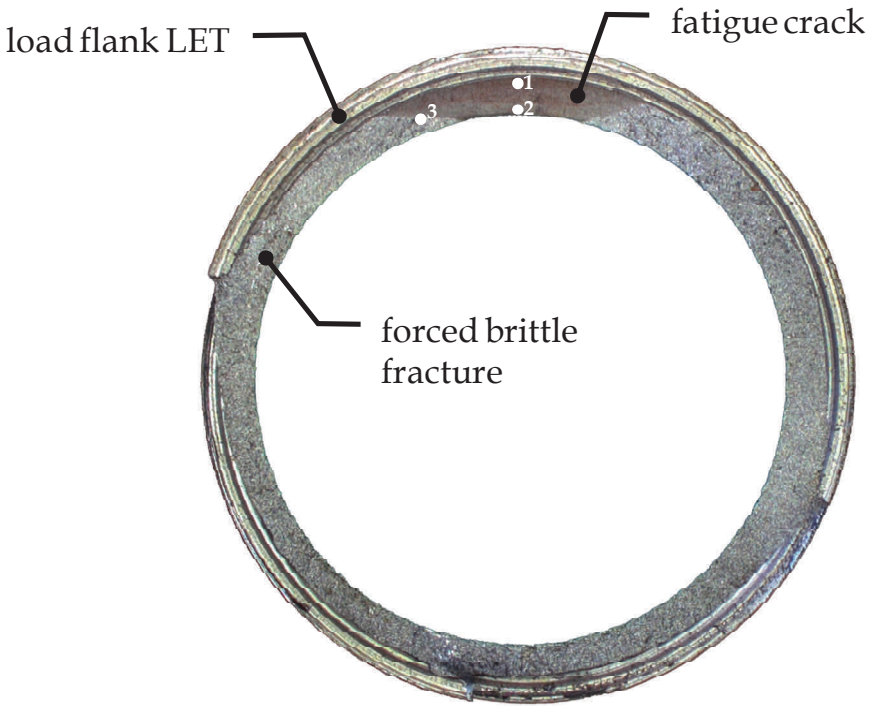

Figure 5.37: Fracture surface of a modified 1″ API Line Pipe specimen with a box wall thickness reduction of 1 mm.

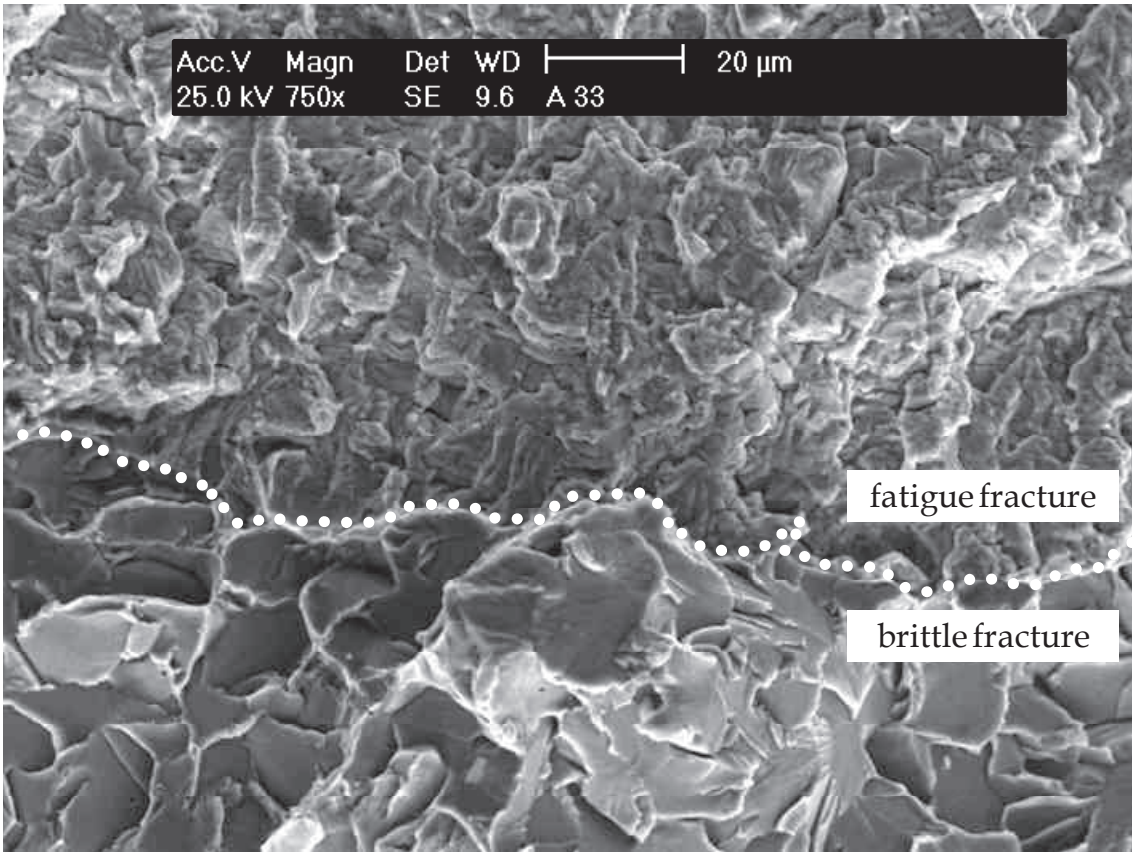

Figure 5.38: SEM micrograph of the boundary between the fatigue crack and the forced brittle fracture (magnification 750x).

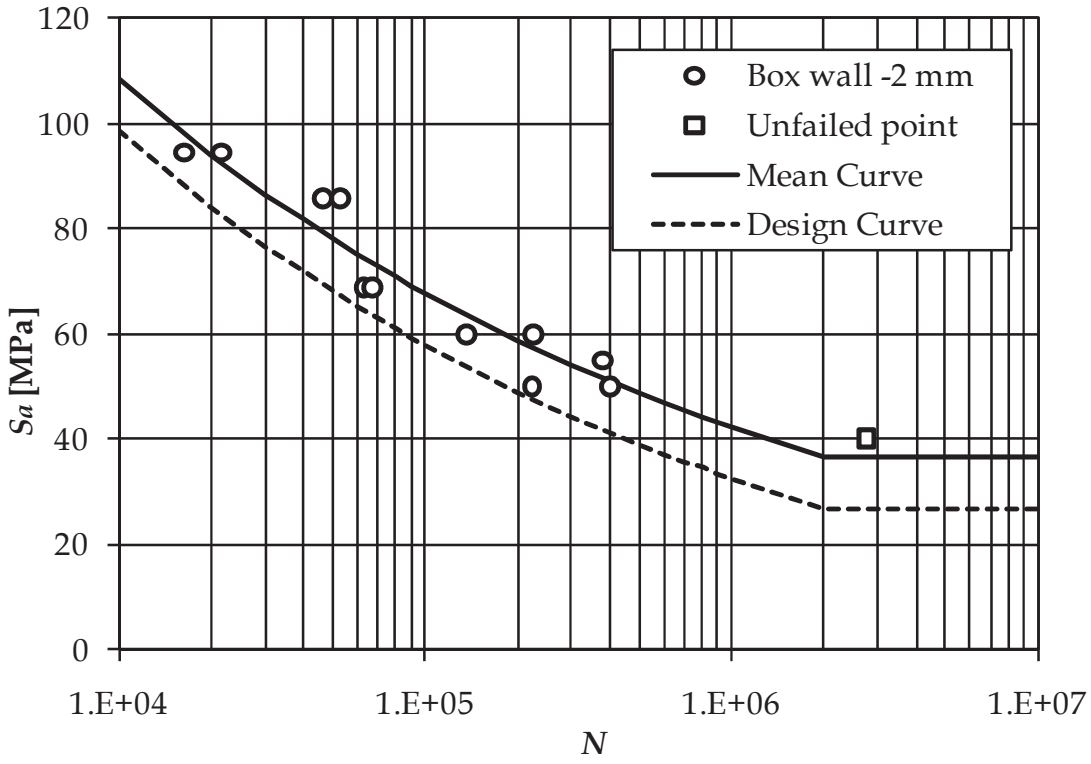

Figure 5.39: S-N curve for the 1″ API Line Pipe connection with box wall thickness reduction of 2 mm (R = 0.1).

4.3.7 Reduced box wall thickness -2 mm

The configuration discussed in this paragraph is analogue to the previous API Line Pipe modification, except that the box wall thickness is reduced by 2 mm (D_b = 36 mm) instead of 1 mm as in the previous case. Fourteen tests are carried out, of which 2 had not failed after 2 million cycles. The test results together with the mean and design curves corresponding to the data are shown in Figure 5.39. The mean curve has a standard deviation of 4.93 MPa compared to the measured data and is described by the following relation.

$$S_a = 711.2 \cdot N^{-0.2042} \tag{5.22}$$

4.3.8 Reduced box recess length

The next tested modified API Line Pipe configuration has a reduced recess length, 5 mm is removed at either side of the box as illustrated in Figure 5.25.b, hence the total box length L_b is reduced to 56.7 mm. In total 11 tests are carried out, of which 2 remained unfailed after 2 million cycles. The test results together with the mean and design curves corresponding to the data are shown in Figure 5.40. The mean curve has a standard deviation of 3.34 MPa compared to the measured data and is described by Eq. (5.23).

$$S_a = 562.1 \cdot N^{-0.1807} \tag{5.23}$$

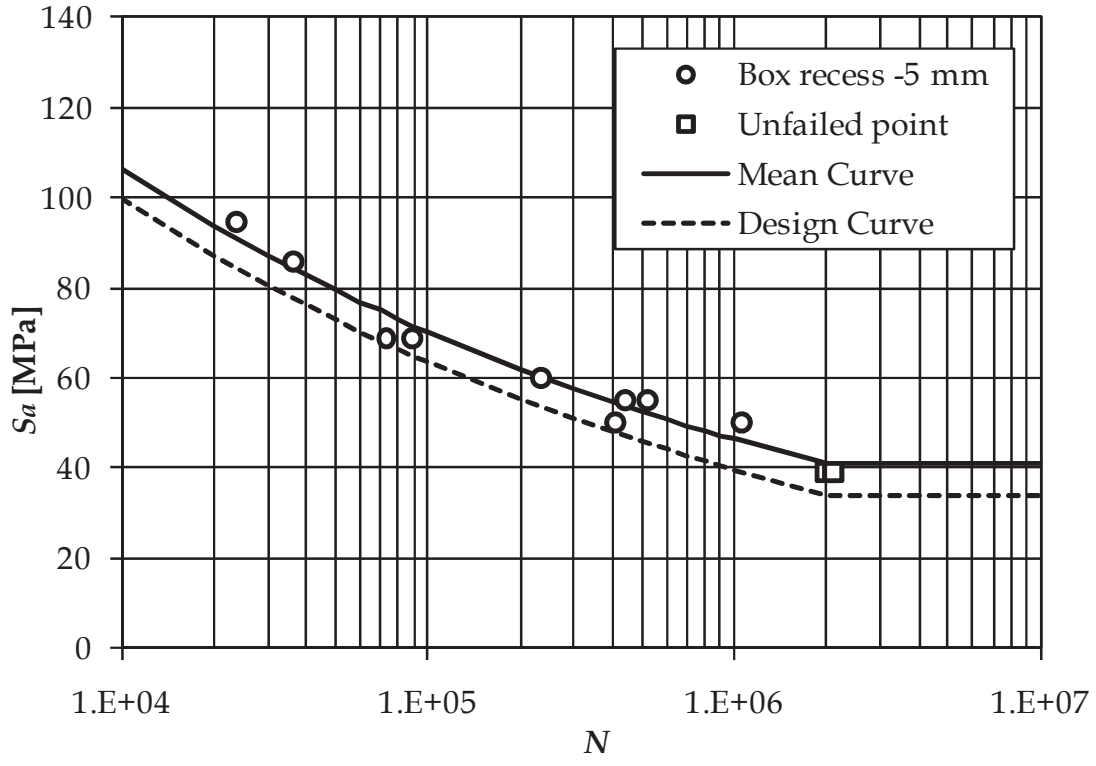

Figure 5.40: S-N curve for the 1″ API Line Pipe connection with box recess length reduction of 5 mm (R = 0.1).

4.3.9 Thick-walled pin configuration

In this modified API Line Pipe configuration, the pins are made out of pipe material with the same outer pin diameter D_p but with an increased wall thickness *WT* as shown in Figure 5.25.c. The wall thickness of the pins is here *WT* = 4.5 mm instead of 3.4 mm as for the standard API Line Pipe pin specimens.

On this configuration 13 tests are carried out, of which 2 remained intact after 2 million cycles. The test results together with the mean and design curves corresponding to the data are shown in Figure 5.41. The mean curve has a standard deviation of 3.50 MPa compared to the measured data and is described by the following relation:

$$S_a = 888.3 \cdot N^{-0.2040} \tag{5.24}$$

It is noted that the stress amplitude S_a is calculated using the bending stress expressed in Eq.(5.16). Since the pin wall thickness is increased in this configuration, a higher force is applied to the specimens to obtain the comparable stress levels as for the other tested configurations.

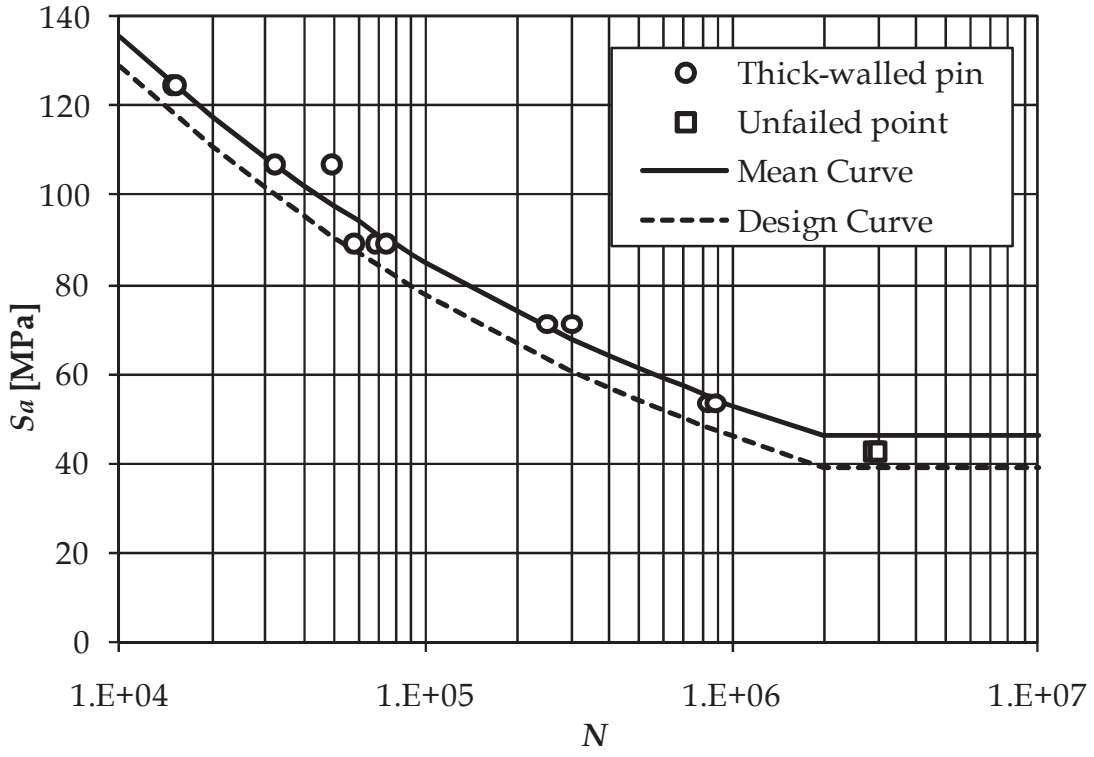

Figure 5.41: S-N curve for the 1″ API Line Pipe connection with thick-walled pin (*R* = 0.1).

4.3.10 Combined pin and box modification

The final tested configuration comprises of a thick-walled pin assembly (pin *WT* = 4.5 mm) with modifications on both the pin and the box as shown in

Figure 5.25.d. In total 16 tests are carried out on this configuration, of which 2 remained unfailed after 2 million cycles. A section view of a failed specimen is shown in Figure 5.43. The test results together with the mean and design curves corresponding to the data are presented in Figure 5.42. The mean curve has a standard deviation of 5.08 MPa compared to the measured data and is given by the following relation:

$$S_a = 1278 \cdot N^{-0.2413} \tag{5.25}$$

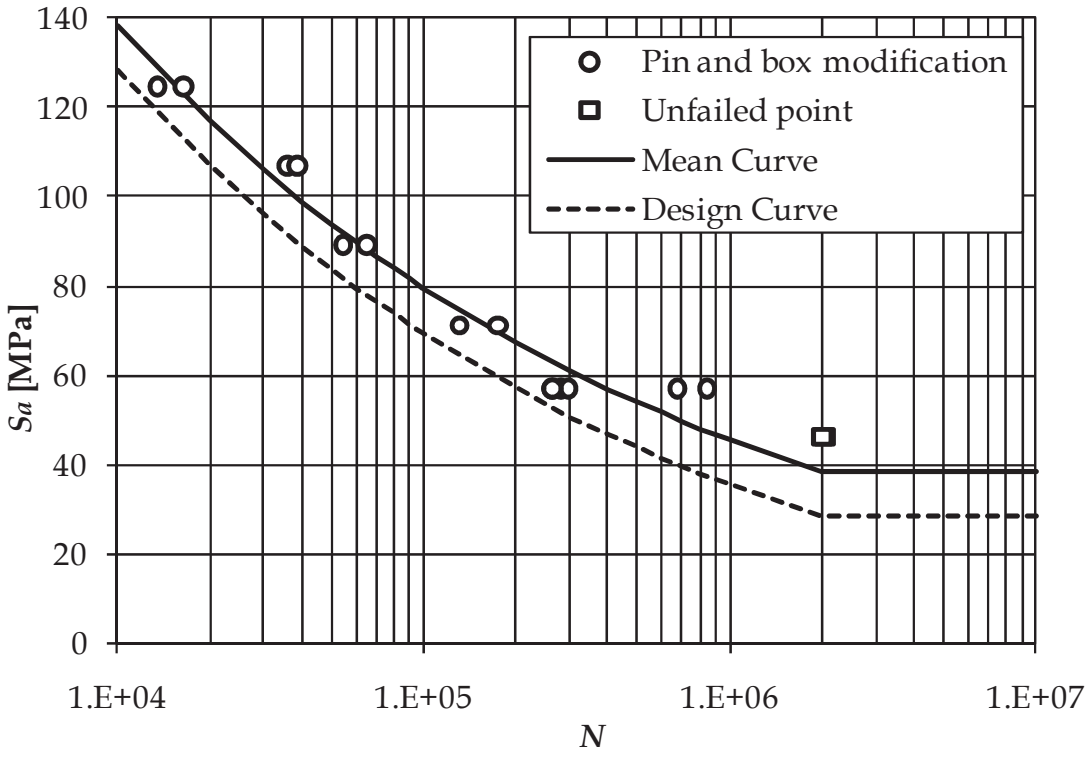

Figure 5.42: S-N curve for the 1″ API Line Pipe connection with pin and box modification (R = 0.1).

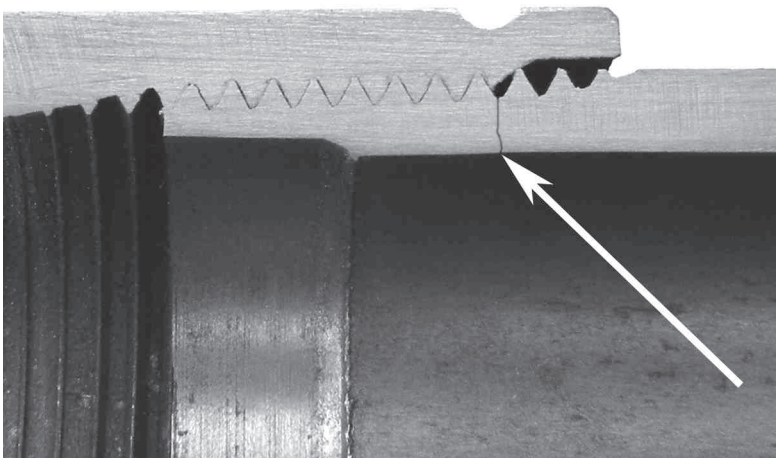

Figure 5.43: Fatigue crack initiated at the LET of the pin of the modified connection.

4.3.11 Small scale test result discussion

4.3.11.1 Comparison of the S-N curves

In Table 5.6 the results of the small scale four-point bending tests are summarized. The respective relations of the mean S-N curves are given. In Figure 5.44 a comparison is made between the API Line Pipe and BSPT configurations. It can be seen that the standard API Line Pipe has the worst fatigue properties since the other S-N curves are laying above the standard API Line Pipe curve. Hence, it is experimentally shown that geometrical changes of a threaded connection, without altering the thread shape itself, can affect the connection's fatigue life. Consequently, the idea introduced in section 3.2.2 of Chapter 2 that a connection's stiffness change can improve its fatigue life is hereby confirmed. Also the BSPT samples, that have a rounded thread shape, show a better fatigue life than the standard API Line Pipe connection.

The connection with the best fatigue behaviour is the thick-walled pin configuration. The configuration with the pin and box modification (shown in Figure 5.43) is manufactured from the same thick-walled pin. Although it has an improved load distribution (this will be shown in Chapter 8) it does not exhibit better fatigue properties compared to the thick-walled configuration.

Connection type	S-N relation	*STD* [MPa]	Number of tests
Standard API Line Pipe	$S_a = 848.7 \cdot N^{-0.2233}$	5.14	15
Standard BSPT	$S_a = 811.8 \cdot N^{-0.2075}$	10.4	8
API Line Pipe + PTFE	$S_a = 597.2 \cdot N^{-0.1866}$	5.74	14
Box wall -1 mm	$S_a = 970.8 \cdot N^{-0.2256}$	4.47	13
Box wall -2 mm	$S_a = 711.2 \cdot N^{-0.2042}$	4.93	14
Box recess -5 mm	$S_a = 562.1 \cdot N^{-0.1807}$	3.34	11
Thick-walled pin	$S_a = 888.3 \cdot N^{-0.2040}$	3.50	13
Pin and box modification	$S_a = 1278 \cdot N^{-0.2413}$	5.08	16

Table 5.6: Summary of the performed small scale four-point bending tests.

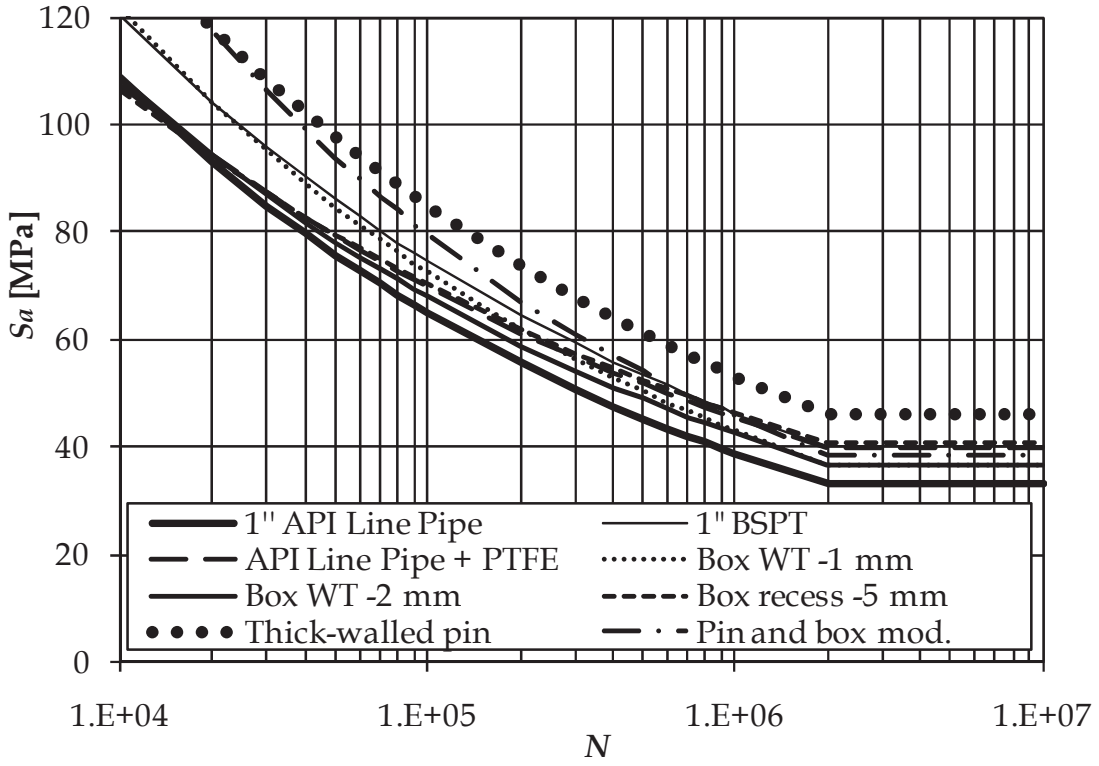

Figure 5.44: Comparison of the mean S-N curves of all experiments carried out on the small scale four-point bending setup.

Worth nothing is the beneficial effect of the PTFE on the fatigue life of the API Line Pipe connection. This corresponds with the observations of Majzoobi et al. [5.18]. During their fatigue tests on different bolt-nut combinations, they clearly showed the beneficial effect of PTFE tape. They showed that the exact influence is dependent of the used nut type. For standard metric nuts the effect is more important in the high-cycle fatigue region. The differences are explained by the observation that the PTFE tape can be eroded due to small sliding of the engaged threads. Hence, when this sliding appears, the beneficial effect of the PTFE tape is destroyed. This corresponds to the observed behaviour of the threaded pipe connections. At high applied loads, the PTFE tape does not improve the fatigue life, while at low stress amplitudes, a beneficial effect can be seen.

A detailed analysis of the presented fatigue data is made in Chapter 8 by comparing the experimental results to standard design curves and using the results of the finite element model described in Chapter 6.

4.3.11.2 Crack growth behaviour

Using the crack depth increase values *da/dN* given in Table 5.5-6 an estimation can be made of the contribution of the crack propagation life N_p to the total fatigue life N. For the three samples that are investigated using SEM, the applied stress amplitude, resulting fatigue life and the crack depth are given in Table 5.7. Additionally the mean value of the crack depth increase *da/dN* is calculated with the crack depth increase at initiation measured at the

thread root (location 1 in Figure 5.33 and Figure 5.37) and at the end of propagation measured at the boundary between the fatigue fracture and brittle fracture region (location 3).

The tabulated crack propagation lives are calculated by dividing the crack depth by the mean crack depth increase value. The total fatigue life N is considered to be the sum of both the initiation life N_i and propagation life N_p as in Eq. (5.26), hence N_i can also be determined.

$$N = N_i + N_p \tag{5.26}$$

Given the facts that this analysis is subjected to a certain amount of scatter (e.g. the difference in total fatigue life of the two discussed connections with PTFE tape) and that determination of the *da/dN* values is based on microscopic measurements, following conclusions can be made: from the results in Table 5.7 it can be seen that the mean *da/dN* value is larger when the total fatigue life is shorter. Since the total crack depth is constant within the tolerances of the connection, this results also in a shorter crack propagation life. Nevertheless, the contribution of the crack propagation life relative to the total connection's life is more important in case of lower values of N. When the total fatigue life is 253 836 cycles, the crack propagation life takes less than 2 % of the total life, while when $N = 19\,663$ the crack propagation phase takes 17 % of the fatigue life. These results are comparable to the values of 15 % and less for the ratio of crack propagation life to total life found in literature as previously mentioned in section 4.6.2 of Chapter 2.

Connection type	API Line Pipe + PTFE	API Line Pipe + PTFE	Box wall -1 mm
Stress amplitude S_a [MPa]	90	90	60
Total fatigue life N	19 663	35 220	253 836
Crack depth [mm]	1.835	1.889	1.812
Mean value of *da/dN* [μm]	0.55	0.50	0.44
Crack propagation life N_p	3336	3778	4118
Crack initiation life N_i	16 327	31 442	249 718
N_p/N	0.170	0.107	0.016

Table 5.7: Crack propagation data.

4.4 Medium scale four-point bending tests

4.4.1 Setup description

The medium scale four-point bending test rig is schematically shown in Figure 5.45. In this setup, the test specimen consists of two pipes (1b) with

threaded ends, connected by the threaded box (1a). The test specimen is carried by two supports positioned 3 m apart on a central rigid frame. A vertical force is applied by the hydraulic cylinder (2) and its magnitude is measured by the loadcell (3). The ball joint (4) connects the loadcell to a transverse beam that transmits the load to two points spaced 1 m apart on the test specimen. The working principles of this setup are similar to those of the small scale four-point bending setup described in section 4.3 and the introduced bending stress in the test specimen can be calculated according to Eq. (5.15-16). The tests are performed at a load ratio of $R = 0.1$ and at a frequency of 2 Hz.

Since fatigue cracks generally initiate at the last engaged thread of the pin the LVDTs (5) are mounted at either side of the coupling. These measure the axial distance between the edge of the coupling and a point on the pin's pipe body close to the coupling, so that the crack opening can be monitored when a fatigue crack is propagating. The used LVDTs have a resolution of 1 μm.

During crack propagation, the bending stiffness of the pipe is reduced and consequently the pipe deflection increases. To measure this deflection, reflective optical markers (6) are attached over the length of the test specimen. The displacement of these points is measured by the dynamic 3D optical displacement measuring device described in Chapter 3.

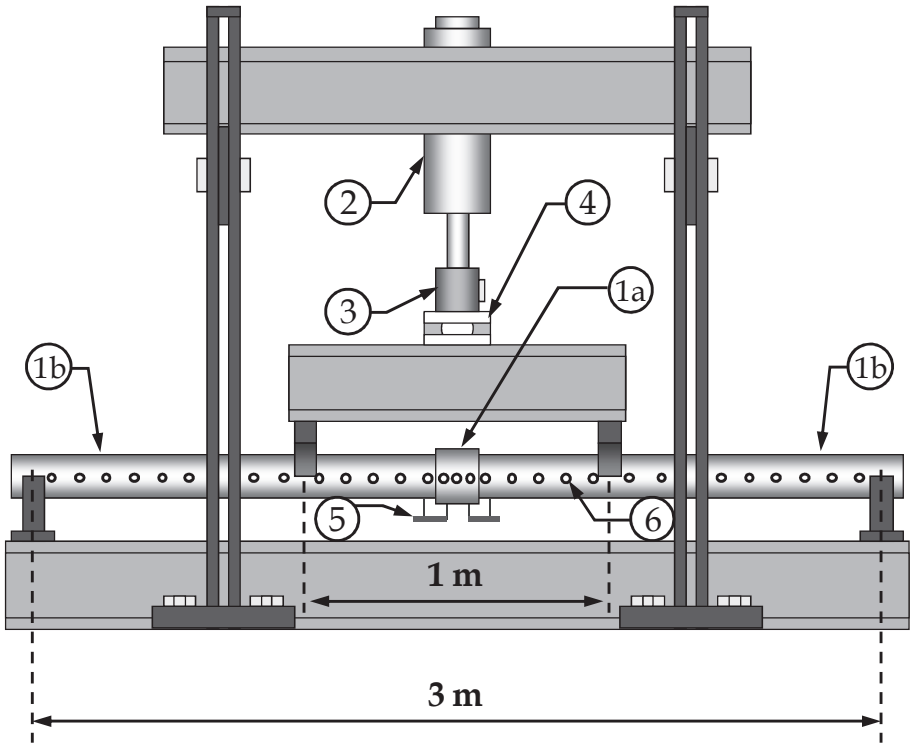

Figure 5.45: Medium scale four-point bending setup for 4.5″ connections.

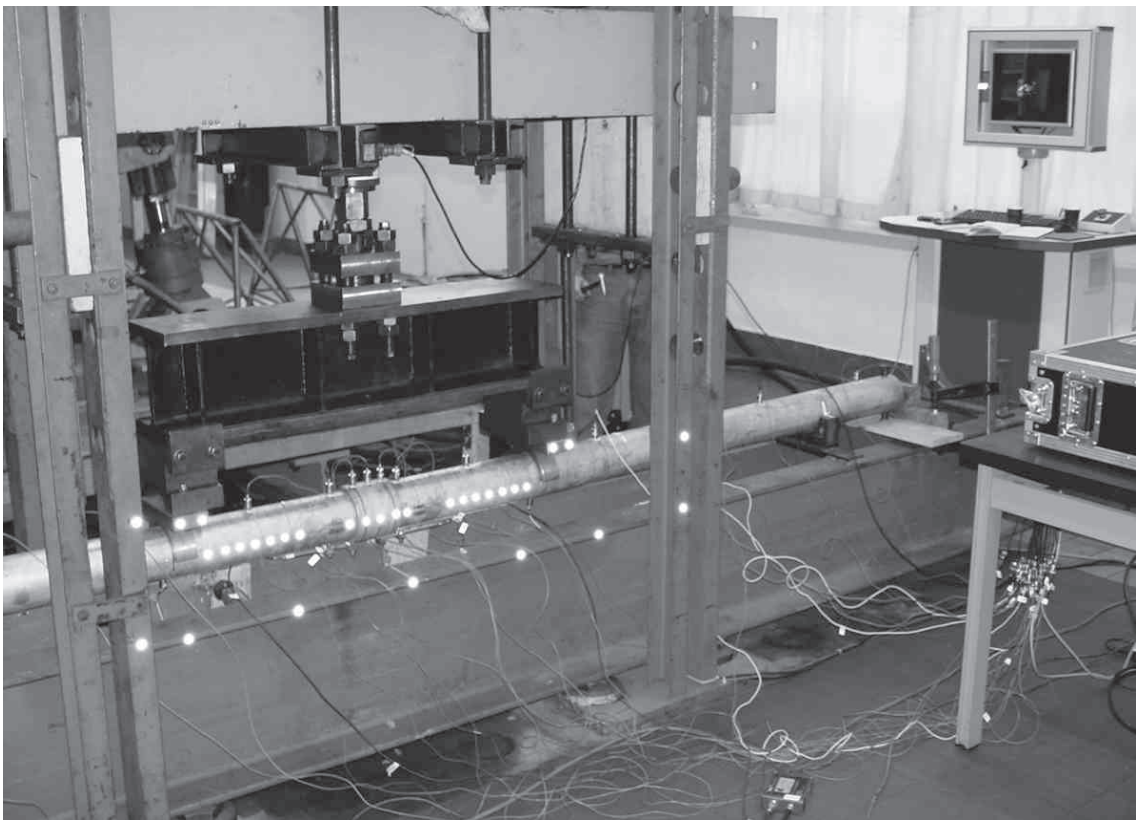

Figure 5.46: 4.5″ API Line Pipe connection with data acquisition for modal analysis and optical measurements.

Additional modal analysis measurements are carried out during the test. This is done by the use of 20 accelerometers along the length of the test specimen. A global view of the test setup can be seen in Figure 5.46, showing the optical measurement markers as clear points and the test specimen with the accelerometers attached.

4.4.2 Test overview

Four tests are carried out on standard 4.5″ API Line Pipe specimens. The applied stress amplitude S_a, the total number of applied cycles during the test N_{test} and the applied crack monitoring techniques are summarized in Table 5.8. The total number of applied load cycles during the test N_{test} should not be treated in the same way as the number of cycles to failure N as used during the small scale four-point bending tests since the medium scale tests are not stopped at the moment a through-wall thickness crack occurs as no leak detection is used. During all tests, LVDT measurements are carried out and beach marking cycles were applied. However, as described in Chapter 3, beach marking requires a certain amount of expertise and good results were only obtained during test 3 and 4. Optical measurements are carried out for tests 2 to 4 and modal analysis measurements in tests 2 and 4. No internal pressure is applied during the tests. In correspondence with the results of the small scale four-point bending results, all cracks initiated at the LET of the pin of the connection.

Test	S_a [MPa]	N_{test}	Crack measurements
1	75.0	20 350	LVDT
2	76.5	12 650	LVDT, optical, modal analysis
3	76.5	24 700	LVDT, optical, beach marking
4	69.8	30 166	LVDT, optical, modal analysis, beach marking

Table 5.8: Overview of the medium scale four-point bending tests on API Line Pipe specimens.

In the following sections, first the crack shapes marked by the beach mark lines are presented to illustrate the crack growth behaviour. Afterwards, the different measurements are related to the crack shapes. An additional quantitative analysis of the crack propagation data will be provided in Chapter 8.

4.4.3 Beach mark lines

4.4.3.1 Beach marking specifications

As mentioned in section 2.2.7 of Chapter 3, the load ratio used and number of beach marking cycles applied is important to obtain clear beach mark lines without affecting the crack propagation. In Table 5.9 an overview is given of tests found in literature where the beach marking technique has been applied. In the table an overview is given of the applicable load ratios during the test and the beach marking blocks as well as the applied number of cycles of the test and beach marking blocks.

Application	R_{test}	R_{beach}	N_{test}	N_{beach}	Source
Drill pipe thread	0.02	0.58	NN	NN	Brennan [5.19]
Cube with edge crack	0.1	0.65 to 0.9	NN	6000 – 110 000	Liu and Bowen [5.20]
Plate surface crack	0.1	0.64	3000 – 40 000	2500 – 20 000	Raghava et al. [5.21]
Cylinder surface crack	0.1	0.73	NN	NN	Cai and Shin [5.22]
Welded structure	0.1	0.53	40 000	100 000	Lihavainen [5.23]

Table 5.9: Overview of typical beach marking parameters (symbols according to Figure 3.12).

In this study, beach marking cycles are applied at a load ratio of $R = 0.85$ in groups of 1000 or 2000 cycles. The resulting beach marks are fine lines, consequently the number of applied beach mark cycles is excluded from the number of load cycles N.

4.4.3.2 Test 3

The fracture surface of test 3 is shown in Figure 5.47.a. The crack initiated at the root of the LET of the pin at the right hand side of the test specimen. At three moments during the test beach marking cycles were applied: after 22 000, 24 000 and 24 250 cycles. The test was terminated after 24 700 cycles. During the beach marking cycles, the load ratio is increased from $R = 0.1$ to 0.85. At 22 000 cycles, 1000 beach marking cycles are applied, during the two subsequent beach marking periods, 2000 beach marking cycles are applied. The resulting beach marking lines can be clearly distinguished. A magnified view of the zones in the four rectangles is given in Figure 5.48. It can be seen that the beach marking process creates a fine line in the fracture surface.

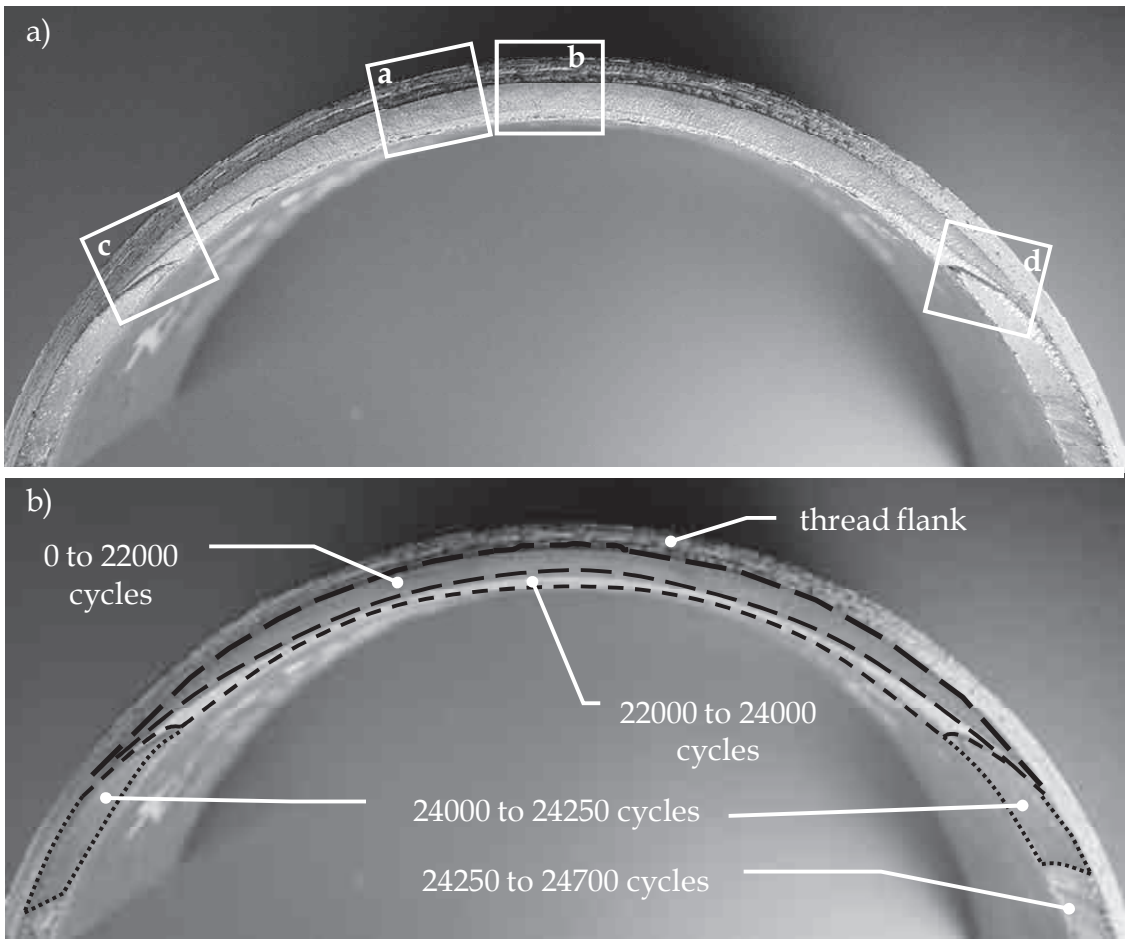

Figure 5.47: a) Fracture surface of test 3, zones in rectangles are magnified in Figure 5.48; b) highlighted zones divided by the beach mark lines.

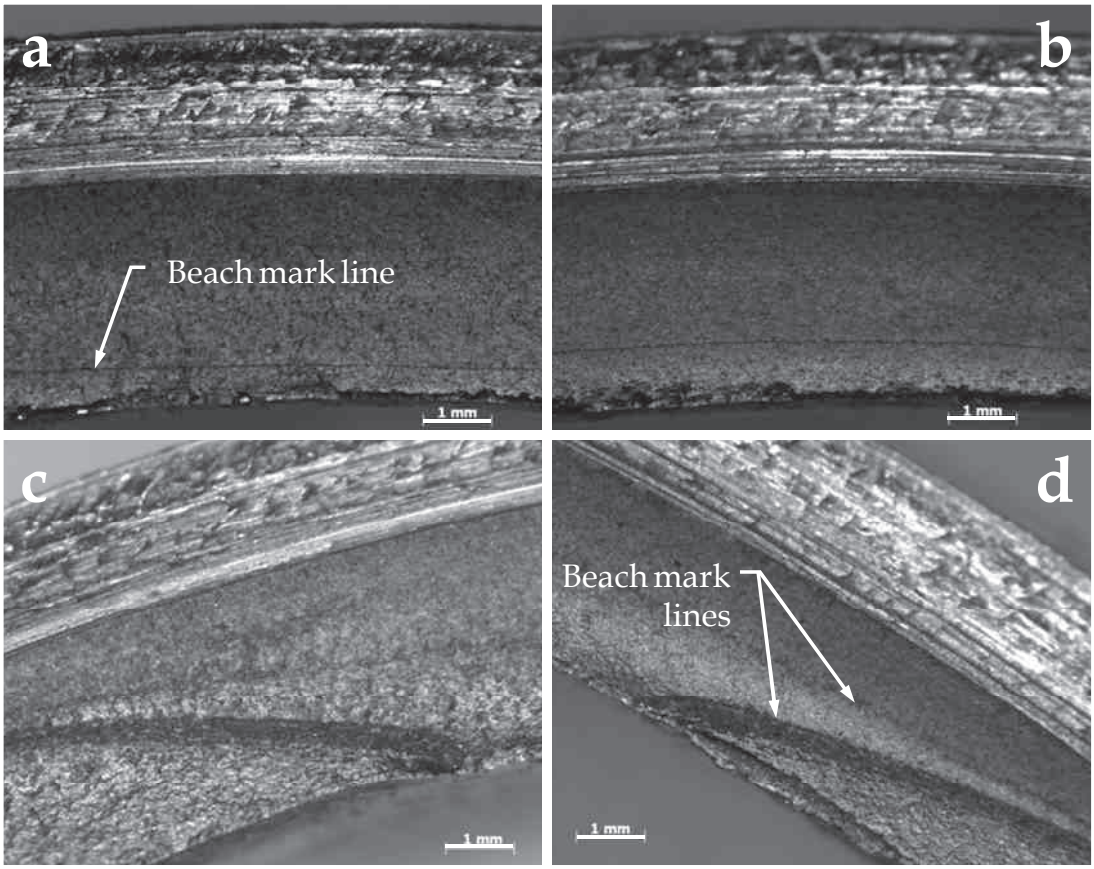

Figure 5.48: Detailed view of the fracture surface with beach mark lines, as indicated in Figure 5.48.

In Figure 5.47.b, the different zones of the fracture surface are highlighted. It can be seen that the crack initiated along the thread root and propagated over a large segment of the circumference between 0 and 22 000 load cycles without creating a through wall thickness crack. During the subsequent 2000 load cycles the crack penetrates the pipe wall, while its increase along the pipe circumference is only limited.

Since the occurrence of a through-wall crack is used as the failure criterion in this research, it can be seen from the first two beach mark lines that the fatigue life N of this specimen is between 22 000 and 24 000 cycles.

After the pipe wall has been breached, the crack propagates rapidly over two different crack fronts as can be seen from the crack zone between 24 000 and 24 250 cycles. During the subsequent cycles the crack growth becomes more and more unstable and the test is finally terminated at 24 700 cycles.

4.4.3.3 Test 4

During test 4, beach marking is applied four times: after 24 000, 26 000, 28 000 and 28 500 cycles, using a load ratio of $R = 0.85$ for 2000 cycles. The test is terminated after $N_{test} = 30\,166$ cycles. Now the beach marking cycles are applied to mark the shape of the fracture surface at certain times before penetrating the pipe wall. The resulting fracture surface of the crack that

occured at the root of the LET of the pin at the left hand side of the specimen is shown in Figure 5.49. With these views the fatigue propagation behaviour, as seen in all previously described small and medium scale tests, is confirmed and the exact crack growth behaviour becomes more clear.

From the highlighted zones in Figure 5.49.b it can be seen that after 24 000 cycles, when the crack depth is limited to about 1.1 mm, it has extended over a considerable length. Hence a long shallow crack is present in the root of the LET of the pin. It continues to propagate in the circumferential direction while only gradually increasing the crack depth. When the total crack length is about one quarter of the entire circumference, the crack fully penetrates the pipe wall and will continue to grow over the two created crack fronts.

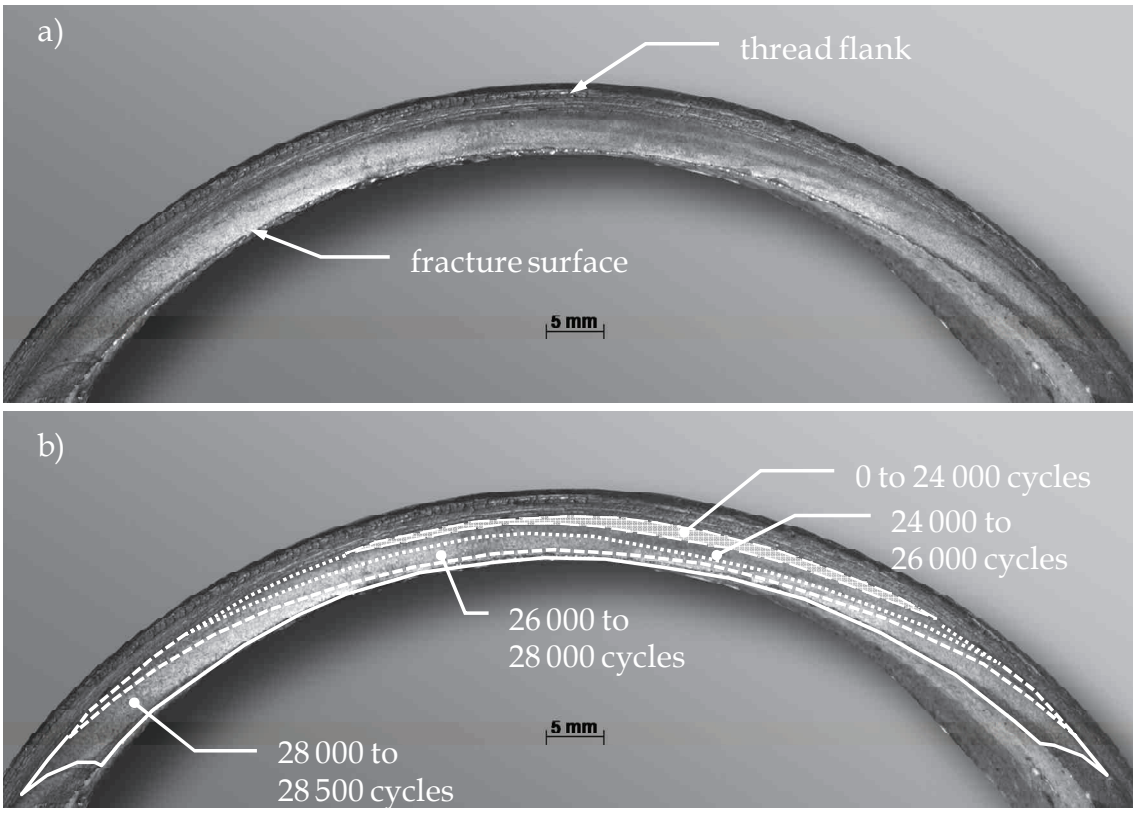

Figure 5.49: a) Fracture surface of test 4; b) zones divided by the beach marks.

4.4.4 Crack opening data

The crack opening measured at the side of the coupling where the crack occured is plotted for tests 3 and 4 respectively in Figure 5.50 and Figure 5.51. The vertical dashed lines in the plot of test 3 in Figure 5.50 indicate the locations where the beach mark cycles were applied at 22 000 and 24 000 cycles. During the interval in between those two lines, the crack penetrates the pipe wall. In Figure 5.51 the dashed lines indicate the beach mark cycles performed at 24 000 and 28 000 cycles during test 4. At 24 000 cycles, the fracture surface in Figure 5.49.b shows a crack with a considerable length, however the measured crack opening at this time is only 0.023 mm. It can be seen that there is no crack opening during the first 21 000 cycles, hence this is

considered to be the crack initiation life. In order to have an objective criterion to determine the number of crack initiation cycles N_i for the other tests, the crack is considered to be initiated when a crack opening value of 0.01 mm is exceeded. This way a crack initiation life of N_i = 21 363 cycles is determined for test 4.

Additionally it is known from the fracture surface of test 4 that the crack penetrated the wall thickness between 28 000 and 28 500 cycles. This is considered to be the point of failure of the connection. It can be seen in Figure 5.51 that after the penetration, the crack opening starts to increase asymptotically. Since the exact moment of penetration N can not be determined, it is assumed that this event took place in the middle of the interval between 28 000 and 28 500 cycles. The corresponding crack opening at N = 28 250 cycles is 0.10 mm.

In order to determine the crack initiation life N_i and the number of cycles to failure N for the other performed tests, the respective number of cycles is used for a crack opening value of 0.01 mm to determine N_i and a crack opening value of 0.10 mm is used to determine N. Using this criterion N = 23 500 cycles for test 3, which lays inside the specified interval as described earlier. The number of crack propagation cycles N_p for the crack to propagate through the pipe wall is determined by Eq. (5.26). The resulting values for the four tests are summarized in Table 5.10. It should be noted that during test 1 an LVDT is used with an accuracy of 0.05 mm, hence the crack initiation and propagation lives could not be obtained for this test.

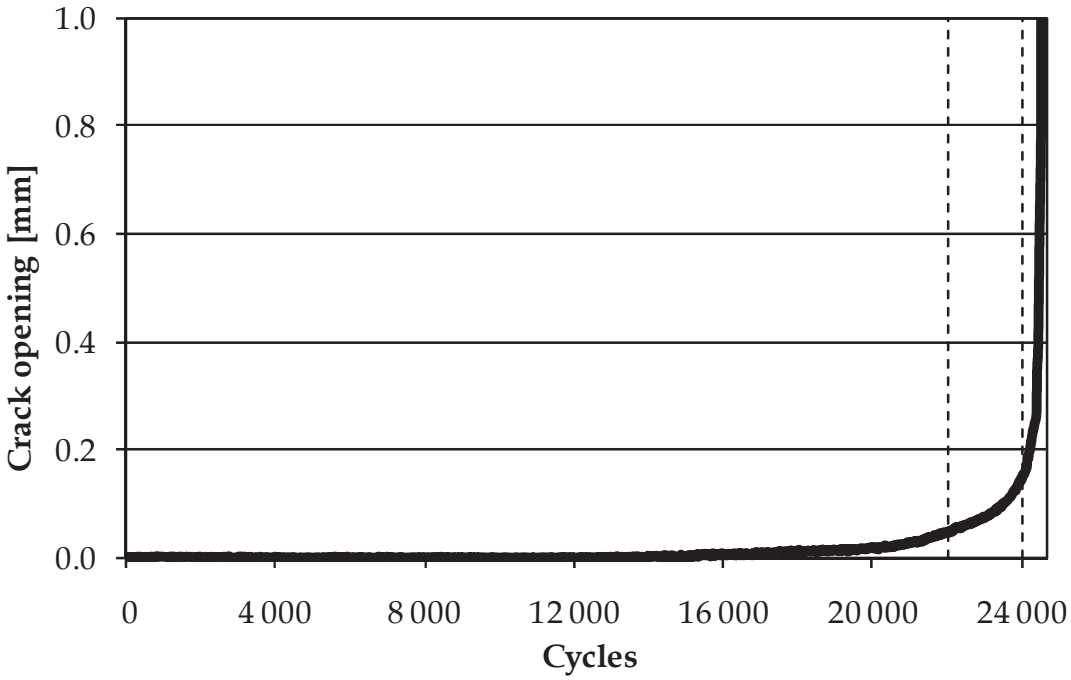

Figure 5.50: Crack opening measured at the right hand side of the coupling during test 3.

Test	N_i	N_p	N	N_p/N	N_{test}
1	na	na	18 650	na	20 350
2	10 025	1509	11 534	0.13	12 650
3	17 720	5780	23 500	0.25	24 700
4	21 363	6887	28 250	0.24	30 166

Table 5.10: Fatigue lives of the 4.5″ API Line Pipe specimens.

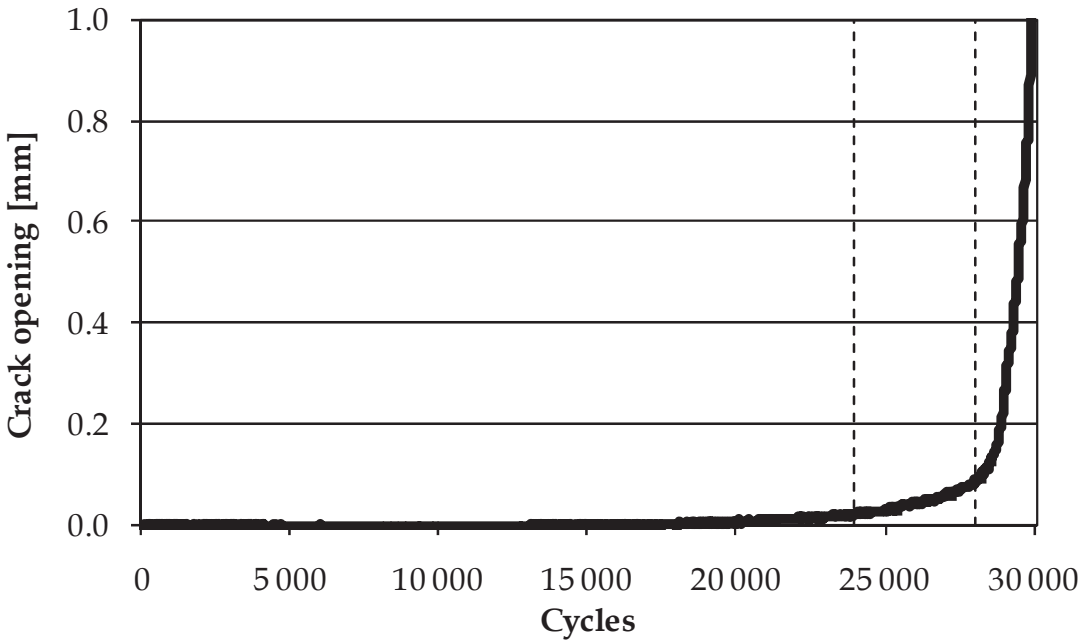

Figure 5.51: Crack opening measured at the left hand side of the coupling during test 4.

4.4.5 Pipe deflection measurements

The dynamic 3D optical displacement measurement system as described in section 2.3.2 of Chapter 3 is used to monitor changes in the pipe deflection as a result of a propagating crack. This is done by capturing 40 images at a frequency of 40 Hz at discrete moments during the test. This means that during each measurement, 2 full load cycles are measured. During the post processing of the data, the maximum displacement of the central marker on the box of each series of 40 images is selected as the pipe deflection. The measured deflection of the attached markers are represented by the vector arrows in Figure 5.52.

In Figure 5.53 the results of test 3 are shown. During this test the optical markers were attached between the two inner load points of the setup and a measurement is carried out every 500 cycles. Three markers are attached to the coupling.

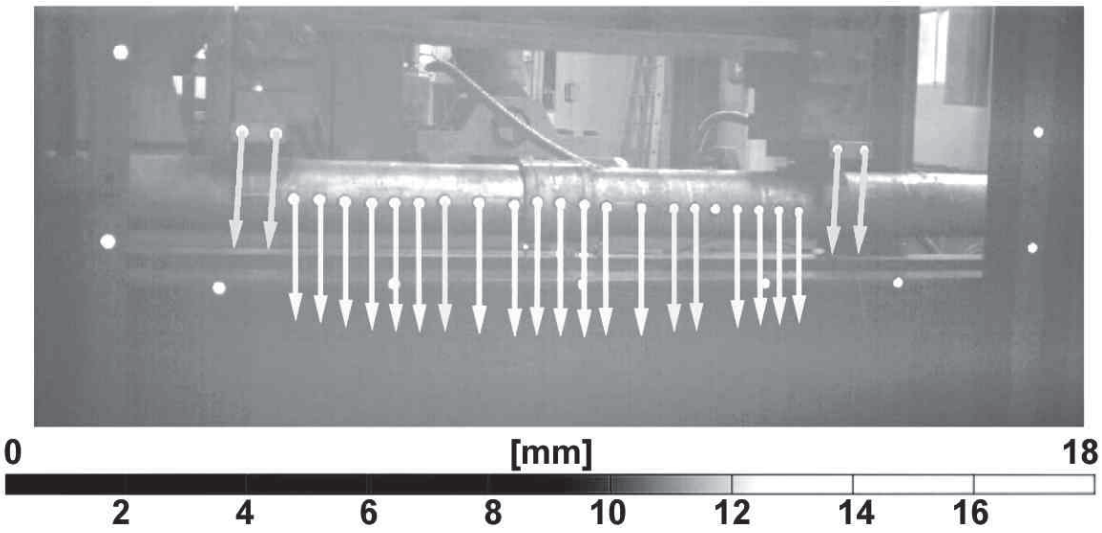

Figure 5.52: Optical displacement measurement.

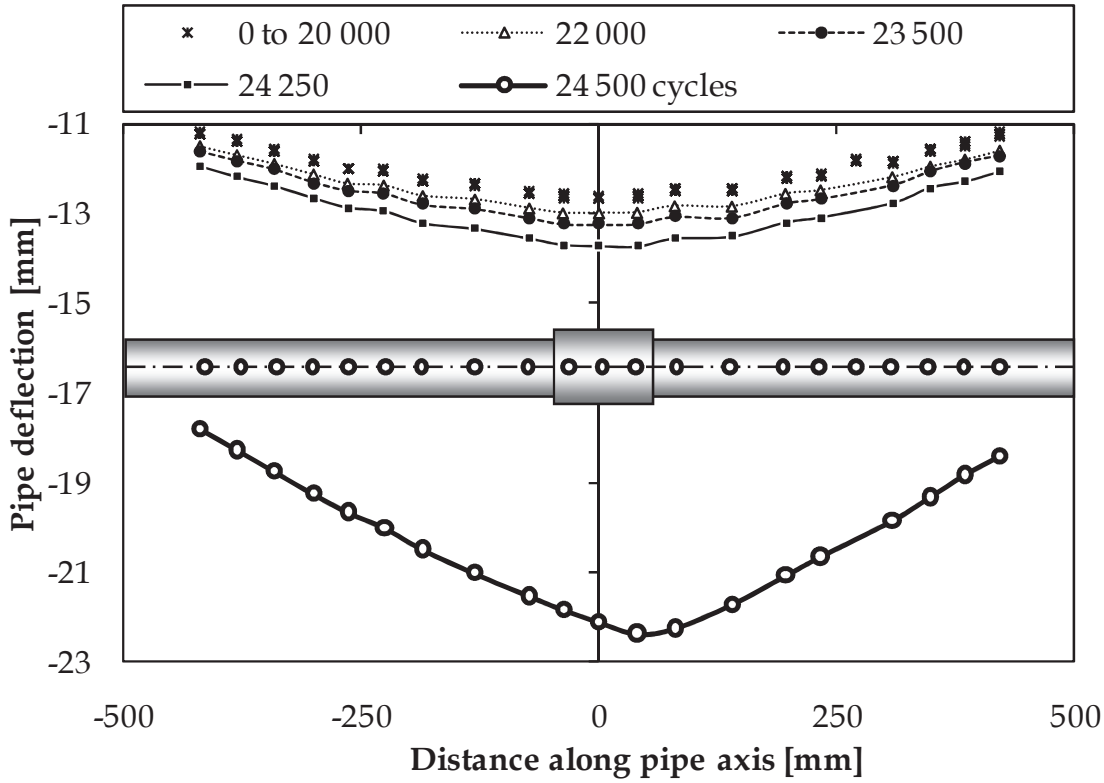

Figure 5.53: Pipe deflection during test 3.

From Figure 5.53 it can be seen that during the first 20 000 cycles no change in deflection is detected although it is known from the crack opening measurements that the crack initiated after 17 720 cycles. Nevertheless, it can be seen that after 23 500 cycles, when the crack penetrates the wall, the pipe deflection starts increasing very rapidly. From the last measurement at 24 500 cycles it is clear that the crack is propagating at the right hand side of the coupling since the deflection becomes asymmetrical and the pipes deformation shape yields to the right.

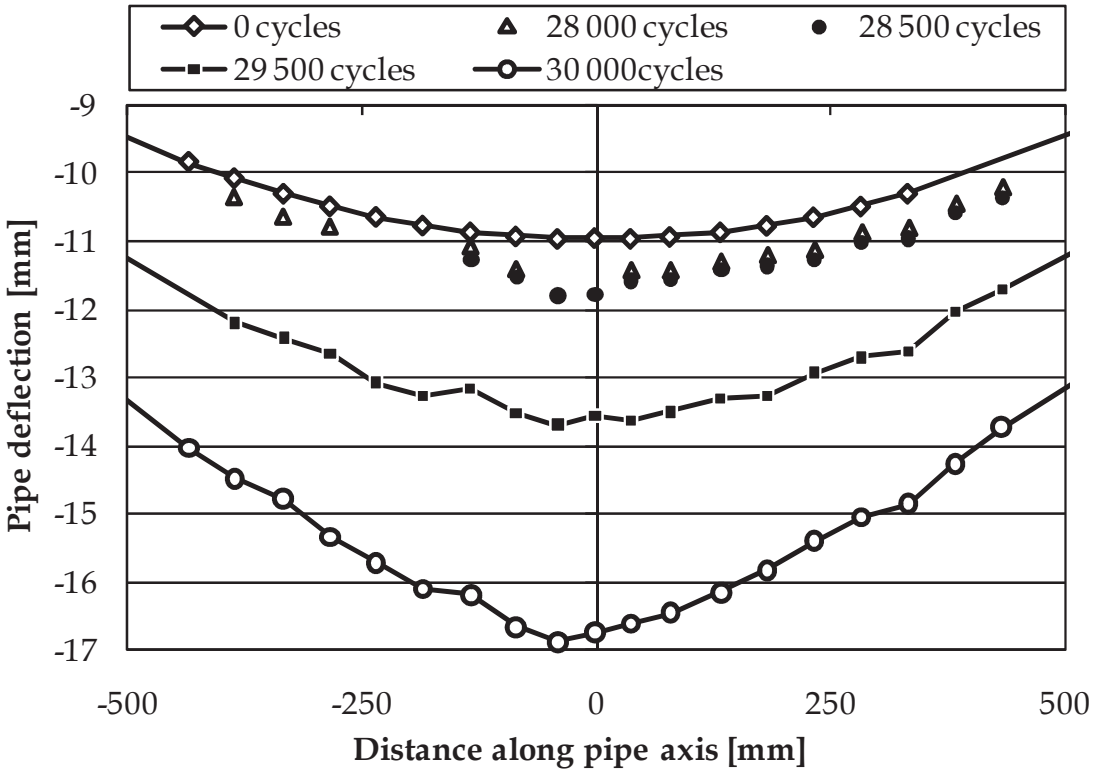

Figure 5.54: Pipe deflection during test 4.

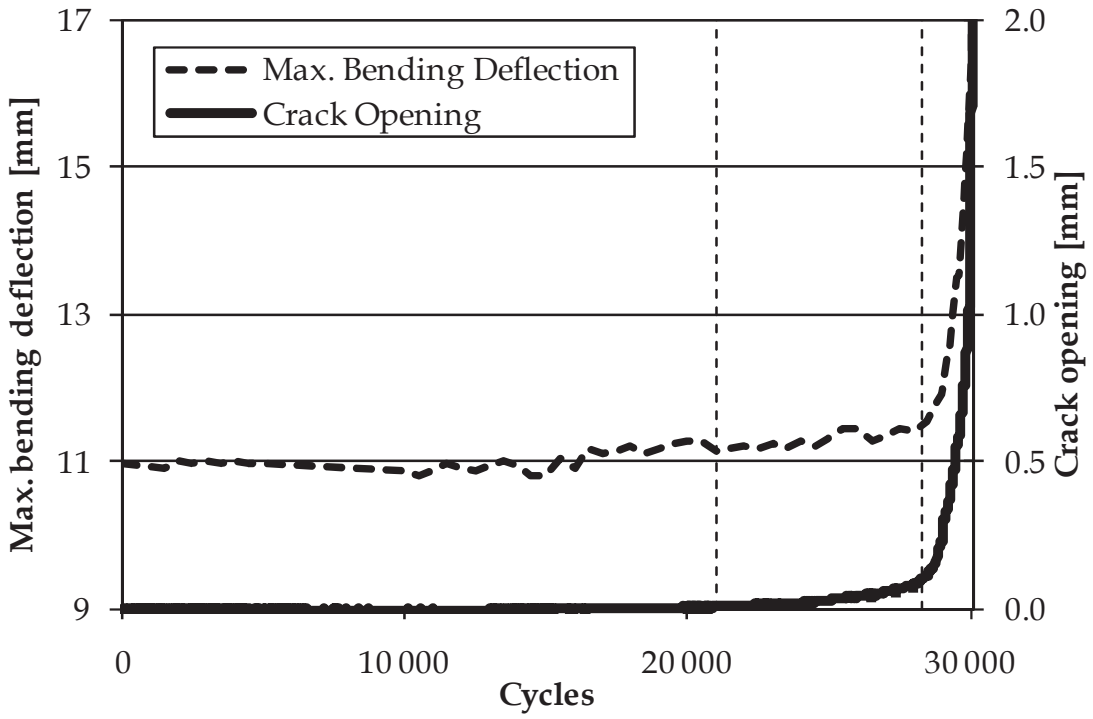

Figure 5.55: Measured bending deflection and crack opening during test 4.

The results obtained during test 4 are similar. As can be seen from Figure 5.54, the pipe deflection starts to change only after 28 000 cycles when the crack has penetrated the pipe wall. During this test the crack propagated at the left hand side of the connection which can be clearly seen by the

asymmetrical shape of the bending deflection at 30 000 cycles. Again the three central markers are attached to the coupling. In Figure 5.55 the deflection of the central point on the box (position $x = 0$) is compared to the corresponding crack opening data. The two dashed vertical lines mark the position of the crack initiation and crack propagation. It can be seen that both signals show a similar behaviour. However, since the accuracy of the optical measurements is less than the crack opening measurement, only the number of cycles to failure can be accurately detected by the optical measurements.

4.4.6 Modal analysis

As indicated in Table 5.8, modal testing measurements are carried out during test 2 and test 4. These measurements are performed using accelerometers mounted along the length of the specimen before, during and after the respective fatigue tests. Before and after the test, classical modal analysis measurements are performed on the unloaded test specimen in a simply supported configuration, only carried by the two outer supports in Figure 5.45 without contact of the transverse beam with the inner load points. In this configuration the pipe is excited by an impact hammer.

During the fatigue test, OMA measurements are carried out after every 1000 cycles. During these measurements the pipe is supported in the four load points. Additionally, the impact hammer is used during the running test for OMAX measurements at specific intervals. The measured input for both the classical modal test and the OMAX measurements is the impulse loading from a load cell that is fixed at the impact hammer head. As output the acceleration spectrum of each accelerometer is measured.

4.4.6.1 Test 2

The first three bending modes identified in the two-support configuration using classical modal analysis are shown in Figure 5.56-59. The modes are expressed as *mass normalized displacements*[2], as is common practice in modal analysis. Both the initial mode shape before the test and the mode shape of the damaged specimen after the test are shown. The location of the two supports are symbolically illustrated by the triangles. Furthermore, the corresponding eigenfrequencies are given in Table 5.11.

It is clear that the eigenfrequencies and mode shapes of the first and third mode change significantly after the specimen is damaged. No significant

---

[2] In modal analysis the displacements are generally normalized, as their absolute values are dependent on the applied excitation force. Normalizing to the mass matrix means that that the generalized mass $u^T \cdot M \cdot u$ is unity. With u the displacement matrix and M the system's mass matrix. This approach gives a better resolution when monitoring stiffness changes than when the maximum displacement is used for the normalization.

change is observed for the second mode. This is logical as mode 2 is the first in-plane asymmetric mode, which has an eigenmode node near the midpoint of the specimen, which is the region where the damage occurs. Mode shapes 1 and 3 of the damaged specimen also show a sudden change in curvature at the centre, indicating severe damage in the connection. In addition it can be noticed that mode shapes 1 and 3 have shifted to the left which is an indication that the damage is concentrated at the left side of the coupling. This corresponds to the visual observation of the crack location and the optical deflection and LVDT measurements.

By analyzing the OMA measurements performed during the test in the four-support configuration, the first bending mode is identified as illustrated in Figure 5.59. The initial eigenfrequency of this bending mode is 260.2 Hz. The reduction of this eigenfrequency during the test is illustrated in Figure 5.60. It can be seen that the eigenfrequency is reduced marginally during the first 10 000 cycles and starts to decrease more importantly after this time.

Eigenfrequency	f_1 **[Hz]**	f_2 **[Hz]**	f_3 **[Hz]**
Initial	37.5	135.1	249.1
Damaged	32.4	132.0	222.5

Table 5.11: First eigenfrequencies of the simply supported specimen of test 2.

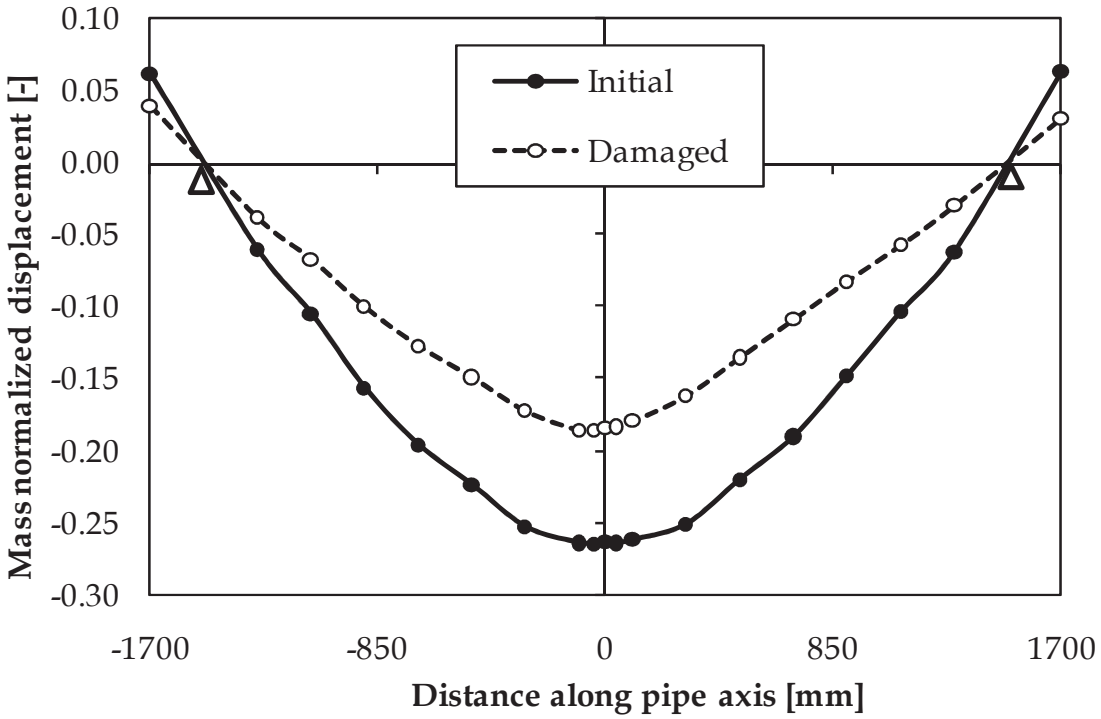

Figure 5.56: First eigenmode before and after test 2.

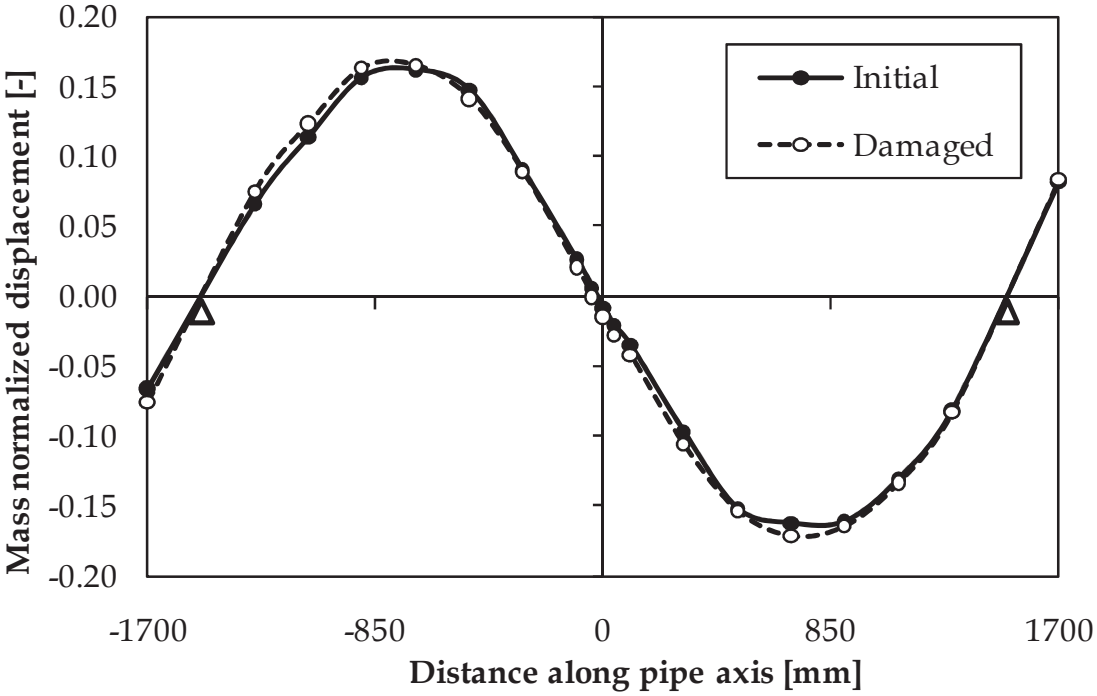

Figure 5.57: Second eigenmode before and after test 2.

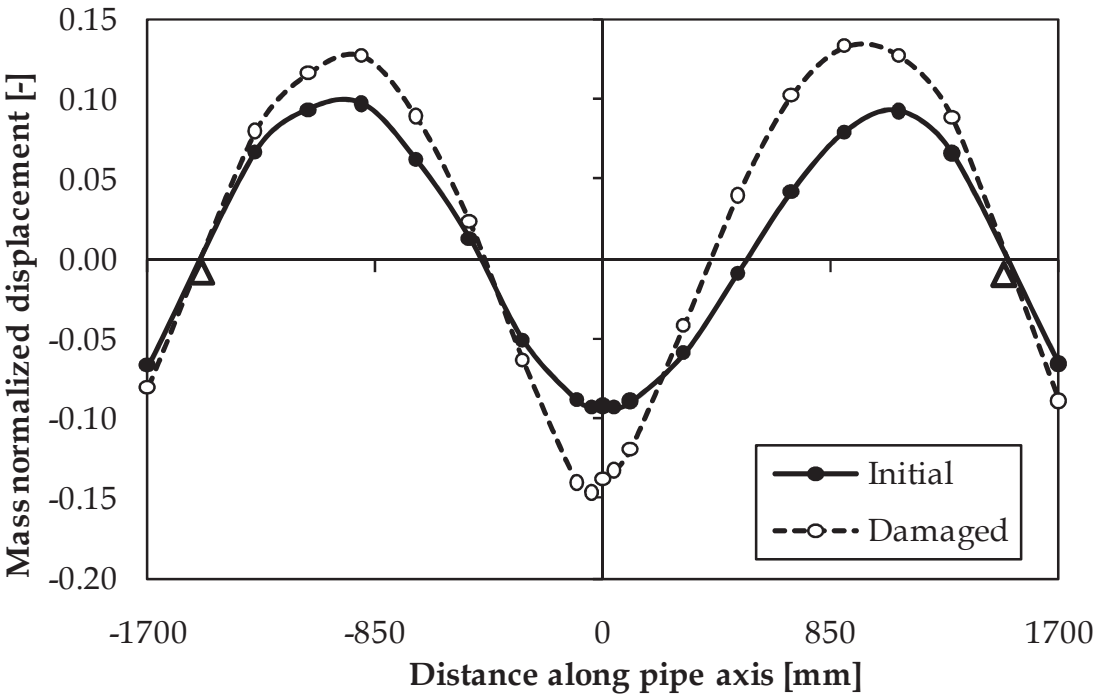

Figure 5.58: Third eigenmode before and after test 2.

It is noted that this moment roughly corresponds to the initiation life in Table 5.10. However, the exact time at which the frequency starts to reduce significantly, can not be easily distinguished.

At two times during the test OMAX measurements are carried out. It can be seen in Figure 5.60 that the results from these measurements correspond very well with the OMA data, demonstrating the validity of the OMAX technique.

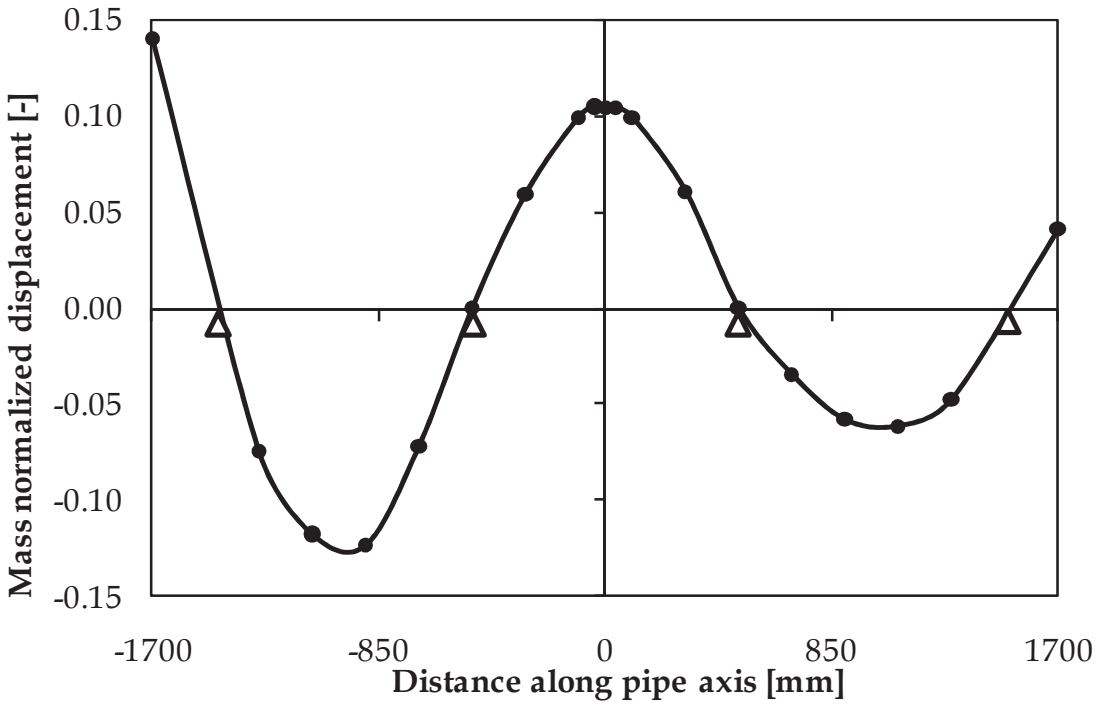

Figure 5.59: First bending mode in the four-support configuration during test 2.

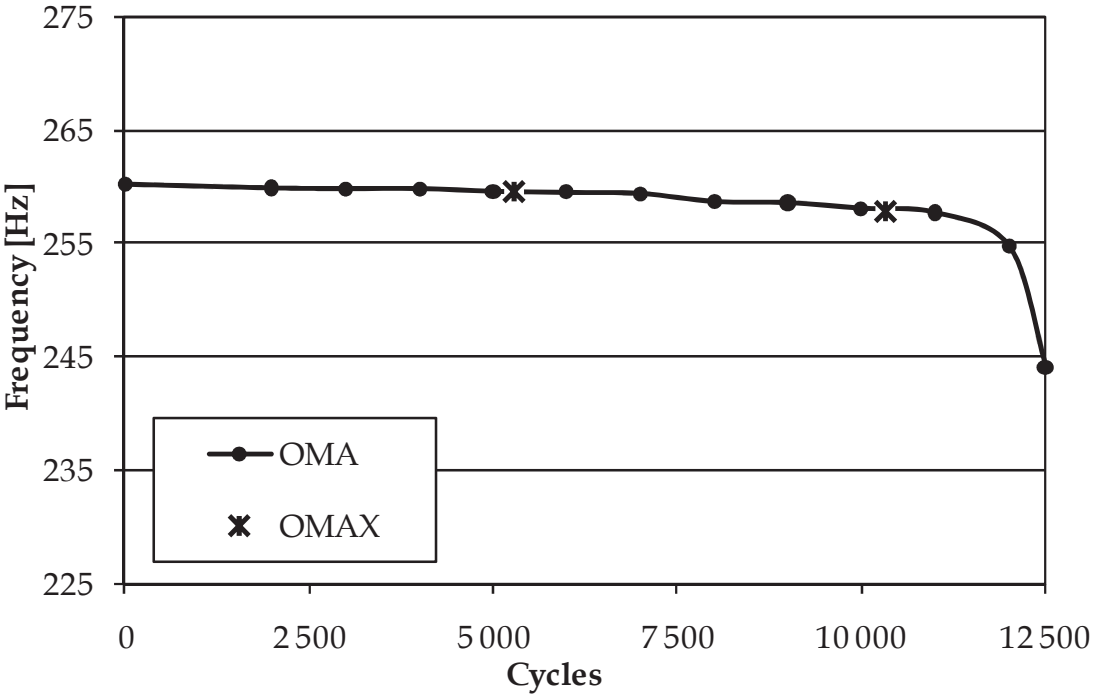

Figure 5.60: Operational modal analysis measurement data of test 2.

4.4.6.2 Test 4

The modal analysis measurements during test 4 are performed in a similar way as in test 2. The eigenfrequencies obtained by classical modal analysis before the test in the two-support configuration show similar values as the specimen of test 2 (35.9, 125.2 and 253.8 Hz).

The results of the OMA and OMAX measurements are shown in Figure 5.61; again a good correspondence can be observed between both operational modal analysis techniques. The initial bending mode has an eigenfrequency of 261.4 Hz, which is comparable to the corresponding initial value during test 2. A marginal frequency reduction takes place during the first 8000 cycles. This change might be caused by a running-in effect, such as small settlement in the supports. Between 8000 and 24 000 cycles, the eigenfrequency of the bending mode remains constant at 259.6 Hz. After 24 000 cycles, the frequency reduction becomes significant, indicating the presence of a fatigue crack. As shown earlier in Table 5.8, the crack initiation life is determined to be N_i = 21 363 cycles, based on the LVDT crack opening measurements. Hence the modal analysis technique detects the presence of the fatigue crack slightly later than the local crack opening measurement.

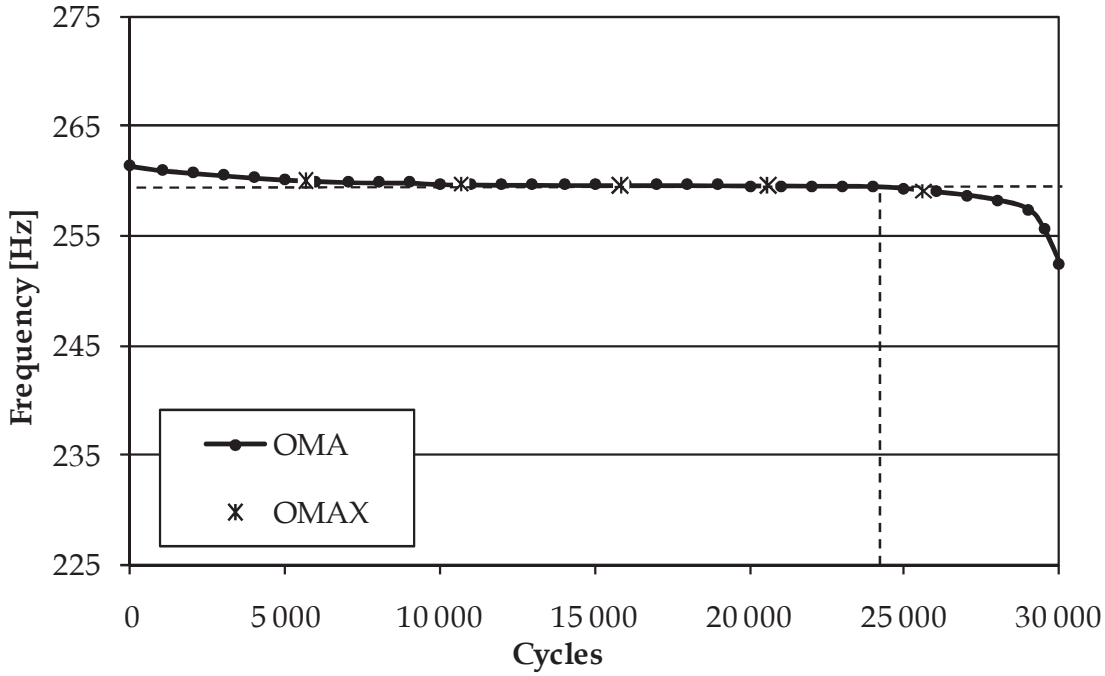

Figure 5.61: Operational modal analysis measurement data of test 4.

4.4.7 Comparison with the axial tension fatigue test results

Test 2 is carried out with a stress amplitude of S_a = 76.5 MPa at the highest stressed fibre, calculated using Eq. (5.16). Hence, the mean stress amplitude over the pipe wall at that location is equal to 72.5 MPa, which is the same value as the stress amplitude during the axial tension fatigue test. During the axial fatigue test, 10 712 load cycles were applied, Tests 2 was subjected to 12 650 cycles. It could be expected that the fatigue life during the axial tension fatigue test is slightly lower than the result of Test 2 in the four-point bending setup. As described in section 4.2.3 of Chapter 2, fatigue data obtained in different loading modes should be corrected with a loading mode factor k_a. It is common practice to use a factor of k_a = 0.9 as the ratio between the fatigue life under axial loading and under bending [5.24]. This is because

in axial tension, the entire circumference is subjected to the same stress level, while under bending, only the bottom fibre is subjected to the highest load.

5 Summary and conclusions

In this chapter the experimental work of this research is presented. Both static and fatigue experiments are carried out. The test rigs that are developed during this research to perform the experiments are outlined.

Using the results of static torque tests, the coefficient of friction of the contacting threads is determined. The obtained value will be used as input in the finite element model described in the next chapter. In addition, the strains measured during the static torque test, axial test and internal pressure test will be used as a validation for this finite element model. The strain values measured during the internal pressure test correspond very well with existing analytical methods.

In total 109 fatigue tests are carried out of which one axial tension fatigue test, 4 medium scale four-point bending tests and 104 small scale four-point bending tests. This amount of results provides a strong experimental basis for further analysis of different connection types. It is pointed out that the number of conducted experiments by far exceeds the number of tests during previous research on the fatigue of threaded pipe connections found in literature. As shown in section 5.2 of Chapter 2 the results of 175 fatigue tests on threaded pipe connections were found in literature, where the most extensive study presents the results of 31 tests. Hence, this study provides important additional experimental data.

The results of the small scale tests show that a local modification of the threaded connection's geometry or contact conditions can have an important influence on the total connection's fatigue life. As a consequence, the idea introduced in section 3.2.2 of Chapter 2 that a connection's stiffness change can improve its fatigue life is hereby confirmed. A more quantitative comparison of these results will be presented Chapter 8.

Several measurement techniques are used to detect fatigue damage during the performed tests. During the small scale tests, internal pressure is used to detect through-thickness cracks. During the medium scale tests, several techniques are used for the first time to detect fatigue damage in threaded connections. The applicability of crack opening measurements, dynamic 3D optical displacement measurements and modal analysis measurements is demonstrated. This way, the fatigue damage in the threaded pipe connections is monitored more accurately than possible until present. The measurements are used to distinguish between crack initiation and propagation and are confirmed by the beach mark lines that are observed in the fracture surface. The ratio of crack propagation life to total life corresponds well with values reported in literature.

Detailed analysis of the fracture surfaces shows that the fatigue cracks initiated at the root of the LET of the pin. This corresponds to documented failure cases and published results of laboratory tests. In addition this is the location where the highest stress concentration is reported to occur. After initiation, a crack propagates gradually over a large segment of the circumference, forming a long shallow crack. When the crack penetrates the wall of the pin, the crack rapidly increases in size along two crack fronts. The crack growth data will be additionally analysed in Chapter 8.

References

[5.1] API Specification 5B, Specification for Threading, Gauging and Thread Inspection of Casing, Tubing and Line Pipe Threads (U.S. Customary Units), American Petroleum Institute, fourteenth ed., 1996.

[5.2] ANSI/ASME B1.20.1-1983, Pipe Threads, General Purpose (Inch), 1983.

[5.3] API Specification 5L, Specification for Line Pipe, American Petroleum Institute, forty-second ed., 2000.

[5.4] DIN 17100, Steels for general structural purposes, as consulted on http://www.tubesolution.com/, retrieved 28/04/2011.

[5.5] EN 10226-1:2004:E, Pipe threads where pressure tight joints are made on the threads – Part 1: Taper external threads and parallel internal threads – Dimensions, tolerances and designation, European Committee for Standardization, 2004.

[5.6] Wawrziniok, O., Handbuch des Materialprüfungswesens, Julius Springer Verlag, Berlin, 1908.

[5.7] Vinson, J.R., Structural Mechanics: The Behaviour of Plates and Shells , John Wiley and Sons, New York, p. 119, 1974.

[5.8] API Bulletin 5C3, Bulletin on Formulas and Calculations for Casing, Tubing, Drill Pipe and Line Pipe Properties, American Petroleum Institute, fifth ed., 1989.

[5.9] Assanelli, A.P., Xu, Q., Benedetto, F., Johnson, D.H., Dvorkin, E.N., Numerical/experimental analysis of an API 8-round connection, Journal of Energy Resources Technology-Transactions of the ASME, 119(2), 81–88, 1997.

[5.10] Yuan, G., Yao, Z., Han, J., Wang, Q., Stress distribution of of oil tubing thread connection during make and break process, Engineering Failure Analysis, 11, 537-545, 2004.

[5.11] Shigley, J.E., Machine Design, Mc Graw-Hill Book Company, New York, pp. 466 (14-3 Press and shrink fits), 1956.

[5.12] Weiner, P.D., Sewel, F.D., New technology for improved tubular connection performance, Journal of Petroleum Engineering, 19(3), 337-343, 1967.

[5.13] Schneider, W.P., Casing and Tubing Connection Stresses, Journal of Petroleum Engineering, 34(8), 1851-1862, 1982.

[5.14] Clinedinst, W.O., Joint strength formulas for API threaded Line Pipe, API 5C3, Appendix 2029, PS Circular 1533, 1976.

[5.15] Clinedinst, W.O., Strength of threaded pipe joints for steel pipe, ASME Petroleum Division Conference, 1964.

[5.16] Venkatesan, S., Kinzel, G.L., Reduction of stress concentration in bolt-nut connectors, ASME Journal of Mechanical Design, 128, 1337-1342, 2006.

[5.17] BS7608:1993, Code of practice for Fatigue Design and Assessment of Steel Structures, British Standards Institution, 1999.

[5.18] Majzoobi, G.H., Farrahi, G.H., Hardy, S.J., Pipelzadeh, M.K., Habibi, N., Experimental results and finite-element predictions of the effect of nut geometry, washer and Teflon tape in the fatigue life of bolts, Fatigue and Facture of Engineering Materials, 28(6), 557-564, 2005.

[5.19] Brennan, F.P., Fatigue and Fracture Mechanics Analysis of Threaded Connections, PhD Thesis, Dept. of Mech. Eng. University College London, 1992.

[5.20] Liu, J., Bowen, P., DC potential drop calibration in matrix-cladded Ti MMC specimens with a corner notch, International Journal of Fatigue, 25, 671-676, 2003.

[5.21] Raghava, G., Mithun, I.K., Gandhi, P., Vaze, K.K. , Bhate, S.R., Bhattacharya, A., Application of beach marking technique to the study of fatigue crack growth in steel plate specimens subjected to tensile loads, Journal of Structural Engineering, 32 (3), 229-232, 2005.

[5.22] Cai, C.Q., Shin, C.S., A normalized area-compliance method for monitoring surface crack development in a cylindrical rod, International Journal of Fatigue, 27, 801-809, 2005.

[5.23] Lihavainen, V.M., A novel approach for assessing the fatigue strength of ultrasonic impact treated welded structures, PhD Thesis, Lappeenranta University of Technology, 2006.

[5.24] Zahavi, E., Life expectancy of machine parts: fatigue design, CRC Press, USA, 1996.

Chapter 6

Finite Element Model

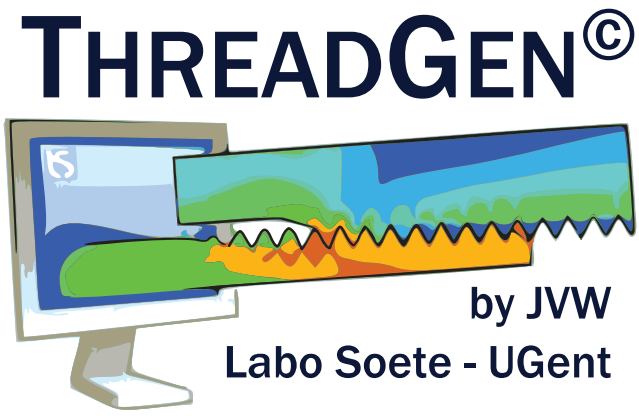

1 Goal

To further understand the experimental results obtained in the previous chapter, a 2D axisymmetric finite model is developed. This numerical model is constructed in a parametric way so that different connection types can be efficiently modelled.

In this chapter the details of this finite element model are provided. First the modelling strategy is defined, followed by a description of the model mesh and applied non-linearities. To illustrate the use of the model a detailed analysis is presented of the standard 4.5" API Line Pipe connection. Afterwards, a comparison is given between the 2D axisymmetric model and a full 3D model. Finally the model is validated by comparing results of the simulations with experimental results described in Chapter 5.

2 Modelling strategy

To simulate the influence of material, contact and geometrical properties on the connection's behaviour, a new modelling tool is developed using a combination of the software packages MATLAB® R2008a and ABAQUS® 6.8-1. The created program is given the name *ThreadGen©*. The used modelling strategy in this program is schematically illustrated in Figure 6.1.

The input of the program consists of the connection's geometric, material and contact properties together with the loading conditions. This data is used during the first stage of the program where a MATLAB pre-processor generates the necessary input files for ABAQUS and stores selected data for transfer to the MATLAB post-processor. Specific parameters related to the numerical analysis such as meshing strategy and element type are included in the generated input files. The choice of the mesh parameters is based on the mesh optimization study presented in section 3.3.1.

Based on the input data, the model geometry is constructed and stored in a Python file together with the necessary material data, load and boundary conditions. In the second stage, this Python file is run by ABAQUS where the finite element analysis is carried out. After the analysis is completed, ABAQUS reads the second Python file that was created by the pre-processor and the relevant data is selected from the output database. Once all data is collected, the MATLAB post-processor routine creates an analysis report containing both graphical and numerical data from the analysis. The generated numerical results are stored in separate files and can also be used for further processing.

When performing parametric studies, multiple variations of a connection can be easily simulated by generating a batch of input scripts in the first stage with the pre-processor. During the second stage, all connections are

automatically simulated and processed. In the third stage the generated output files are processed automatically.

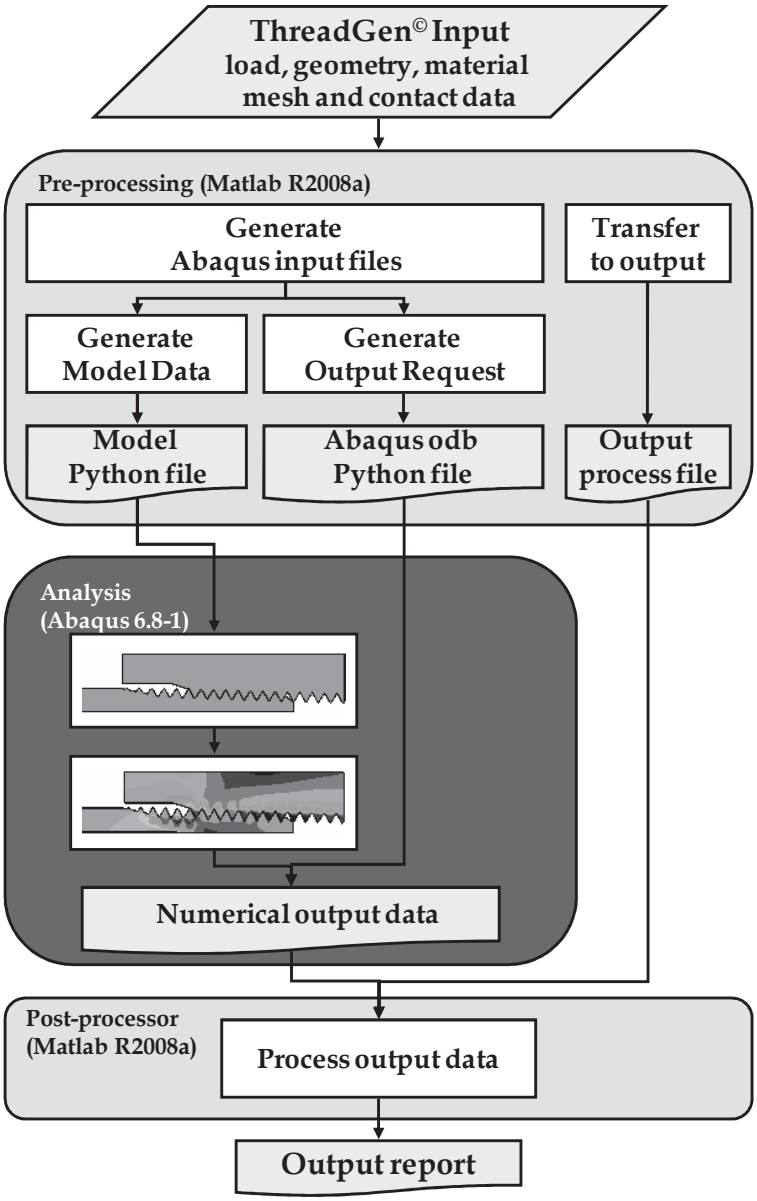

Figure 6.1: Structure of the parametric program.

3 Finite element model

3.1 Model geometry

In analogy to the models found in literature and described in section 2.2.3 of Chapter 2, a 2D axisymmetric geometry is used to model the threaded connections. Although this is a widely accepted method, it is originally based on comparisons with photo-elastic models under simple loading conditions and assuming fully elastic behaviour of the connection. To justify the choice of the 2D approach, a comparison is made with a full 3D model in section 5 of this chapter.

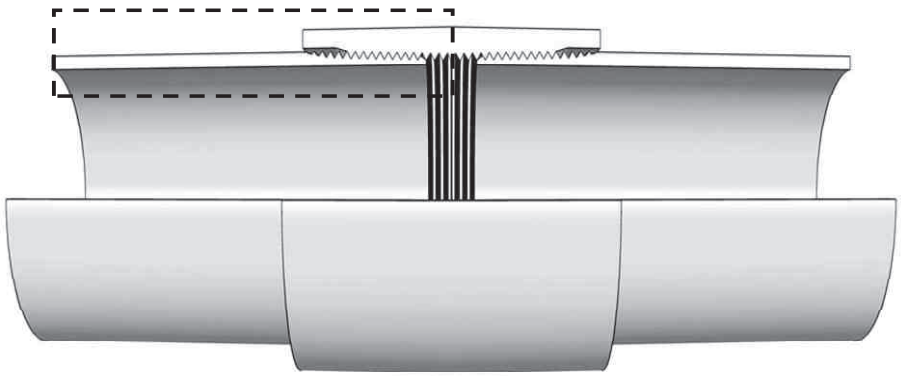

Figure 6.2: Section view of an API Line Pipe connection.

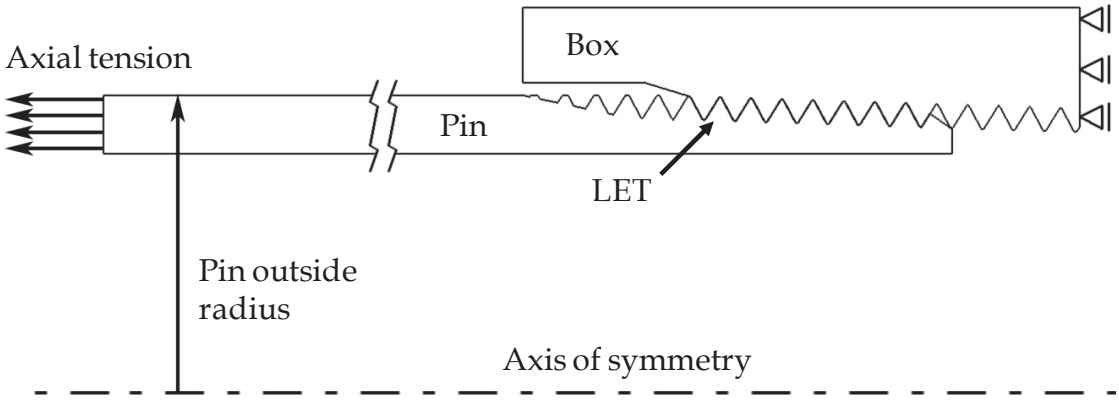

Figure 6.3: 2D axisymmetric model of an API Line Pipe connection.

The parametric model is optimized to simulate API Line Pipe connections as schematically shown in Figure 6.2 and configurations derived from this standard connection type. In addition, it will be shown later that other types such as BSPT connections can be easily modelled.

Next to the use of axisymmetry, a plane of symmetry is assumed at the coupling's centre of the threaded and coupled API Line Pipe connection (see boundary conditions at the right of Figure 6.3), hence the model comprises only the region inside the dashed line in Figure 6.2. The resulting axisymmetric model is schematically shown in Figure 6.3 and consists of a separate pin and box part. The unthreaded pipe body of the pin is sufficiently long (100 mm for the 4.5" API Line Pipe connection model) to eliminate boundary effects when an external tensile stress is applied at its free end.

The geometry of the pin and box are constructed using a limited number of parameters so that different connection sizes and modifications can be easily simulated. To do this, the construction of the global pin and box geometry is separated from the construction of the connection's threads. In Figure 6.4 it is illustrated that the global pin geometry is generated using six points. It is clear that the points 1 to 4 are defined by the pin outside diameter, the wall thickness and the total length of the pin. To construct the points 5 and 6, the

thread taper is used and the lengths L_1, L_2 and L_4 are introduced as defined in the API 5B specifications [6.1]. L_2 is the effective thread length and L_4 is the length between the pin end and the thread vanish point, which means the region between the points 1 and 6 is the thread runout region. L_1 defines the position of the hand-tight plane towards which the threads engage in the hand-tight situation without the make-up torque applied. The corresponding diameter of the pitch line at the hand-tight plane is given by E_1. The used coordinate system has a horizontal axis that coincides with the axis of symmetry of the pin and a vertical axis that runs through the vanish point as shown in Figure 6.4.

The construction of the box global geometry is performed in a similar way as the pin geometry and is illustrated in Figure 6.5. The box is positioned at an axial distance t from the origin which corresponds to the axial distance for the number of make-up turns. (In API 5B [6.1] it is specified that the face of the box should advance up to the vanish point for power-tight make-up). This way, if placed in the same coordinate system, the pin and box are constructed in their hand-tight position. As the pin geometry, the box is also constructed using six points. Points 1 to 4 are generated using the distance A, the box outer diameter D_b, box length L_b and the values Q and q that define respectively the box recess diameter and box recess length.

The points 5 and 6 are determined by using the chamfer angle γ, the length L_5, diameter E_1 and the thread taper angle which does not necessarily has to be equal to the taper angle of the pin.

After the global connection geometry is constructed, the threads are introduced. The thread shape is defined in Figure 6.6 and is based on a triangular thread shape with a fully developed thread height H and pitch length p. The thread angle of the API Line Pipe connection is 60°, but this value can be altered to model other thread types. The thread crest and root are truncated over a certain truncation height respectively t_c and t_r.

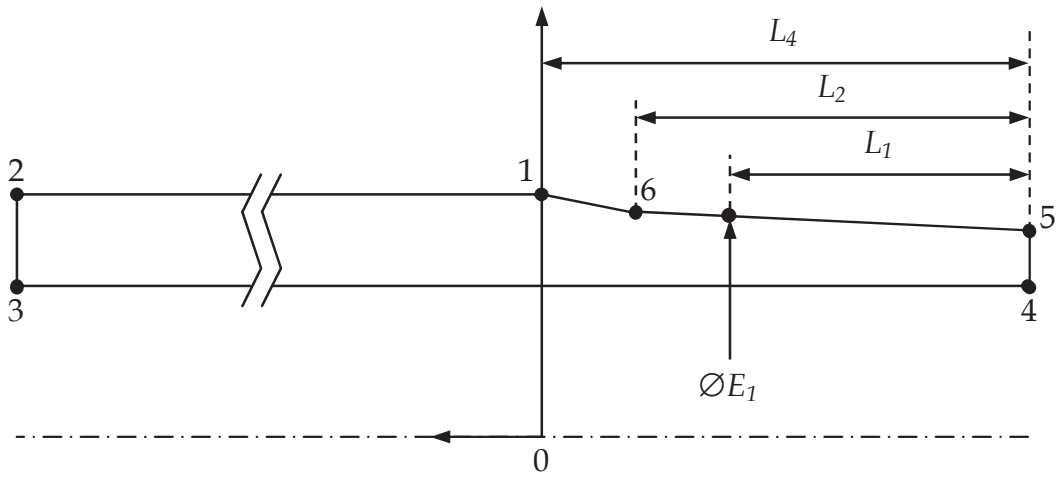

Figure 6.4: Construction of the global pin geometry.

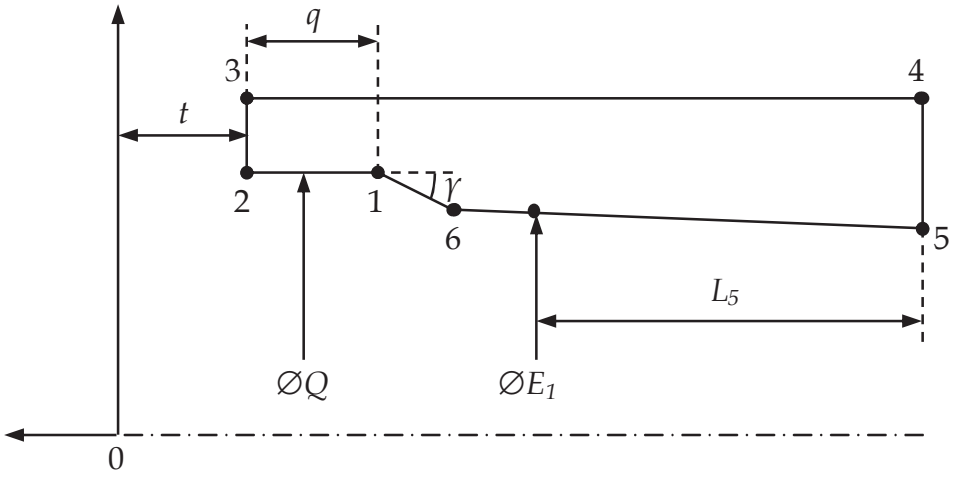

Figure 6.5: Construction of the global box geometry.

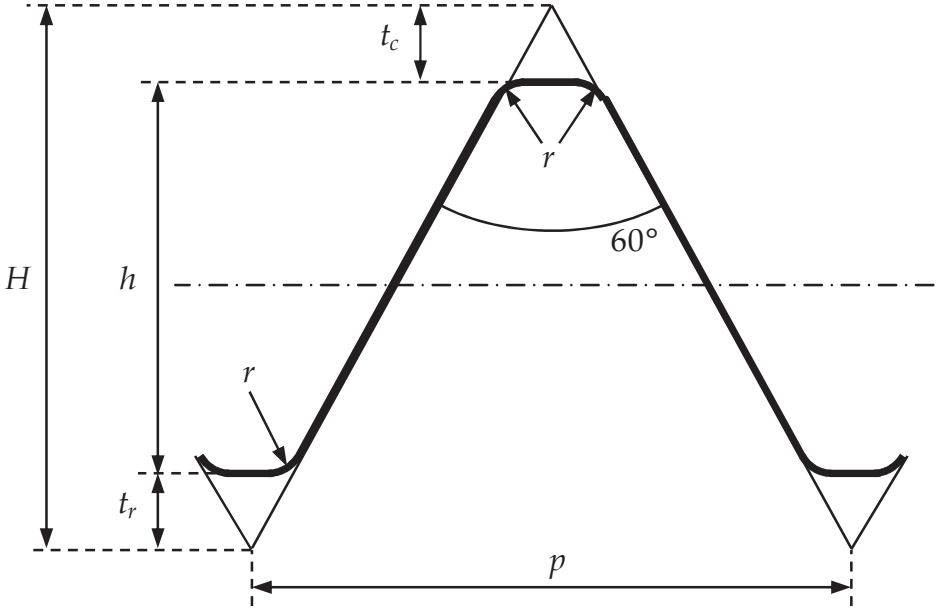

Figure 6.6: Construction of the threads.

In addition a fillet radius r is used since a sharp edge would result in a stress singularity in the model and in practice a thread cutting tool has a certain small radius. It is also noted that by increasing this radius to the appropriate values, round thread shapes can be modelled. For the standard API Line Pipe geometry a fillet radius of $r = 0.05$ mm is applied.

3.2 Model non-linearities

To include the necessary non-linear behaviour in the finite element model elastic-plastic material behaviour and elaborate contact interactions are in introduced.

3.2.1 Material properties

Non-linear material behaviour is provided by the use of a multilinear elastic-plastic material model with isotropic hardening. The material data used in this study is either based on the experimentally determined stress-strain behaviour of the pipeline steel (determined by tensile testing as described in Chapter 5) or on the minimum specified material properties of the applicable standards.

3.2.2 Contact definition and make-up

The contact between the pin and box threads is defined by a node to surface interaction and allows for finite sliding. Being the most rigid part of the connection, the box threads are defined as the master surface and the pin threads as the slave pair. The effect of friction is included by the use of a Coulomb friction model with an isotropic coefficient of friction.

Since a 2D axisymmetric model is used, the make-up turns can not be modelled by a rotation. For this reason, a certain interference or radial overlap between pin and box is provided in the model, which corresponds to the number of make-up turns as by Eq. (5.4). This is schematically shown in Figure 6.7. The thread surfaces are then brought into contact using the interference fit option in ABAQUS®.

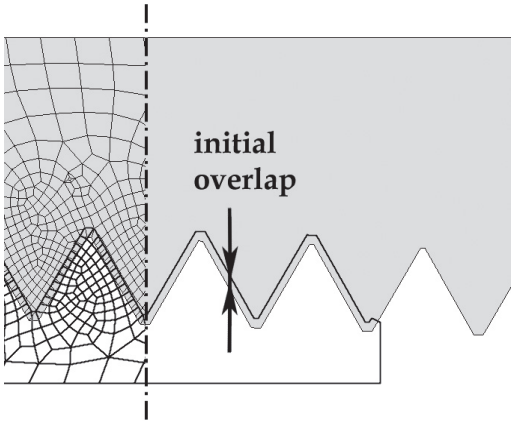

Figure 6.7: Radial overlap to model make-up.

3.3 Mesh details

3.3.1 Mesh optimization study

To mesh the geometric model, CAX4R elements are used. These are 4-node axisymmetric quadrilateral elements with reduced integration. In order to determine the optimal mesh size of the threaded connection model, a mesh optimization study is carried out on the 4.5" API Line Pipe geometry.

The complete model mesh is defined by 5 parameters as shown in Figure 6.8. The global seed size defines the basic size of the mesh in the pin and the box.

Since the stress distribution around the thread surfaces is to be studied in detail, a smaller local seed size is used for the threads of the box and the thread runout region of the pin. Because the pin threads are the slave surface of the contact pair they require a finer mesh than the box threads. Additionally, because it is known from the experiments that fatigue cracks initiate at the thread roots of the pin, the smallest elements are used at that location. The resulting mesh of the pin threads is defined by three additional parameters. Both the thread crest and thread root have their own seed size. The thread flanks have a specific number of elements using biased seeding, which means the element size reduces linearly from crest to root. A bias ratio of five is used, which is the ratio between the size of the largest element at the crest and the smallest element at the root.

During the mesh optimization study, all five parameters are changed to see the influence on the stress field and the resulting calculation time. The simulations are carried out on a central server system which is a cluster of quad-core CPU's. In Table 6.1 the results of six simulations from the mesh optimization study are summarized; they are sorted by increasing number of elements in the model. The most coarse and finest meshes listed in the table are illustrated in respectively Figure 6.9 a and b. The first model contains 1452 elements and is analysed in 24 s, while the latter consists of 56 984 elements and takes over 21 min. to calculate. The relation between number of elements and calculation time is approximately linear.

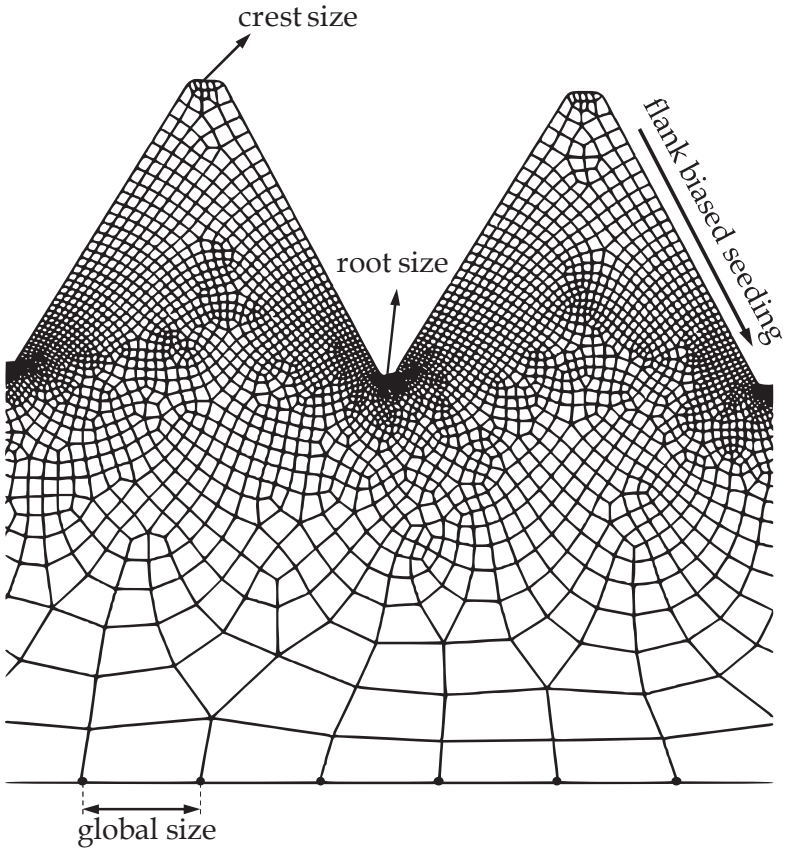

Figure 6.8: Mesh parameters.

To evaluate to obtained accuracy of the stress field around the LET of the pin, the von Mises stress as a function of the radial distance from the LET is plotted for 5 different meshes in Figure 6.10. The three mesh configurations with global mesh size of 6, 4 and 2 mm are compared with the finest mesh of Table 6.1. The latter is given by the full black line in the plot. The mesh configuration selected for this study is represented by the circular data points and corresponds with the mesh configuration with a calculation time of 5 min in Table 6.1.

Global size [mm]	Local size [mm]	Crest size [mm]	Root size [mm]	# Flank elements	Calcul. time [m:s]	Model # elements
6	1.2	0.30	0.060	10	0:24	1452
4	0.8	0.20	0.040	20	0:45	3264
2	0.4	0.10	0.020	25	1:47	6127
1	0.3	0.05	0.015	30	3:40	13 757
1	0.2	0.05	0.010	35	5:00	19 781
1	0.2	0.05	0.005	45	8:19	27 889
1	0.1	0.05	0.001	50	21:40	56 984

Table 6.1: Comparison of different mesh details.

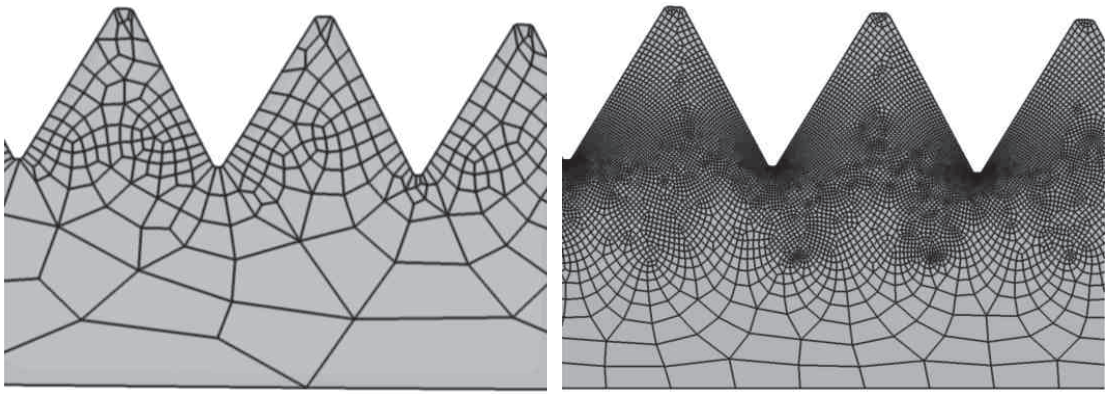

a) b)

Figure 6.9: a) Coarse mesh with global mesh size of 6 mm; b) fine mesh with root element size of 0.001 mm.

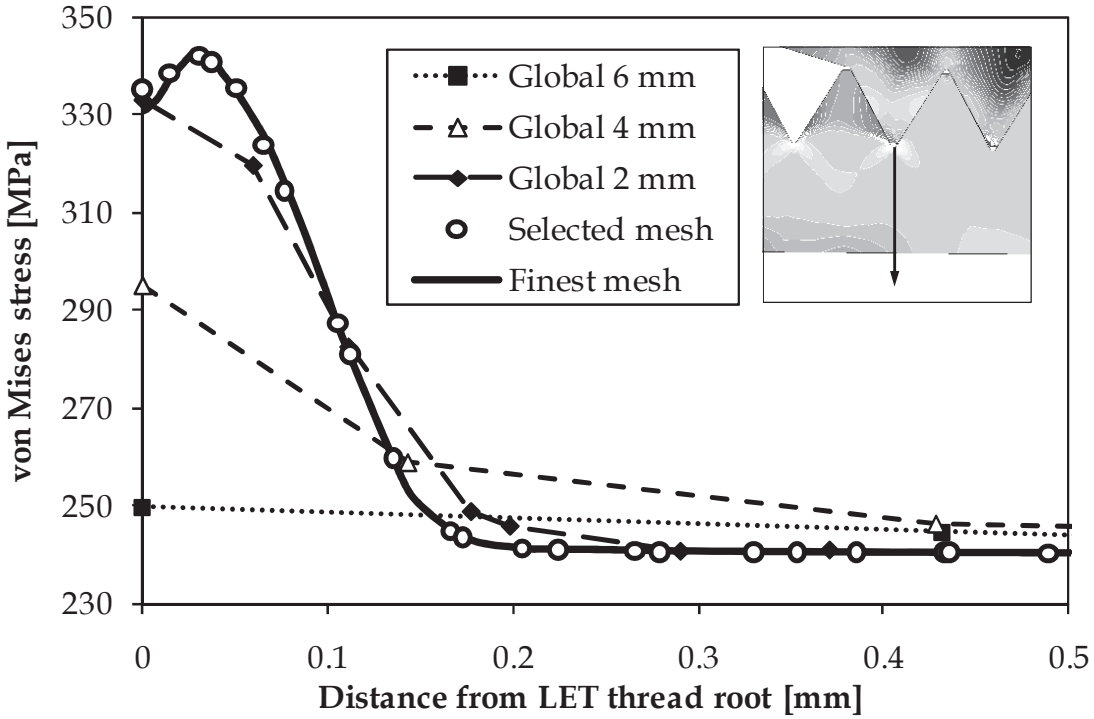

Figure 6.10: Comparison of the stress field (von Mises values) around the LET for different meshes.

3.3.2 Model mesh

The optimized model mesh of the 4.5″ API Line Pipe connection is shown in Figure 6.11. It consists of 19 781 elements of which 14 111 are pin elements and 5670 box elements.

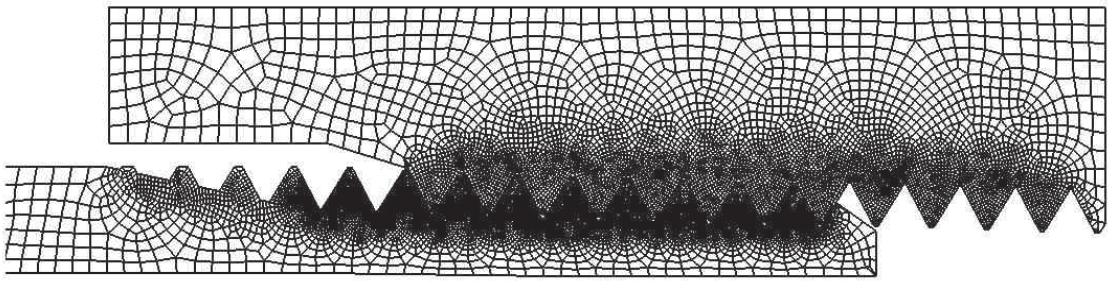

Figure 6.11: 4.5″ API Line Pipe model mesh.

Global seed size	pin *WT/6*
Local seed size	global / 5
Pin thread crest seed	global / 20
Pin thread root seed	global / 100
Number of elements at pin flanks	35

Table 6.2: Rules for determining mesh parameters.

Since ThreadGen© is a parametric program, all mesh parameters are defined as a function of the connection's geometry. The followed rules to determine mesh parameters in this study are summarized in Table 6.2.

4 Analysis of a 4.5″ API Line Pipe connection

To illustrate the output of the finite element model, the analysis results of the standard 4.5″ API Line Pipe connection are presented. The used elastic-plastic material model, shown in Figure 6.12, is based on the minimum properties of API Grade B steel as specified by API 5L [6.2]. The material model uses a Young's modulus of 208 GPa and a Poisson coefficient of 0.3. The material's yield strength is 241 MPa and the ultimate tensile stress value (true stress) is 521 MPa, the corresponding elongation is 23%. A coefficient of friction μ = 0.12 is used for the contact between the threads.

The analysis is carried out in two consecutive steps. In the first step the make-up of the connection is simulated. Unless mentioned otherwise, an effective number of 1 make-up turn is used throughout the simulations on the 4.5″ connection. This value lays within the range of the API 5B specifications [6.1] and is close to the value of 0.80 effective make-up turns measured in the torque tests. During the second step an additional uniform axial tensile stress is applied, as illustrated in Figure 6.3. In the following paragraphs the resulting stress state and load distribution are discussed.

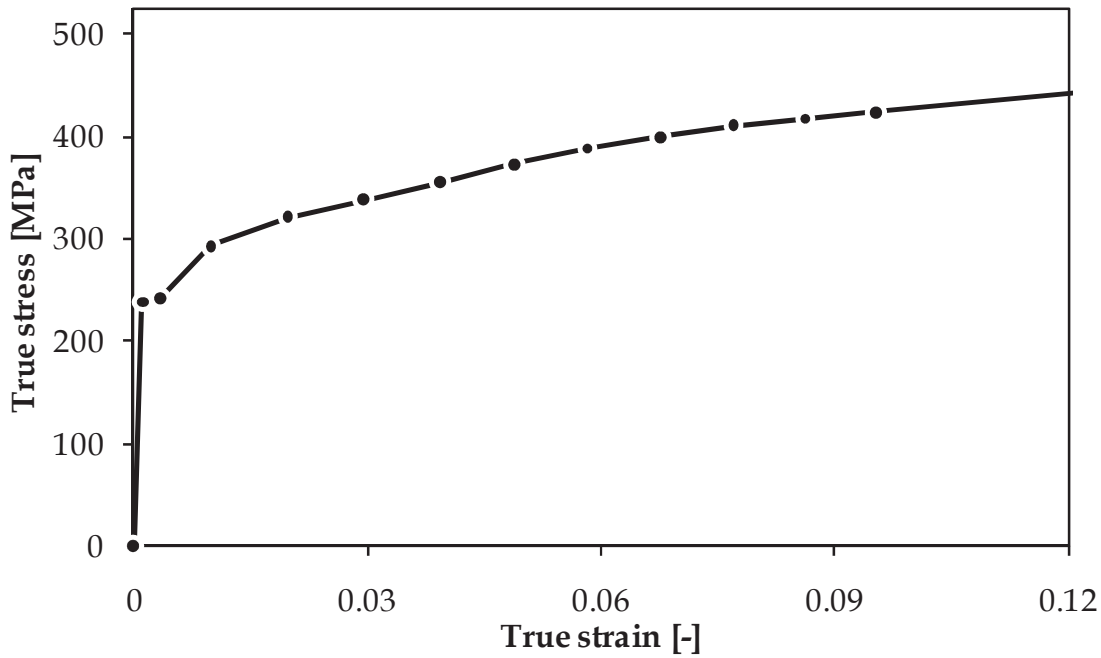

Figure 6.12: Multilinear elastic plastic material model based on the minimum properties of API Grade B steel.

4.1 Stresses

The von Mises equivalent stress distribution for both calculated steps is shown in Figure 6.13. Note that the stresses in the pin over the length of the engaged threads are very high and exceed the material's yield strength even in the make-up stage, which corresponds to the observations made during the three consecutive make-up tests described in section 3.2 in Chapter 5. In addition, this is in agreement with the plastic deformation of the engaged threads of an API Round connection during make-up modelled by Dvorkin and Toscano [6.3]. With this it is illustrated that the use of elastic-plastic material behaviour is indispensable.

When the axial load is applied, the highest stress concentration appears at the root of the last engaged thread of the pin (indicated by the arrow in Figure 6.13.b). This corresponds again to the results obtained by Dvorkin and Toscano [6.3] for the analysis of an API Round connection.

To analyse the stresses more in detail, the different stress components for the make-up stage and the made up connection with an additional axial load of 150 MPa are shown respectively in Figure 6.14 and Figure 6.15.

From Figure 6.14.c it can be seen that the high von Mises stress during make-up is mainly the result of the acting hoop stress. The hoop stress in the pin has a negative sign, which indicates a compressive stress while the hoop stress in the box is positive, being a tensile stress. This is because during make-up the pin is forced to move into the box. Hence at the engaged threads the pin is compressed in a uniform way, while the box is expanded. Due to its larger wall thickness, the box is a more rigid part than the pin, and the amplitude of the hoop stress in the pin is higher than in the box. It can be seen that the compressive hoop stress in the pin decreases when moving further away from the engaged threads.

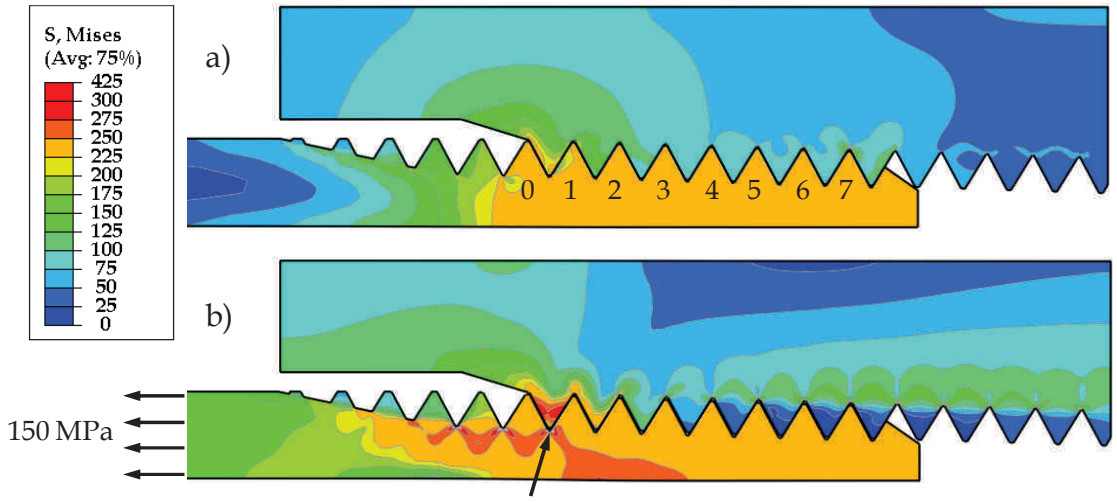

Figure 6.13: Von Mises stress distribution a) at make-up; b) with an external axial tensile stress of 150 MPa.

From Figure 6.14.b and d it can be seen that the radial and shear stress are low, apart from some local effects around the LET of the pin.

The axial stress is given in Figure 6.14.a. In the thread runout region of the pin, the axial stress changes from a compressive stress at the inside wall of the pin to a tensile stress at the outside. This is the consequence of bending of the pin due to make-up deformation. A similar bending situation appears at the box recess region where the axial stress changes from being tensile at the outside wall to compressive near the inside diameter. Important to note is that at the LET of the pin an axial tensile stress appears over the wall thickness of the pin even though no external axial stress is applied. This is caused by the bending of the box recess, causing a local axial tensile stress situation at the LET of the pin.

The stress situation after application of the external axial load of 150 MPa is presented in Figure 6.15. From Figure 6.15.b and d it is clear that the radial and shear stress remain low.

Since a uniform axial tensile stress is applied over the wall of the free end of the pin, the axial stress distribution is changed as can be seen in Figure 6.15.a. The axial stress in the pin reduces over the engaged threads of the pin from left to right because the axial load is transferred by the engaged threads to the box. Accordingly the axial stress in the box increases from left to right over the engaged threads. In the pin the axial stress causes high stress concentrations around the root of the LET and also at the root of the threads in the thread runout region.

The maximum axial stress acts at the LET of the pin and is 596 MPa. This corresponds to a stress concentration factor of 3.97 relative to the applied axial tensile stress of 150 MPa. A similar stress concentration factor of 3.7 was calculated by Shoji and Sawa [6.4] for metric bolts which have a comparable triangular thread shape with thread angle of 60°.

Due to the applied axial stress, the hoop stress is partly affected as illustrated in Figure 6.15.c. Although the main hoop stress is still compressive in the pin and tensile in the box, the high axial stress at the LET and thread runout reduces the hoop stress due to the Poisson effect.

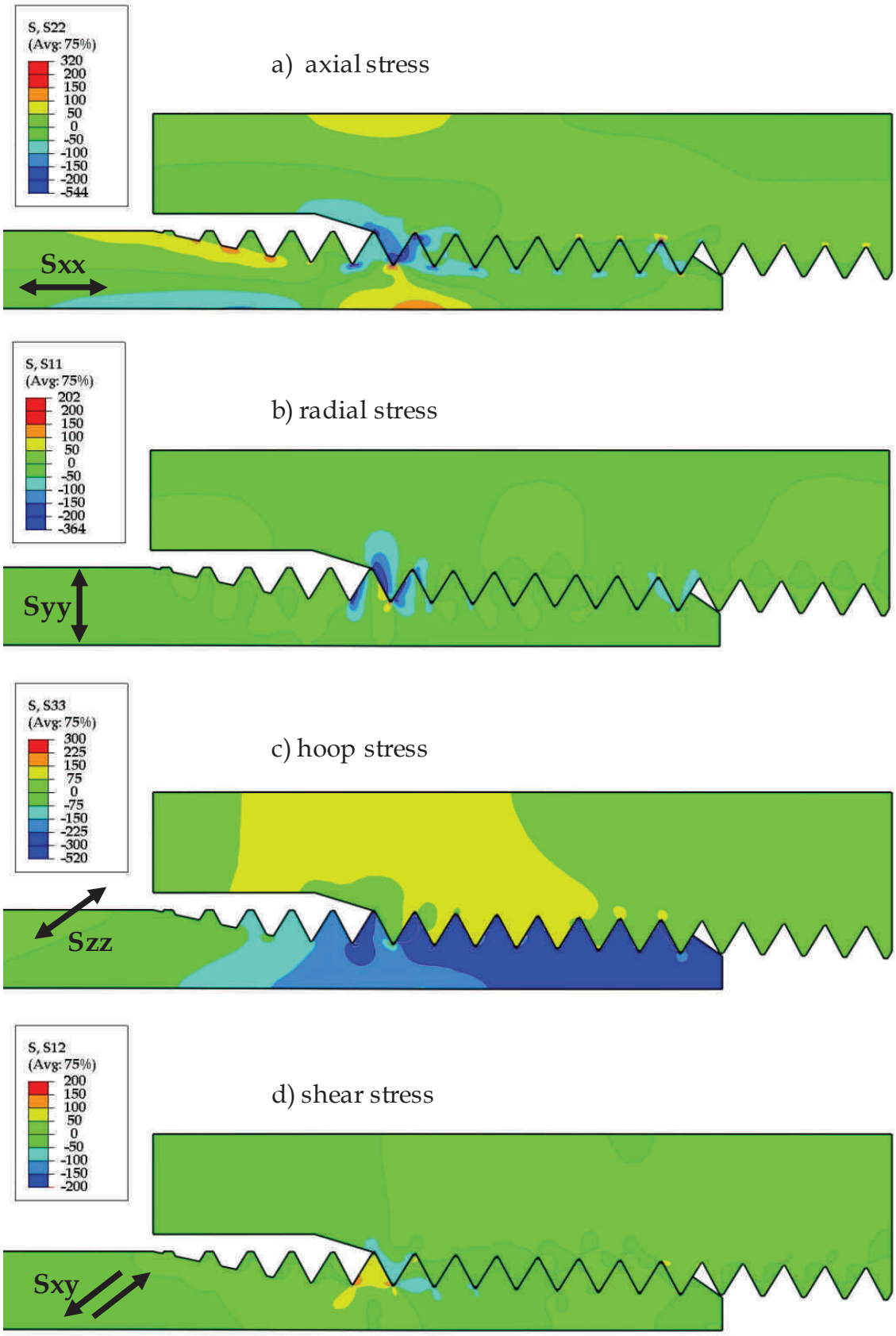

Figure 6.14: Stress components in a made up connection.

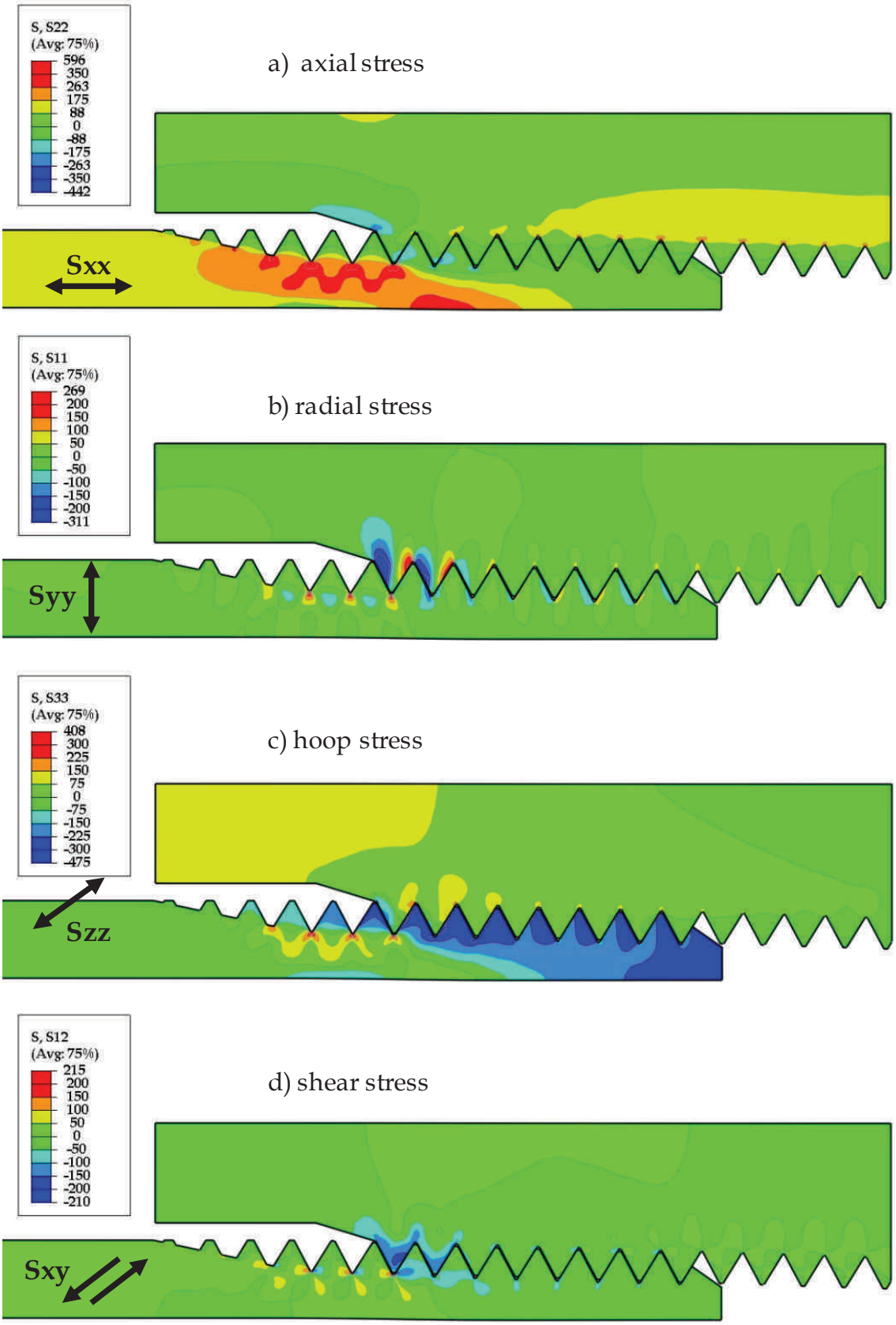

Figure 6.15: Stress components in a made up connection with an additional axial tensile stress of 150 MPa.

4.2 Plasticity at thread root

As known from the local strain approach described in section 4.3 of Chapter 2, the local strain range is a determining factor for a components fatigue life. The highest equivalent plastic strain ε_p appears at the root of the LET of the pin. This is shown in Figure 6.16 for both make-up as for the connection with an additional axial tensile stress of 100 MPa. After make-up the equivalent plastic strain reaches 0.7 %. With the additional axial tensile stress of 100 MPa, ε_p increases to 2.0 % and when the stress is increased to 150 MPa the maximum ε_p-value is 9.6 %. These values are in the same order of magnitude as the values obtained by Dvorkin and Toscano [6.3] in their analysis of an API Round connection.

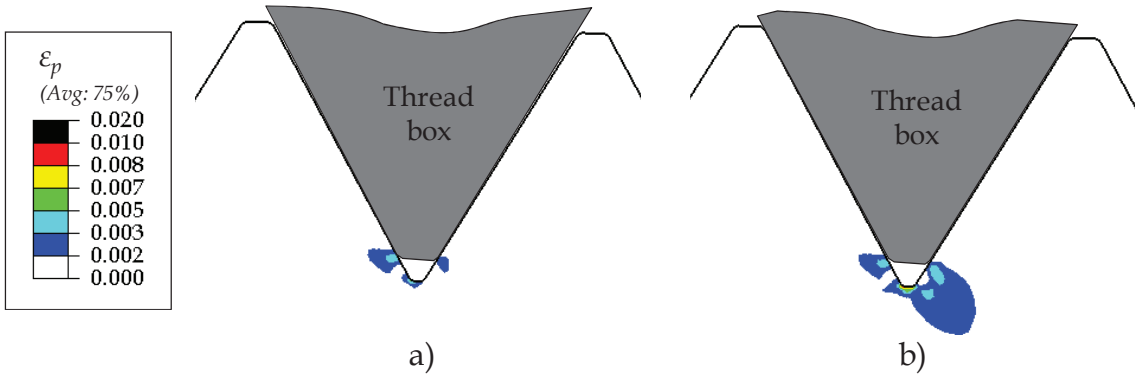

Figure 6.16: Equivalent plastic strain at the root of the LET of the pin, a) at make-up; b) with an additional axial tensile stress of 100 MPa.

4.3 Separation

As described analytically in section 3.3.2 of Chapter 5, the applied axial load is transferred by contact forces acting on the threads. Due to the triangular thread profile, these contact forces have an important radial component, the so-called separation force. When the applied axial tensile stress exceeds a certain value, the separation force will cause a sliding of the threads and an opening will be created between the thread stab flanks as in Figure 6.17. It can be seen that this opening remains limited in value up to an axial tensile stress of 125 MPa. Afterwards, an important opening increase can be observed. A similar thread opening behaviour was obtained by Assanelli et al. [6.5] for an API Round connection. Yet, the appearing opening between the thread flanks is highly undesirable since a fluid inside the pipe can find its way out through the created helical path, for increased loads the thread sliding causes thread jump-out and under dynamic loading conditions the sliding can initiate fretting fatigue cracks [6.6].

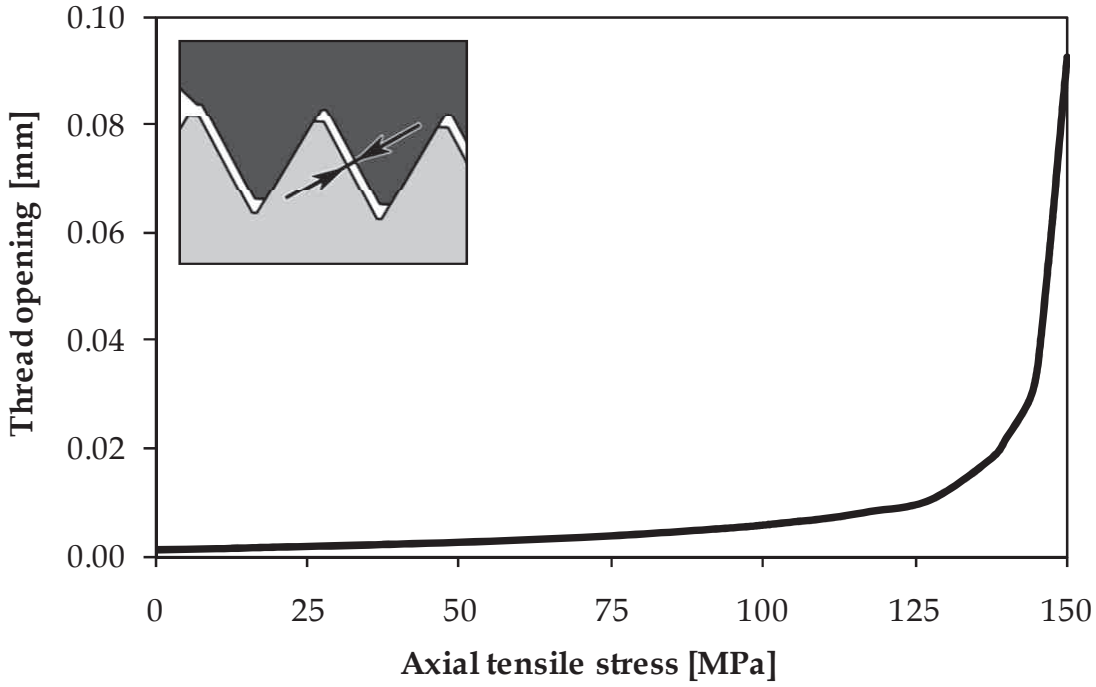

Figure 6.17: Thread opening as a function of the applied axial stress.

4.4 Load distribution

It is clear from Figure 6.15.b that an important part of the axial load is transferred from pin to box by the LET of the pin. Hence, the stress concentration at the last engaged thread of the pin is caused by the non-uniform distribution of the axial load over the different threads. This load distribution is plotted in Figure 6.18.

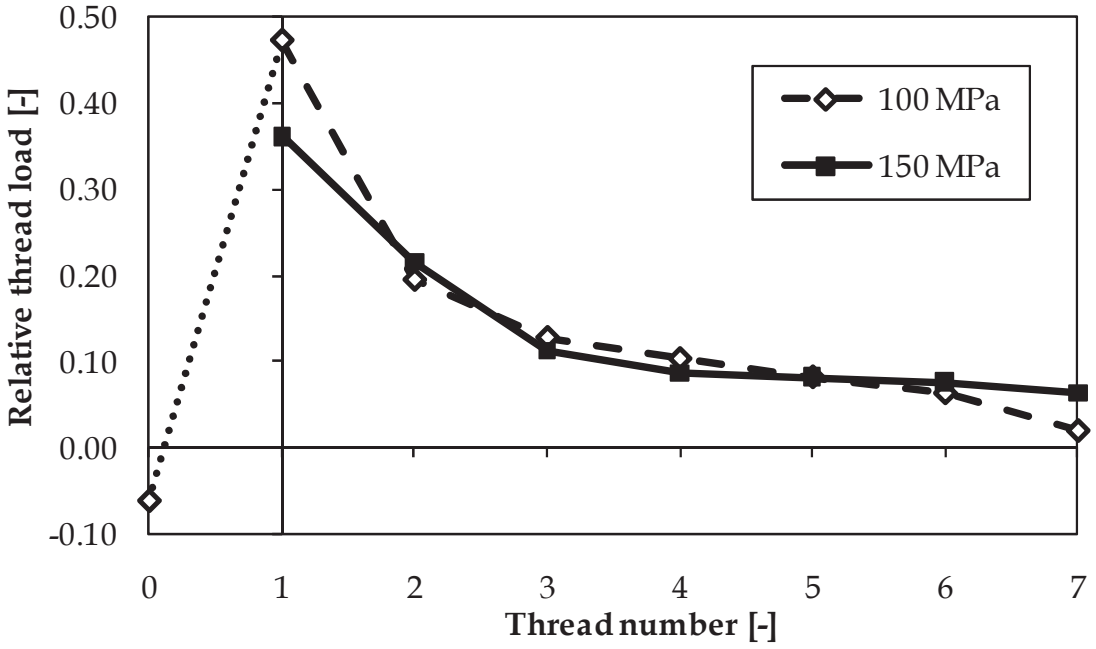

Figure 6.18: Relative thread load distribution; thread numbering as in Figure 6.13.

In this figure the relative thread load as a percentage of the total axial load is given for each engaged pin thread. The threads are numbered from 0 to 7 according to Figure 6.13 with thread number 1 being the LET of the pin. Thread number zero is not fully engaged, it only contacts the box thread with its stab flank, while its load flank is unloaded. This means thread 0 can only transfer negative relative loads.

From Figure 6.18 it can be seen that when an external tensile stress of 100 MPa is applied, the LET carries 47 % of the total load. This is highly undesirable since it means almost half the load is carried by just one thread while the remaining half is divided over six engaged threads. The thread number 0 carries a negative load which is a compression caused by the bending of the pin during make-up. When the external stress is increased to 150 MPa, the LET starts to bend, transmitting part of its load to the other threads. Furthermore, at this applied stress, separation of the thread load flanks has occurred, eliminating the compressive load on thread 0. This way the load carried by the LET is reduced to 36 % of the total load.

5 2D axisymmetric vs 3D modelling

5.1 3D model details

As mentioned in section 2.2.4 of Chapter 2, the use of 2D axisymmetric models instead of full 3D models is widely accepted in literature and has the advantage of shorter calculation times. Still, the majority of the performed experimental tests of this study are carried out under four-point bending. Since MacDonald and Deans [6.7] showed that an axisymmetric approach is only valid when the wall thickness to diameter ratio is sufficiently small, it is important to check the validity of using 2D axisymmetric models to represent a bending load case.

Since the standard 1” API Line Pipe connection has a larger wall thickness to diameter ratio than the standard 4.5” API Line Pipe connection, the 1” configuration is evaluated both by a 2D axisymmetric model and a full 3D model. The 3D model is constructed by revolving the 2D axisymmetric geometry, so the exact thread helix is neglected. Nonetheless, both models use the same elaborate contact definitions, with a coefficient of friction of 0.12 and a multilinear elastic-plastic material model based on the results of tensile testing of the 1” specimen material, as shown in Figure 6.19. Hence, both models include the necessary non-linearities for accurate modelling of a threaded pipe connection. For both models, a plane of symmetry is introduced at the centre of the box. The 2D axisymmetric model is meshed according to the mesh parameters given in Table 6.2, but the 3D model has a coarser mesh to reduce the model’s calculation time.

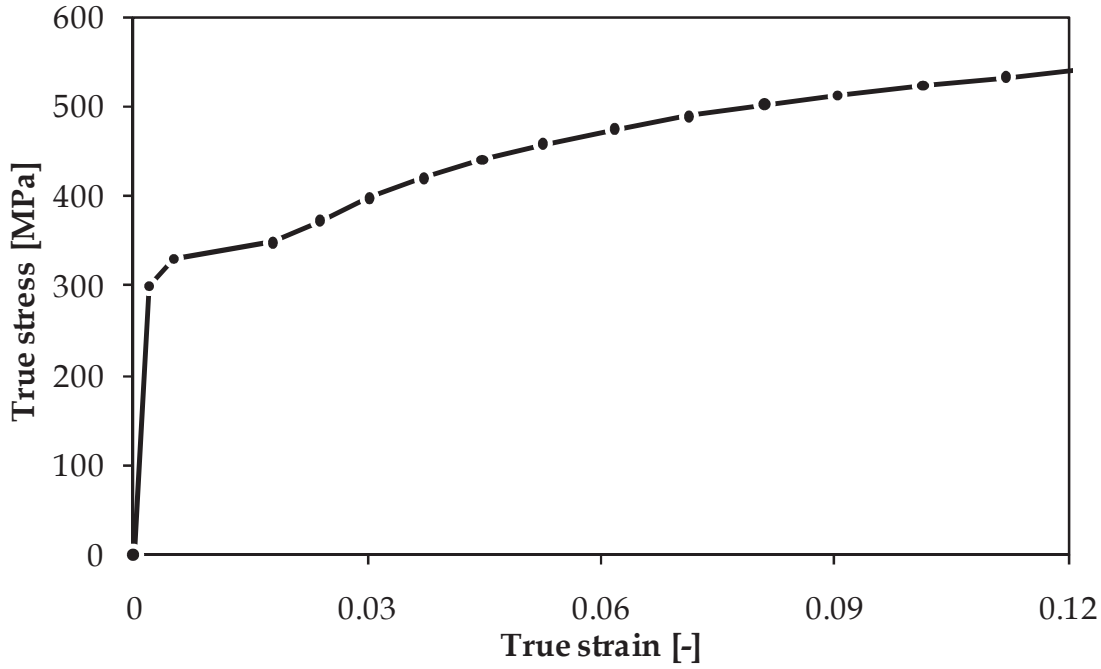

Figure 6.19: Multilinear elastic plastic material model based on tensile test results of three 1" API Grade B steel tubes.

5.2 Make-up

In Figure 6.20 the resulting von Mises stress distributions for both the 3D and 2D axisymmetric model are given for the made up coupling without any additional load. Note that there is a very good correspondence between both stress fields. As a comparison, the von Mises stress of all nodes along the inside wall of the pin and the outside wall of the box is plotted for the 2D axisymmetric and the 3D model in Figure 6.20. The x-distance is measured along the x-axis, with $x = 0$ the plane of symmetry at the centre of the box. Along the outside wall of the box, the stress increases from the first to last engaged threads. Further along the x-axis, the box stress decreases again. The pin stress along the engaged threads is nearly constant, as the stress values reach the material's yield strength and plastic deformation occurs during make-up. Further along the x-axis, the pin stresses become zero.

It can be seen that difference between the stress along the pin for both models is negligible (root mean square RMS deviation = 4.1 MPa or 0.8 % of the maximum appearing von Mises stress). The resulting stresses in the box deviate a little more between both models (RMS deviation = 13.6 MPa), but still a good agreement can be observed. This difference is explained by the coarser mesh in the 3D model of the box that had a seed size of 2.0 mm compared to 0.6 mm for the axisymmetric model.

From these observations it may be concluded that the 2D axisymmetric model is a good approximation for the 3D threaded couplings in the make-up situation as shown previously by Zhong [6.8].

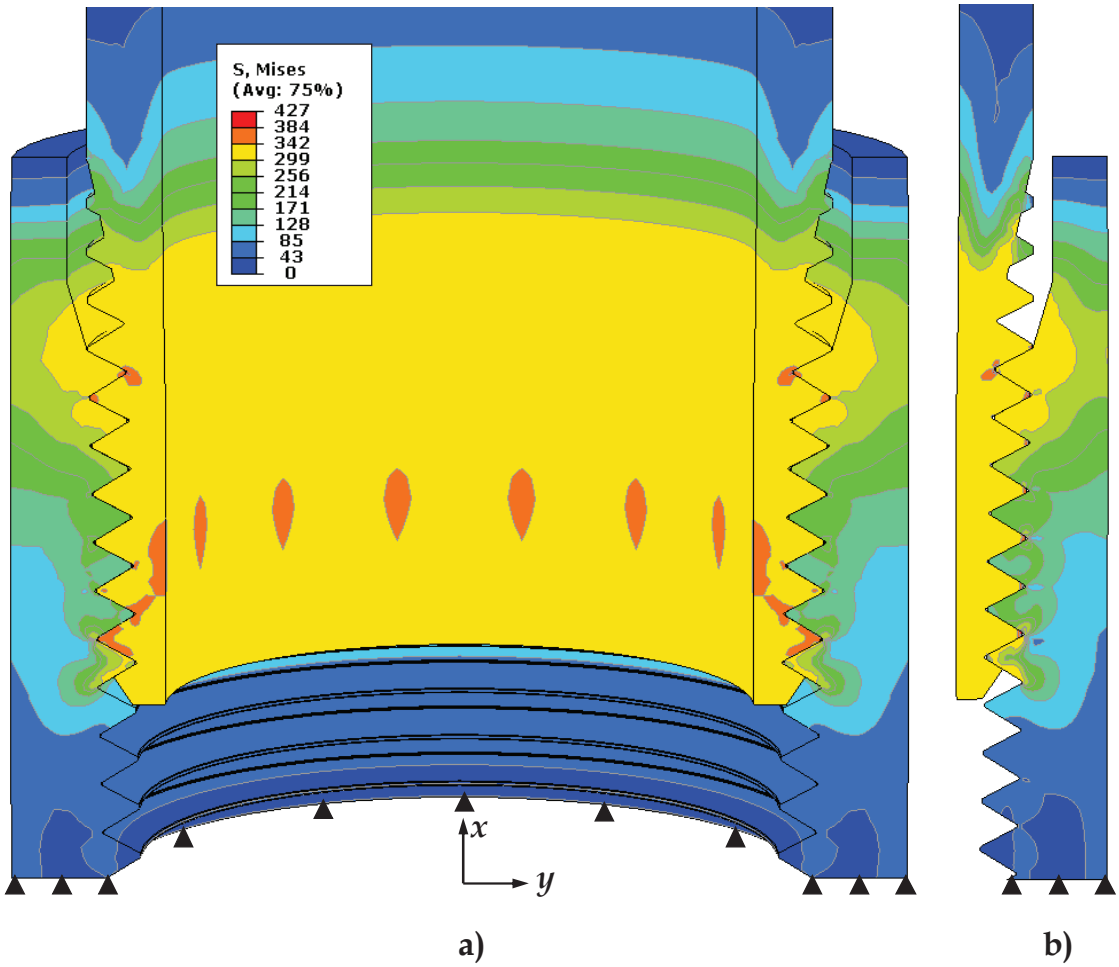

Figure 6.20: Comparison between von Mises stress due to make-up for a) the 3D model and b) the 2D axisymmetric model.

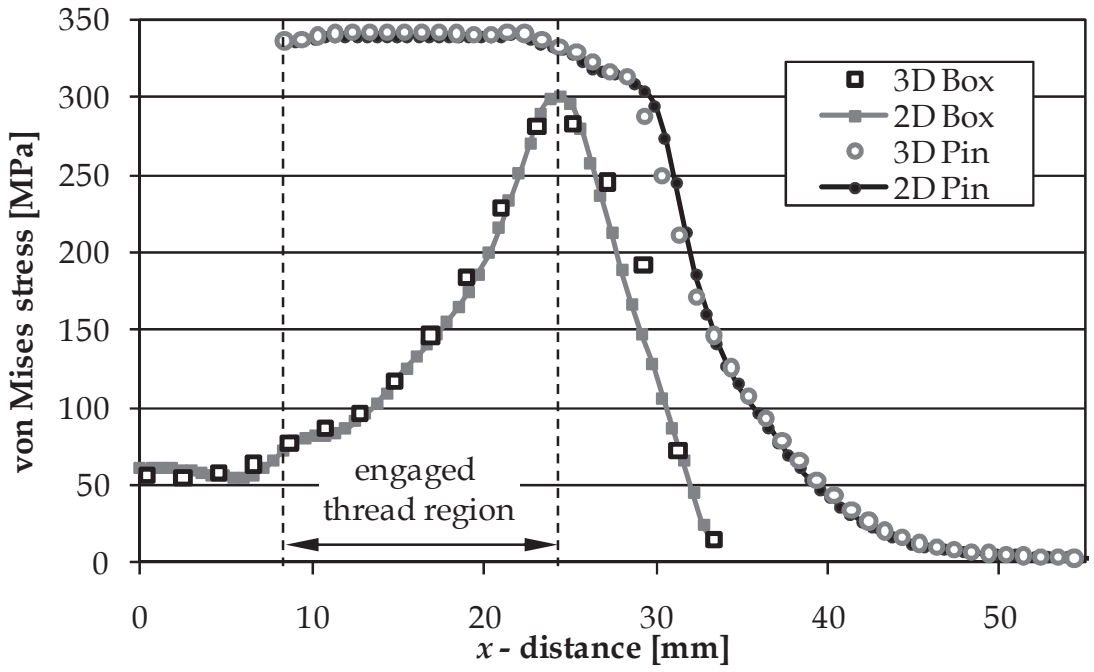

Figure 6.21: Von Mises stress along the inside pin wall and outside box wall after make-up.

5.3 Bending load

The application of the bending loads in the 3D model is schematically shown in Figure 6.22. To get a more comprehensive view in this figure, the 3D finite element model is mirrored around its plane of symmetry indicated by the centreline. The forces are applied similar to the situation in the small scale four-point bending experimental setup.

In Figure 6.23 the results for additional bending of the made up 3D model are compared to the results of the made up 2D axisymmetric model with an additional uniform axial tensile stress. The applied force in the 3D model is chosen in such a way that the mean stress over the wall thickness of the pin at the tensile side (the right side in Figure 6.23.a) is equal to 100 MPa. As schematically illustrated in Figure 6.23.a, the actual maximum tensile stress in the 3D model is 111.3 MPa, and the tensile stress at the inside wall of the pin is 88.7 MPa. This way the resulting force over the wall thickness of the pin in this section is equal for both the 2D and 3D model. To prove the good correspondence between the two models, the nodal stresses along the wall of the pin and box are plotted in Figure 6.24. For the pin it can be seen that along the entire threaded region ($8.3 < x < 33.4$ mm) the von Mises stress in the two models is very close (RMS deviation = 2.7 MPa). Outside this region, the stress difference is caused by the difference in loading conditions. As explained in the previous paragraph, the bending stress at the inside wall of the 3D model can only reach a value of 88.7 MPa, while on the 2D model a uniform axial tensile stress of 100 MPa is applied. Since the wall thickness to diameter ratio is sufficiently small, this difference remains limited. For the stress along the outside wall of the box, again a good qualitative correspondence is observed (RMS deviation = 14.3 MPa which is similar to the deviation at make-up). It is believed that even better results can be obtained if the mesh density in the box is higher.

The stress around the LET of the pin (x = 23.5 mm), where fatigue cracks are observed to initiate, is of prime interest. Since the difference between the results of the two models are negligible at this location and along the entire engaged thread length, it is concluded that the proposed 2D axisymmetric model is a good approximation to study bending situations.

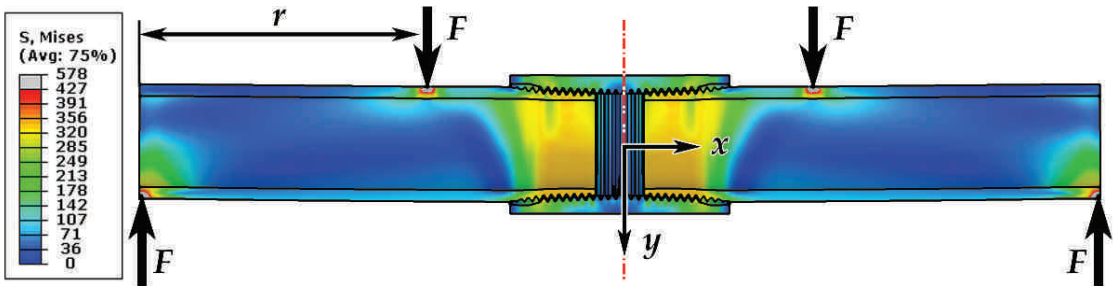

Figure 6.22: Four-point bending forces.

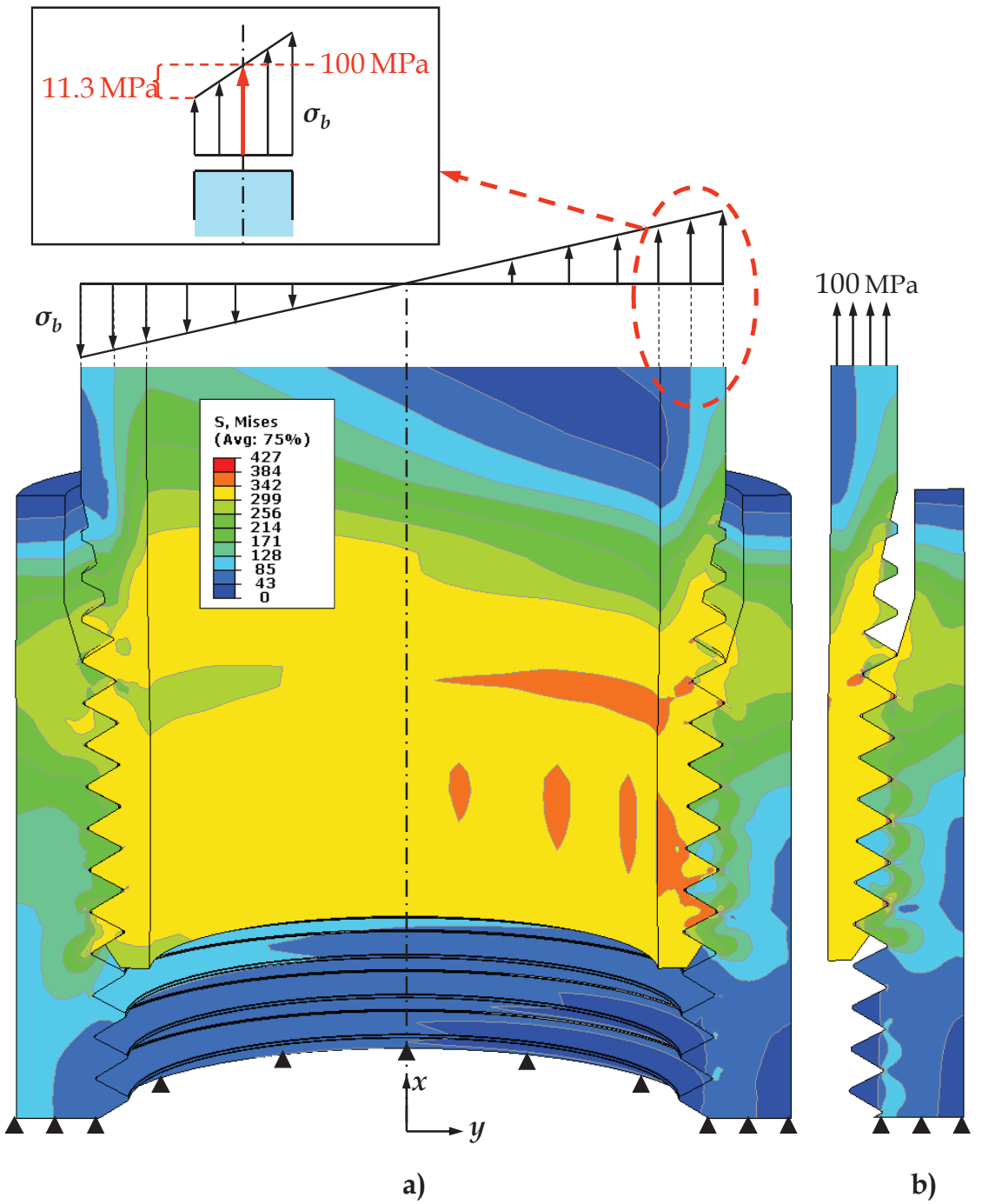

Figure 6.23: Comparison between the von Mises stress for a) bending in the 3D model and b) the corresponding axial tension in the 2D axisymmetric model.

Table 6.3 summarizes the advantages of the 2D model: the simulation of the 2D axisymmetric 1″ API Line Pipe model takes about 6 minutes of calculation time, while the 3D model takes 28 times longer on the same computer system. Additionally, to avoid even longer calculation times, the mesh of the 3D model is considerably coarser. In the 2D model the thread roots of the pin are seeded with 22 elements, while in the 3D model only 3 elements are used. Therefore the stress field at the thread roots in the 2D model is resolved more accurately than in the 3D model.

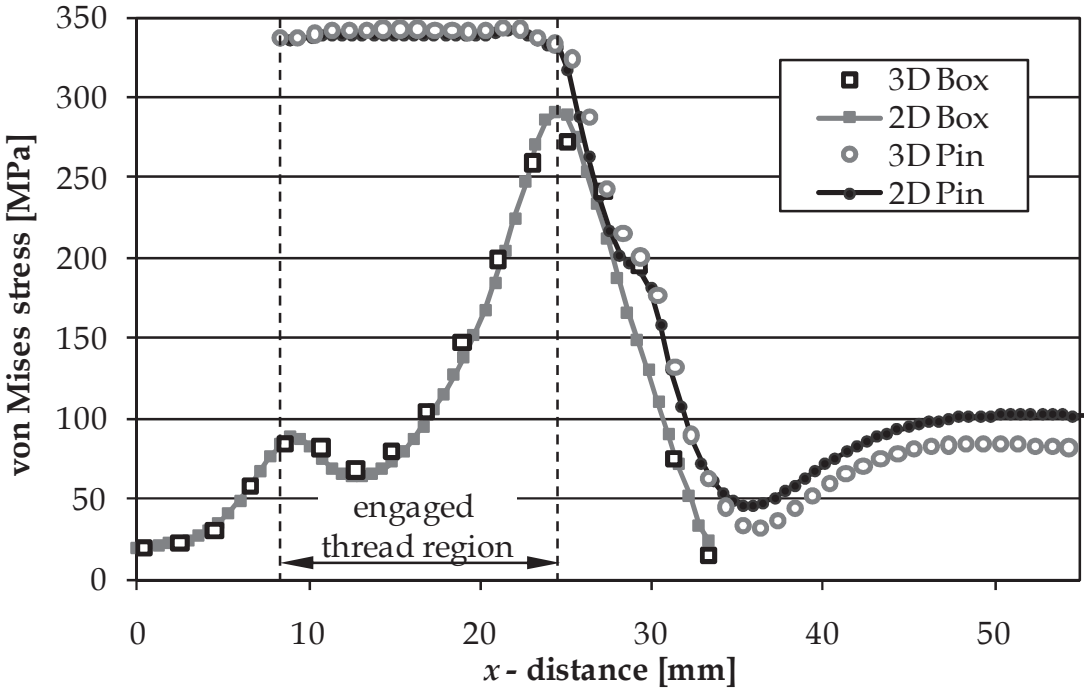

Figure 6.24: Von Mises stress along the inside pin wall and outside box wall for the made up connection with an additional load.

	2D axisymmetric model	**3D model**
Calculation time	6 min	2 h 51 min
Total number of elements	13 515	69 762
Elements around thread root	22	3

Table 6.3: Calculation details of the 2D and 3D model.

6 Model validation

In this section the finite element model is validated by comparing the experimental results of the static tests described in Chapter 5 with the corresponding results of the 2D axisymmetric finite element program.

6.1 Make-up validation

To validate the modelling of the make-up stage, the strains measured on the made-up connection are compared with the modelled strain values. As described in section 3.2.3 of Chapter 5 the effective number of 0.80 make-up turns taking into account the necessary rotation for the settlement of the connection during the experiments is used in the models. Furthermore, the actual measured thread taper values of pin and box are used in the model.

The resulting axial, hoop and shear strains are respectively shown in Figure 6.25, Figure 6.26 and Figure 6.27. The points in the graphs are the values measured by the strain gauges (SG) and the lines are the simulated strains along the inside wall of the pin and the outside wall of the box. The gauge length of the strain gauges is 3 mm. Hence, the measured values are the mean strains over a region with a length of 3 mm. A good qualitative and quantitative correlation can be observed. Since the box is the most rigid part of the threaded connection, the magnitude of the strains in the box is generally smaller than the magnitude of the pin strains. The maximum axial strain values appear around the location of the LET at the inside wall of the pin. Similar to the hoop stress situation described in section 4.1, the hoop strains in the pin are compressive and tensile in the box. It is also confirmed that the shear strains remain limited. The overall correspondence is good. The root mean square deviation (RMS) between all measured and modelled strains is 78 με. Compared to results found in literature, previously described in Chapter 2, the measurements show the same trends as the axial and hoop strain measurements from the make-up tests of Yuan et al. [6.9-10] carried out on API Round Non-Upset Tubing T&C threaded connections.

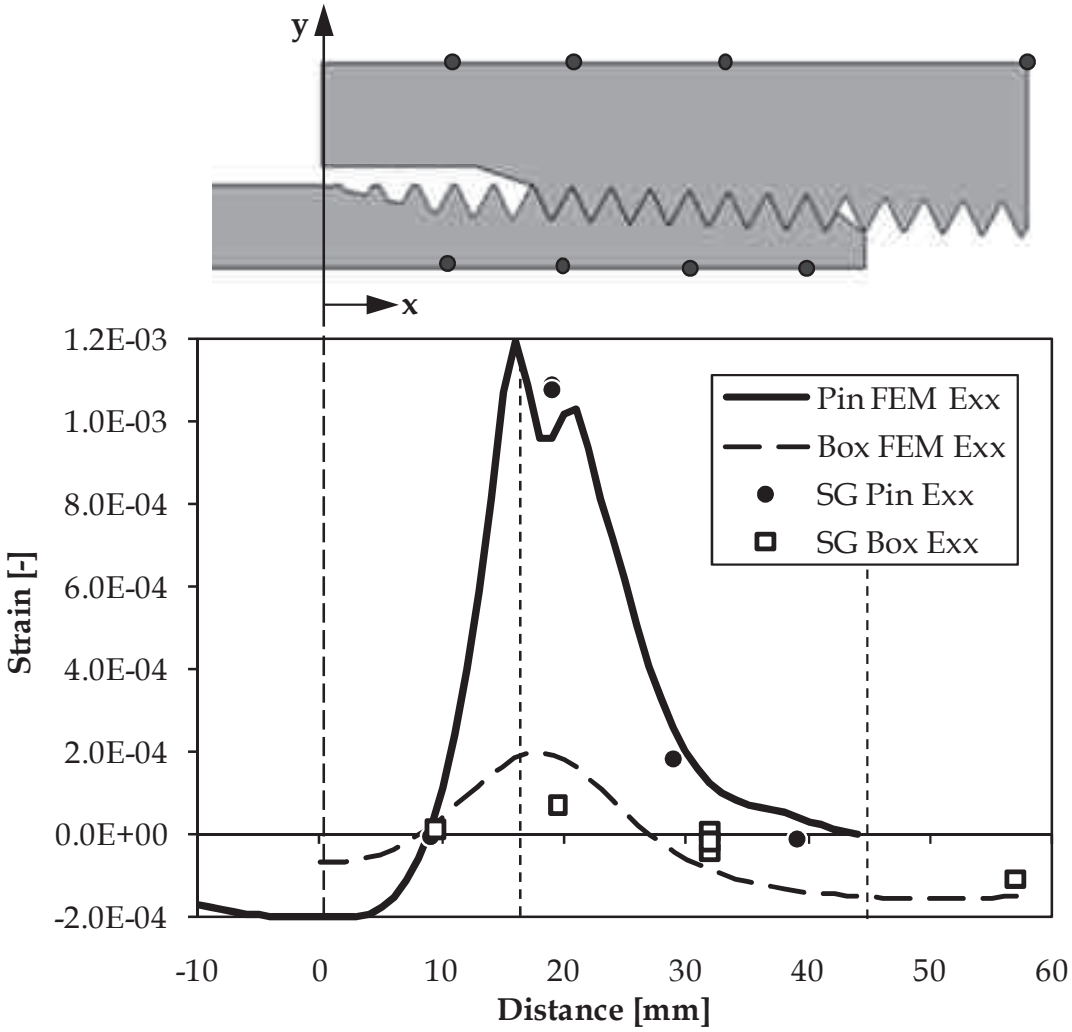

Figure 6.25: Experimental vs. simulated axial strain values due to make-up.

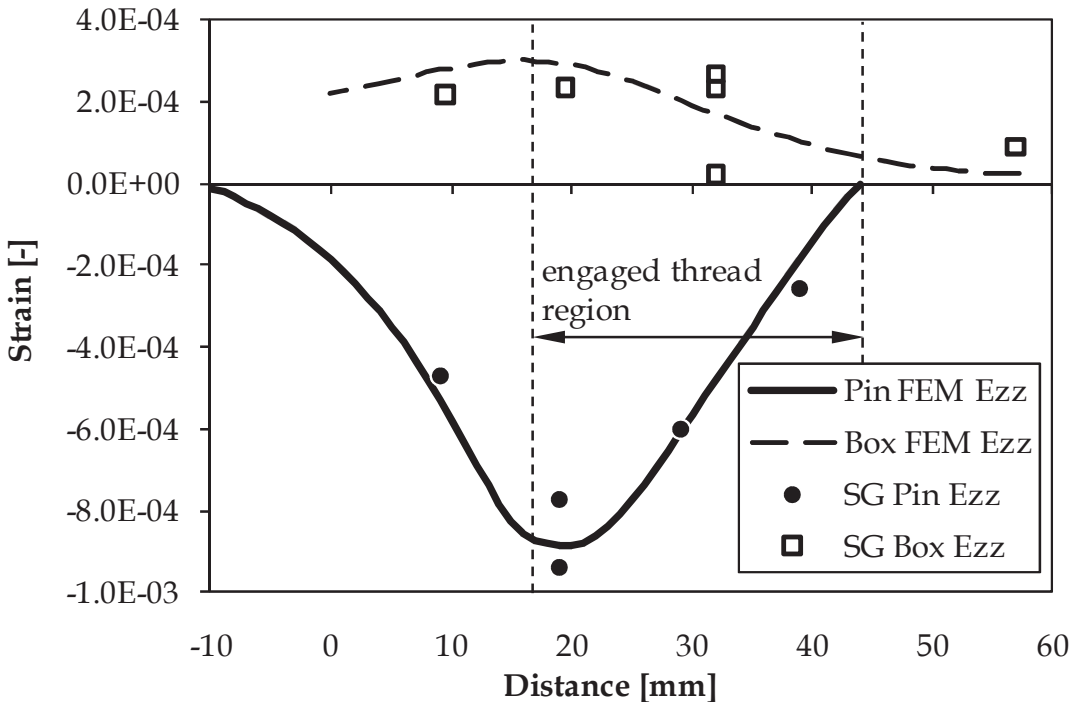

Figure 6.26: Experimental vs. simulated hoop strain values due to make-up.

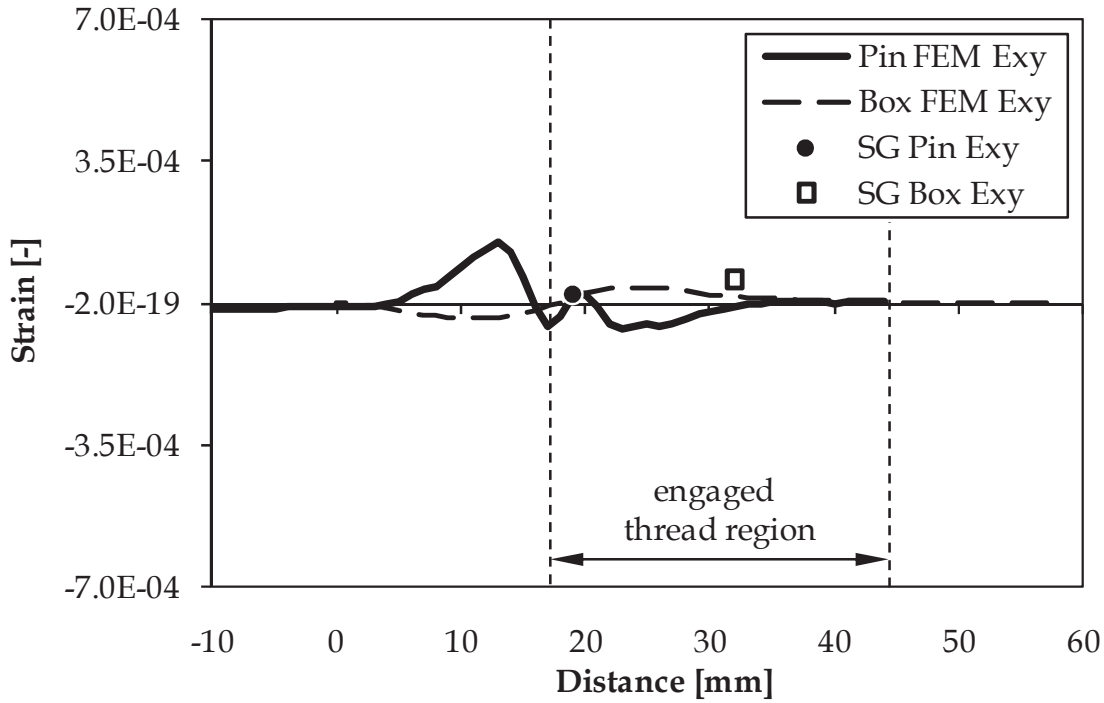

Figure 6.27: Experimental vs. simulated shear strain values due to make-up.

6.2 Axial tension validation

During the axial tension test described in section 3.3 of Chapter 5, a uniform axial tensile load is applied on a 4.5" API Line Pipe connection. Hence, an axisymmetric load case is created. The strains measured during this test serve as a validation for the 2D axisymmetric model with a uniform axial load. In

Figure 6.28-30 the strains are compared for a uniform axial tensile stress of 150 MPa. The strains are given relative to the made-up situation.

Strain gauges 1 and 3 on the pin (as given in Figure 5.8) failed during the test, hence for these locations no measured strain value is given.

For all strain components, the results obtained by the finite element model are in good agreement with the measured strains. The RMS deviation is 84 με, which is comparable to the deviation obtained for the connection make-up validation test. Consequently, the model is validated for the axisymmetric load cases of make-up and axial tensile loading.

Compared to the strain measurements of a premium shouldered connection subject to an axial load of Dvorkin et al. [6.11], the strains measured in this study show similar trends. However, the torque shoulder of the premium connection affects the strain distribution.

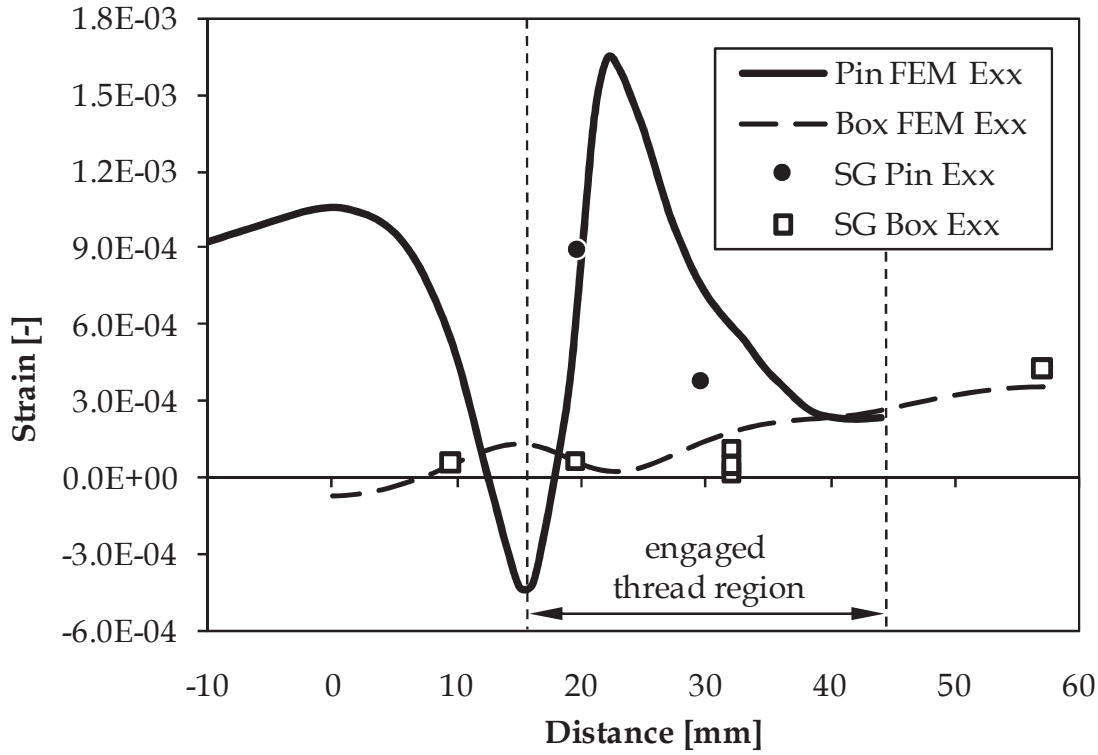

Figure 6.28: Experimental vs. simulated axial strain values due to an axial tensile stress of 150 MPa.

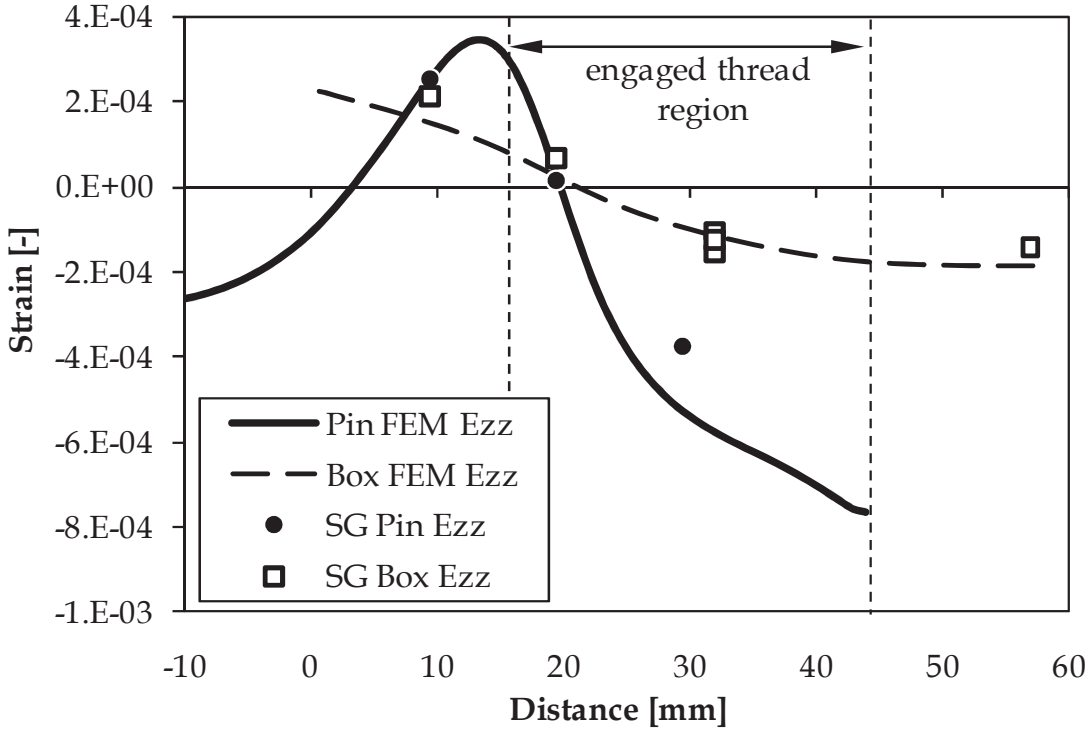

Figure 6.29: Experimental vs. simulated hoop strain values due to an axial tensile stress of 150 MPa.

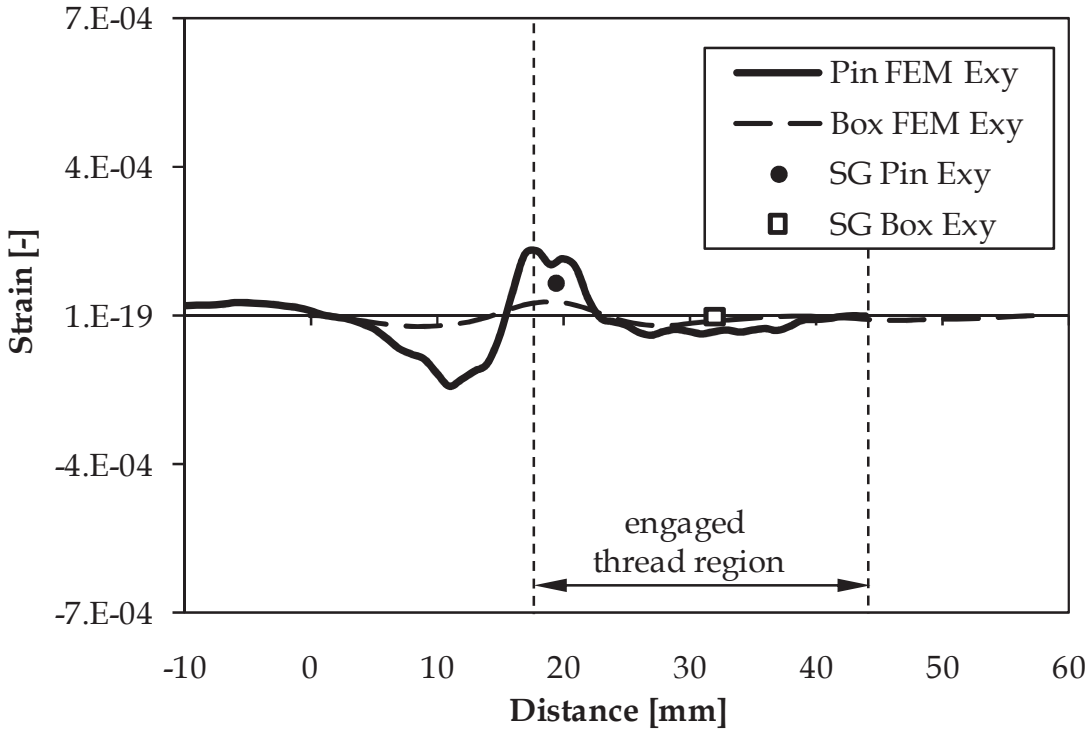

Figure 6.30: Experimental vs. modelled shear strain values due to an axial tensile stress of 150 MPa.

6.3 Bending validation

During the first test on the 4.5" API Line Pipe specimens carried out on the medium scale four-point bending setup, axial strain gauges were attached on the outer fibre of the pipe body of the pin and on the outer fibre of the box at the location of the LET. In Figure 6.31 the measured axial strains are given as a function of the applied bending stress and compared to the modelled values. It is noted that in this figure only the strains induced by the bending stress are given relative to the make-up situation. The simulated values of the bending stress in the pipe body are the mean of the bending stress over the wall thickness of the pipe at the bottom section of the pipe where the maximum axial tensile stress appears.

Again both a good quantitative and qualitative correspondence is observed. The RMS deviation between the measured and modelled values is 33 με. This result does not only provide part of the necessary validation of the FEM in general, but more specifically confirms that the 2D axisymmetric approach can be used to model bending. Hence these observations confirm the results obtained by the comparison of the 2D with the 3D model in section 5.3. It can even be seen that the measured axial strain in the pin is slightly lower than the simulated value, as was also the case in section 5.3 due to the use of an equivalent axisymmetric load in the 2D model.

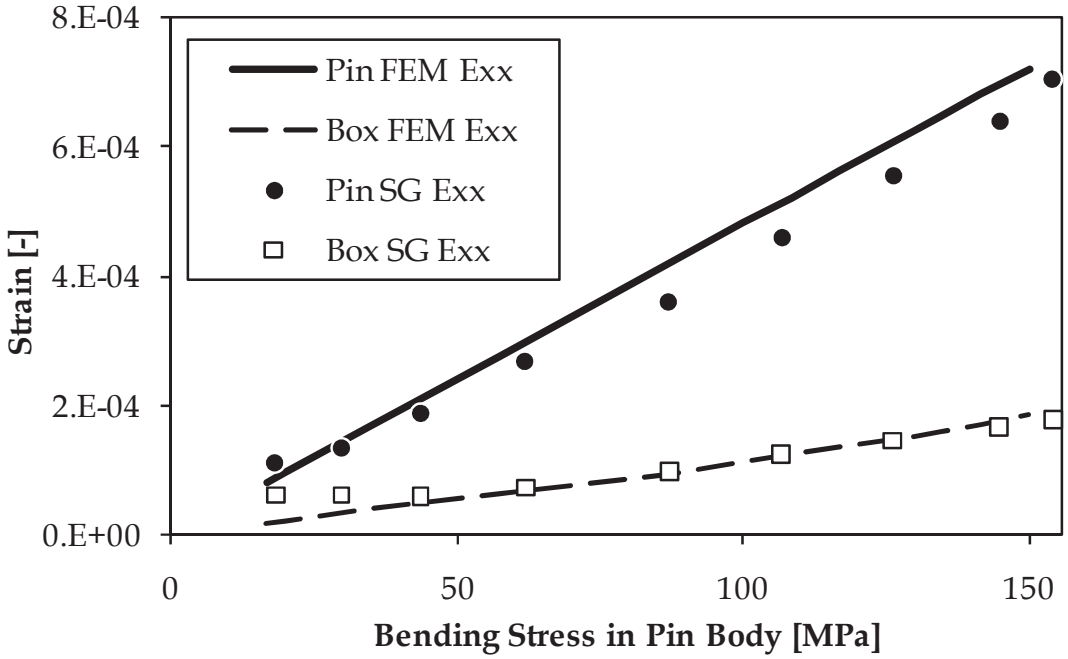

Figure 6.31: Experimental vs. simulated axial strain values of a 4.5" API Line Pipe specimen in the medium scale four-point bending setup.

6.4 Internal pressure validation

The last validation test performed, is the internal pressure test described in section 3.4 of Chapter 5. In that section it was already pointed out that the

measured strains in the pipe body are identical to the analytically calculated values by the linear elastic theory of Lamé.

In Figure 6.32-33 the measured strains at an internal pressure of 500 bar are compared to the results of the finite element model. The strains at the outside wall of the pin and box are plotted, the values are given relative to the made up situation.. It is noteworthy that the hoop strains in the box are lower than in the pin since the box is the more rigid part. The difference between the measured and simulated strain values is negligible, the RMS deviation is 35 με. Hence, the validity for the FE model to simulate internal pressure is hereby provided.

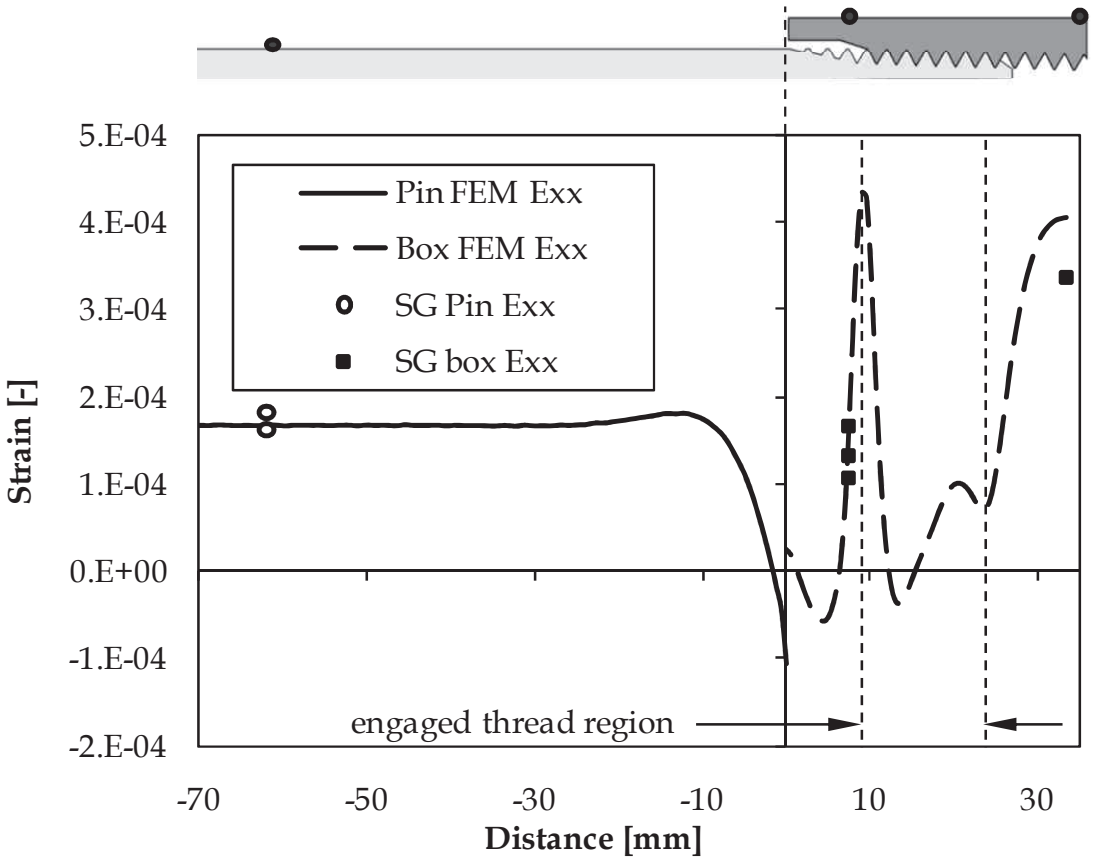

Figure 6.32: Experimental vs. simulated axial strain values of a 1″ API Line Pipe specimen subjected to an internal pressure of 500 bar.

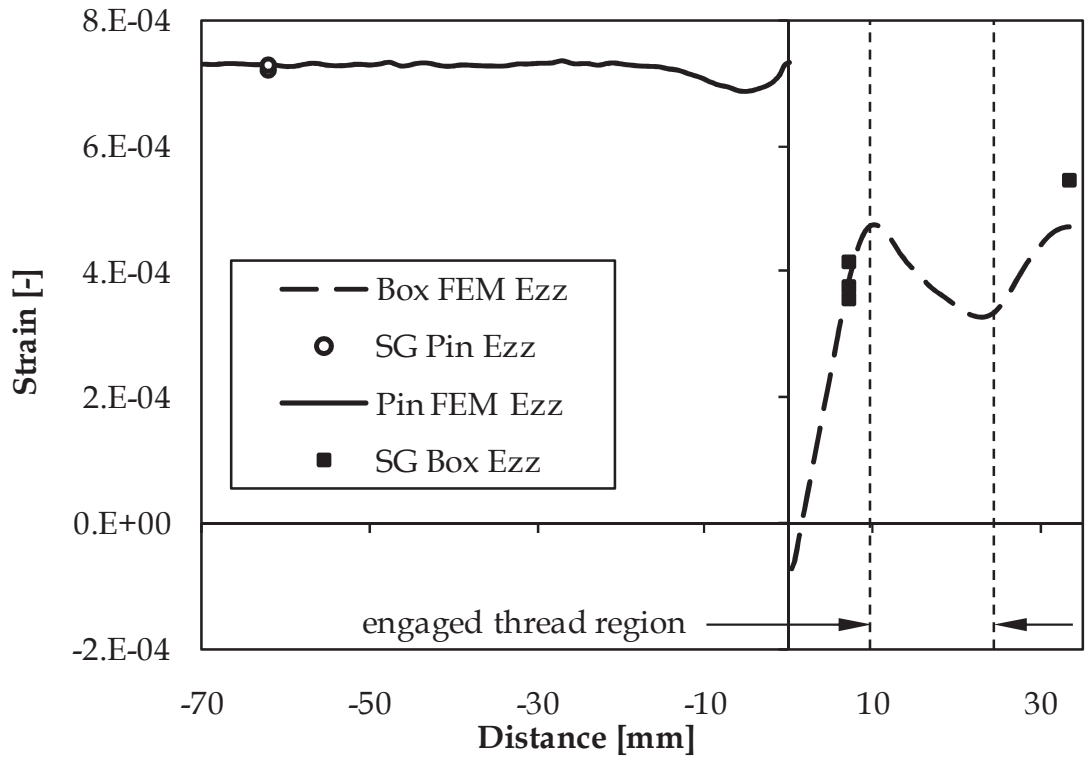

Figure 6.33: Experimental vs. simulated hoop strain values of a 1″ API Line Pipe specimen subjected to an internal pressure of 500 bar

7 Summary and conclusion

In this chapter the parametric finite element program ThreadGen© is introduced. With this program it is possible to create a 2D axisymmetric model geometry of a threaded connection and to perform a detailed stress analysis based on a number of geometrical parameters. The model mesh is automatically generated and elaborate contact behaviour is included. Next to this, the necessity of using elastic-plastic material properties is shown by the appearance of plastic deformation during the make-up stage.

To validate the 2D approach, a comparison is made with a full 3D model. As also found in literature, the stress state resulting from make-up for both models is as good as identical. In addition, a comparison is made between a 3D model under four-point bending and a 2D axisymmetric model with an equivalent uniform axial tensile stress. It is shown that also for these load cases, the stress states around the engaged threads are similar. This means that the used approach is suitable to analyse the results of the performed experimental four-point bending tests.

Furthermore the validity of the model is proven experimentally. This is done by comparing simulated strain values with strain gauge measurements for four different load cases: make-up, axial tension, bending and internal pressure. For all load cases the differences between the measured and modelled strains are negligible.

In previous work the validity of 2D axisymmetric models was always assumed. These assumptions were based on the results of photo-elastic scale models under simple linear elastic load cases. In this chapter however, the validity of these assumptions is rigorously proven and extended to real elastic-plastic material behaviour and non-linear contact properties. Hence, a fully validated model is presented that is suitable of modelling a wide variety of load cases.

References

[6.1] API Specification 5B, Specification for Threading, Gauging and Thread Inspection of Casing, Tubing and Line Pipe Threads (U.S. Customary Units), American Petroleum Institute, fourteenth ed., 1996.

[6.2] API Specification 5L, Specification for Line Pipe, American Petroleum Institute, forty-second ed., 2000.

[6.3] Dvorkin, E.N., Toscano, R.G., Finite element models in the steel industry: Part II: Analysis of tubular products performance, Computers & Structures, 81(8), 575-594, 2003.

[6.4] Shoji, Y., Sawa, T., Stress concentration at the root of bolt thread, ASME Pressure Vessels and Piping Conference, PVP2010-25857, 2010.

[6.5] Assanelli, A.P., Xu, Q., Benedetto, F., Johnson, D.H., Dvorkin, E.N., Numerical/experimental analysis of an API 8-round connection, Journal of Energy Resources Technology-Transactions of the ASME, 119(2), 81-88, 1997.

[6.6] Sanctus, C., Fretting fatigue of aluminium alloy in contact with steel in oil drill pipe connections, modelling to interpret test results, International Journal of Fatigue, 30(4), 677-688, 2008.

[6.7] MacDonald, K.A., Deans, W.F., Stress Analysis of Drillstring Threaded Connections Using The Finite Element Method, Engineering Failure Analysis, 2(1), 1-30, 1995.

[6.8] Zhong, A., Thread connection response to critical pressures, Abaqus users' conference, Paris, France, 690-706, 2007.

[6.9] Yuan, G., Yao, Z., Han, J., Wang, Q., Stress distribution of of oil tubing thread connection during make and break process, Engineering Failure Analysis, 11, 537-545, 2004.

[6.10] Yuan, G., Yao, Z., Wang, Q., Tang, Z., Numerical and experimental distribution of temperature and stress fields in API Round threaded connection, Engineering Failure Analysis, 13(8), 1275-1284, 2006.

[6.11] Dvorkin, E.N., Assanelli, A.P., Toscano, R.G., Performance of the QMITC Element in Two-Dimensional Elasto-Plastic Analysis, Computers & Structures, 58(6), 1099-1129, 1996.

Chapter 7

Parametric Study

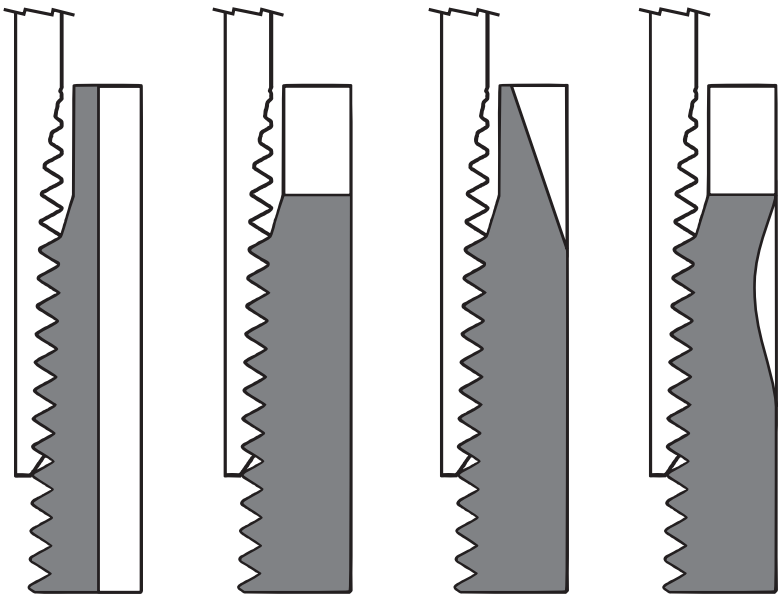

1 Goal

Using the fully validated program ThreadGen presented in the previous chapter, a parametric study is carried out to study the influence of several features on the behaviour of a threaded connection. For this parametric study, the standard 4.5" API Line Pipe connection is used as a reference. The other simulated configurations are obtained by changing this connection's geometry, dimensions or contact properties

As mentioned in the literature review of Chapter 2, the load distribution over the connection's threads is generally considered as one of the defining factors for the strength of a threaded connection. Since an unequal load distribution inevitably causes stress concentrations, the load distribution is often considered as a measure for the fatigue life of a connection [7.1-6]. For this reason, the load distribution is represented by the percentage of the load carried by the LET and this value is compared for different connection designs. In addition, the corresponding values of the thread opening (as introduced in section 4.3 of Chapter 6) are taken into account, since a connection showing a smaller thread opening is less prone to leaking and thread jumpout [7.7].

In this chapter, first the influence of the contact conditions and thread parameters is investigated. Then the box geometry modifications are evaluated, followed by modifications of the pin geometry. Finally a comparison is made between the different considered features.

2 Influence of the thread and contact conditions

2.1 Coefficient of friction

As mentioned in section 2.3.1 of Chapter 2 a wide variety of values for the coefficient of friction (COF, μ) are used, ranging from 0.02 to 0.20 and beyond. Although simulations showed that the value used does not affect the load distribution over the threads, it has an important influence on the thread opening as can be seen in Figure 7.1. The opening at an external gross axial tensile stress of 150 MPa varies from 0.03 mm when μ = 0.16 to 0.41 mm for the frictionless situation (μ = 0). This illustrates the importance of accurate knowledge of the COF to perform accurate finite element simulations.

The graph further reveals that the opening remains negligible until a certain limit stress S_L is reached. From that moment, the separation force causes the threads to slide and the thread opening increases significantly. It can be seen from the graph that the limit stress increases with increasing COF and that paths of the opening during sliding are parallel for the different COF's. Based on the simulations, an empirical relation is formulated for the limit stress S_L

[MPa] and the opening O [mm] of the standard 4.5″ API Line Pipe connection, with S the applied axial tensile stress in the pin body.

$$S_L = 124 + \mu \cdot 169 \tag{7.1}$$

$$O = 0.014\,(S - S_L) + 0.025 \qquad \text{for} \qquad S > S_L \tag{7.2}$$

This relation is only valid for the standard 4.5″ API Line Pipe geometry. As the connection's separation is linked to the jump-out behaviour described in section 3.3.2 of Chapter 5, it is dependent on the thread angle and other connection dimensions.

When the maximum stress during the cyclic loading of a fatigue test exceeds the limit stress, the thread sliding can cause fretting damage at the contact surface. During all experiments in the medium scale four-point bending setup, the limit stress (for $\mu = 0.12$) is exceeded and it was observed that the thread grease at the engaged threads coloured black, which is an indication of fretting corrosion. The appearance of fretting fatigue in threaded connections is studied more in detail by Santus [7.8] but is not further investigated in this work.

During all subsequent simulations the COF equals 0.12 since this value is obtained during the first torque test described in section 3.2.4 of Chapter 5.

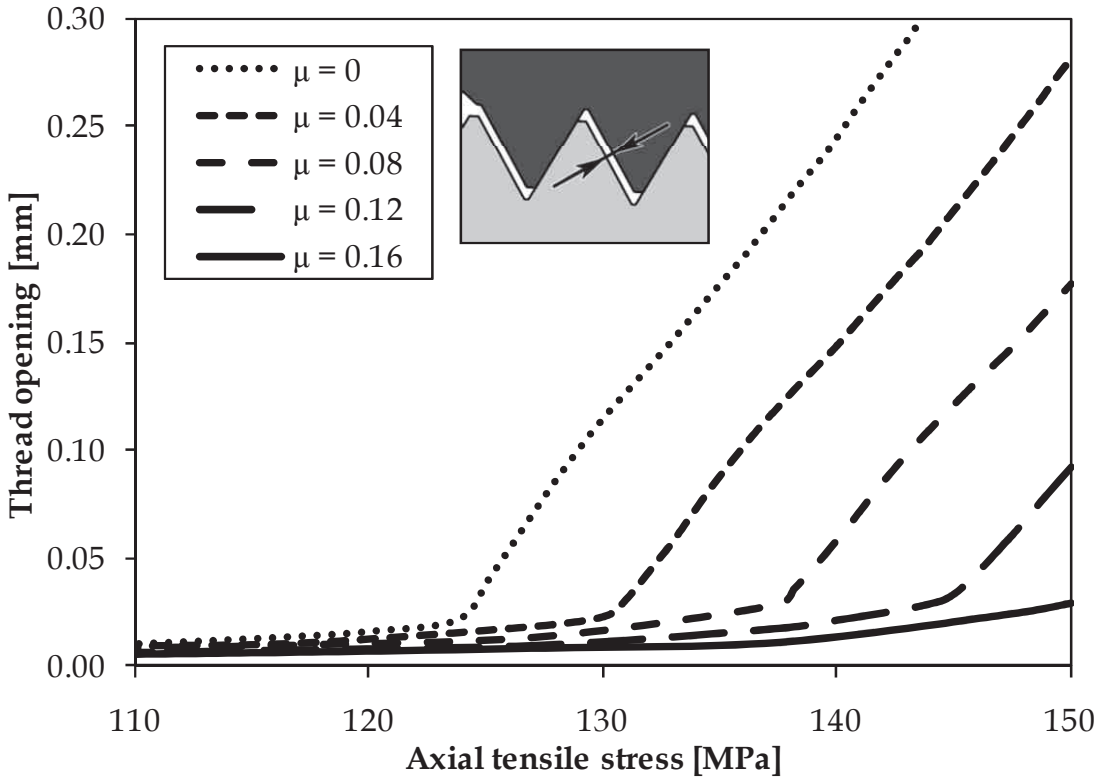

Figure 7.1: Influence of the coefficient of friction on thread opening.

2.2 Number of make-up turns

According to the API 5B specifications, the number of make-up turns for the 4.5" API Line Pipe connection should lay between 1 and 3. Besides, it was shown during the discussion of the torque tests in section 3.2.3 of Chapter 5 that the effective number of make-up turns used in the finite element model should be shifted over 0.3 turns due to the settlement of the connection. Hence, to study the influence of the acceptable make-up range on the connection behaviour, values should be considered between 0.7 and 2.7 turns. As mentioned previously in Chapter 6, all simulations on the 4.5" connection are evaluated with a single effective make-up turn, unless stated otherwise. This is based on the results of the torque experiments.

In Figure 7.2, both the thread load at the LET of the pin and the thread opening are evaluated every 0.25 turns between 0.25 and 3 rotations. Since the thread opening becomes significant only after a certain limit stress, it is evaluated at the highest applied gross axial tensile stress of 150 MPa. At this stress, however, the LET is bended, changing the load distribution over the threads. In addition, this stress is relatively high for fatigue applications. Hence, the relative thread load is defined at a lower external axial stress of 100 MPa where the load distribution is more representative for the overall behaviour of the connection.

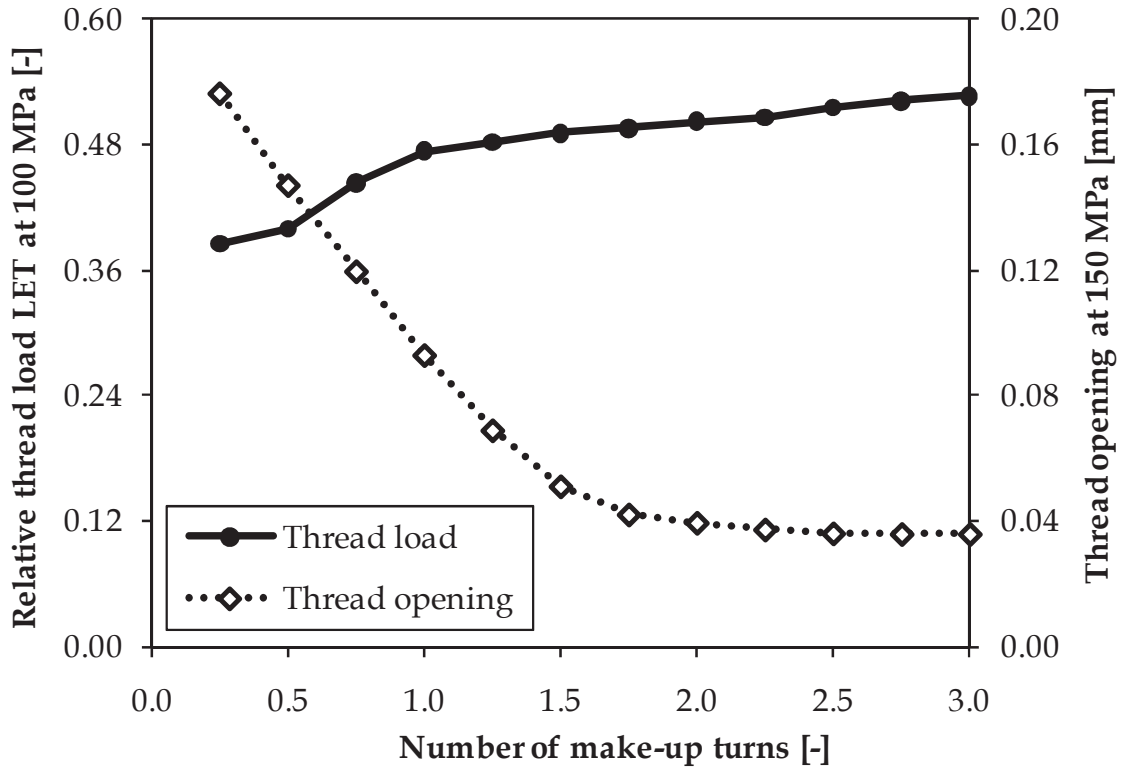

Figure 7.2: Influence of the number of make-up turns on the relative thread load and thread opening.

It is clear that the thread load at the LET of the pin increases gradually from 47% to 53% for 1 to 3 make-up turns. For lower values, the thread load decreases more significantly to 36%. Although this trend promotes a number of make-up turns as low as possible, it has the clear downside that the thread opening becomes more and more important because the frictional forces that prevent separation of the threads are reduced. Furthermore it is obvious that a very low number of make-up turns would result in an insufficiently tightened connection. In addition, it was shown by Newport and Glinka [7.9] and pointed out in section 2.2.2 of Chapter 2 that in fatigue applications, a certain make-up stress is beneficial for a connection's fatigue life as the preload reduces the local stress range at the threads. This will be confirmed by the fatigue analysis in the next chapter.

2.3 Taper difference

The taper angle of both pin and box of the API Line Pipe connection is specified to have a nominal value of 3.576° and can be maximum 3.873° or minimum 3.428°. By comparing different simulations, it is found that within this range, the exact taper angle does not have a significant influence on the connection's behaviour, whereas a taper mismatch, characterized by the taper difference Δt, can cause an important change. The taper difference Δt [°] is defined by:

$$\Delta t = \alpha_{box} - \alpha_{pin} \tag{7.3}$$

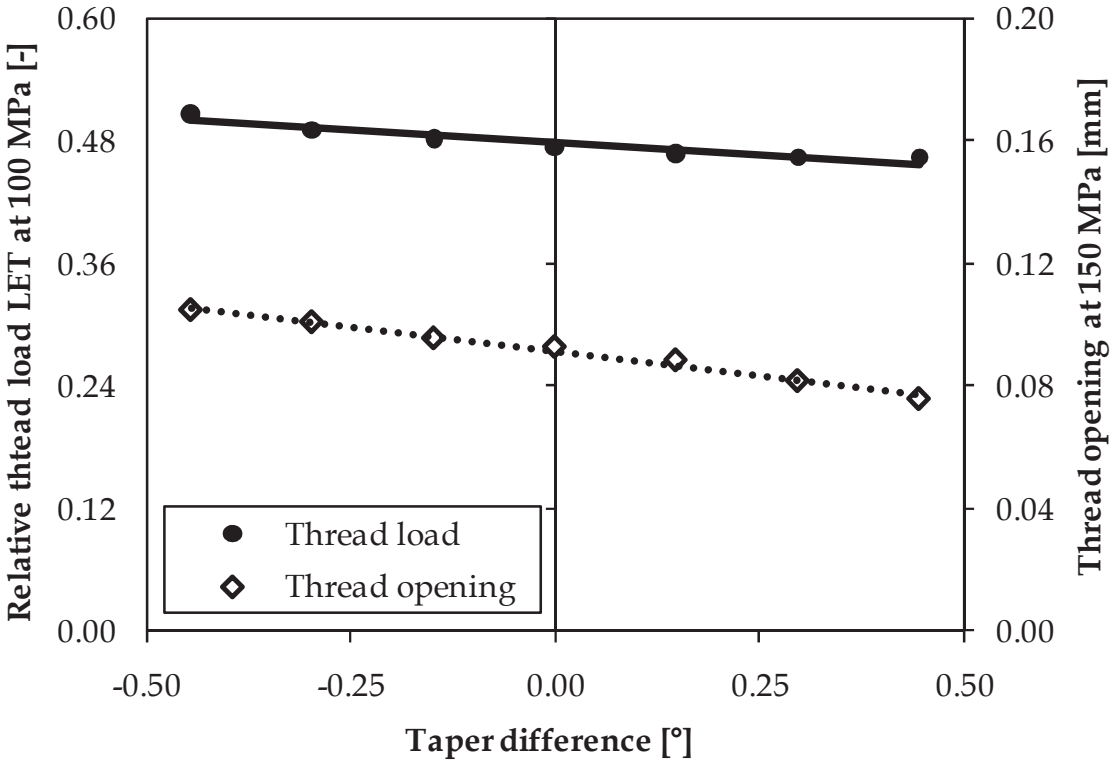

Figure 7.3: Influence of taper mismatch on relative thread load and opening.

Although the changes are limited, it can be seen in Figure 7.3 that both the thread load at the LET of the pin and thread opening decrease with increasing taper difference. Hence a positive taper mismatch is beneficial for the properties of the threaded connection. This is because a positive taper mismatch provides a larger overclosure at the first engaged threads of the pin, while the last engaged threads of the pin have a decreased overclosure. This way part of the load is transferred to the first engaged threads of the pin and a more uniform load distribution is obtained.

2.4 Thread pitch

Figure 7.4 shows the influence of the thread pitch, given as the number of threads per inch *tpi*. The standard 4.5" API Line Pipe connection carries 8 threads per inch. Decreasing the pitch length or increasing the *tpi*, decreases the load on the LET of the pin. This is because, when the pitch length is shorter, the thread height is reduced since the thread angle of 60° is fixed. The smaller threads have a lower stiffness and will transfer the load more easily to the different threads. This corresponds to the results obtained by Newport [7.1] using the hybrid modelling technique. The smaller, less rigid threads also result in an increased thread opening.

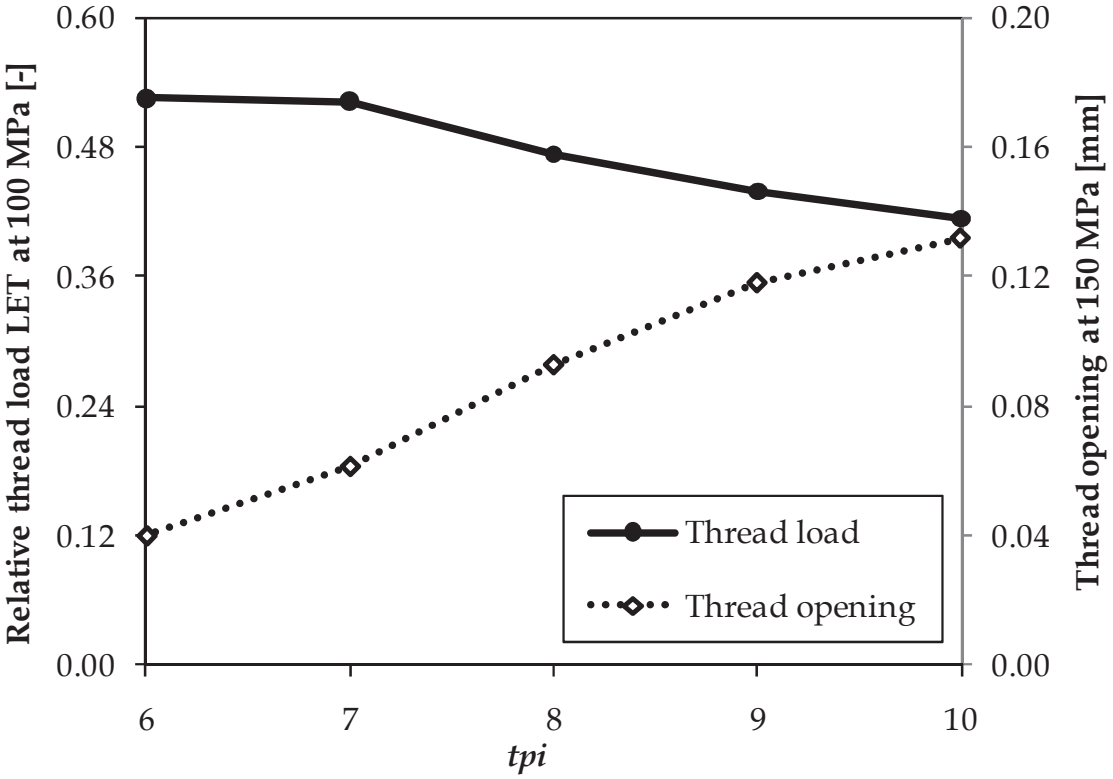

Figure 7.4: Influence of thread pitch on relative thread load and opening.

2.5 Thread type

The influence of the thread type on a connection's fatigue performance is mainly determined by its stress concentration factor.

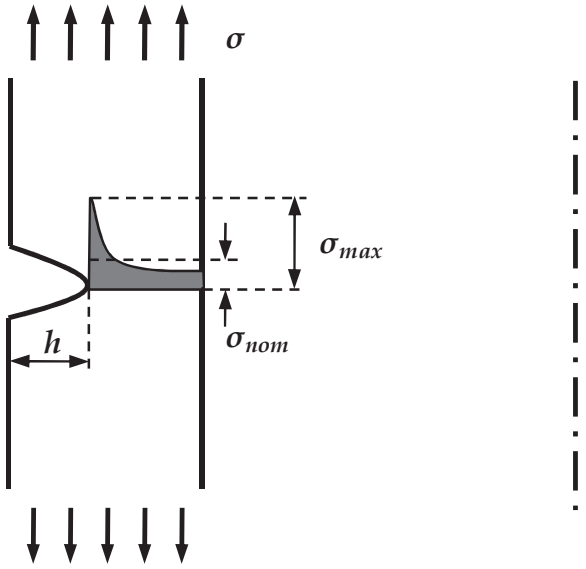

Figure 7.5: Local stresses at a notch in a tube.

When evaluating stress concentrations, it is common practice to make a comparison between the *gross stress concentration factor* K_{tg} and the *net stress concentration factor* K_{tn}. Both factors are explained using Figure 7.5. When a notched tube is subjected to a certain gross stress σ, a stress concentration with a maximum value σ_{max} is induced. The relation (7.4) between this gross stress and maximum value defines K_{tg}. This factor, however, includes a certain size effect, since it will change e.g. when the wall thickness is increased while keeping the same notch size.

$$K_{tg} = \frac{\sigma_{max}}{\sigma} \tag{7.4}$$

$$K_{tn} = \frac{\sigma_{max}}{\sigma_{nom}} \tag{7.5}$$

In order to obtain a stress concentration factor which is more dependent on the notch than on the tube geometry, the net stress concentration factor is defined. This factor is given by the relation (7.5) as the ratio between the maximum appearing notch stress and the nominal stress value over the section of the pipe at the notch location.

To compare the geometrical stress concentration factors of different thread types, a tube with an outer diameter of 114.3 mm and wall thickness of 6 mm is modelled with a single notch shaped like the considered thread. Linear elastic material properties are used and each thread is meshed with a seed size of 0.01 mm. The obtained stress concentration factors are summarized in Table 7.1.

Thread type	Thread height h [mm]	Root radius [mm]	Thread angle	K_{tn}	K_{tg}
API Line Pipe	2.413	0.050	60°	7.9	13.6
API Line Pipe increased wall	2.413	0.050	60°	8.1	11.6
API Round	1.810	0.432	60°	4.2	6.1
BSPT	1.479	0.317	55°	4.4	5.9
API Buttress	1.575	0.203	13°	3.8	5.2

Table 7.1: Geometrical stress concentration factors for different thread types.

The gross and net stress concentration factors of the standard 4.5" API Line Pipe thread shape are respectively 13.6 and 7.9. It can be noted that these values are considerably higher than those obtained with the finite element model, as discussed in section 4.1 of Chapter 6, since in the current evaluation a linear elastic model is used and consequently no plastic relaxation can appear. In addition, the same thread is evaluated in a pipe with a wall thickness of 8.6 mm instead of 6 mm. For this configuration a decreased value of K_{tg} is found, while the K_{tn} value is similar. This illustrates the difference between the two stress concentration factors.

The API Round thread shape is a triangular thread with rounded crests and roots. This smoother thread shape has a clear influence on the appearing stress concentration since the net stress concentration factor is almost half the value of the API Line Pipe thread. The BSPT thread type is similar to the API Round thread, but has a smaller root radius. This results in a slightly higher K_{tn} value of 4.4. Nevertheless, the gross stress concentration factor of the BSPT thread is slightly lower than that of the API Round type since the BSPT thread height is lower.

The final considered thread type is the API buttress thread. Due to its trapezoidal shape with rounded edges and limited thread height, this thread type exhibits the lowest gross and net stress concentration factors.

3 Influence of the box geometry

It is known from Newport [7.1] that changing the hoop stiffness of pin or box affects the load distribution over the threads. The exact correlations and the effect on the overall behaviour of the connection, however, remain unknown. In this study, the influence of the box geometry is evaluated by considering the four different box modifications illustrated in Figure 7.6.

The first modified configuration (Figure 7.6.a) provides a global stiffness reduction of the box by reducing the box wall. Configurations b to d apply to local box stiffness reductions. In Figure 7.6.b the box stiffness is altered by reducing the box recess length. Configuration c is based on the patent of Delange and Evans [7.2] and configuration d contains a bevelled groove as in the patent of Verdillon [7.3].

3.1 Global box wall thickness reduction

In Figure 7.7 the hoop stresses at the inside wall of the pin and the outside wall of the box are plotted for different values of the box wall thickness. When the wall thickness of the box is increased, it becomes more rigid. This means that the deformation of the box during make-up will be smaller and lower tensile hoop stresses will appear. Consequently, for the same number of make-up turns, the pin needs to deform more. For the standard connection, the engaged threads of the pin are exceeding the material's yield strength at make-up.

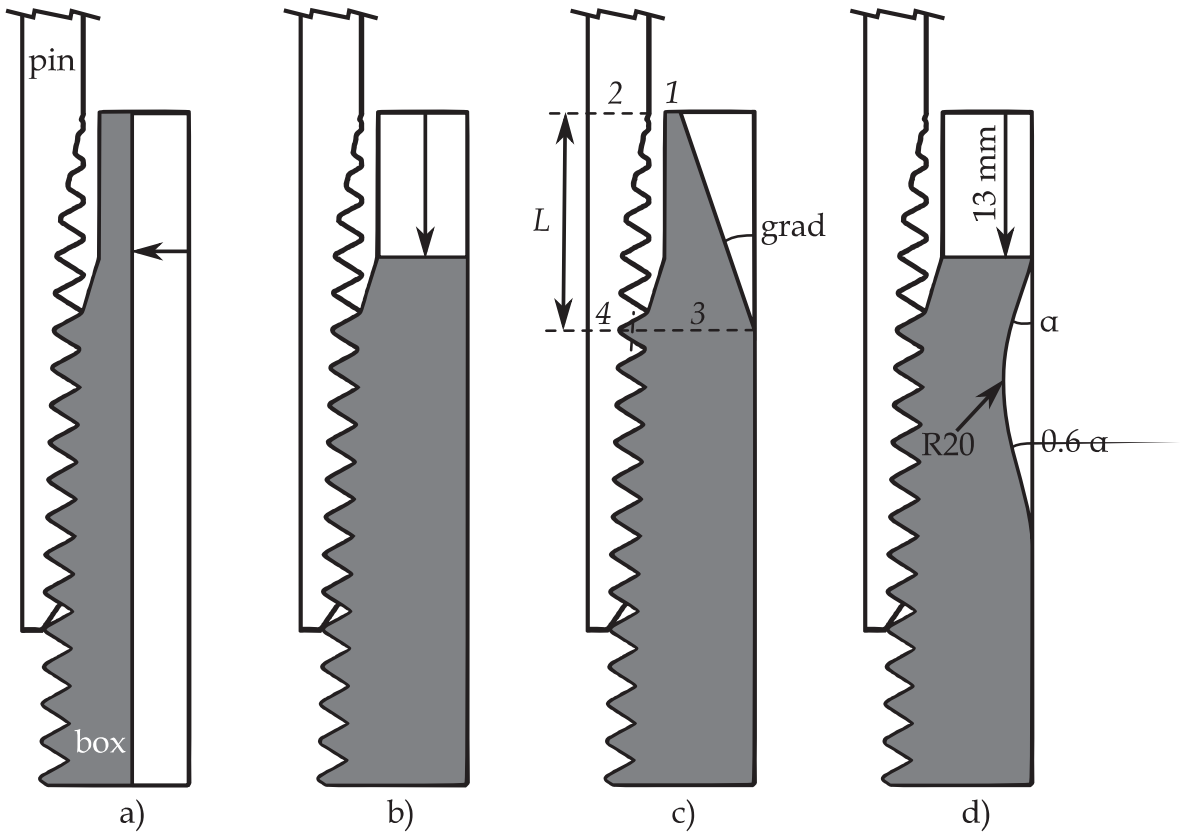

Figure 7.6: Different box modifications: a) wall thickness change; b) recess change; c) gradient; d) bevelled groove.

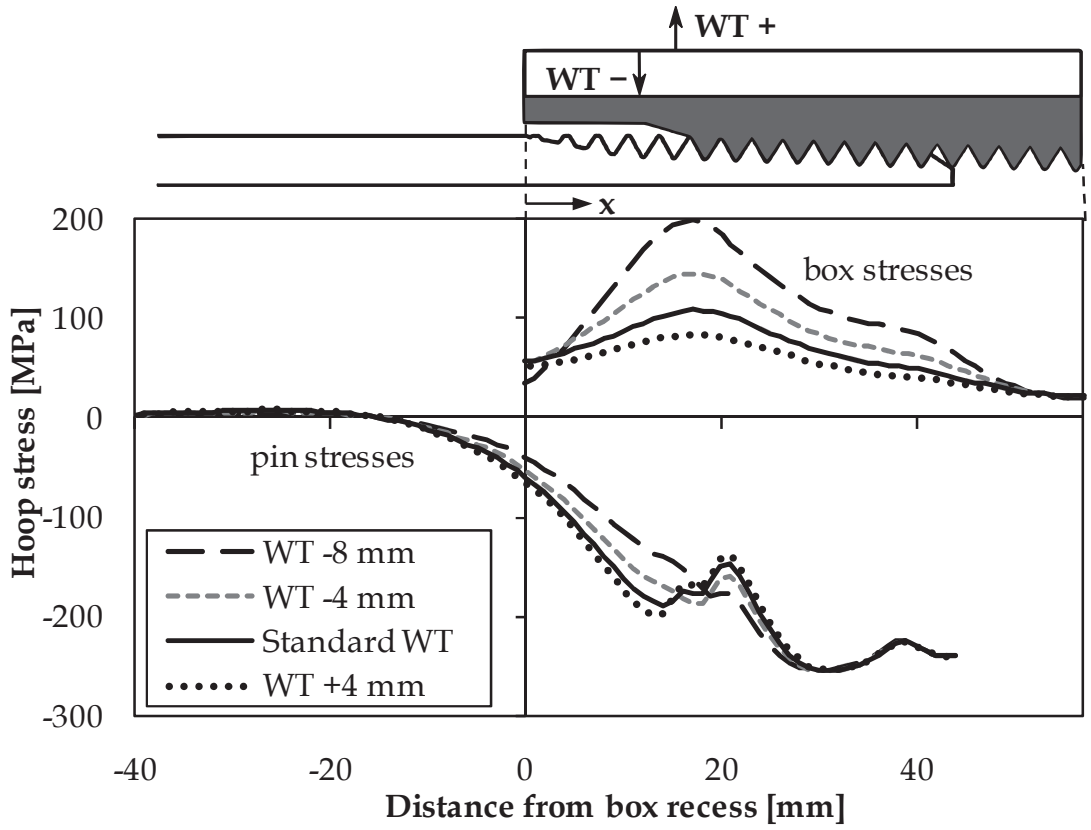

Figure 7.7: Hoop stress at the inside wall of the pin and the outside wall of the box at make-up for different values of the box wall thickness.

A further increase in plastic deformation, for the connection with the increased box wall, does not change the pin hoop stress significantly. But in the runout region of the pin, which does not yield at make-up, the magnitude of the compressive hoop stresses are increased due to the higher box stiffness. When the box wall is decreased, the box stresses increase and the pin stresses decrease in the runout region.

The influence of the box wall thickness on the axial and von Mises equivalent stress caused by make-up is similar to the described effects on the hoop stress.

The influence of a box wall thickness change on a loaded connection is illustrated in Figure 7.8 which shows the results of 16 simulations. With a thinner box, the relative thread load on the LET of the pin is reduced, since the load is transferred more easily due to the increased box flexibility. A relative thread load at the LET of about 41% at an external axial load of 100 MPa can be achieved when the box wall thickness is reduced with 10 mm. However, due to the increased deformation of the box, the thread flank opening will be larger. An increase of the box wall thickness does not result in an increased load at the LET due to the high level of plastic deformation in the connection, but does reduce the thread opening as a consequence of the more rigid assembly.

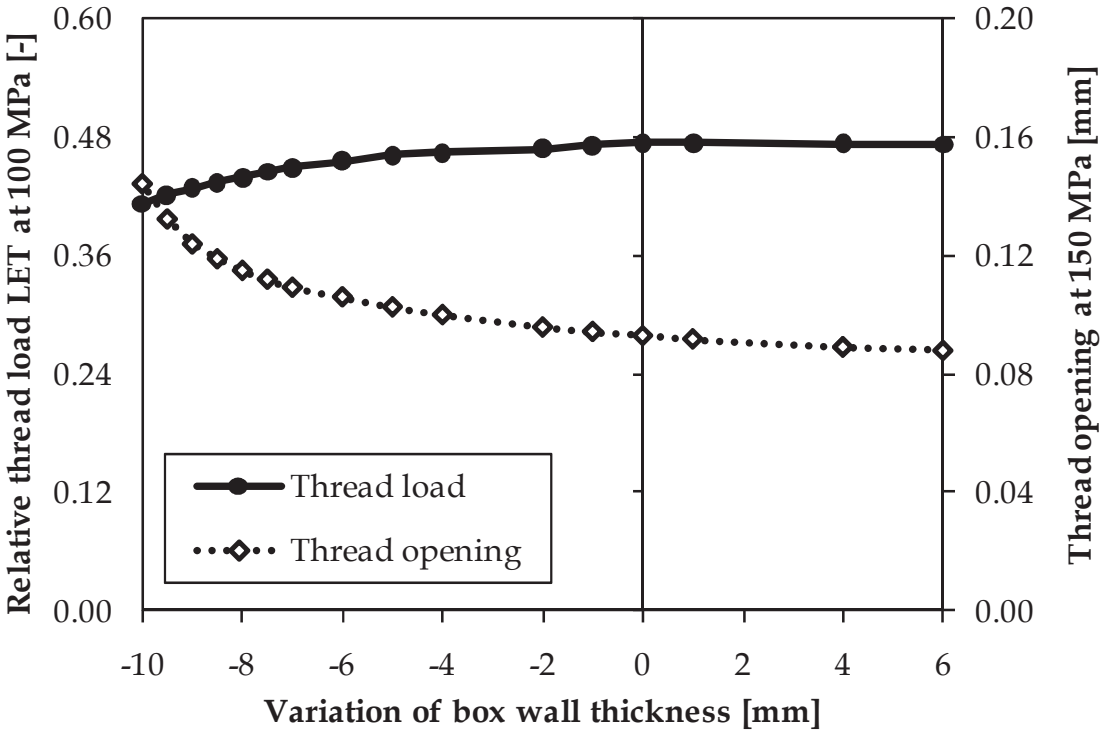

Figure 7.8: Influence of the box wall thickness on relative thread load and opening.

3.2 Local stiffness reduction features

3.2.1 Box recess length

As discussed during the stress analysis of the connection described in section 4.1 of Chapter 6, bending of the box recess causes an increased axial stress in the made up connection. From Figure 7.9 it is clear that this stress can be reduced by decreasing the box recess length (this modification is shown in Figure 7.6.b). By removing the box recess completely (recess length -16 mm) only compressive axial stresses are introduced during make-up. Although the axial stresses in the box are lowered, the maximum box hoop stress increases with a reduced recess length, as is clear from Figure 7.10. Consequently, the hoop stress in the thread runout of the pin is reduced. As can be expected from the previous results, this creates a reduction in thread load on the LET of the pin together with an increased opening.

In Figure 7.11 and Figure 7.12 the results of 36 simulations are summarized to illustrate the influence of the box recess length on respectively the relative thread load and thread opening for different values of the box wall thickness. The effects of the box wall thickness and recess length modifications can be superimposed up to a certain extent. Only when a large box wall thickness reduction is combined with a large recess decrease, the thread opening increases much more importantly.

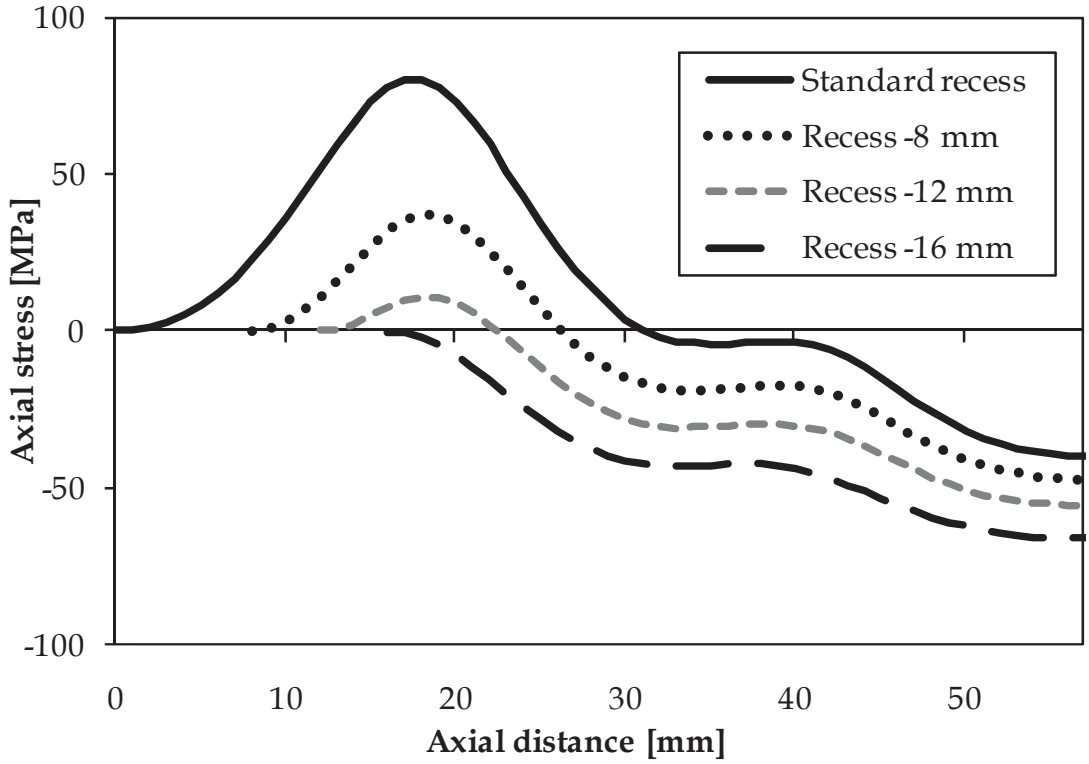

Figure 7.9: Hoop stress at outside wall of the box at make-up for different values of the box recess length.

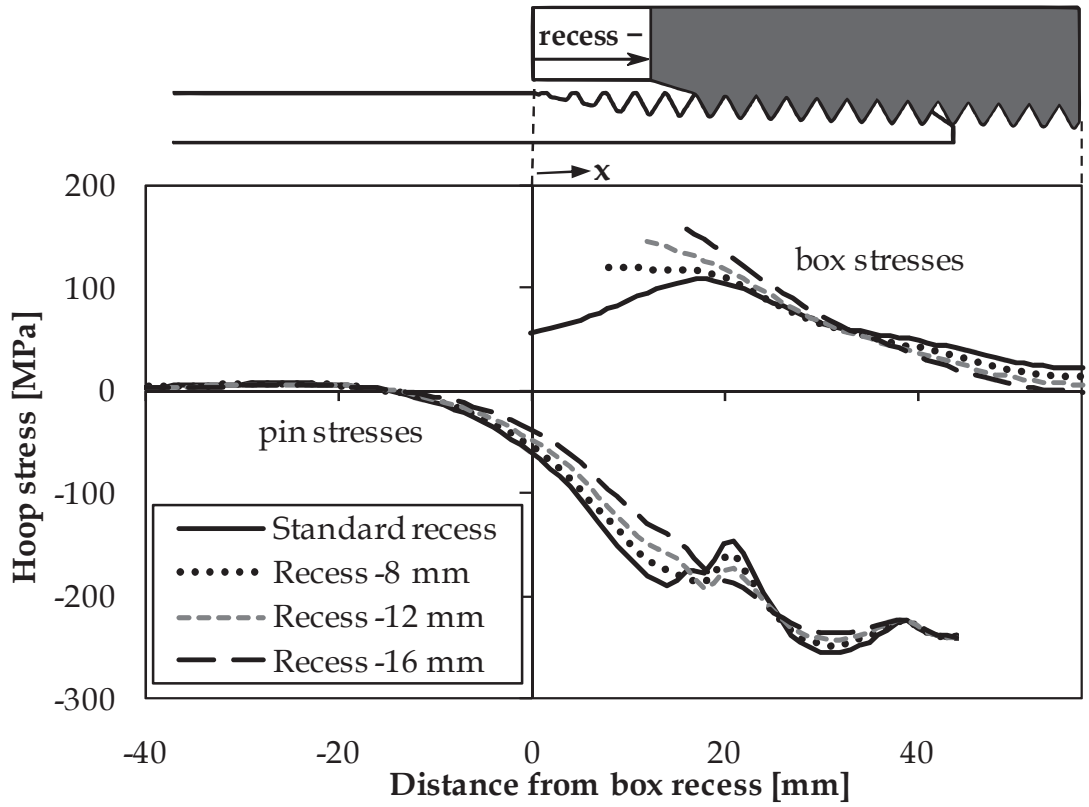

Figure 7.10: Hoop stress at the inside wall of the pin and the outside wall of the box at make-up for different values of the box recess length.

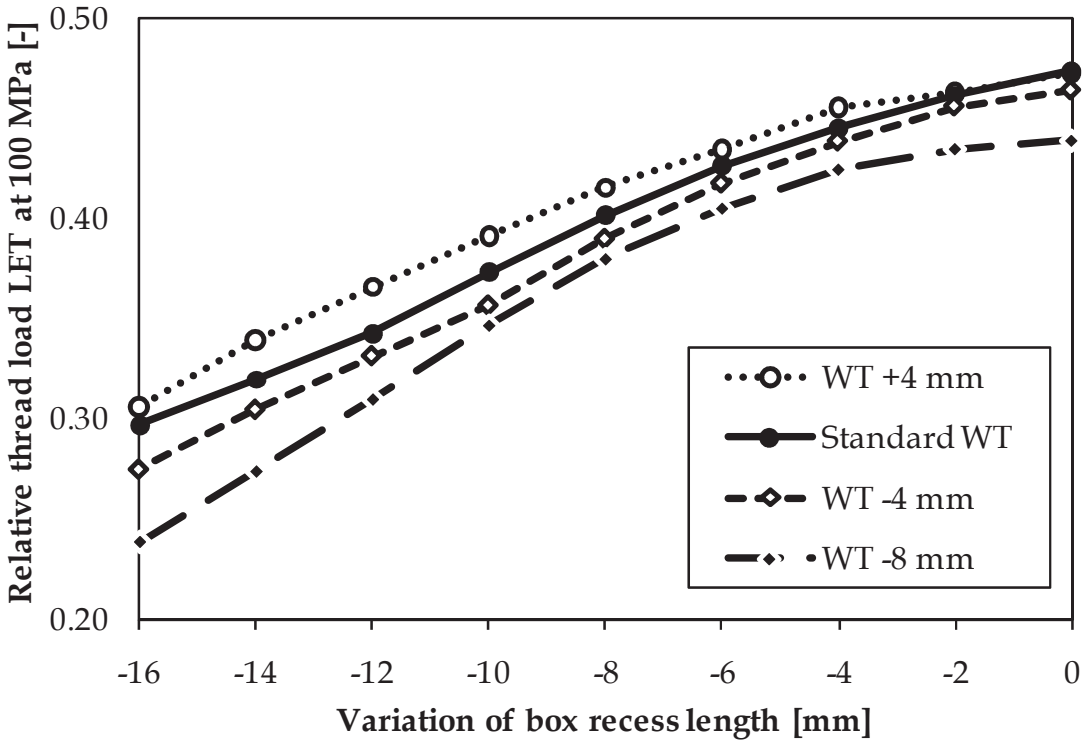

Figure 7.11: Influence of the box recess length on relative thread load for different box wall thickness values.

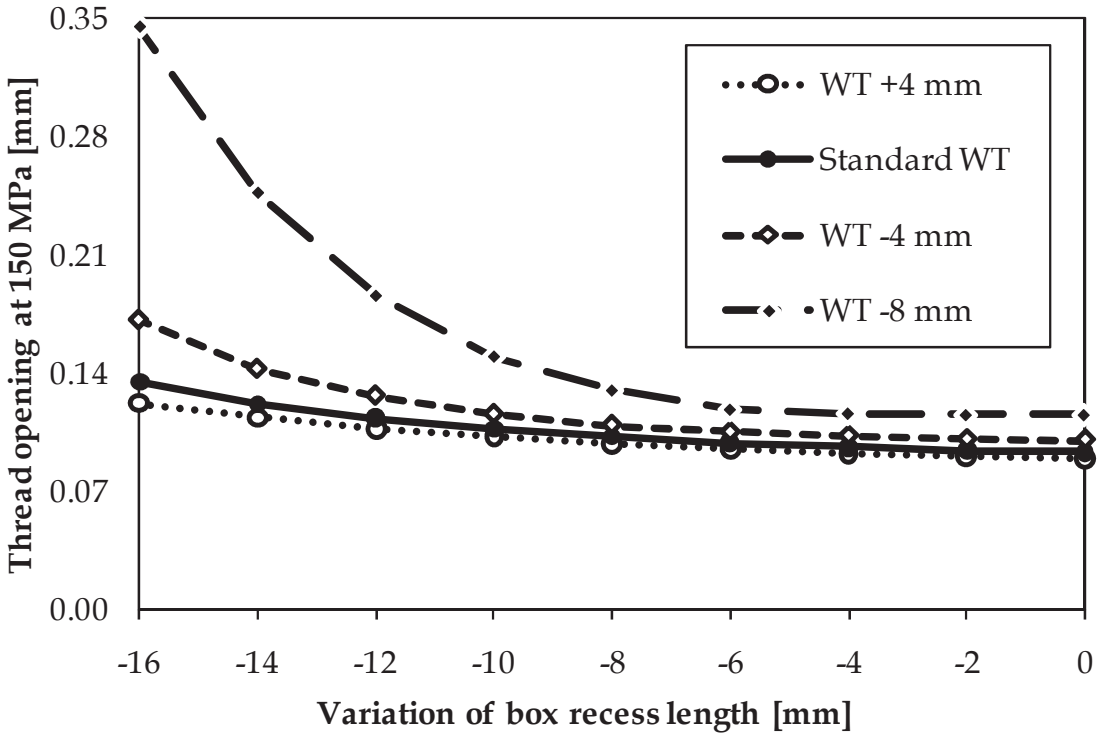

Figure 7.12: Influence of the box recess length on thread opening for different box wall thickness values.

In general, a recess length decrease results in an important decrease of the thread load at the LET. For the standard connection, the relative thread load can be reduced from 47% to 30% of the total load by decreasing the recess length with 16 mm, while the increase in thread opening remains limited. It is noted that the only practical function of the box recess is to work as a guide while assembling the pipe. Hence, in practice the recess could be removed and replaced by a temporary guiding system that is mounted on the coupling during make-up and dismounted afterwards. The thread load can be further decreased by choosing a decreased box wall thickness. However, an optimum is to be determined to keep an acceptable thread opening value.

3.2.2 Stiffness gradient

During the overview of the patented box modifications in section 3.2.2 of Chapter 2, the box modification of DeLange and Evans [7.2] is described. They proposed a *stiffness gradient* of the recess region of the box (as illustrated in Figure 7.6.c) to obtain a better fatigue performance. Hereby the stiffness of the pin or box is equal to the area moment of inertia I_z at a certain section. The stiffness gradient is defined by Delange and Evans as the difference in stiffness ratio between box and pin divided by the length L of the chamfer as noted in Eq. (7.6).

$$\nabla I_z = \frac{\frac{I_{z,1}}{I_{z,2}} - \frac{I_{z,3}}{I_{z,4}}}{L} \tag{7.6}$$

In this equation $I_{z,1}$ and $I_{z,2}$ are respectively the stiffness of the box and pin section at the end of the box recess. The position of both sections is indicated by the numbers 1 and 2 in Figure 7.6.c. It is specified that the chamfer should start at the location of the last fully engaged thread of the pin. Hence, $I_{z,3}$ and $I_{z,4}$ are the stiffness of the box and pin section at LET of the pin calculated at the pitch line of the threads. The gradient is changed from 0 to 1.6. The resulting values of thread load and opening for the loaded connections are plotted in Figure 7.13. An increased stiffness gradient does improve the performance of the connection, which confirms the claims made in the patent. Nevertheless, the improvement is minimal, since the minimum value of the relative thread load is still 44% while with a recess length reduction of 16 mm a value as low as 30% is obtained.

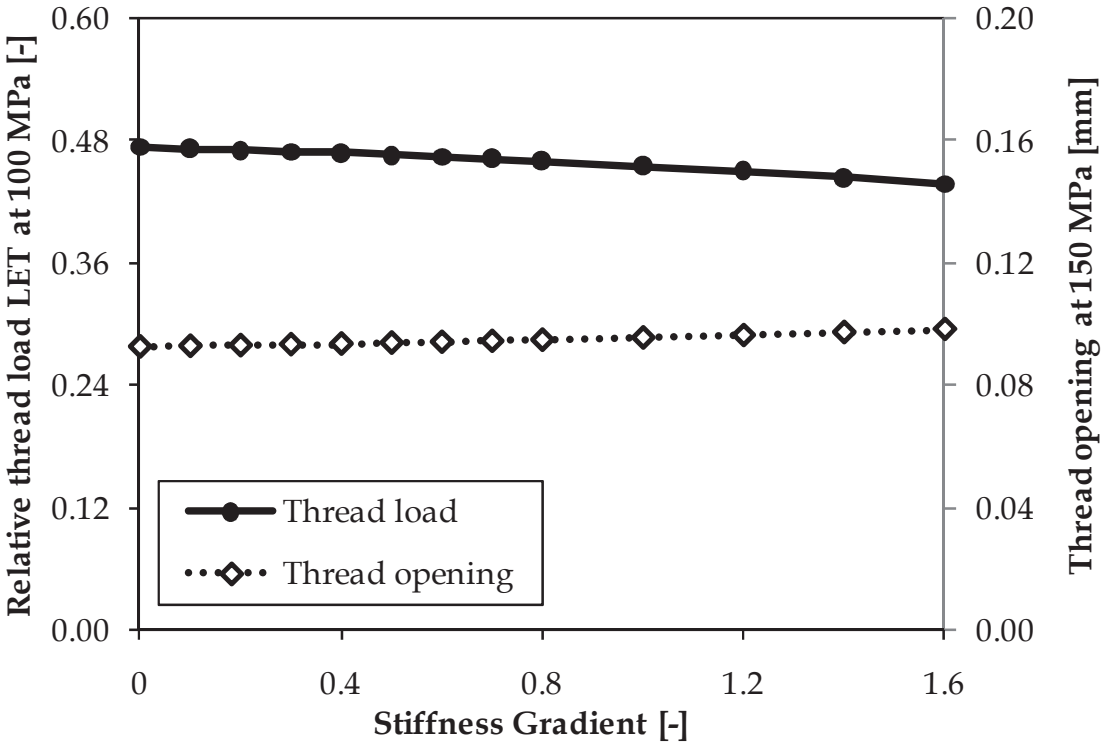

Figure 7.13: Influence of the stiffness gradient on relative thread load and opening.

3.2.3 Bevelled groove

The final discussed box modification consists of a coupling with a recess length reduction of 13 mm combined with the bevelled groove design described in the patent of Verdillon [7.3]. In this patent, described earlier in section 3.2.2 of Chapter 2, the box is waisted by a groove beneath the last engaged threads of the pin in order to obtain a more uniform load distribution. According to the description given in the patent [7.3], the groove is constructed by two sloped edges connected by rounded root. The root should be in the region between the two last engaged threads and a root radius of 20 mm is chosen, as illustrated in Figure 7.6.d. The first edge starts at the right end of the recess and makes an angle α with the original outside wall of the box. This angle will be referred to as the 'primary angle' of the groove. The second edge encloses an angle of 0.6 α with the outside wall of the box.

The primary angle is varied between 0° and 30°. The resulting values of the relative thread load and opening are given in Figure 7.14. The relative thread load at the LET of the pin is reduced from 33% for the box with a recess reduction of 13 mm to 31% for the same box with an additional groove with a 30° primary angle. Hence, as in the case of the patented stiffness gradient, this modification only has a minimal effect on the thread load. The thread opening increase is more important, which is undesirable.

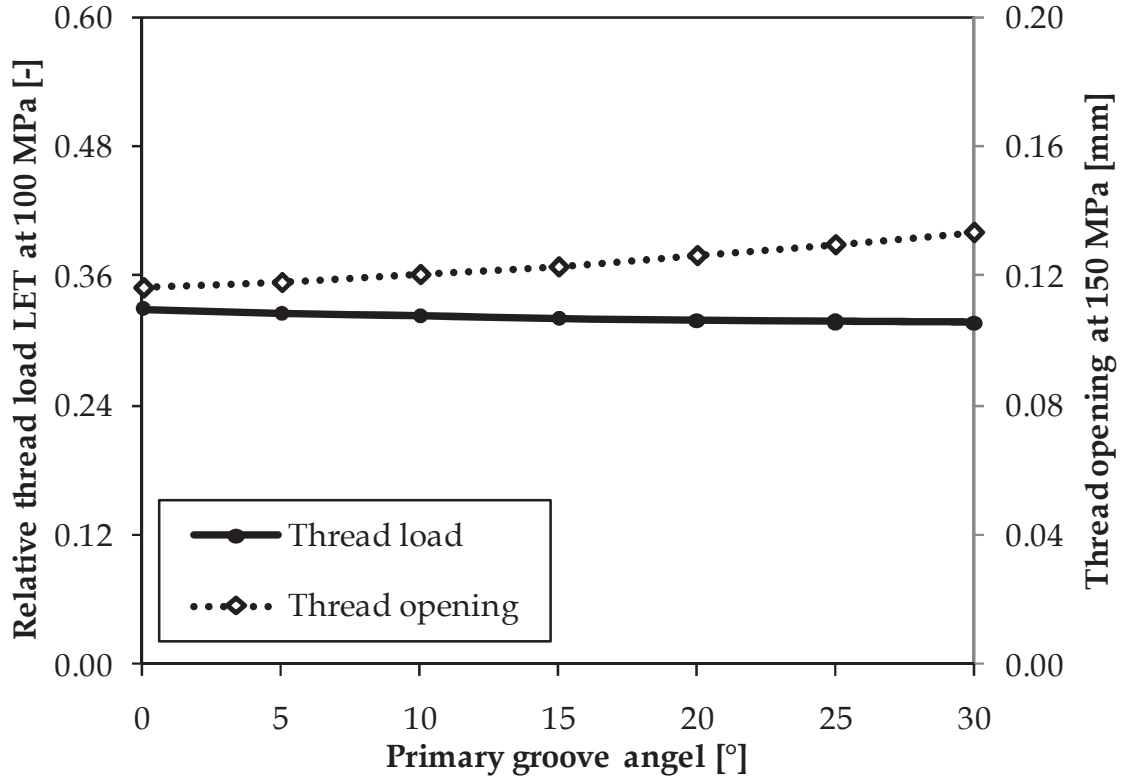

Figure 7.14: Influence of the primary groove angle of the bevelled groove design on relative thread load and opening.

It is worth noting that it is claimed in the patent of Verdillon that the bevelled groove is beneficial for all thread types. However, since the thread load decrease is minimal and the thread opening increases significantly, it is advisable not to use this modification in combination with triangular threads. The groove might give better results for trapezoidal or buttress threads since their thread angle is much smaller. Because of this, the thread forces will be better aligned to the axial direction. Hence the radial tooth force components will be much smaller, reducing the thread opening.

4 Influence of the pin geometry

Next to the discussed box modifications, two pin modifications are evaluated. Firstly, the stiffness ratio between pin and box is changed by modifying the pin wall thickness, secondly the length of the pin is changed, which alters the number of engaged threads of the connection. Both modifications are illustrated in Figure 7.15.

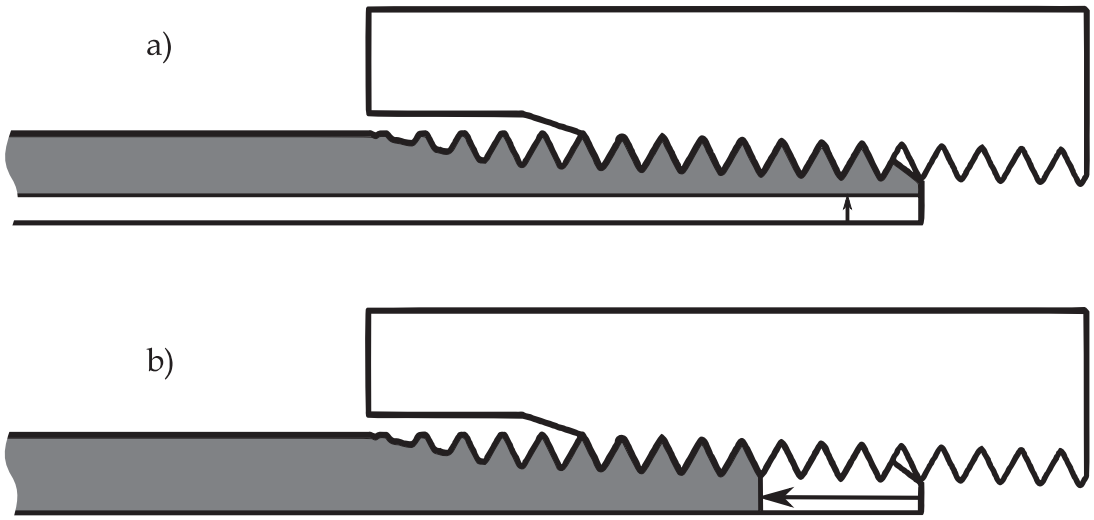

Figure 7.15: Pin modifications: a) pin wall thickness; b) number of engaged threads.

4.1 Pin wall thickness

Because the hoop stiffness ratio of the pin and box is more determining for the thread load than the exact stiffness value themselves, a pin wall thickness change has the inverse effect of a change of the box wall thickness. The resulting behaviour of a loaded connection is summarized in Figure 7.16. When the pin wall thickness is increased, it becomes more rigid. Consequently the load on the LET is decreased.

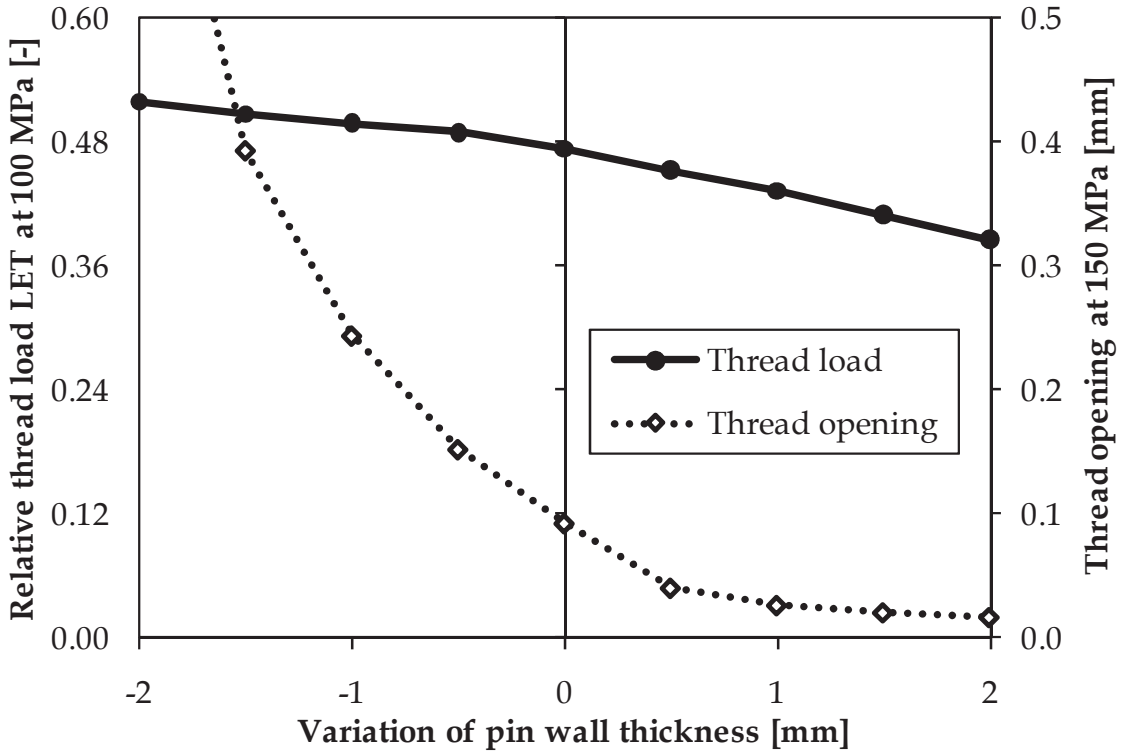

Figure 7.16: Influence of pin wall thickness on thread load and opening.

Important to note is that an increased pin wall means an increase in total force on the connection, as the external applied axial gross stress over the pin wall is kept constant. Nevertheless, the stiffer pin configuration also shows a decreased thread opening value.

4.2 Pin engaged thread length

When the pin length is changed, the number of engaged threads is affected. The standard 4.5" API Line Pipe connection, has 7 fully engaged threads. When the number of engaged threads is decreased, it can be expected that the load on the LET increases significantly (as illustrated in Figure 7.17) since the same load has to be carried by fewer threads. In addition, the thread opening increases significantly. This is because the hoop stiffness is reduced by its shorter length which means the make-up stress will be lower as well as the necessary separation force to create an opening.

When a number of engaged threads larger than 7 is chosen, the thread load at the LET does not change significantly. This is because the load on the added threads is close to zero. The thread opening, however, is reduced significantly when 8 engaged threads are used, but a further pin length increase has no advantages. From these observations one may conclude that the optimal number of engaged threads is 8 instead of 7.

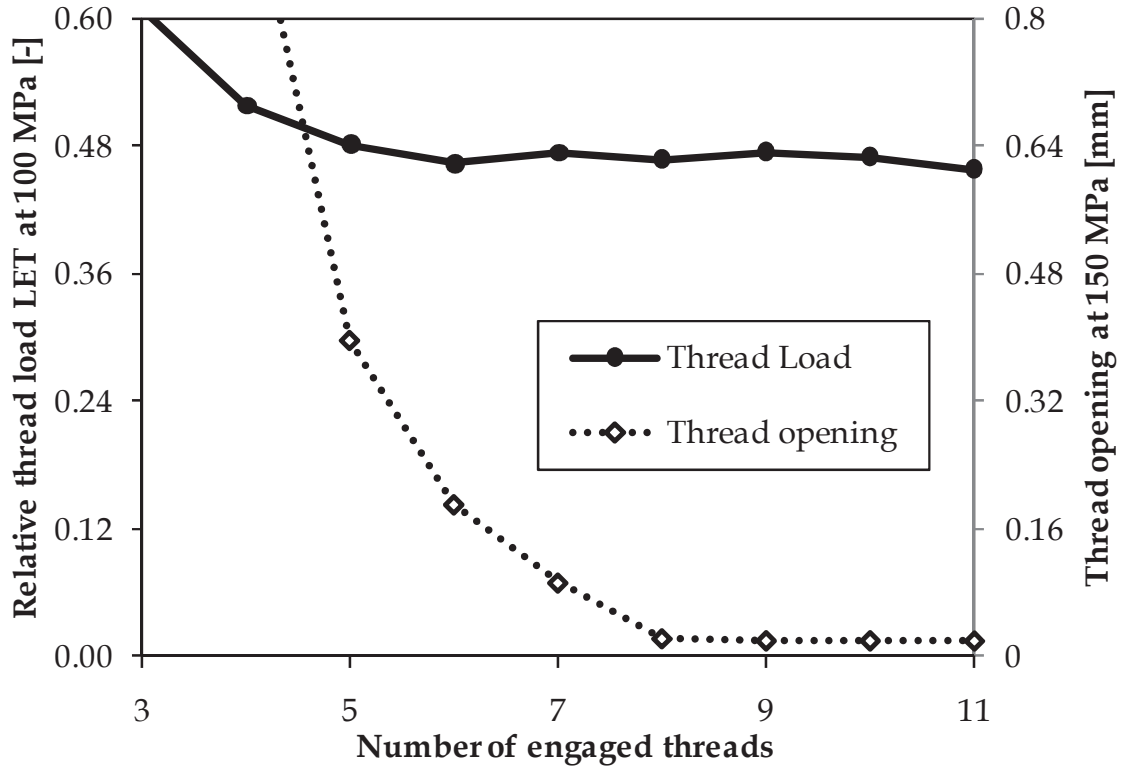

Figure 7.17: Influence of engaged thread length on relative thread load and opening.

This is in correspondence with the optimal value of 12 threads obtained for a shouldered buttress connection as determined by Newport [7.1] using the hybrid modelling technique (as mentioned in the literature study of Chapter 2). The presence of the shoulder would in his case increase the load on the first engaged thread of the pin, next to the high load concentration on the LET. Due to these two maxima in the thread load distribution, the obtained optimal number of threads is higher than in the present study.

5 Summary and conclusions

In this chapter the validated parametric program ThreadGen© is used to determine the effects of contact conditions, thread type and box and pin geometry.

Following trends are observed when considering the contact conditions and thread properties:

- The coefficient of friction between the threads of pin and box has an important influence on the thread opening, but does not affect the load distribution.
- The thread opening can be decreased by applying a higher number of make-up turns, but this introduces an increased loading of the LET of the pin.
- The relative thread load on the LET of the pin of an axially loaded connection can be reduced by using a thread with a smaller pitch length. This more flexible thread transfers the load better over all engaged threads, but also tends to create an increased thread opening.
- Both the relative load on the LET and the thread opening can be reduced when a positive taper difference is applied between the pin and box threads.
- The stress concentration factors of different thread types are compared. As could be expected, the thread root radius has an important influence on the resulting stress distribution. The buttress thread shape is found to create the lowest stress concentration.

The stiffness ratio between pin and box can be changed by altering their dimensions and the load distribution can be influenced. To obtain a reduced relative thread load at the LET of the pin:

- A local box stiffness reduction can be used. For example the stiffness gradient or bevelled groove design result in a slightly improved load distribution.

- A more significant reduction of the thread load can be obtained by reducing the box recess length. This also causes a limited increase in the thread opening.
- By applying a relative stiffness reduction of the box, the thread load can also be reduced. This can either be done by decreasing the box wall or increasing the thickness of the pin wall. The thread opening however, increases for a box wall reduction, but decreases for a pin wall increase.
- Reducing the engaged thread length can significantly increase the load at the LET, while having more than 7 engaged threads does not improve this value any more. Furthermore, the thread opening can be reduced by having 8 engaged threads, which is identified to be the optimum pin length.

Hence it can be concluded that important changes in thread load distribution can be obtained by changing globally or locally the pin and box geometry or dimensions.

As stated in section 2.2.3 of Chapter 2, the pressure sealing of premium connections can be provided by metal-to-metal seals instead of using sealing threads. Hence, the value of the thread opening becomes less important. When optimizing a connection, it might be appropriate to combine several design features. The thread shape can be optimized to obtain a low stress concentration factor and reduce the local strains at the thread roots; the connection geometry and make-up conditions can be optimized to improve the load distribution over the threads and the resulting local stresses and strains at the threads; metal-to-metal seals can be added to ensure appropriate leak resistance.

References

[7.1] Newport, A., Stress and Fatigue Analysis of Threaded Tether Connections, PhD Dissertation, Dept. of Mech. Eng. University College London, 1989.

[7.2] De Lange, R.W., Evans, M.E., Threaded and coupled connection for improved fatigue resistance, United States Patent, US 6609735 B1, 2003.

[7.3] Verdillon, L., Threaded tubular element for fatigue resistant threaded tubular joint and resulting threaded tubular joint, United States Patent, US 6729658 B2, 2004.

[7.4] Venkatesan, S., Kinzel, G.L., Reduction of stress concentration in bolt-nut connectors, ASME Journal of Mechanical Design, 128, 1337-1342, 2006.

[7.5] Pallini, J.W., Munk, B.N., Riha, J.B., Lyle, R.D., Threaded Pipe Connector, United States Patent, US 2007/0063517 A1, 2007.

[7.6] Shahani, A.R., Sharifi, S.M.H., Contact stress analysis and calculation of stress concentration factors at the tool joint of a drill pipe, Materials and Design, 30(9), 3615-3621, 2009.

[7.7] Assanelli, A.P., Xu, Q., Benedetto, F., Johnson, D.H., Dvorkin, E.N., Numerical/experimental analysis of an API 8-round connection, Journal of Energy Resources Technology-Transactions of the ASME, 119(2), 81-88, 1997.

[7.8] Santus, C., Fretting fatigue of aluminum alloy in contact with steel in oil drill pipe connections, modeling to interpret test results, International Journal of Fatigue, 30, 677-688, 2008.

[7.9] Newport, A., Glinka, G., Concentration of Cyclic Stresses in Preloaded Threaded Connections, Journal of Engineering Mechanics, 117(6), 1257-1273, 1991.

Chapter 8
Fatigue Analysis

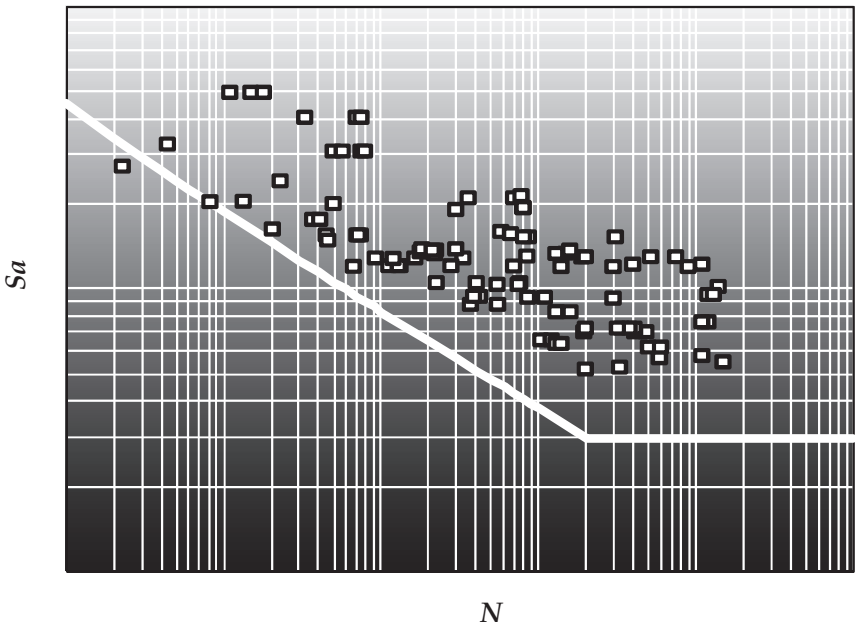

1 Goal

In this chapter the experimentally obtained fatigue data is discussed more in detail. First the fatigue life data is compared to published data and the applicable standard design curves presented in Chapter 2 and a comparison is made with results obtained by the finite element model. In the second part of this chapter, the crack growth data obtained in the medium scale tests is further discussed.

Final goal is to compare different approaches to assess the fatigue performance of threaded connection designs in order to come to an accurate and practical approach.

2 Fatigue analysis

2.1 Comparison with literature data

In Figure 8.1 a comparison is made between the experimentally obtained fatigue data and published results previously described in section 5.2 of Chapter 2. In this graph the stress amplitude is expressed relative to the tensile strength of the connection's material. It can be seen that the obtained data is in line with results from previous studies.

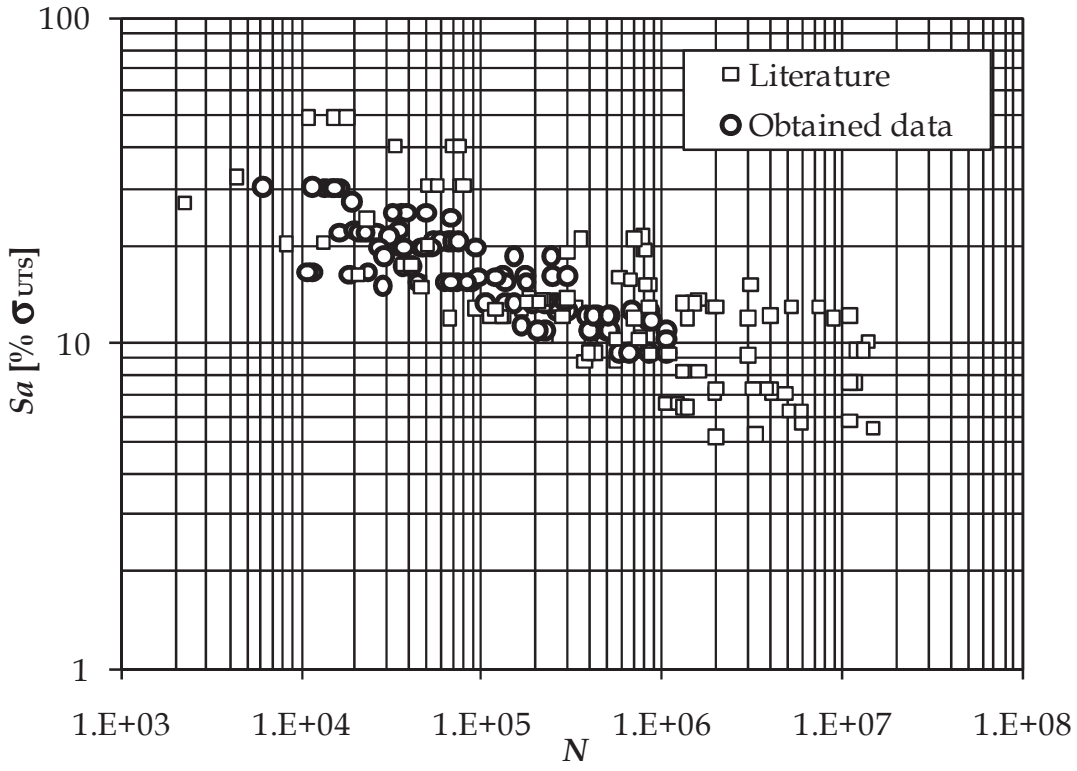

Figure 8.1: Comparison of the data obtained in this study with data from literature.

2.2 Comparison with existing standards

Two standard design curves for threaded pipe connections and a design curve for threaded fasteners were introduced in section 4.6.1 of Chapter 2.

In Figure 8.2 the results are shown of the 90 failed 1″ test specimens, obtained using the small scale four-point bending setup together with the fatigue life data of the 5 tests on the 4.5″ API Line Pipe specimens (axial tension and medium scale four-point bending). The 1″ data points are represented by circles, the 4.5″ results are represented by black squares. Additionally, the ASME-B31 and DNV-B design curves are added. Since these curves are given for a load ratio $R = -1$, the experimental test data is corrected using the Goodman equation (2.5).

Note that all data points are situated well above the ASME-B31 design curve, which means this curve is over-conservative. Hence, the use of this curve would lead to unnecessarily over-dimensioned connections.

The DNV-B curve is obtained by correcting the standard curve Eq. (2.22) with the stress concentration factor 3.97 obtained by the finite element model. Important to note is that only 2 of 95 data points are situated below the DNV-B curve. Accordingly 97.9 % of the data points are situated above the curve. Since the design curve is based on a mean curve minus twice the standard deviation, it is associated with a 95.4 % probability of survival which is in good correspondence with the obtained value. Due to this good match, it is clear that the DNV approach is more suitable for evaluating the fatigue performance of threaded connections than the ASME-B31 curve. However, a more detailed analysis of the different configurations is hard. As plastic deformation occurs during make-up, the von Mises stress at the thread root shows little difference for the different connection types and almost identical stress concentration factors are obtained. Hence the DNV-B curve can be used as a general design curve, but it is not possible to rigorously predict the influence of different design features on the connection's fatigue life.

The S-N plot of Figure 8.3 compares the fatigue data to the BS 7608 curve. In this curve, the stress amplitude is represented as a percentage of the experimentally determined material's ultimate tensile strength. Both the data points of the failed specimens and of the specimens that did not fail after at least $2 \cdot 10^6$ cycles are plotted. Again only two data points are below the curve, which is acceptable considering the 95.4 % probability of survival of the curve. Nevertheless it can be observed that the 4.5″ API Line Pipe results in the low cycle region are laying closely to the curve, while all other data points at the high cycle region are well above it. Hence, the design curve does become more conservative in the high cycle region which makes it less accurate than the DNV approach. It can be concluded that the use of standard design curves leads to conservative results and no accurate distinction can be made between different connection designs.

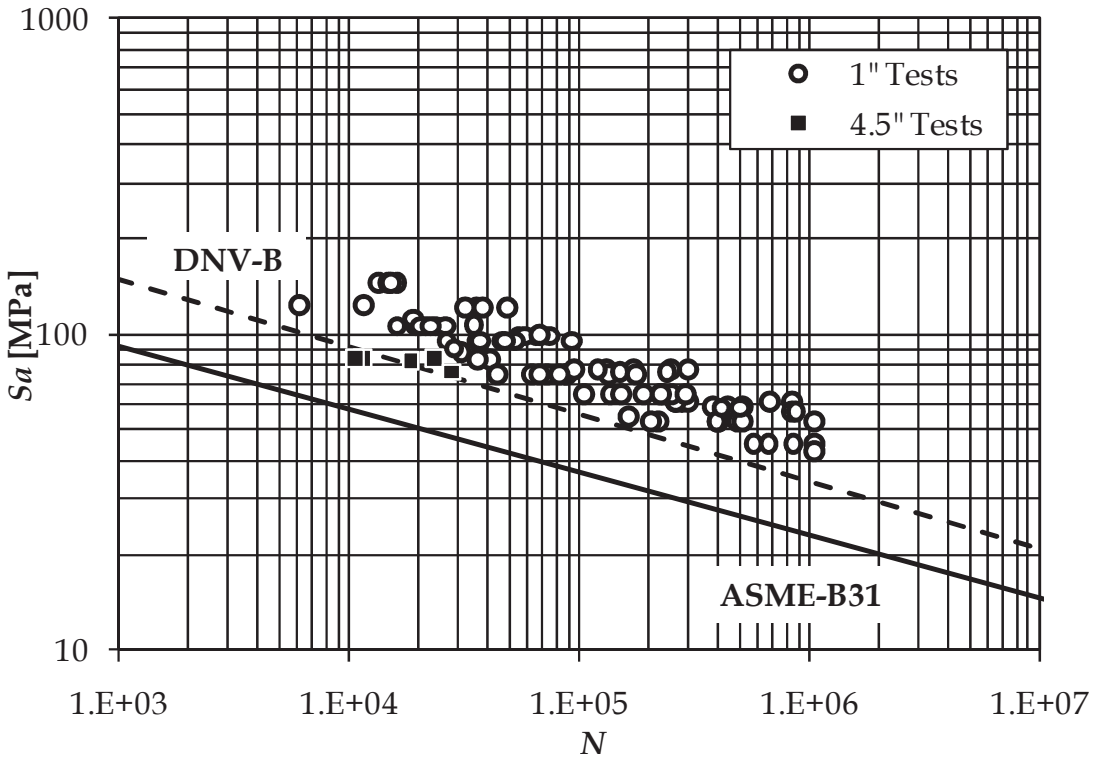

Figure 8.2: Comparison of the experimental test data with existing design curves for threaded pipe connections (*R = -1*).

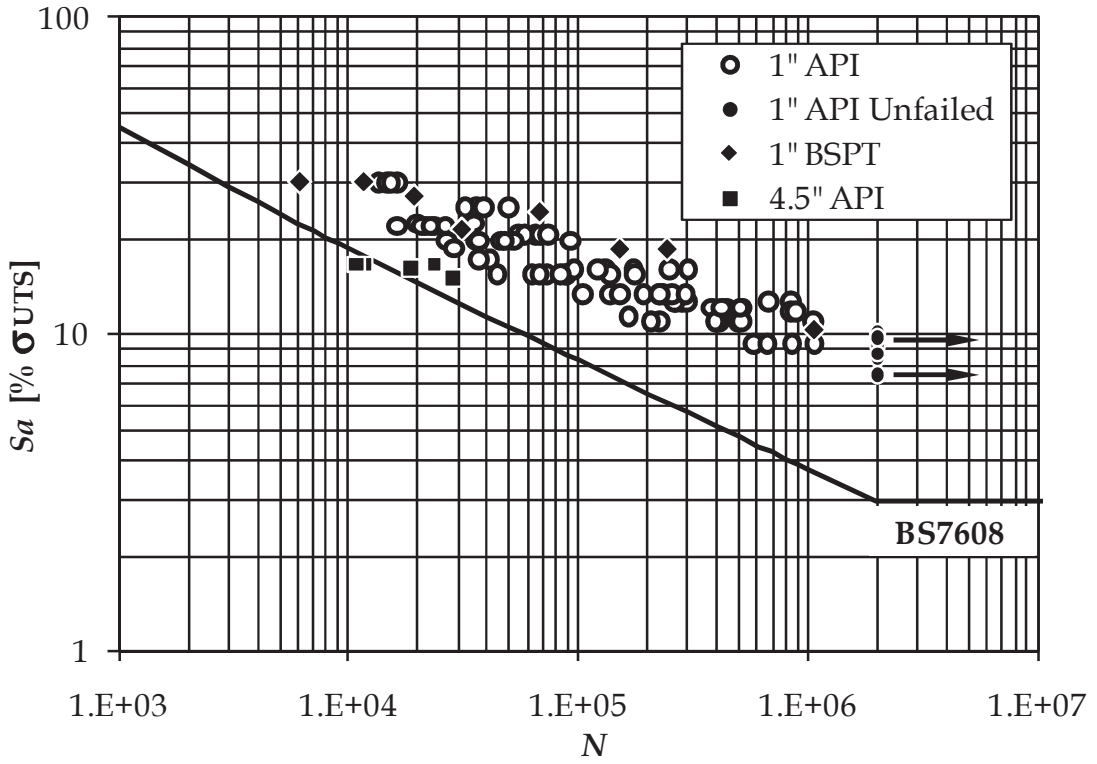

Figure 8.3: Comparison of the experimental data with the BS7608 design curve (*R = -1*).

2.3 Comparison with load distribution

As explained in Chapter 7, it is common practice to use the thread load distribution as a measure for the fatigue life of a threaded connection. To check this assumption, the thread load distributions are calculated for the 1″ configurations tested on the small scale four-point bending setup as described in section 4.3 of Chapter 5. The relative load carried by the LET for the different configurations is summarized in Table 8.1. The load distributions of four configurations are illustrated in Figure 8.4. They are plotted as a percentage of the total load carried by the coupling and thread 1 corresponds to the LET. Note that for the standard API Line Pipe connection, the thread 6 carries a negative load. This is caused by bending of the pin due to make-up deformation, which puts a compressive load on this thread. The standard API Line Pipe connection is used as a reference to other configurations. The LET of this connection carries 51.0 % of the total load. The modified API Line Pipe configurations with a thick-walled pin and with a box wall thickness reduction of 2 mm both show a more uniform load distribution. The respective percentages of the load carried by the LET are reduced to 42.3 % and 37.3 %, which are significantly lower than for the standard API Line Pipe configuration. For the BSPT configuration a relative thread load of 81.5% at the LET is calculated. This high value is caused by the taper mismatch of a straight box and a tapered pin. This taper difference results in only three engaged threads and a highly concentrated load on the LET.

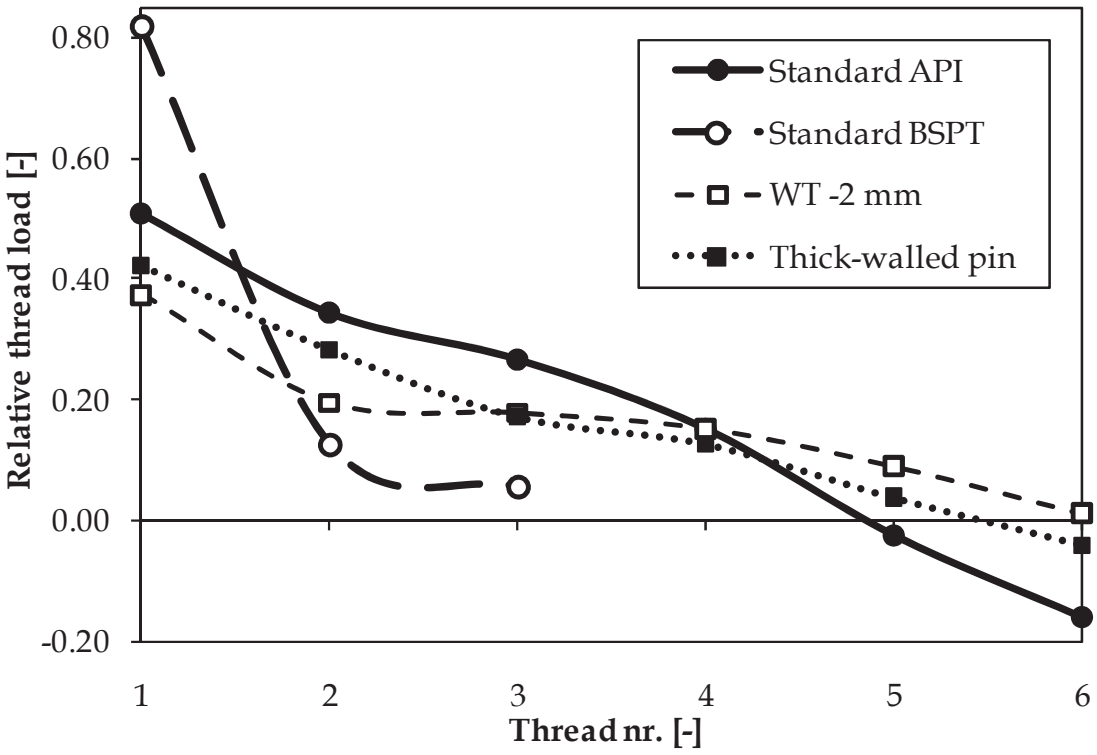

Figure 8.4: Thread load distribution of 1″ configurations.

Connection configuration	Fatigue stress at 10^5 cycles [MPa]	Fatigue stress improve [%]	Relative thread load at LET [-]	Thread load improve [%]
Standard API Line Pipe	64.9	-	0.510	-
Box wall -2 mm	67.8	4.5	0.373	26.9
Box recess -5 mm	70.2	8.2	0.477	6.5
Box wall -1 mm	72.3	11.4	0.456	10.6
Standard BSPT	74.5	14.8	0.815	-59.8
Pin and box modific.	79.5	22.5	0.385	24.5
Thick-walled pin	84.9	30.8	0.423	17.1

Table 8.1: Comparison of the fatigue stress at 10^5 cycles with the LET relative thread load for the tested 1" configurations.

In Table 8.1 the relative thread load at the LET of the pin as obtained through numerical analyses is put against the allowable fatigue stress at a fatigue life of 10^5 cycles as derived from the experimentally determined S-N curves (see Table 5.6). In the table, the configurations are sorted by increasing fatigue stress. Additionally, the improvement of the relative thread load at the LET with respect to the standard API Line Pipe configuration is compared to the improvement in fatigue stress amplitude. These results are also plotted in Figure 8.5. It is clear that the commonly assumed relation between thread load and fatigue life is not justified. Three configurations (box recess reduction, box wall thickness -1 mm and thick-walled pin) exhibit a linear relation between relative thread load and fatigue stress improvement, but the other configurations diverge significantly. The BSPT configuration can be subjected to a much higher fatigue stress than expected from the high load carried by the LET. This might be explained by two separate reasons. First, the crests and roots of the BSPT threads are rounded, while the API Line Pipe threads have a sharper truncated triangular shape. Hence, as shown in section 2.5 of Chapter 7, the net stress concentration factor of the BSPT threads ($K_{tn} = 4.4$) is lower than of the API Line Pipe threads ($K_{tn} = 7.9$), which is beneficial for the fatigue life of the connection. Next to this, the BSPT connection has sealing threads. Hence the thread crests and roots of pin and box are in contact with each other and a certain amount of compressive stress is introduced at the thread roots, which can also improve the connection's fatigue life [8.1-2]. Despite the unfavourable load distribution, the BSPT exhibits a better fatigue life than the standard API Line Pipe connection due to the improved thread shape.

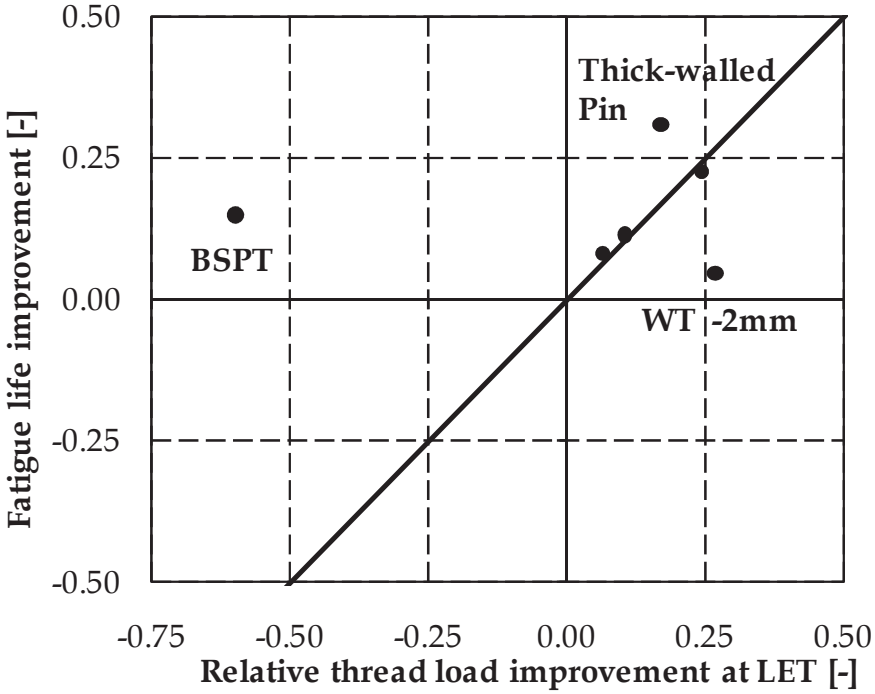

Figure 8.5: Comparison of the relative thread load and fatigue life improvement.

The thick-walled pin configuration too can resist a higher fatigue stress than expected, while the modified pin and box configuration (see Figure 5.25.d), which is manufactured from the same thick-walled pin specimens, behaves as expected. On the other hand, the configuration with a box wall thickness reduction of 2 mm has the most uniform load distribution, but only a minimal fatigue stress improvement. These differences can not be explained by merely considering the thread load distribution.

However, when the equivalent plastic strain at the root of the last engaged thread is compared for the different API Line Pipe configurations, the non-conformance of both the thick-walled pin and box wall -2 mm configurations is confirmed. In Figure 8.6 the equivalent plastic strain ε_p at the root of the LET (mean value over e certain region, as will be described in section 2.4.1) is plotted as a function of the applied pipe gross axial tensile stress for the API Line Pipe configurations. The equivalent plastic strain at make-up (axial tensile stress = 0 MPa) can be related to the relative thread load at the LET. This is made clear by the tabulated values of $\varepsilon_{p,make\text{-}up}$ and the relative thread load in Table 8.2: a decreased equivalent plastic strain at make-up corresponds to a decreased relative thread load. When the pipe axial tensile stress is applied, this relation no longer holds true. Only for the three configurations for which the fatigue life improvement is linear to the relative thread load improvement, the plastic strain describes a curve parallel to that of the standard 1" API Line Pipe connection. The two configurations for which the fatigue life does not relate to the relative thread load, show a different behaviour of the equivalent plastic strain.

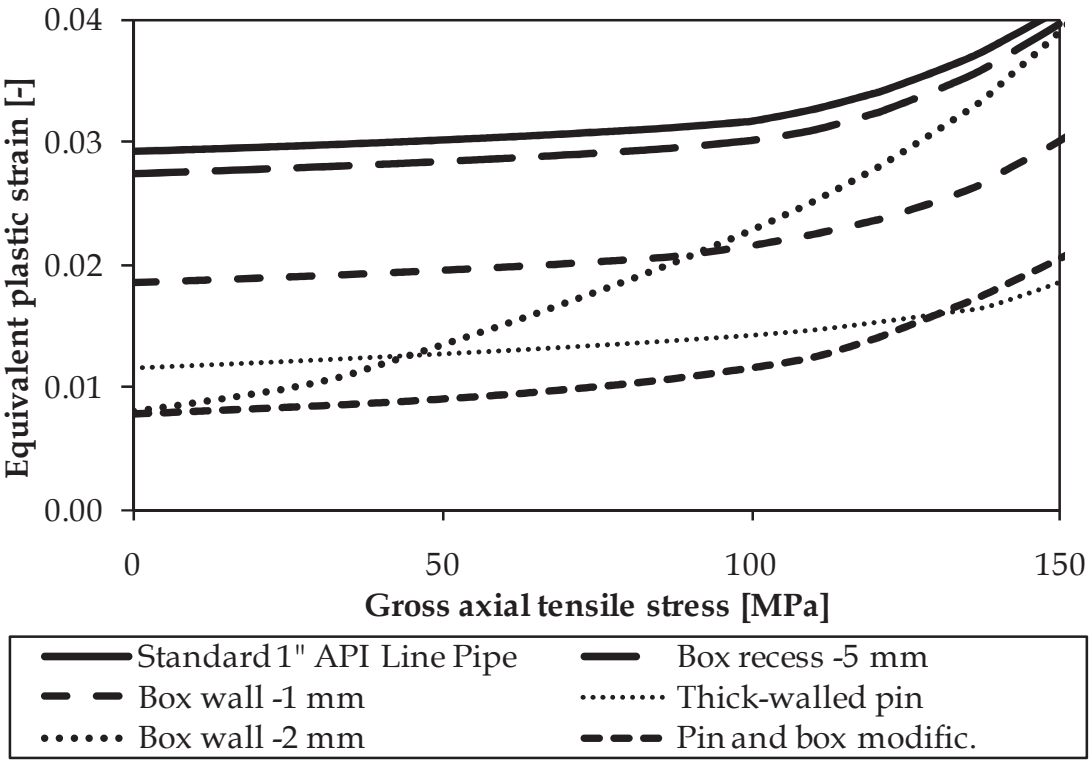

Figure 8.6: Equivalent plastic strain at the LET of the pin as a function of the pipe gross axial tensile stress.

Connection configuration	**Relative thread load at LET [-]**	$\varepsilon_{p,make\text{-}up}$ **at LET [-]**	$\frac{\Delta\varepsilon_p}{\Delta S}$ **at 100 MPa** $\cdot 10^5$ **[MPa^{-1}]**
Standard 1" API Line Pipe	0.510	0.029	9.8
Box recess -5 mm	0.477	0.027	8.4
Box wall -1 mm	0.456	0.019	9.3
Thick-walled pin	0.423	0.012	4.3
Pin and box modific.	0.385	0.008	8.7
Box wall -2 mm	0.373	0.008	23.4

Table 8.2: Equivalent plastic strain and relative thread load data for the 1″ API Line Pipe configurations.

To quantify these results, the slope of the plastic strain curves $\Delta\varepsilon_p/\Delta S$ is evaluated at an axial tensile stress of S = 100 MPa and added in Table 8.2. A steep slope means that the strain range during a fatigue test will be higher. Consequently, a shorter fatigue life might be expected, as it is known from the local strain approach described in section 4.3 of Chapter 2 that a higher strain range reduces the fatigue life. Except for the thick-walled pin and

box wall -2 mm configurations, the $\Delta\varepsilon_p/\Delta S$-values are similar (values between $8.7 \cdot 10^{-5}$ and $9.8 \cdot 10^{-5}$ MPa^{-1}) and the fatigue life of these configurations can be related to the relative thread load. For the thick-walled pin configuration, $\Delta\varepsilon_p/\Delta S$ is only $4.3 \cdot 10^{-5}$ MPa^{-1}, which is considerably lower and the fatigue life is also higher than expected from the relative thread load. Conversely, the box wall -2 mm configuration shows a much higher value of $\Delta\varepsilon_p/\Delta S = 23.4 \cdot 10^{-5}$ MPa^{-1} and the fatigue life is also lower than expected from the relative thread load.

It can be concluded that a more uniform load distribution over a threaded connection does not necessarily result in improved fatigue properties. This is because the thread load is a measure for the axial stresses over the connection, while the local stress and strain at the root of the LET are also altered by other stress and strain components such as the hoop stress introduced during make-up, which can additionally be affected by a changed connection stiffness. Hence a connection's fatigue performance can not be evaluated by it's load distribution alone.

2.4 Damage evolution law

Before presenting the fatigue analysis using the damage evolution law, it is mentioned that attempts were made to apply the Dang Van criterion according the methodology described in section 4.6.3 of Chapter 2. However, the Dang Van parameters κ and λ could not be determined accurately enough. When using the S-N curves of the small scale four-point bending tests, the values of the hydrostatic pressure σ_H and shear stress τ did not differ sufficiently for the different curves. It might be part of future research to determine κ and λ by fatigue testing of standard plain test specimens.

2.4.1 Application to the finite element model

To account for the local multiaxiality at the root of the LET in the evaluation of a threaded connection's fatigue life, the damage evolution law (DEL) is used, as introduced in section 4.5.2 of Chapter 2. The main relation is repeated below.

$$N = \frac{\Delta\sigma_{eq}^{-(\beta+m)} R_V^{-\beta/2}}{a(\beta+m+1)} \tag{8.1}$$

This model combines the values of the von Mises equivalent stress σ_{eq} and the hydrostatic pressure σ_H (present in the triaxiality function R_V) as determined at the root of the LET in the finite element model. However, the extraction of numerical data from finite element results should be performed rigorously [8.3]. Using data from a single element could result in inaccurate or mesh-dependent solutions. Therefore a methodology based on the *area method* (AM) and the *theory of critical distance* (TCD) is used.

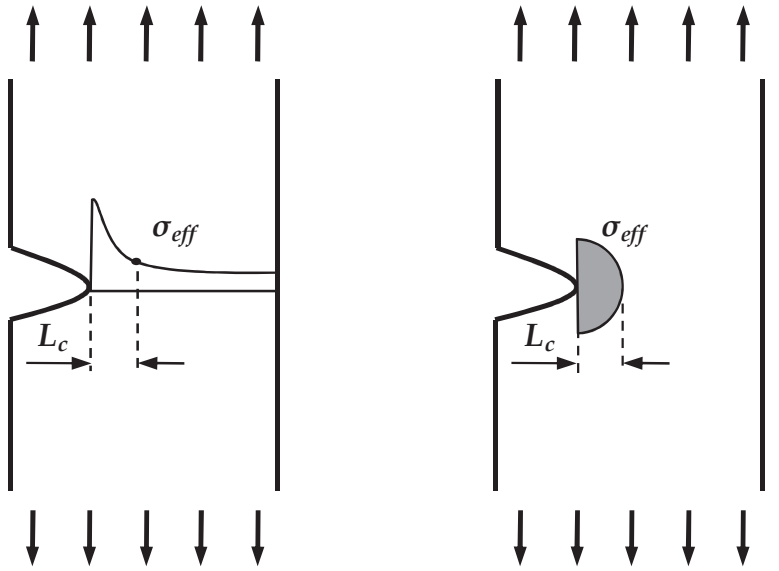

a) b)

Figure 8.7: a) critical distance evaluation, b) area method.

The TCD (or hot-spot approach) was developed by Peterson [8.4] to extract notch factors from linear elastic stress analyses. He assumed that the stress at a certain critical distance L_c from a notch root can be used for fatigue evaluation as illustrated in Figure 8.7.a. As this approach only helps to extract data from linear elastic finite element analysis, but still uses data extracted from a single element, the area method was developed by Taylor [8.6]. In this last approach, the stresses are averaged over a semicircular area centred at the notch tip having a radius equal to the critical distance L_c as illustrated in Figure 8.7.b. Hereby L_c is defined by Eq. (8.2).

$$L_c = \frac{1}{\pi}\left(\frac{\Delta K_{th}}{\Delta \sigma_0}\right)^2 \tag{8.2}$$

Where ΔK_{th} is the threshold value of ΔK for fatigue crack growth and $\Delta\sigma_0$ is the plain specimen fatigue limit (stress range) of the material. Common values for medium strength steels (such as API Grade B steel) are $\Delta K_{th} = 8$ MPa·m$^{1/2}$ [8.7] and $\sigma_0 = 0.45 \cdot \sigma_{UTS}$ [8.8]. With these values, the critical distance for the API Grade B steel becomes 0.1 mm. This corresponds well to the critical distance values from 0.09 to 0.11 mm for V-notches in a steel grade with similar strength properties [8.3]. The area method has been applied to threaded pipe connections before by Santus [8.9] in his study on the fretting fatigue behaviour of drill pipe connections. Furthermore it is mentioned that even more advanced area methods exist, where the size of the critical area is changed according to the applied fatigue stress [8.10]. However, in this study a semicircular area with a fixed radius of 0.1 mm is used to determine the effective stress values from the finite element analyses. This region contains approximately 100 elements in each analysed geometry.

2.4.2 Determination of fatigue parameters

In the damage evolution law Eq. (8.1) $\Delta\sigma_{eq}$ and R_V are obtained from the simulations, a and β are damage parameters and m is the strain hardening exponent of the connection material (m = 9.49 by fitting the experimentally determined stress-strain curve of the Grade B steel to the Ramberg-Osgood relation). Since a and β are unknown material constants, the experimental data from the standard API Line Pipe connection is used to determine their value. This is done by evaluating the finite element model at 9 different levels of stress amplitude. For each of these stress levels, the triaxiality function R_V and the equivalent stress range $\Delta\sigma_{eq}$ are calculated and substituted in the damage evolution law Eq. (8.1). The values of the damage parameters are then found using regression analysis to calculate the best least-squares fit between the calculated cycles to failure and the mean curve of the experimental data of the standard API Line Pipe samples given by Eq. (5.18). This methodology results in the following values: $a = 1.50 \cdot 10^{-7}$ and β = -8.23. Consequently, the damage evolution law becomes:

$$N = 2.95 \cdot 10^{6} \cdot \Delta\sigma_{eq}^{-1.26} \cdot R_V^{4.12} \tag{8.3}$$

In Figure 8.8 the corresponding results of the fitted damage evolution law are compared to the mean curve of the experimental data of the standard API Line Pipe connection.

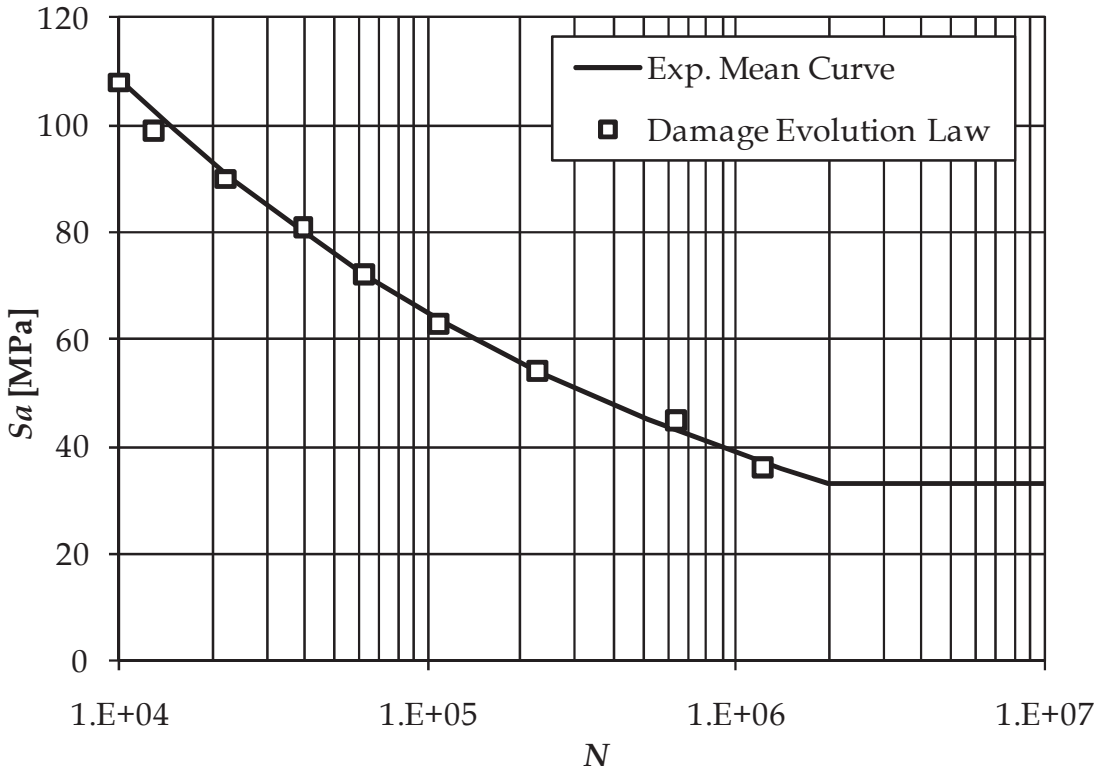

Figure 8.8: Comparison between the mean curve of the 1″ standard API Line Pipe results and the damage evolution law.

S_a [MPa]	R_V [-]	$\Delta\sigma_{eq}$ [MPa]	N [-]
36	1.14	3	1 221 250
45	1.15	5	635 193
54	1.16	13	225 763
63	1.17	23	107 975
72	1.18	37	61 886
81	1.19	54	39 518
90	1.19	87	22 125
99	1.19	137	12 968
108	1.20	167	10 012

Table 8.3: Numerical data of the damage evolution law.

It can be seen that for all 9 stress levels where the DEL is evaluated, the obtained fatigue life is in good correspondence with the experimental mean curve. The standard deviation *STD* is only 1.83 MPa. Also the values of the fatigue life N, the triaxiality function R_V and the von Mises equivalent stress range $\Delta\sigma_{eq}$ are given in Table 8.3 for the 9 evaluated values of the stress amplitude S_a. The triaxiality function only slightly increases with increasing stress amplitude, while $\Delta\sigma_{eq}$ is highly dependent of the applied stress level.

To investigate the sensitivity of the critical distance used in the area method, the damage parameters a and β are determined two additional times using the same methodology for a critical distance of 0.08 and 0.12 mm respectively. The resulting values are shown in Table 8.4. The value of β does not show a significant change. The damage parameter a increases for an increased critical distance. However, the change remains relatively small and it can be stated that small deviations in the number of elements included in the critical area do not significantly affect the value of the damage parameters.

L_c [mm]	a	β	# elements in critical area
0.08	$1.54 \cdot 10^{-7}$	-8.08	80
0.10	$1.50 \cdot 10^{-7}$	-8.23	107
0.12	$1.85 \cdot 10^{-7}$	-8.14	127

Table 8.4: Damage parameters for different critical distance values.

2.4.3 Application to the experimental results

The determined damage parameters a and β should be valid for all types of threaded connections consisting of Grade B steel. The obtained damage evolution law Eq. (8.3) is now used to evaluate the fatigue performance of the 5 tested 1″ configurations manufactured from the API Line Pipe samples. In Figure 8.9 and Table 8.5 the results for the configuration with a box wall thickness reduction of 1 mm are illustrated. The DEL data points in the graph are obtained by inserting the simulated values of R_V and $\Delta\sigma_{eq}$ in Eq. (8.3). It is clear that there is a good correspondence between the predictions of the DEL and the experimental mean curve (STD = 2.97 MPa). As a comparison, the mean curve of the standard API Line Pipe connection is provided. It can be seen that the DEL predicts a similar increase of the connection's fatigue life.

The triaxiality R_V in the connection with reduced box wall thickness is higher than for the standard API Line Pipe connection, while only a limited increase of $\Delta\sigma_{eq}$ appears, as can be seen by comparing the results in Table 8.5 and Table 8.3. A change in triaxiality R_V affects the fatigue limit of the S-N curve in the plot, without having an influence on the slope of the curve, while $\Delta\sigma_{eq}$ affects both slope and fatigue limit. As can be seen from Eq. (8.3) an increased R_V is beneficial for the fatigue life, while a rise of $\Delta\sigma_{eq}$ will decrease it.

The results of the four additional tested configurations are shown in Figure 8.10. The results of the configuration with a box wall thickness reduction of 2 mm are provided in Figure 8.10.a.

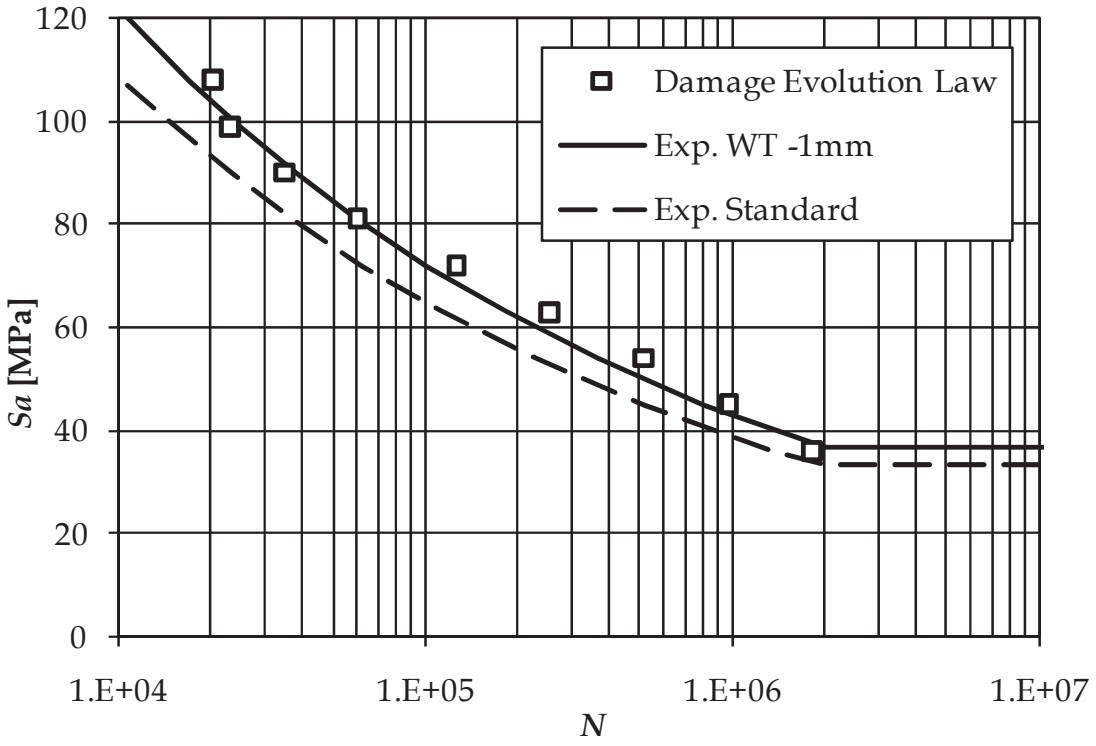

Figure 8.9: Comparison between the experimental mean curve and the damage evolution law of the 1″ configuration with a box wall thickness reduction of 1 mm.

S_a [MPa]	R_V [-]	$\Delta\sigma_{eq}$ [MPa]	N [-]
36	1.43	5	1 815 593
45	1.44	8	979 137
54	1.45	13	515 366
63	1.46	24	255 270
72	1.47	43	126 327
81	1.48	79	60 197
90	1.49	126	34 600
99	1.50	177	23 145
108	1.51	201	20 346

Table 8.5: Numerical data of the damage evolution law (box WT -1 mm).

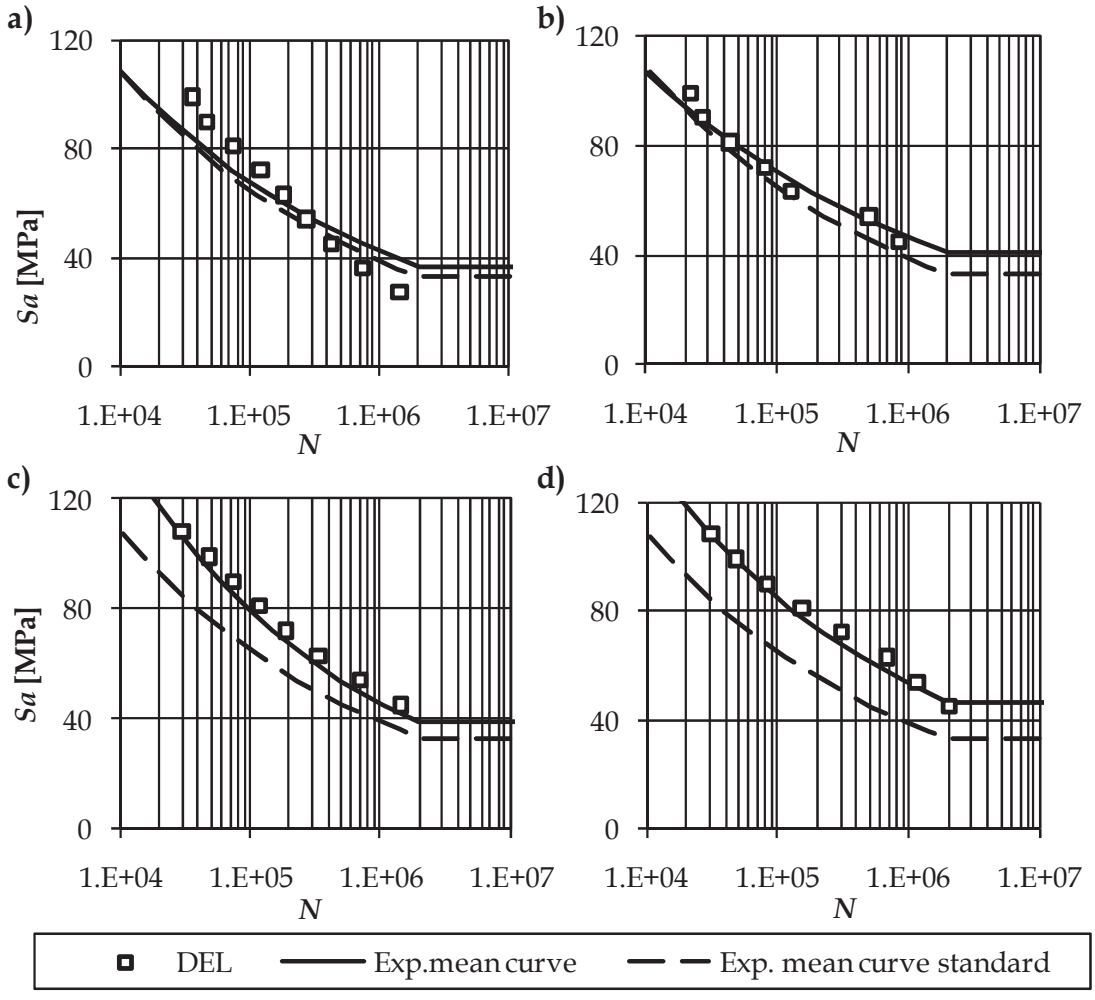

Figure 8.10: DEL and experimental data for a) box WT -2 mm; b) box recess -5 mm; c) pin and box modification; d) thick-walled pin.

Connection configuration	Fatigue stress at 10^5 cycles [MPa]	Fatigue stress improvement [%]	DEL fatigue stress at 10^5 cycles [MPa]	DEL fatigue stress improvement [%]	R_V [-]	$\Delta\sigma_{eq}$ [MPa]
Standard API Line Pipe	64.90	-	64.56	-	1.18	25.6
Box wall -2 mm	67.80	4.5	73.03	13.1	1.79	102.7
Box recess -5 mm	70.19	8.2	71.13	10.2	1.45	50.5
Box wall -1 mm	72.34	11.5	73.89	14.5	1.47	57.2
Pin and box modific.	79.45	22.4	83.81	29.8	1.65	78.6
Thick-walled pin	84.87	30.8	86.85	34.5	1.60	70.9

Table 8.6: Comparison of the fatigue stress at 10^5 cycles with the tested 1″ configurations.

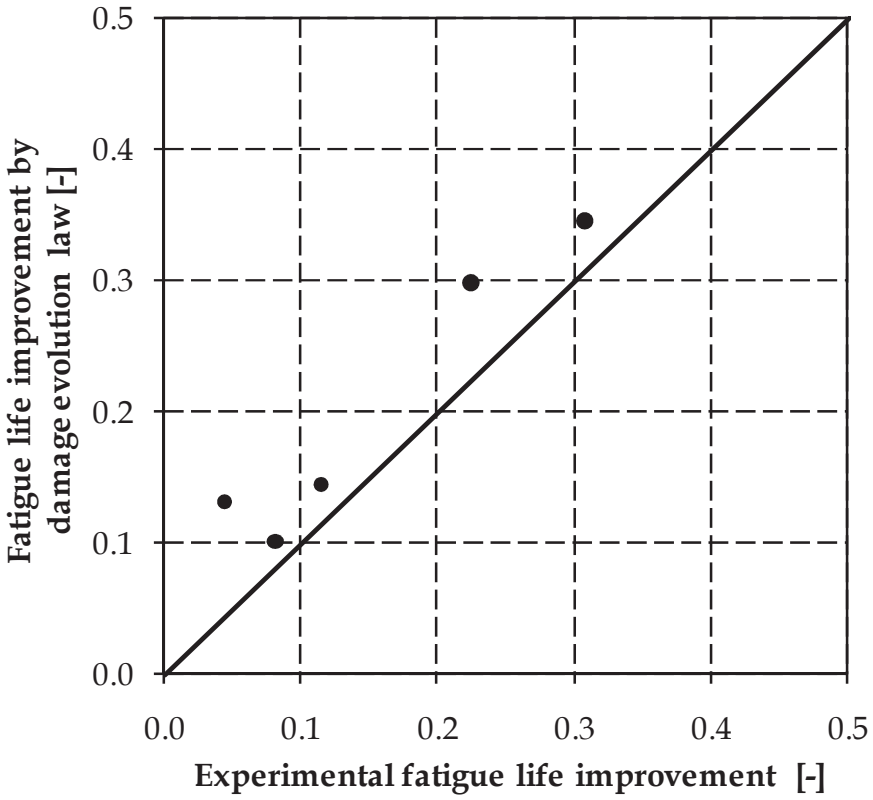

Figure 8.11: Comparison between experimentally obtained and calculated fatigue life improvement values.

For this configuration there is only a moderate agreement since the DEL predicts a curve with a slope that is too steep. This indicates that the prediction of the von Mises stress range is inaccurate. The standard deviation between the DEL data and the experimental mean curve is 9.20 MPa. This is relatively high compared to the results for the other three configurations in Figure 8.10 where the standard deviation is about 3 MPa. The trends predicted by the DEL for these configurations correspond also much better to the experimental results.

In Table 8.6 the predicted and experimental values are compared based on the fatigue stress values at 10^5 cycles. Next to the values as such, the improvement in terms of percentage are given. These values are additionally plotted in Figure 8.11. From this figure it is clear that, although the predictions are unconservative –for every configuration a higher fatigue stress is predicted than experimentally determined- they follow the same trend. All modified configurations show a higher value of the triaxiality function R_V than the standard API Line Pipe connection, which explains the better fatigue properties. However, the beneficial effect of the increased triaxiality function is in some cases countered by a higher von Mises stress range. The configuration with the 2 mm box wall thickness reduction deviates the most. The DEL predicts a fatigue stress improvement of 13.1 % while only an improvement of 4.5 % is measured. It is noted that the values of both R_V and $\Delta\sigma_{eq}$ are the highest for the configuration with a box wall reduction of 2 mm. These high values might explain the less accurate prediction. The correspondence for the other configurations is better. Altogether the DEL is able to predict the trends observed during the experiments.

For the 4.5" API Line Pipe tests on the medium scale four-point bending setup, insufficient tests have been carried out to construct an experimental fatigue curve. Nevertheless, the results of Test 4 are evaluated using the DEL. In this test a fatigue life of N = 28 250 cycles (see Table 5.10) was obtained at a stress amplitude of 69.8 MPa (see Table 5.8). For this stress level, following values are obtained from the finite element model: R_V = 1.41 and $\Delta\sigma_{eq}$ = 122.5 MPa. When these values are substituted in the DEL Eq. (8.3) a fatigue life is obtained of N = 28 000 cycles, which fits the experimental results.

2.4.4 Application to geometry changes

The effect of a change of the box wall thickness, the box recess length and the pin wall thickness on a connection's fatigue life has been demonstrated in the previous paragraphs. To quantify the influence of the other geometry changes described in the parametric study of Chapter 7, the damage evolution law is used to evaluate these modified connections. As in Chapter 7, these configurations are derived from the standard 4.5" API Line Pipe connection.

Connection configuration	$N \cdot 10^{-5}$ by DEL at S_{max} = 100 MPa	Relative thread load LET at 100 MPa [-]	$\frac{\Delta\varepsilon_p}{\Delta S}$ at 100 MPa $\cdot 10^5$ [MPa^{-1}]
Thread pitch – *10 tpi*	6.3	0.414	5.2
Stiffness gradient – *1.6*	3.4	0.437	8.8
Standard 4.5″ API Line Pipe	3.2	0.474	8.9
Pin engaged thread length – *8 threads*	3.2	0.468	8.5
Taper difference – *0.30°*	2.7	0.464	13.6
Bevelled groove – *30°* primary groove angle	1.8	0.317	13.7
Number of make-up turns – *0.5 turns*	0.2	0.399	11.7

Table 8.7: Comparison of different configurations described in the parametric study of Chapter 7.

Table 8.7 summarizes the results. Six different configurations are compared to the standard 4.5″ API Line Pipe connection. For each configuration, following information is provided: the fatigue life calculated by the DEL for a stress amplitude of 45 MPa (maximum stress is 100 MPa as $R = 0.1$); the relative thread load at the LET at an axial tensile stress of 100 MPa and the slope of the plastic strain curve $\Delta\varepsilon_p/\Delta S$ at an axial tensile stress of 100 MPa. The results are ordered by decreasing fatigue life. As pointed out in section 2.4 of Chapter 7, increasing the number of threads per inch, reduces both the thread load at the LET and the thread opening. Additionally, this has a positive effect on the connection's fatigue life. In Table 8.7 it can be seen that a connection with 10 threads per inch has a predicted fatigue life of 630 000 cycles compared to 320 000 cycles for the standard connection that has 8 threads per inch. These improved fatigue properties are confirmed by the combination of the reduced relative thread load and the low $\Delta\varepsilon_p/\Delta S$ value.

The previously discussed patented stiffness gradient (Figure 7.6.c and [8.11]) showed a slightly improved thread load, together with a negligible change in local strain range $\Delta\varepsilon_p/\Delta S$. This feature gives a slightly improved fatigue life for a stiffness gradient of 1.6.

The patented bevelled groove (Figure 7.6.d and [8.12]) had no effect on the relative thread load. During the parametric study, section 3.2.3 of Chapter 7, the bevelled groove has been applied to a configuration with a reduced box recess length. It has been shown experimentally that reducing the box recess length is beneficial for the connection's fatigue life. However, when the

bevelled groove is added, the $\Delta\varepsilon_p/\Delta S$-value is increased and the fatigue life is significantly reduced. Hence, this feature is predicted to be ineffective to improve the fatigue behaviour of API Line Pipe connections.

As indicated in section 4.2 of Chapter 7, increasing the pin engaged thread length reduces the thread opening, without affecting the relative thread load at the LET. From that point of view the optimum thread length is 8, instead of the standard number of 7 engaged threads for the 4.5" API Line Pipe connection. However, from Table 8.7 it is clear that due to the negligible changes in thread load and local strain range $\Delta\varepsilon_p/\Delta S$, this pin length increase does not affect the connection's fatigue life.

The last configuration discussed in this section has the same geometry as the standard connection, but is made up with only 0.5 turns instead of the standard value of 1 turn. Although this configuration has a reduced relative thread load, the local strain range at the thread root is increased significantly. This configuration has a fatigue life of only 20 000 cycles compared to 320 000 cycles of the configuration made-up with a single turn. These results are in correspondence with the findings of Newport and Glinka [8.13] who showed that the preload due to make-up can significantly reduce the dynamic stress range at the threads of a conical connection.

3 Crack growth analysis

In this section the crack propagation behaviour in a threaded connection is discussed more in detail. From the observations made during the experiments described in Chapter 5, it is clear that fatigue cracks initiate at the root of the LET of the pin and propagate over a wide segment of the circumference before penetrating the pipe wall. Hence, the appearing crack shapes do not resemble the semi-elliptical cracks used in the crack analysis of threaded pipe joints by Bahai et al. [8.14] and Zhao et al. [8.15]. In the following paragraph, the crack shapes obtained by the beach mark lines on the 4.5" API Line Pipe samples are used to perform further crack growth analysis.

3.1 Analysis of the bending deflection

To verify that the observed beach mark lines correspond to the specified number of fatigue cycles, the optical deflection measurements and crack opening measurements are compared with a simplified finite element model of a threaded connection containing a crack as shown in the section view of Figure 8.12. In this simplified linear elastic model, the 4.5" API Line Pipe specimen as tested in the medium scale four-point bending setup is modelled without taking into account the exact contact interface and thread geometry. Only the outer coupling geometry is considered. The exact shape of the coupling thread is not incorporated into the model in order to reduce its complexity and calculation time.

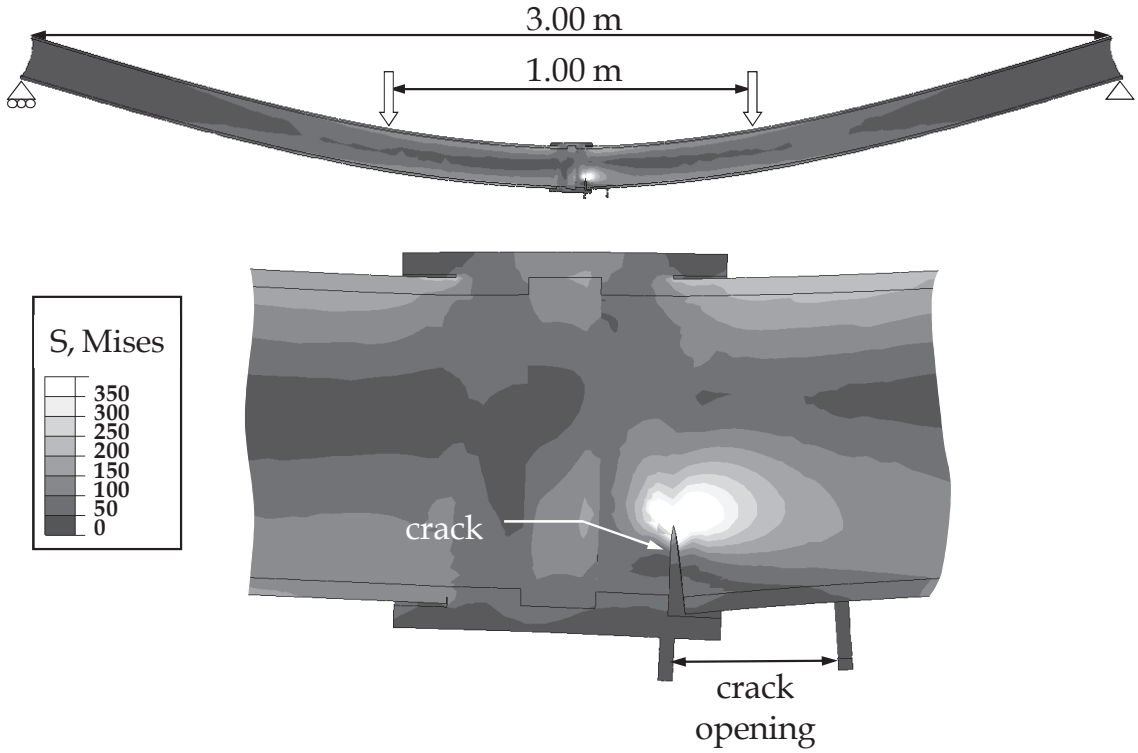

Figure 8.12: Finite element model of the cracked pipe assembly (deformation scale factor = 22).

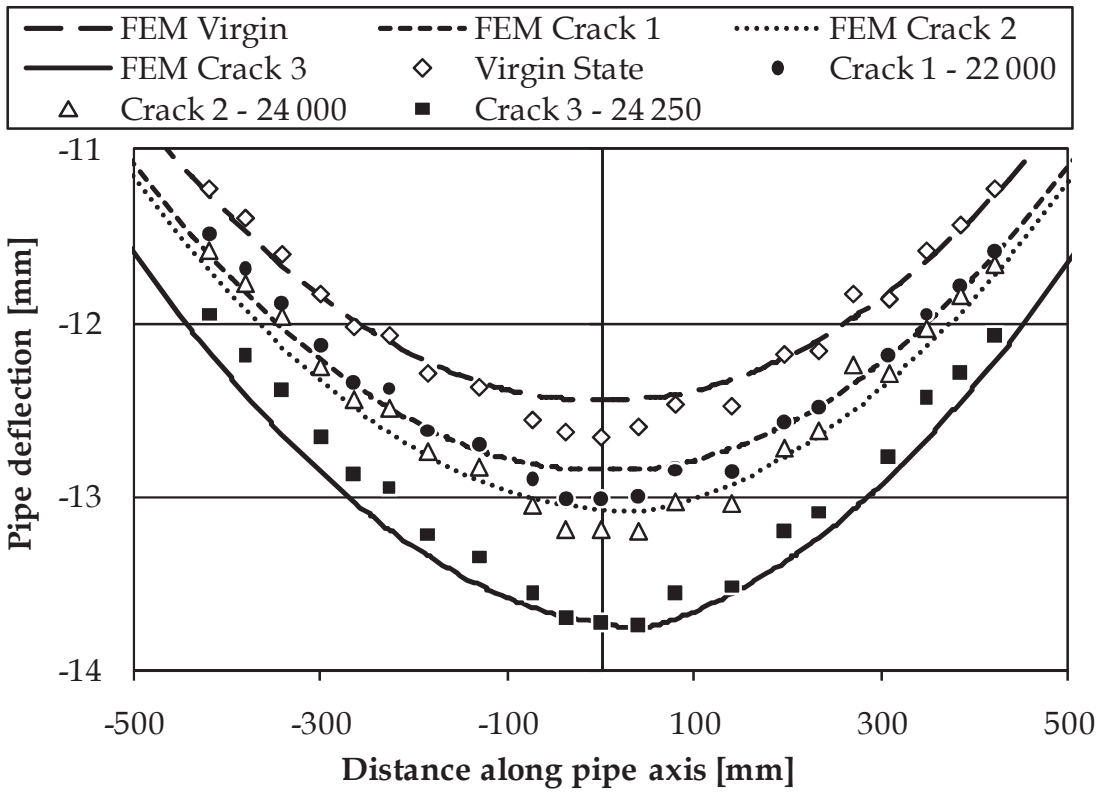

Figure 8.13: Comparison of the simulated and measured bending deflection during Test 3 of the medium scale four-point bending tests.

	Virgin state	Crack 1	Crack 2	Crack 3
Number of cycles [-]	0	22 000	24 000	24 250
Max. deflection FEM [mm]	12.4	12.8	13.1	13.8
Max. measured deflection [mm]	12.7	13.0	13.2	13.7
RMS deviation deflection shape [mm]	0.10	0.09	0.11	0.16
Crack opening FEM [mm]	0	0.04	0.17	0.31
Crack opening LVDT [mm]	0	0.05	0.17	0.27

Table 8.8: Overview of the fatigue crack growth results of Test 3.

Additionally, linear elastic material behaviour is used, which gives a local stress around the crack tip that exceeds the material's tensile stress. However, this has a limited effect on the global pipe deflection.

Three crack shapes are subsequently modelled using the 'crack seam' option in ABAQUS with the crack geometries based on the beach mark lines found on the fracture surface of Figure 5.48. The simulated deflection shapes for the virgin pipe assembly without a crack and for the pipes with the three different crack shapes are compared to the experimental measurements in Figure 8.13. The FE results are given by the lines, while the measurements of the individual optical markers are given by the plotted points. The measured trends are confirmed by the modelled deflections.

In Table 8.8 the results of the experimental measurements and the finite element simulations are summarized. The RMS deviation between the simulated and measured deflection is 0.10 mm for the virgin pipe, 0.09 mm for crack 1, 0.11 mm for crack 2 and 0.16 mm for the third crack. Hence, the mean deviation for the different deflections is 0.12 mm. The maximum deflection of the uncracked pipe is 12.5 mm. After 22 000 cycles this deflection is increased by 0.58 mm. It can be seen that the deformation for the cracked pipes becomes asymmetric. Because of the presence of the crack at the right side of the coupling, this side deflects more. This trend can be clearly seen in both the experimental and numerical results. After 22 000 cycles, the crack has a depth of 2.73 mm. Since this corresponds to a deflection increase of 0.58 mm and since the mean deviation between the measured and modelled deflections is 0.12 mm, it can be stated that the crack depth can be estimated with an accuracy of 0.6 mm (= 2.73 mm · 0.12/0.58). This is less accurate than the crack sizing techniques described in Chapter 3. As previously summarized in Table 3.1, these more conventional techniques have an accuracy from 0.1 to 0.5 mm. However, all sizing techniques using electric or magnetic fields can only be applied offline since the connection

should be uncoupled and a crack has to exceed a certain minimum size before it can be detected. When ultrasonic inspection with advanced signal processing would be used, there is no need to uncouple the connection, but the test should be paused to get accurate measurements. Hence, although the presented optical dynamic 3D measurement technique is less accurate than conventional methods for crack depth sizing, it can be successfully used for online monitoring during laboratory tests without the need to interrupt the test.

3.2 Analysis of the crack opening

Apart from the optical displacement measurements, crack opening measurements were carried out during the medium scale four-point bending tests. In order to further analyse these measurements, the points to attach the LVDT's are included in the FE model as shown in Figure 8.12. This way the measured crack opening can be related to the simulations. In Figure 8.14 the measured maximum crack opening during each load cycle of Test 3 is plotted together with the simulated values for the three different cracks, the latter are the discrete points in the graph. Again a good correspondence between the experimental and modelled values can be observed (RMS deviation = 0.031 mm). During Test 4 of the medium scale four-point bending tests, four beach mark lines were introduced. Similar as for Test 3, the observed crack shapes are inserted in the simplified FE model. The crack opening data is compared in Figure 8.15. Here the observed trends are again confirmed by the numerical simulations (RMS deviation = 0.034 mm). Between 24 000 and 28 000 cycles, the crack opening increases only gradually. The crack propagates the pipe wall between 28 000 and 28 500 cycles and for the beach mark line at 28 500 cycles, a significant crack opening is obtained.

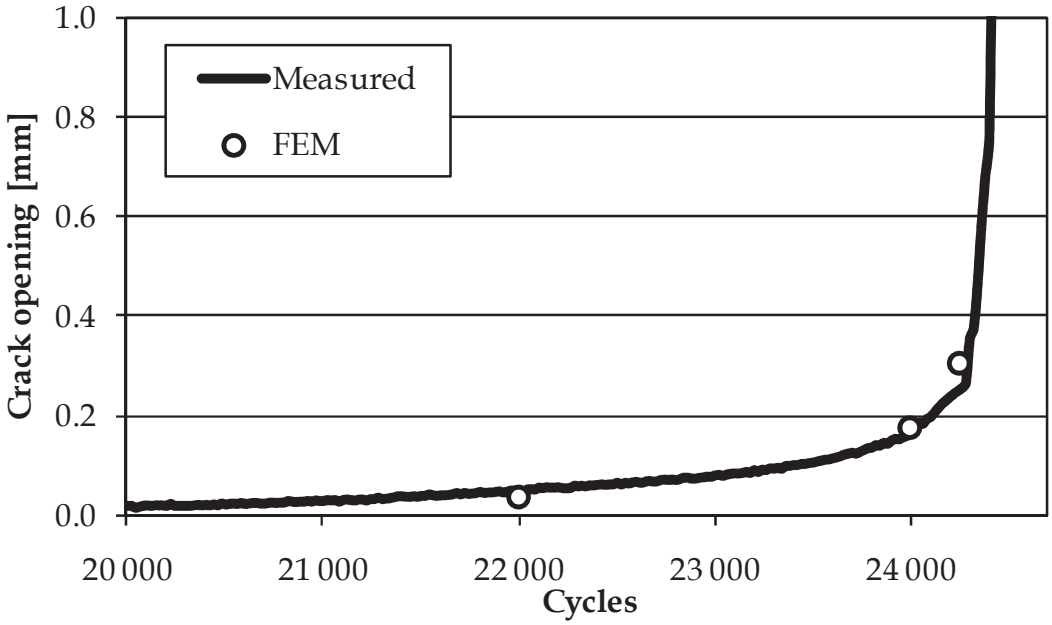

Figure 8.14: Crack opening data of Test 3.

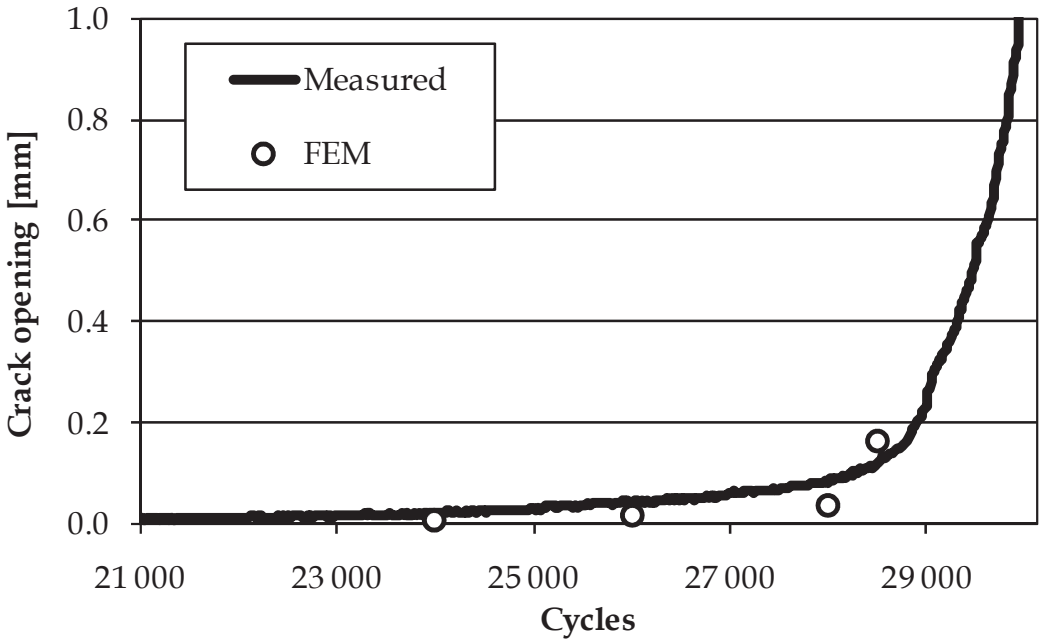

Figure 8.15: Crack opening data of Test 4.

Since the results of both tests are consistent with the results from the simplified FE model, it is confirmed that the observed beach mark lines correspond to the crack shapes at the specified number of cycles. In addition, it can be stated that although the model does not contain any information about the connection's threads, it is a useful tool to describe the crack growth behaviour.

3.3 Fracture mechanics approach

Since four different beach mark lines are present on the fracture surface of Test 4 (see Figure 5.50), a detailed crack growth analysis is carried out on this test specimen. This is done by using the fracture mechanics calculations according to the ASME BPVC VIII-3-app. D [8.16]. In this approach a crack at the root of a thread is considered as an annular flaw, instead of assuming a semi-elliptical crack shape. Considering the observed crack shapes, this seems to be a better assumption.

The stress intensity factor K_I for a certain crack depth a is calculated according to Eq. (8.4).

$$K_I = F\sqrt{\pi a} \tag{8.4}$$

Where the factor F is defined by:

$$F = A_0 F_1 + \frac{2aA_1F_2}{\pi} + \frac{a^2A_2F_3}{2} + \frac{4a^3A_3F4}{3\pi} \tag{8.5}$$

In Eq. (8.5) the F_1, F_2, F_3 and F_4 are magnification factors relative to the crack geometry. The four coefficients A_0, A_1, A_2 and A_3 are determined by the

Buchalet-Bamford method [8.17] in which the distribution of stresses σ normal to the plane containing the annular crack is approximated by a third order polynomial Eq. (8.6).

$$\sigma = A_0 + A_1 x + A_2 x^2 + A_3 x^3 \tag{8.6}$$

where x is the radial distance from the free crack surface or $x = 0$ in the root of the LET. The stress distribution is calculated by a linear elastic analysis and the coefficients are determined by the best least squares fit of the polynomial. If a single polynomial is not sufficient to fit the stress distribution, it is acceptable to split the distribution into several regions and describe each region by a different polynomial.

Since the crack is considered to be annular, the 2D axisymmetric FE model from Chapter 6, now with linear elastic material properties, is used to obtain the stress distribution. In Figure 8.16 the resulting axial stress distribution at the LET is plotted for the minimum and maximum axial load. The load is applied as a uniform stress over the wall of the pin with a magnitude of 15.5 MPa and 155 MPa respectively. Two polynomials are used to describe each curve. The first polynomial describes the region $0 < x < 0.36$ mm, the second describes the region $0.36 < x < 3.5$ mm. The boundary between both regions is indicated by the dashed vertical line in the graph.

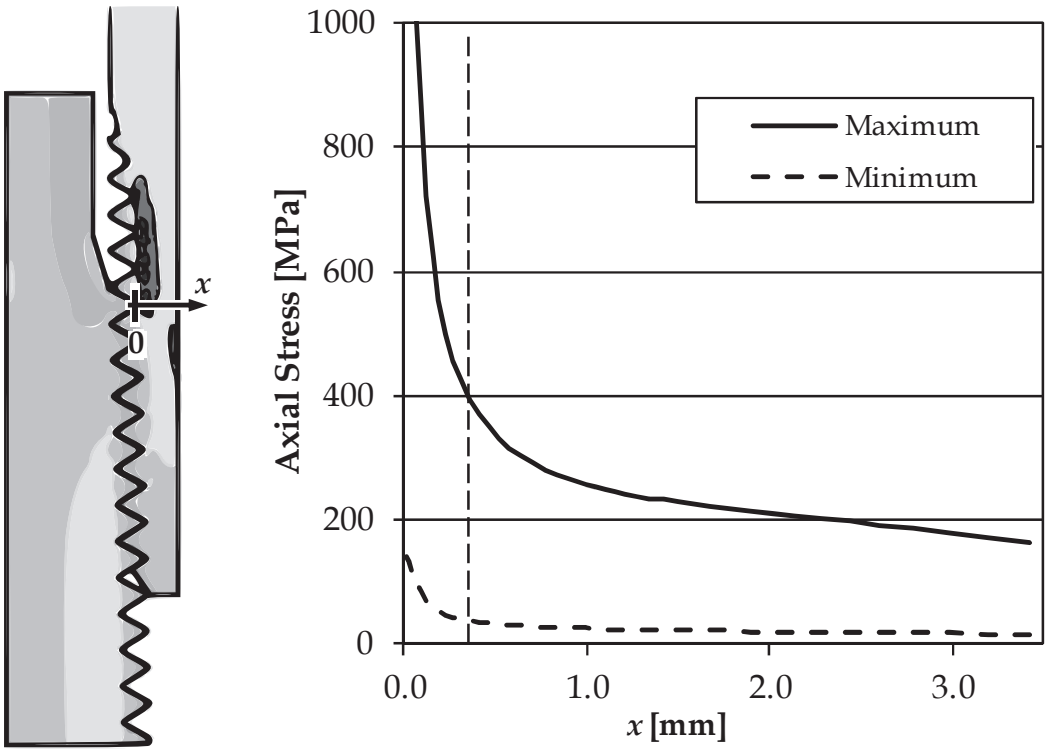

Figure 8.16: Axial stress distribution at the LET using linear elastic properties.

For each polynomial the coefficients A_0 to A_3 are determined. The fatigue crack growth rate is then calculated using the Paris Law Eq. (8.7), where N is the number of fatigue cycles, f is the crack growth rate factor and ΔK is the range of the stress intensity factor corresponding to the minimum and maximum applied load.

$$\frac{da}{dN} = C \cdot f \cdot \Delta K^m \tag{8.7}$$

The factors C and m are material constants with values for API 5L Grade B material according to [8.18]: $C = 1.38 \cdot 10^{-12}$ $(\text{MPa}\cdot\text{m}^{1/2})^{-m}$ and $m = 3.37$. The crack growth rate factor f is determined by fitting the crack growth rate of Eq. (8.7) to the measured crack depth increase between 24 000 and 26 000 cycles. This resulted in a value of $f = 1.96$.

Using these factors, the number of cycles required to achieve a certain crack depth increase can be calculated by integrating the Paris Law. This is done for the four measured crack depths at the beach marking lines. The results are summarized in Table 8.9. In the second column the crack depth increase values, as measured on the fracture surface, are used as inputs in the calculations. The initial crack depth on the first row is set to 0.1 mm since a finite value is necessary for the calculations, a value of 0 mm would lead to an infinite number of cycles. The calculated number of cycles are obtained by integrating Eq. (8.7). The measured number of cycles is the duration between the application of the beach marking cycles.

It can be seen that there is a good correlation between the calculated and measured number of cycles. Moreover, it is confirmed by the crack growth calculations that the crack initiated at approximately 21 000 cycles as estimated from the crack opening data. Because the total number of calculated cycles to reach the final crack depth of 3.6 mm is 7502 cycles and this crack depth is reached during the experiment at 28 500 cycles.

Total number of cycles	Crack depth increase [mm]	Initial crack depth [mm]	Calculated number of cycles	Measured number of cycles
24 000	1.2	0.1	3313	3000
26 000	1.0	1.2	2012	2000
28 000	1.0	2.2	1583	2000
28 500	0.4	3.2	594	500

Table 8.9: Crack growth rates during Test 4.

4 Summary and conclusions

In this chapter the experimentally obtained fatigue data is compared to standardized fatigue assessment techniques and to the results from the finite element model. It is also shown that the obtained experimental results are in line with results described in literature. Comparison of the fatigue results to standard fatigue curves shows that standard curves are either too conservative or not accurate enough to predict the exact fatigue behaviour of different connection designs.

The general concept of using a connection's thread load distribution as a measure for its fatigue life is shown to be inaccurate. The main reason for this is that the load distribution is mainly defined by the distribution of axial stresses over the connection. The make-up introduces important hoop stresses that contribute to the local stresses and equivalent plastic strain around the root of the LET and that consequently affects the connection's fatigue life. To account for this multiaxiality, a damage evolution law is used. This model combines information about the local multiaxial stress distribution at the thread root of the LET of the pin obtained from the finite element model with experimentally obtained damage parameters. With this damage evolution law, the experimentally observed trends can be explained. It is shown that creating a more uniform load distribution can be beneficial if the equivalent stress range and equivalent plastic strain range at the LET remain limited and if the value of the triaxiality function R_V is increased.

In the final part of this chapter it is shown that the 2D axisymmetric FE model can be used to predict fatigue crack growth in combination with the ASME BPVC approach where a crack is considered to be an annular flaw instead of using the typical semi-elliptical shape used throughout fracture mechanics.

References

[8.1] Knight, M.J., Brennan, F.P., Dover, W.D., Effect of residual stress on ACFM crack measurements in drill collar threaded connections, NDT&E International, 37, 337-343, 2003.

[8.2] Korin, I., Perez Ipiña, J., Controlled residual stresses introduction to improve fatigue resistance of rotary shouldered connections used in oil drilling industry, International Journal of Pressure Vessels and Piping, 87, 696-703, 2010.

[8.3] Stavrovský, V., Papuga, J., Ruzicka, M., Multiaxial approach for local elastic stress analysis, Procedia Engineering, 2010, 2, 1721-1729.

[8.4] Peterson, R.E., Notch Sensitivity, Metal Fatigue, MacGraw Hill, New-York, USA, 1959 (as referred in Pluvinage [8.5] p.10).

[8.5] Pluvinage, G., Fracture and fatigue emanating from stress concentrators, Kluwer Academic Publishers, Dordrecht, The Netherlands, 2003.

[8.6] Taylor, D., Geometrical effects in fatigue: a unifying theoretical model, International Journal of Fatigue, 1999, 21, 413-420.

[8.7] Boyer, H.E., Atlas of fatigue curves, American Society for Metals, Ohio, USA, 2003.

[8.8] Janosch, J.J., FITNET fitness-for-service (FFS) – Fatigue Module - MK8, GKSS Research Centre, Germany, 2008.

[8.9] Santus, C., Fretting fatigue of aluminum alloy in contact with steel in oil drill pipe connections, modeling to interpret test results, International Journal of Fatigue, 30, 677-688, 2008.

[8.10] Susmel, L., Taylor, D., The theory of critical distances to estimate lifetime of notched components subjected to variable amplitude uniaxial fatigue loading, International Journal of Fatigue, 2011, 33, 900-911.

[8.11] De Lange, R.W., Evans, M.E., Threaded and coupled connection for improved fatigue resistance, United States Patent, US 6609735 B1, 2003.

[8.12] Verdillon, L., Threaded tubular element for fatigue resistant threaded tubular joint and resulting threaded tubular joint, United States Patent, US 6729658 B2, 2004.

[8.13] Newport, A., Glinka, G., Concentration of Cyclic Stresses in Preloaded Threaded Connections, Journal of Engineering Mechanics, 117(6), 1257-1273, 1991.

[8.14] Bahai, H., Glinka, G., Esat, I.I., Numerical and experimental evaluation of SIF for threaded connectors, Engineering Fracture Mechanics, 54(6), 835-845, 1996.

[8.15] Zhao, H.,Kuang, Z.B.,Li, Z.H., Stress-intensity factor for a semi-elliptical surface crack at the thread root of a screwed-pipe joint, Computers & Structures, 59(3), 419-424, 1996.

[8.16] ASME Boiler and Pressure Vessel Code VIII.3-2010, Rules for Construction of Pressure Vessels, American Society of Mechanical Engineers, 2010.

[8.17] Buchalet, C.B., Bamford, W.H., 1976, Stress Intensity Factor Solutions for Continuous Surface Flaws in Reactor Pressure Vessels, Mechanics for Crack Growth, ASTM STP 590, 385-402, 1976 as referred in [8.16]).

[8.18] Lam, P.S., Sindelar, R.L., Duncan, A.J., Adams, T.M., Literature Survey of Gaseous Hydrogen Effects on the Mechanical Properties of Carbon and Low Alloy Steels, ASME Journal of Pressure Vessel Technology, 131(4), 041408, 2009.

Chapter 9

Conclusions and Future Research

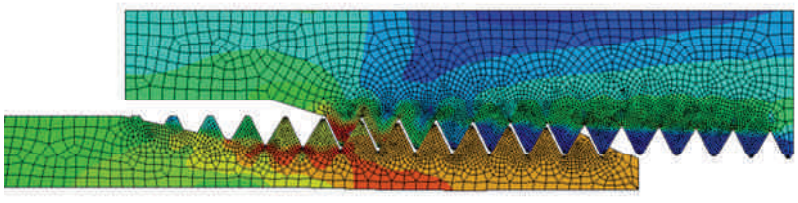

1 General conclusions

1.1 Summary

The aim of this work is to provide a better understanding of the fatigue mechanisms of threaded pipe connections and to study the effect of different design features on a connection's fatigue life.

The experimental data available in literature is limited. Published studies generally comprise experiments on a single connection type. In addition, as no uniformity in testing setup, loading conditions and damage detection techniques exists, results from different studies can not be used for a detailed fatigue analysis to compare the designs. Furthermore, current design curves in codes and standards lead to overly conservative or inaccurate results.

In this study, the API Line Pipe connection is used as a reference. Several modifications and design features are applied to this connection type. A parametric finite element model is developed to evaluate the influence of connection properties and design features on the threaded connection's fatigue behaviour. Besides, an experimental test program is carried out, comprising 109 fatigue tests, to create an extensive experimental database. The results from the simulations and the experiments are combined in a multiaxial fatigue analysis and the observed trends are explained. Based on these main results, guidelines for future development of fatigue resistant premium threaded connections are formulated in section 1.4.

1.2 Methodology used in this work

1.2.1 Finite element modelling

In this study, a parametric 2D axisymmetric finite element model is developed. It is important that elaborate contact conditions and the correct value of the coefficient of friction between the threads in contact are included. The use of elastic-plastic material behaviour is of utmost importance, as plastic deformation can already appear during the make-up stage. The required material properties are obtained by tensile testing and the coefficient of friction is derived from the results of a torque test.

Compared to full 3D models, the 2D axisymmetric approach has the advantage of a much shorter calculation time, without significant loss in accuracy. This is illustrated by a comparison of the stresses in a 2D axisymmetric and 3D model during make-up and a comparison between a 3D model under four-point bending and a 2D axisymmetric model with an equivalent uniform axial tensile stress. The validity of the model is proven experimentally by comparing simulated strain values with strain gauge measurements for four different load cases: make-up, axial tension, bending

and internal pressure. For all load cases, the differences between the measured and modelled strains are negligible.

1.2.2 Experimental testing

1.2.2.1 Test setups

In this work both static and fatigue tests have been carried out in setups that were either newly designed or adapted existing setups. The static tests used for model validation comprise torque tests, an axial tension test, a bending test and an internal pressure test. Fatigue tests on threaded pipe connections are carried out in three setups: axial tension, small scale four-point bending and medium scale four-point bending. The majority of the tests is carried out on small scale 1" specimens. The medium scale tests are conducted on 4.5" specimens. In the future, full scale tests can be carried out on the resonant bending fatigue setup (see section 1.2.2.3).

1.2.2.2 Measurement techniques

During the experiments, attention is paid to elaborate instrumentation. As until present no direct online monitoring technique exists for crack sizing in threaded pipe connections, several existing techniques have been applied to monitor crack propagation indirectly. During the small scale tests, internal pressure is used to detect through-thickness cracks. During the medium scale tests, more elaborate techniques are applied to detect fatigue damage. The applicability of crack opening measurements, dynamic 3D optical displacement measurements and modal analysis measurements is demonstrated. By these techniques the fatigue damage in the threaded pipe connections is monitored more accurately than previously possible. However, they are only suitable for use in laboratory conditions. The measurements are used to distinguish between crack initiation and propagation and are confirmed by the beach mark lines that are observed in the fracture surface. The crack opening measurement gives the most accurate results. However, it can only be applied in four-point bending tests, since the crack initiation location along the pipe circumference should be known. The dynamic 3D optical displacement measurements and modal analysis measurements can also be applied to resonant bending tests.

1.2.2.3 Resonant bending fatigue setup

To perform fatigue tests in the future on large diameter or full-scale threaded connections, a resonant bending fatigue setup is developed and built. This setup is designed for fatigue testing of pipe joints from 6" to 20". It comprises a drive unit with two variable excentric masses, supports that are designed to allow continuous control of their position and extensive measuring equipment to monitor the deformation shape and deflection amplitude of the pipe and of the supports. A bending stress range of up to 490 MPa can be

applied, which is considerably higher than the reported maximum stress ranges of other existing resonant bending fatigue setups for pipes.

Two mathematical models are developed to predict the dynamic behaviour of a pipe in the setup. An analytical model is used to calculate the eigenmodes and eigenfrequencies of a free floating pipe. Secondly, a more complex semi-analytical model, using component mode synthesis, describes the pipe in the test rig.

To prove the suitability of the setup, two plain pipes (without a threaded connection) have been tested. Artificial notches were produced in one of these pipes, which was tested until a through-thickness fatigue crack appeared. The measurements are in very good agreement with the mathematical models. For a given pipe diameter, wall thickness and pipe length, the models can accurately predict the necessity to fill the pipe with water, the required mass of the endweigths, the system's natural frequency and the position of the supports. Using strain gauge measurements it is shown that the deflection-stress relation, obtained by the models, accurately predicts the stress corresponding to a specific deflection amplitude.

1.3 Main results

1.3.1 Trends in fatigue life

The general concept of using a connection's thread load distribution as a measure for its fatigue life is proven to be inaccurate. The main reason for this is that the load distribution is related to the axial stresses over the connection. However, the fatigue life of a threaded connection is determined by the local multiaxial stress and strain at the root of the LET. These local conditions are not only the result of the axial load distribution, but they are also affected by other stress and strain components such as the hoop stress introduced during make-up, which can additionally be affected by a changed connection stiffness.

Using a damage evolution law, the multiaxiality at the thread root is accounted for. This model combines data from the simulations with experimentally obtained damage parameters and is able to explain the experimentally observed trends. It is shown that creating a more uniform load distribution can be beneficial if the equivalent stress range and equivalent plastic strain range at the LET remain limited.

A range of design features and modifications, used in patented fatigue resistant threaded connections, are evaluated and compared using the damage evolution law. Their effectiveness to improve a connection's fatigue life is investigated. The results are summarized in Table 9.1, a distinction is made between positive features that improve a connection's fatigue life and negative features that result in a fatigue life reduction.

Feature	Description
Positive features	
Make-up	Application of a sufficient number of make-up turns can significantly reduce the local dynamic stress and strain range at the root of the LET. Although this increases the thread load, this is positive for the connection's fatigue life.
Thread type	Applying a thread type with a low stress concentration factor will reduce the local stresses at the thread root and consequently improve the connection's fatigue life.
Thread pitch	Reducing the thread pitch length (or increasing the number of threads per inch) increases the fatigue life due to a thread load reduction and reduction of local plastic strain range at the last engaged thread.
Pin and box wall thickness	Changing the relative stiffness of the pin and box by altering their wall thickness can be used to obtain a more uniform load distribution which can result in an improved fatigue life. However, when the stiffness of the box becomes too small relative to the pin stiffness, the local strain range at the LET root will increase, and the positive effect is reduced.
Box recess	The box recess length can be reduced to improve the thread load and strain range at the LET and to obtain a higher fatigue life. In addition, applying a chamfer to the box recess (as in the patented stiffness gradient shown in Figure 7.6.c) can also deliver a slight fatigue life improvement.
Negative features	
Pin engaged thread length	Increasing the pin engaged thread length to more than 7 reduces the thread opening, but does not affect the fatigue life.
Taper difference	A positive taper difference ($\alpha_{box} > \alpha_{pin}$) gives a slight improvement of the thread load, but reduces the make-up stresses at the LET of the pin. Consequently, the local strain range increases and the fatigue life is reduced.
Bevelled groove	The patented bevelled groove design (Figure 7.6.d) is ineffective to improve the API Line Pipe connection's fatigue life. The resulting thread load distribution improvement is negligible, and the local strain range at the LET root is significantly increased.

Table 9.1: Overview of the influence of different features on a connection's fatigue life.

1.3.2 Fatigue crack growth

The contribution of the crack propagation life to the total fatigue life of the connection ranges from 2 % for a high total life ($N > 100\,000$ cycles) up to 25 % for a lower total life.

Fatigue cracks initiate at the root of the LET of the pin, which is the location where the highest local stress and strain are calculated in the finite element model. After initiation, a crack propagates gradually over a large segment of the circumference, forming a long shallow crack. When the crack penetrates the wall of the pin, the crack rapidly increases in size along two crack fronts.

The observed crack shapes, visualised by the beach mark lines, do not have a semi-elliptical shape as is commonly used in fracture mechanics. However, the ASME BPVC recommends an approach where a crack is considered to be an annular flaw. Consequently, this approach is able to accurately predict the fatigue crack growth.

1.4 Guidelines for fatigue resistant connection designs

As the multiaxial stress distribution and strain range around the last engaged thread of the pin are affected by the connection geometry, the thread type as well as the make-up conditions, it might be appropriate to combine several design features when optimizing a connection. A multiaxial fatigue analysis technique, such as the damage evolution law, should be used to quantify the effect on the fatigue life of the new design. The positive features from Table 9.1 can hereby be used as a guide.

- The thread shape can be optimized to obtain a low stress concentration factor and reduce the local strains at the thread roots. The API Buttress thread can be used as a starting point, since this thread type shows the lowest stress concentration factor.
- An important factor to take into account is the thread pitch. A shorter pitch length can be beneficial for the fatigue life.
- The connection global geometry in combination with the make-up conditions can be optimized to improve the load distribution over the threads and the resulting local stresses and strains at the threads.
- Metal-to-metal seals can be added to ensure appropriate leak resistance when sealing is not provided by the threads.
- Thread lubricants or compounds can be used in practice, but these can affect the coefficient of friction in the contacting threads. In order to obtain reliable predictions, the correct friction value should be used in the finite element analysis.

2 Recommendations for future research

2.1 Connection design optimization

Using the damage evolution law, it becomes possible to optimize a connection design for fatigue purposes. Next to the considered features, more advanced thread types, can be included. In addition the effect of torque shoulders and sealing surfaces can be studied. More advanced multiaxial fatigue models have been developed during the last years and might be applied to threaded pipe connections. A detailed comparison can be made of these models with the experimental results in order to select the most reliable and best applicable technique.

The parametric finite element program is constructed in such a way that advanced optimization, using special algorithms, is possible. When such an optimization algorithm would be implemented, a series of simulations has to be carried out. Each connection geometry, generated by such an algorithm, would be based on the resulting fatigue lives of the previous geometries, calculated by the damage evolution law. The usefulness of such techniques is already shown by Ekh and Schön [9.1] in their analysis of bolted lap joints and by Han and Yamazaki [9.2] in the shape optimization of the threads of bolt-nut fasteners. A suitable optimization technique could be the *genetic algorithm*, as used by Kradinov et al. [9.3] for optimizing bolted lap joints.

2.2 Experiments and measurement techniques

For experimental validation of the modelling results, the resonant bending fatigue setup can be used to test full scale connections. To monitor fatigue crack growth, the dynamic 3D optical displacement measurement system and advanced modal analysis can be used. However, these are still indirect crack growth measurement systems. The development of an online crack monitoring technique, that could be used in the field and is not limited to laboratory conditions, remains an important challenge.

2.3 Additional load cases

Low cycle fatigue behaviour of threaded joints is of importance in relation to the seismic performance of piping systems. As recently pointed out by Ryu et al. [9.4], threaded connections are often used in the uncoupled secondary systems (e.g. fire extinguishing piping) and the seismic performance of these components is hardly documented. Additional load cases can be considered. For example in casing drilling applications, the connection's fatigue properties are of importance during the drilling installation. Afterwards, the connection's response to internal pressure, external pressure and static loads becomes predominant. These load cases can be incorporated in the finite element simulations.

References

[9.1] Ekh, J., Schön, J., Finite element modeling and optimization of load transfer in Multi-fastener joints using structural elements, Composite Structures, 82, 245-256, 2008.

[9.2] Han, J., Yamazaki, K., A novel technique of shape optimization for the contact parts of bolt-nut fastening structures, Engineering Optimization, 36(6), 691-703, 2004.

[9.3] Kradinov, V., Madenci, E., Ambur, D.R., Application of genetic algorithm for optimum design of bolted composite lap joints, Composite Structures, 77, 149-159, 2007.

[9.4] Ryu, Y., Behrouzi, A., Melesse, T., Matzen, V.C., Inelastic behavior of threaded piping connections: reconciliation of experimental and analytic results, ASME Pressure Vessels and Piping Division Conference, PVP2011-57949, 2011.

Publications

List of scientific publications of Jeroen Van Wittenberghe.

A1 - Peer reviewed journal publications included in Science Citation Index

1. **Van Wittenberghe, J.**, Ost, W., Rezaei, A., De Baets, P., Zsidai, L., Kalácska, G., Test setup for friction force measurements of large-scale composite bearings, Experimental Techniques, 33(1), 45-50, 2009.
2. Ost, W., De Baets, P., **Van Wittenberghe, J.**, Failure investigation and redesign of piston- and pump shafts, Engineering Failure Analysis, 16(4), 1174-1187, 2009.
3. **Van Wittenberghe, J.**, De Baets, P., De Waele, W., Non-Linear contact analysis of different API Line Pipe coupling modifications, ASME Journal of Pressure Vessel Technology, 132(5), 2010.
4. Bonny, K., De Baets, P., **Van Wittenberghe, J.**, Perez Delgado, Y., Vleugels, J., Van Der Biest, O., Lauwers, B., Influence of electrical discharge machining on sliding friction and wear of WC–Ni cemented carbide, Tribology International, 43, 2333-2344, 2010.
5. **Van Wittenberghe, J.**, De Baets, P., De Waele, W., Bui, T.T., De Roeck, G., Fatigue crack propagation measurements in a threaded pipe connection using an optical dynamic 3D analysis technique, Engineering Failure Analysis, 18(3), 1115-1121, 2011.
6. **Van Wittenberghe, J.**, De Baets, P., De Waele, W., Ost, W., Verstraete, M., Hertelé, S., Resonant bending fatigue test setup for pipes with optical displacement measuring system, ASME Journal of Offshore Mechanics and Arctic Engineering, accepted for publication, 2011.
7. **Van Wittenberghe, J.**, De Baets, P., De Waele, W., De Pauw, J., The influence of coupling geometry on the fatigue life of NPT threaded pipe couplings, ASME Journal of Pressure Vessel Technology, Accepted for publication, 2011.

8. **Van Wittenberghe, J.**, Ost, W., De Baets, P., Testing the friction characteristics of industrial drum brake linings, Experimental Techniques, doi:10.1111/j.1747-1567.2010.00675.x scheduled for publication, 36(1), 2012.

A2 - Peer reviewed journal publications

1. **Van Wittenberghe, J.**, De Baets, P., De Waele, W., Analysis of the make-up and break-out behaviour of API line pipe threaded connections, Mechanical Engineering Letters, 2, 210-219, 2009.
2. Ost, W., De Baets, P., Van Autrève, S., **Van Wittenberghe, J.**, Zsidai, L., Kalácska, G., Tribotesting of large-scale specimens : the necessity of proper design, Mechanical Engineering Letters, 2, 17-26, 2009.
3. **Van Wittenberghe, J.**, Galle, T., De Baets, P., De Waele, W., Numerical modelling and experimental validation of a threaded pipe connection under axial tension, Mechanical Engineering Letters, 5, 89-94, 2011.

B3 – Book editor

1. Proceedings of the Day of Research 2010, editor: **Van Wittenberghe, J.**, Ghent University – Laboratory Soete, ISBN 978-9-49072-600-3, 2010.
2. Sustainable Construction & Design, vol. 2, editor: **Van Wittenberghe, J.**, Ghent University – Laboratory Soete, ISBN 978-9-49072-601-0, 2011.

C - Conference proceedings

1. **Van Wittenberghe, J.**, De Baets, P., Degrieck, J., De Waele, W., Fatigue behaviour of threaded pipe connections, 8e UGent - FirW Doctoraatssymposium, 2007.
2. Van Autrève, S., Ost, W., **Van Wittenberghe, J.**, De Baets, P., Evaluating self-lubricating materials for large scale bearings functioning under seawater conditions, Proceedings of the first i-SUP conference, 171-175, 2008.
3. **Van Wittenberghe, J.**, De Baets, P., De Waele, W., Analysis of a preloaded conical threaded pipe connection, Selected Topics of Contemporary Solid Mechanics, 2008.
4. **Van Wittenberghe, J.**, De Baets, P., De Waele, W., Modelling of preloaded threaded pipe connections, Proceedings of the 8th National Congress on Theoretical and Applied Mechanics, 149-156, 2009.

5. **Van Wittenberghe, J.**, De Baets, P., De Waele, W., Van Autrève, S., Numerical and experimental study of the fatigue of threaded pipe couplings, WIT Transactions on Engineering Sciences, WIT Press, 163-174, 2009.

6. **Van Wittenberghe, J.**, De Baets, P., De Waele, W., Hertelé, S., Parametric model for evaluating the performance of threaded pipe connections, International Conference on Advanced Computational Engineering and Experimenting, 2009.

7. Hertelé, S., De Waele, W., Denys, R., **Van Wittenberghe, J.**, Numerical evaluation of the CMOD of defects in pipeline girth welds under remote plastic deformation, International Conference on Advanced Computational Engineering and Experimenting, 2009.

8. **Van Wittenberghe, J.**, De Baets, P., De Waele, W., Non-linear contact analysis of an API line pipe coupling, Proceedings of the ASME Pressure Vessel and Piping Conference, 2009.

9. **Van Wittenberghe, J.**, Ost, W., Van Autrève, S., De Baets, P., Friction characteristics of industrial drum brake linings, World Tribology Congress, 2009.

10. Van Autrève, S., Ost, W., **Van Wittenberghe, J.**, De Baets, P., Experimental investigation of the frictional stability of engineering plastics, World Tribology Congress, 2009.

11. Bonny, K., De Baets, P., **Van Wittenberghe, J.**, Van Autrève, S., Vleugels, J., Van der Biest, O., Lauwers, B., Influence of surface finishing operations on the dry sliding friction and wear response of zirconia composites, World Tribology Congress, 2009.

12. **Van Wittenberghe, J.**, De Baets, P., De Waele, W., Influence of changes in box geometry on the performance of API line pipe threaded connections, Pipeline Technology, 2009.

13. Bonny, K., Perez Delgado, Y., Van Autrève, S., **Van Wittenberghe, J.**, De Baets, P., Lauwers, B., Vleugels, J., Van der Biest, O., Influence of surface finishing operations on reciprocating sliding friction and wear response of WC-based cemented carbides, ASME/STLE International Joint Tribology Conference, 2009.

14. **Van Wittenberghe, J.**, De Pauw, J., De Baets, P., De Waele, W., Fatigue life assessment of preloaded API Line Pipe threaded connections, Fatigue Design, 2009.

15. **Van Wittenberghe, J.**, De Baets, P., De Waele, W., Study of the static and fatigue behaviour of threaded pipe connections, 10de UGent - FirW Doctoraatssymposium, 2009.

16. **Van Wittenberghe, J.**, De Baets, P., De Waele, W., De Pauw, J., Ost, W., Bui, T.T., De Roeck, G., Fatigue investigation of threaded pipe connections, Proceedings of the Day of Research, 182-189, 2010.

17. Meertens, B., De Baets, P., De Waele, W., **Van Wittenberghe, J.**, Fatigue behaviour of threaded pipe couplings - experimental research, Proceedings of the Day of Research, 50-57, 2010.

18. Ost, W., **Van Wittenberghe, J.**, De Baets, P., How design quirks and conditions of use conspire to structural failure : a case study" Proceedings of the Day of Research, 144-150, 2010.

19. De Pauw, J., **Van Wittenberghe, J.**, De Baets, P., Traction and wear mechanisms during roll-slip contact, Proceedings of the Day of Research, 59-67, 2010.

20. **Van Wittenberghe, J.**, De Baets, P., De Waele, W., De Pauw, J., Ost, W., Verstraete, M., Hertelé, S., Resonant bending fatigue test setup with optical measuring system for large diameter pipes, Proceedings of the 8th International Pipeline Conference, ASME, 2010.

21. Hertelé, S., De Waele, W., Denys, R., **Van Wittenberghe, J.**, Verstraete, M., Investigation of pipe strain measurements in a curved wide plate specimen, Proceedings of the 8th International Pipeline Conference, ASME, 2010.

22. Hertelé, S., De Waele, W., Denys, R., **Van Wittenberghe, J.**, Limit load and reference stress for curved wide plates, Proceedings of the 8th International Pipeline Conference, ASME, 2010.

23. **Van Wittenberghe, J.**, De Pauw, J., De Baets, P., De Waele, W., Experimental determination of the fatigue life of modified threaded pipe couplings, Procedia Engineering, 2(1), 1849-1858, 2010.

24. **Van Wittenberghe, J.**, De Baets, P., De Waele, W., De Pauw, J., Fatigue life improvement of threaded pipe couplings, Proceedings of the ASME Pressure Vessel and Piping Conference, 2010.

25. Bonny, K., Perez, Y., **Van Wittenberghe, J.**, De Baets, P., Vleugels, J., Lauwers, B., Effect of surface finishing on tribological properties of ZrO2-based composites, Nordic Conference on Tribology, 14th edition, 2010.

26. Bui, T.T., De Roeck, G., **Van Wittenberghe, J.**, De Baets, P., De Waele, W., A modal approach to identify fatigue damage in threaded connections of large scale tubular structures, Proceedings of ISMA2010, 795-807, 2010.

27. **Van Wittenberghe, J.**, De Baets, P., De Waele, W., Threaded pipe connections under dynamic loading conditions, 11e UGent - FirW Doctoraatssymposium, 2010.

28. **Van Wittenberghe, J.**, De Baets, P., De Waele, W., Timothy, G., Bui, T.T., De Roeck, G., Design characteristics that improve the fatigue life of

threaded pipe connections, Sustainable Construction & Design, 334-341, 2011.

29. Bui, T. T., De Roeck, G., **Van Wittenberghe, J.**, De Baets, P., De Waele, W., Fatigue damage identification in threaded connection of tubular structures through in-situ modal tests, Sustainable Construction & Design, 207-216, 2011.
30. Claeys, J., **Van Wittenberghe, J.,** De Baets, P., De Waele, W., Characterisation of a resonant bending fatigue setup for pipes, Sustainable Construction & Design, 424-431, 2011.
31. Seys, J., Roeygens, K., **Van Wittenberghe, J.**, Galle, T., De Baets, P., De Waele, W., Failure behaviour of preloaded API line pipe threaded connections, 407-415, 2011.
32. Galle, T., De Waele, W., De Baets, P., **Van Wittenberghe, J.**, Influence of design features on the structural integrity of threaded pipe connections, Sustainable Construction & Design , 237-245, 2011.
33. **Van Wittenberghe, J.**, De Baets, P., De Waele, W., Bui, T.T., De Roeck, G., Dynamic 3D optical measurement system for the characterisation of the behaviour of a pipe in a resonant bending test rig, 8th international conference on structural dynamics, 3554-3560, 2011.
34. Bui, T.T., Reynders, E., De Roeck, G., **Van Wittenberghe, J.**, De Baets, P., De Waele, W., A modal approach to identify fatigue damage in threaded connections of large scale tubular structures in a resonant bending test rig, 8th international conference on structural dynamics, 1623-1628, 2011.
35. **Van Wittenberghe, J.**, De Baets, P., De Waele, W., Fatigue crack growth behaviour of threaded pipe couplings, Proceedings of the ASME Pressure Vessel and Piping Conference, 2011.
36. **Van Wittenberghe, J.**, Galle, T., De Baets, P., De Waele, W., Numerical modelling and experimental validation of a threaded pipe connection under axial tension, Synergy Conference, 2011.
37. Galle, T., De Waele, W., De Baets, P., **Van Wittenberghe, J.**, Experimental procedure for the evaluation of the structural integrity of threaded API Line Pipe Couplings, Synergy Conference, 2011.

Reviewer of international journal articles and conferences

International Journal of Fatigue (2), Tribology International (1), Experimental Techniques (1), Engineering Failure Analysis (1), Journal of Mechanical Science and Technology (1), Contact and Surface Conference 2011 (4).